

GRAND / LEWIS

IN - 02 - 37561

RF Project 712620/762009  
Interim Technical Report

AN EXPERIMENTAL STUDY OF THE AERODYNAMICS OF A  
NACA 0012 AIRFOIL WITH A SIMULATED GLAZE ICE ACCRETION

Michael B. Bragg  
Department of Aero and Astro Engineering

(NASA-CF-179897) AN EXPERIMENTAL STUDY OF  
THE AERODYNAMICS OF A NACA 0012 AIRFOIL WITH  
A SIMULATED GLAZE ICE ACCRETION Interim  
Technical Report (Ohio State Univ.) 318 p

N87-11701

Unclas  
CSCL 01A G3/02 44889

NASA-LEWIS RESEARCH CENTER  
21000 Brookpark Road  
Cleveland, Ohio 44135

Grant No. NAG 3-28

November 1986



**The Ohio State University  
Research Foundation**

1314 Kinnear Road  
Columbus, Ohio 43212



AN EXPERIMENTAL STUDY OF THE AERODYNAMICS  
OF A  
NACA 0012 AIRFOIL WITH A SIMULATED GLAZE ICE ACCRETION

M. B. Bragg

The Ohio State University  
Columbus, Ohio

AARL TR 8602



## ABSTRACT

An experimental study has been conducted in the Ohio State University subsonic wind tunnel to measure the detailed aerodynamic characteristics of an airfoil with a simulated glaze ice accretion. A NACA 0012 model with interchangeable leading edges and pressure taps every one percent chord was used. Surface pressure and wake data were taken on the airfoil clean, with forced transition and with a simulated glaze ice shape. Lift and drag penalties due to the ice shape were found and the surface pressure clearly showed that large separation bubbles were present. Both total pressure and split-film probes were used to measure velocity profiles, both for the clean model and for the model with a simulated ice accretion. A large region of flow separation was seen in the velocity profiles and was correlated to the pressure measurements. Clean airfoil data were found to compare well to existing airfoil analysis methods.

PRECEDING PAGE BLANK NOT FILMED



# TABLE OF CONTENTS

	<u>Page</u>
ABSTRACT	iii
TABLE OF CONTENTS	v
NOMENCLATURE	vii
I. INTRODUCTION	1
II. EXPERIMENTAL APPARATUS	3
Wind Tunnel and Model	3
Velocity Profile Measurements	6
Data Acquisition and Reduction	7
III. DATA REDUCTION	8
Pressure Data	8
Split Film Data	
IV. RESULTS AND DISCUSSION	11
Pressure and Force Measurements	12
Velocity Profile Measurements	19
Data Presentation	24
V. SUMMARY	27
REFERENCES	30
TABLES	32
FIGURES	37
APPENDIX A: RUN SUMMARIES	59
APPENDIX B: PRESSURE DISTRIBUTIONS	67
APPENDIX C: WAKE SURVEYS	237
APPENDIX D: VELOCITY PROFILES	259

PRECEDING PAGE BLANK NOT FILMED





## NOMENCLATURE

<u>Symbol</u>	<u>Description</u>
$c$	Airfoil chord length
$C_d$	Airfoil drag coefficient, $\text{Drag}/q_\infty c$
$C_l$	Airfoil lift coefficient, $\text{Lift}/q_\infty c$
$C_m$	Airfoil moment coefficient about $x=c/4$ , Moment/ $q_\infty c^2$
$C_p$	Pressure coefficient, $P-P_\infty/q_\infty$
$\bar{d}$	Volume median diameter
$E_1, E_2$	Hot film output voltage
$k$	$E_1/E_2$
LWC	Liquid water content
$m$	Mach number
$P$	Pressure
$q$	Dynamic pressure
$Re$	Reynolds number
$u, v$	Streamwise and normal velocity components
$V_{tot}$	Total velocity measured by hot film probe
$x, y$	chordwise and normal coordinate, or $y$ can be the boundary layer coordinate
Y-SEP	Y location of separation streamline
Y-STAG	Y location of u component stagnation streamline
$\alpha$	Angle of attack
$\delta^*$	Boundary layer displacement thickness
$\Theta$	Boundary layer momentum thickness

### Subscripts

$l$	lower surface
$u$	upper surface
$\infty$	freestream condition

PRECEDING PAGE BLANK NOT FILMED



## I. INTRODUCTION

Ice formation on an airfoil often leads to a sizeable leading edge protuberance. This protuberance causes a leading edge separation bubble to form, thus reducing the lift and increasing the drag. As the angle of attack is increased, the bubble will eventually fail to re-attach causing a reduction in airfoil stall angle and maximum lift. For unprotected airfoils, these aerodynamic penalties are important and further research is needed before they can be accurately predicted.

Airfoil aerodynamic penalties have been investigated by other researchers, primarily by making lift and drag measurements. Jacobs [1] in 1932 measured the lift, drag and moment change due to various protuberances on a NACA 0012 airfoil. While these protuberances were not specifically ice simulations, the data show the sensitivity of the airfoil to any leading edge disturbance. In the 1950's the NACA investigated the effects of ice on airfoil performance. Some of these results can be found in the work of Gray [2,3], on the NACA 65-212 and NACA 65A004 airfoil with actual ice accretions. These data show the adverse effects of ice on airfoil performance, but report only the integrated lift, drag and moment data. More recent studies such as that by Korkan, et. al. [4], Lee [5] and Flemming [6] have also reported lift, drag and moment effects on airfoils with simulated ice shapes.

In an attempt to obtain more detailed flowfield data, Bragg et.al. [7,8] have obtained surface pressures on airfoils with simulated rime and glaze ice shapes. These data give not only the integrated lift, drag and moment data, but provide information on

the length of the bubble, re-attachment and trailing edge separation. Flow visualization data reported by Bragg [9], give the first information about the glaze ice separation bubble geometry. Approximate bubble shapes reduced from photographs of oil flow on a splitter plate are presented for two different glaze ice shapes at two angles of attack.

Recently sophisticated computational tools have begun to be applied to the problem of an airfoil with leading edge ice accretion. Potapczak [10] used a parabolized Navier-Stokes code to predict the aerodynamic characteristics of an airfoil with and without ice. Cebeci [11] has modified his interactive boundary layer technique to make similar calculations. The results of these calculations are encouraging, but more experimental data are needed to fully develop and validate these methods.

This report presents the initial results of a detailed experiment to study the effect of a particular glaze ice shape on a NACA 0012 airfoil. Part of this work has been published previously by Bragg and Coirier [12,13] in summary form. The purpose of this report is to present a single report with as much of the detailed data as possible. It should be noted that this work is continuing and more and better data are currently being acquired, and plans for more tests are being made. It was, however, felt that a report presenting the data gathered to date would be valuable at this time.

## II. EXPERIMENTAL APPARATUS

### Wind Tunnel and Model

These tests were conducted in the Ohio State University's subsonic wind tunnel located at the Aeronautical and Astronautical Research Laboratory. The tunnel is of conventional design with approximately a three-by-five foot test section, eight feet in length. The tunnel operates at speeds from zero to 220 feet per second at Reynolds number of up to  $1.3 \times 10^6$  per foot. The tunnel is of open return type and uses four turbulence screens and honeycomb in the settling chamber to reduce the tunnel turbulence. The tunnel will accommodate airfoils mounted vertically in the test section or three-dimensional models, strut mounted using an internal strain gauge balance. Tunnel speed, Reynolds number and Mach number are measured through facility transducers.

Standard wind tunnel instrumentation was used for this test. Pressure measurements were made using a Scanivalve system. Two scanivalves capable of measuring 48 pressures each were used. The valves were connected in series sharing one pressure transducer to reduce calibration time and improve the accuracy of the measurements. No cut-off valves were used for this test. A single traversing total pressure probe was used to measure the airfoil wake. The probe was located approximately one chord length downstream of the model trailing edge and was traversed automatically by the computer system.

Two different NACA 0012 models were used for this test. Both models were 21 inches in chord and had a span of 39 inches. The models were mounted vertically in the tunnel providing a height (actually width since the model was mounted vertically) to chord ratio of 2.62. Simulated ice shapes were used with both models which were constructed to approximately duplicate an actual measured ice accretion. The ice was accreted in the NASA Lewis Research Center's Icing Research Tunnel on a NACA 0012 airfoil, also of 21 inch chord [14]. In Figure 1. the measured ice shape, as recorded from an actual tracing, compared to the one used in this test.

Data were first taken on NACA 0012 Model No. 1 while construction was continuing on the more complex model. This model was made from a section of a UH1H helicopter rotor blade. Since the model had twist, all data were taken and the angle of attack was reported on the model center line. The model used external one-eighth inch tubing to provide surface pressure information (pressure belts) and the wooden ice shape was internally tapped. Although pressure data and wake data were acquired on this model, see reference 12, it is considered preliminary and will not be presented here. Split film measurements of the separation bubble were taken using this model and will be presented. NACA 0012 airfoil coordinates clean (i.e. no ice shape attached) are given in Table 1. The coordinates of the airfoil plus ice shape for Model No. 1 are given in Table 2.

NACA Model No. 2 was built for this experiment with some special features. The model has a 21-inch chord and was cut from mahogany using a numerical control machine and laminated together to

form the 39-inch span. A unique feature of this model is its interchangeable leading edges. Past experiences using simulated ice on airfoils has identified a problem with the proper placement of the ice shape over the clean leading edge. To avoid this problem, the current model has the ice shape as an integrable part of the first 15 percent of the model (about 3 inches). In this way, the first 15 percent of the model could be attached precisely to the main model section, and the exact airfoil plus ice shape geometry would be accurately known. Experience with earlier simulated models demonstrated the need for a very dense placement of surface pressure taps. The current model was internally tapped with approximately 90 surface pressure ports. The upper surface was instrumented with a tap every one percent (0.21 inches) surface length back to the forty percent chord station. Another 40 taps were located around the rest of the airfoil, on the model centerline. Eight taps were located spanwise at the five percent station to ensure the two-dimensionality of the flow. The entire ice shape was also instrumented with internal pressure taps every one percent surface length resulting in 19 taps ahead of the five percent chord station.

The basic airfoil coordinates for Model No. 2 are the same as those in Table 1. The ice shape is also basically the same, although due to the construction technique some slight differences do exist from the ice shape of Model No. 1. Therefore, the ice shape plus airfoil coordinates for Model No. 2 can be found in Table 3. All the force and surface pressure data shown in this report will be from Model No. 2.

### Velocity Profile Measurements

In order to measure the velocity profiles in the separation bubble, a probe capable of determining flow reversal must be accurately positioned in the model boundary layer. A split film probe, TSI model 1288, was chosen. Here two separate films are placed, front and back, on the same 0.006 inch diameter rod. The plane of the split is parallel to the axis of the probe, perpendicular to the freestream flow, thus allowing for the determination of flow reversal. The probe was modified by incorporating a special shield [10]. The shield was set so that it touched the model before the probe, allowing probe protection and setting the probe a known distance off the surface of the model to start each run. This system worked well and prevented damaging the very delicate probe. The hot film data channels were both taken using TSI 1053B anemometers with TSI 1057 signal conditioners.

The entire tunnel set-up is shown in Figure 2. A close-up of the traverse system is shown in Figure 3. A two-dimensional traversing system was used to position the probe in the horizontal plane, containing the airfoil section on the tunnel centerline. The bottom traverse positioned the probe axially from a position approximately 15 percent chord ahead of the model to a point at the airfoil 65 percent chord station. A L.C. Smith BBR30180 traverse was placed on this traverse and provided the probe positioning out from the model. The hot-film probe was supported through a TSI probe support and shield which slid through an airfoil shaped strut extending into the tunnel. This steel strut was rigidly mounted to



the fixed end of the top traverse and moved chordwise (along the tunnel axis) through a sealed slide arrangement. Both traverses were driven by d.c. motors and may be either positioned locally or through the computer system. Probe position was determined using standard potentiometers. Using this system probe positioning tolerance including all errors through digitizing, was no more than +0.003 inches or +0.00014 chord-lengths out from the model and no more than +0.010 inches or +0.00048 chord-lengths in the chordwise direction.

On the airfoil without ice, boundary layer profiles were measured using a traversed total pressure probe. The traversing system, and therefore positioning tolerances, were the same as that used for the split film measurements. The probe was constructed of 1/32-inch stainless steel tubing compressed at the tip to reduce its height to approximately 0.020 inches. The probe was positioned on the surface by hand, then traversed out from the wall by the computer controlled traversing system.

#### Data Acquisition and Reduction

The data were gathered online by the in-house Digital Computer and Data Acquisition System. The system currently based on a Harris H100 computer, a 48-bit machine expandable to 768 K bytes internal memory, with virtual memory address space to 12 M bytes. Two analog-to-digital (A/D) systems were used to acquire these data. A high speed Datel model 256 system with a throughput rate exceeding 100 kHz was used to acquire the hot film data. A medium speed RTP system with 8 kHz throughput was used to sample tunnel conditions

and probe position. The system was operated through a CRT terminal with disk and tape data storage, as well as printed and plotted data hardcopy, all were available through the laboratory's computer facility.

### III. DATA REDUCTION

#### Pressure Data

The pressure data, both model surface pressures and wake data were reduced in the usual way. Models pressures were converted into pressure coefficients using the expression

$$C_p = \frac{P - P_\infty}{1/2 \rho_\infty U^2} \quad (1)$$

Here all pressure differences were measured directly from the Scanivalve. The pressure coefficients were then integrated to obtain the lift and moment coefficients. It should be noted that since no cut-off valves were used, as much as 90 seconds could elapse between the time the first and last surface pressures were measured. Therefore, the tunnel dynamic pressure was sampled simultaneously with each surface pressure to provide the correct dynamic pressure to be used in eq. (1).

Airfoil drag was obtained from the total pressure survey made in the airfoil wake. Since the survey was made one chord-length downstream of the model, the static pressure was assumed to be just the free stream value. The airfoil drag was then found from the following expression

$$C_d = 2 \int \sqrt{\frac{P_{tw} - P_{\infty}}{q_{\infty}}} (1 - \sqrt{\frac{P_{tw} - P_{\infty}}{q_{\infty}}}) d\left(\frac{Y}{c}\right) \quad (2)$$

In the implementation of this equation allowances were made for any tunnel speed variation which occurred during the traverse. The variation in tunnel speed across the tunnel due to model and wake blockage at high angles of attack was also incorporated.

The lift, drag and moment coefficients, as well as the model angle of attack, have been corrected for tunnel wall interference. These corrections used the procedures outlined by Rae and Pope [15]. The coefficients and angle of attack were corrected for solid blockage, streamline curvature and wake blockage; due to the test section design, no buoyancy corrections were made. The primary effect of these corrections was a reduction in the airfoil lift curve slope on the order of ten percent. Both the corrected and uncorrected values are given in the data tables. No attempt has been made in this report to correct the measured surface pressure distributions.

Velocity profiles were obtained from the boundary layer total pressure probe by assuming a constant static pressure across the boundary layer. Using a surface static pressure tap at the same chordwise location as the boundary layer total probe, the dynamic pressure at each location in the boundary layer was measured. For incompressible flow this was easily converted into a boundary layer velocity using the Bernoulli equation. Probe wall proximity and probe Reynolds number correction were found to be small, therefore,

all total pressure probe boundary layer velocity profiles are reported uncorrected.

### Split Film Data

The split film probe data reduction utilized calibration data of voltage versus velocity for a range of 0-300 ft/sec and several flow angles. The total velocity sensed by the probe was determined from

$$V_{tot} = f[(E_1 + E_2)^2] \quad (3)$$

Here  $E_1$  and  $E_2$  are the voltages from the front and back of the film, respectively, both corrected for ambient temperature effects. The function  $f$  is a fourth order polynomial. The streamwise velocity component,  $u$ , and the perpendicular component,  $v$ , could be determined knowing the flow angle,  $\theta$ . Where  $\theta$  is 90 degrees in the free stream. Using the expression for  $\sin \theta$  given in reference 16,

$$\sin \theta = \left[ \frac{E_1^2 - k^2 E_2^2}{(E_1^2 - k^2 E_2^2)_{\max}} \right]^{h(V_{tot})} \quad (4)$$

The constant  $k$  is the ratio of  $E_1$ , to  $E_2$  at  $\theta = 0$  degrees and is a function of velocity. The denominator is the value of  $E_1^2 - k^2 E_2^2$  at  $\theta = +90$  degrees depending on the sign of the numerator.

The term  $h(V_{tot})$  was assumed to be one, independent of velocity. This was curve fit based on the calibration data as a polynomial in  $V$ . Then  $u$  and  $v$  are

$$v = V_{tot} \sin\theta, \quad u = \sqrt{V_{tot}^2 - v^2} \quad (5)$$

with  $u$  greater than zero if  $E_1^2 - k^2 E_2^2$  is greater than zero. Note that with a two element split film probe the flow angle can at best be determined only in the range  $-90^\circ \leq \theta \leq 90^\circ$ . Therefore, the sign of the  $v$  component cannot be determined. When using many samples to determine a time averaged velocity, only the average  $u$  component can be calculated. The average  $v$  component and average total velocity are unknown. Therefore all velocity data presented here are the average streamwise component,  $u$ . RMS values were calculated but are not discussed, since no attempt was made to document the split film frequency response. Note that each split film velocity value presented in this report is really an average of 2048 data samples. These data were taken at a rate of 5 KHz using a 10 KHz low pass filter.

#### IV. RESULTS AND DISCUSSION

In this section some of the more important results obtained from these tests are summarized. All of the data, except the split film measurements, were obtained on the NACA 0012 Model No. 2. A more complete set of data is presented in the appendices.

## Pressure and Force Measurements

Initial tests were conducted on the NACA 0012 Model No. 2 without the ice shape. This is usually referred to as the clean configuration. Due to the slight seam in the model at the 15 percent chord location where the leading edge section meets the main model body, there was some question regarding its affect on the boundary layer transition location. To remove this question, and for ease in comparing these measurements to the computational results, tests were run with the boundary layer tripped at the five percent chord location on the upper and lower surface. The trip strip used was carborundum grit, nominally 0.009 inches in diameter, attached to the model using double-sided tape. The trip was approximately 0.25 inches in the chordwise direction with the back edge at the 0.05,  $x/c$  location. Only results from measurements at positive angles of attack are shown for the clean airfoil, with or without trip. Negative angles to stall were tested, but were similar to those at positive angles of attack. All data presented here have been corrected for tunnel wall effects by applying the correction method of Rae and Pope [15].

In Figure 4, the lift as a function of angle of attack for the clean model is shown. Presented are the data for a Reynolds number of  $1.5 \times 10^6$  and Mach number of 0.12. Also shown are the theoretical predictions from the airfoil analysis codes of Eppler [17] and Smetana [18]. The lift curve slope compares well to the results of Smetana since this code iterates on the displacements thickness to include the decambering of the airfoil due to boundary layer growth.

Eppler merely assumes a lift curve slope of  $2\pi$  per radian and this overpredicts these data. The Eppler code does contain a simple  $C_{l,max}$  prediction which predicts a maximum lift of approximately 1.12 at  $1.5 \times 10^6$  Reynolds number. Using the plot of reference 15, a  $C_{l,max}$  of 1.22 occurs at an effective Reynolds number of approximately  $2 \times 10^6$ . Tests were also run at  $0.9$  and  $2.0 \times 10^6$  in Reynolds number with little affect on the lift.

The drag performance of this airfoil was measured and presented in Figure 5. Here the experiment as well as the theories of references [17] and [18] are shown with natural transition and fixed transition. Both theories show more of a drag bucket than is reflected in the experiment, although some bucket is also seen in the data. At zero degrees angle of attack the experimental data have a drag coefficient of 0.0075 with 0.0070 and 0.0067 predicted by [17] and [18], respectively. This is probably due to some early transition on the wind tunnel model since the data with the boundary layer tripped compare very well to theory. With transition fixed at the 5 percent station, the measured drag rises to 0.0106 with the theories only 2 or 3 drag counts higher. The comparison remains excellent until the theories fail to predict the large drag rise associated with separation at high angle of attack. Experimental and theoretical results were also obtained at  $0.9$  and  $2.0 \times 10^6$  in Reynolds number. The drag increased with decreasing Reynolds number as expected.

The measured and predicted pitching moment about the quarter chord location is shown in Figure 6. For the natural transition case, the experimental data show a slightly positive  $C_m$  which becomes larger with increasing angle of attack due to the boundary layer growth. The theory due to Smetana reflects this trend but underpredicts its magnitude. Near stall, Smetana's  $C_m$  prediction is poor as would be expected. Eppler predicts the  $C_m$  trend near stall, but since it includes no boundary layer effects, it does poorly at low angle of attack. Fixed transition had little affect on the  $C_m$  in the experimental or theoretical data. Changing the Reynolds number from  $0.9$  to  $2.0 \times 10^6$  also had little affect on  $C_m$ .

In Figure 7, the measured pressures are compared to those predicted by the Smetana code. Comparisons were made at matched lift coefficient since the pressure coefficient data has not been corrected for the tunnel wall interference. The experimental data are for uncorrected angles of attack of 2 and 6 degrees. The comparisons are excellent with only some small deviation near the 15 percent chord location. This is probably due to the slight discontinuity where the model leading edge joins the main element. Note that with the very dense distribution of measured pressures near the leading edge, every symbol represents a measured pressure, the peak pressure was obtained in good agreement to the theory. Changes in  $C_p$  with Reynolds number and with the boundary layer trip were small as expected.



After completing the clean NACA 0012 Model No. 2 tests just described the ice shape shown in Figure 1 was installed. The ice shape was tested with no transition strip and with no distributed roughness. Since the airfoil was symmetric, the clean NACA 0012 performed the same at positive and negative angles of attack. However, with the ice shape, the airfoil was no longer symmetric and this was reflected in its aerodynamic characteristics. The ice shape was then tested to  $C_{l,max}$  for both positive and negative angles of attack. For ease in data presentation, the negative angles of attack are plotted as positive in Figures 8 and 9 and labelled, "Ice - Lower Horn". In this way, the data are presented as if the ice shape was removed and then inverted, upper and lower surfaces, for these tests. Five pressure taps were located, equally spaced spanwise, on both the upper and lower surfaces at an  $x/c$  of 0.05. These taps were compared to ensure the two-dimensionality of the flow, particularly when large separation zones were present. These taps compared well across the span and indicated that the flow was indeed two-dimensional at all conditions examined.

In Figure 8, the lift coefficient as a function of angle of attack for the NACA 0012 clean and with the glaze ice shape is shown. A large  $C_{l,max}$  penalty is seen for the airfoil with glaze ice due to either the upper or lower surface horn. The maximum lift decreased from the clean value of over 1.2, to the iced value of about 0.55, over a 50 percent decrease. The angle of attack for stall was also reduced about 50 percent. It is interesting that while the upper and lower surface horns were quite different in shape and location,

their affect on the airfoil lift was remarkably similar. Stall for the airfoil with ice shape was due to the failure of the leading edge separation bubble to re-attach at the higher angles of attack. This will be seen more clearly when the pressure distributions are examined. These data were also duplicated at Reynolds numbers of 0.9 and  $2.0 \times 10^6$  with little affect on the lift.

The effect of the ice accretion on drag is shown in Figure 9. As expected, the drag increase due to the ice was significant, from 0.0075 at  $\alpha = 0$  degrees clean to 0.0260 with the glaze ice shape. The drag rose quickly with angle of attack for the glaze shape since it stalled at only seven degrees angle of attack. The drag rise corresponding to the lower surface horn (negative angles of attack) was slightly larger than that from the upper surface horn (positive angles of attack), although the trend was very similar. While this ice shape did not correspond directly to any of those measured by Olsen [17], it was quite similar to one of the shapes reported there and the drag values reported by Olsen compare well to those in Figure 9. Again, these data were repeated at .9 and  $2.0 \times 10^6$  Reynolds number and no significant effects were noted.

Figure 10 shows the pitching moment coefficient measured on the clean and iced airfoil. The ice shape cambers the airfoil which can be seen by noting the pitching moment at zero degrees angle of attack. The upper horn ice shape data indicate a positive cambering since the  $C_m$  here is less than zero. As the angle of attack was increased, the separation bubble on the upper surface grew, thickening the boundary layer and decambering the airfoil causing a positive

increase in the moment coefficient. This continued until the airfoil started to stall and the moment becomes a large negative, nose down, value. The affect of the ice shape on the pitching moment, even at the low angles of attack, may be significant in rotorcraft applications. No significant Reynolds number effects were seen on the measured pitching moment coefficient.

Pressure distributions for the airfoil with simulated ice are shown in the next four figures. These pressure distributions have not been corrected for wind tunnel wall effects. As seen in Figure 7, these corrections are not necessary. Therefore, the  $C_p$ 's here are uncorrected and the angle of attack and lift coefficient indicated on the figures for each distribution are also uncorrected values.

In Figure 11, the pressure distributions for the NACA 0012 clean and with simulated ice are shown at an angle of attack of four degrees. Note first the zone of almost constant pressure occurring on the iced pressure distribution at a  $C_p$  level of approximately -1.4 . This is the separation bubble aft of the upper surface horn. The flow accelerated from the stagnation point as it moved toward the upper surface horn and separated as it attempts to flow over the tip of the ice horn. The separation zone was characterized by fairly constant but slightly falling pressure ( $C_p$  was decreasing as the flow accelerated) for approximately ten percent chord; then the pressure rose rapidly and ultimately returned to the clean value at about the 40 percent chord station. Hot-film measurements indicated re-attachment somewhat downstream of the minimum pressure point. At

a  $C_p$  of approximately -0.4 a constant pressure region corresponding to the lower surface bubble was seen. This also occurred at a much lower pressure than the clean airfoil experienced at this same location since the flow accelerated rapidly toward the lower surface horn before separation occurred. The uncorrected lift coefficient at four degrees angle of attack dropped from 0.439 clean to 0.376 iced, due to the separation.

The measured pressure distributions for the airfoil with simulated glaze ice are shown for various angles of attack in Figures 12 and 13. In Figure 12, pressures for 0, 2 and 4 degrees angle of attack are shown. The circles represent the zero angle of attack measured pressures. Here the lower and upper surface separation zones were at  $C_p$ 's of approximately -0.9 and -0.7, respectively. As the angle of attack was increased, these constant pressure zones occurred at decreasing pressures for the upper surface separation and increasing pressures for the lower. Note also that at  $\alpha = 0$  degrees the upper surface separation occurred at a higher pressure than the lower surface separation. At 2 and 4 degrees, this was reversed with the upper surface separation zone occurring at a lower pressure level.

In Figure 13, the pressure distributions for angles of attack of 4, 6 and 8 degrees are shown. Here, as the airfoil begins to approach stall, the upper surface separation bubble grew rapidly in length and the constant pressure zone occurred at higher pressures. Remember that the airfoil stalled at approximately seven degrees angle of attack. As the angle of attack increased the trailing edge

pressure is seen to fall, as do the pressures on the entire aft portion of the airfoil. At eight degrees angle of attack, the airfoil has stalled and the scatter in the leading edge, upper surface measured pressures was an indication of the unsteadiness of the flow in this region.

A comparison of the 4 and -4 degree pressure distributions are shown in Figure 14 so that the relative affect of the two ice horns on the pressure distribution may be more easily compared. The suction side separation zone can be seen, as discussed earlier, to be slightly longer and to have a more gentle pressure recovery for the -4 degree case. Both suction and pressure side separation occurred at lower pressures for the positive 4 degree measurements. The constant pressure separation zones all started at the leading edge of the particular ice horn concerned. These plots show that the lower surface horn does, indeed, cause a more severe aerodynamic penalty at negative angles of attack than the upper surface horn does at positive angles. This is an interesting result since these negative angle of attack cases are not usually considered. This finding would be important for any surface which must operate at both positive and negative angles of attack, such as the horizontal stabilizer. It may also have application to airfoils which operate at lower angles of attack than that at which the ice is accreted.

#### Velocity Profile Measurements

Velocity profile data were taken using a total pressure probe on the NACA 0012 Model No. 2 and a split film probe using Model No. 1. The purpose of these data was to measure the detailed boundary

layer and separation zone mean velocity profiles for comparison to the computational results.

Total pressure boundary layer surveys were taken on the model with the trip strip installed and at a Reynolds number of  $1.5 \times 10^6$ . The surveys were reduced in the standard way by assuming no pressure gradient through the boundary layer and, therefore, applying the measured surface static pressure through the boundary layer. Using the measured total pressure, the velocity profile in the boundary layer was determined. In Figure 15, a sample of the measured profiles are shown. The profiles shown are the measured velocity divided by the local edge velocity. The vertical lines are  $1.25 U/U_e$  apart. The  $y/c$  location, measured above the surface, of 0.02 is shown which corresponds to 0.42 inches. Profiles at several chordwise locations are shown at an angle of attack of four degrees in Figure 15. Since the boundary layer was tripped at  $x/c = .05$ , all of the measured profiles are turbulent. The boundary layer displacement thickness,  $\delta^*/c$ , calculated from the measured profiles versus  $x/c$  for both the  $\alpha = 0$  and  $\alpha = 4$  degree cases, are shown in Figure 16. Also shown are the predicted values from the Smetana analysis. Overall, the comparisons are quite good except at the 10 and 20 percent stations where the experiment showed a much larger displacement thickness. This was probably due to the trip strip initially increasing the displacement thickness more than would be due to transition alone. Further downstream of the trip the measurements and theory compared very well.

Whenever a separation zone is being probed, as with the split-film probe used in this test, the problem of probe interference must be considered. In Figure 17 a sketch of the NACA 0012 airfoil and the traversing system used for these experiments is shown. While the traversing mechanism itself was outside of the tunnel, a substantial probe support strut was required to properly position the probe. The entire traverse system consisted of the traversing mechanism (not shown), the strut, sleeve and the probe itself.

Surface pressures were measured on the airfoil with the probe at various locations to quantify the affect of the probe on the separation bubble. In Figure 18 the pressure distribution on the airfoil with simulated glaze ice is compared with and without the probe present. The probe and support system when located at the  $x/c = 0.03$  location was seen to lower the pressure in the bubble. If pressure level can be used as a basis for flow re-attachment, the probe and support moved the point of bubble re-attachment forward. The lower surface and the aft part of the upper surface did not appear to be significantly affected by the presence of the probe. The position of the probe in the bubble was shown to be important, Figure 19. Here the probe and support were positioned at three different chordwise locations and the surface pressures recorded. The probe at  $x/c = 0.11$  had the largest affect on bubble re-attachment which occurred around  $x/c = 0.20$ . Only the  $x/c = 0.19$  position had little affect on the pressure level in the relatively constant pressure region of the bubble. Tests were also made by positioning the strut and sleeve but not placing the probe in the bubble. These tests showed that the strut and sleeve could be modified so as not

to affect the separation zone pressures, however, once the probe was inserted into the bubble the pressures were always affected.

The interference studies showed that the presence of the probe affected the bubble in all cases tested. The primary results were a decreased plateau pressure in the bubble, and an increased pressure in the re-attachment region. The probe appeared to cause early bubble re-attachment, shortening the bubble by a few percent chord. Therefore, all the split-film data where the probe was in the separation bubble included this probe interference error for which no correction has been made.

In Figures 20 through 22, the velocity profiles are shown for the NACA 0012 Model No. 1, upper surface, in the vicinity of the glaze ice shape. All runs were made at a Reynolds number based on chord of  $1.5 \times 10^6$  and a Mach number of 0.12. Note that the velocity shown was actually the streamwise component of the total boundary layer velocity and was nondimensionalized by the edge velocity. The edge velocity was defined as the maximum velocity measured for each profile. The vertical lines on the plot are the zero velocity reference line for each profile. So points to the left indicate negative velocity or reversed flow. These vertical lines are spaced a distance apart of 1.25 times the local edge velocity. The height scale nondimensionalized by the airfoil chord of 21 inches and is measured from the airfoil surface. All airfoil angles of attack are uncorrected.

The bubble shapes are also represented in Figures 20 through 22. The dashed lines are the stagnation streamline and are merely



taken from the point above the surface where the measured streamwise velocity zero (i.e. the velocity changes from negative to positive). The solid lines are the dividing stream lines. These were found by integrating the mass flow in the streamwise direction. The point above the surface where the net mass flow is zero defines the dividing streamline.

The profiles for the  $-0.15$  degree case are shown in Figure 20. If it is assumed that separation occurred at the leading edge of the upper surface horn,  $x/c = -.0225$ , then the first profile was only  $-.0025c$  downstream. Therefore a relatively large reversed flow region developed very quickly. The reversed flow region grew initially, then decreased until the bubble re-attached around an  $x/c$  of  $.08$ . The last profile is a fairly characteristic turbulent profile. From the streamline plot it is clear that the reversed flow region was relatively thick and slow moving. Conversely, the shear layer was thin and rapidly accelerated to the edge velocity.

Figure 21 is similar but for the  $1.85$  degree angle of attack case. Here, as expected, the bubble was thicker and larger than the previous case. Re-attachment occurred around the 12 percent chord location. Note in the  $x/c = .14$  profile a change in second derivative that occurred about one-fifth of the way up on the profile. This appears to be characteristic of all the re-attached profiles measured to date.

In Figure 22 the profiles are shown for a model angle of attack of  $3.85^\circ$ . Here the bubble was extremely large as shown. In Figure 22, re-attachment occurred around the 18 percent airfoil station.

Note that for this bubble, reversed flow extended up from the airfoil over one-half inch in some cases. Figure 22 also shows three profiles further downstream, aft of re-attachment. Note that here the height scale is different from the other plots. These were clearly turbulent profiles. Re-attachment appeared to be at approximately 18 percent chord for the 3.85 degree case. Note that this was uncorrected and probe interference has probably shortened all the bubble length measurements.

### Data Presentation

The detailed results, run by run, are given in the appendices. In Appendix A the wind tunnel run summaries are tabulated. The runs are listed in order by run number and separated into groups according to the model and configuration. For example, NACA 0012 Model No. 2 with Glaze Ice appears as one of the group headings. For the runs where pressure data were taken, both the uncorrected or raw data, and the corrected values are given for the angle of attack; lift, drag and pitching moment coefficients. Mach number and Reynolds number are also given. For the data runs where velocity profile data were taken, no force coefficient data are available. In this case the uncorrected angle of attack, tunnel velocity, Reynolds number, Mach number, and calculated boundary layer thicknesses are given. In the tables AOA is just the angle of attack in degrees and VEL and U-EDGE are the tunnel velocity and boundary layer edge velocity, respectively, in feet per second.

It should be noted that many run numbers are missing. Blocks of run numbers are often missing which represent tunnel runs on other models and projects. In some instances one or two runs may be

omitted when the data is bad or questionable due to an equipment or software problem.

In Appendix B the pressure coefficient plots are given in run number order. Each symbol represents a measured pressure with the apex of the triangular symbol up, for upper surface taps, and down, for lower surface taps. Some taps were removed from the plots due to blockage in the pressure lines. Tabulated on each plot are the tunnel conditions and the corrected angle of attack and corrected integrated force coefficients. The nomenclature is straight-forward with the possible exception of the term CDW. Since the OSU software is also capable of calculating and outputting the integrated pressure drag coefficient, the total airfoil corrected drag coefficient obtained from the wake survey probe is given as CDW. This corresponds to the CD value in the table of Appendix A.

The model construction did cause some inconsistencies in the data which should be explained. The model was constructed with a removable leading edge which caused a spanwise seam in the model at the 15 percent chord location. This slight discontinuity in the airfoil surface can be seen in the pressure distribution plots, particularly on the upper surface where taps were located every one percent chord. Some asymmetry, about zero degrees angle of attack, was also seen in the integrated coefficients due to this model seam, since it was slightly smoother on one side than the other. Although an effort was made to smooth the seams, this was not completely successful. This asymmetry was most evident in the drag data on the clean model. Due to what is thought to be different laminar boundary layer transition points, the drag was somewhat asymmetric about

zero degrees angle of attack. Also contributing to this was the surface pressure tap installation. From previous experience at OSU it is known that the presence of these taps increases the airfoil drag since they act as boundary layer trips and as surface roughness. This model has many more taps on the upper surface than on the lower, which may explain in part why the drag was higher at negative angles of attack. Even when the boundary layer trip was installed at the five percent chord location, this asymmetry was present. On the runs of the NACA 0012 Model No. 2 with boundary layer trip, a small discontinuity was seen in the pressure plots near the forty percent chord station on the upper surface. This was the point where the pressure measurement was switched to a second Scanivalve. Apparently some small deviation in transducer reference pressure was present. Unfortunately, this was not discovered until after the experiment was completed, but the data are still of acceptable quality and are included here.

In Appendix C selected wake traces are presented. It was not felt that these data would be useful to most readers, so only a representative sample of these plots are presented here. In these figures the dynamic pressure in the wake, assuming that the wake static is just the tunnel freestream static pressure, were plotted versus the position in the wake. Since only the relative positions of the data are used in the data reduction, no attempt has been made to maintain a common coordinate system for all runs. The wake deficit is then a measure of the total airfoil drag. Since, as in the integration of the pressure distributions of Appendix B, the tunnel dynamic pressure is measured to correspond to each wake

point, integrating these plots alone will not give the exact drag value reported here. The tunnel speed variation correction is, however, small and the two values should be very close.

The detailed velocity measurements are presented in Appendix D. Two sets of measurements are found here; the split-film results on Model No. 1 with glaze ice and the total probe boundary layer measurements on Model No. 2 with the trip strip. These runs can be easily distinguished by the plot title or run number. In addition to the data listed for each run in the table of Appendix A, the important parameters are given on each plot. These include run number, uncorrected angle of attack in degrees, the probe chordwise location, the freestream velocity in ft/sec and the model chord Reynolds number in millions. Each symbol represents the measured velocity at a particular height above the model where Y is always zero on the surface. The total pressure data has somewhat more scatter than the split-film data since each total probe data point represents only one data sample instead of the 2048 samples averaged for each split-film velocity.

#### SUMMARY

An experimental program has been conducted to document the aerodynamic characteristics and flow field about a NACA 0012 airfoil with simulated glaze ice. Two different NACA 0012 models were used for the tests.

NACA 0012 Model No. 2 was instrumented with an extremely dense distribution of surface pressure taps to provide additional details concerning the large separation zones aft of the ice horns. Airfoil

lift and drag were severely affected by the ice shape as was expected. However, the surface pressure provided additional information about the separation bubbles. The bubbles are characterized by a region of almost constant, but slightly falling pressure, followed by a region of pressure recovery. Work on Model No. 1 has shown that re-attachment occurred in this pressure recovery region. The lower surface horn caused a larger separation zone and a more severe aerodynamic penalty when tested at negative angles of attack than did the upper surface horns at positive angles of attack. This is an interesting result which should be studied further. Model No. 2 was also used to document the baseline performance of the NACA 0012 airfoil. These tests were conducted with natural transition and transition fixed at the five percent chord location on both surfaces. The forced transition data compared well to theoretical results in all aerodynamic quantities including the measured boundary layer parameters.

Velocity profile measurements were performed in the separated flow region behind the upper surface glaze ice horn. Using split-film anemometry on the NACA 0012 Model No. 1, streamwise velocity profiles have been measured at several chordwise locations and angles of attack. These profiles have shown the bubble extent and the large regions of reversed flow.

Much of the detailed data from these experiments can be found in the appendices. In addition to the run summary tables, plots of surface pressures, wake total pressure profiles and velocity profiles are also in the appendices. It is hoped that these data will be useful in testing and developing airfoil performance in

icing computer codes and providing a better understanding of the flow field.

## REFERENCES

1. Jacobs, E. N., "Airfoil Section Characteristics as Affected by Protuberances", NACA Report No. 446, 1932.
2. Gray, V. H. and Von Glahn, Uwe H., "Effects of Ice and Frost Formations on Drag of NACA 65-212 Airfoil for Various Modes of Thermal Ice Protection", NACA TN 2962, 1953.
3. Gray, V. H. and Von Glahn, Uwe H., "Aerodynamic Effects Caused by Icing of an Unswept NACA 65A004 Airfoil", NACA TN 4151, 1957.
4. Korkan, K. D., Cross, E. J. Jr., and Cornell, C. C., "Experimental Study of Performance Degradation of a Model Helicopter Main Rotor with Simulated Ice Shape", AIAA Paper No. 84-0184, presented at the 22nd Aerospace Sciences Meeting, Reno, Nevada, Jan. 9-12, 1984.
5. Lee, J. D. and Shaw, R. J., "The Aerodynamics of Rotor Blades with Ice Shapes Accreted in Hover and in Level Flight", paper presented at the 41st Annual Forum of the American Helicopter Society, Ft. Worth, Texas, May, 1985.
6. Flemming, R. J., Shaw, R. J. and Lee, J. D., "The Performance Characteristics of Simulated Ice on Rotor Airfoils", paper presented at the 41st Annual Forum of the American Helicopter Society, Ft. Worth, Texas, May 1985.
7. Bragg, M. B., Zaguli, R. J., and Gregorek, G. M., "Wind Tunnel Evaluation of Airfoil Performance Using Simulated Ice Shapes", NASA CR 167960, 1982.
8. Bragg, M. B. and Gregorek, G. M., "Wind Tunnel Investigation of Airfoil Performance Degradation Due to Icing", AIAA Paper No. 82-0582, presented at the 12th Aerodynamic Testing Conference, Williamsburg, Virginia, March 22-24, 1982.
9. Bragg, M. B., "Predicting Airfoil Performance with Rime and Glaze Ice Accretions", AIAA Paper No. 84-0106, presented at the 22nd Aerospace Sciences Meeting, Reno, Nevada, Jan. 9-12, 1984.
10. Potapczuk, M. G. and Gerhart, P. M. "Progress in the Development of a Navier-Stokes Solver for Evaluation of Iced Airfoil Performance", AIAA Paper No. 85-0410, presented at the 23rd Aerospace Sciences Meeting, Reno, Nevada, Jan. 14-17, 1985.
11. Cebeci, T., "Interactive Boundary-Layer Analysis of Iced Airfoils", Airfoil Performance-in-Icing Workshop, NASA Lewis Research Center, July 17-18, 1986.



12. Bragg, M. B. and Coirier, W. J., "Detailed Measurements of the Flowfield in the Vicinity of an Airfoil with Glaze Ice", AIAA Paper No. 85-0409, presented at the 23rd Aerospace Sciences Meeting, Reno, Nevada, Jan. 14-17, 1985.
13. Bragg, M. B., and Coirier, W. J., "Aerodynamic Measurements of an Airfoil with Simulated Glaze Ice", AIAA-86-0484, paper presented at the 24th Aerospace Sciences Meeting, Reno, NV, Jan. 6-9, 1986.
14. Shaw, R. J., private communication, March 1982.
15. Rae, W. H., Jr. and Pope, A., Low-Speed Wind Tunnel Testing, 2nd ed., John Wiley and Sons, New York, 1984.
16. Boerner, Th. and Leutheusser, H. J., "Calibration of Split-Fibre Probe for Use in Bubbly Two-Phase Flow", DISA Information, No. 29, January 1984.
17. Eppler, Richard and Somers, Dan M., "A Computer Program for the Design and Analysis of Low-Speed Airfoils", NASA TM 80210, August 1980.
18. Smetana, F. O., Summey, D. C., Smith, N. S. and Carden, R .K., "Light Aircraft Lift, Drag, and Moment Prediction - A Review and Analysis", NASA CR-2523, May 1975.
19. Olsen, W., Shaw, R. and Newton, J., "Ice Shapes and the resulting Drag Increase for a NACA 0012 airfoil", NASA TM 83556, 1983.

TABLE 1. COORDINATES FOR THE NACA 0012  
MODEL NO. 2 - CLEAN CONFIGURATION

No.	$X_u$	$Y_u$	$X_l$	$Y_l$
1	0.00000	0.00000	0.00000	0.00000
2	0.00309	0.00967	0.00309	-0.00967
3	0.00621	0.01356	0.00621	-0.01356
4	0.01380	0.01984	0.02230	-0.02481
5	0.02230	0.02481	0.04080	-0.03256
6	0.03140	0.02899	0.08000	-0.04307
7	0.04080	0.03256	0.12000	-0.04988
8	0.05000	0.03555	0.16000	-0.05442
9	0.06000	0.03838	0.20000	-0.05738
10	0.07000	0.04086	0.24000	-0.05913
11	0.08000	0.04307	0.28000	-0.05993
12	0.09000	0.04505	0.32000	-0.05993
13	0.10000	0.04683	0.36000	-0.05926
14	0.11000	0.04843	0.40000	-0.05803
15	0.12000	0.04988	0.44000	-0.05631
16	0.13000	0.05119	0.50000	-0.05294
17	0.14000	0.05238	0.56000	-0.04878
18	0.15000	0.05345	0.60000	-0.04563
19	0.16000	0.05442	0.65000	-0.04132
20	0.17000	0.05529	0.70000	-0.03664
21	0.18000	0.05607	0.75000	-0.03160
22	0.19000	0.05676	0.80000	-0.02623
23	0.20000	0.05738	0.85000	-0.02053
24	0.21000	0.05792	0.90000	-0.01448
25	0.22000	0.05839	0.95000	-0.00807
26	0.23000	0.05879	0.97500	-0.00471
27	0.24000	0.05913	1.00000	0.00000
28	0.25000	0.05941		
29	0.26000	0.05864		
30	0.27000	0.05981		
31	0.28000	0.05993		
32	0.29000	0.06000		
33	0.30000	0.06002		
34	0.31000	0.05999		
35	0.32000	0.05993		
36	0.33000	0.05982		
37	0.34000	0.05967		
38	0.35000	0.05949		
39	0.36000	0.05926		
40	0.37000	0.05900		
41	0.38000	0.05871		
42	0.39000	0.05839		
43	0.40000	0.05803		
44	0.42000	0.05723		
45	0.44000	0.05631		

TABLE 1. (continued)

No.	$X_u$	$Y_u$
46	0.47000	0.05473
47	0.50000	0.05294
48	0.53000	0.05095
49	0.56000	0.04878
50	0.60000	0.04563
51	0.65000	0.04132
52	0.70000	0.03664
53	0.75000	0.03160
54	0.80000	0.02623
55	0.85000	0.02053
56	0.90000	0.01448
57	0.95000	0.00807
58	0.97500	0.00471
59	1.00000	0.00000
-----		
-----		

TABLE 2. COORDINATES FOR THE NACA 0012  
MODEL NO. 1 - GLAZE ICE CONFIGURATION

No.	X <sub>u</sub>	Y <sub>u</sub>	X <sub>l</sub>	Y <sub>l</sub>
1	-0.02557	0.02729*	-0.02557	0.02729
2	-0.02501	0.02877*	-0.02000	0.00621
3	-0.02445	0.02922*	-0.01800	0.00097
4	-0.02389	0.02945*	-0.01200	-0.01151
5	-0.02333	0.02952*	-0.00600	-0.02115
6	-0.00305	0.02632	0.00000	-0.02907
7	0.01857	0.02263	0.00600	-0.03577
8	0.03140	0.02899	0.01200	-0.04155
9	0.05000	0.03555	0.02166	-0.05215*
10	0.06000	0.03838	0.02278	-0.05283*
11	0.08000	0.04307	0.02333	-0.05290*
12	0.10000	0.04683	0.02389	-0.05283*
13	0.12000	0.04988	0.04798	-0.04683
14	0.14000	0.05238	0.06952	-0.04026
15	0.16000	0.05442	0.09900	-0.04700
16	0.18000	0.05607	0.12000	-0.04988
17	0.20000	0.05738	0.16000	-0.05442
18	0.22000	0.05839	0.20000	-0.05738
19	0.24000	0.05913	0.24000	-0.05913
20	0.26000	0.05864	0.28000	-0.05993
21	0.28000	0.05993	0.32000	-0.05993
22	0.30000	0.06002	0.36000	-0.05926
23	0.32000	0.05993	0.40000	-0.05803
24	0.34000	0.05967	0.44000	-0.05631
25	0.36000	0.05926	0.50000	-0.05294
26	0.38000	0.05871	0.56000	-0.04878
27	0.40000	0.05803	0.60000	-0.04563
28	0.42000	0.05723	0.65000	-0.04132
29	0.44000	0.05631	0.70000	-0.03664
30	0.47000	0.05473	0.75000	-0.03160
31	0.50000	0.05294	0.80000	-0.02623
32	0.53000	0.05095	0.85000	-0.02053
33	0.56000	0.04878	0.90000	-0.01448
34	0.60000	0.04563	0.95000	-0.00807
35	0.65000	0.04132	0.97500	-0.00471
36	0.70000	0.03664	1.00000	0.00000
37	0.75000	0.03160		
38	0.80000	0.02623		
39	0.85000	0.02053		
40	0.90000	0.01448		
41	0.95000	0.00807		
42	0.97500	0.00471		
43	1.00000	0.00000		

\* NOTE: Upper and lower surface horn radius of curvature,  $r/c = 0.002232$  .

TABLE 3. COORDINATES FOR THE NACA 0012  
MODEL NO. 2 - ICED CONFIGURATION

No.	X <sub>u</sub>	Y <sub>u</sub>	X <sub>l</sub>	Y <sub>l</sub>
1	-0.02660	0.01690*	-0.02660	0.01690
2	-0.02450	0.02870*	-0.02220	0.00390
3	-0.02080	0.03060*	-0.01750	-0.00700
4	-0.01000	0.02880	-0.01070	-0.01840
5	-0.00010	0.02680	-0.00360	-0.02840
6	0.01000	0.02500	0.00590	-0.03930
7	0.02210	0.02670	0.01500	-0.04740
8	0.03110	0.03000	0.02580	-0.05330**
9	0.04070	0.03330	0.03000	-0.05300**
10	0.04910	0.03610	0.03970	-0.05030
11	0.05950	0.03900	0.04950	-0.04730
12	0.06940	0.04140	0.06000	-0.04410
13	0.07940	0.04350	0.06950	-0.04210
14	0.08910	0.04550	0.07930	-0.04360
15	0.09900	0.04720	0.10940	-0.04870
16	0.10970	0.04870	0.11930	-0.05000
17	0.11970	0.05000	0.12900	-0.05110
18	0.12969	0.05140	0.14000	-0.05200
19	0.14000	0.05240	0.16000	-0.05442
20	0.16000	0.05442	0.20000	-0.05738
21	0.17000	0.05500	0.24000	-0.05913
22	0.18000	0.05607	0.28000	-0.05993
23	0.19000	0.05676	0.32000	-0.05993
24	0.20000	0.05738	0.36000	-0.05926
25	0.21000	0.05792	0.40000	-0.05803
26	0.22000	0.05839	0.44000	-0.05631
27	0.23000	0.05879	0.50000	-0.05294
28	0.24000	0.05913	0.56000	-0.04878
29	0.25000	0.05941	0.60000	-0.04563
30	0.26000	0.05864	0.70000	-0.03664
31	0.28000	0.05993	0.75000	-0.03160
32	0.30000	0.06002	0.85000	-0.02053
33	0.32000	0.05993	0.90000	-0.01448
34	0.34000	0.05967	0.95000	-0.00807
35	0.36000	0.05926	0.97500	-0.00471
36	0.38000	0.05871	1.00000	0.00000
37	0.40000	0.05800		
38	0.42000	0.05700		
39	0.44000	0.05631		
40	0.47000	0.05473		
41	0.50000	0.05294		
42	0.53000	0.05095		
43	0.56000	0.04878		
44	0.60000	0.04563		
45	0.70000	0.03664		

TABLE 3. (continued)

No.	$X_u$	$Y_u$
46	0.75000	0.03160
47	0.80000	0.02623
48	0.85000	0.02053
49	0.90000	0.01448
50	0.95000	0.00807
51	0.97500	0.00471
52	1.00000	0.00000

\* NOTE: Upper surface horn radius of curvature,  $(r/c)_u = 0.00595$  .

\*\* NOTE: Lower surface horn radius of curvature,  $(r/c)_l = 0.01042$  .

# NACA 0012 ICING CONDITIONS

$\alpha = 4^\circ$        $V = 130 \text{ mph}$

$\bar{d} = 20\mu\text{m}$        $\text{LWC} = 2.1 \text{ g/m}^3$

$T = 18^\circ\text{F}$

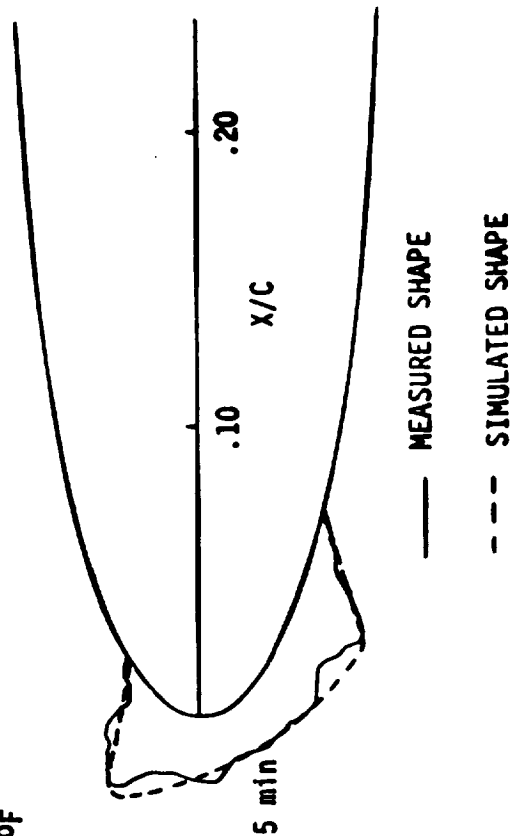


FIGURE 1. COMPARISON OF THE MEASURED AND SIMULATED ICE SHAPE.

ORIGINAL PAGE IS  
OF POOR QUALITY



FIGURE 2. OHIO STATE UNIVERSITY SUBSONIC WIND TUNNEL.



ORIGIN  
OF PLOTTING

ORIGINAL PAGE IS  
OF POOR QUALITY

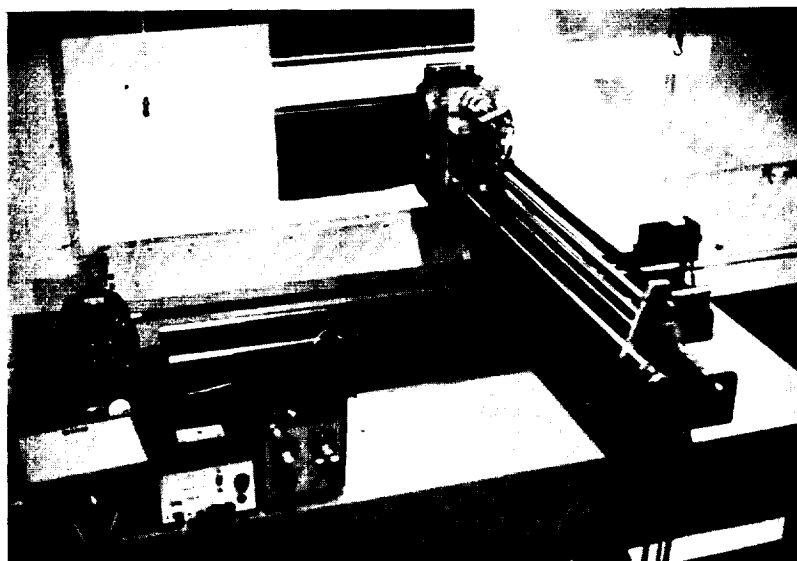


FIGURE 3. TWO-DIMENSIONAL TRAVERSE SYSTEM.

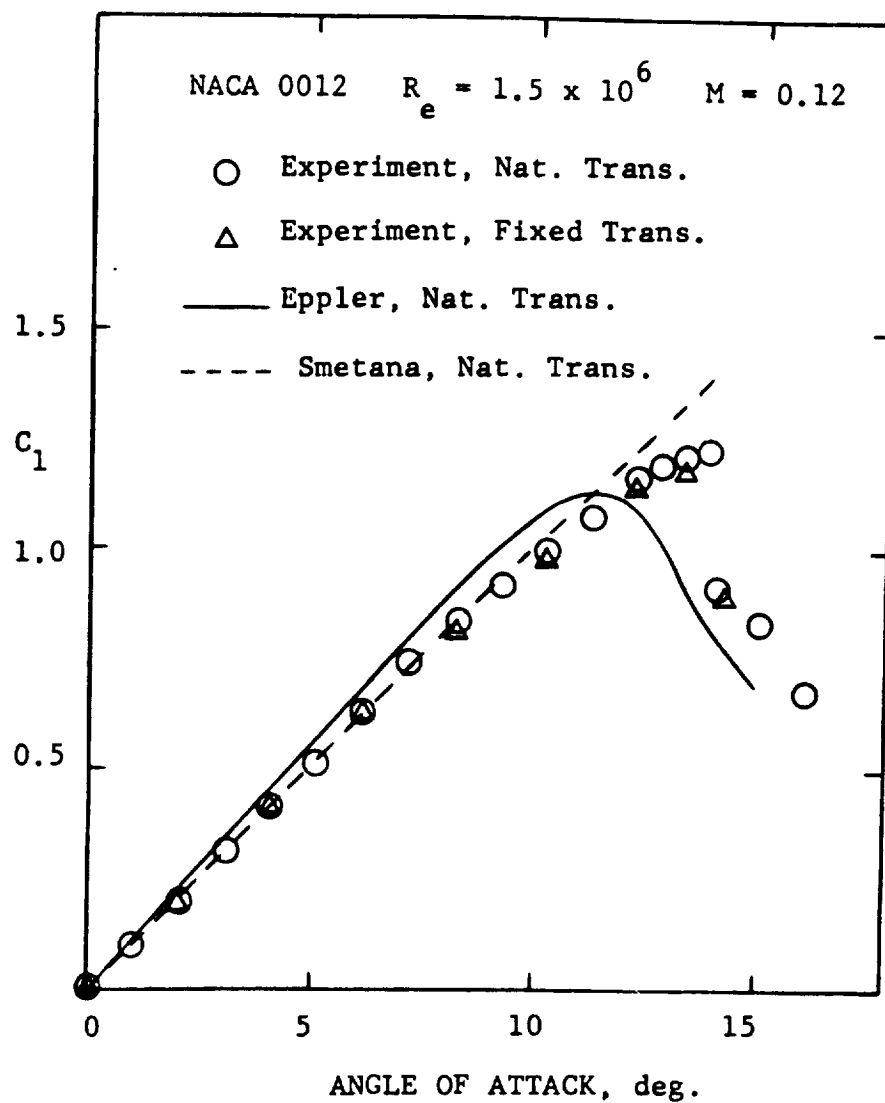


FIGURE 4. COMPARISON OF MEASURED LIFT WITH NATURAL AND FIXED TRANSITION TO THEORY.

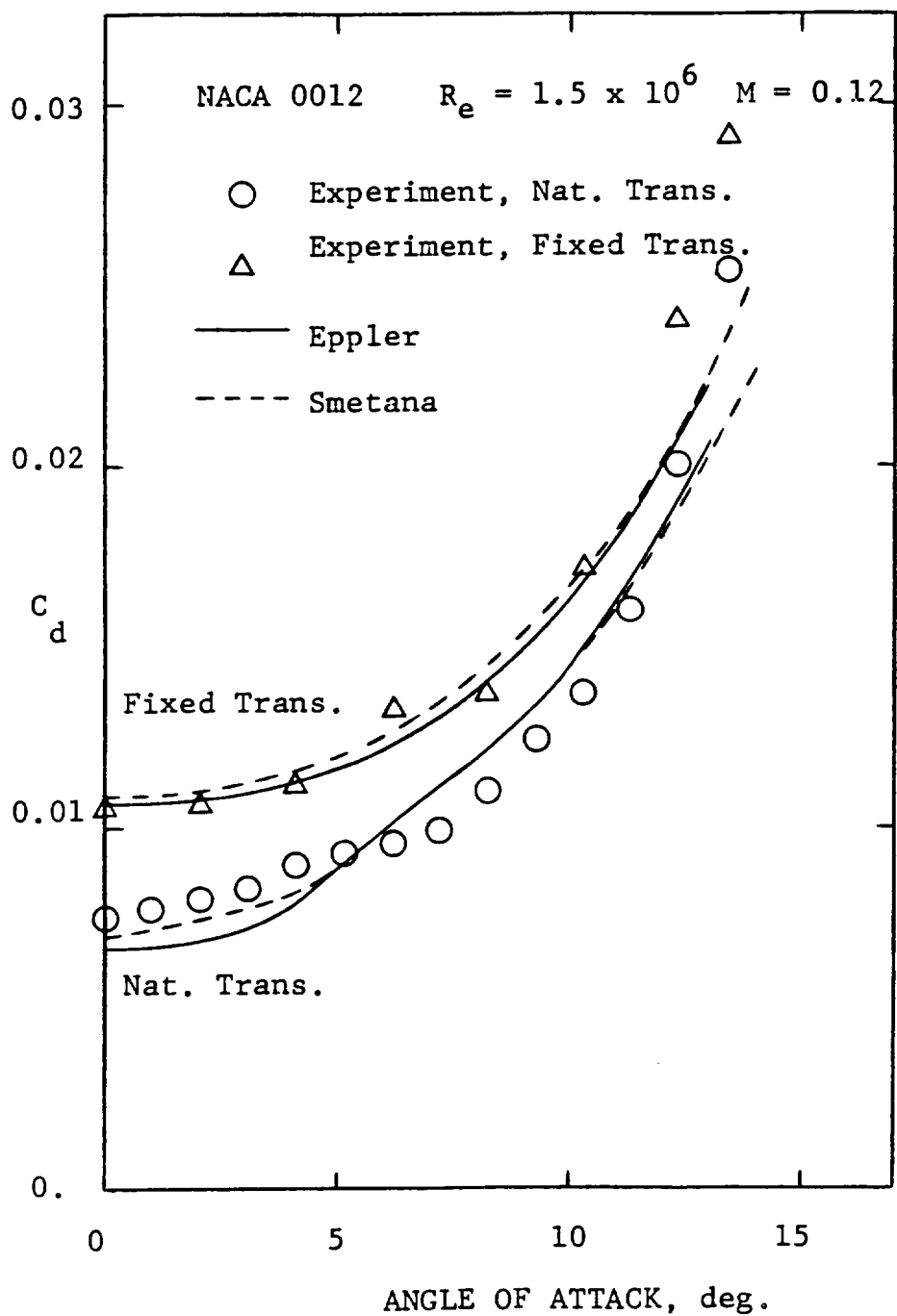


FIGURE 5. COMPARISON OF MEASURED DRAG WITH NATURAL AND FIXED TRANSITION TO THEORY.

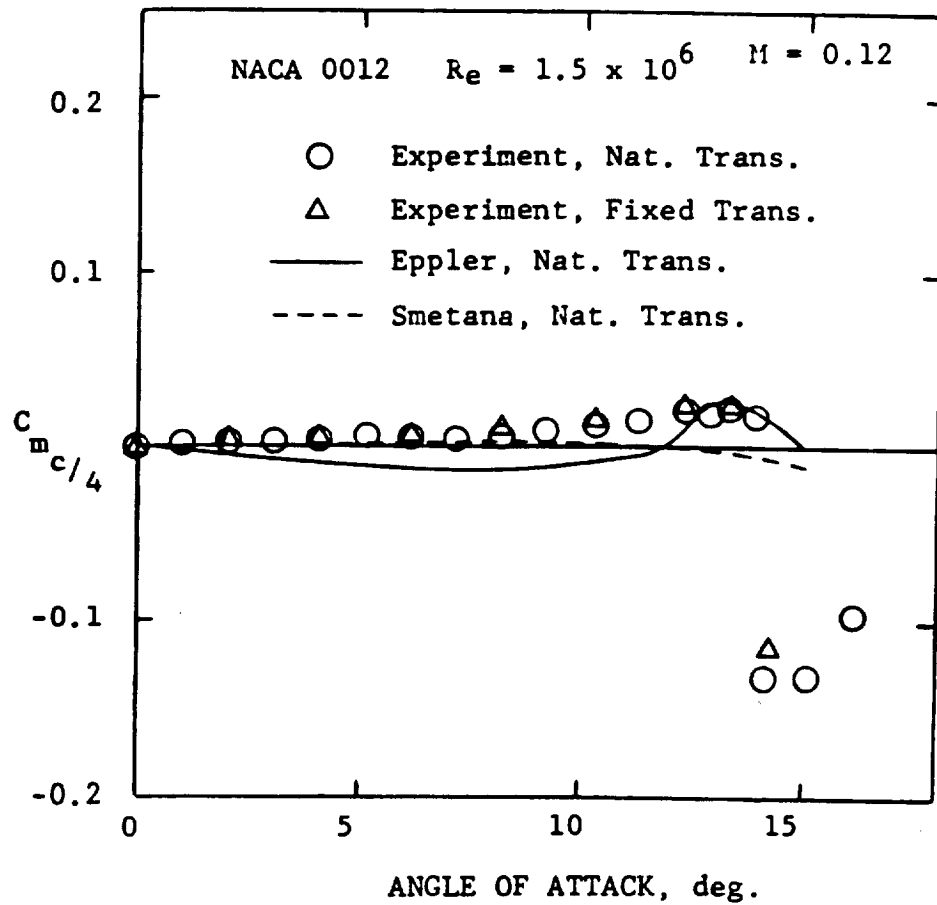


FIGURE 6. MEASURED AIRFOIL PITCHING MOMENT WITH AND WITHOUT SIMULATED GLAZE ICE.

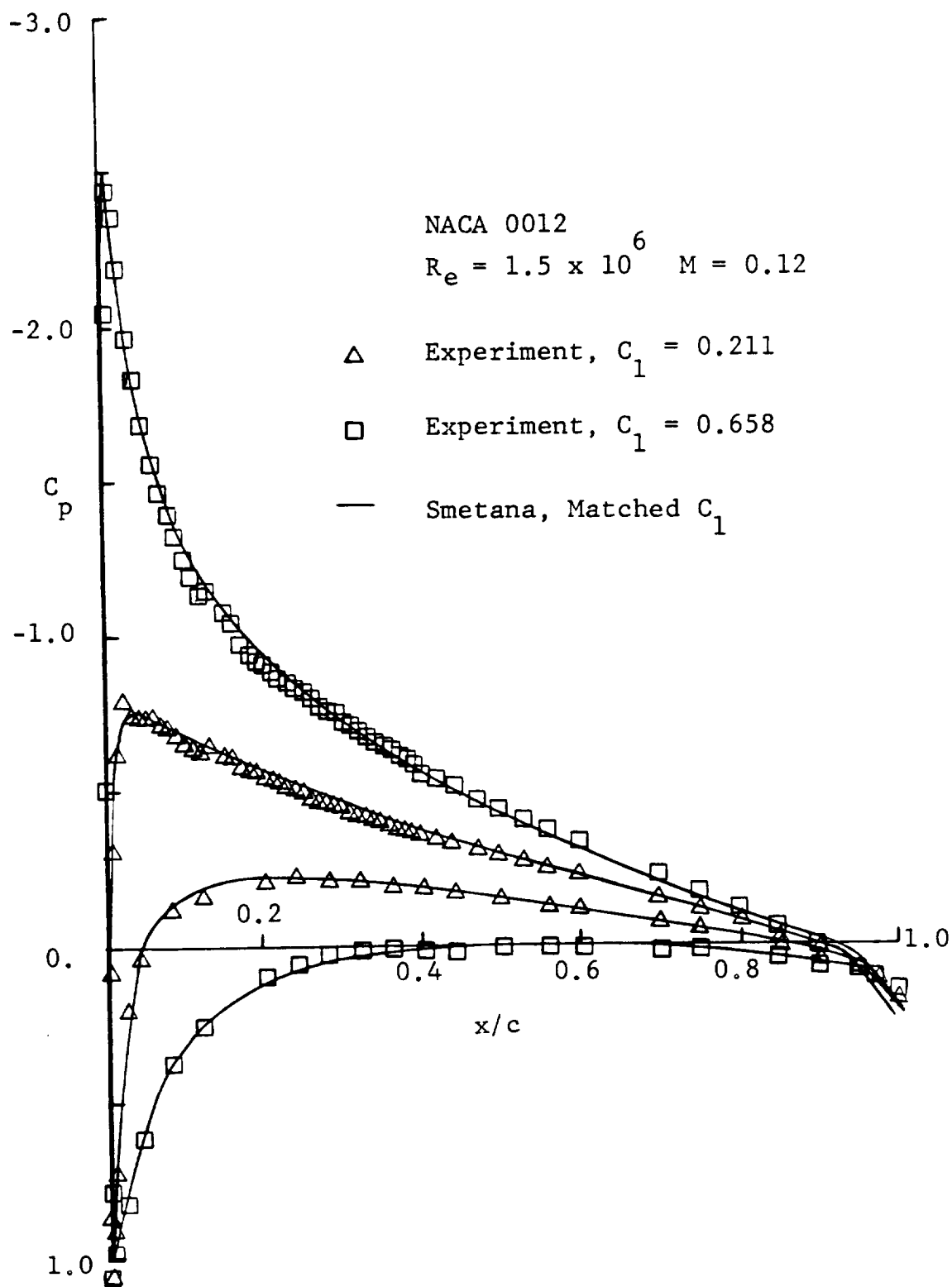


FIGURE 7. MEASURED SURFACE PRESSURES COMPARED TO THEORY AT TWO ANGLES OF ATTACK.

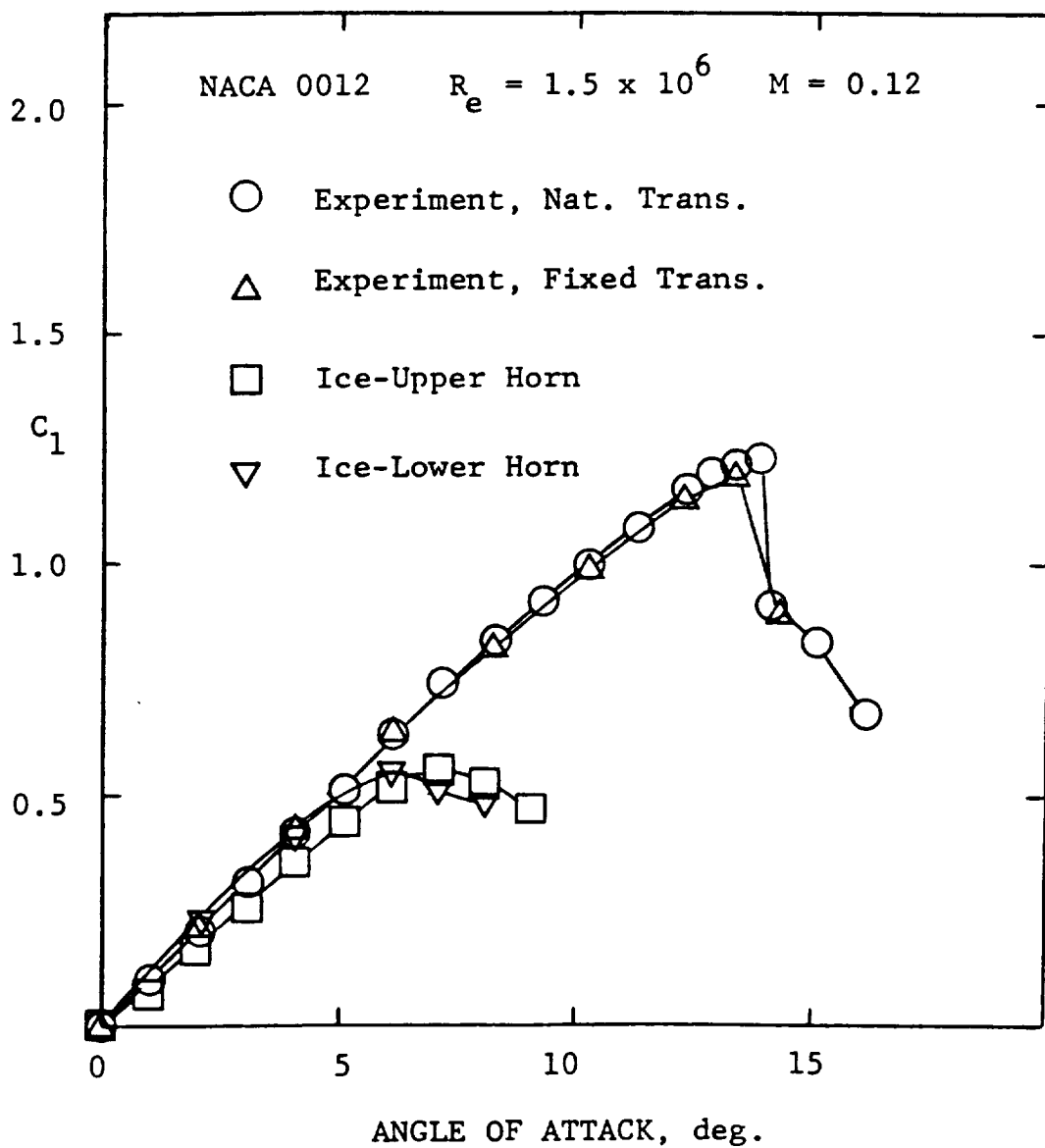


FIGURE 8. MEASURED AIRFOIL LIFT WITH AND WITHOUT SIMULATED GLAZE ICE.

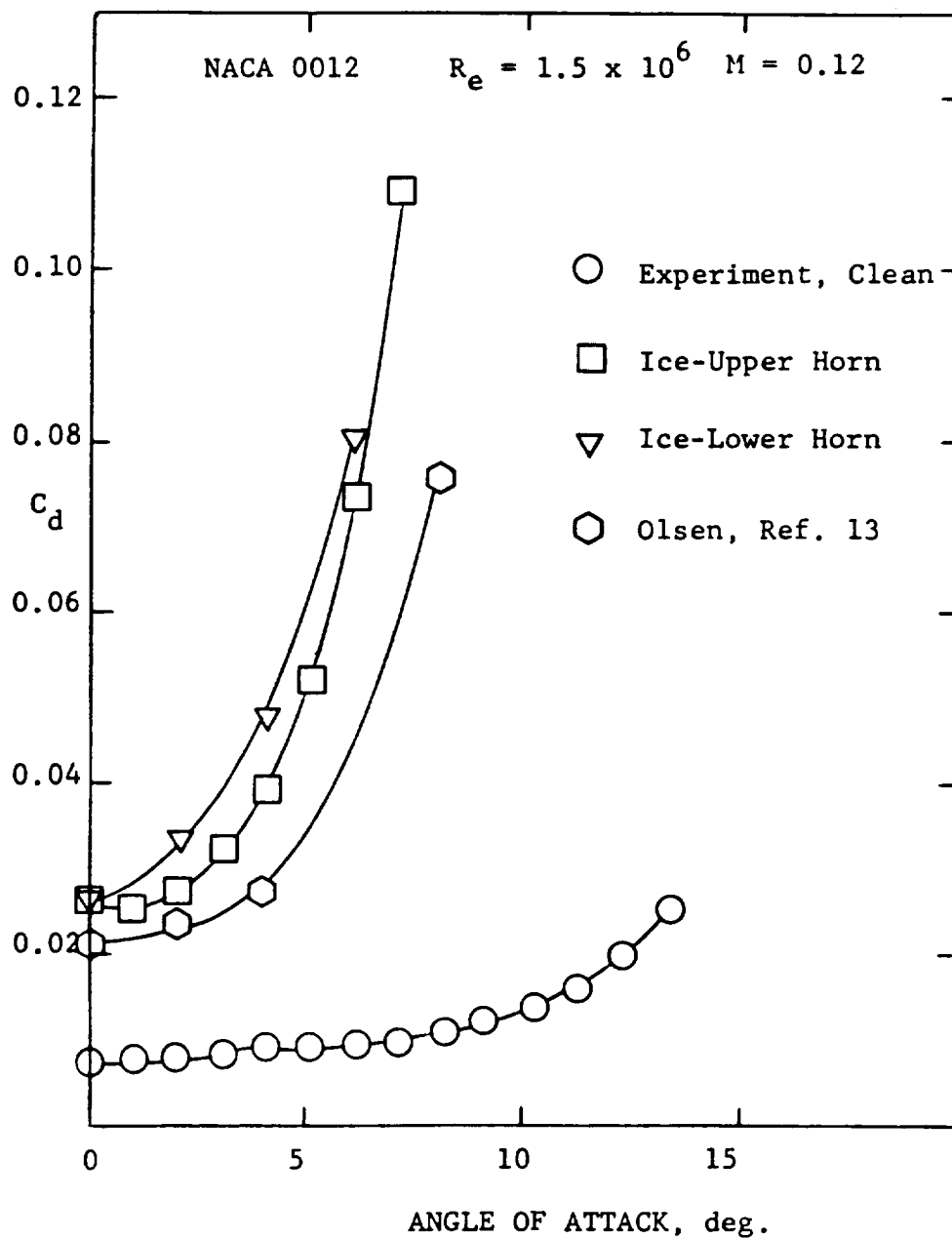


FIGURE 9. MEASURED AIRFOIL DRAG WITH AND WITHOUT SIMULATED GLAZE ICE.

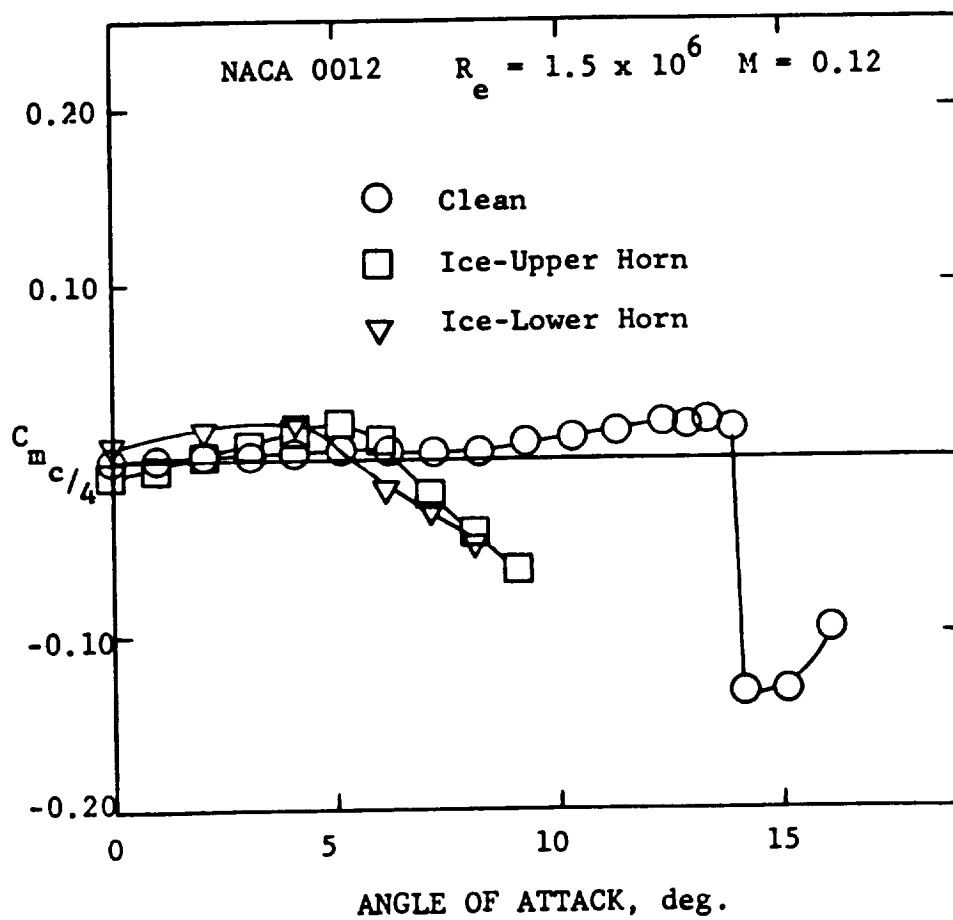


FIGURE 10. COMPARISON OF MEASURED PITCHING MOMENT WITH NATURAL AND FIXED TRANSITION TO THEORY.



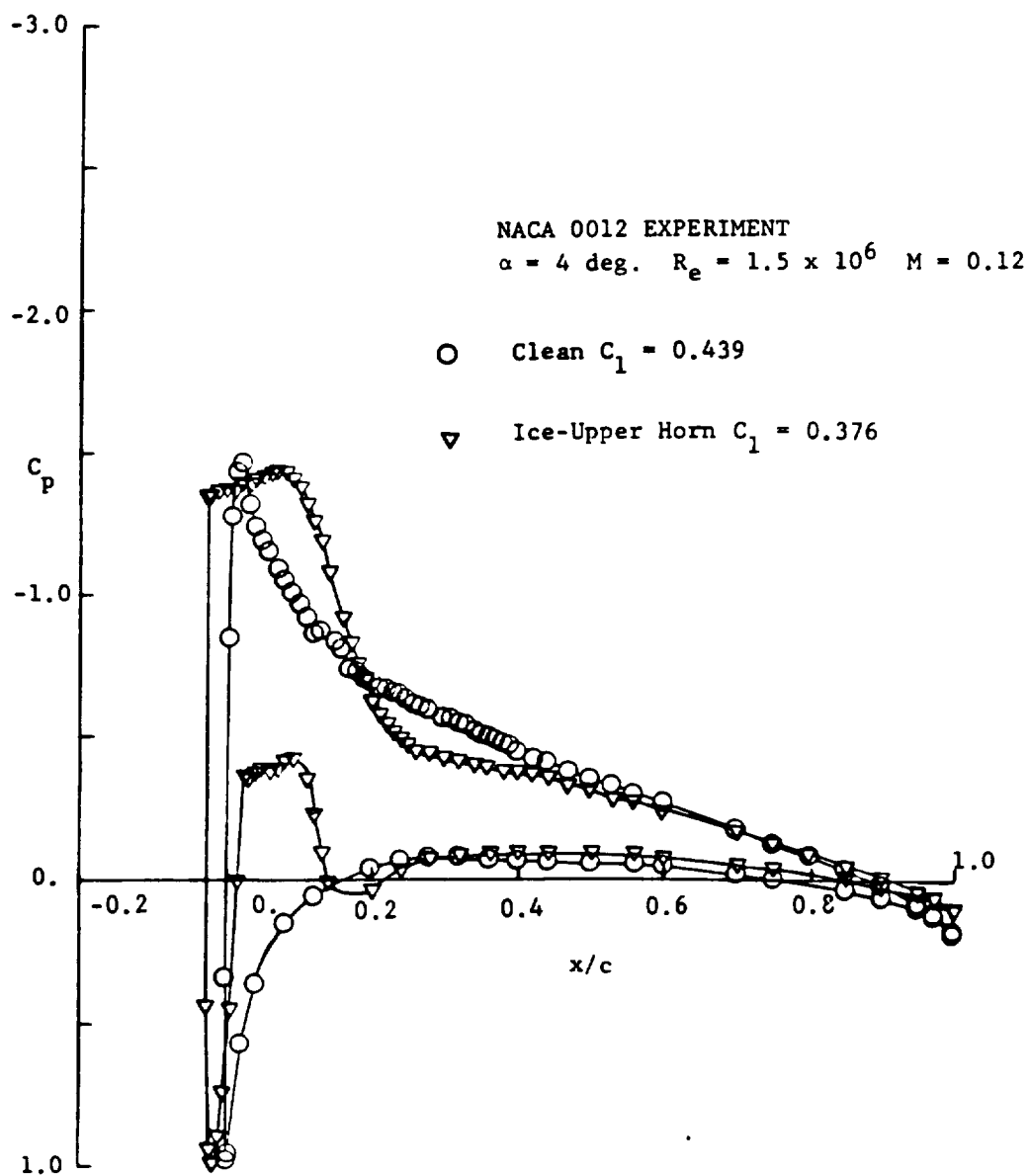


FIGURE 11. MEASURED SURFACE PRESSURES WITH AND WITHOUT  
 SIMULATED GLAZE ICE AT  $\alpha = 4 \text{ DEG.}$

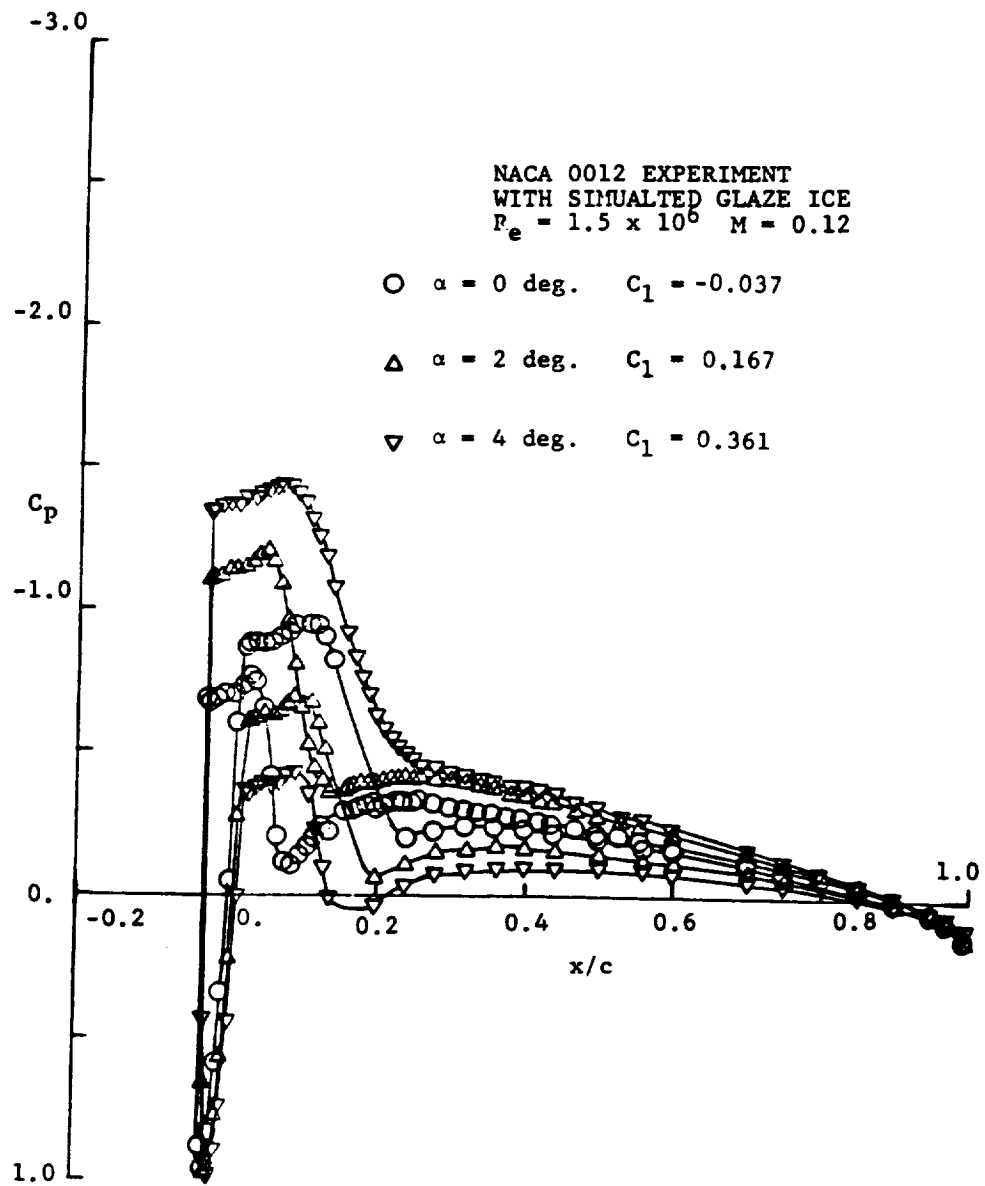


FIGURE 12. MEASURED SURFACE PRESSURES WITH SIMULATED ICE AT LOW ANGLES OF ATTACK.

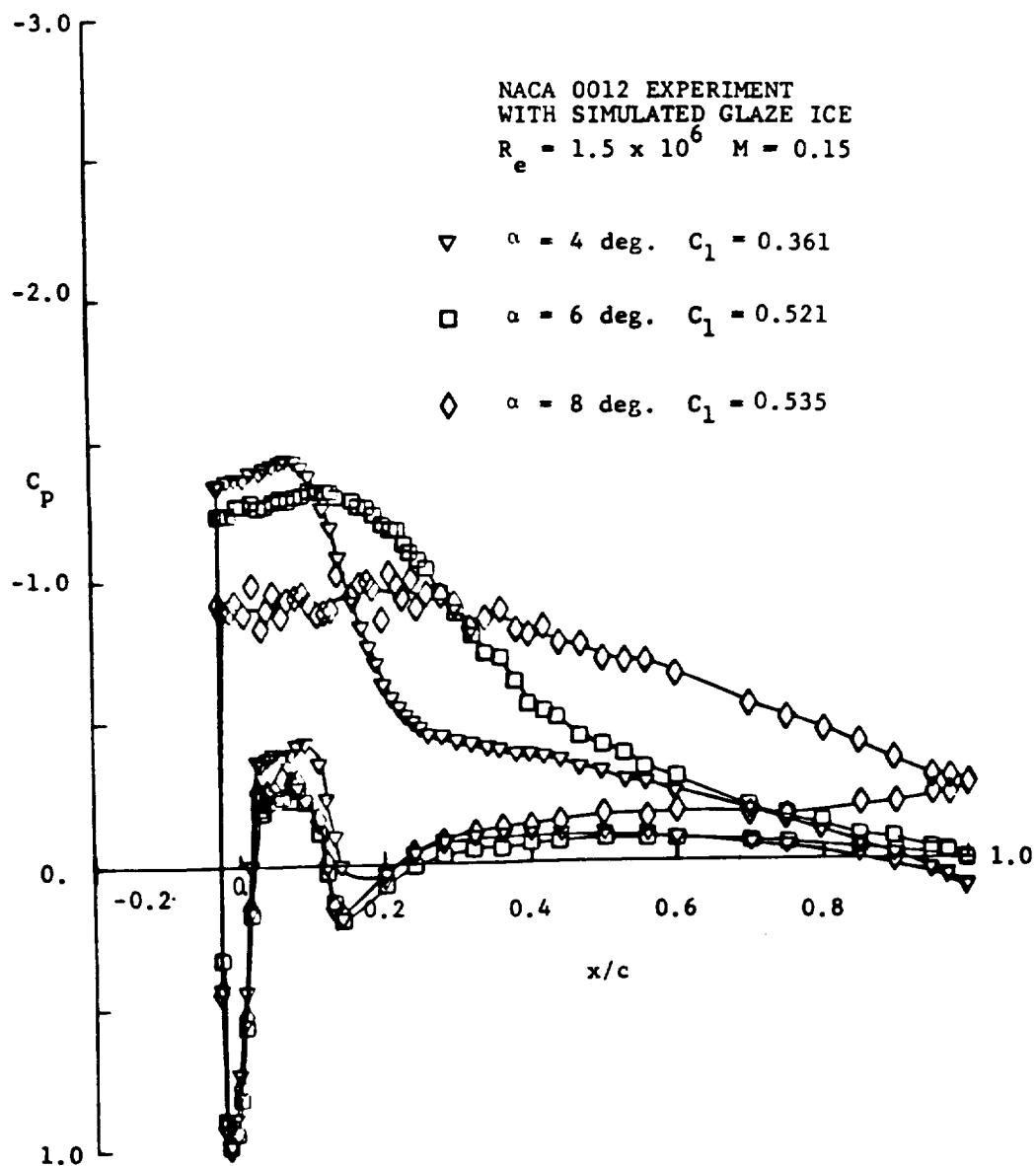


FIGURE 13. MEASURED SURFACE PRESSURES WITH SIMULATED ICE AT HIGH ANGLES OF ATTACK.

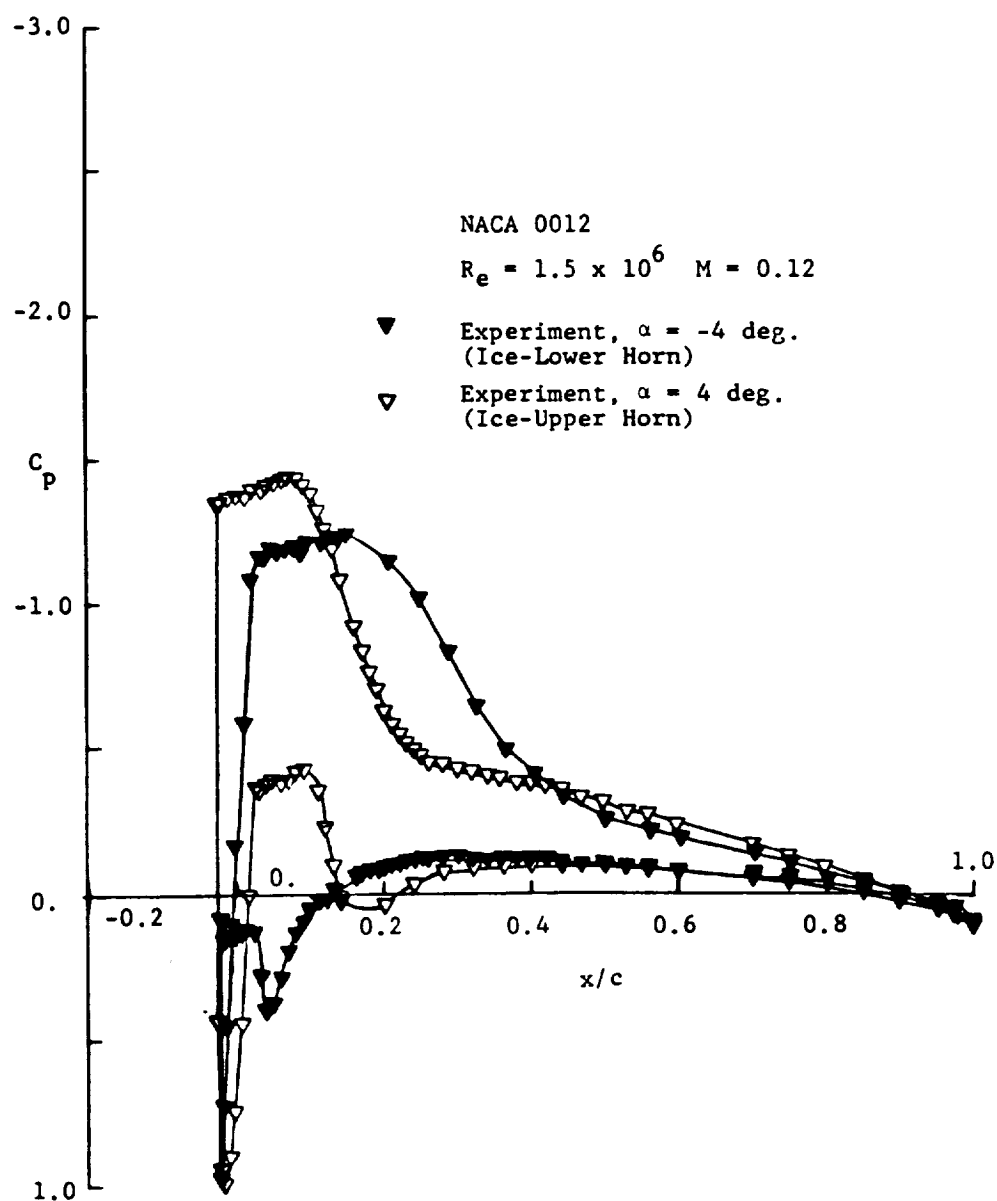


FIGURE 14. MEASURED SURFACE PRESSURES WITH SIMULATED ICE AT  $\alpha = -4$  and 4 DEG.

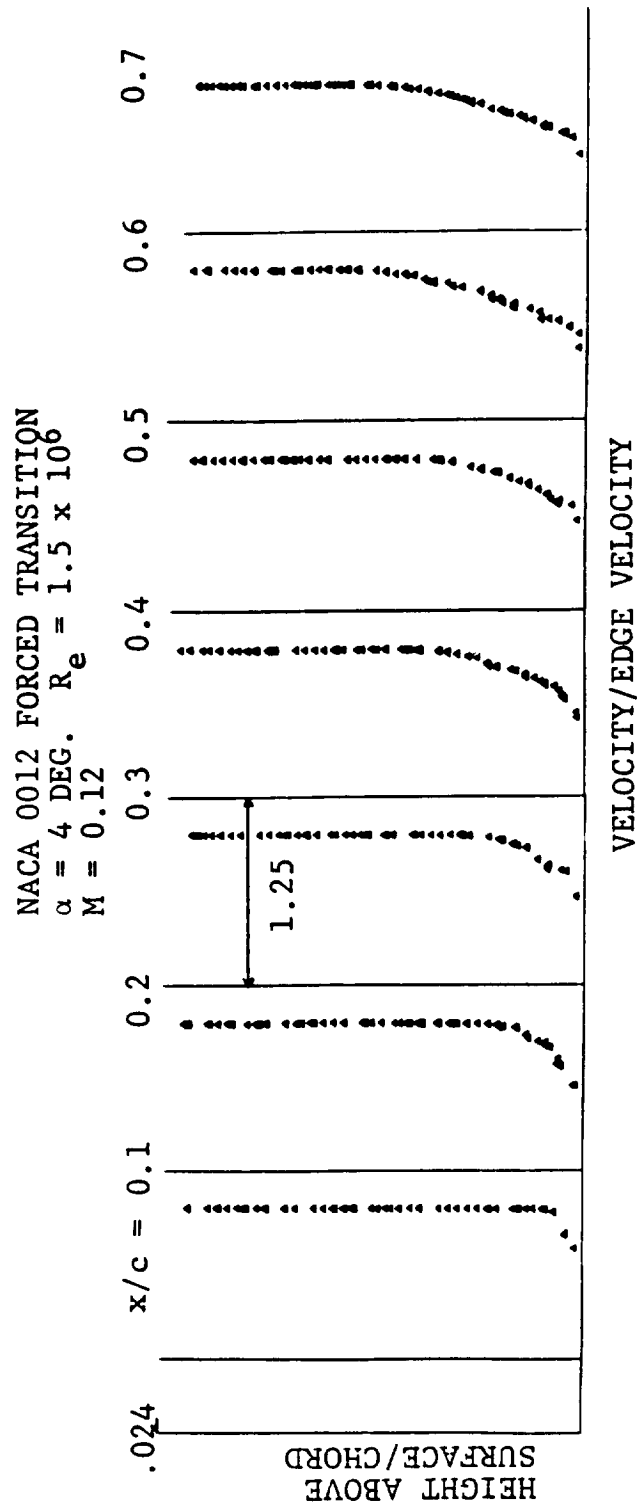


FIGURE 15. MEASURED BOUNDARY LAYER VELOCITY PROFILES ON A NACA 0012  
 AT  $\alpha = 4$  DEG. WITH FIXED TRANSITION.

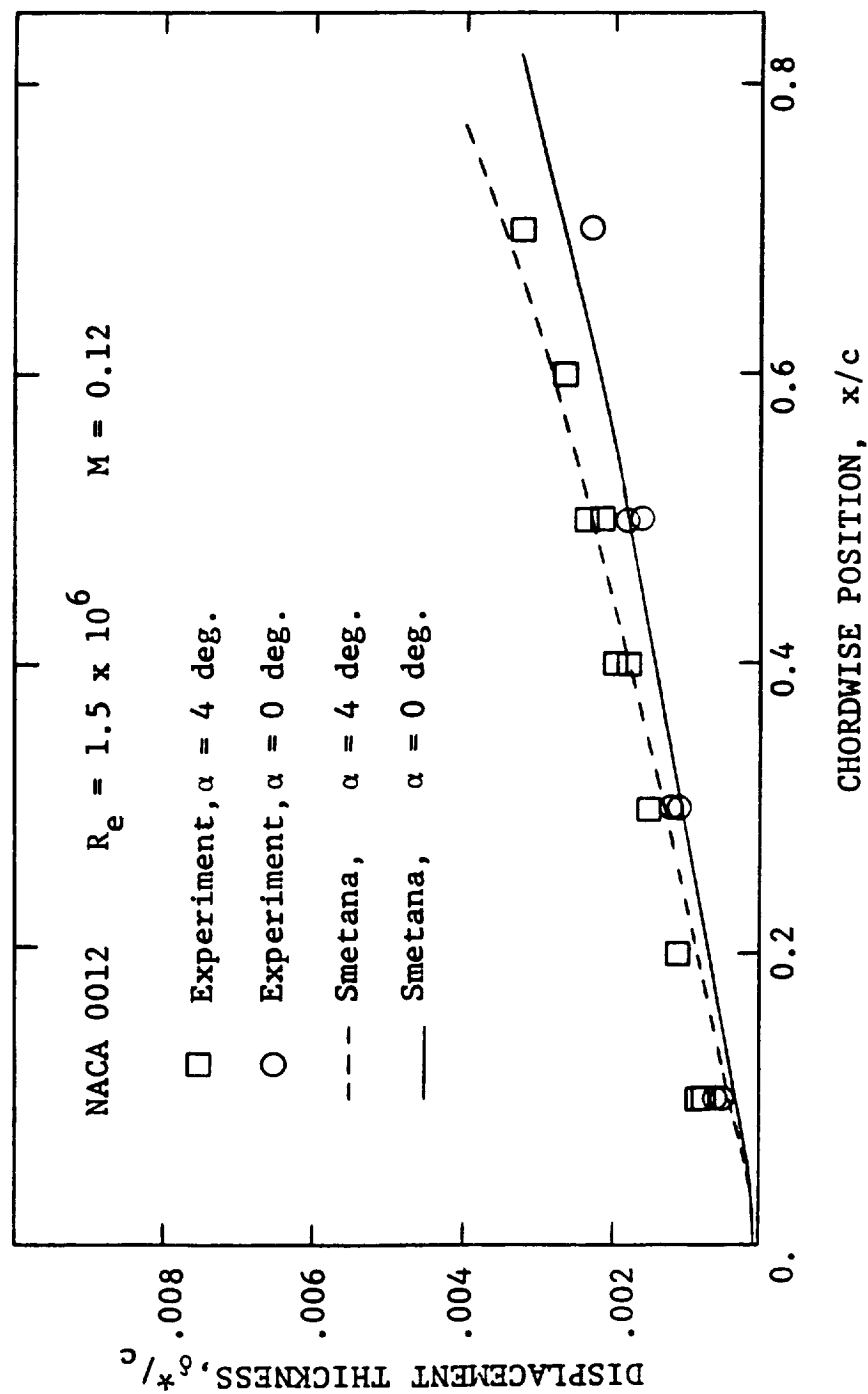


FIGURE 16. EXPERIMENTAL AND THEORETICAL BOUNDARY LAYER DISPLACEMENT THICKNESSES FOR A NACA 0012 WITH FIXED TRANSITION.

# EXISTING HOT FILM SUPPORT SYSTEM

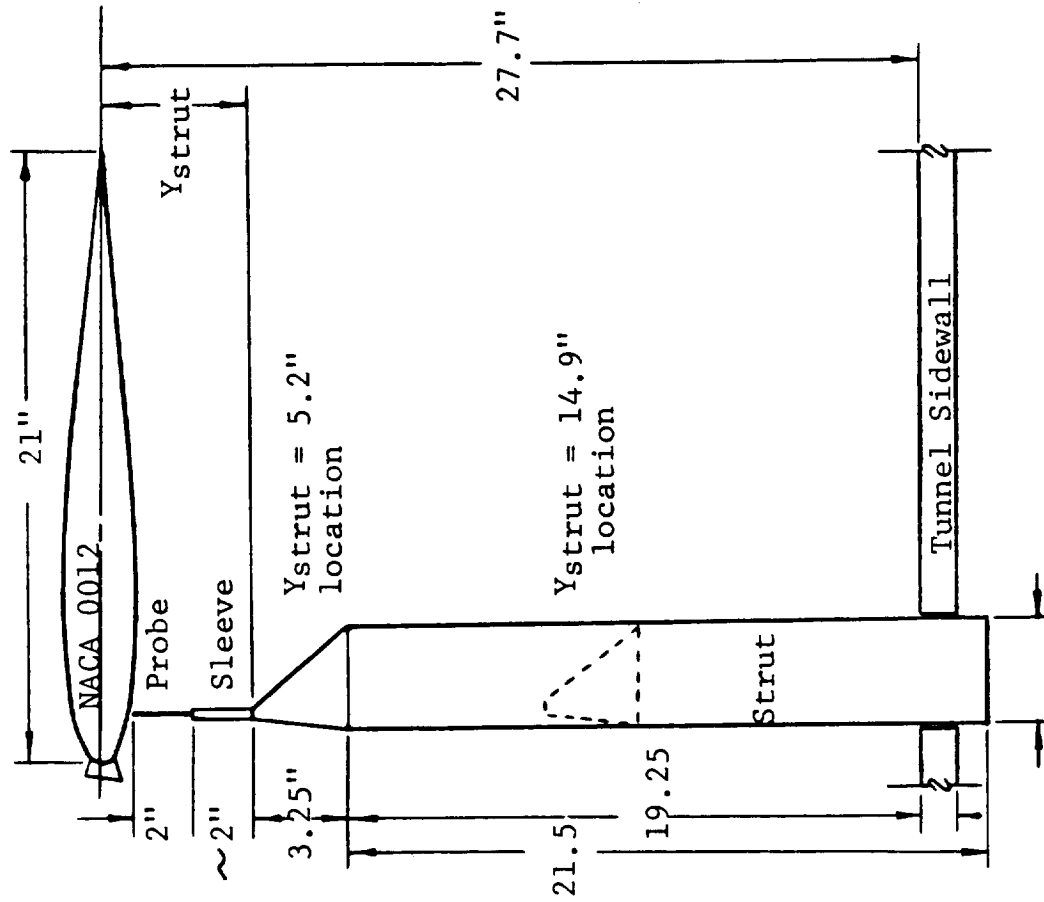


FIGURE 17. HOT FILM SUPPORT SYSTEM

# STRUT INTERFERENCE TEST

NACA 0012 Glaze Ice  $\alpha = 4$  deg.  $Re = .9 \times 10^6$

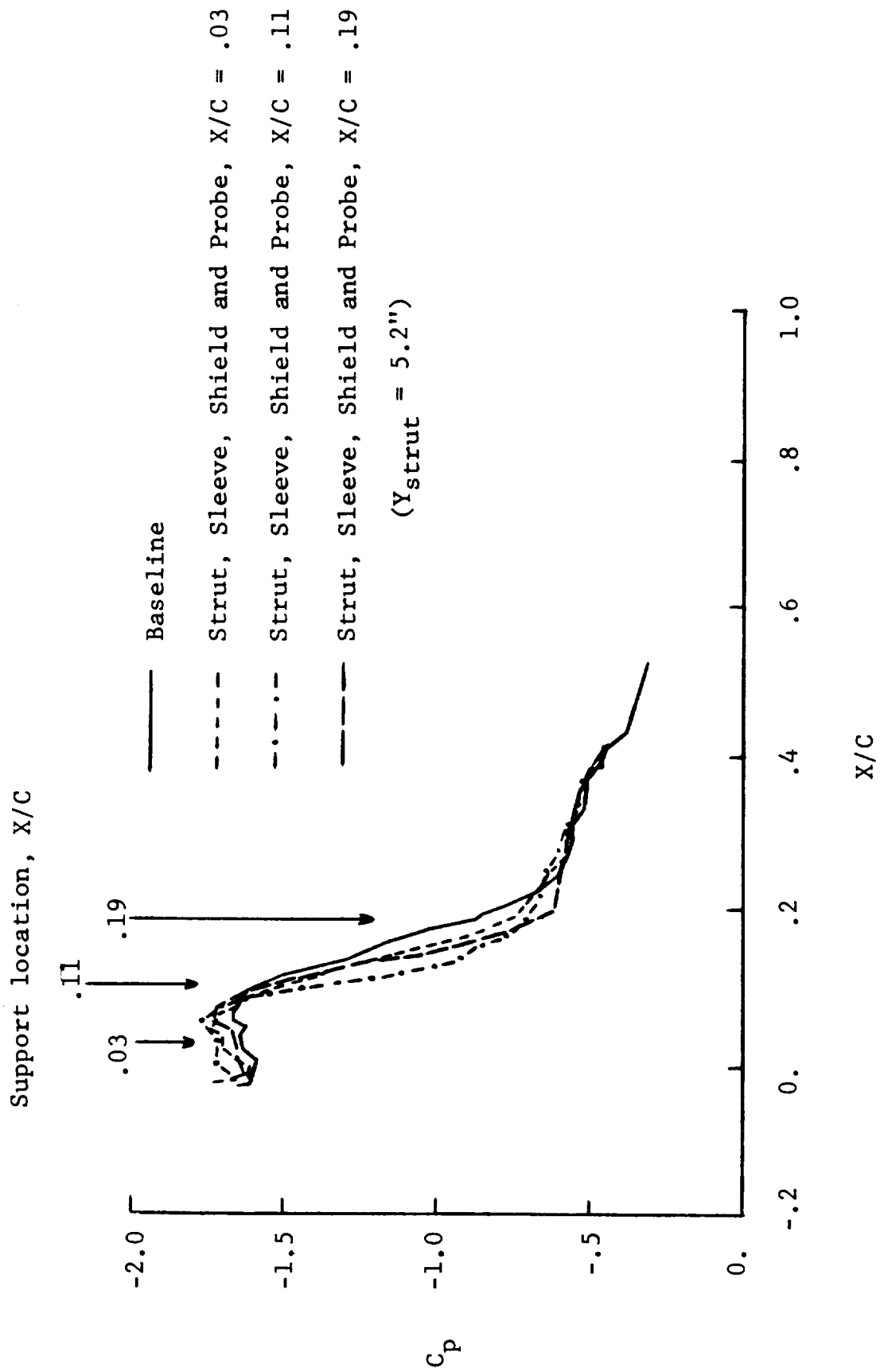
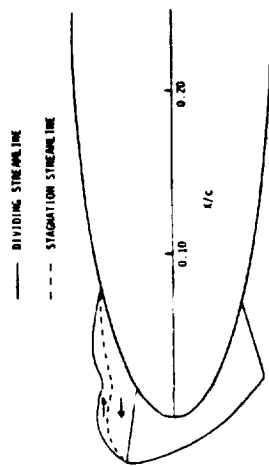


FIGURE 19. EFFECT OF PROBE ON AIRFOIL PRESSURE DISTRIBUTIONS FOR VARIOUS CHORDWISE LOCATIONS.





NACA 0012 WITH GLAZE ICE

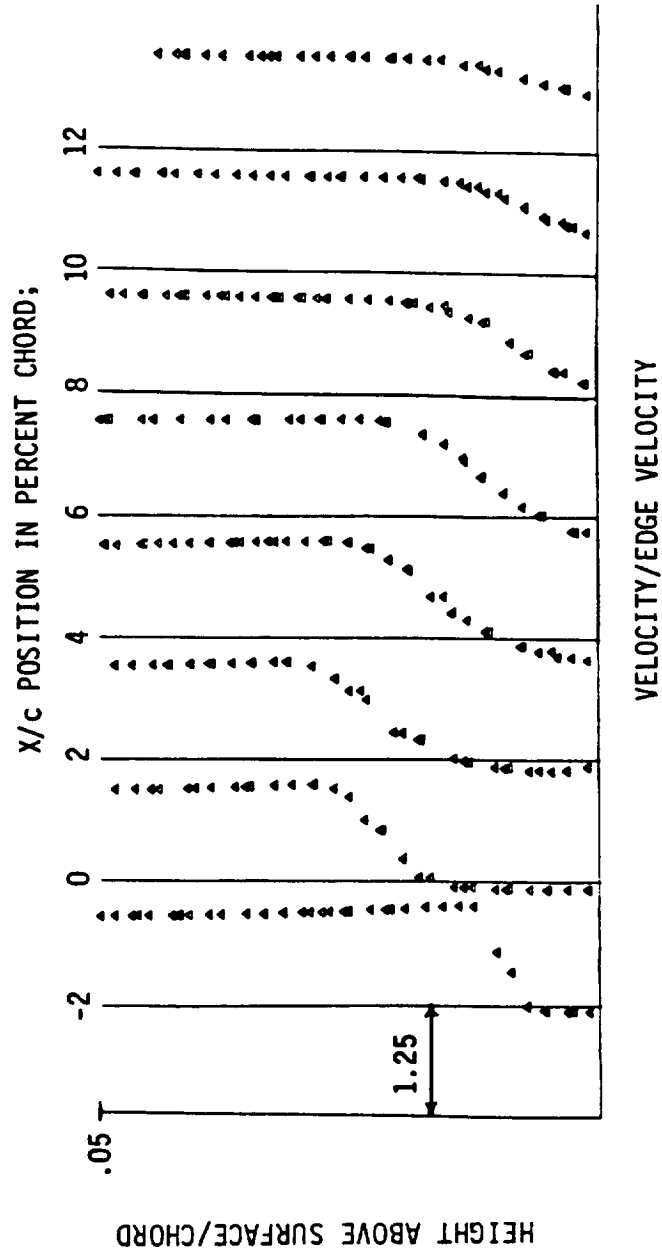
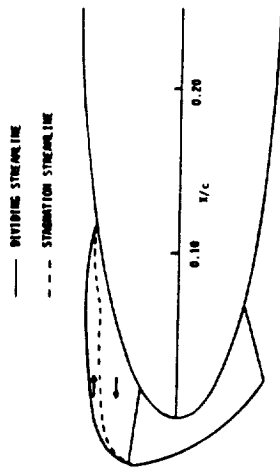


FIGURE 20. STREAMWISE COMPONENT OF VELOCITY PROFILES FOR A NACA 0012 AIRFOIL AT AN ANGLE OF ATTACK OF  $-0.15^\circ$ .  $Re = 1.5 \times 10^6$ , AND  $M = 0.12$ .



NACA 0012 WITH GLAZE ICE

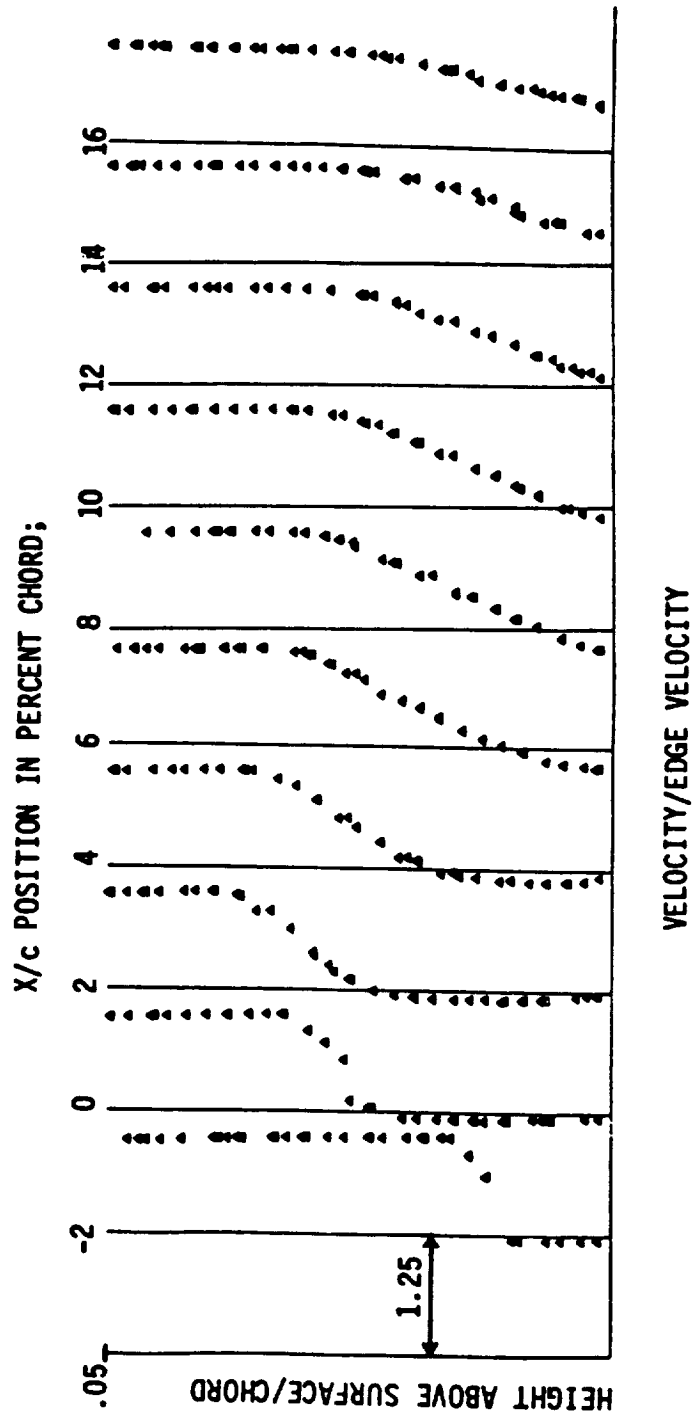


FIGURE 21. STREAMWISE COMPONENT OF VELOCITY PROFILES FOR A NACA 0012 AIRFOIL AT AN ANGLE OF ATTACK OF 1.85 DEG.,  $Re = 1.5 \times 10^6$ , AND  $M = 0.12$ .

NACA 0012 WITH GLAZE ICE

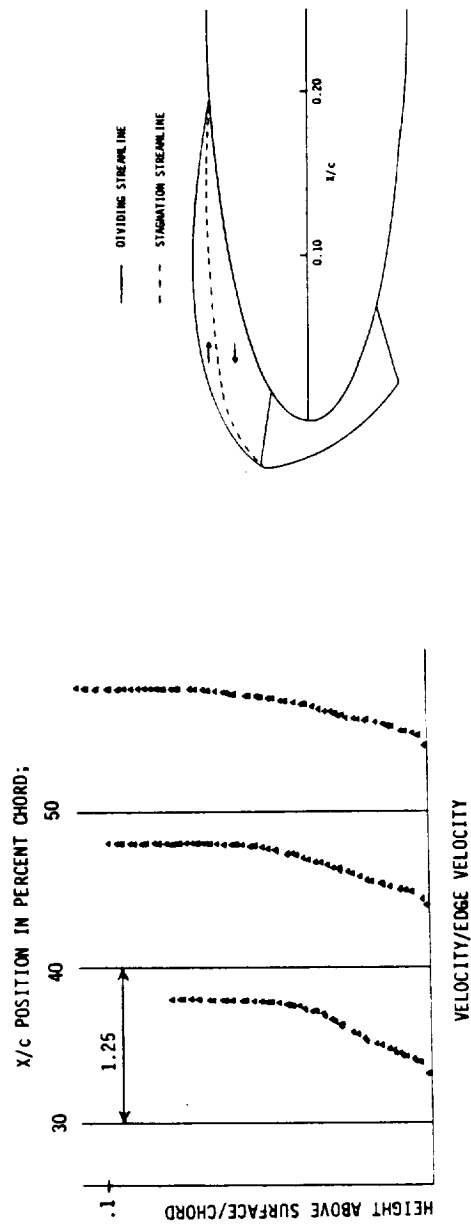
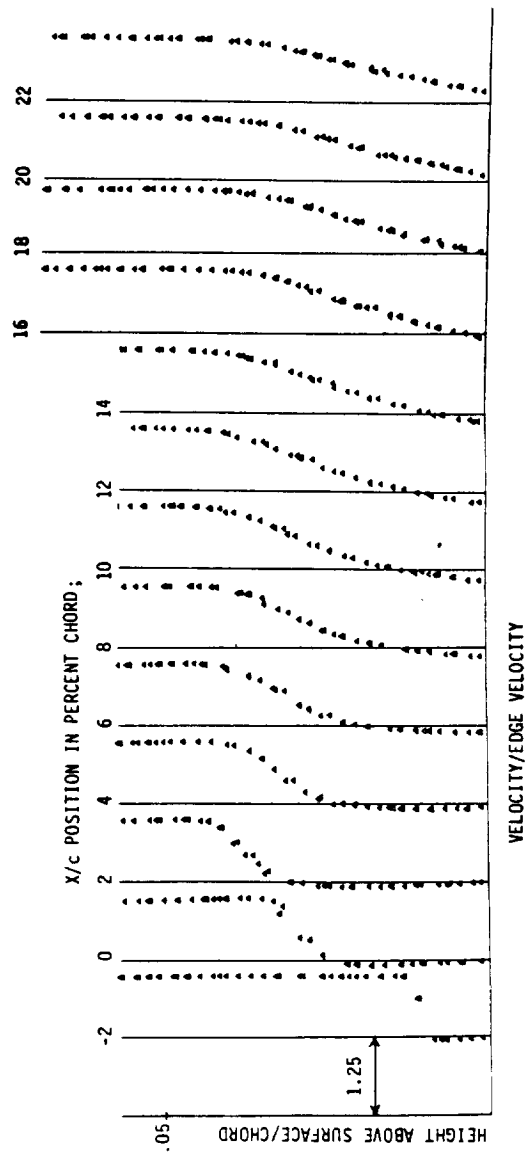


FIGURE 22. STREAMWISE COMPONENT OF VELOCITY PROFILES FOR A NACA 0012 AIRFOIL AT AN ANGLE OF ATTACK OF 3.85 DEG.,  $Re = 1.5 \times 10^6$ , AND  $M = 0.12$ .



## APPENDIX A

### RUN SUMMARIES

NACA 0012 MODEL NO. 1 - GLAZE ICE CONFIGURATION  
SPLIT FILM VELOCITY PROFILES

RUN	AOA (deg)	X/C	Re $\times 10^{-6}$	VEL (ft/s)	U-EDGE (ft/s)	$\delta^*$ /C $\times 10^3$	$\theta$ /C $\times 10^3$	Y-STAG/C	Y-SEP/C
236	-0.15	0.00	1.46	131.7	171.7	0.02146	0.42626	0.014721	0.020143
238	-0.15	-0.02	1.46	131.7	166.9	0.00950	0.35212	0.006662	0.008399
239	-0.15	0.02	1.46	131.7	170.0	0.02144	1.07510	0.012993	0.018715
240	-0.15	0.04	1.46	131.7	167.4	0.01697	0.77877	0.008640	0.014875
241	-0.15	0.06	1.42	133.5	176.1	0.01214	1.79805	0.004461	0.008394
242	-0.15	0.08	1.42	133.5	169.2	0.00737	3.05670	--	--
243	-0.15	0.10	1.44	132.7	160.6	0.00489	2.90518	--	--
244	-0.15	0.12	1.44	132.7	160.7	0.00375	2.56528	--	--
245	1.85	-0.02	1.44	132.7	184.2	0.01161	0.21754	0.008947	0.010372
246	1.85	0.00	1.44	132.7	200.5	0.01265	-0.17896	0.020703	0.025558
247	1.85	0.02	1.44	132.7	201.7	0.03009	0.46930	0.021808	0.028466
248	1.85	0.04	1.44	132.7	201.8	0.02606	0.91716	0.016222	0.023689
249	1.85	0.06	1.44	132.9	199.4	0.02066	1.88002	0.009068	0.016413
250	1.85	0.08	1.44	132.5	191.8	0.01703	2.68549	0.006024	0.011304
251	1.85	0.10	1.44	132.5	185.3	0.01478	3.49155	0.004404	0.006891
252	1.85	0.12	1.44	132.5	176.7	0.01116	4.33792	--	--
254	1.85	0.14	1.51	130.0	167.3	0.00835	4.28289	--	--
255	1.85	0.16	1.51	130.0	165.5	0.00704	4.42153	--	--
257	3.85	-0.02	1.51	130.0	180.0	0.01041	0.27493	0.008068	0.009076
258	3.85	0.00	1.51	130.0	202.4	0.02907	0.14864	0.022242	0.027926
262	3.85	0.02	1.54	129.0	200.0	0.03682	0.57272	--	--
263	3.85	0.04	1.53	129.3	197.9	0.03195	1.15141	0.019096	0.029356
264	3.85	0.06	1.53	129.3	197.6	0.03110	1.91804	0.018119	0.027221
265	3.85	0.08	1.53	129.3	198.2	0.02875	2.72787	0.012555	0.022697
267	3.85	0.10	1.49	130.6	212.3	0.02849	3.10515	0.012515	0.021727
268	3.85	0.12	1.49	130.6	208.9	0.02717	3.90636	0.009639	0.018506
269	3.85	0.14	1.49	130.6	205.6	0.02418	4.80094	0.007583	0.012813
270	3.85	0.16	1.49	130.6	197.4	0.02072	5.57149	0.002420	0.004897
271	3.85	0.18	1.49	130.6	192.9	0.01939	6.21330	--	--
272	3.85	0.20	1.49	130.6	186.8	0.01797	6.96573	--	--
273	3.85	0.22	1.49	130.6	183.3	0.01687	7.44755	--	--
274	3.85	0.30	1.49	130.6	175.4	0.01279	7.94107	--	--
275	3.85	0.40	1.49	130.6	169.5	0.01223	8.40160	--	--
276	3.85	0.50	1.49	130.6	166.5	0.01297	9.47147	--	--

NACA 0012 MODEL NO. 2 - CLEAN CONFIGURATION

RUN	ALPHA <sub>u</sub> (deg)	ALPHA (deg)	CL <sub>u</sub>	CL	CD <sub>u</sub>	CD	CM <sub>u</sub>	CM	MACH	Re x10 <sup>-6</sup>
364	0.00	0.00	-0.005	-0.005	0.0080	0.0078	0.0004	0.0003	0.126	1.465
365	0.00	0.00	-0.003	-0.003	0.0078	0.0076	0.0006	0.0005	0.126	1.484
366	1.00	1.03	0.101	0.096	0.0080	0.0078	0.0010	0.0017	0.126	1.484
367	2.00	2.06	0.208	0.198	0.0083	0.0081	0.0010	0.0025	0.126	1.489
368	3.00	3.09	0.318	0.303	0.0085	0.0083	0.0011	0.0034	0.126	1.506
369	4.00	4.12	0.434	0.414	0.0092	0.0090	0.0023	0.0053	0.126	1.507
370	5.00	5.15	0.535	0.511	0.0095	0.0093	0.0027	0.0065	0.126	1.499
371	6.00	6.18	0.652	0.622	0.0098	0.0096	0.0010	0.0056	0.126	1.500
372	7.00	7.21	0.774	0.738	0.0101	0.0099	-0.0014	0.0041	0.126	1.499
373	8.00	8.24	0.870	0.829	0.0114	0.0111	0.0004	0.0066	0.126	1.500
374	9.00	9.27	0.962	0.917	0.0127	0.0124	0.0036	0.0105	0.126	1.501
375	10.00	10.29	1.052	1.003	0.0142	0.0139	0.0058	0.0132	0.125	1.493
376	11.00	11.32	1.134	1.080	0.0165	0.0161	0.0088	0.0168	0.126	1.497
377	12.00	12.35	1.217	1.159	0.0205	0.0200	0.0127	0.0212	0.125	1.494
378	13.00	13.37	1.279	1.216	0.0261	0.0254	0.0152	0.0240	0.125	1.494
379	14.00	14.10	0.908	0.862	0.0317	0.0308	-0.1319	-0.1228	0.118	1.407
380	15.00	15.10	0.876	0.831	0.0373	0.0362	-0.1310	-0.1220	0.117	1.388
381	16.00	16.09	0.713	0.676	0.0429	0.0416	-0.0959	-0.0887	0.117	1.394
382	12.50	12.86	1.256	1.194	0.0233	0.0227	0.0146	0.0233	0.126	1.500
384	13.50	13.87	1.298	1.234	0.0289	0.0281	0.0179	0.0268	0.126	1.497
385	4.00	4.12	0.423	0.403	0.0092	0.0090	0.0021	0.0051	0.126	1.469
386	0.00	0.00	-0.007	-0.006	0.0072	0.0070	0.0004	0.0004	0.125	1.455
387	-2.00	-2.06	-0.228	-0.217	0.0078	0.0076	-0.0005	-0.0021	0.126	1.463
388	-4.00	-4.12	-0.437	-0.417	0.0075	0.0073	-0.0037	-0.0067	0.125	1.452
389	-6.00	-6.18	-0.681	-0.650	0.0067	0.0065	0.0011	-0.0038	0.125	1.459
390	-8.00	-8.24	-0.900	-0.857	0.0127	0.0124	0.0009	-0.0055	0.126	1.469
391	-6.00	-6.19	-0.683	-0.651	0.0069	0.0067	0.0010	-0.0039	0.126	1.462
392	-5.00	-5.16	-0.563	-0.537	0.0077	0.0075	-0.0031	-0.0070	0.125	1.455
393	-10.00	-10.30	-1.084	-1.032	0.0170	0.0166	-0.0061	-0.0137	0.127	1.478
394	-10.00	-10.30	-1.077	-1.025	0.0170	0.0166	-0.0063	-0.0139	0.125	1.458
395	-12.00	-12.35	-1.240	-1.178	0.0272	0.0265	-0.0114	-0.0200	0.125	1.458
396	-14.00	-14.16	-1.015	-0.963	0.0374	0.0363	0.1055	0.0960	0.116	1.353
397	-15.00	-15.17	-1.057	-1.002	0.0425	0.0412	0.1087	0.0987	0.115	1.333
398	-13.00	-13.37	-1.299	-1.233	0.0323	0.0314	-0.0159	-0.0248	0.125	1.455
399	-13.50	-13.87	-1.191	-1.129	0.0349	0.0339	-0.0445	-0.0520	0.117	1.360
400	0.00	0.00	-0.015	-0.014	0.0087	0.0085	0.0003	0.0002	0.168	2.018
401	1.00	1.03	0.097	0.093	0.0081	0.0079	0.0002	0.0008	0.168	2.025
402	2.00	2.06	0.203	0.194	0.0083	0.0081	0.0006	0.0020	0.168	2.017
403	3.00	3.08	0.301	0.287	0.0086	0.0084	0.0002	0.0024	0.168	2.022
404	4.00	4.11	0.407	0.388	0.0087	0.0085	0.0008	0.0037	0.168	2.016
405	5.00	5.14	0.523	0.499	0.0098	0.0096	0.0017	0.0054	0.167	2.011
406	6.00	6.17	0.622	0.594	0.0099	0.0097	0.0004	0.0048	0.168	2.016
407	7.00	7.20	0.742	0.708	0.0099	0.0097	-0.0009	0.0045	0.167	2.009
408	7.00	7.20	0.744	0.710	0.0089	0.0087	-0.0010	0.0044	0.166	1.964
409	5.00	5.14	0.523	0.499	0.0087	0.0085	0.0012	0.0050	0.166	1.964
410	3.00	3.08	0.300	0.286	0.0083	0.0081	0.0001	0.0023	0.165	1.955
412	0.00	0.00	-0.004	-0.004	0.0076	0.0074	0.0004	0.0004	0.167	1.980
413	8.00	8.23	0.843	0.803	0.0112	0.0109	0.0001	0.0062	0.166	1.959

RUN	ALPHA <sub>u</sub> (deg)	ALPHA (deg)	CL <sub>u</sub>	CL	CD <sub>u</sub>	CD	CM <sub>u</sub>	CM	MACH	Re x10 <sup>-6</sup>
414	-2.00	-2.06	-0.224	-0.213	0.0071	0.0069	0.0000	-0.0016	0.167	1.970
415	-2.00	-2.06	-0.222	-0.212	0.0076	0.0074	0.0000	-0.0016	0.166	1.960
416	-4.00	-4.12	-0.420	-0.401	0.0082	0.0080	-0.0014	-0.0044	0.167	1.970
417	-6.00	-6.18	-0.646	-0.616	0.0085	0.0083	-0.0015	-0.0061	0.168	1.981
418	-8.00	-8.24	-0.868	-0.827	0.0114	0.0111	0.0003	-0.0059	0.167	1.974
420	9.00	9.26	0.929	0.886	0.0119	0.0116	0.0023	0.0089	0.165	1.948
421	10.00	10.28	1.014	0.967	0.0140	0.0137	0.0048	0.0120	0.165	1.948
422	11.00	11.31	1.098	1.046	0.0158	0.0154	0.0069	0.0146	0.164	1.942
423	12.00	12.33	1.184	1.127	0.0184	0.0179	0.0093	0.0176	0.164	1.940
425	13.00	13.36	1.254	1.193	0.0220	0.0214	0.0116	0.0204	0.163	1.935
426	14.00	14.15	0.965	0.917	0.0256	0.0249	-0.1052	-0.0963	0.148	1.749
427	13.50	13.68	1.034	0.983	0.0238	0.0232	-0.0942	-0.0850	0.151	1.788
428	-10.00	-10.29	-1.035	-0.986	0.0165	0.0161	-0.0040	-0.0113	0.166	1.958
429	-10.00	-10.29	-1.034	-0.985	0.0165	0.0161	-0.0036	-0.0109	0.166	1.960
430	-12.00	-12.34	-1.201	-1.142	0.0227	0.0221	-0.0100	-0.0183	0.166	1.957
431	-14.00	-14.20	-1.110	-1.054	0.0289	0.0281	0.0919	0.0822	0.153	1.800
432	-13.00	-13.36	-1.267	-1.205	0.0258	0.0251	-0.0120	-0.0208	0.166	1.955
433	-13.50	-13.87	-1.292	-1.228	0.0274	0.0267	-0.0129	-0.0218	0.165	1.951

NACA 0012 MODEL NO. 2 - ICED CONFIGURATION

RUN	ALPHA <sub>u</sub> (deg)	ALPHA (deg)	CL <sub>u</sub>	CL	CD <sub>u</sub>	CD	CM <sub>u</sub>	CM	MACH	Re x10 <sup>-6</sup>
434	0.00	-0.02	-0.039	-0.037	0.0282	0.0274	-0.0106	-0.0106	0.127	1.476
435	4.00	4.12	0.381	0.361	0.0399	0.0387	0.0134	0.0158	0.127	1.467
436	4.00	4.12	0.385	0.364	0.0401	0.0389	0.0140	0.0164	0.123	1.421
437	4.00	4.12	0.380	0.361	0.0401	0.0389	0.0147	0.0171	0.123	1.420
438	4.00	4.12	0.380	0.361	0.0390	0.0379	0.0135	0.0159	0.123	1.421
439	0.00	-0.02	-0.043	-0.041	0.0258	0.0251	-0.0103	-0.0104	0.124	1.428
440	1.00	1.01	0.070	0.066	0.0261	0.0254	-0.0056	-0.0050	0.124	1.429
441	2.00	2.05	0.176	0.167	0.0283	0.0275	0.0007	0.0019	0.124	1.426
442	3.00	3.08	0.274	0.260	0.0333	0.0324	0.0066	0.0084	0.124	1.457
443	4.00	4.12	0.380	0.360	0.0405	0.0393	0.0144	0.0167	0.123	1.455
444	5.00	5.15	0.478	0.452	0.0537	0.0520	0.0177	0.0207	0.123	1.452
445	6.00	6.16	0.553	0.521	0.0763	0.0735	0.0075	0.0112	0.122	1.443
446	7.00	7.14	0.601	0.561	0.1141	0.1092	-0.0252	-0.0201	0.121	1.431
447	8.00	8.10	0.577	0.535	0.1519	0.1442	-0.0549	-0.0485	0.121	1.438
448	9.00	9.07	0.521	0.479	0.1897	0.1787	-0.0704	-0.0633	0.120	1.429
449	0.00	-0.02	-0.038	-0.036	0.0270	0.0263	-0.0095	-0.0096	0.124	1.483
450	-2.00	-2.09	-0.251	-0.238	0.0345	0.0335	-0.0172	-0.0187	0.124	1.482
451	-4.00	-4.14	-0.444	-0.420	0.0494	0.0479	-0.0194	-0.0220	0.123	1.477
452	-4.00	-4.14	-0.443	-0.420	0.0503	0.0487	-0.0203	-0.0230	0.123	1.406
453	-6.00	-6.13	-0.577	-0.544	0.0649	0.0627	0.0218	0.0171	0.121	1.392
454	-8.00	-8.08	-0.516	-0.486	0.0798	0.0769	0.0553	0.0500	0.120	1.379
455	-7.00	-7.11	-0.547	-0.515	0.0724	0.0698	0.0332	0.0284	0.120	1.377
456	-6.00	-6.13	-0.580	-0.547	0.0649	0.0627	0.0232	0.0185	0.121	1.389
457	-5.00	-5.15	-0.536	-0.505	0.0686	0.0662	-0.0043	-0.0079	0.122	1.402
458	0.00	-0.02	-0.043	-0.041	0.0272	0.0265	-0.0101	-0.0102	0.161	1.883
459	2.00	2.05	0.167	0.159	0.0287	0.0279	0.0008	0.0020	0.161	1.880
460	4.00	4.11	0.364	0.345	0.0417	0.0405	0.0135	0.0158	0.160	1.870



RUN	ALPHA <sub>u</sub> (deg)	ALPHA (deg)	CL <sub>u</sub>	CL	CD <sub>u</sub>	CD	CM <sub>u</sub>	CM	MACH	Re x10 <sup>-6</sup>
461	6.00	6.15	0.535	0.504	0.0769	0.0741	0.0052	0.0088	0.157	1.840
462	8.00	8.11	0.575	0.537	0.1121	0.1073	-0.0443	-0.0387	0.154	1.798
463	7.00	7.12	0.568	0.532	0.0945	0.0908	-0.0294	-0.0244	0.155	1.815
464	9.00	9.06	0.489	0.455	0.1297	0.1237	-0.0679	-0.0618	0.152	1.775
465	-2.00	-2.08	-0.238	-0.226	0.0342	0.0332	-0.0178	-0.0192	0.160	1.875
466	-2.00	-2.09	-0.239	-0.227	0.0342	0.0332	-0.0181	-0.0194	0.161	1.904
467	-4.00	-4.14	-0.424	-0.401	0.0506	0.0490	-0.0199	-0.0225	0.160	1.890
468	-6.00	-6.15	-0.546	-0.513	0.0837	0.0806	0.0038	-0.0002	0.157	1.858
469	-8.00	-8.16	-0.644	-0.601	0.1168	0.1117	0.0187	0.0135	0.154	1.826
470	-9.00	-9.16	-0.688	-0.640	0.1334	0.1271	0.0280	0.0221	0.153	1.806
471	-10.00	-10.16	-0.729	-0.676	0.1499	0.1424	0.0360	0.0294	0.150	1.777
472	-10.00	-10.05	-0.414	-0.384	0.1499	0.1424	0.0549	0.0496	0.152	1.794
473	-8.00	-8.10	-0.545	-0.508	0.1168	0.1117	0.0491	0.0435	0.153	1.814
474	-6.00	-6.13	-0.537	-0.504	0.0900	0.0865	0.0144	0.0101	0.157	1.859
475	-4.00	-4.14	-0.426	-0.403	0.0506	0.0490	-0.0185	-0.0211	0.160	1.894
476	-7.00	-7.13	-0.582	-0.546	0.0947	0.0909	0.0261	0.0211	0.156	1.840
477	0.00	-0.02	-0.048	-0.046	0.0250	0.0243	-0.0104	-0.0106	0.075	0.848
478	2.00	2.05	0.182	0.173	0.0278	0.0271	0.0002	0.0015	0.075	0.853
479	4.00	4.12	0.396	0.375	0.0392	0.0381	0.0143	0.0168	0.075	0.849
480	6.00	6.17	0.575	0.542	0.0718	0.0693	0.0122	0.0160	0.074	0.844
481	8.00	8.11	0.596	0.558	0.1044	0.1001	-0.0490	-0.0432	0.073	0.830
482	9.00	9.08	0.571	0.533	0.1210	0.1156	-0.0735	-0.0668	0.073	0.826
483	7.00	7.14	0.624	0.586	0.0880	0.0846	-0.0243	-0.0192	0.074	0.836
484	-2.00	-2.09	-0.269	-0.256	0.0302	0.0294	-0.0187	-0.0203	0.075	0.849
485	-4.00	-4.15	-0.470	-0.445	0.0477	0.0462	-0.0208	-0.0237	0.075	0.845
486	-6.00	-6.14	-0.603	-0.566	0.0839	0.0807	0.0216	0.0167	0.074	0.834
487	-8.00	-8.07	-0.528	-0.494	0.1044	0.1001	0.0651	0.0592	0.073	0.826
488	-7.00	-7.10	-0.581	-0.546	0.0880	0.0846	0.0527	0.0470	0.074	0.833
489	-5.00	-5.17	-0.567	-0.535	0.0669	0.0646	-0.0094	-0.0132	0.074	0.842
490	0.00	-0.03	-0.050	-0.047	0.0250	0.0243	-0.0105	-0.0107	0.075	0.862
491	2.00	2.05	0.177	0.169	0.0278	0.0271	0.0011	0.0023	0.075	0.861
492	4.00	4.12	0.398	0.378	0.0392	0.0381	0.0143	0.0168	0.074	0.857
493	6.00	6.17	0.583	0.549	0.0718	0.0693	0.0117	0.0155	0.074	0.851
494	-4.00	-4.15	-0.469	-0.444	0.0477	0.0462	-0.0210	-0.0238	0.074	0.856
495	-2.00	-2.09	-0.258	-0.245	0.0302	0.0294	-0.0196	-0.0211	0.075	0.861
500	0.00	0.00	-0.011	-0.010	0.0078	0.0076	0.0006	0.0005	0.075	0.872
501	2.00	2.06	0.213	0.203	0.0077	0.0075	0.0013	0.0028	0.075	0.873
502	4.00	4.12	0.435	0.415	0.0088	0.0086	0.0030	0.0060	0.076	0.875
503	6.00	6.19	0.691	0.659	0.0089	0.0087	-0.0026	0.0024	0.076	0.876
504	8.00	8.24	0.888	0.846	0.0129	0.0126	0.0021	0.0084	0.076	0.875
505	10.00	10.30	1.061	1.010	0.0165	0.0161	0.0086	0.0160	0.076	0.876
506	10.00	10.30	1.061	1.010	0.0169	0.0165	0.0092	0.0166	0.076	0.876
507	12.00	12.34	1.189	1.131	0.0244	0.0238	0.0166	0.0247	0.075	0.873
508	14.00	14.12	0.842	0.800	0.0319	0.0310	-0.1027	-0.0946	0.072	0.832
509	13.00	13.32	1.166	1.108	0.0282	0.0274	0.0011	0.0094	0.075	0.871
510	12.50	12.84	1.188	1.129	0.0263	0.0256	0.0170	0.0251	0.075	0.872
511	-2.00	-2.06	-0.233	-0.222	0.0082	0.0080	-0.0010	-0.0026	0.076	0.879
512	-4.00	-4.13	-0.452	-0.431	0.0100	0.0098	-0.0035	-0.0067	0.076	0.896
513	-6.00	-6.19	-0.714	-0.681	0.0137	0.0134	0.0061	0.0009	0.076	0.899
514	-6.00	-6.19	-0.710	-0.677	0.0133	0.0130	0.0060	0.0008	0.076	0.895

RUN	ALPHA <sub>u</sub> (deg)	ALPHA (deg)	CL <sub>u</sub>	CL	CD <sub>u</sub>	CD	CM <sub>u</sub>	CM	MACH	Re x10 <sup>-6</sup>
515	4.00	4.12	0.433	0.413	0.0080	0.0078	0.0024	0.0055	0.076	0.901
516	-8.00	-8.25	-0.909	-0.866	0.0146	0.0142	-0.0029	-0.0093	0.076	0.900
517	-10.00	-10.31	-1.093	-1.040	0.0192	0.0187	-0.0097	-0.0173	0.076	0.902
518	-12.00	-12.35	-1.210	-1.150	0.0269	0.0262	-0.0163	-0.0246	0.076	0.894
519	-14.00	-14.12	-0.847	-0.804	0.0346	0.0336	0.1031	0.0949	0.073	0.858
520	-13.00	-13.32	-1.164	-1.105	0.0308	0.0300	0.0005	-0.0078	0.076	0.895
521	-12.50	-12.85	-1.197	-1.138	0.0288	0.0280	-0.0191	-0.0272	0.076	0.900

NACA 0012 MODEL NO. 2 - CLEAN CONFIGURATION  
TRIP AT X/C = 0.05 (BOTH UPPER AND LOWER SURFACES)

RUN	ALPHA <sub>u</sub> (deg)	ALPHA (deg)	CL <sub>u</sub>	CL	CD <sub>u</sub>	CD	CM <sub>u</sub>	CM	MACH	Re x10 <sup>-6</sup>
748	0.00	0.00	-0.006	-0.006	0.0081	0.0079	-0.0025	-0.0025	0.116	1.387
749	8.00	8.25	0.875	0.832	0.0108	0.0105	-0.0015	0.0051	0.116	1.386
750	8.00	8.25	0.880	0.837	0.0111	0.0108	-0.0025	0.0042	0.116	1.387
751	0.00	0.00	-0.006	-0.006	0.0109	0.0106	-0.0001	-0.0002	0.116	1.374
* 752	2.00	2.06	0.217	0.207	0.0111	0.0108	0.0007	0.0023	0.117	1.384
* 753	4.00	4.13	0.438	0.417	0.0115	0.0112	0.0004	0.0037	0.116	1.380
* 754	2.00	2.06	0.208	0.198	0.0110	0.0107	-0.0013	0.0003	0.117	1.385
* 755	4.00	4.12	0.430	0.409	0.0116	0.0113	-0.0012	0.0021	0.117	1.391
* 756	6.00	6.19	0.653	0.620	0.0136	0.0133	0.0006	0.0055	0.116	1.381
* 757	8.00	8.25	0.849	0.806	0.0139	0.0135	0.0045	0.0109	0.117	1.390
* 758	10.00	10.31	1.038	0.986	0.0176	0.0171	0.0083	0.0161	0.115	1.370
* 759	12.00	12.36	1.198	1.136	0.0247	0.0240	0.0139	0.0226	0.116	1.373
760	14.00	14.13	0.932	0.882	0.0318	0.0309	-0.1248	-0.1151	0.109	1.293
761	13.00	13.38	1.247	1.181	0.0299	0.0290	0.0167	0.0257	0.116	1.375
762	-4.00	-4.14	-0.463	-0.440	0.0125	0.0122	-0.0030	-0.0065	0.117	1.394
763	-8.00	-8.26	-0.856	-0.812	0.0173	0.0168	-0.0055	-0.0119	0.116	1.380
764	-13.00	-13.37	-1.190	-1.127	0.0283	0.0275	-0.0184	-0.0270	0.109	1.295
765	-14.00	-14.19	-0.939	-0.889	0.0318	0.0309	0.0728	0.0641	0.113	1.337
766	-12.00	-12.36	-1.174	-1.112	0.0285	0.0277	-0.0160	-0.0246	0.116	1.376

\* NOTE: Pressure difference between transducers.

NACA 0012 MODEL NO. 2 - CLEAN CONFIGURATION  
 TRIP AT X/C = 0.05  
 TOTAL BOUNDARY LAYER PROBE VELOCITY PROFILES

RUN	AOA	X/C	Re	VEL	U-EDGE	$\delta^*/C$	$\Theta/C$
	(deg)		$\times 10^{-6}$	(ft/s)	(ft/s)	$\times 10^3$	$\times 10^3$
788	3.85	0.03	1.43	131.8	151.8	3.20166	2.10189
789	3.85	0.03	1.41	130.7	151.1	3.21301	2.10328
790	3.85	0.02	1.42	131.6	163.9	2.15226	1.42940
791	3.85	0.02	1.42	131.1	163.3	2.33087	1.50410
792	3.85	0.02	1.42	131.3	162.9	2.37040	1.57792
793	3.85	0.02	1.41	130.8	162.8	2.76799	1.79168
794	3.85	0.01	1.42	131.2	162.7	1.53397	0.93361
795	3.85	0.01	1.42	131.0	163.9	1.69846	1.02513
796	3.85	0.00	1.42	131.3	194.0	0.77307	0.43989
797	3.85	0.00	1.43	132.5	194.8	0.88946	0.55715
798	-0.15	0.03	1.43	131.1	148.0	2.30661	1.57829
799	-0.15	0.03	1.43	132.4	147.9	2.28867	1.52718
801	-0.15	0.02	1.44	132.0	155.8	1.58051	1.03879
802	-0.15	0.02	1.43	130.4	155.5	1.80664	1.17000
803	-0.15	0.01	1.44	131.8	159.4	1.10019	0.67952
804	-0.15	0.01	1.44	131.6	159.4	1.24502	0.77926
805	-0.15	0.00	1.44	131.5	159.2	0.53174	0.24111
807	-0.15	0.00	1.44	131.6	159.8	0.62718	0.33051
808	-0.15	0.01	1.49	132.9	179.8	1.12362	0.65278
811	-0.15	0.02	1.48	132.8	168.2	1.72779	1.12934
812	-0.15	0.02	1.48	132.3	168.0	1.95480	1.22531
813	-0.15	0.03	1.48	132.2	155.4	2.63122	1.74612



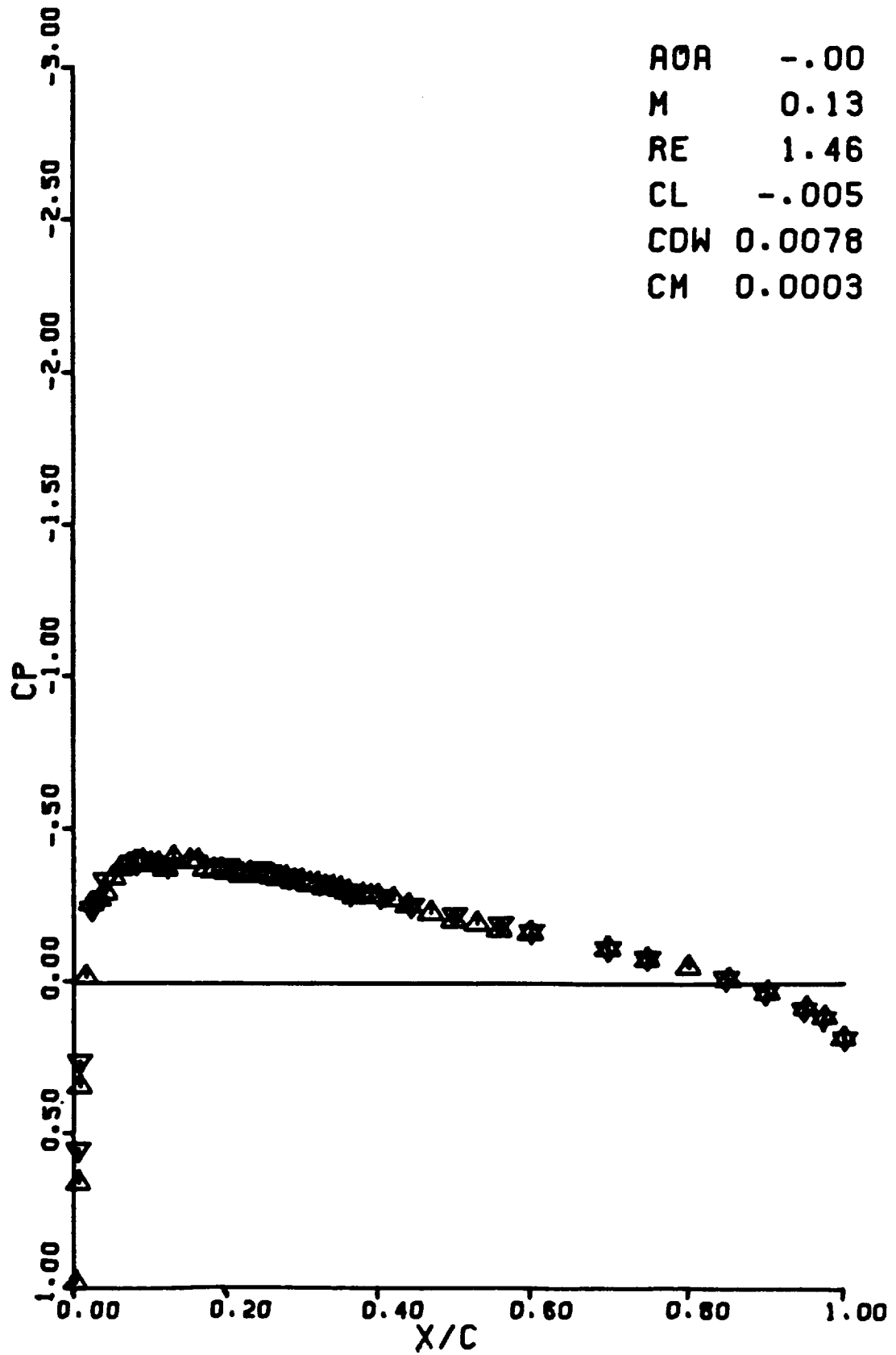
APPENDIX B

PRESSURE DISTRIBUTIONS

PRECEDING PAGE BLANK NOT FILMED

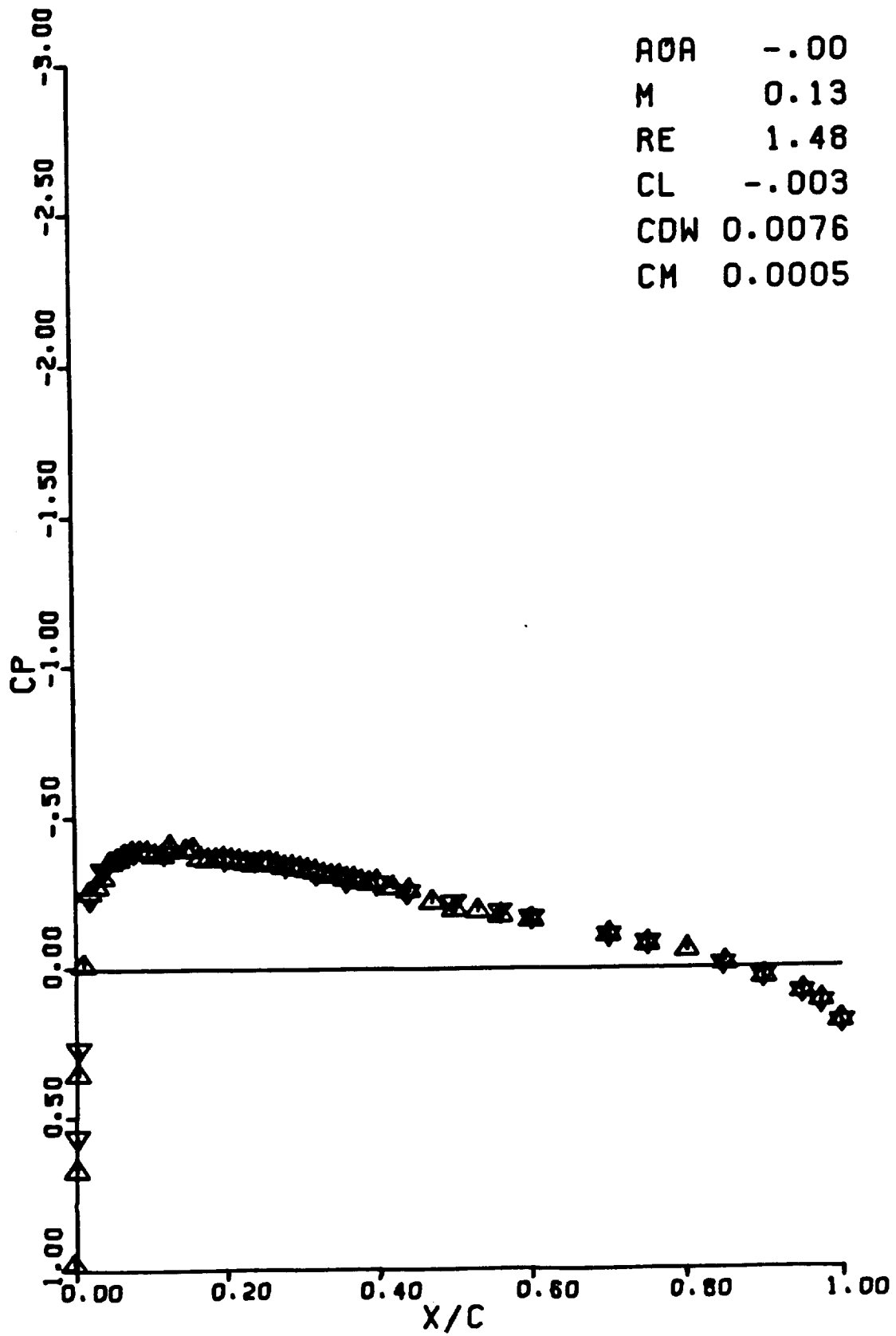
RUN 0364

AOA -.00  
M 0.13  
RE 1.46  
CL -.005  
CDW 0.0078  
CM 0.0003



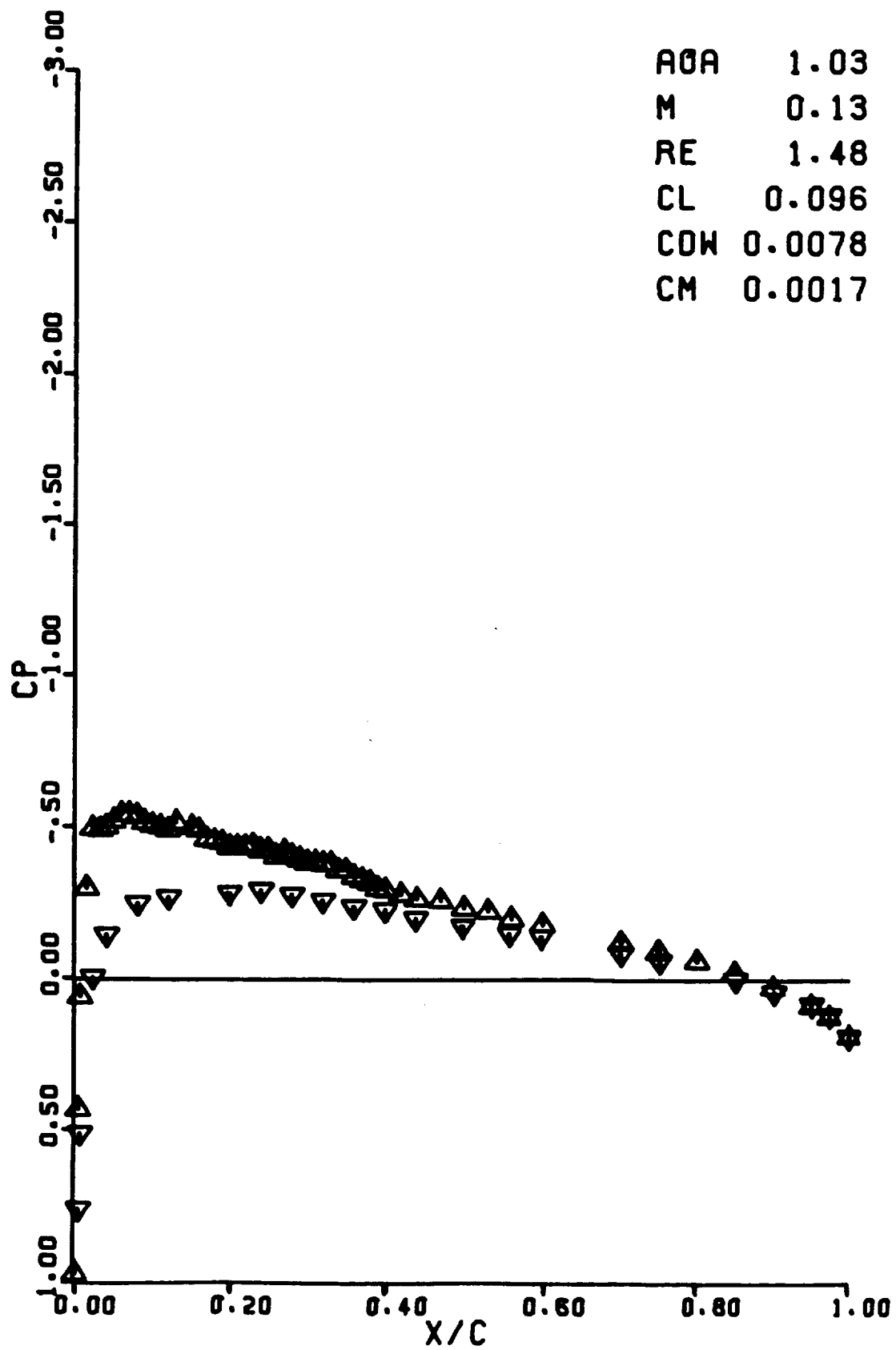
RUN 0365

AOA -.00  
M 0.13  
RE 1.48  
CL -.003  
CDW 0.0076  
CM 0.0005



RUN 0366

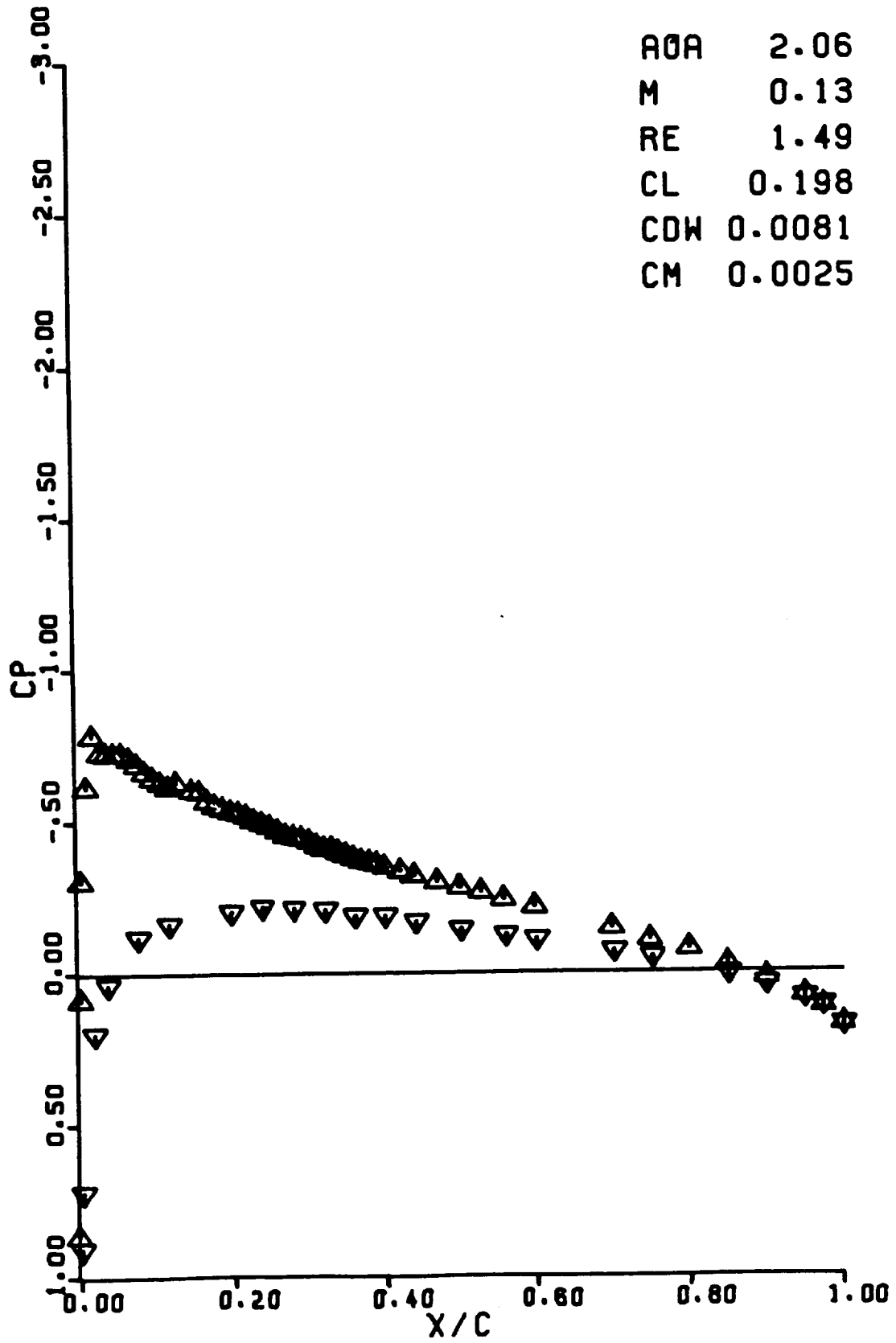
AOA 1.03  
M 0.13  
RE 1.48  
CL 0.096  
CDW 0.0078  
CM 0.0017





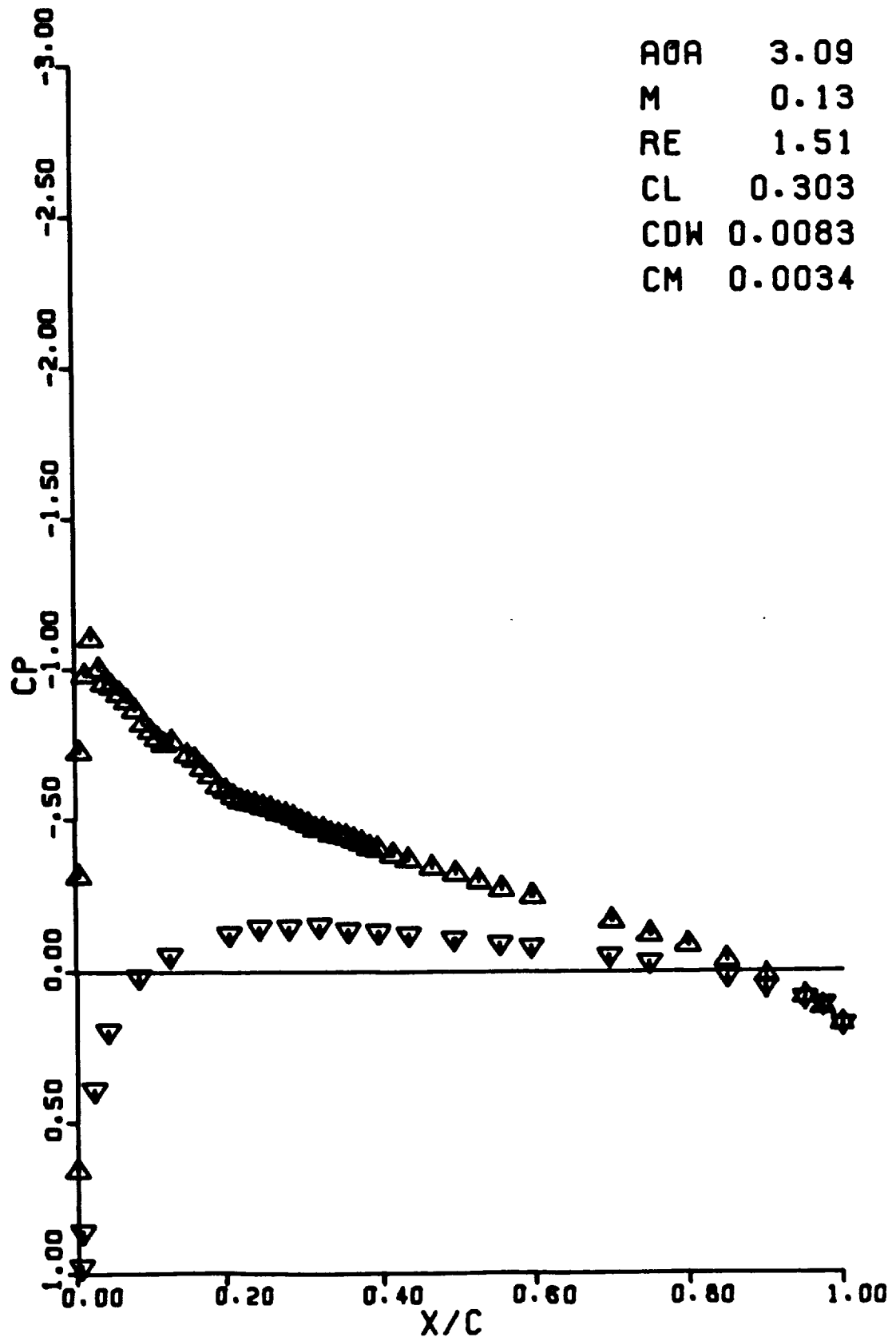
RUN 0367

AOA 2.06  
M 0.13  
RE 1.49  
CL 0.198  
CDW 0.0081  
CM 0.0025



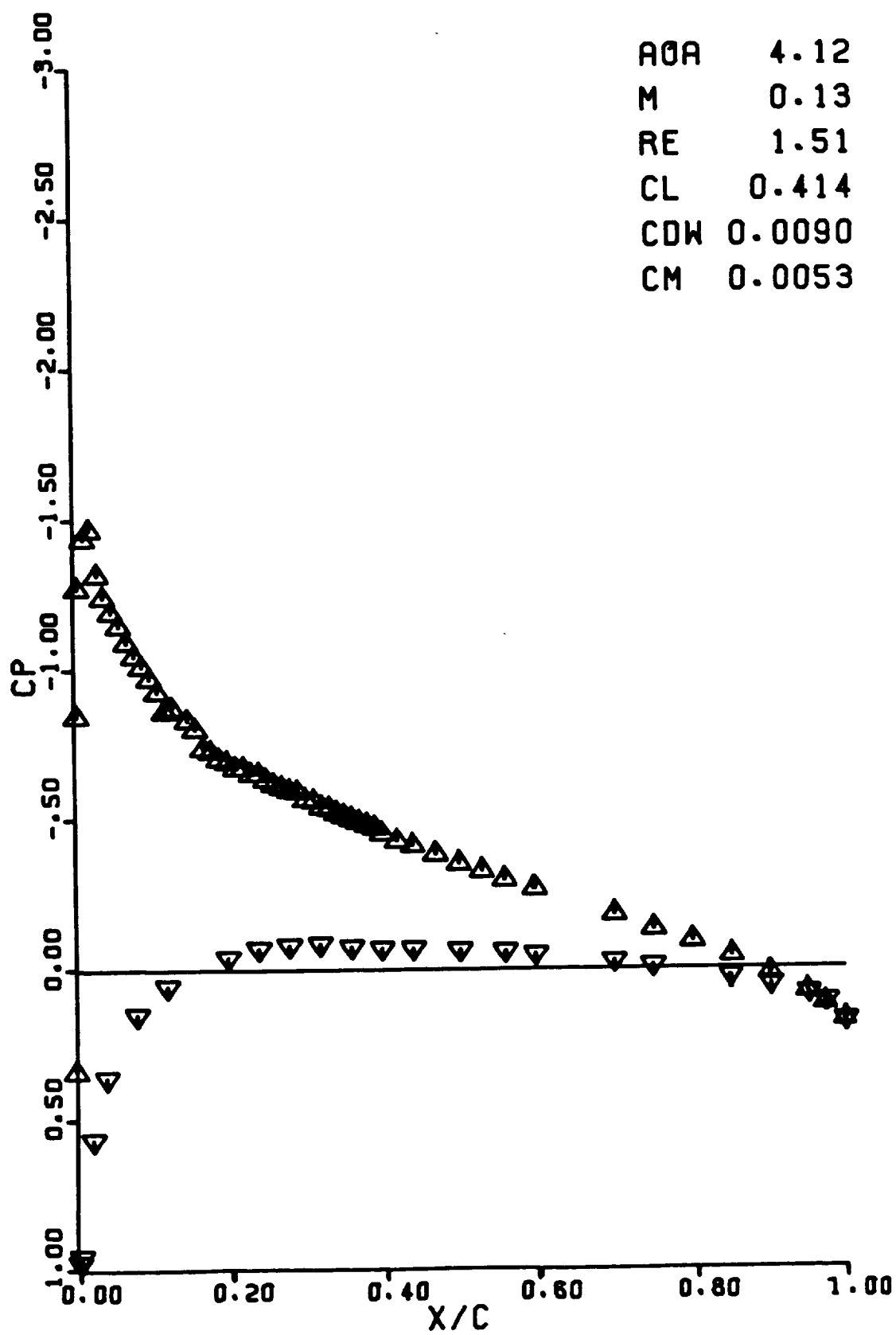
RUN 0368

AOA 3.09  
M 0.13  
RE 1.51  
CL 0.303  
CDW 0.0083  
CM 0.0034



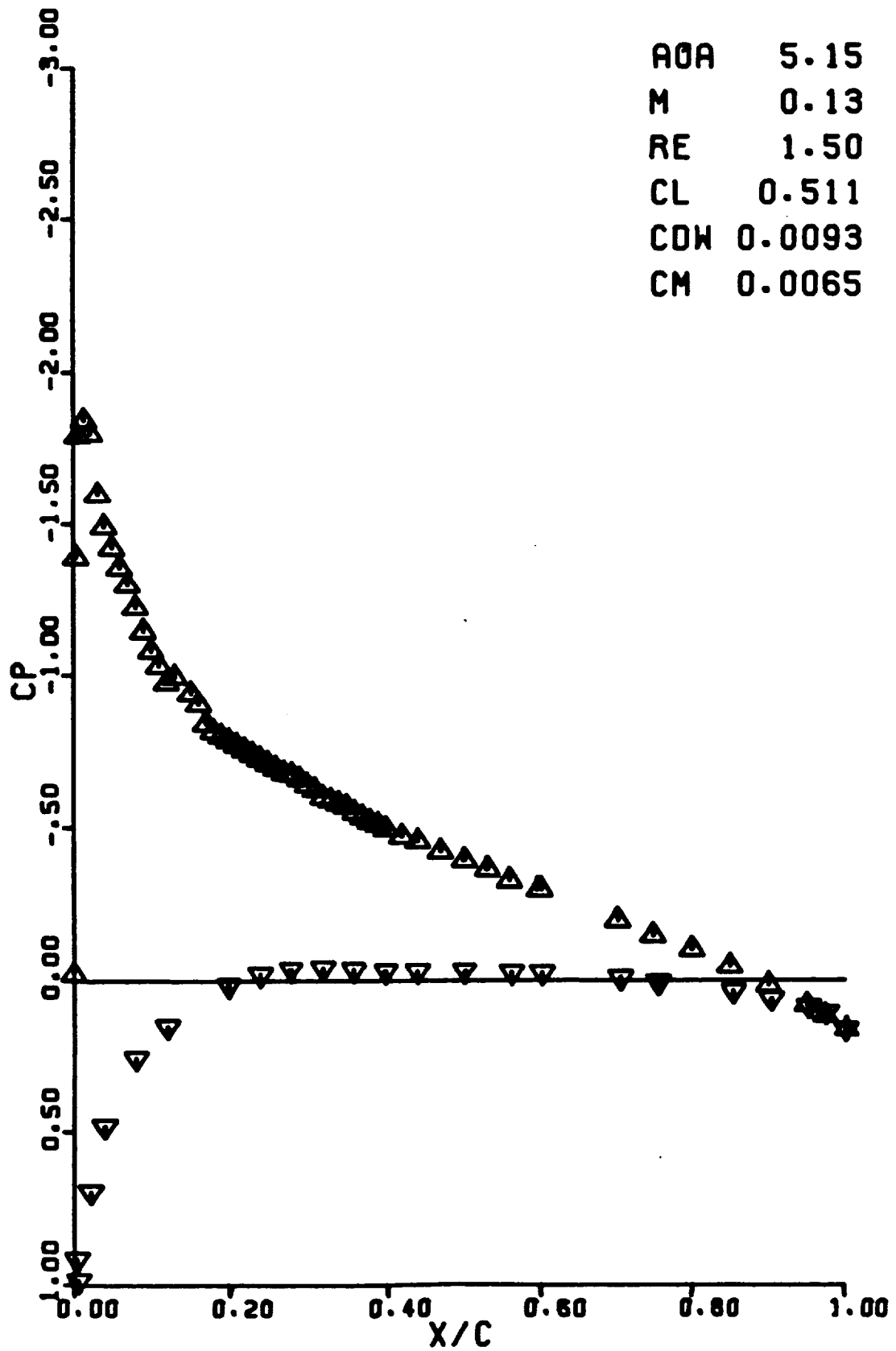
RUN 0369

AOA 4.12  
M 0.13  
RE 1.51  
CL 0.414  
CDW 0.0090  
CM 0.0053



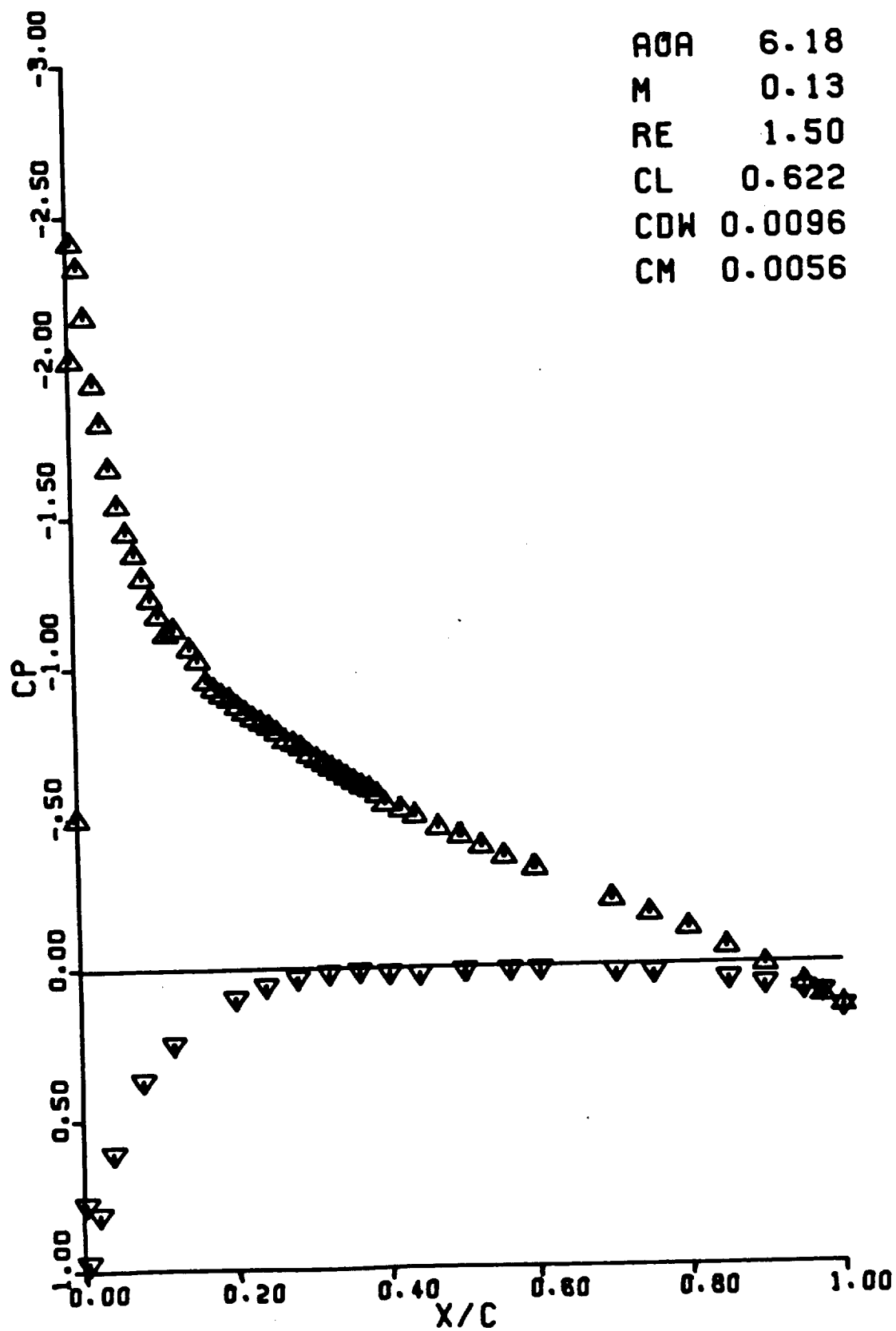
RUN 0370

AOA 5.15  
M 0.13  
RE 1.50  
CL 0.511  
CDW 0.0093  
CM 0.0065



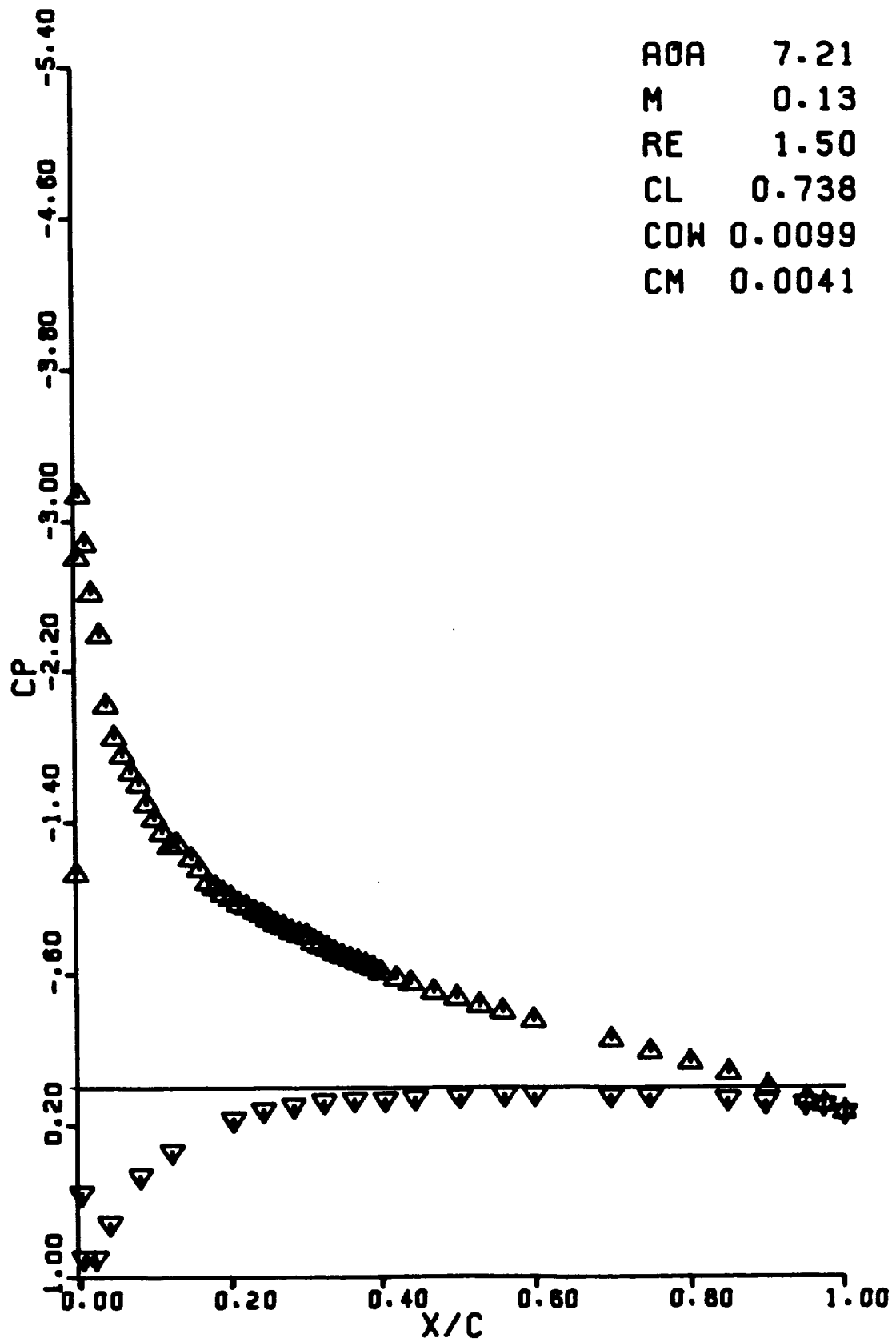
RUN 0371

AOA 6.18  
M 0.13  
RE 1.50  
CL 0.622  
CDW 0.0096  
CM 0.0056



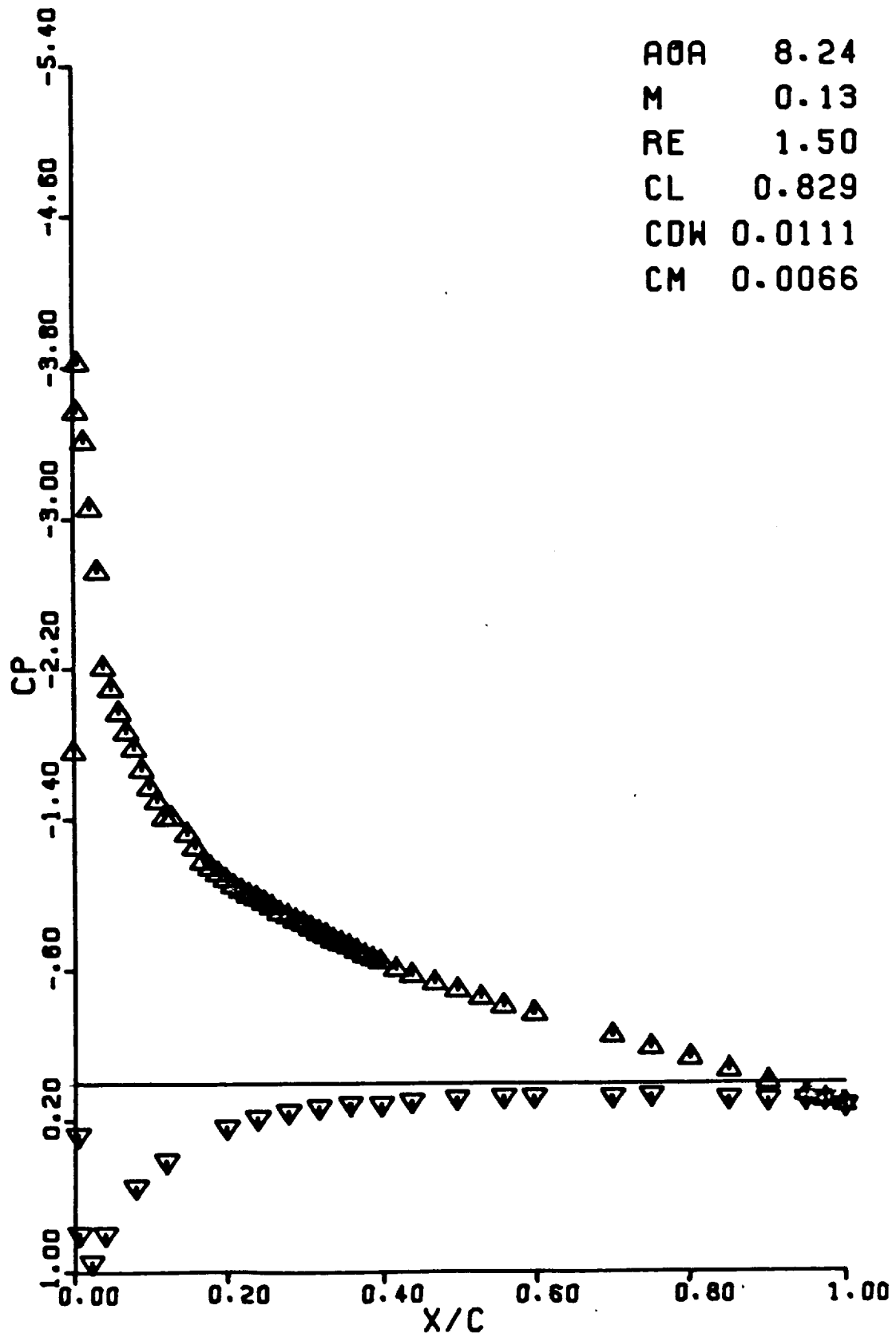
RUN 0372

AOA 7.21  
M 0.13  
RE 1.50  
CL 0.738  
CDW 0.0099  
CM 0.0041



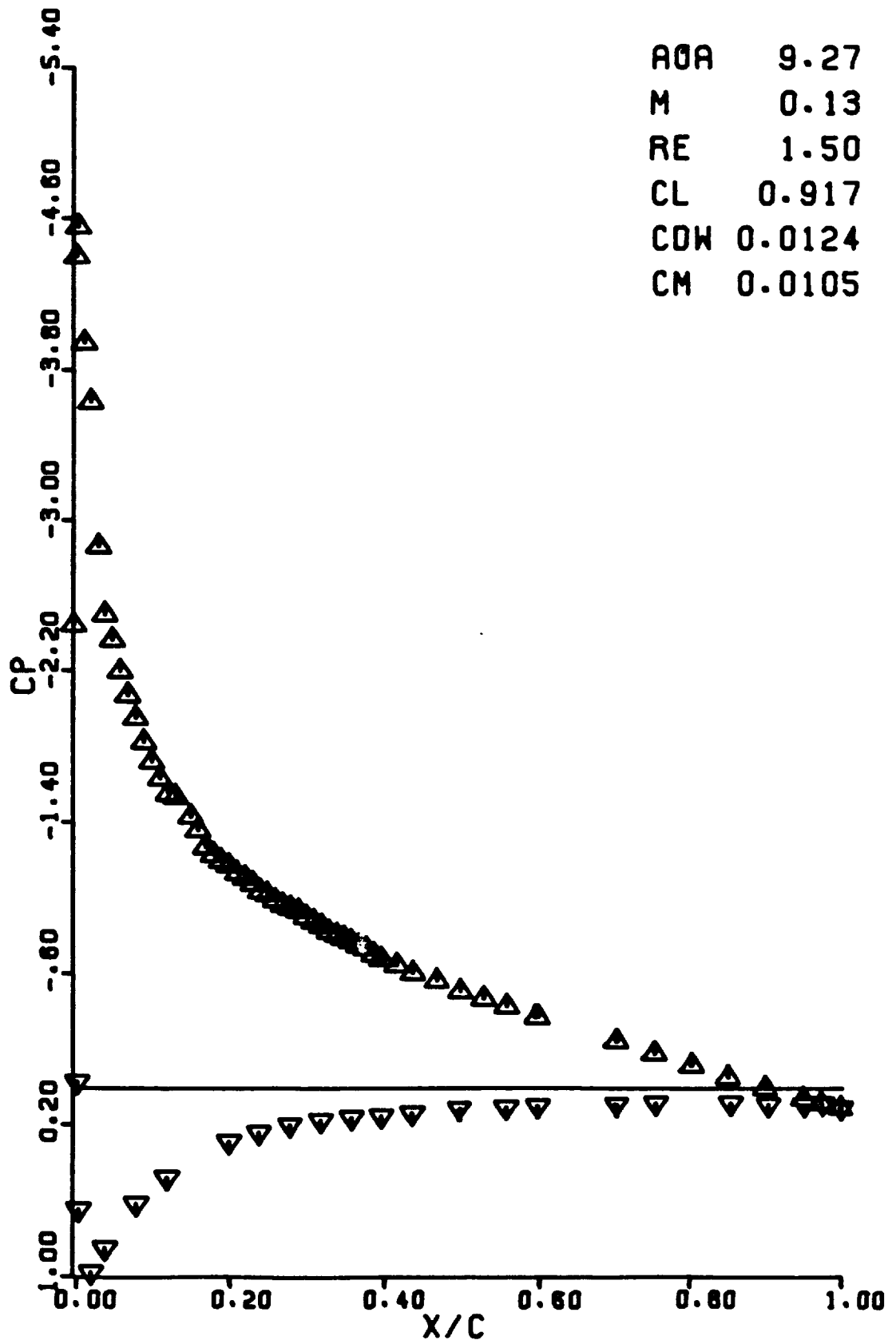
RUN 0373

AOA 8.24  
M 0.13  
RE 1.50  
CL 0.829  
CDW 0.0111  
CM 0.0066



RUN 0374

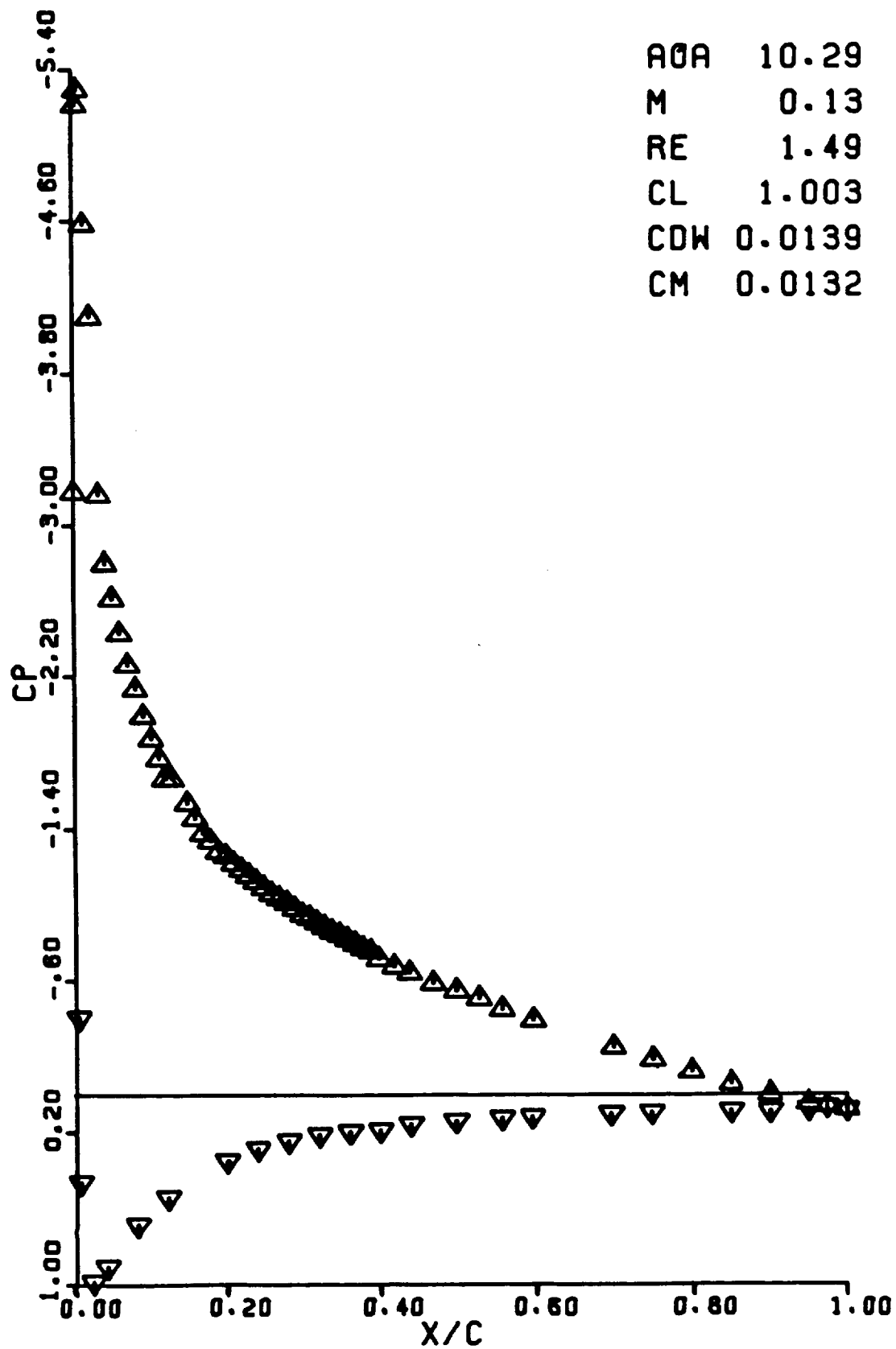
AOA 9.27  
M 0.13  
RE 1.50  
CL 0.917  
CDW 0.0124  
CM 0.0105





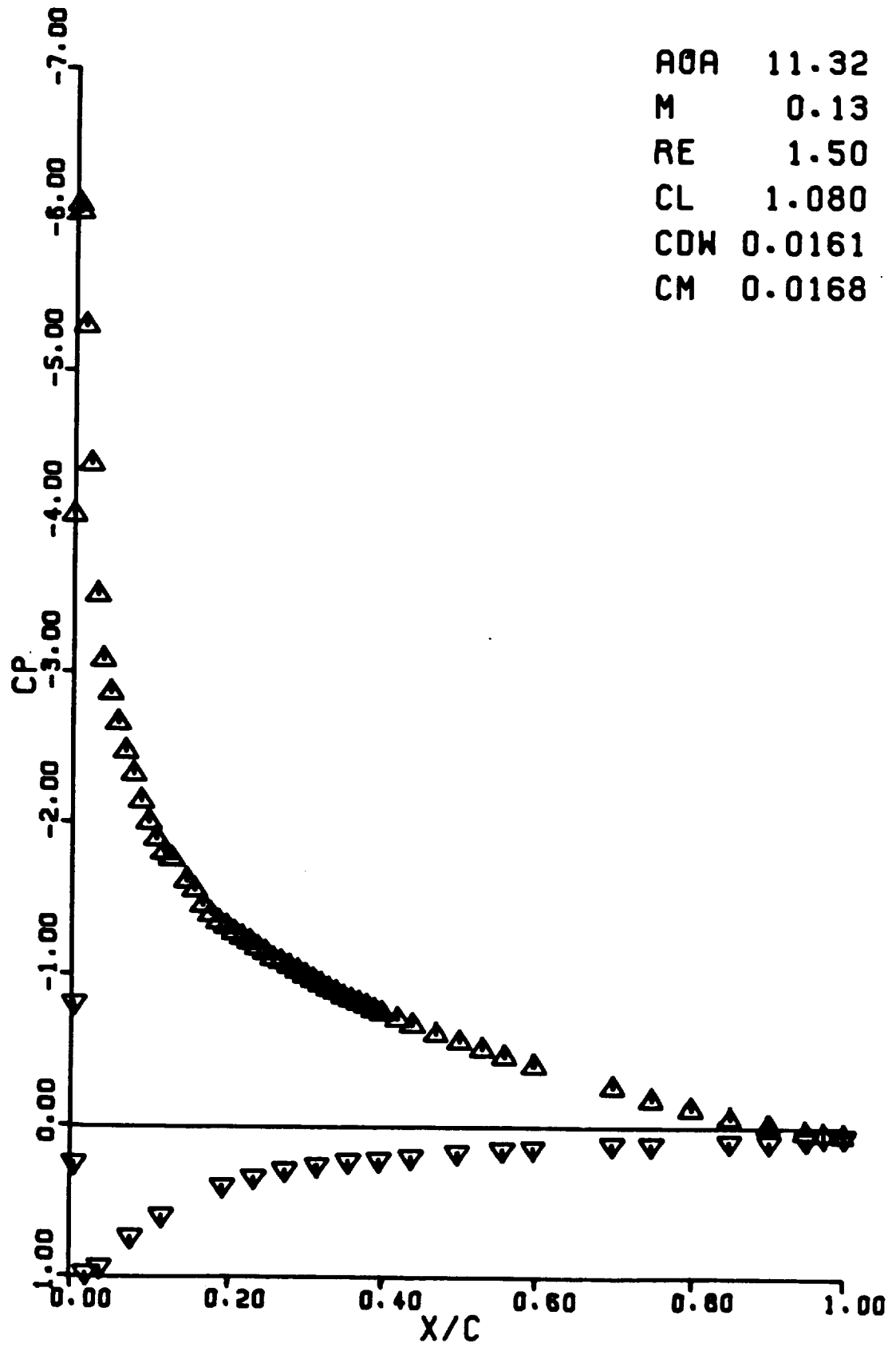
RUN 0375

AOA 10.29  
M 0.13  
RE 1.49  
CL 1.003  
CDW 0.0139  
CM 0.0132



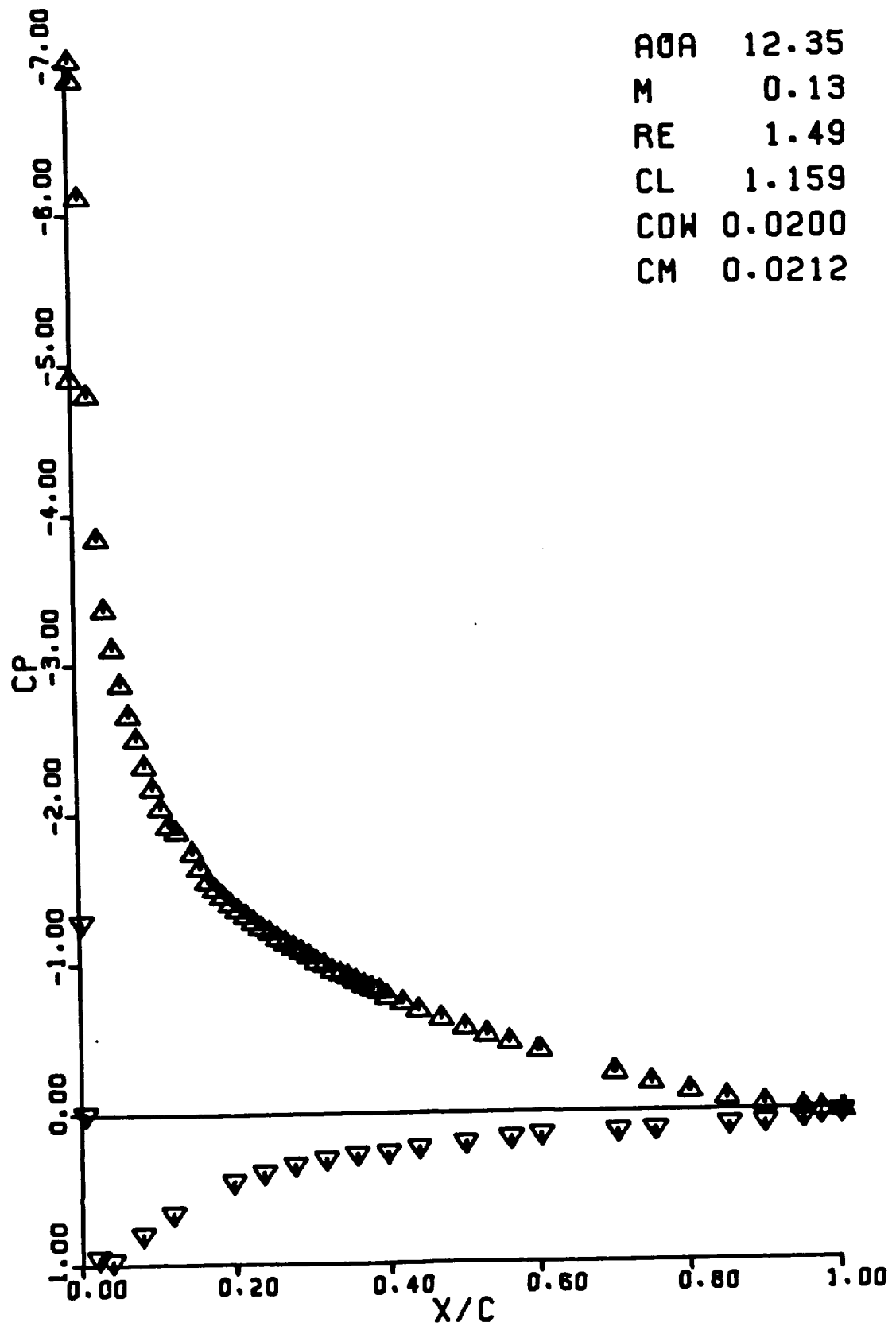
RUN 0376

AOA 11.32  
M 0.13  
RE 1.50  
CL 1.080  
CDW 0.0161  
CM 0.0168



RUN 0377

AOA 12.35  
M 0.13  
RE 1.49  
CL 1.159  
CDW 0.0200  
CM 0.0212



RUN 0378

AOA 13.37

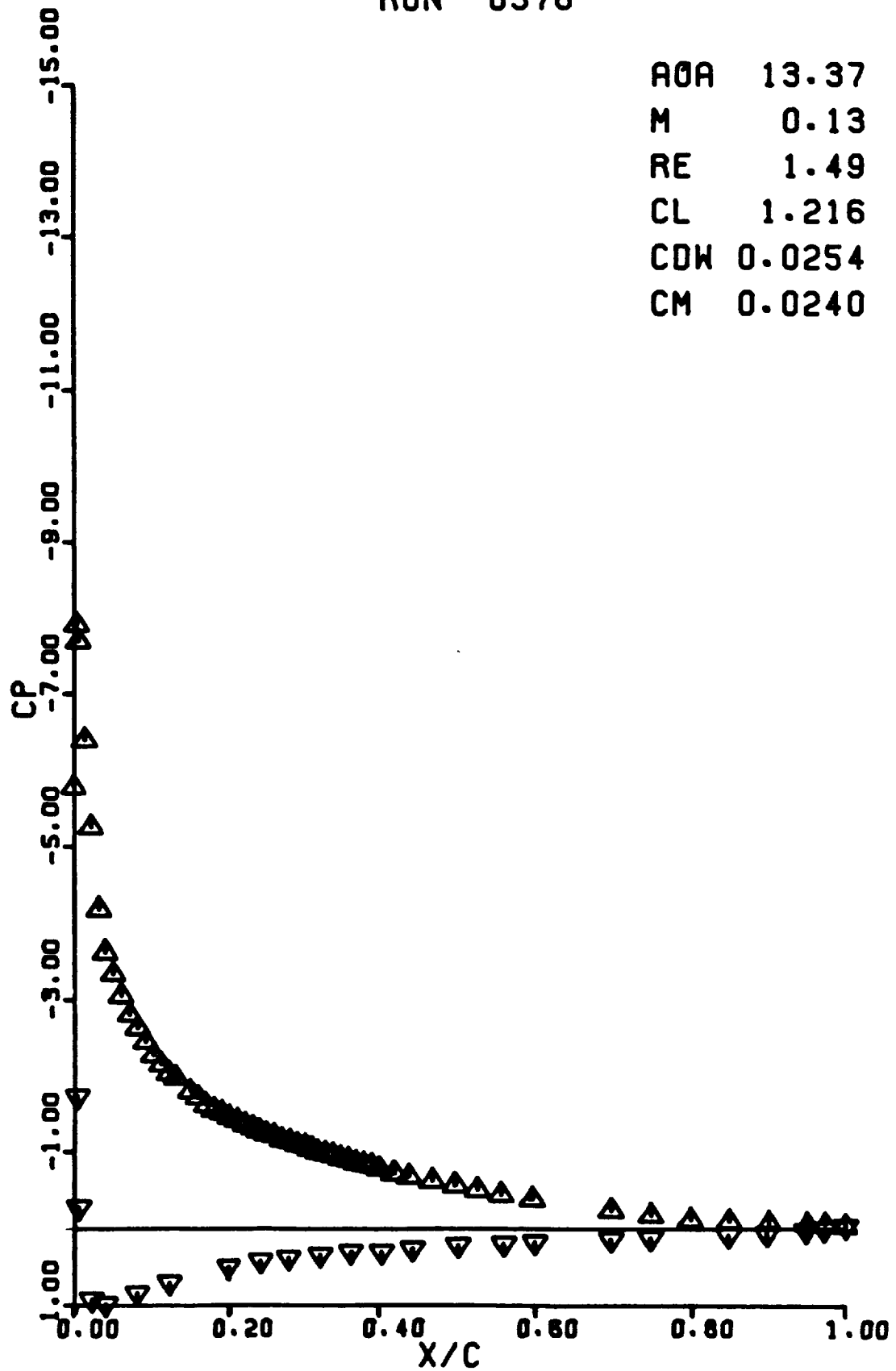
M 0.13

RE 1.49

CL 1.216

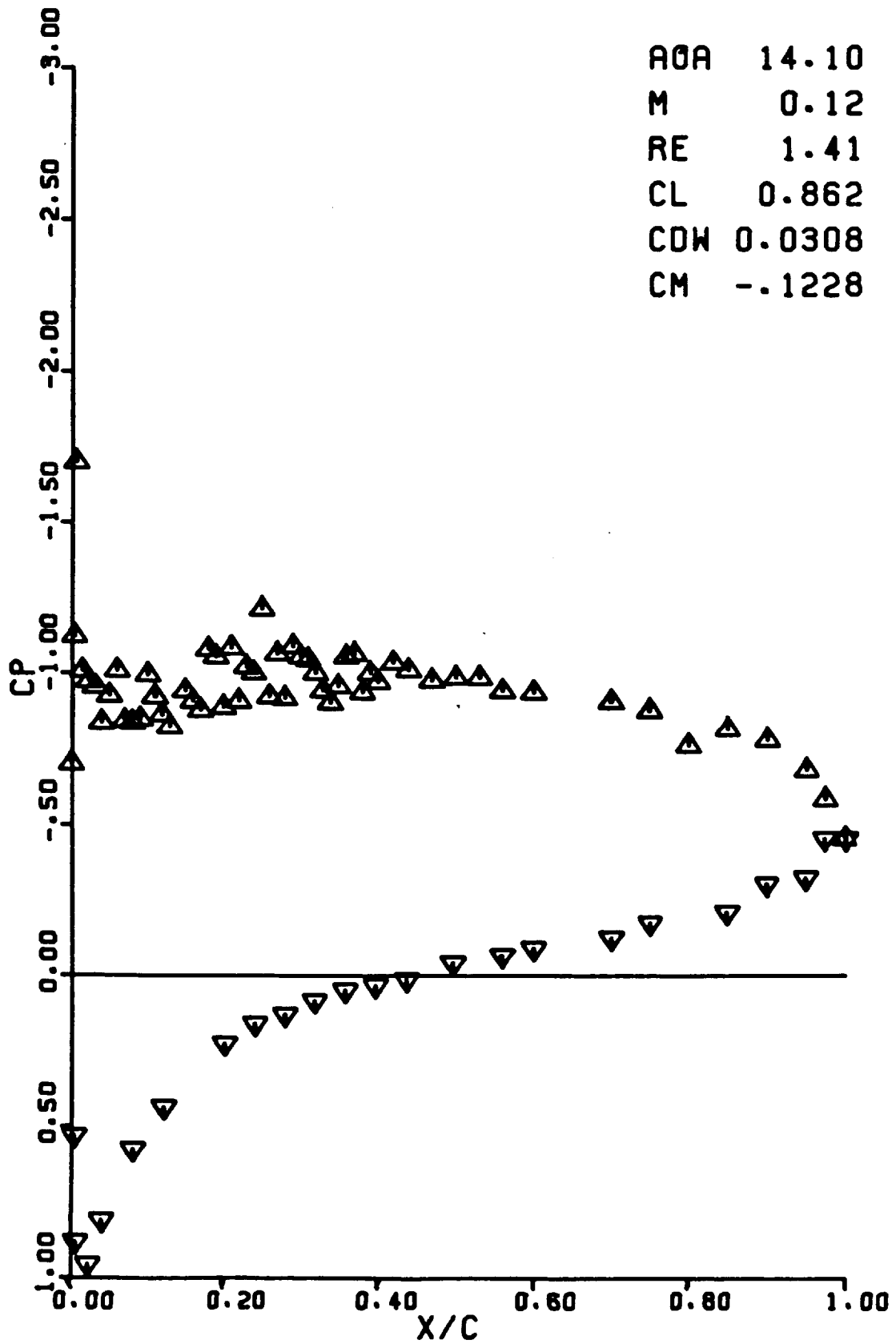
CDW 0.0254

CM 0.0240



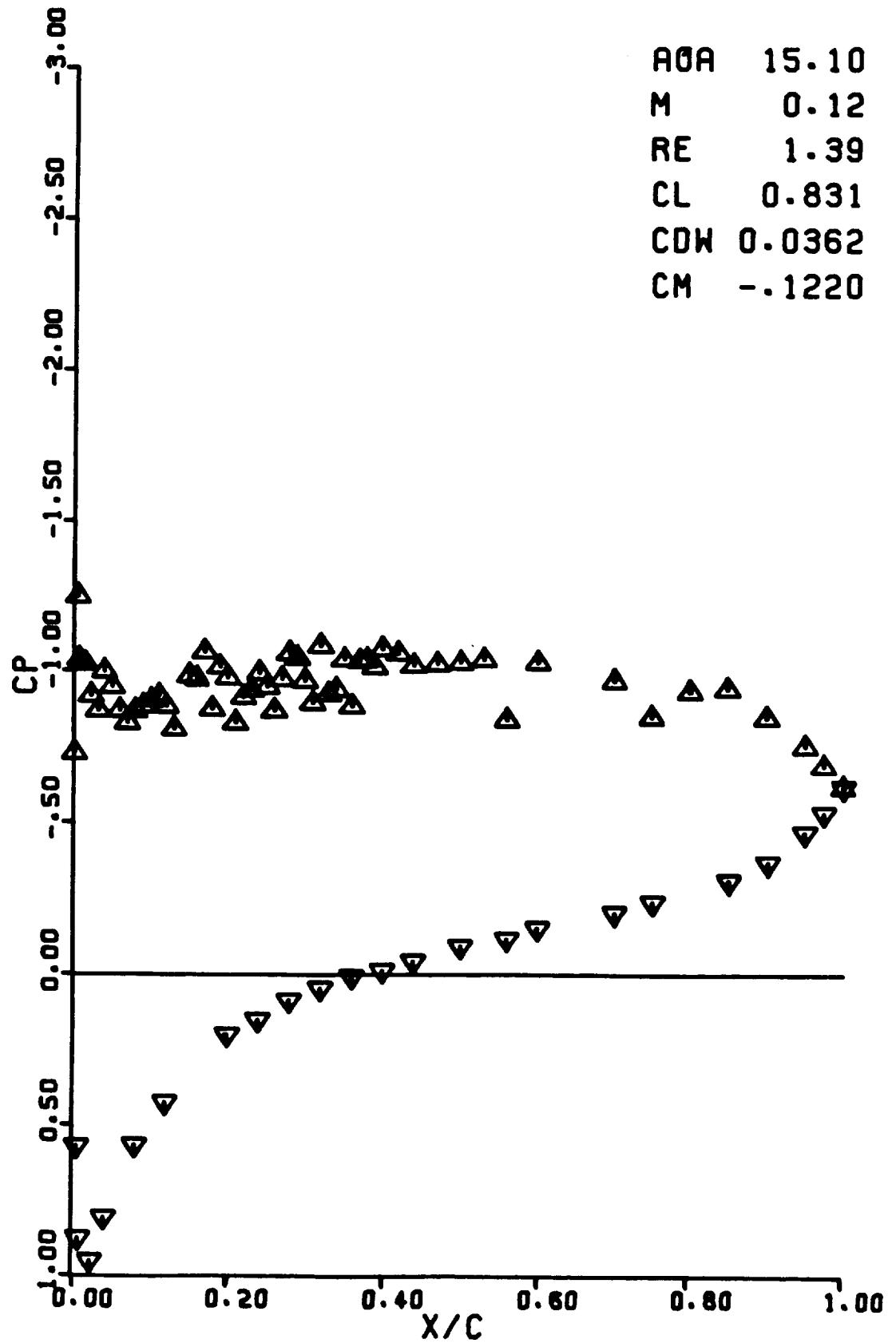
RUN 0379

AOA 14.10  
M 0.12  
RE 1.41  
CL 0.862  
CDW 0.0308  
CM -.1228



RUN 0380

AOA 15.10  
M 0.12  
RE 1.39  
CL 0.831  
CDW 0.0362  
CM -.1220



RUN 0381

AOA 16.09

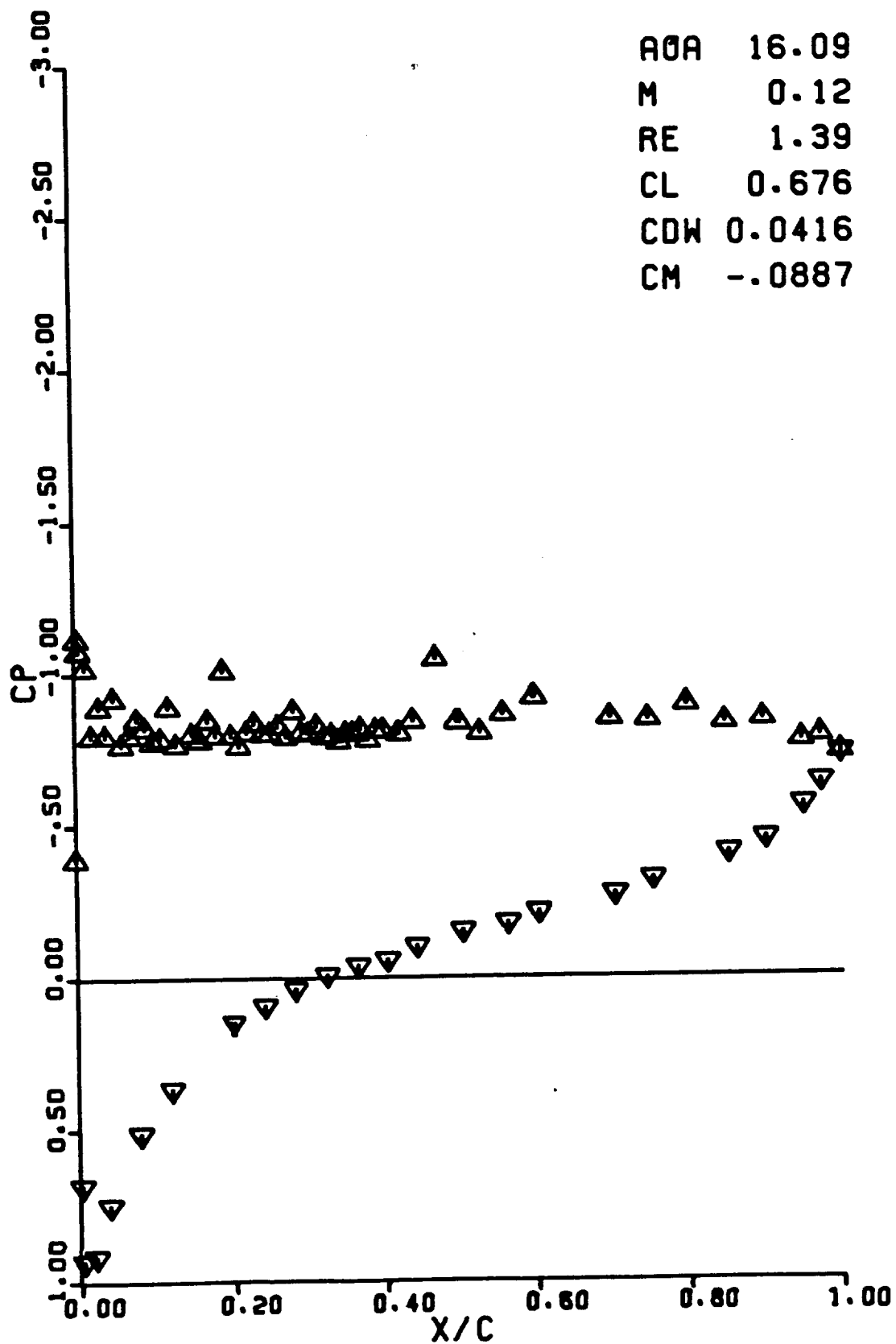
M 0.12

RE 1.39

CL 0.676

CDW 0.0416

CM -.0887



RUN 0382

AOA 12.86

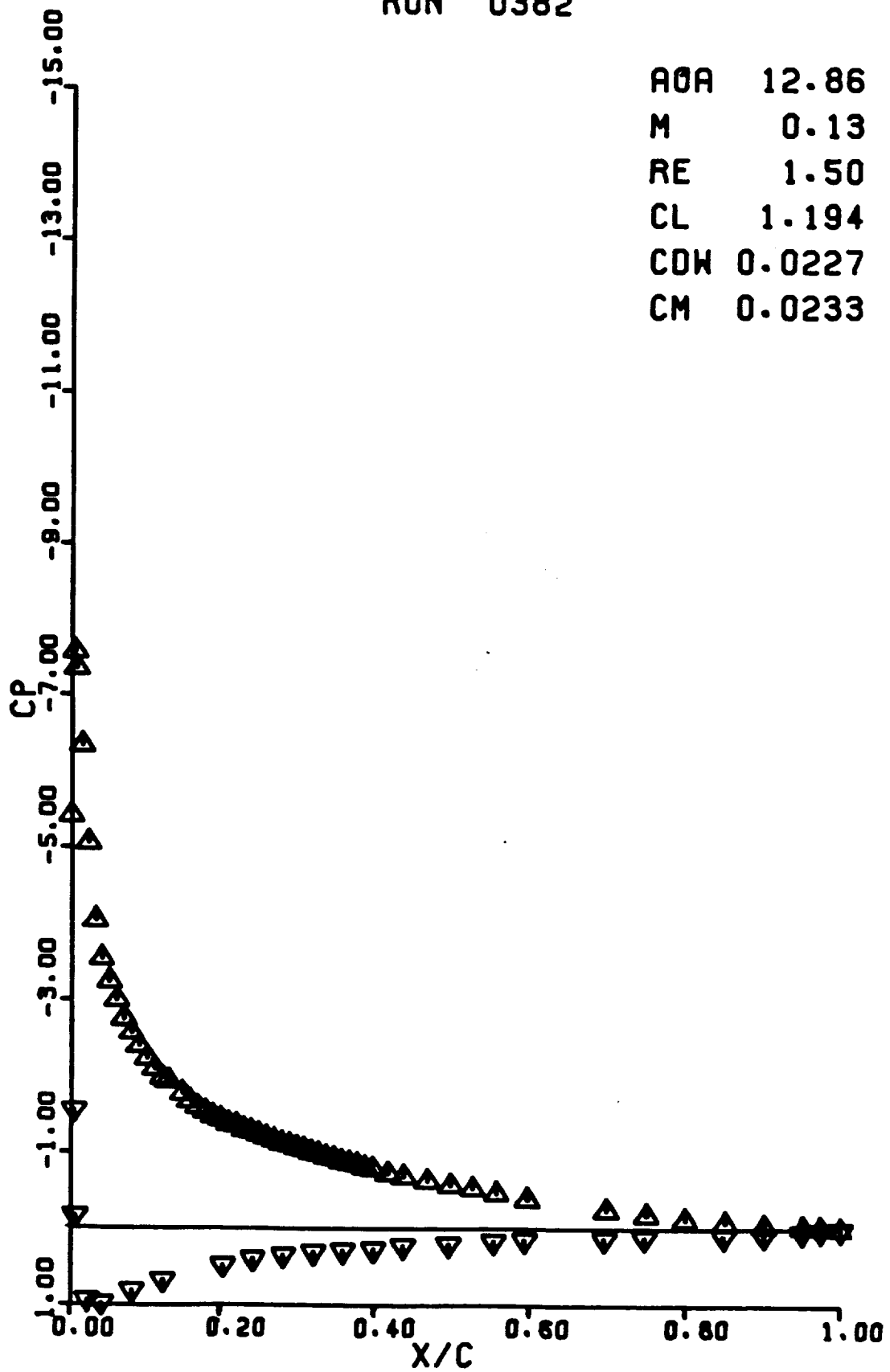
M 0.13

RE 1.50

CL 1.194

CDW 0.0227

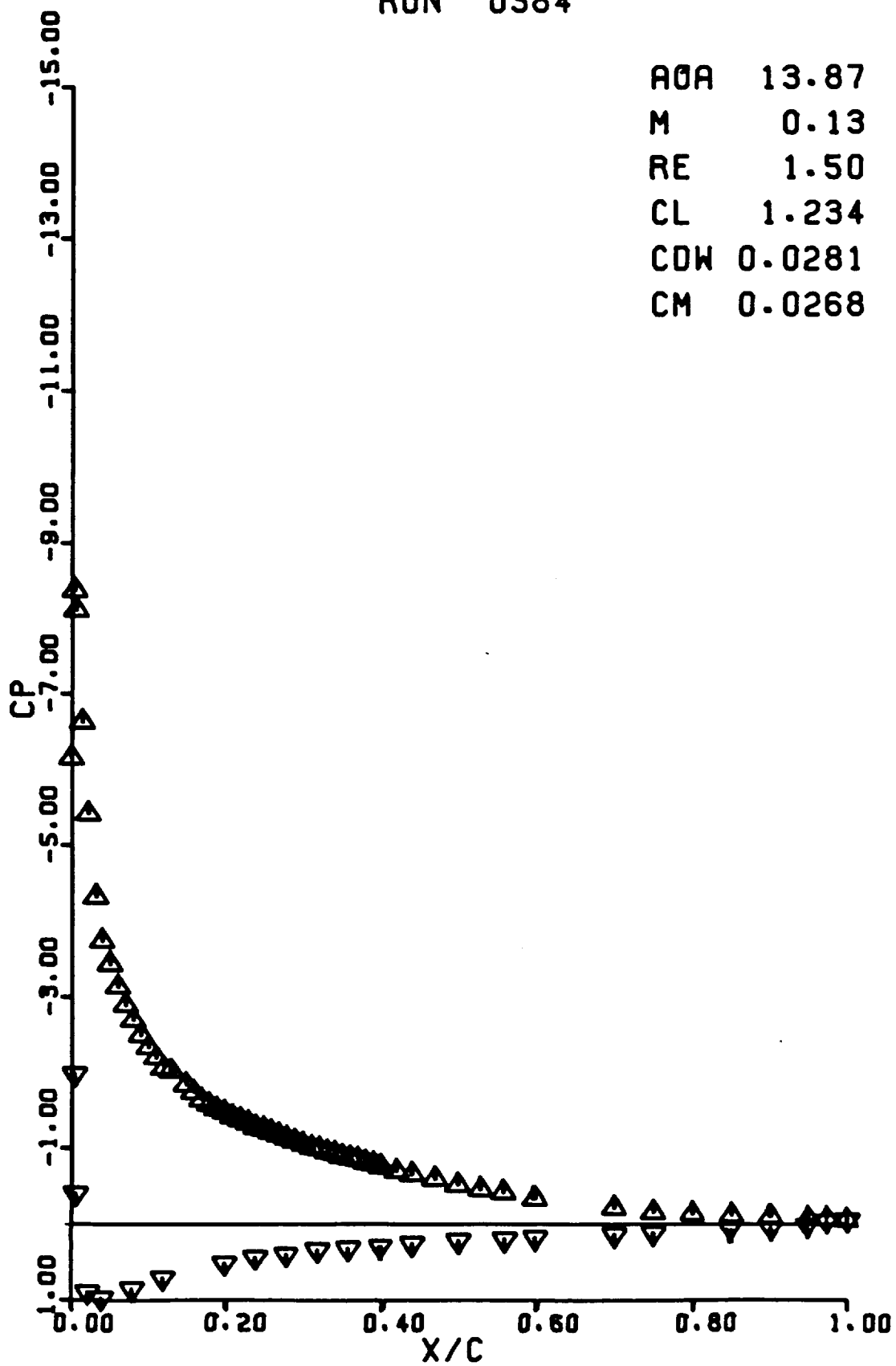
CM 0.0233





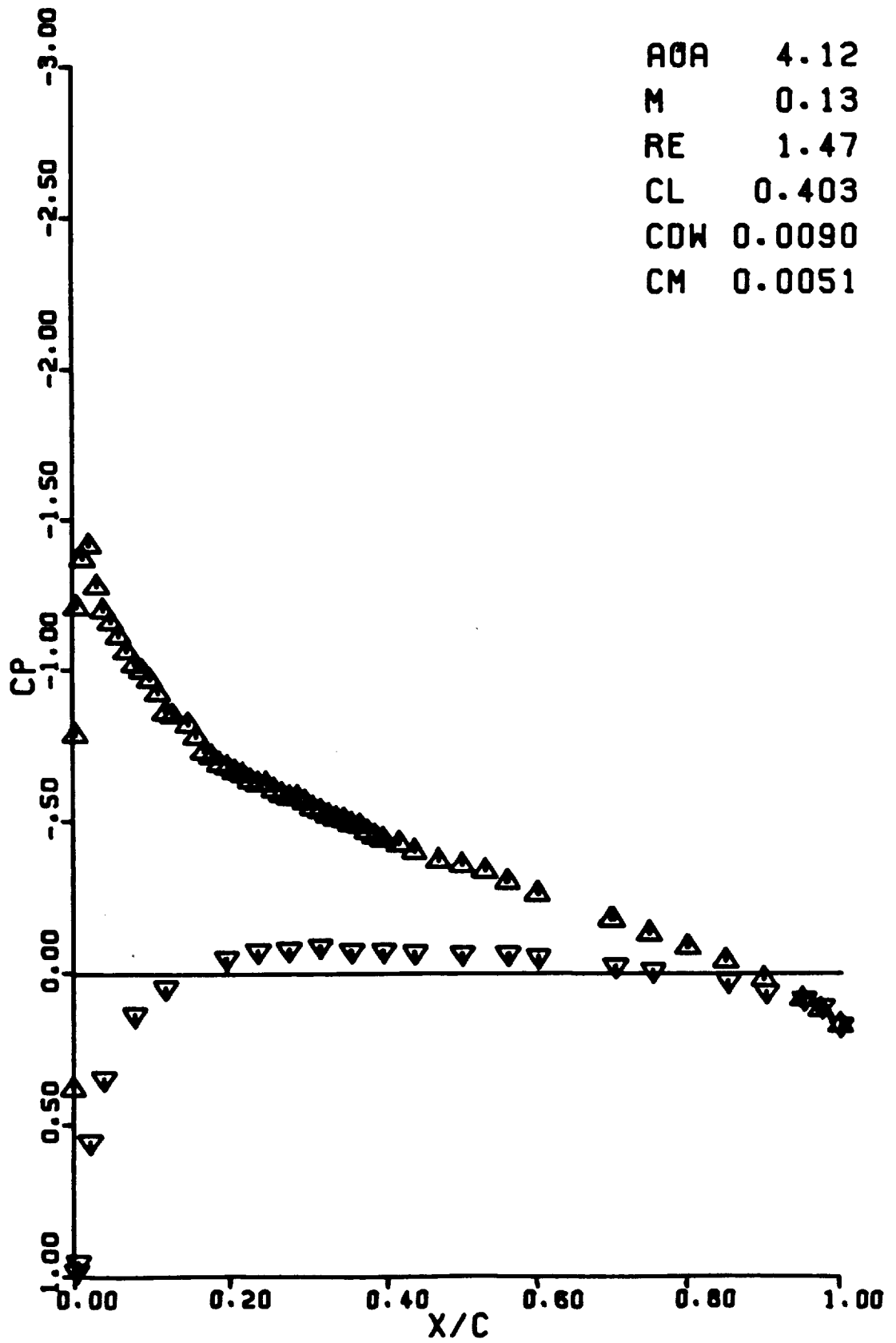
RUN 0384

AOA 13.87  
M 0.13  
RE 1.50  
CL 1.234  
CDW 0.0281  
CM 0.0268

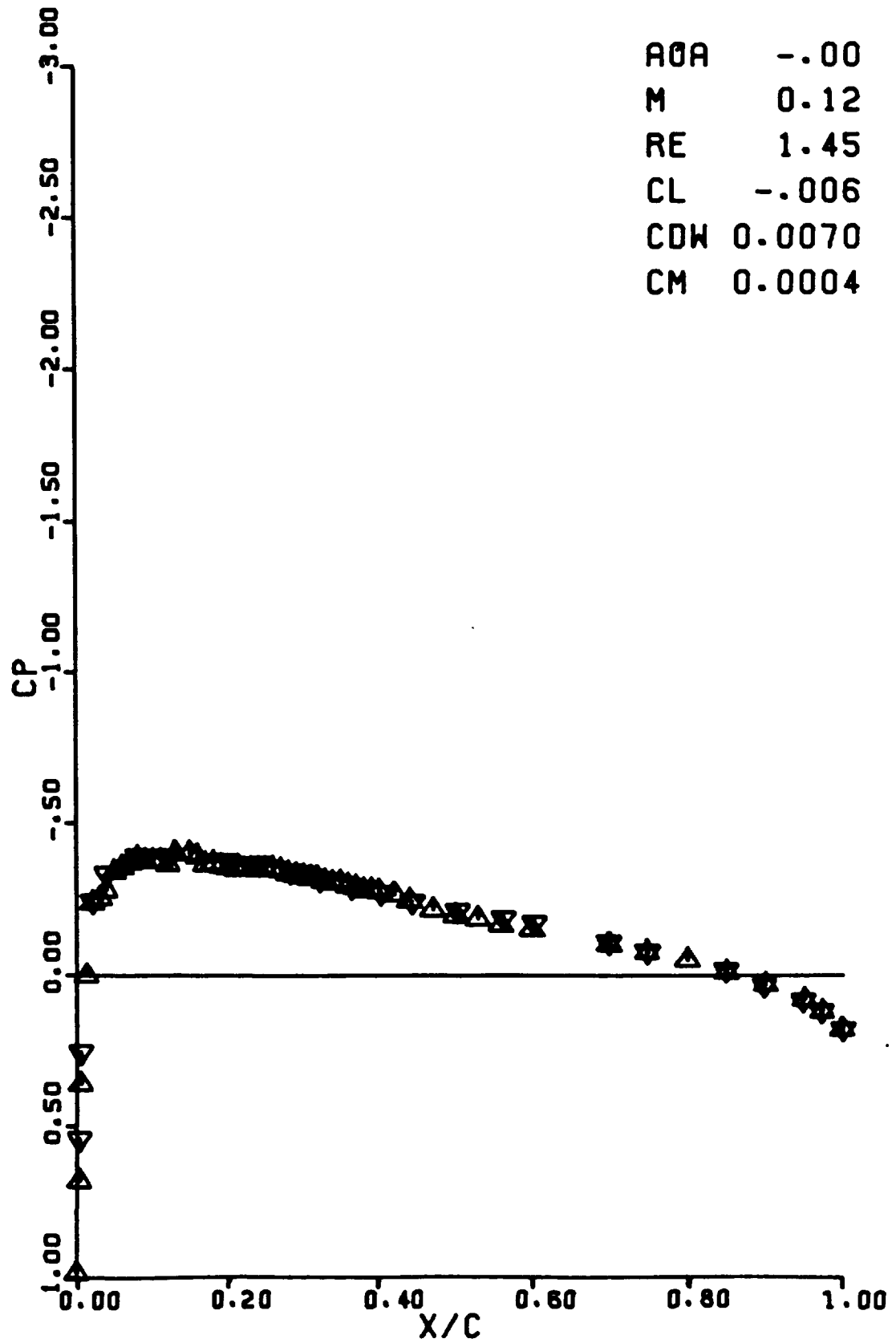


RUN 0385

AOA 4.12  
M 0.13  
RE 1.47  
CL 0.403  
CDW 0.0090  
CM 0.0051

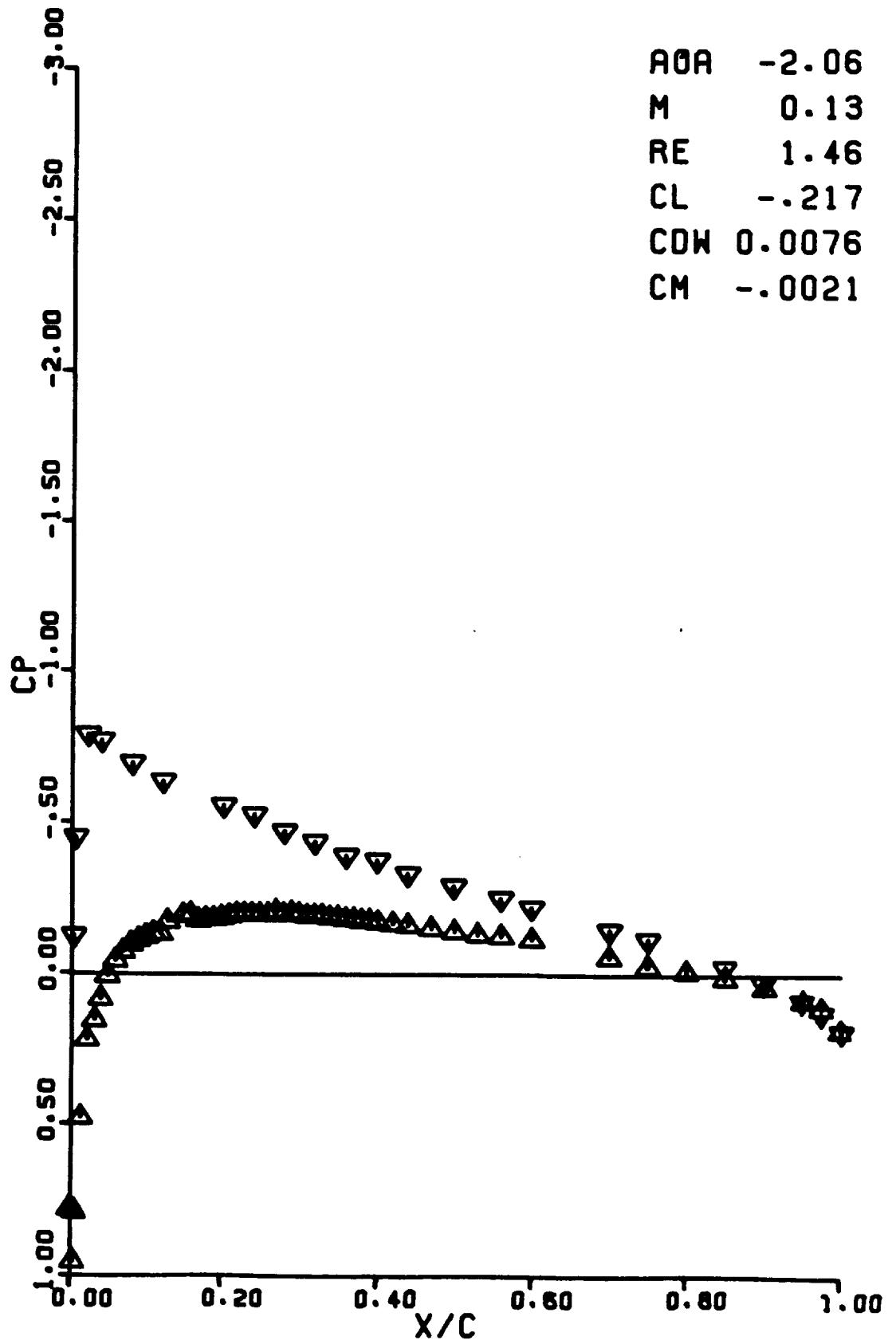


RUN 0386



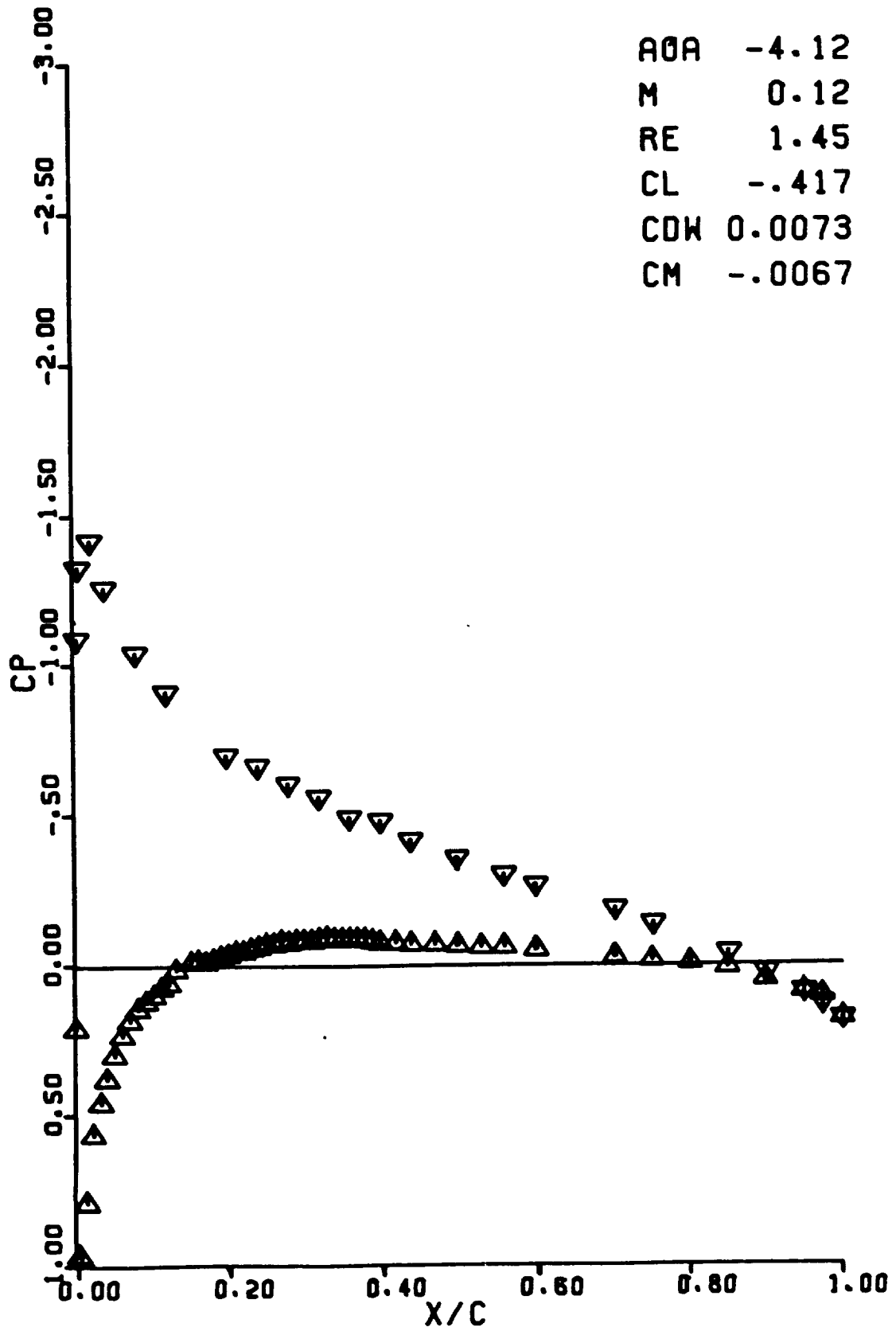
RUN 0387

AOA -2.06  
M 0.13  
RE 1.46  
CL -.217  
CDW 0.0076  
CM -.0021



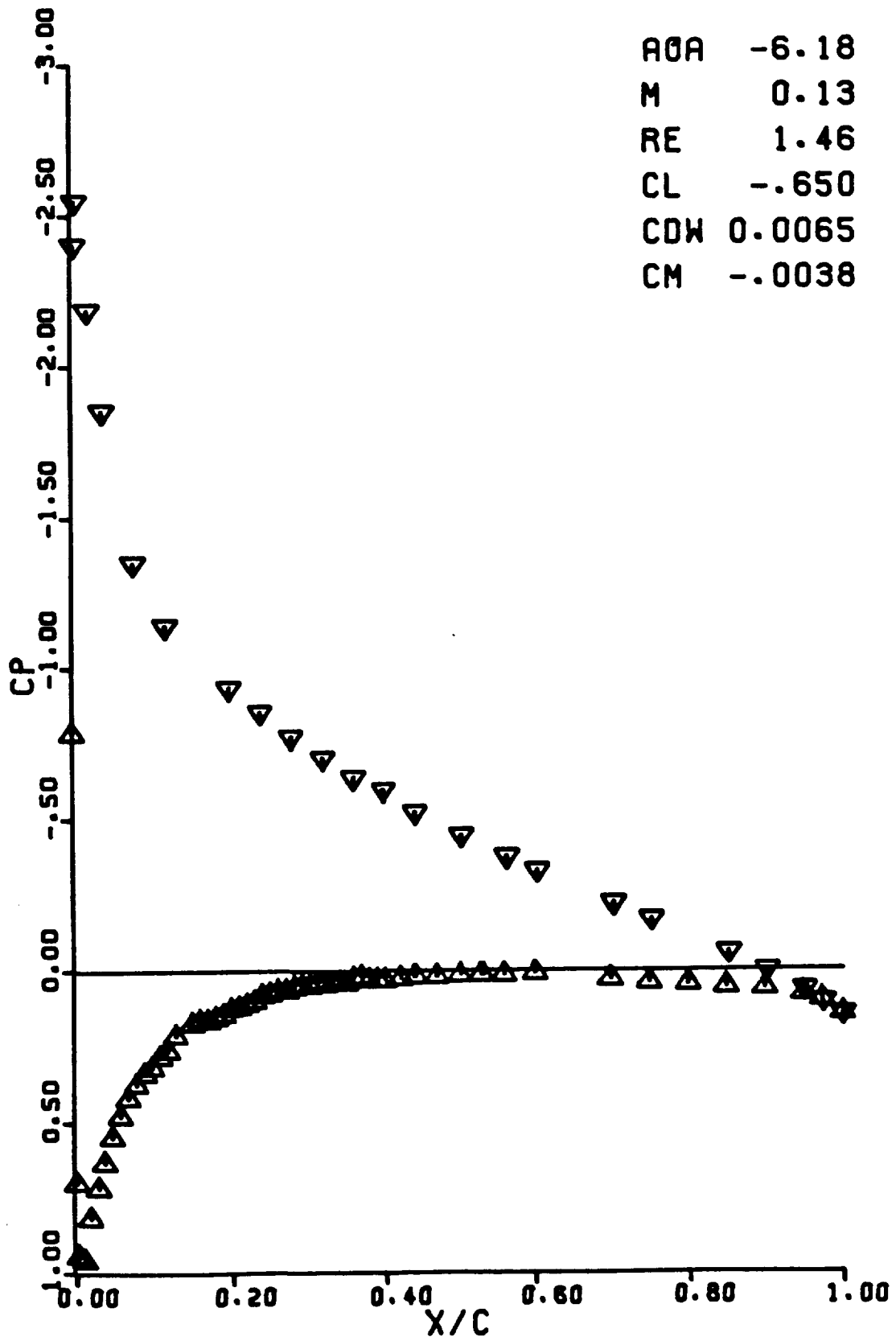
RUN 0388

AOA -4.12  
M 0.12  
RE 1.45  
CL -.417  
CDW 0.0073  
CM -.0067



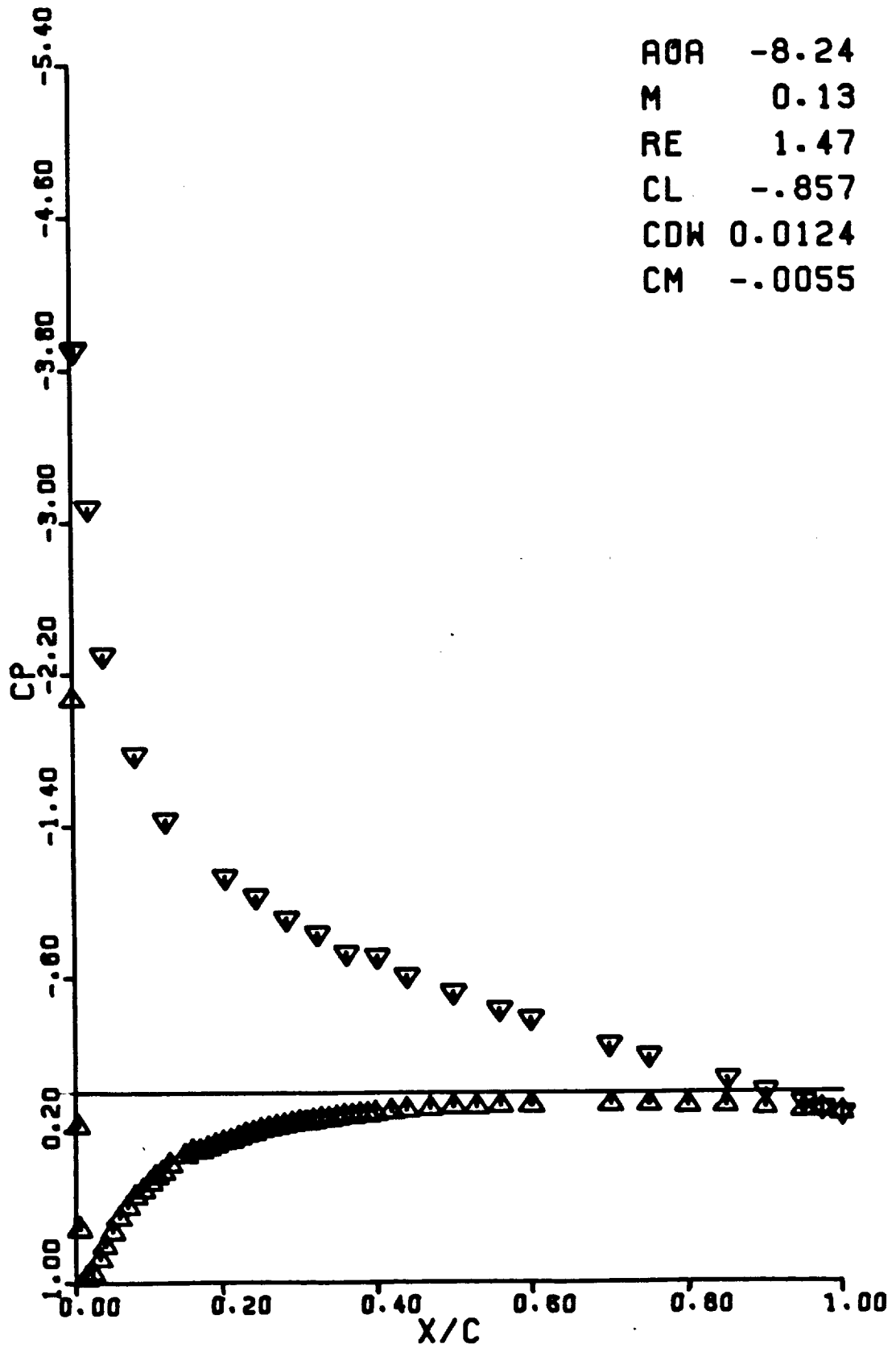
RUN 0389

AOA -6.18  
M 0.13  
RE 1.46  
CL -.650  
CDW 0.0065  
CM -.0038

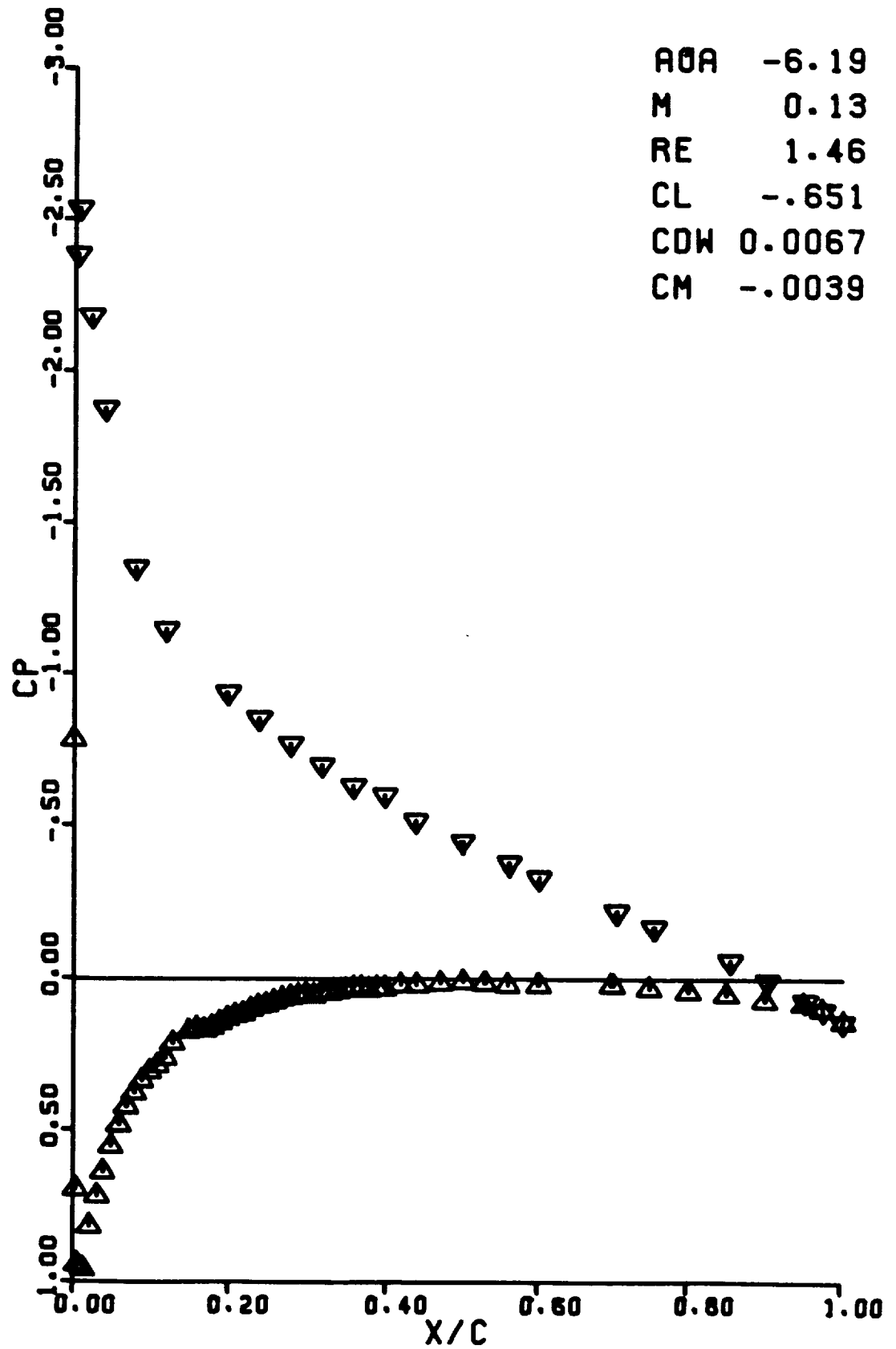


RUN 0390

AOA -8.24  
M 0.13  
RE 1.47  
CL -.857  
CDW 0.0124  
CM -.0055



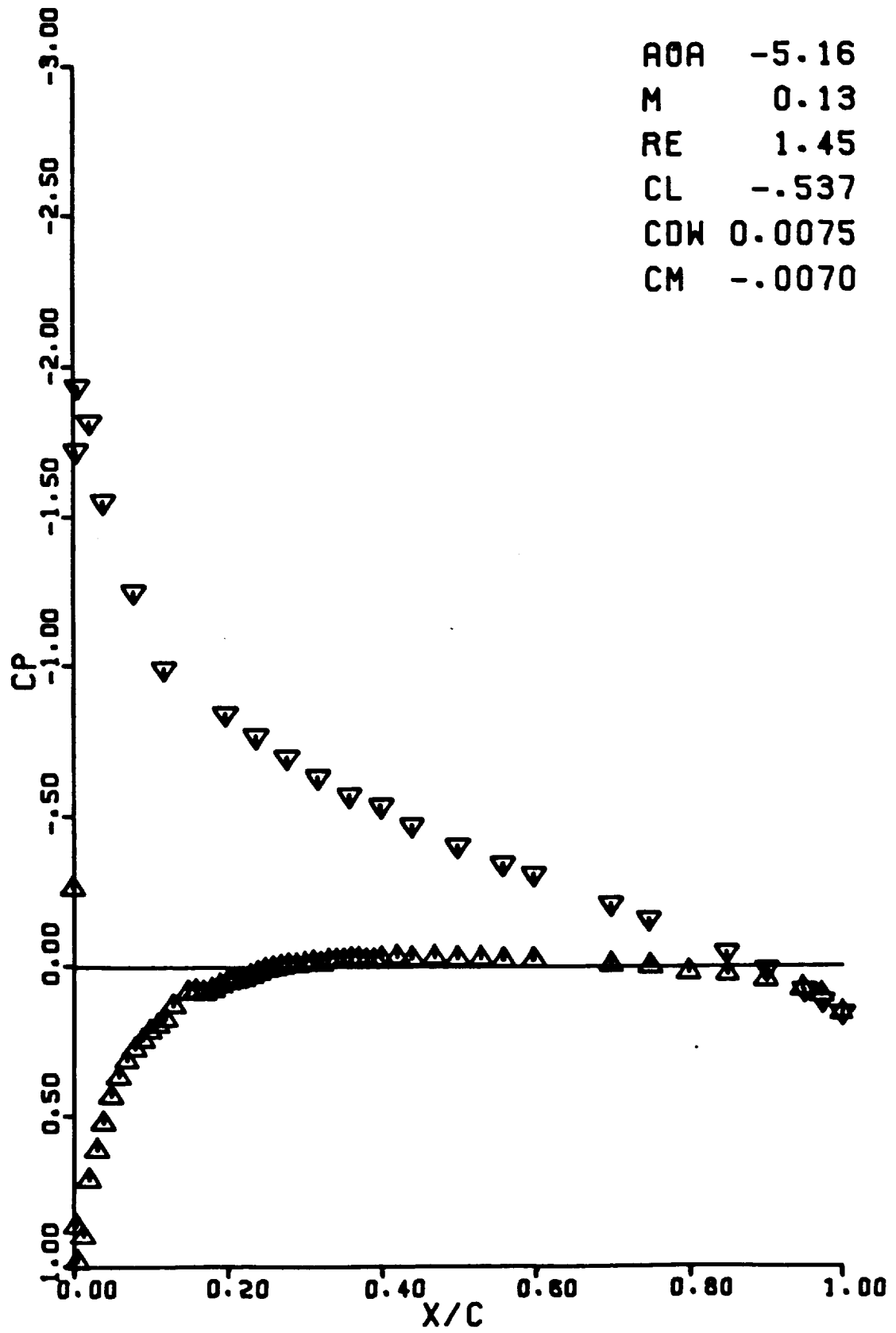
RUN 0391





RUN 0392

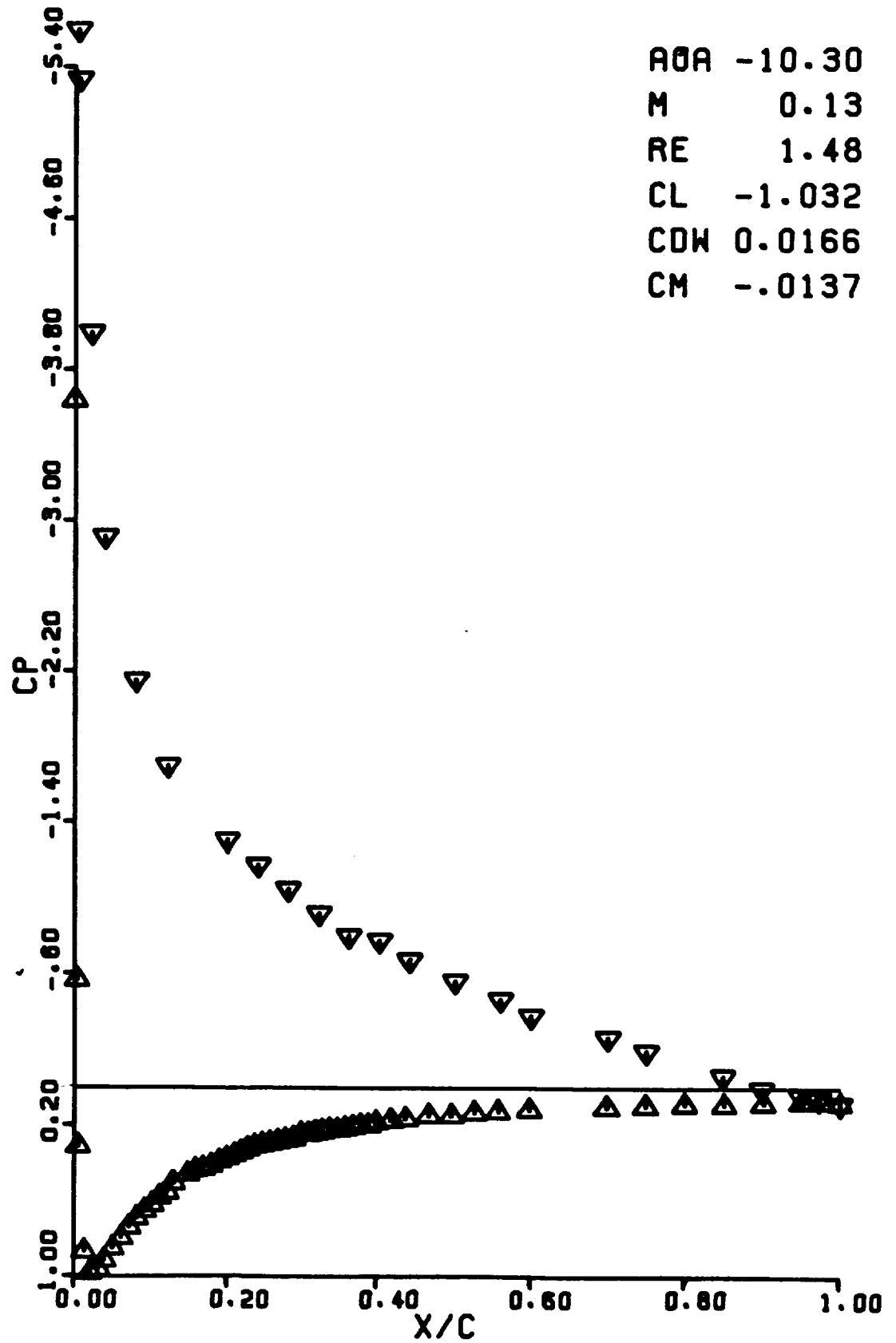
AOA -5.16  
M 0.13  
RE 1.45  
CL -.537  
CDW 0.0075  
CM -.0070



C.2

RUN 0393

AOA -10.30  
M 0.13  
RE 1.48  
CL -1.032  
CDW 0.0166  
CM -.0137



RUN 0394

AOA -10.30

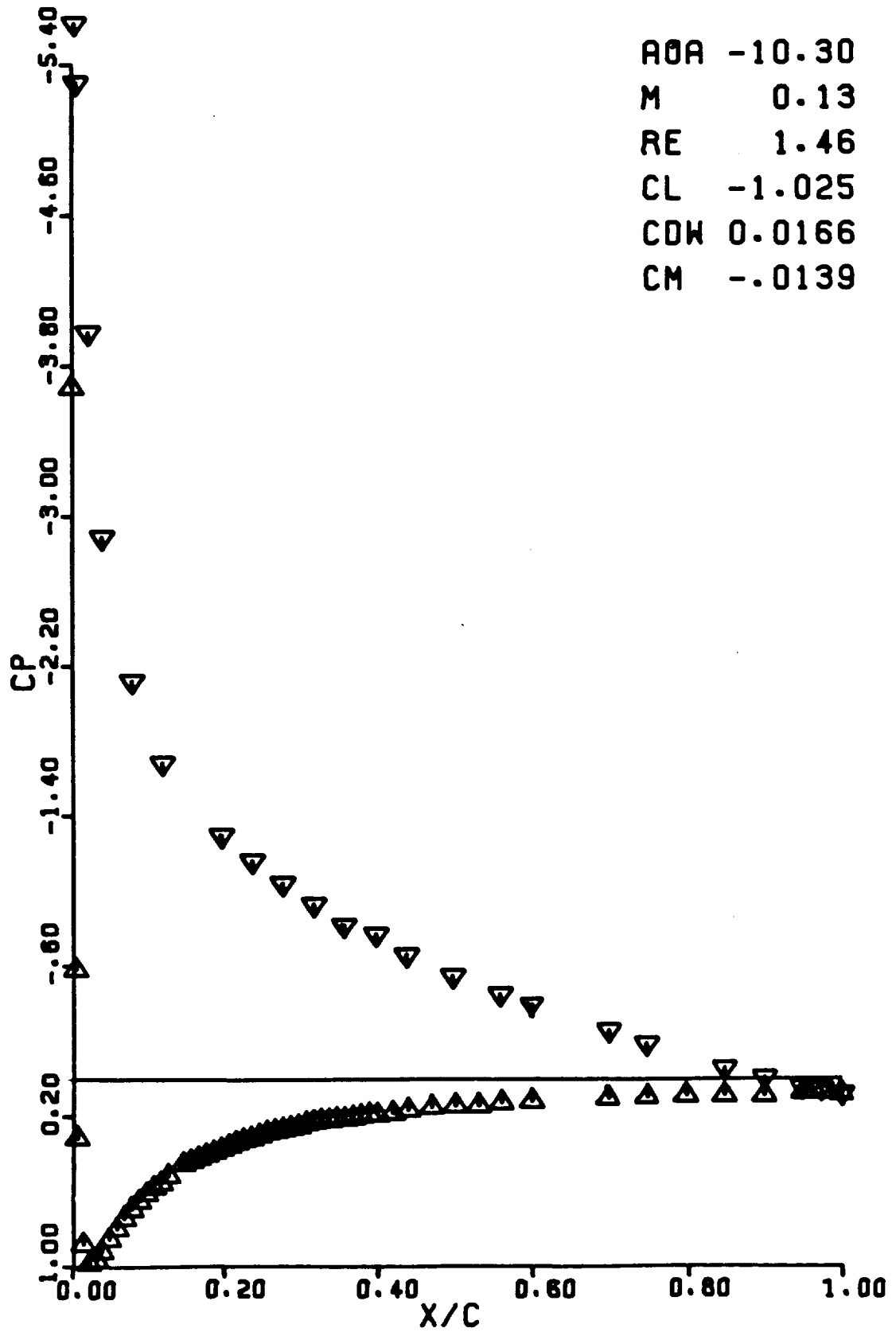
M 0.13

RE 1.46

CL -1.025

CDW 0.0166

CM -.0139



RUN 0395

AOA -12.35

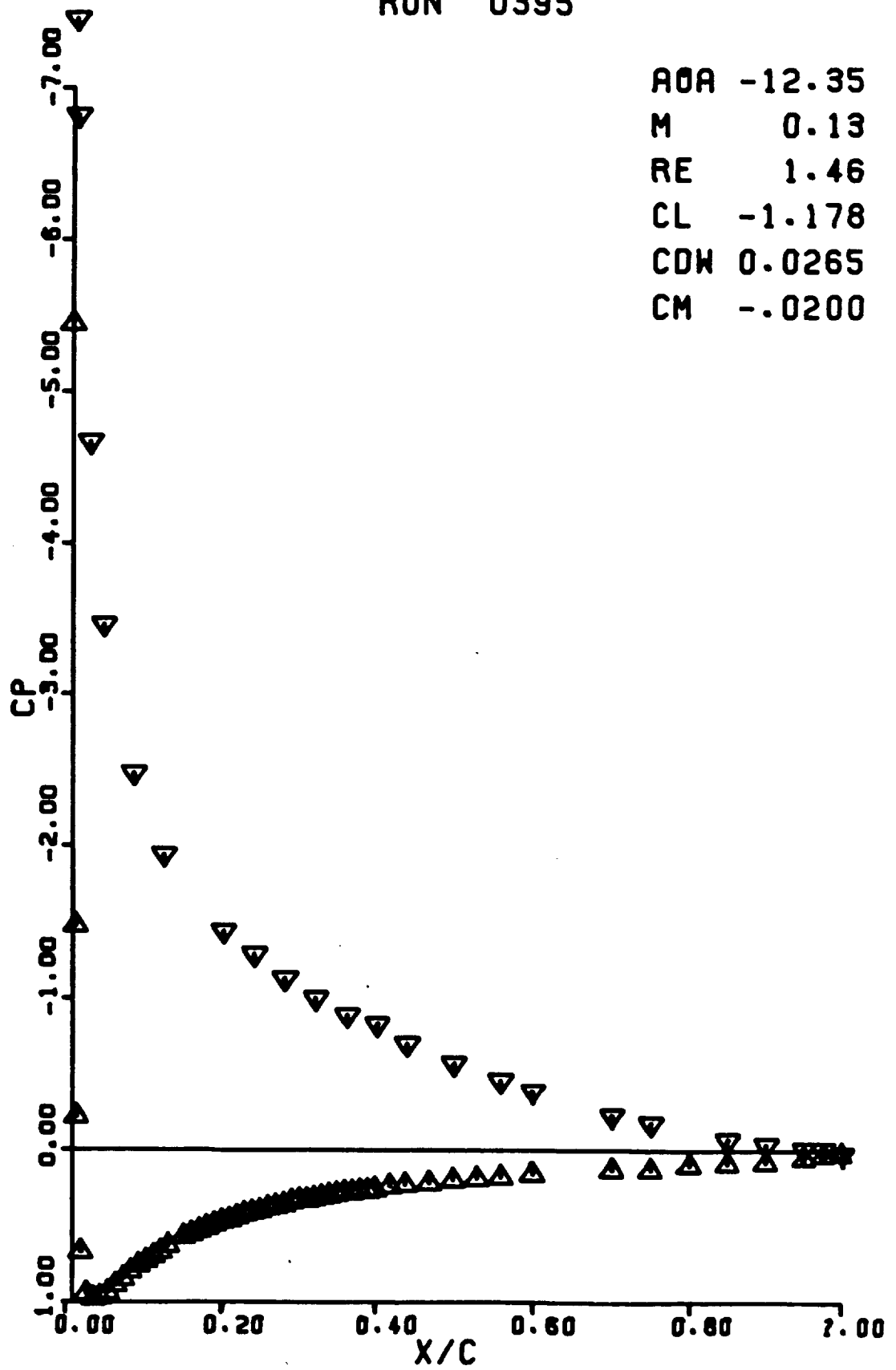
M 0.13

RE 1.46

CL -1.178

CDW 0.0265

CM -.0200



RUN 0396

AOA -14.16

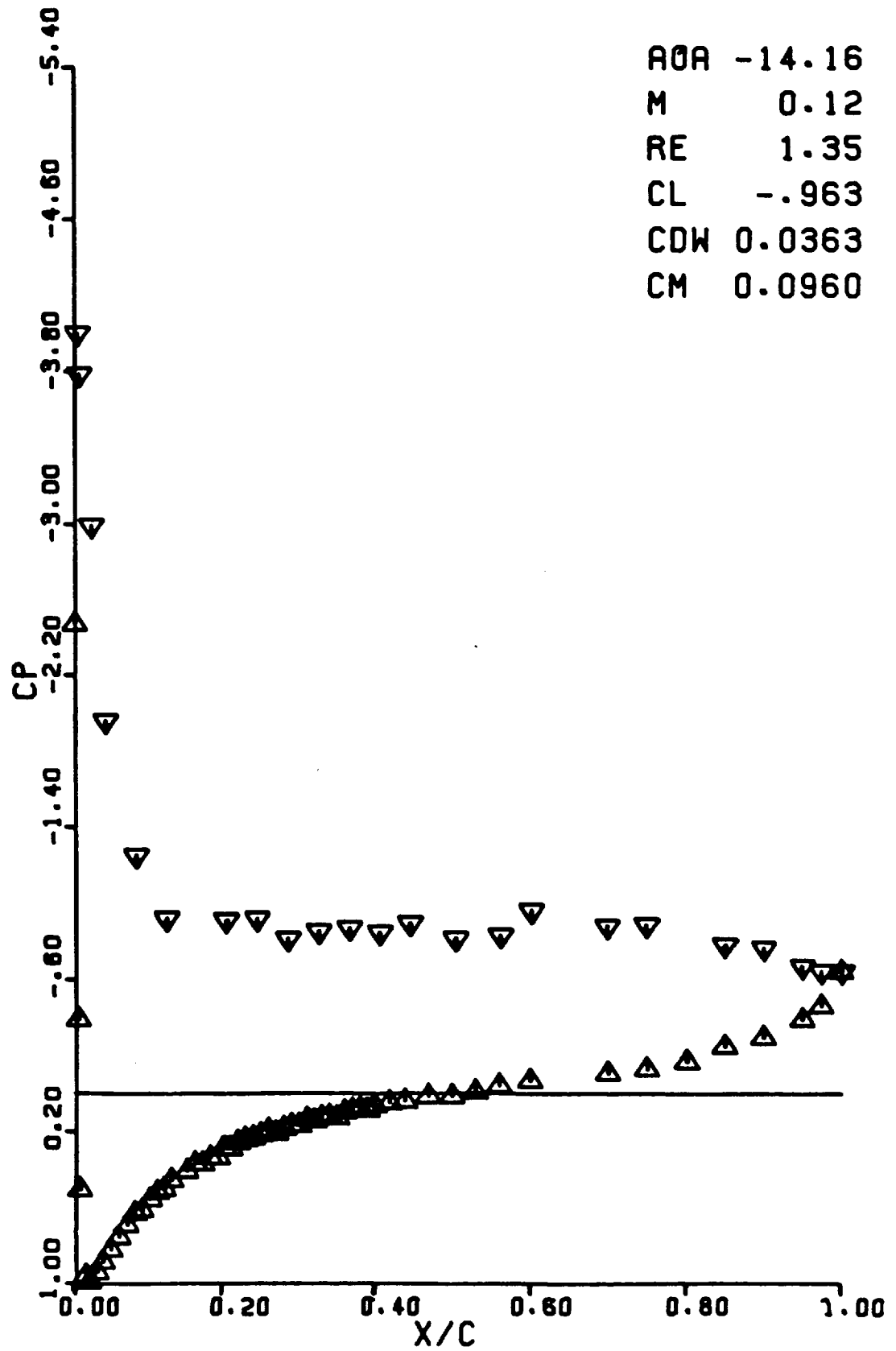
M 0.12

RE 1.35

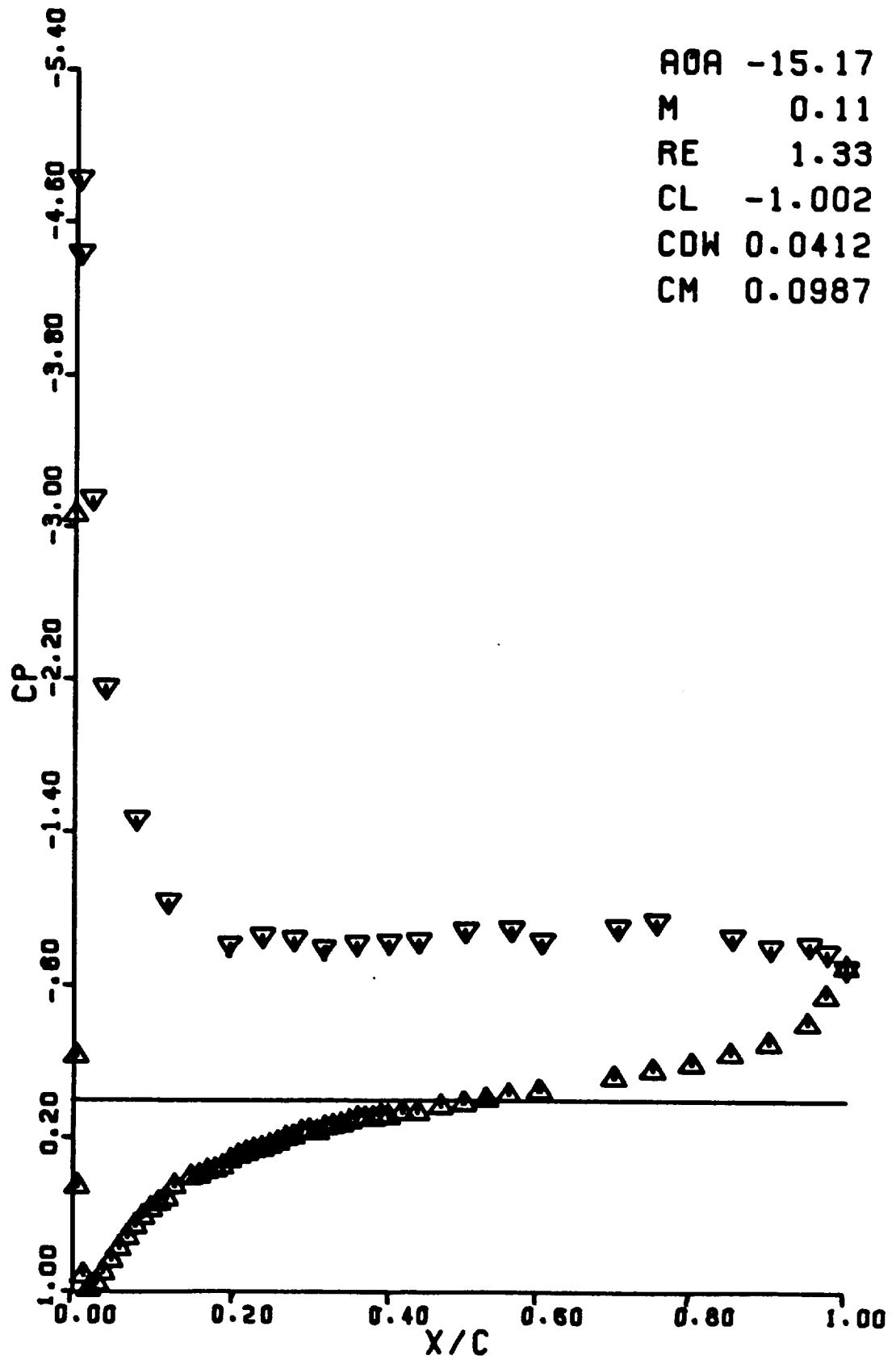
CL -.963

CDW 0.0363

CM 0.0960



RUN 0397



RUN 0398

AOA -13.37

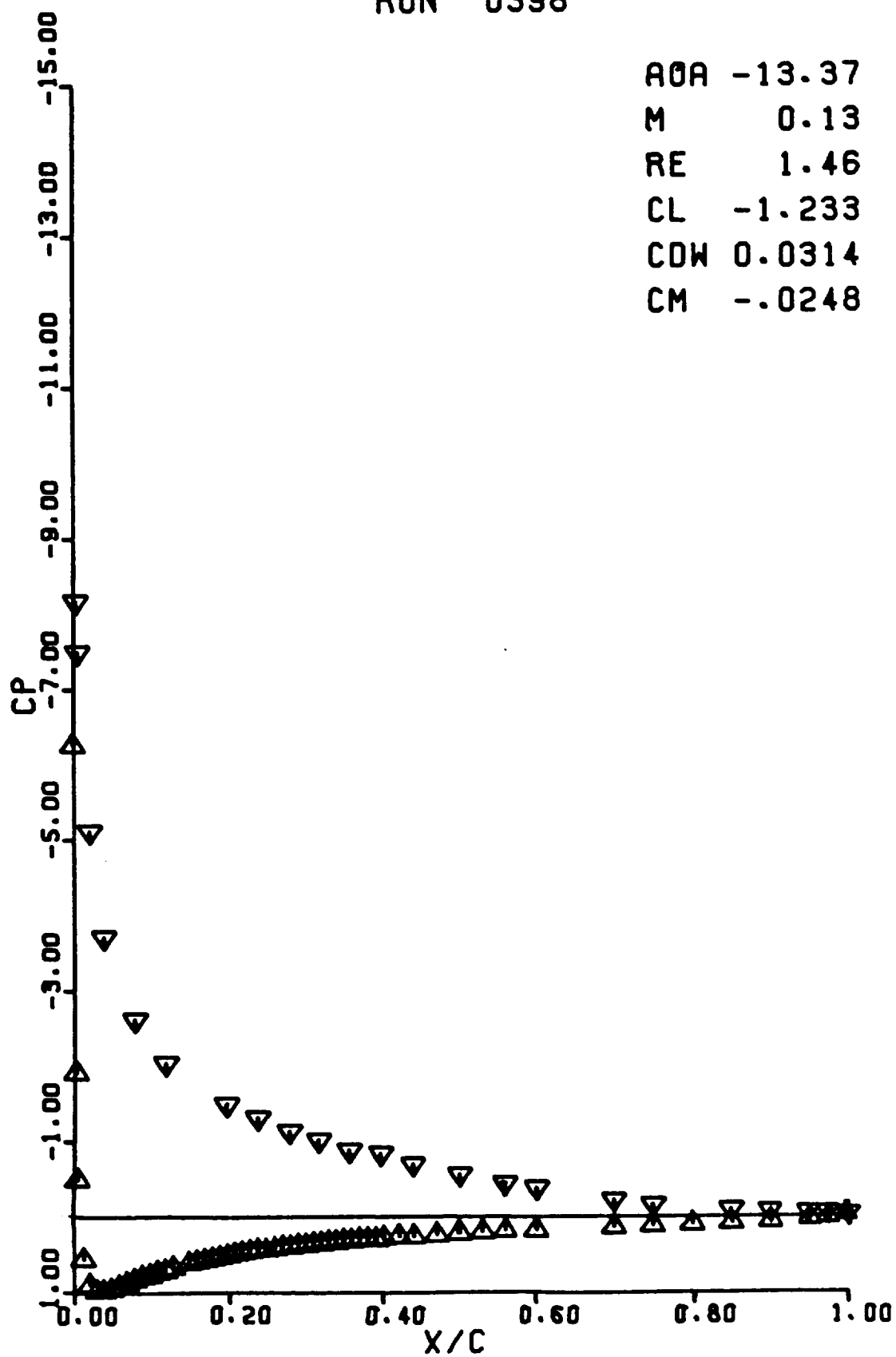
M 0.13

RE 1.46

CL -1.233

CDW 0.0314

CM -.0248



RUN 0399

AOA -13.87

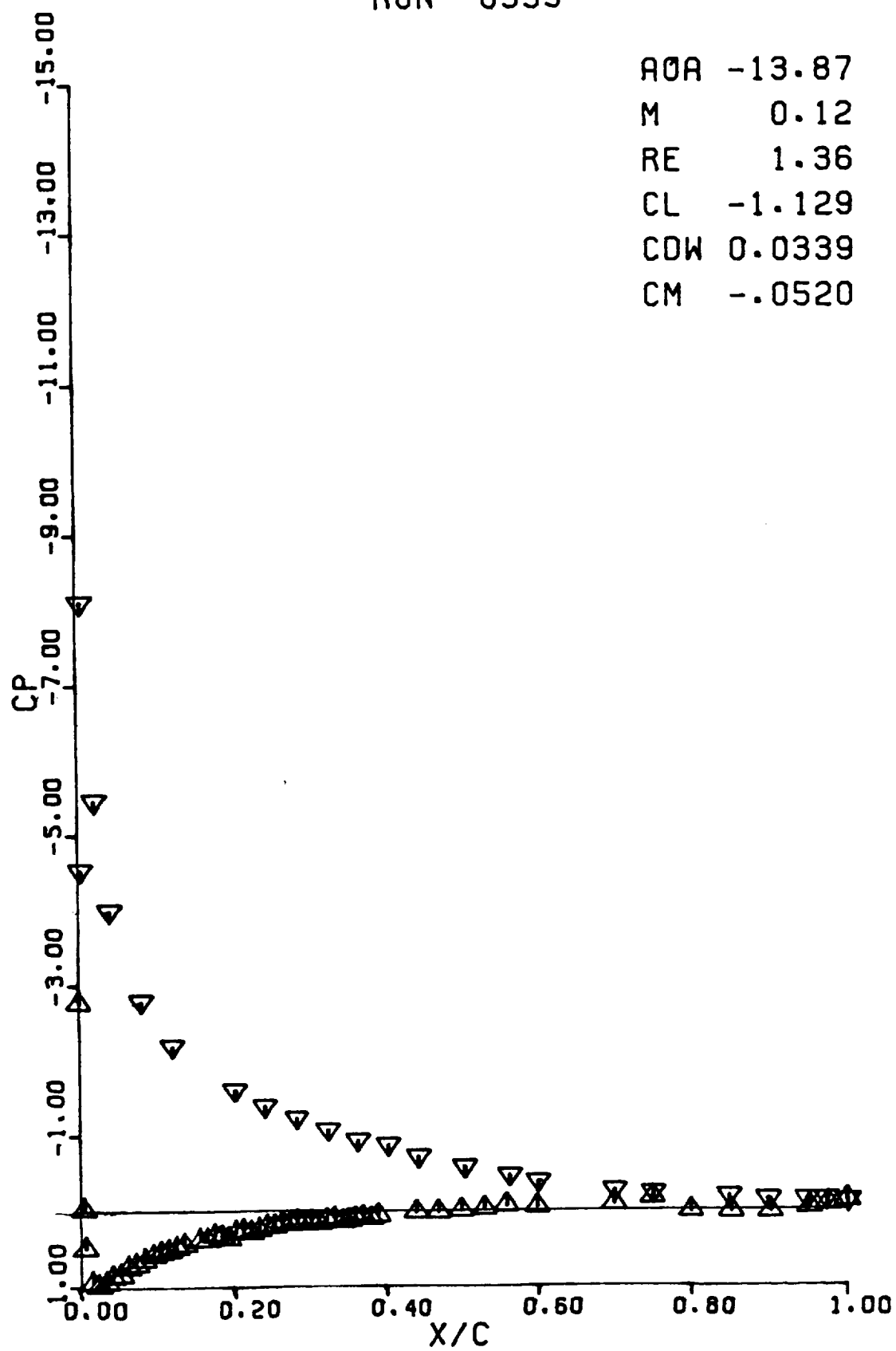
M 0.12

RE 1.36

CL -1.129

CDW 0.0339

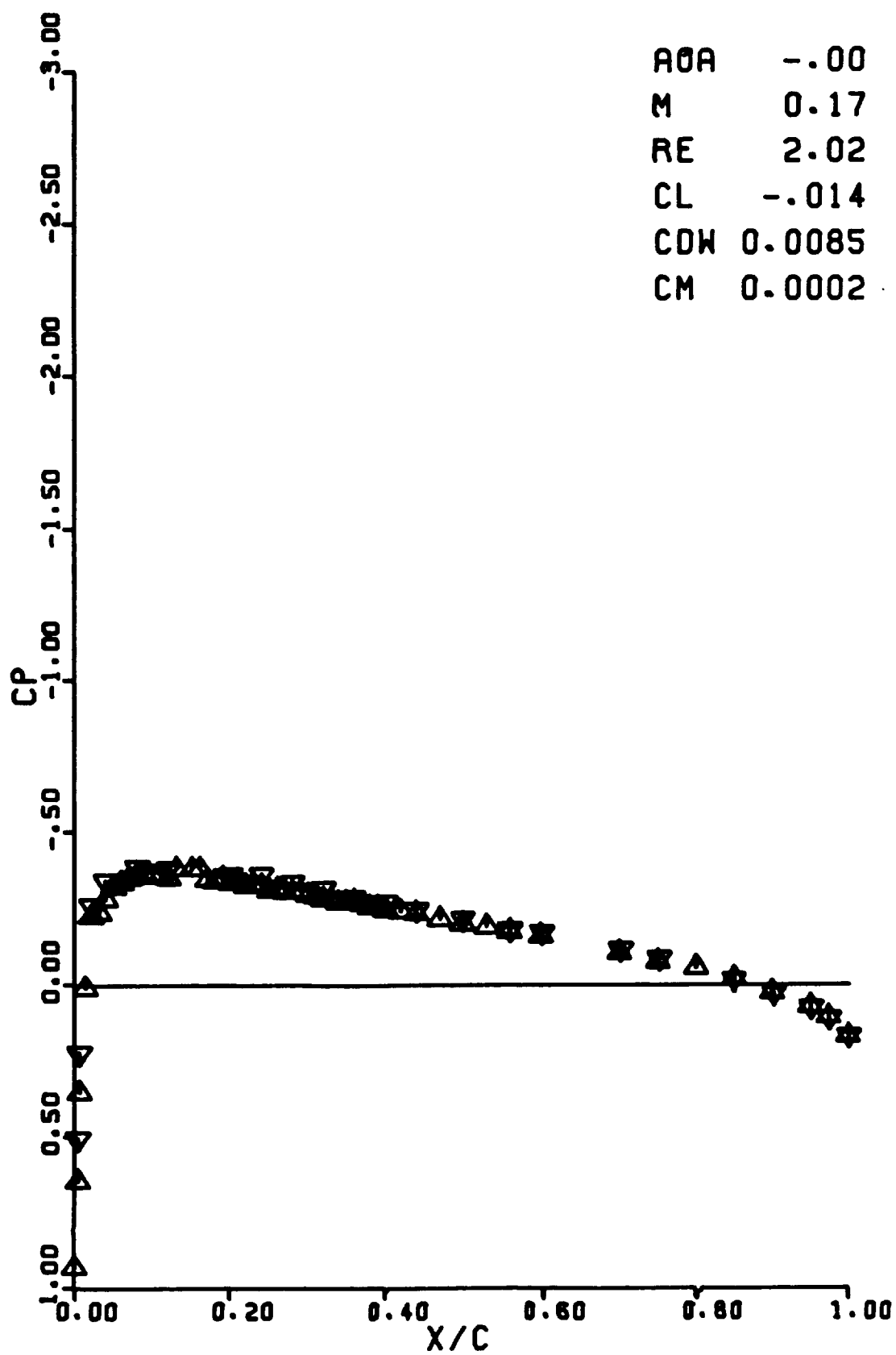
CM -.0520





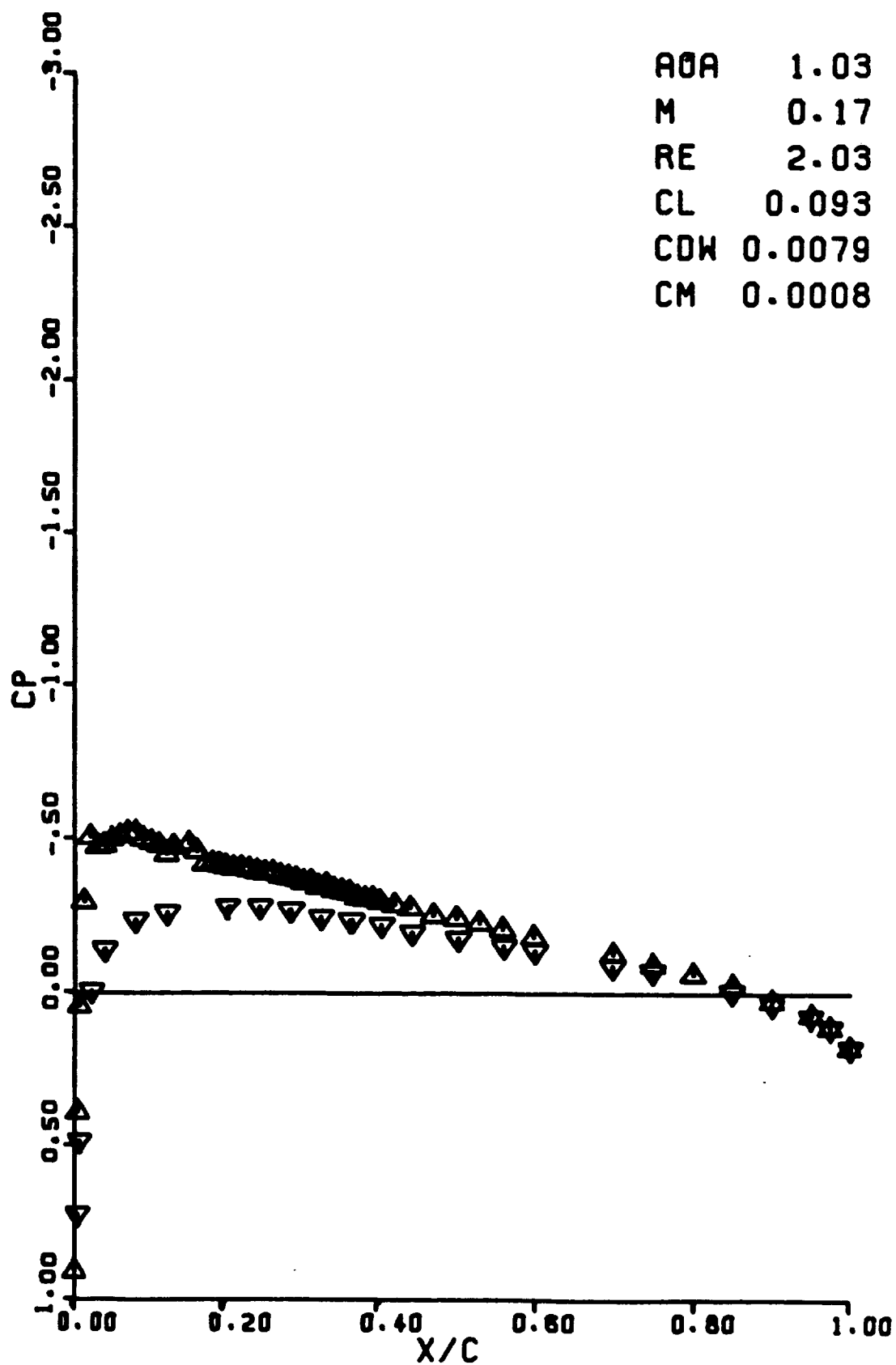
RUN 0400

AOA -.00  
M 0.17  
RE 2.02  
CL -.014  
CDW 0.0085  
CM 0.0002



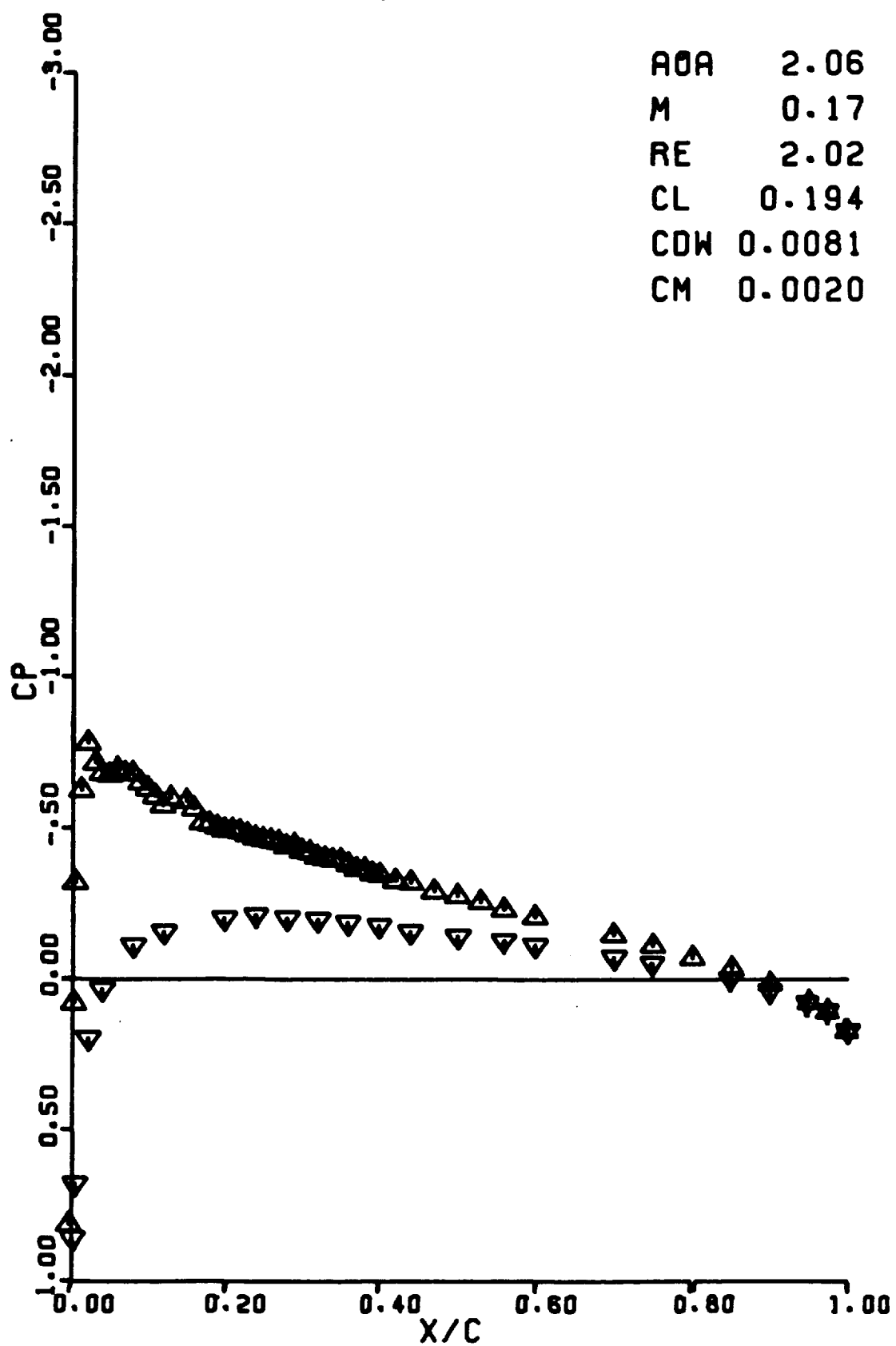
RUN 0401

AOA 1.03  
M 0.17  
RE 2.03  
CL 0.093  
CDW 0.0079  
CM 0.0008



RUN 0402

AOA 2.06  
M 0.17  
RE 2.02  
CL 0.194  
CDW 0.0081  
CM 0.0020



RUN 0403

AOA 3.08

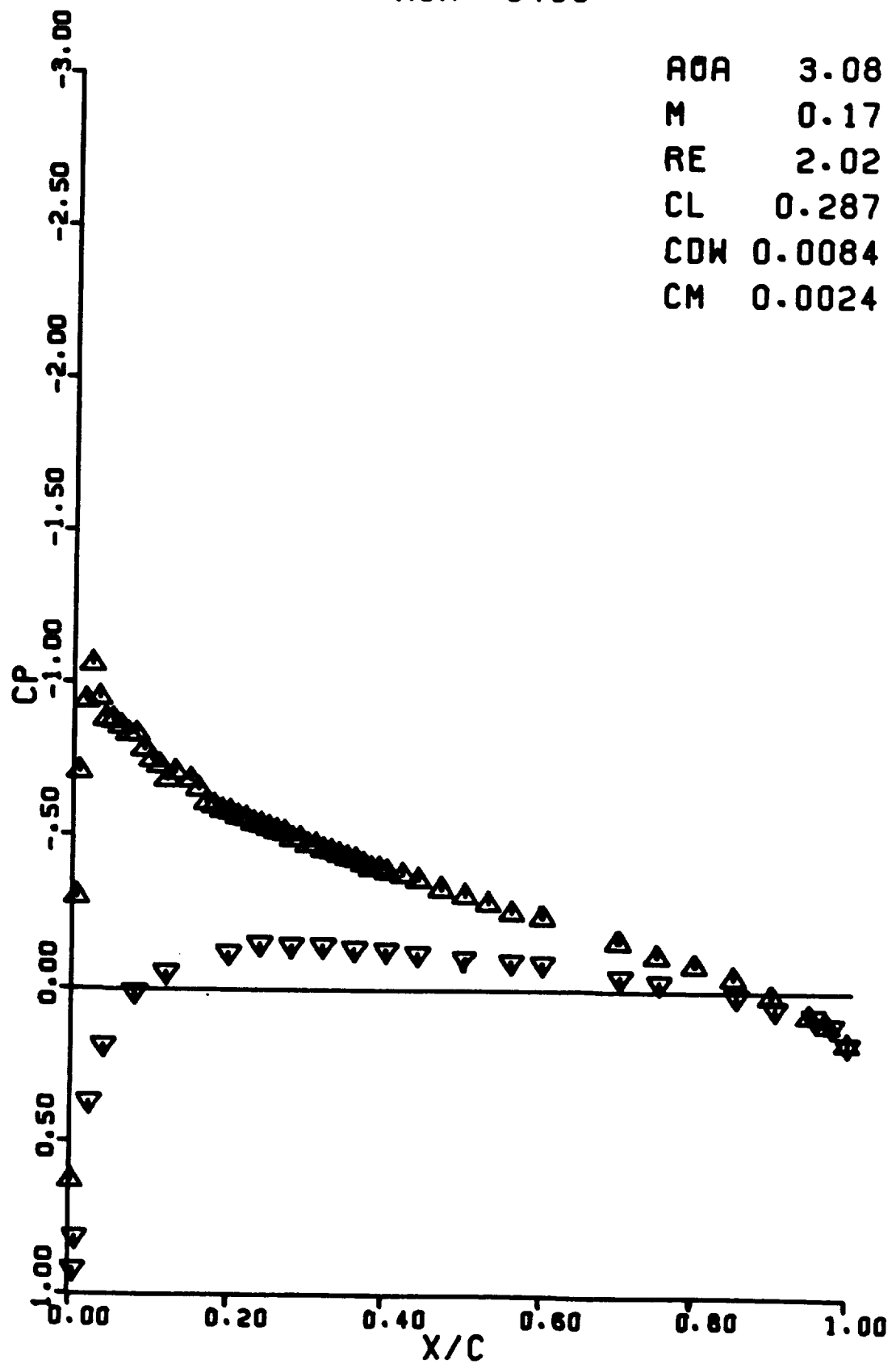
M 0.17

RE 2.02

CL 0.287

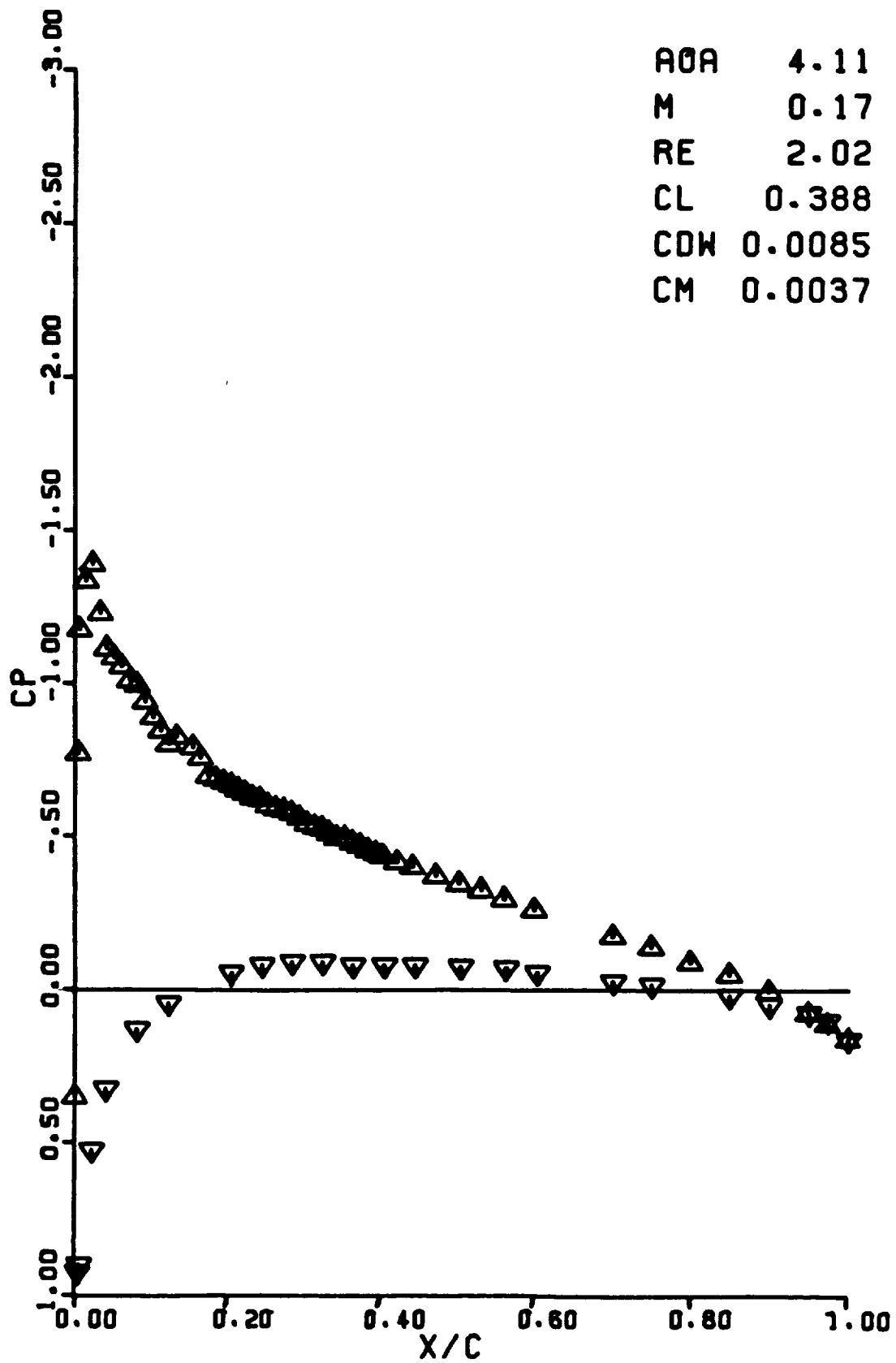
CDW 0.0084

CM 0.0024



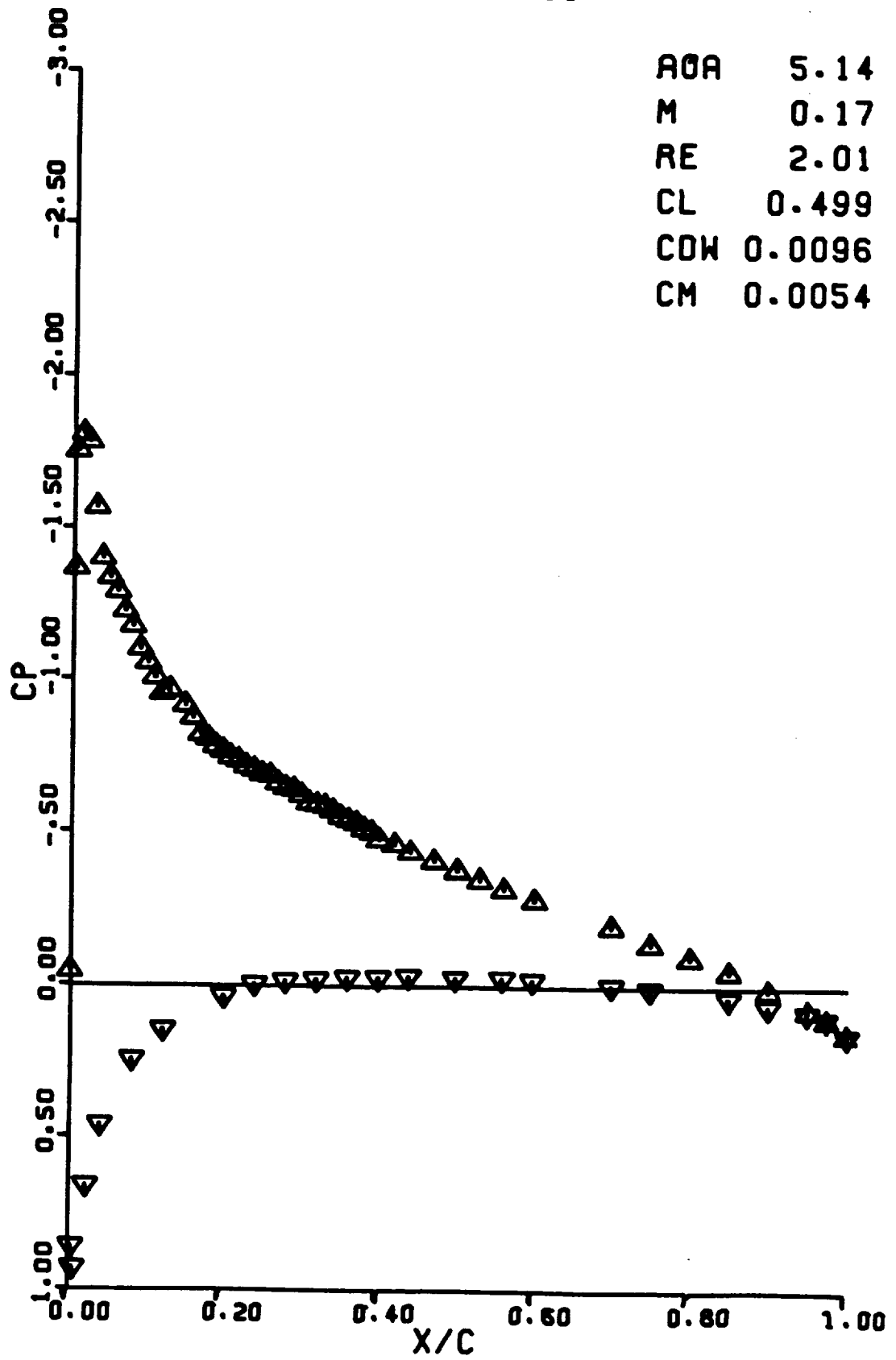
RUN 0404

AOA 4.11  
M 0.17  
RE 2.02  
CL 0.388  
CDW 0.0085  
CM 0.0037



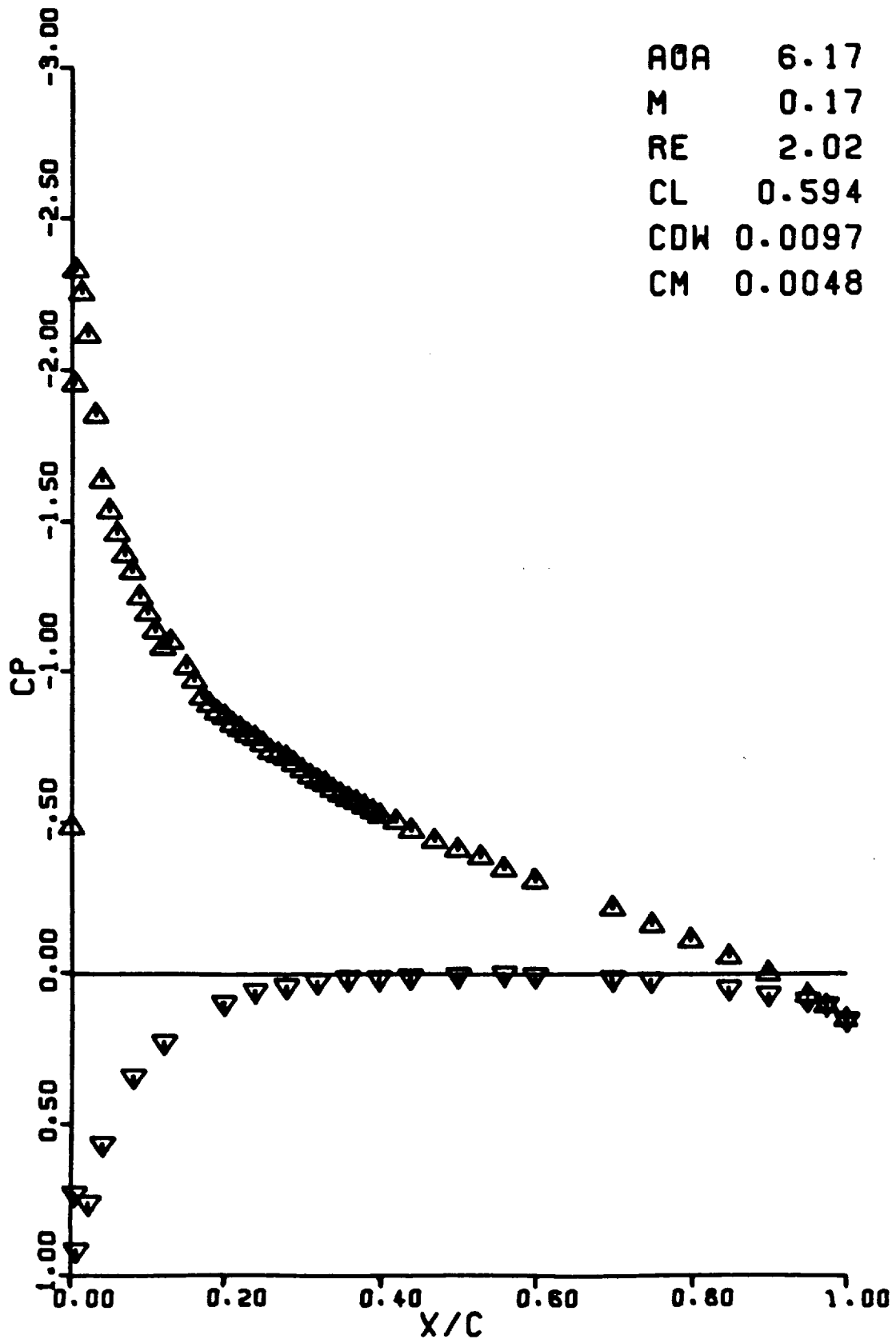
RUN 0405

AOA 5.14  
M 0.17  
RE 2.01  
CL 0.499  
CDW 0.0096  
CM 0.0054



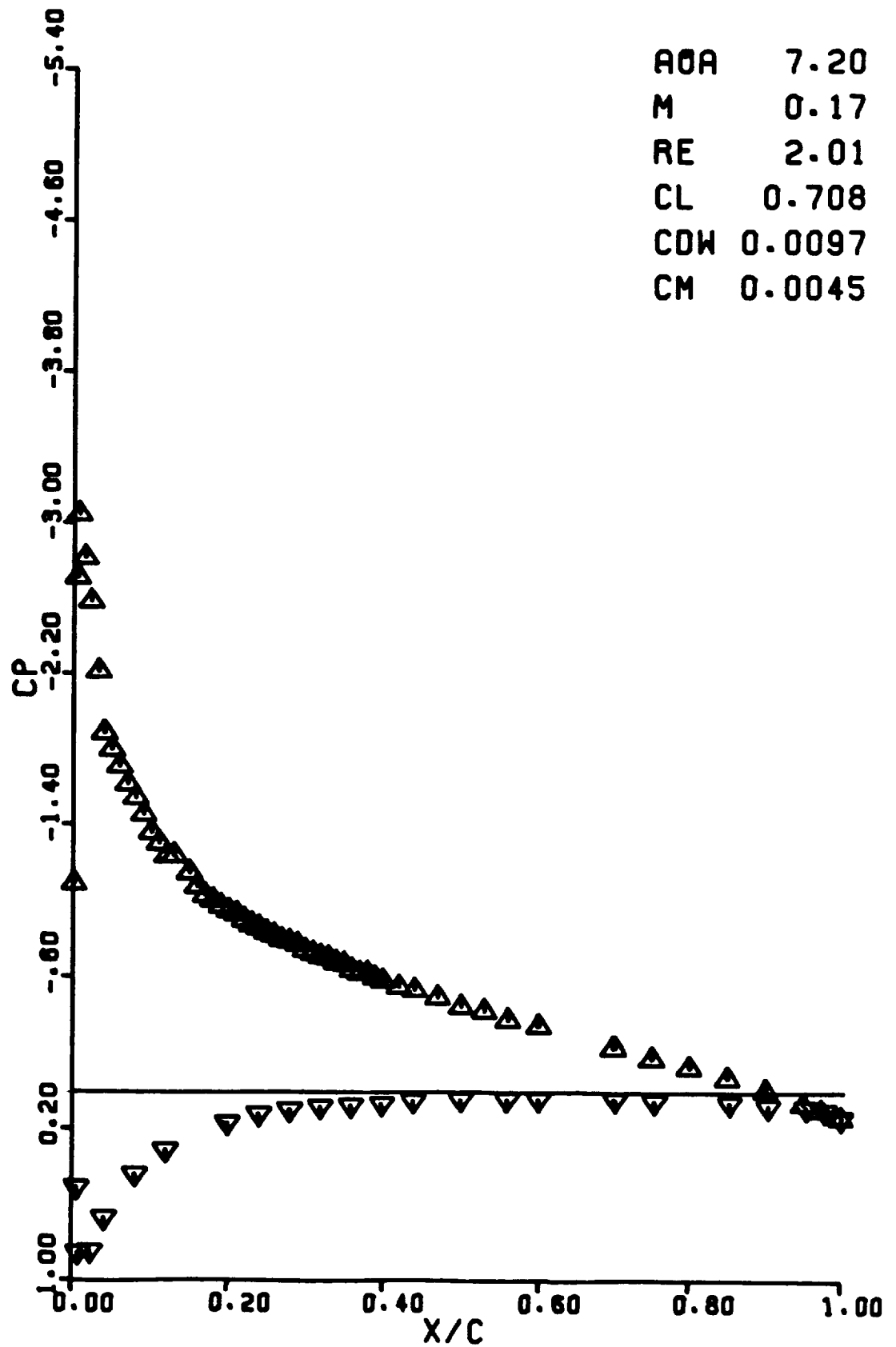
RUN 0406

AOA 6.17  
M 0.17  
RE 2.02  
CL 0.594  
CDW 0.0097  
CM 0.0048



RUN 0407

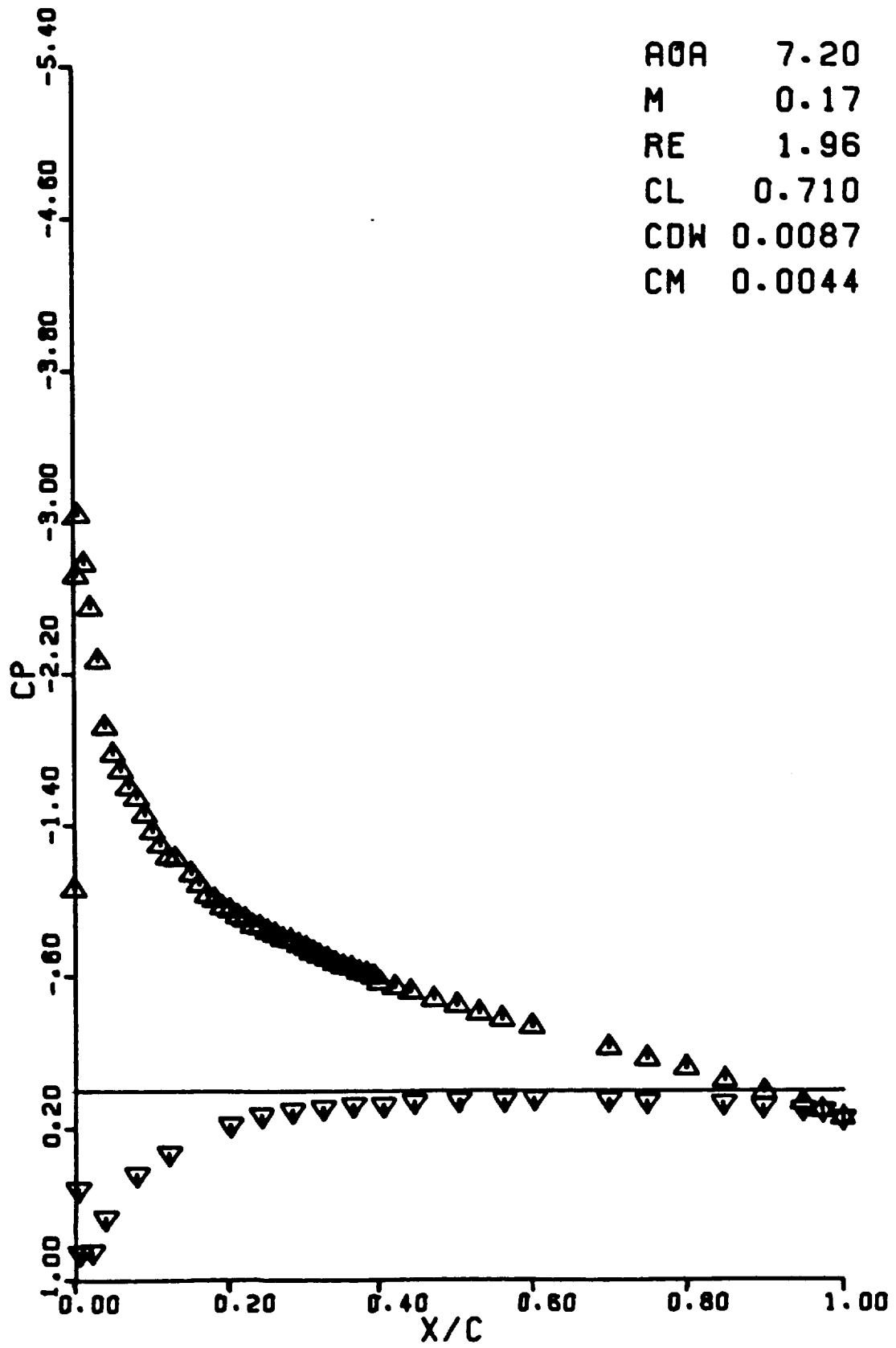
AOA 7.20  
M 0.17  
RE 2.01  
CL 0.708  
CDW 0.0097  
CM 0.0045





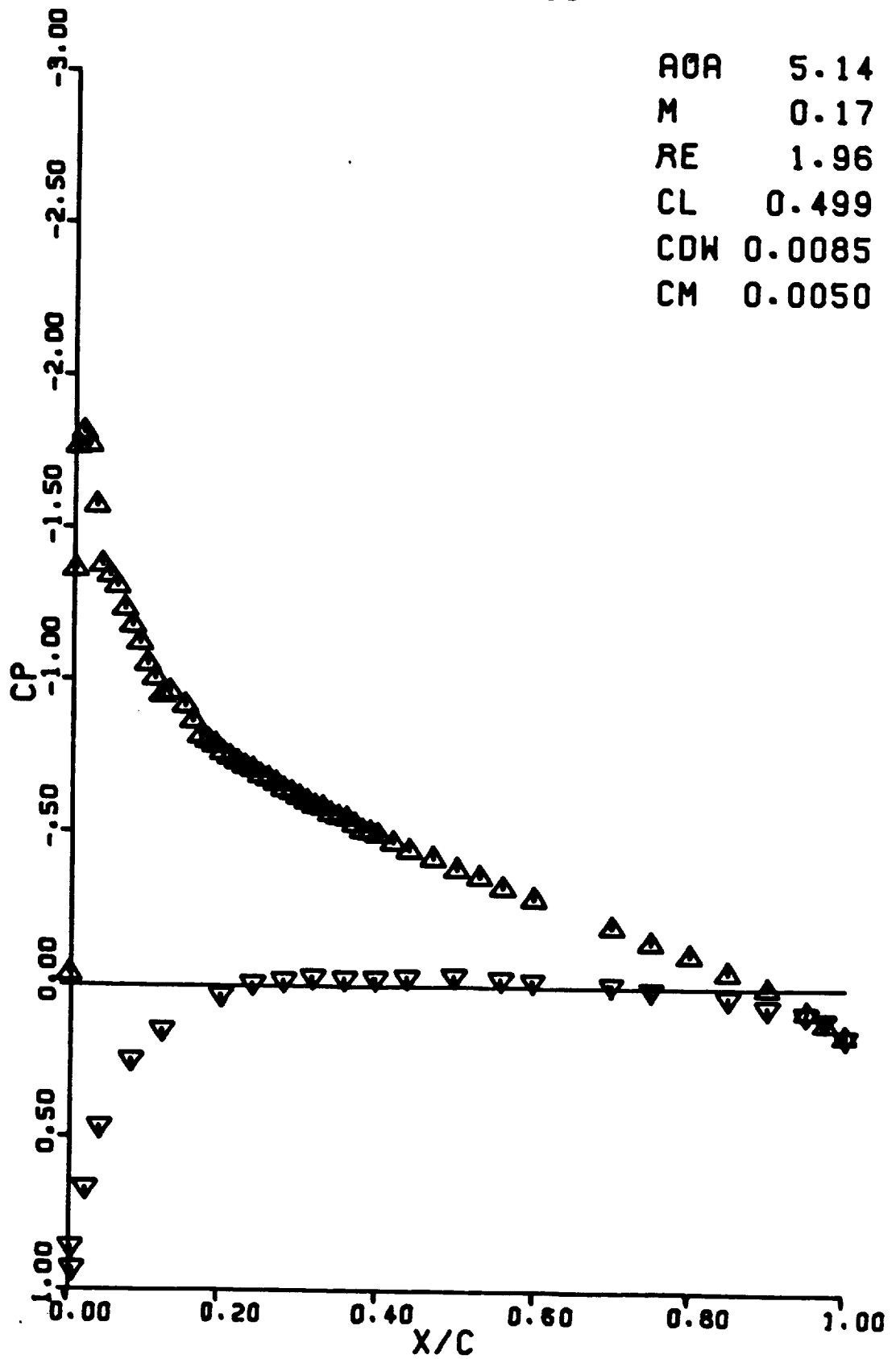
RUN 0408

AOA 7.20  
M 0.17  
RE 1.96  
CL 0.710  
CDW 0.0087  
CM 0.0044



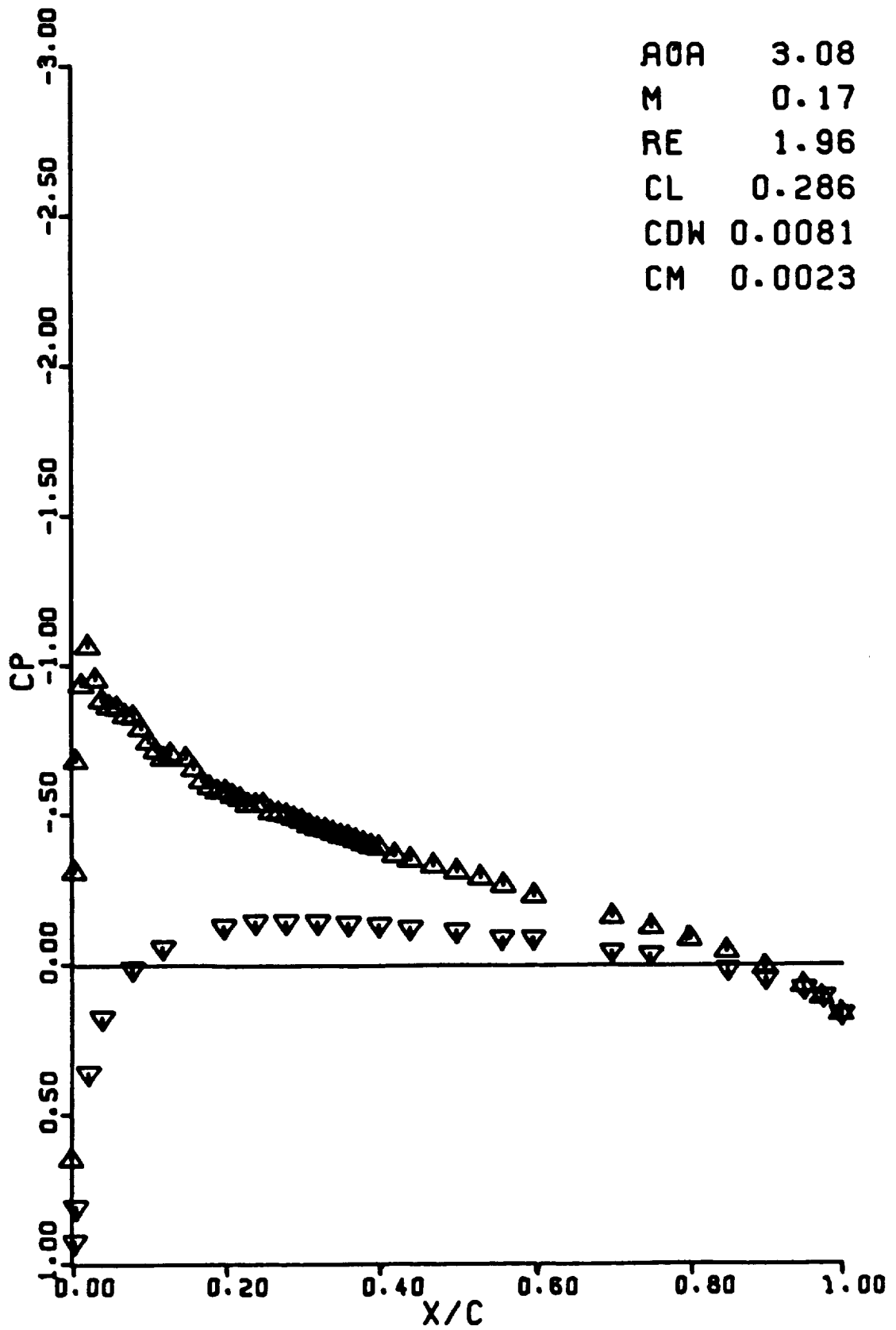
RUN 0409

AOA 5.14  
M 0.17  
RE 1.96  
CL 0.499  
CDW 0.0085  
CM 0.0050



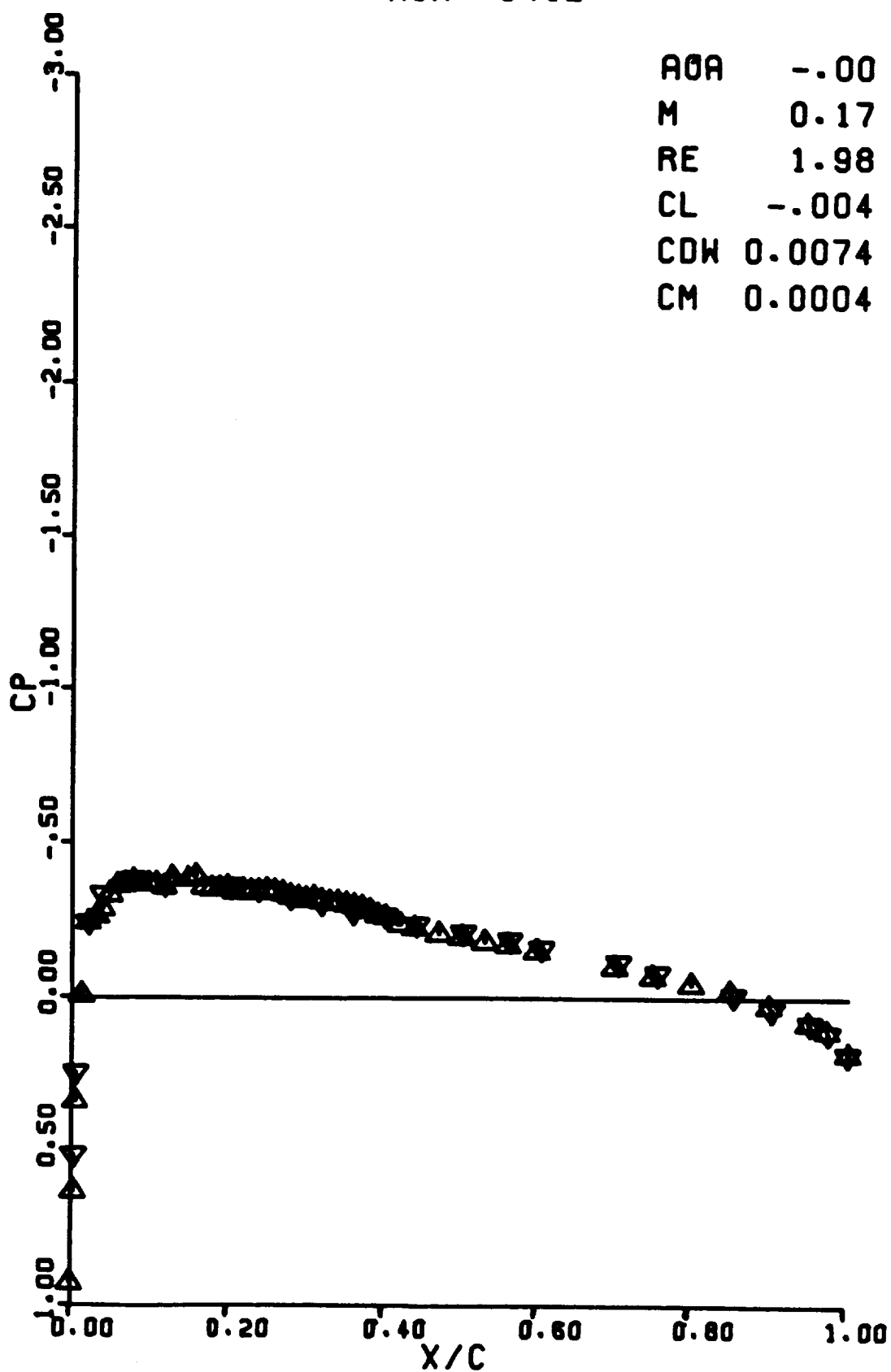
RUN 0410

AOA 3.08  
M 0.17  
RE 1.96  
CL 0.286  
CDW 0.0081  
CM 0.0023



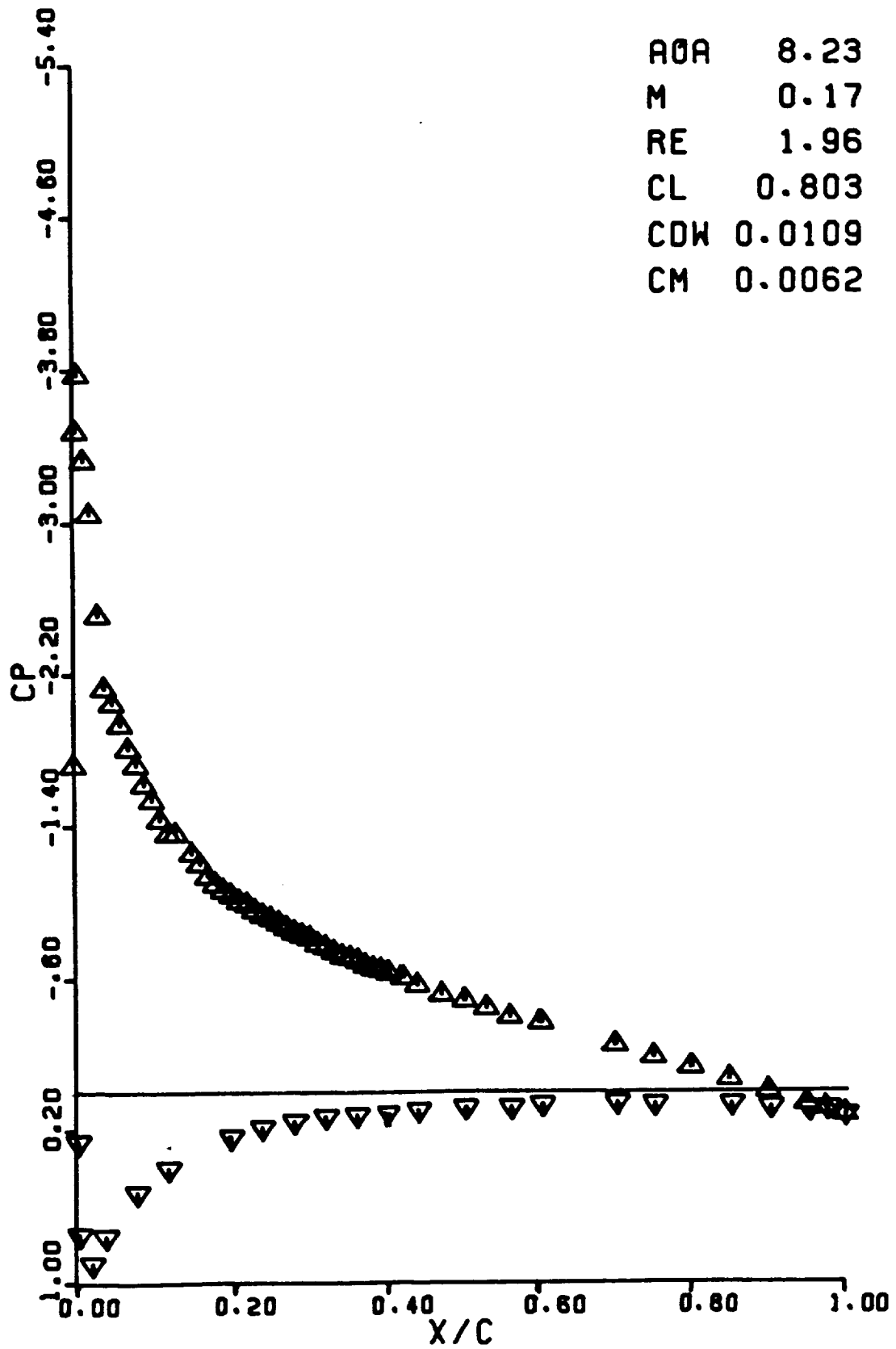
RUN 0412

AOA -.00  
M 0.17  
RE 1.98  
CL -.004  
CDW 0.0074  
CM 0.0004

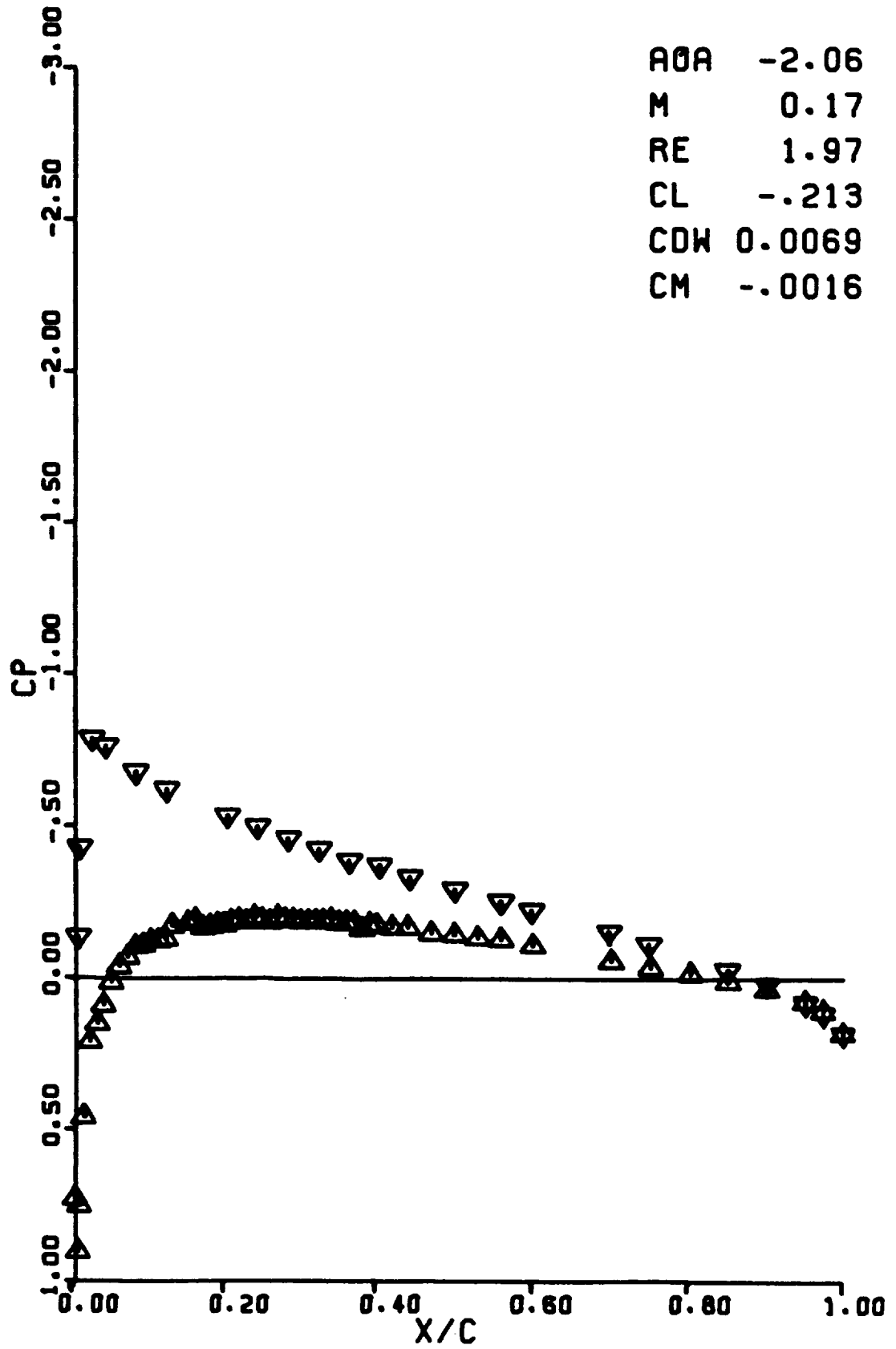


RUN 0413

AOA 8.23  
M 0.17  
RE 1.96  
CL 0.803  
CDW 0.0109  
CM 0.0062

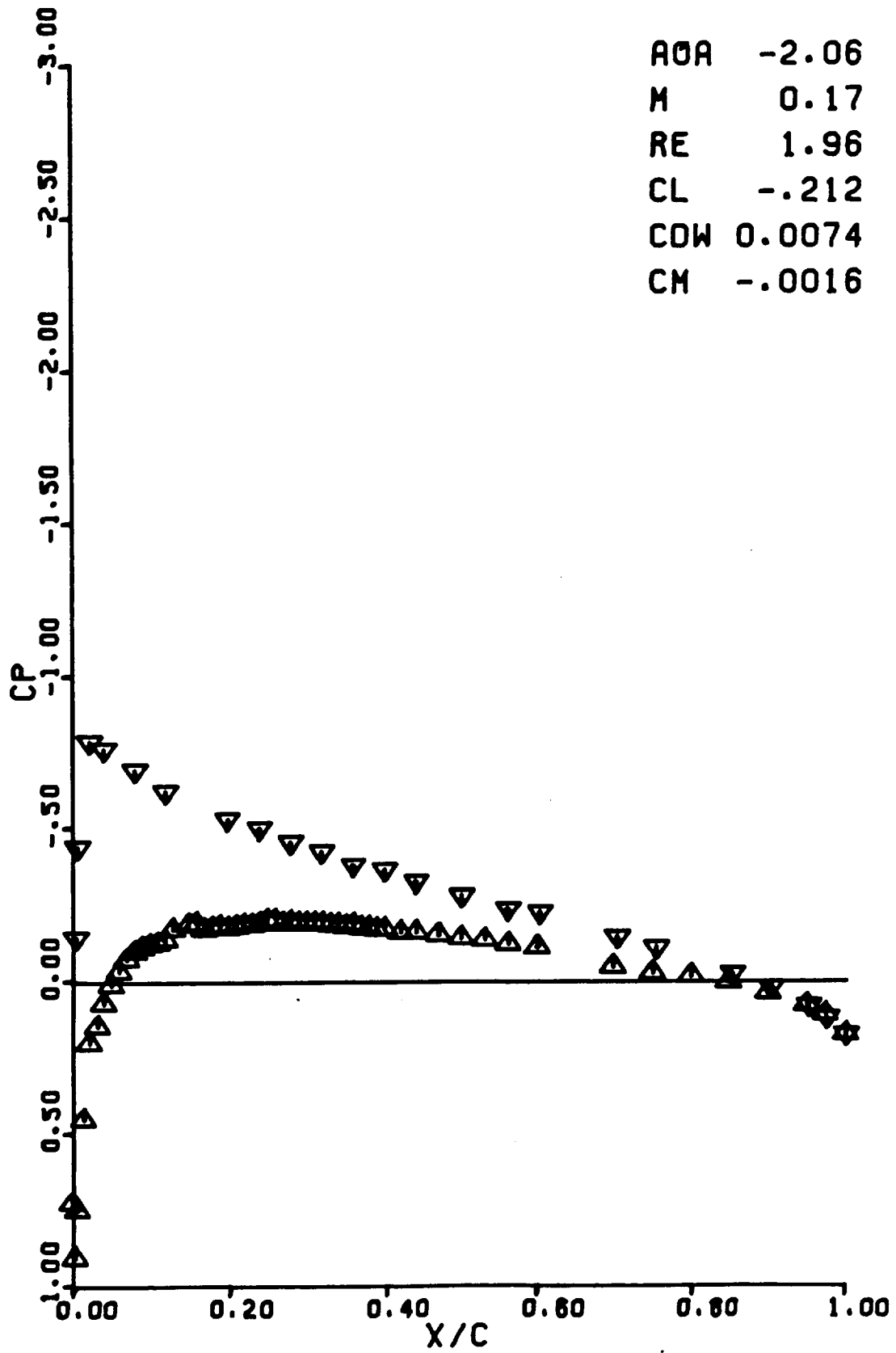


RUN 0414



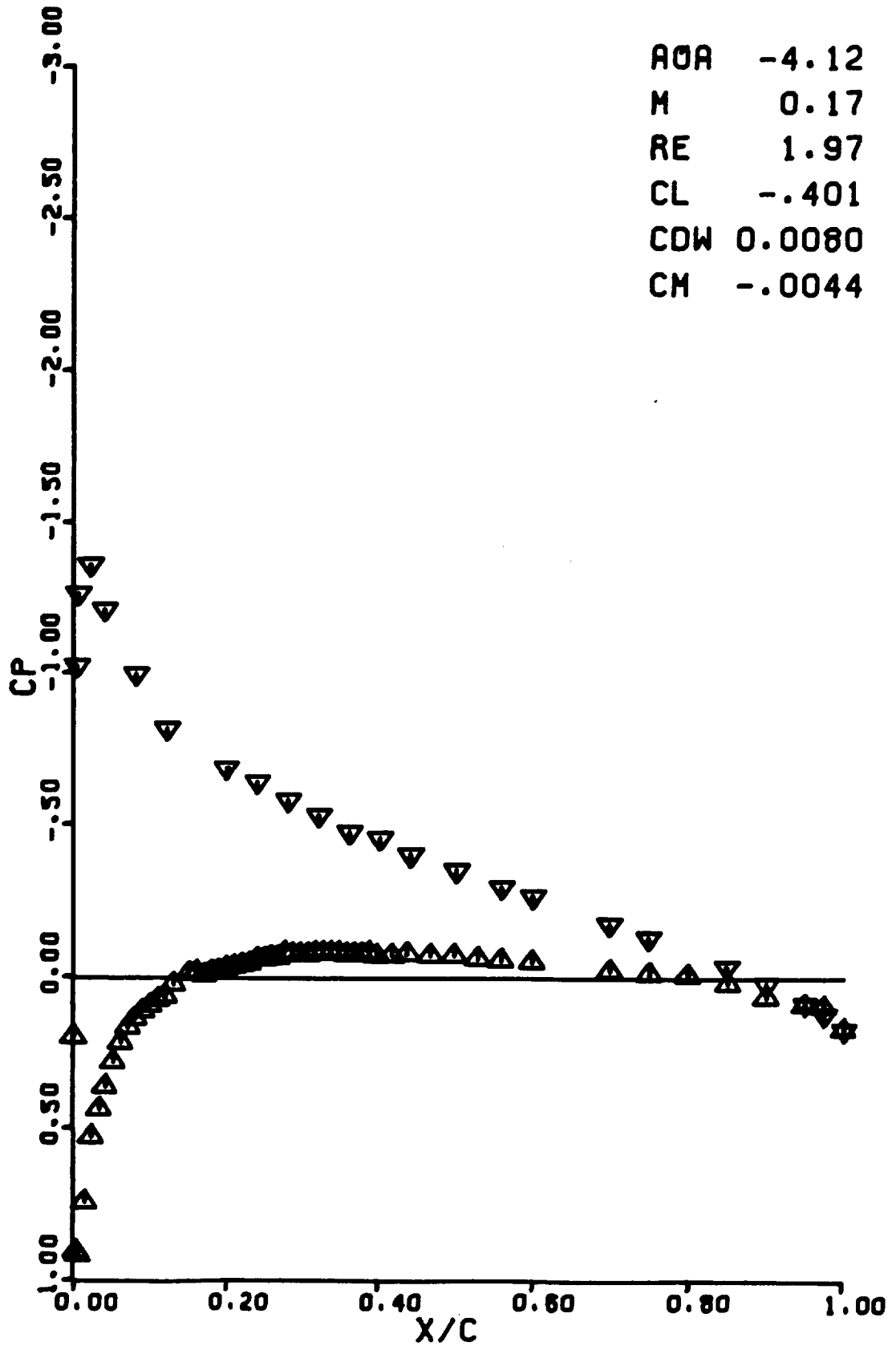
RUN 0415

AOA -2.06  
M 0.17  
RE 1.96  
CL -.212  
CDW 0.0074  
CM -.0016



RUN 0416

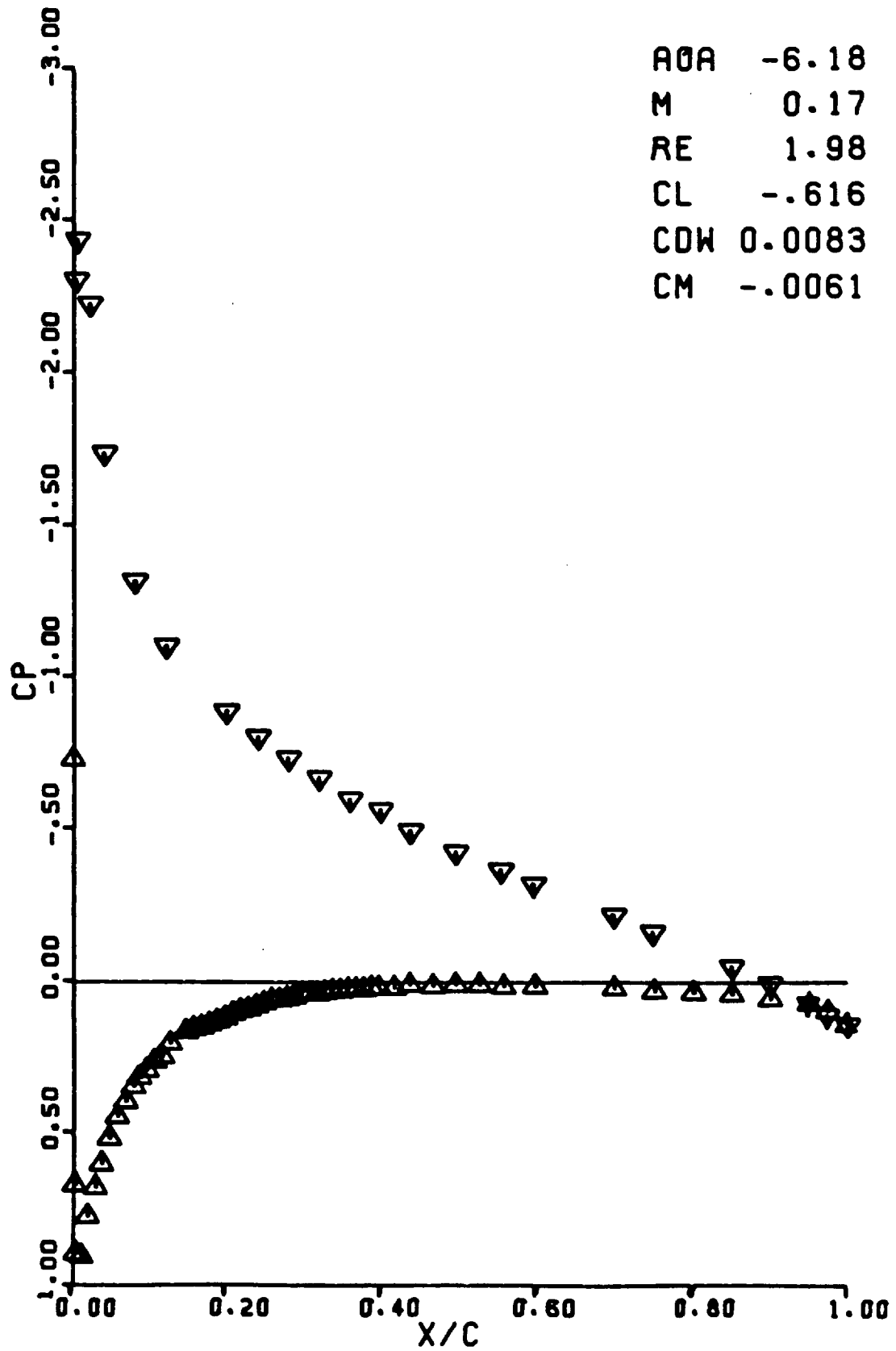
AOA -4.12  
M 0.17  
RE 1.97  
CL -.401  
CDW 0.0080  
CM -.0044





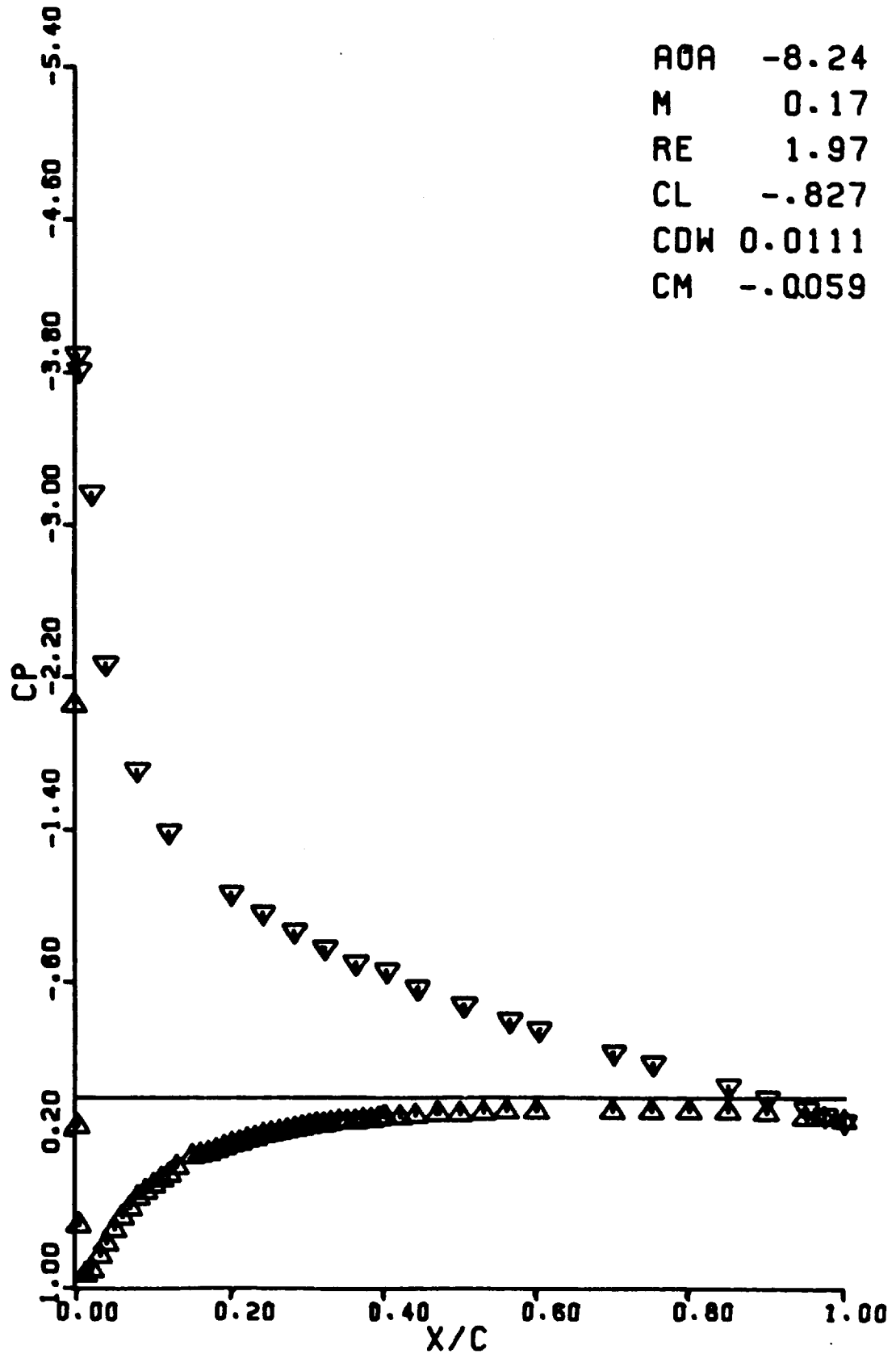
RUN 0417

AOA -6.18  
M 0.17  
RE 1.98  
CL -.616  
CDW 0.0083  
CM -.0061



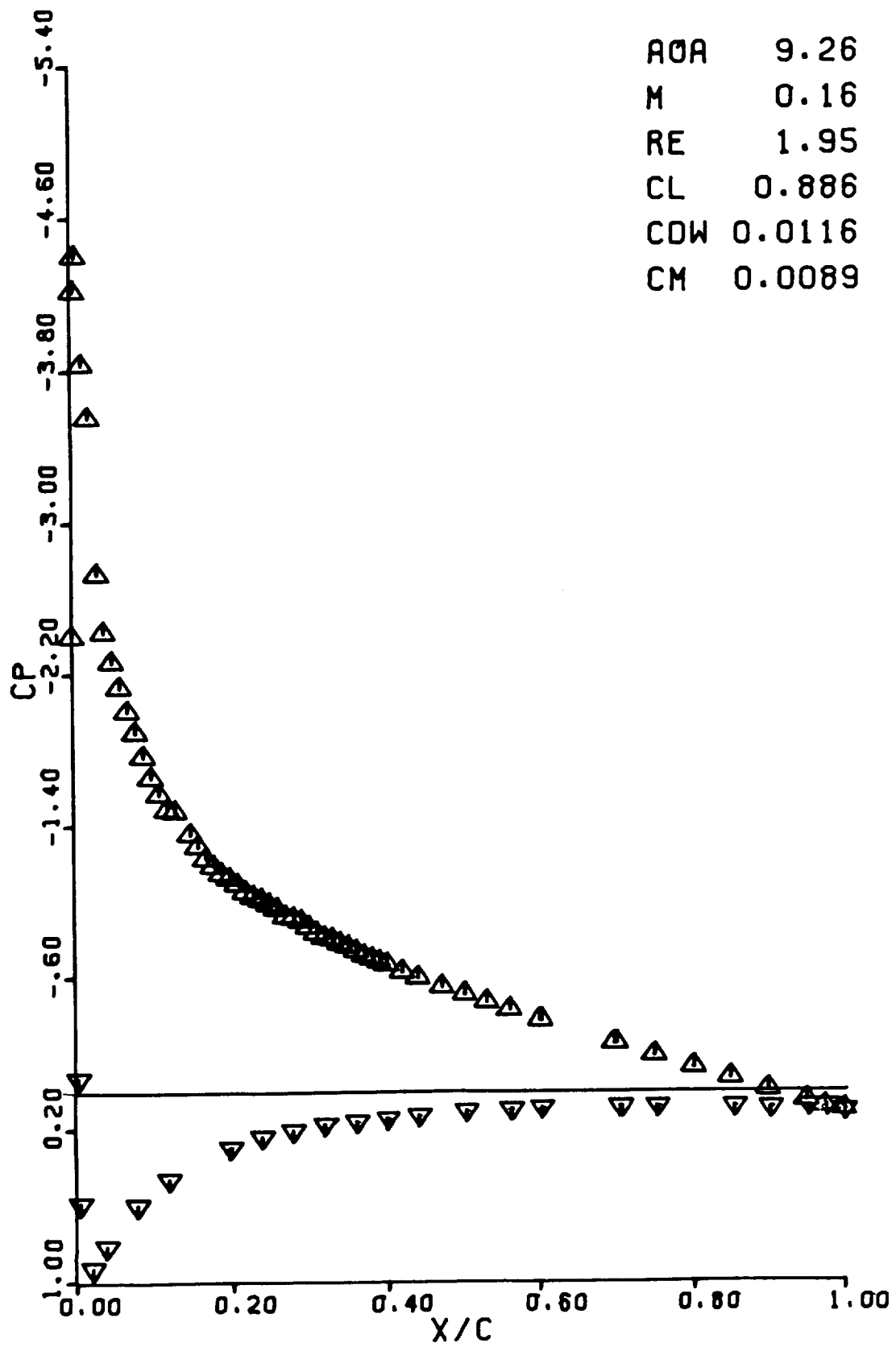
RUN 0418

AOA -8.24  
M 0.17  
RE 1.97  
CL -.827  
CDW 0.0111  
CM -.0059



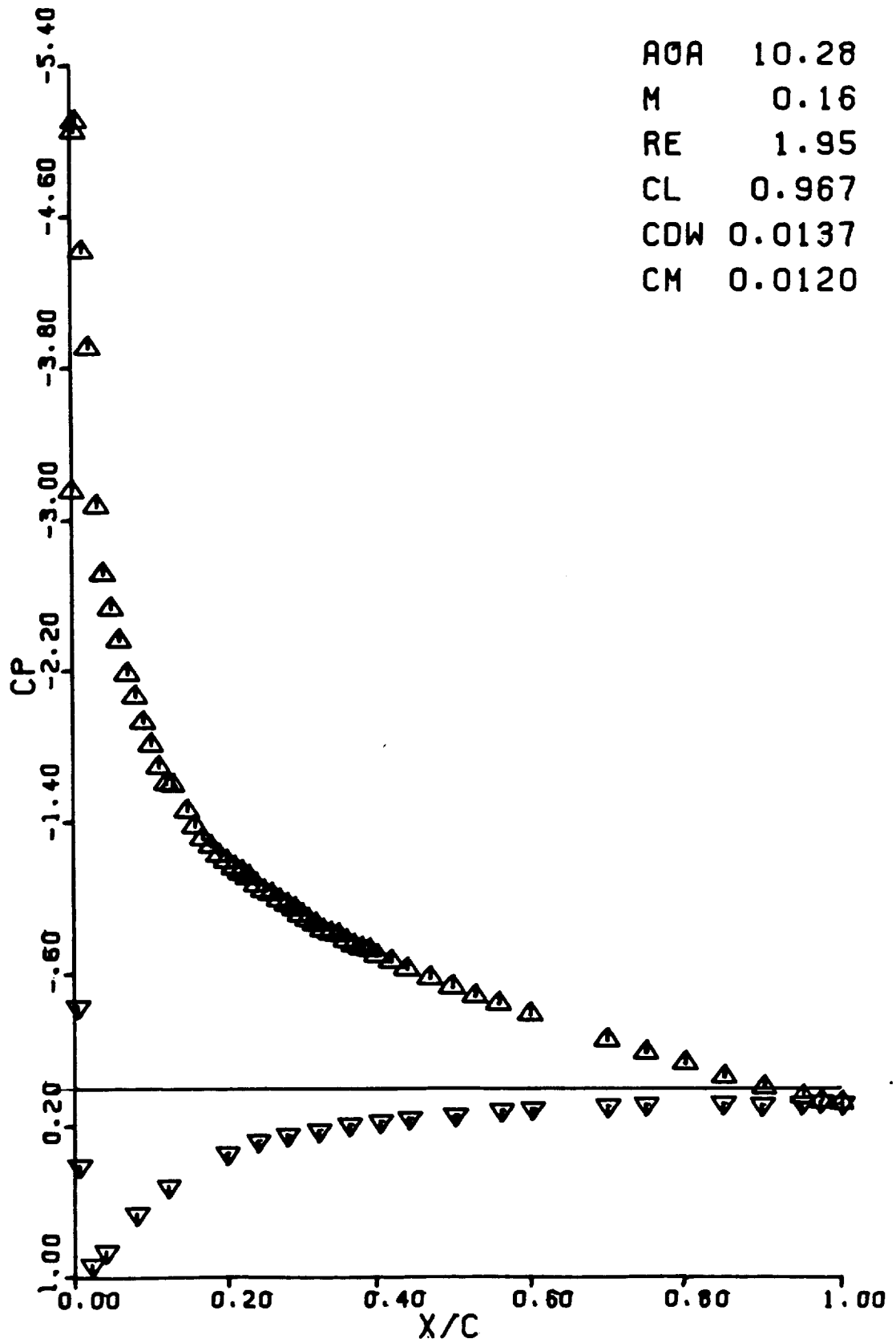
RUN 0420

AOA 9.26  
M 0.16  
RE 1.95  
CL 0.886  
CDW 0.0116  
CM 0.0089



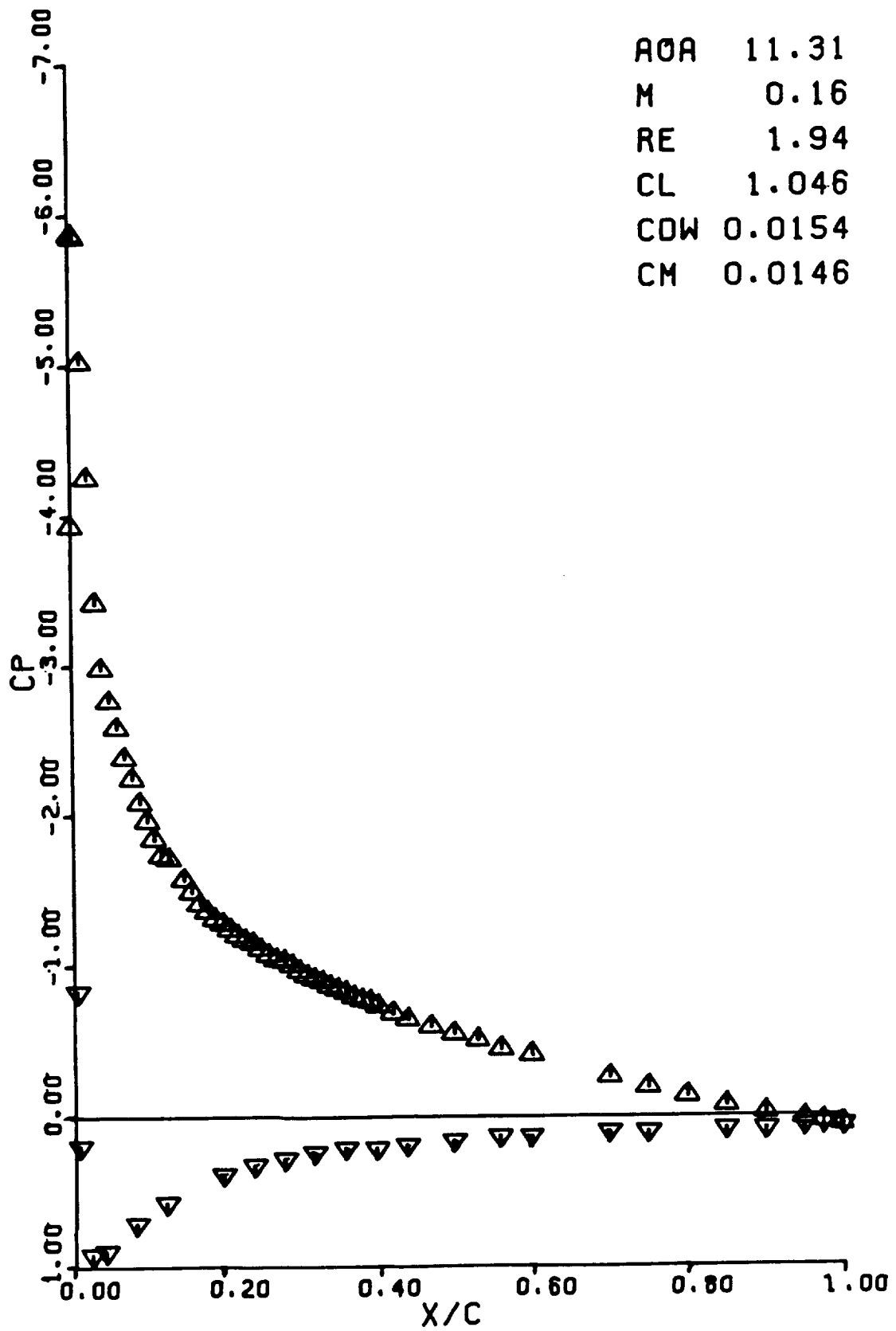
RUN 0421

AOA 10.28  
M 0.16  
RE 1.95  
CL 0.967  
CDW 0.0137  
CM 0.0120



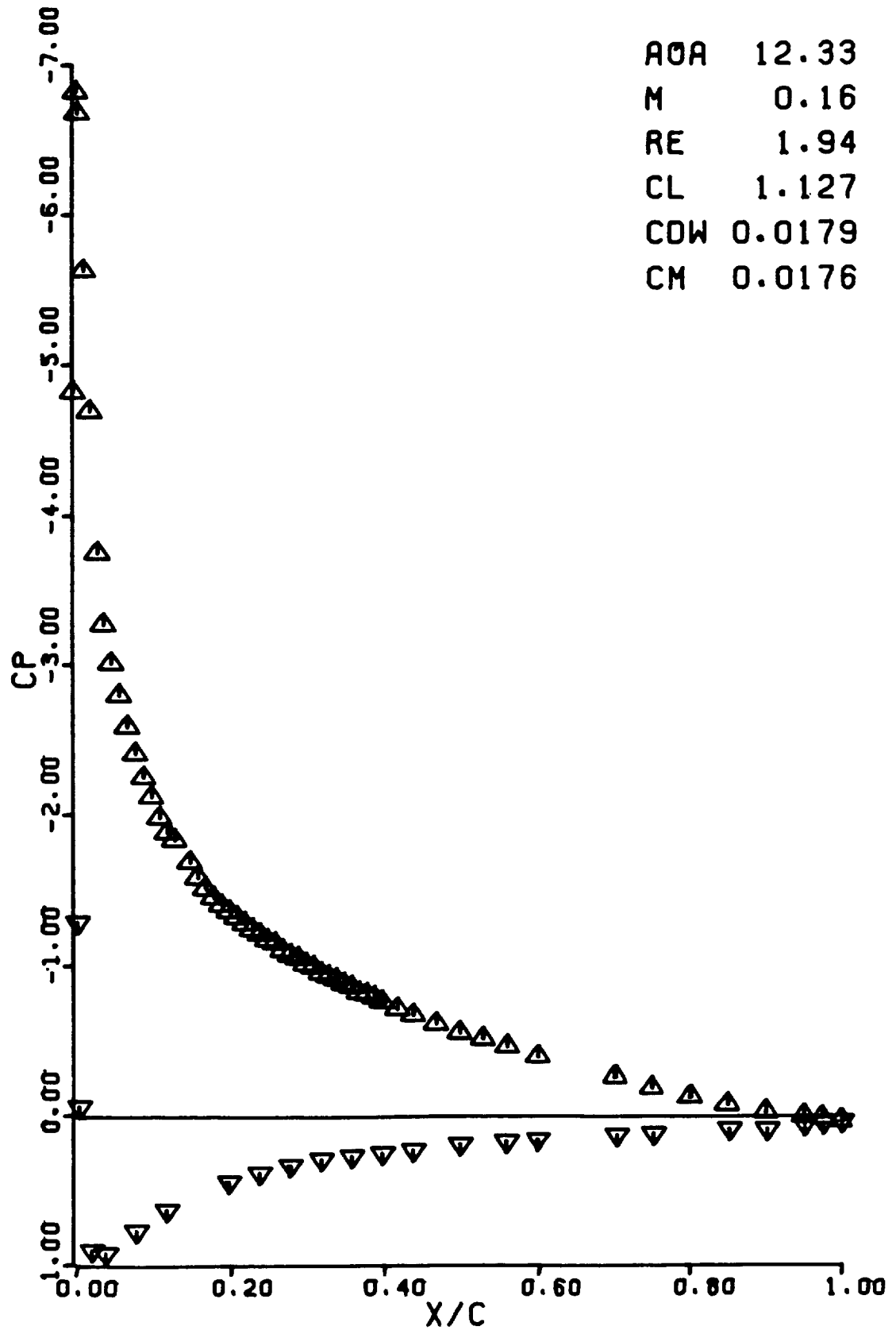
RUN 0422

AOA 11.31  
M 0.16  
RE 1.94  
CL 1.046  
CDW 0.0154  
CM 0.0146



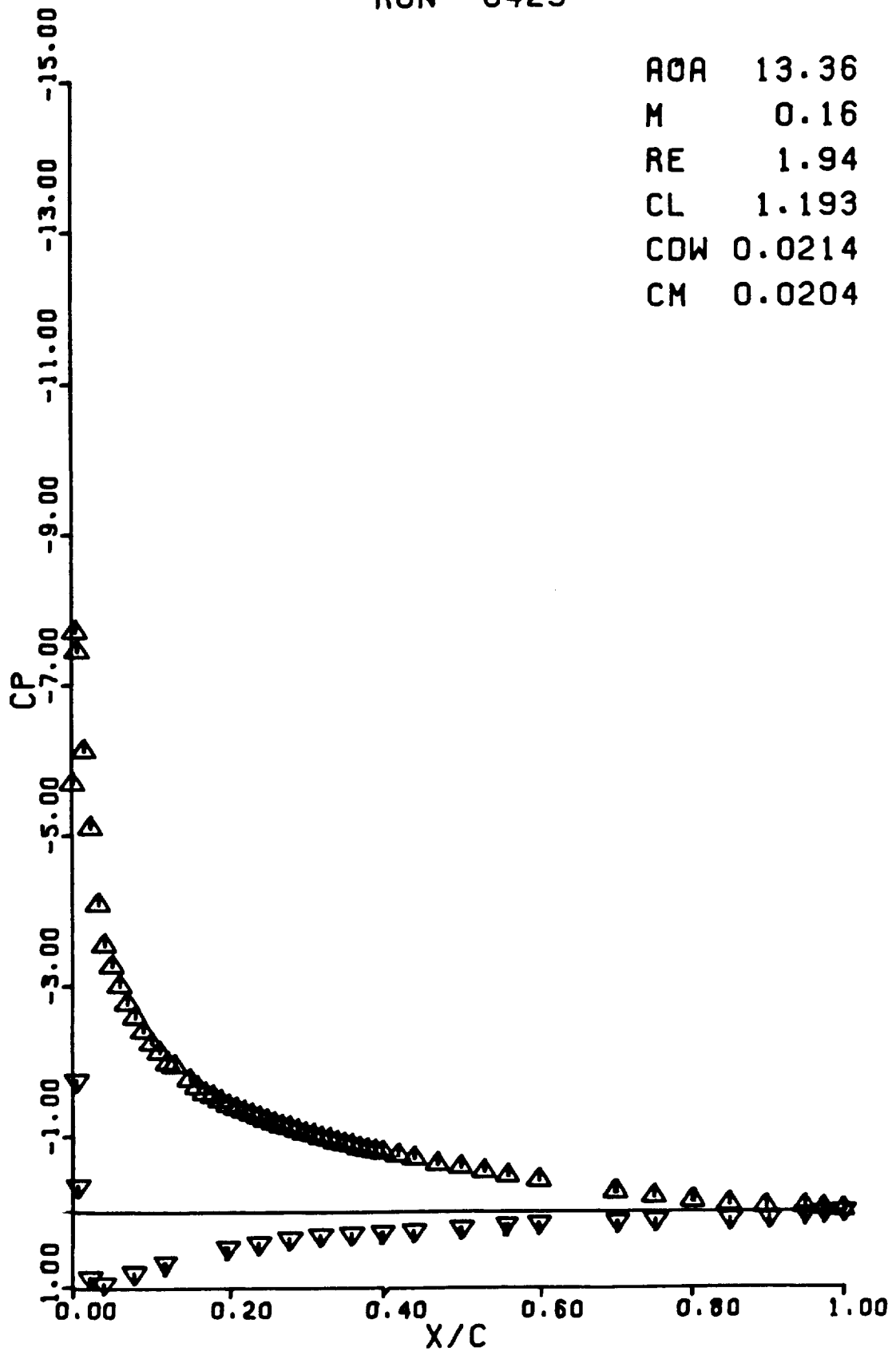
RUN 0423

AOA 12.33  
M 0.16  
RE 1.94  
CL 1.127  
CDW 0.0179  
CM 0.0176

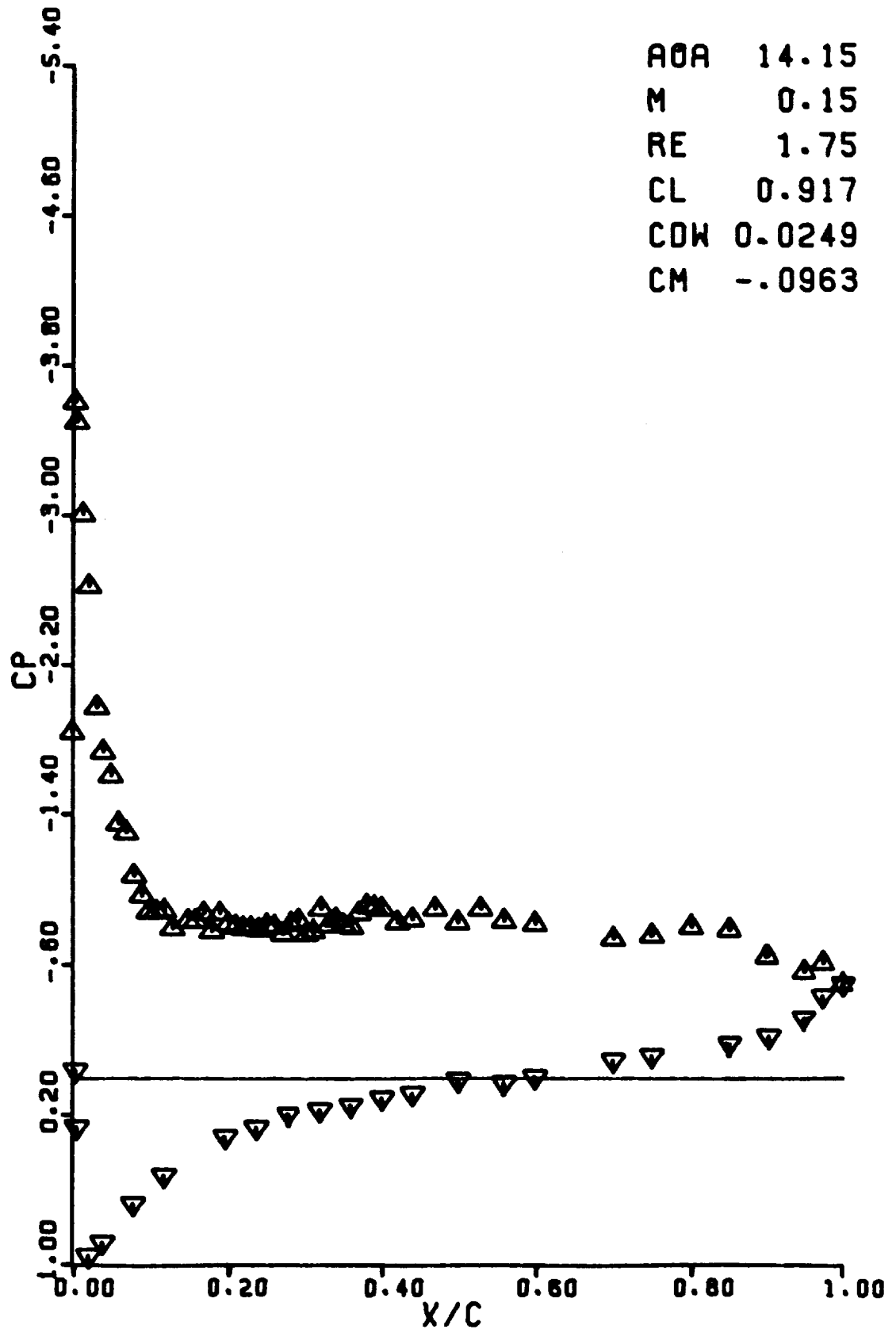


RUN 0425

AOA 13.36  
M 0.16  
RE 1.94  
CL 1.193  
CDW 0.0214  
CM 0.0204



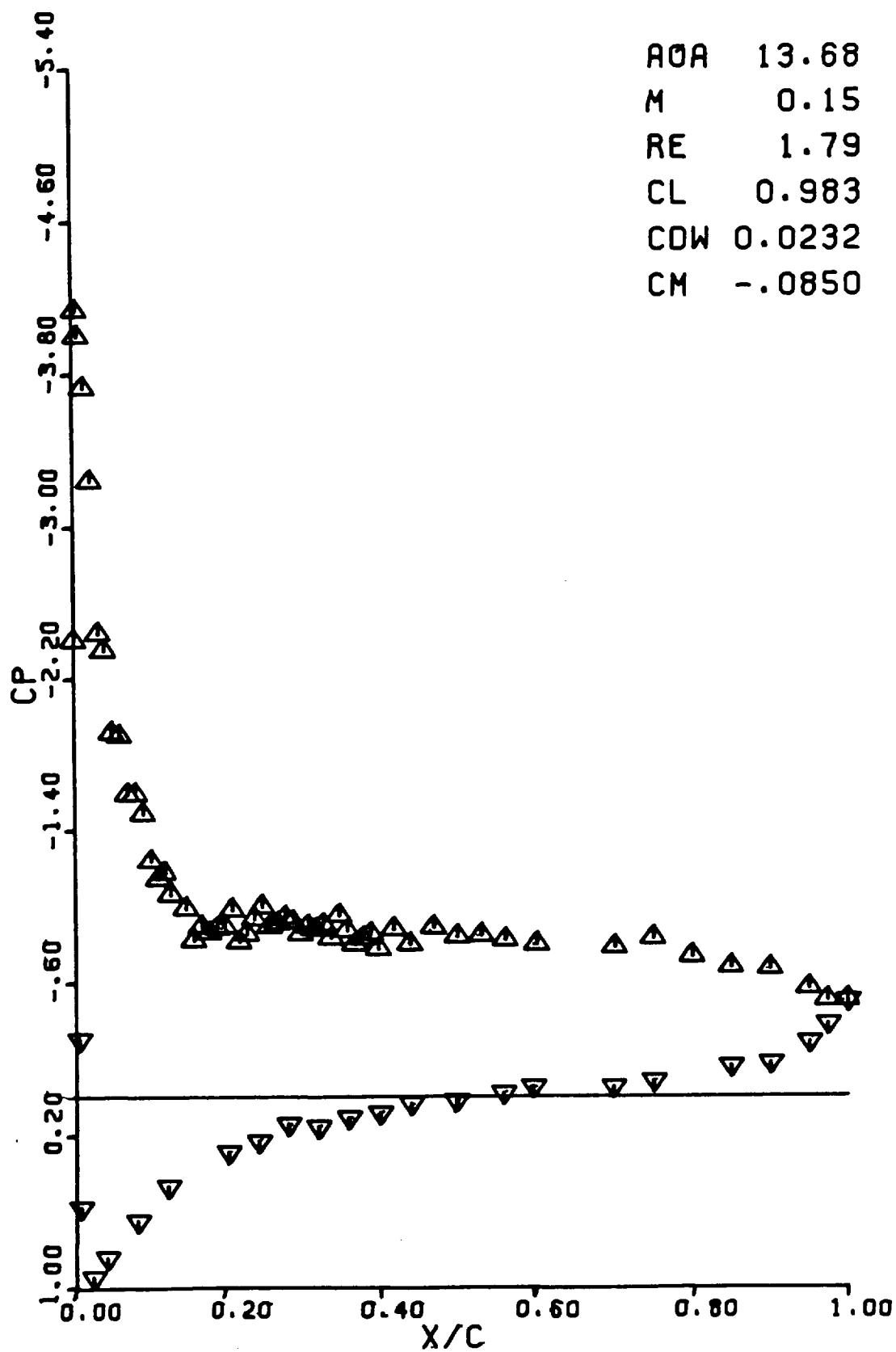
RUN 0426





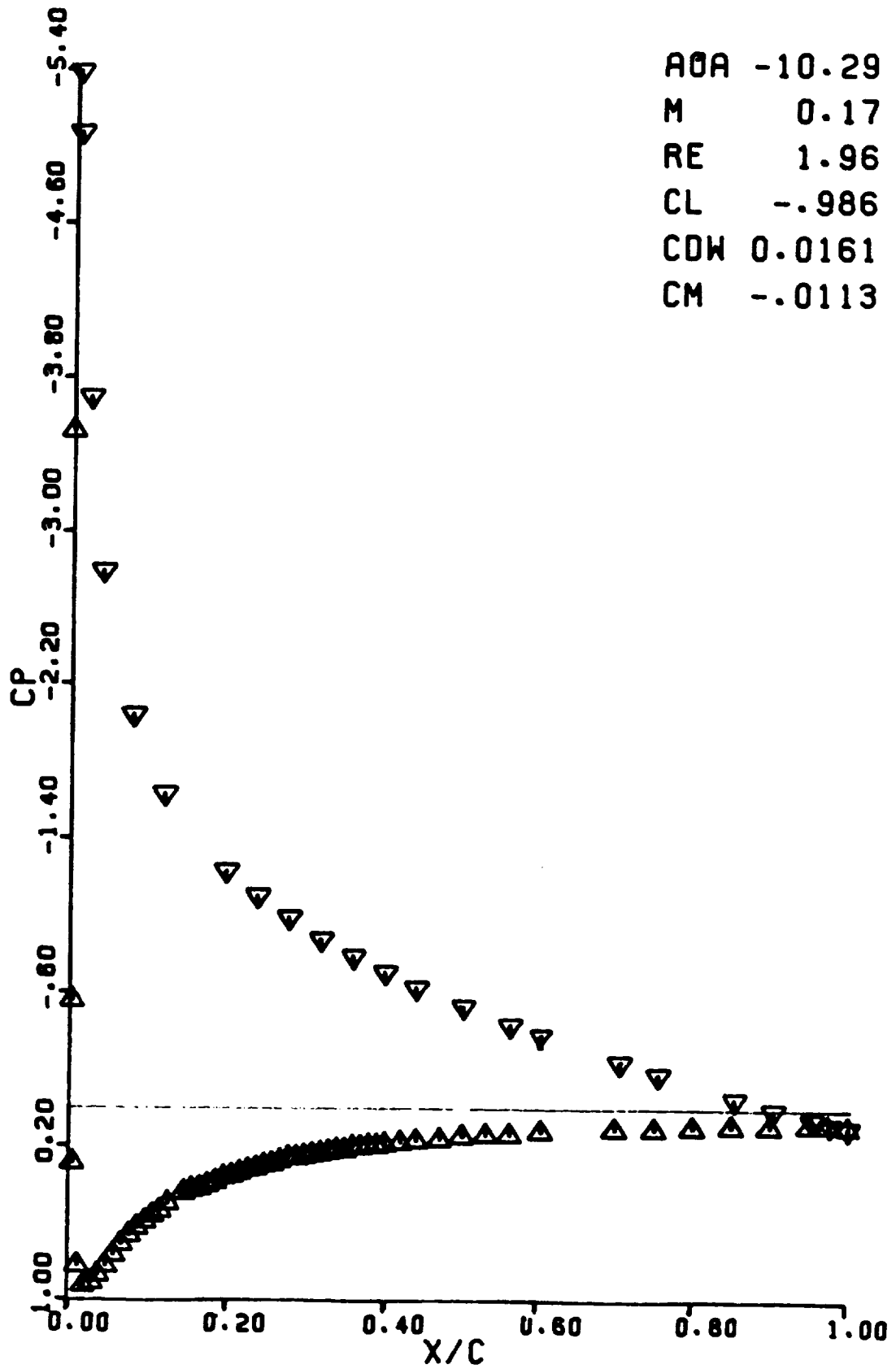
RUN 0427

AOA 13.68  
M 0.15  
RE 1.79  
CL 0.983  
CDW 0.0232  
CM -.0850



RUN 0428

AOA -10.29  
M 0.17  
RE 1.96  
CL -.986  
CDW 0.0161  
CM -.0113



RUN 0429

AOA -10.29

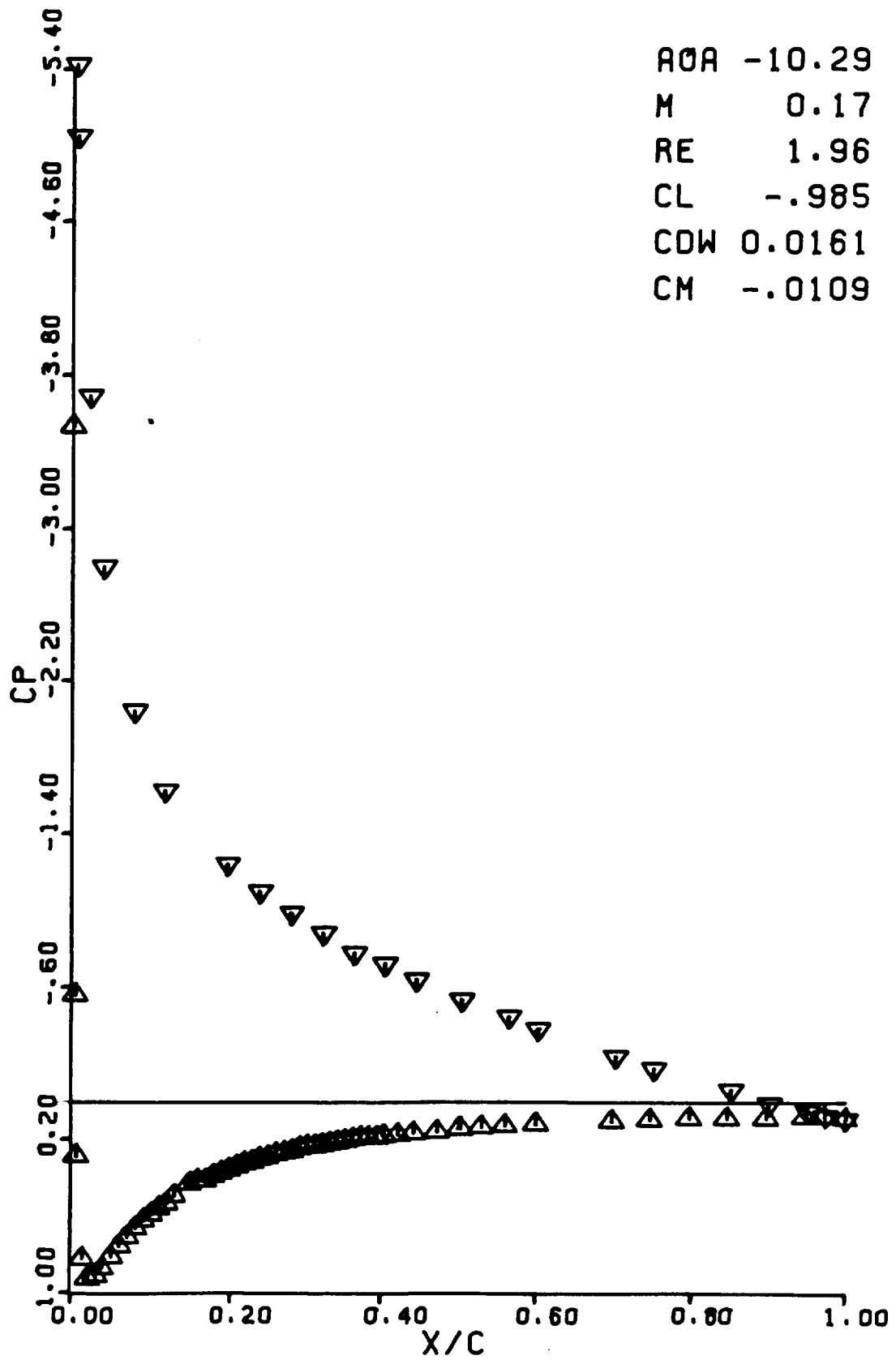
M 0.17

RE 1.96

CL -.985

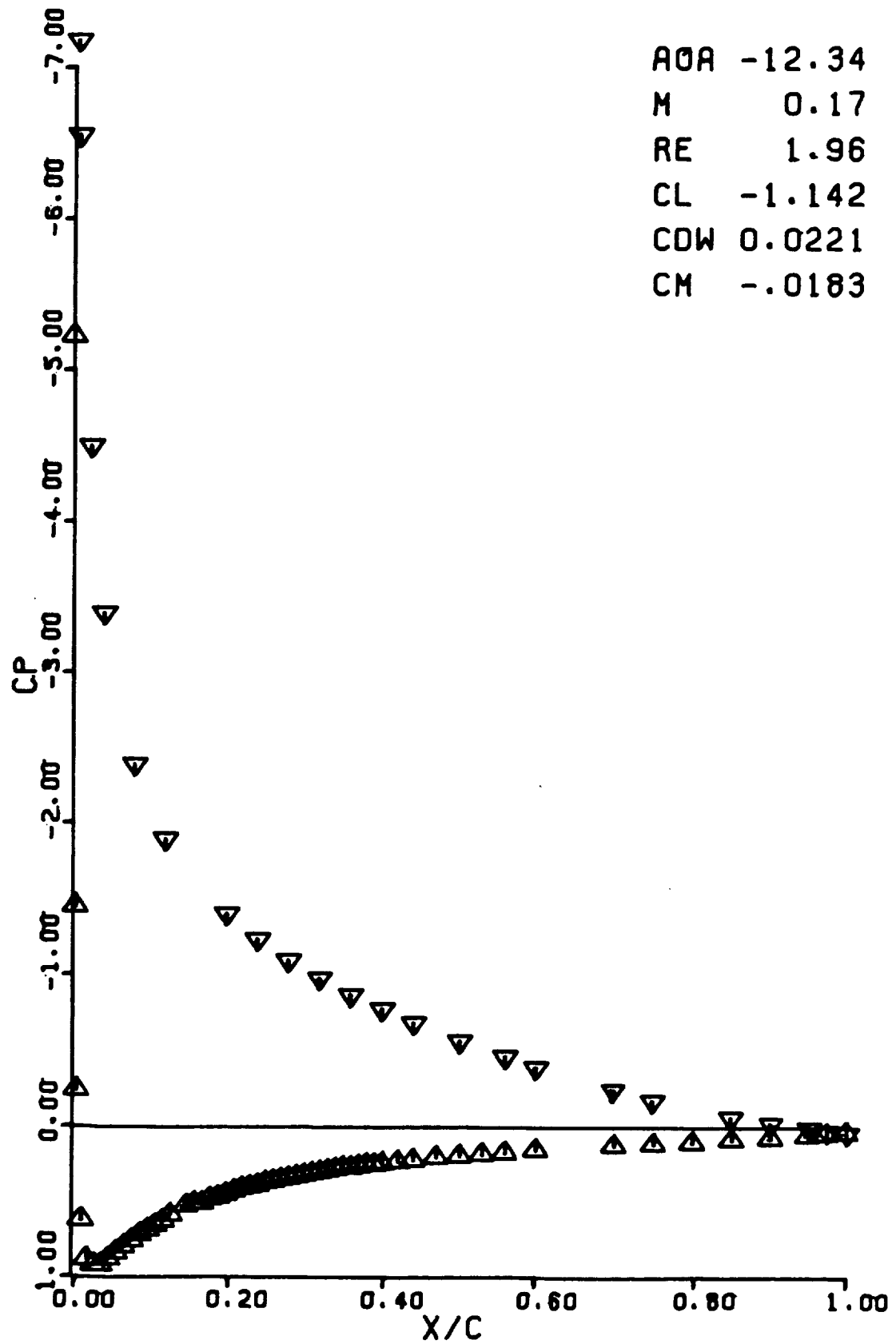
CDW 0.0161

CM -.0109



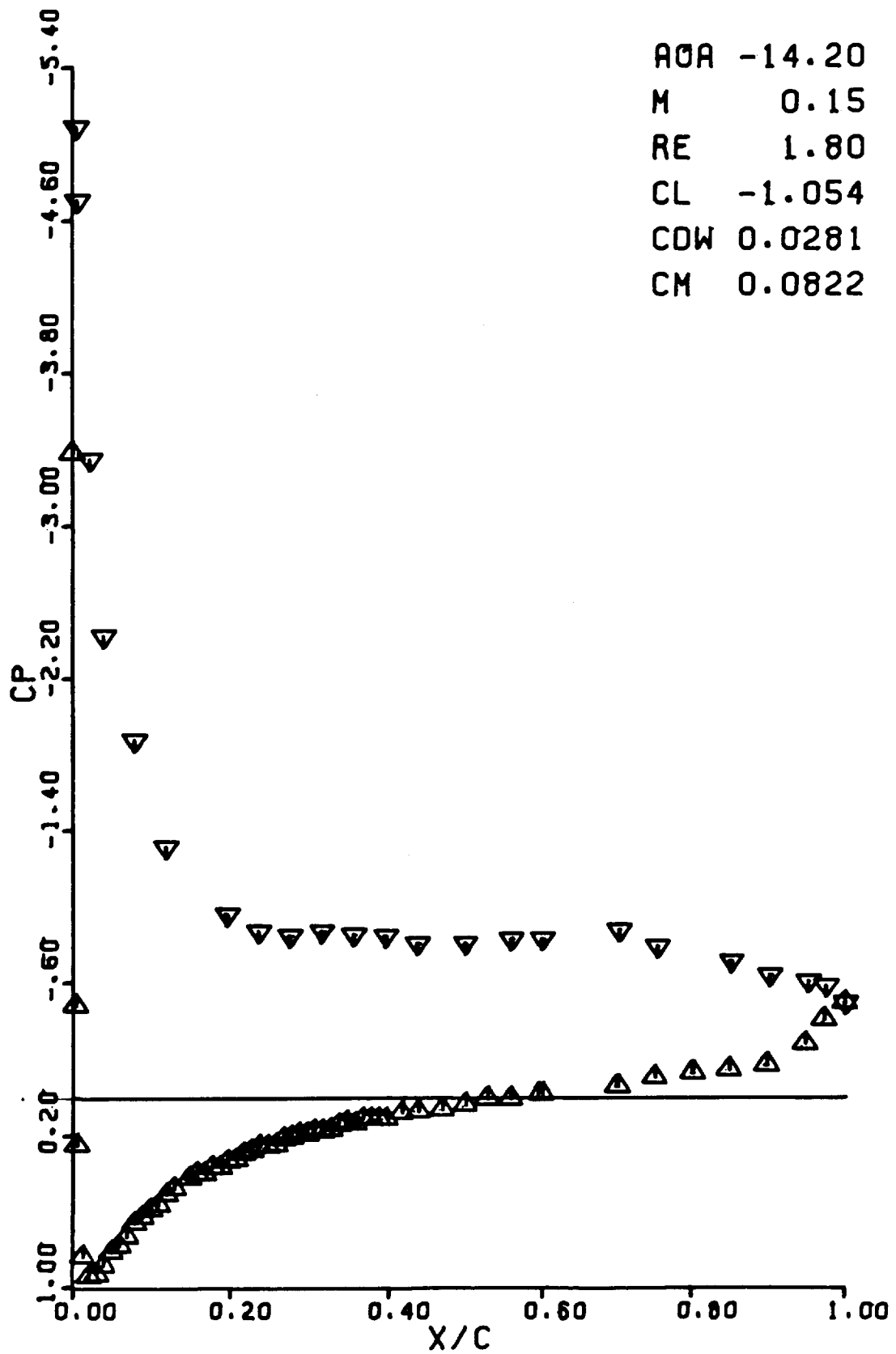
RUN 0430

AOA -12.34  
M 0.17  
RE 1.96  
CL -1.142  
CDW 0.0221  
CM -.0183



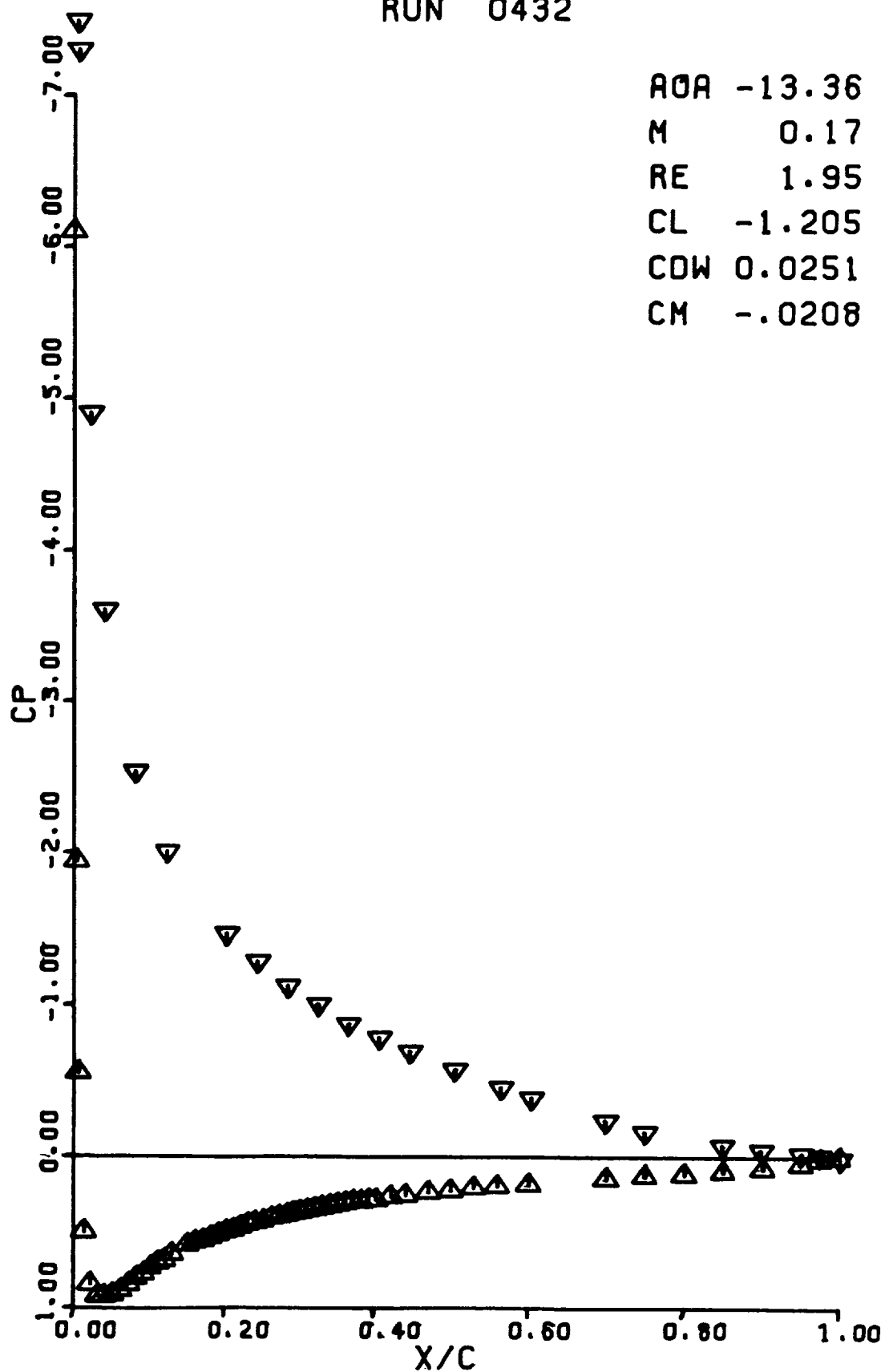
RUN 0431

AOA -14.20  
M 0.15  
RE 1.80  
CL -1.054  
CDW 0.0281  
CM 0.0822



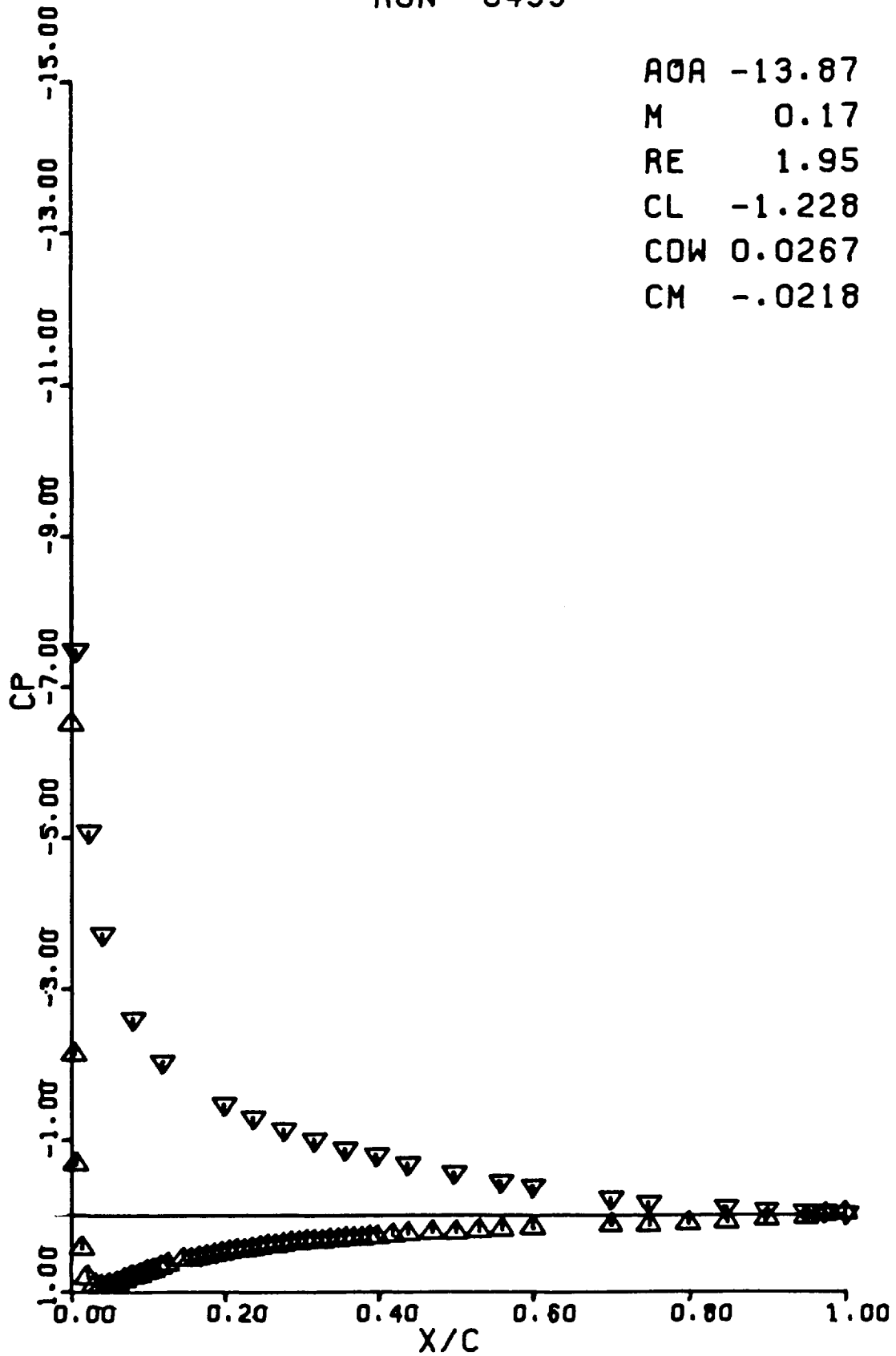
RUN 0432

AOA -13.36  
M 0.17  
RE 1.95  
CL -1.205  
CDW 0.0251  
CM -.0208

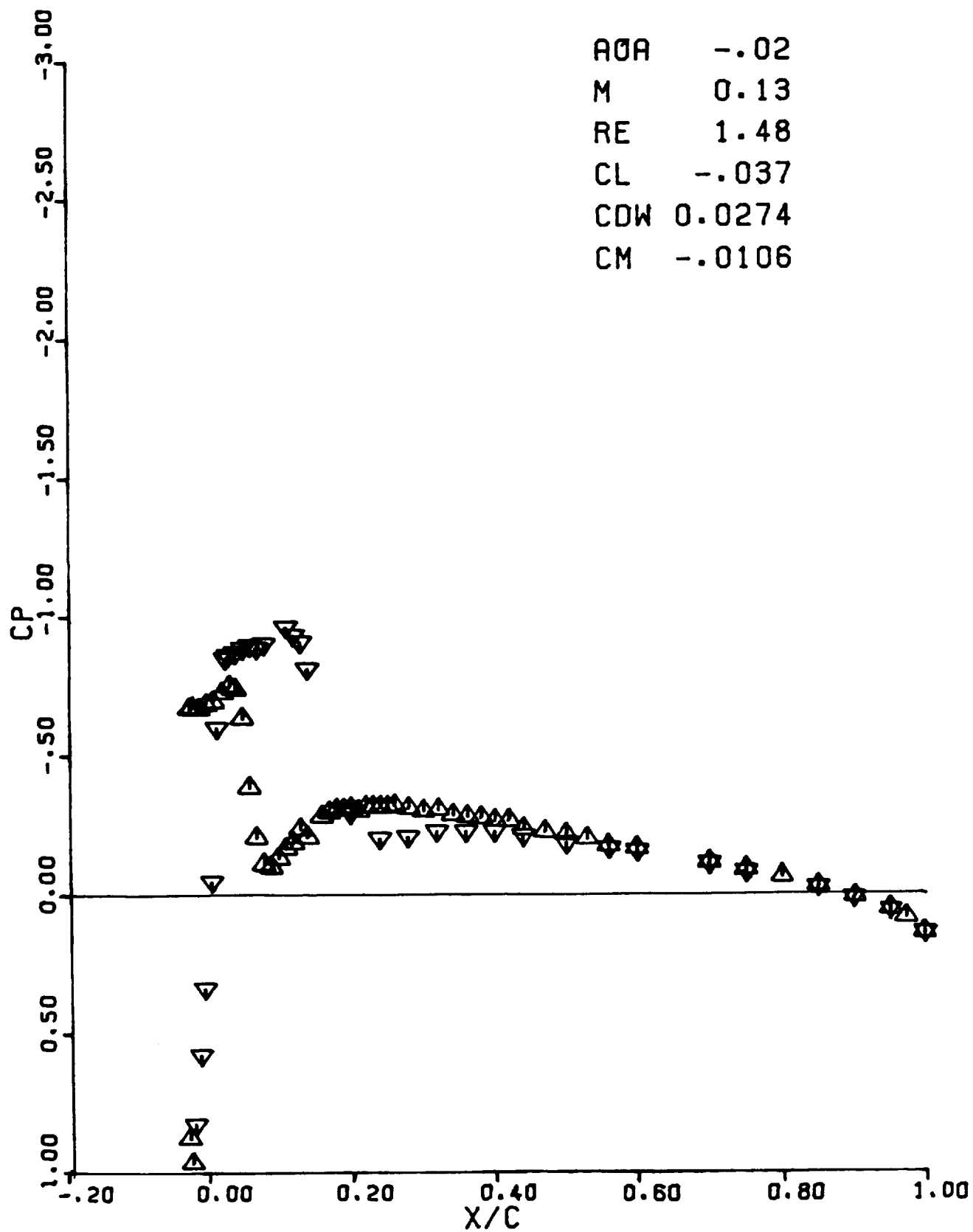


RUN 0433

AOA -13.87  
M 0.17  
RE 1.95  
CL -1.228  
CDW 0.0267  
CM -.0218



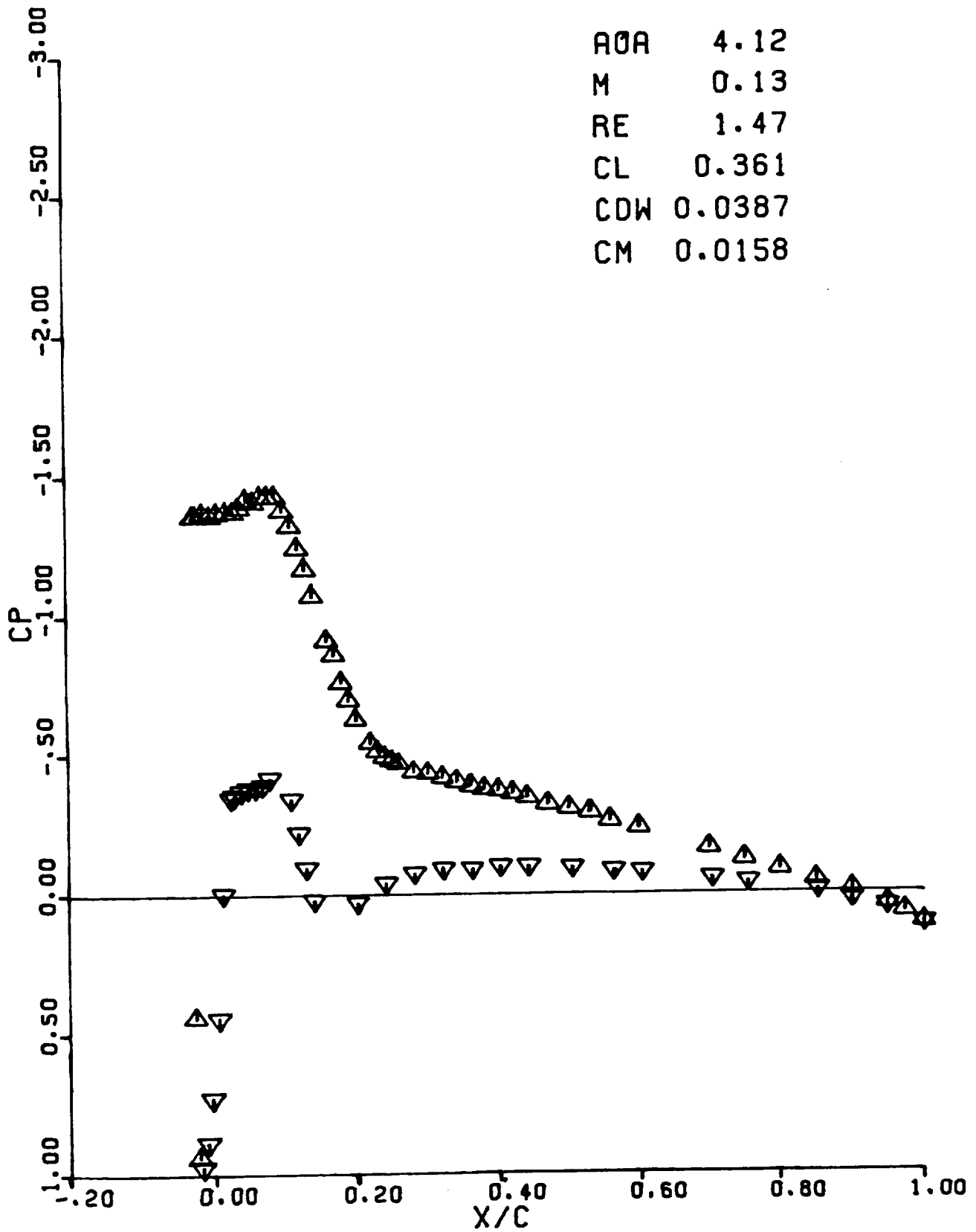
RUN 0434





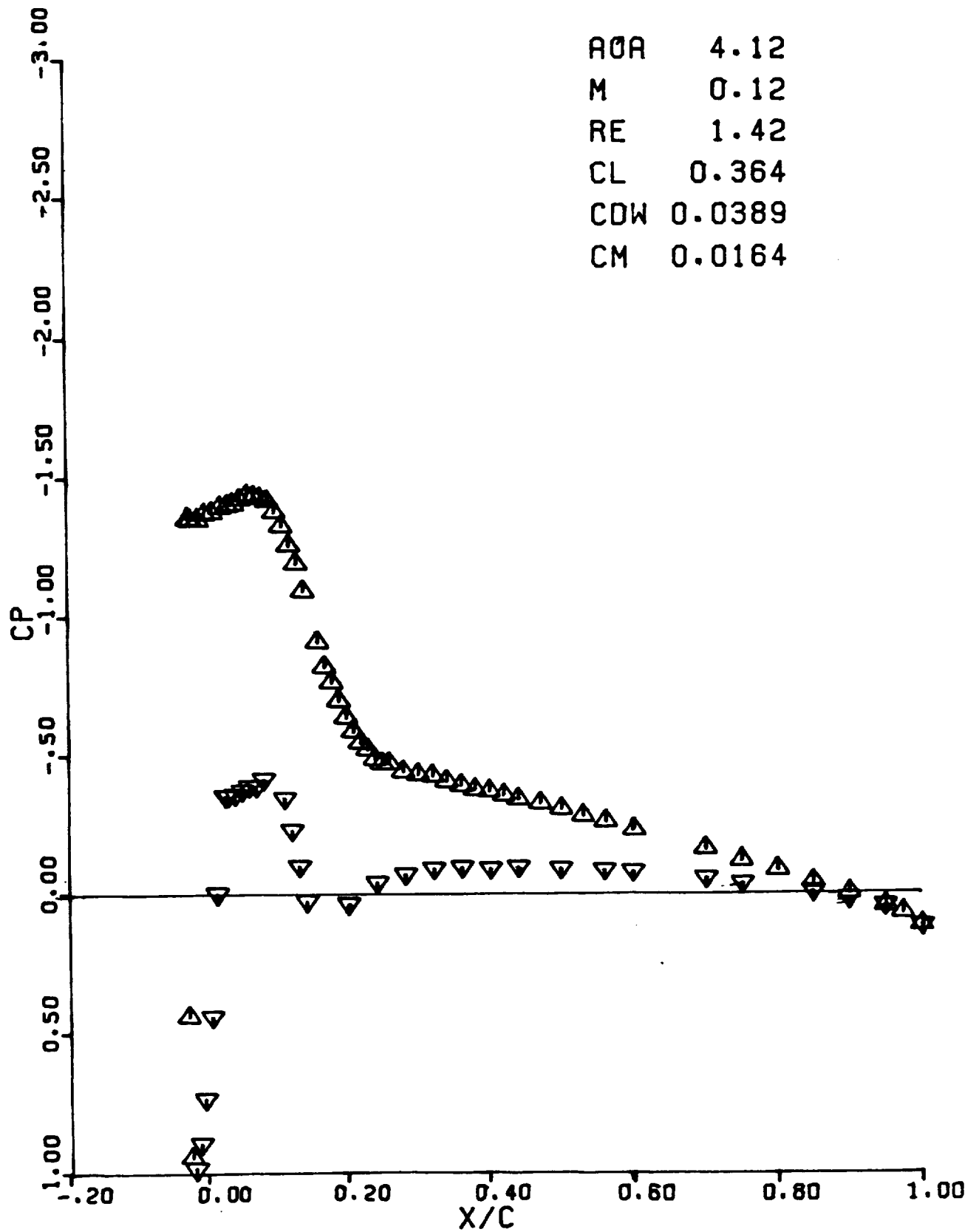
RUN 0435

AOA 4.12  
M 0.13  
RE 1.47  
CL 0.361  
CDW 0.0387  
CM 0.0158



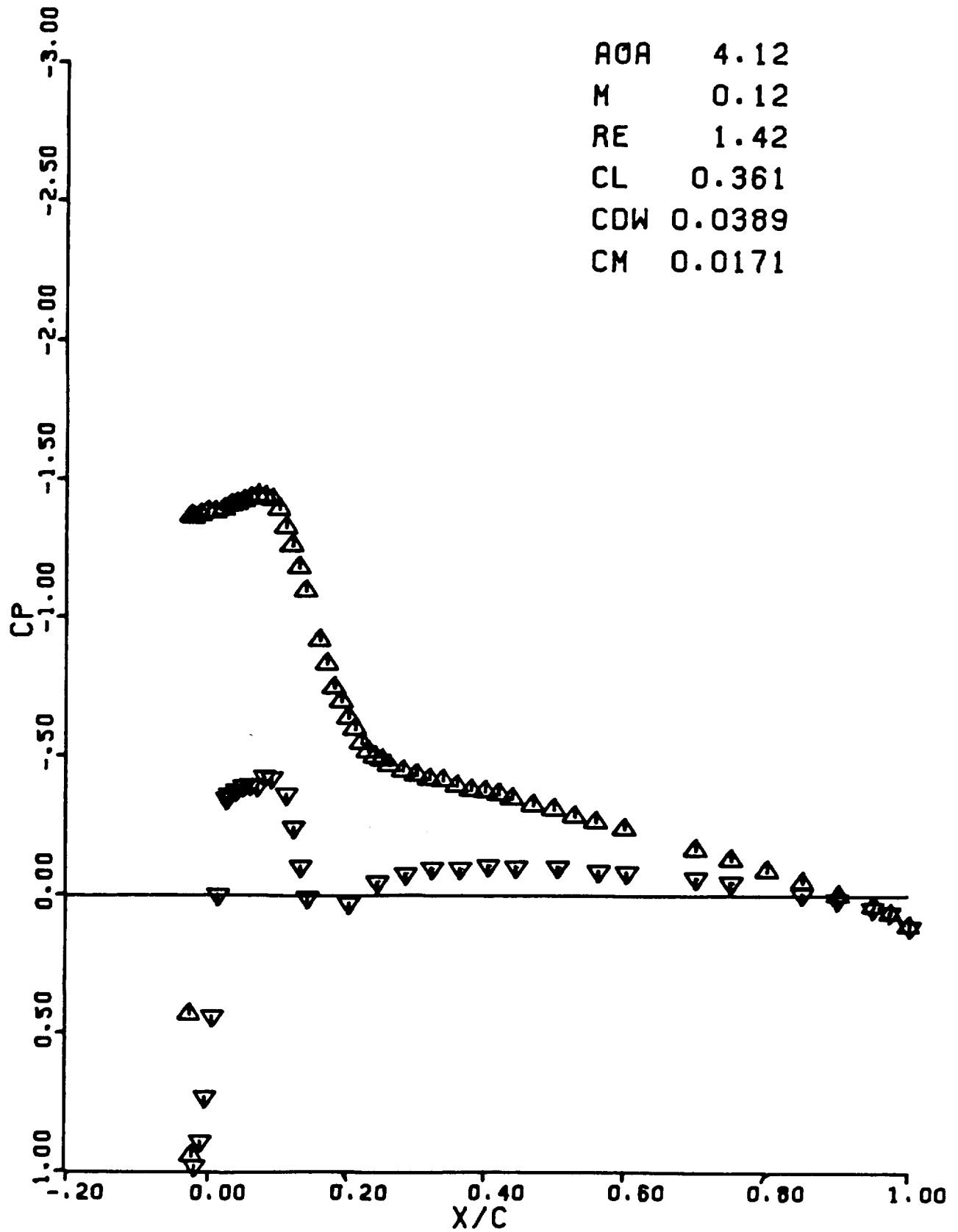
RUN 0436

AOA 4.12  
M 0.12  
RE 1.42  
CL 0.364  
CDW 0.0389  
CM 0.0164



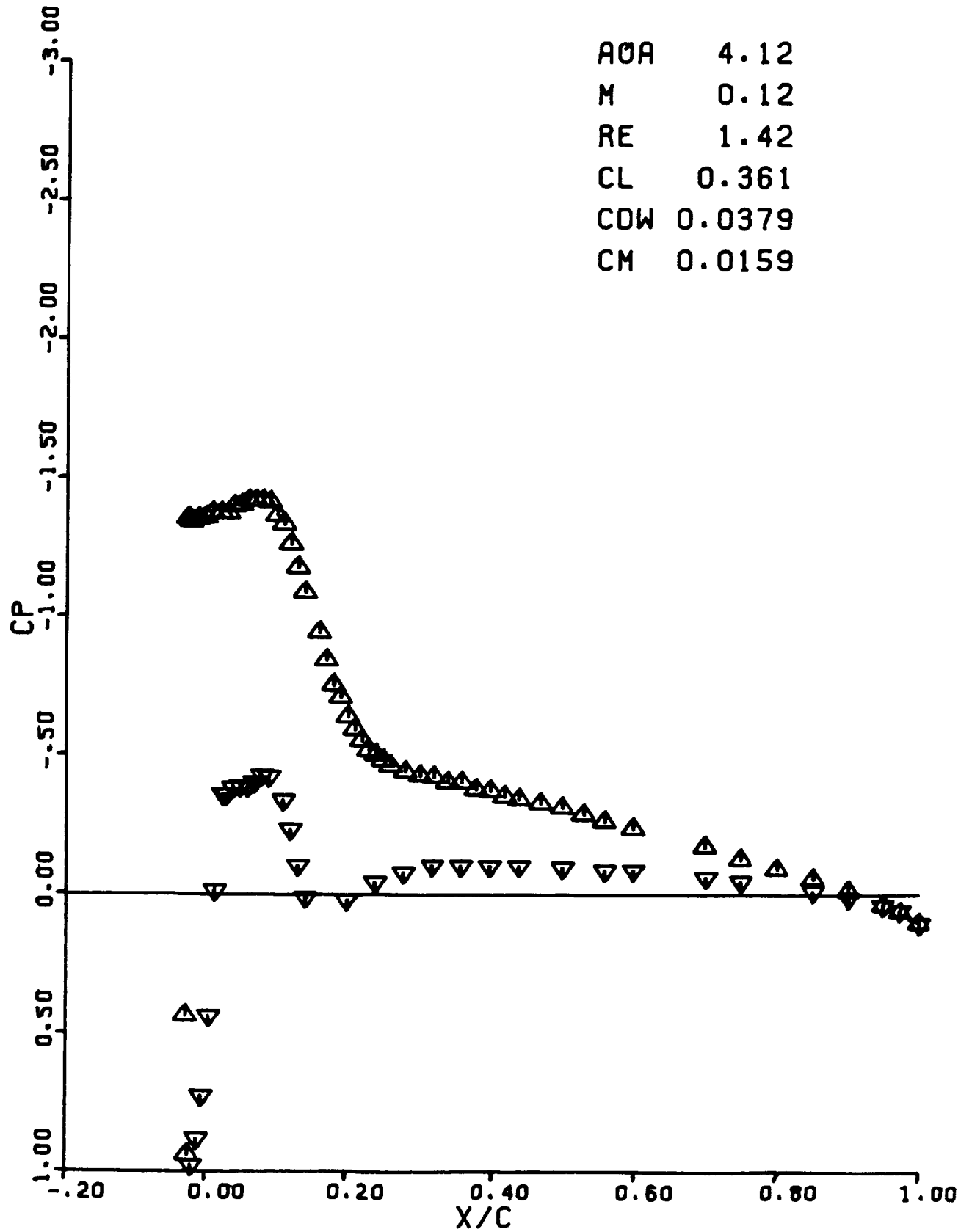
RUN 0437

AOA 4.12  
M 0.12  
RE 1.42  
CL 0.361  
CDW 0.0389  
CM 0.0171

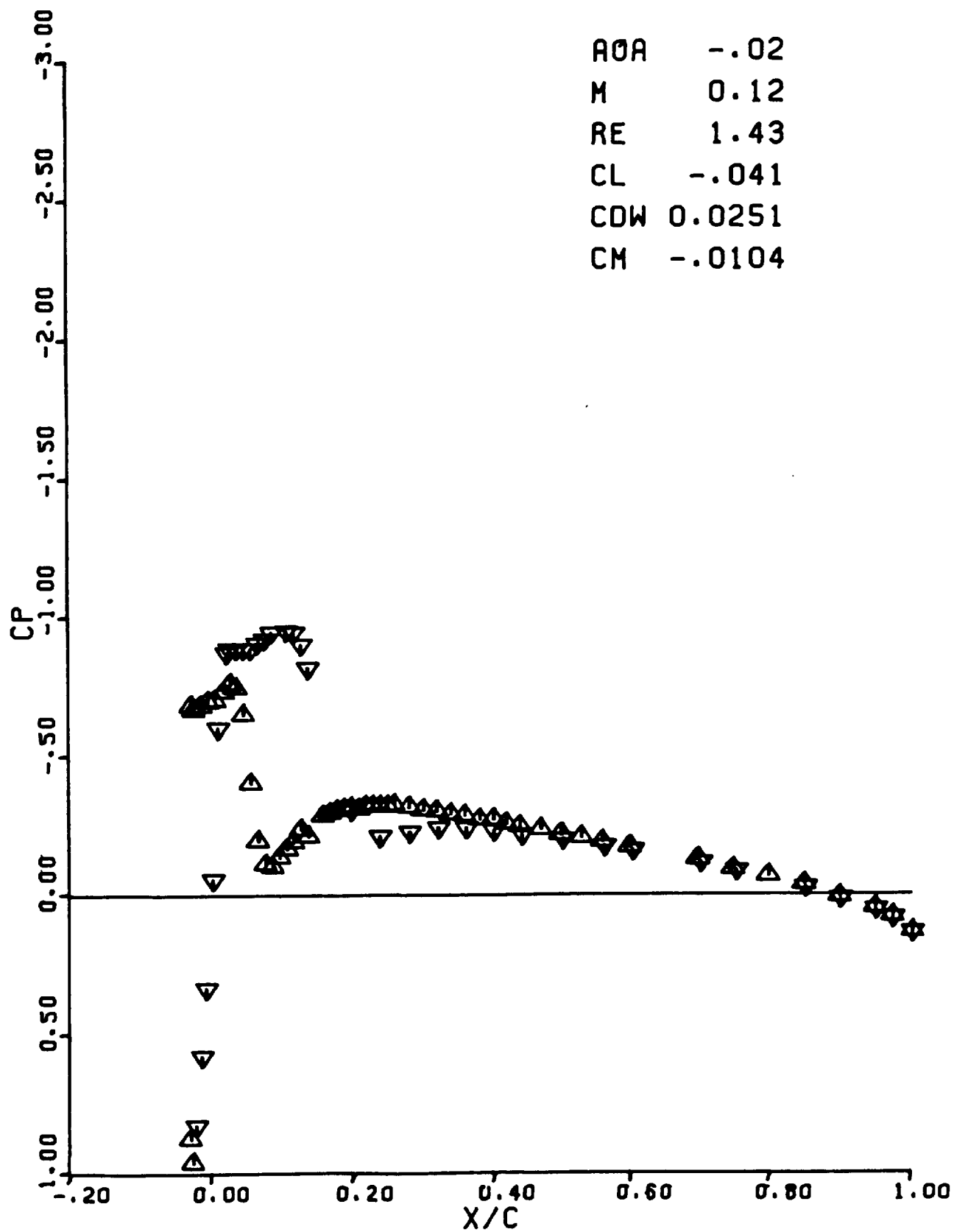


RUN 0438

AOA 4.12  
M 0.12  
RE 1.42  
CL 0.361  
CDW 0.0379  
CM 0.0159

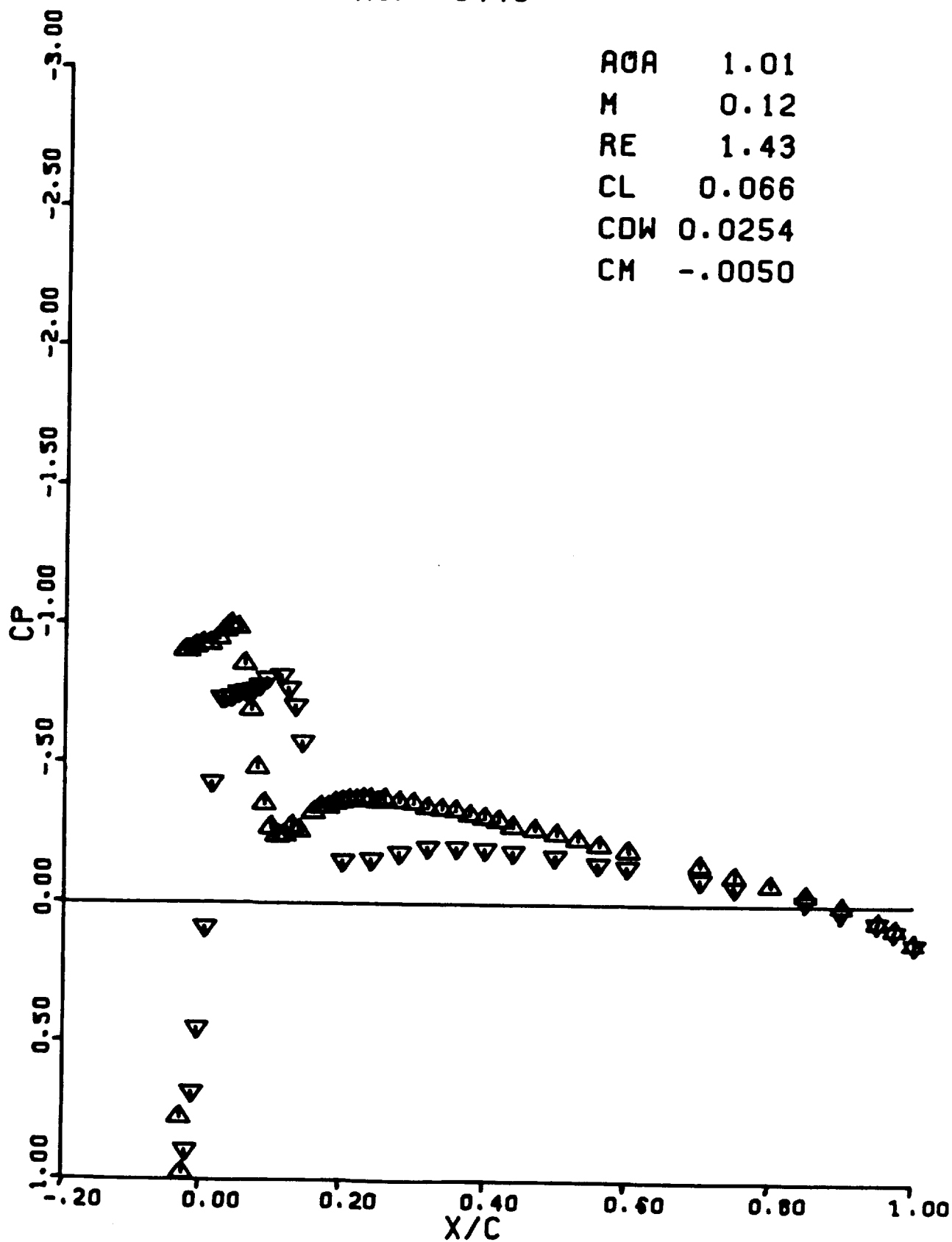


RUN 0439



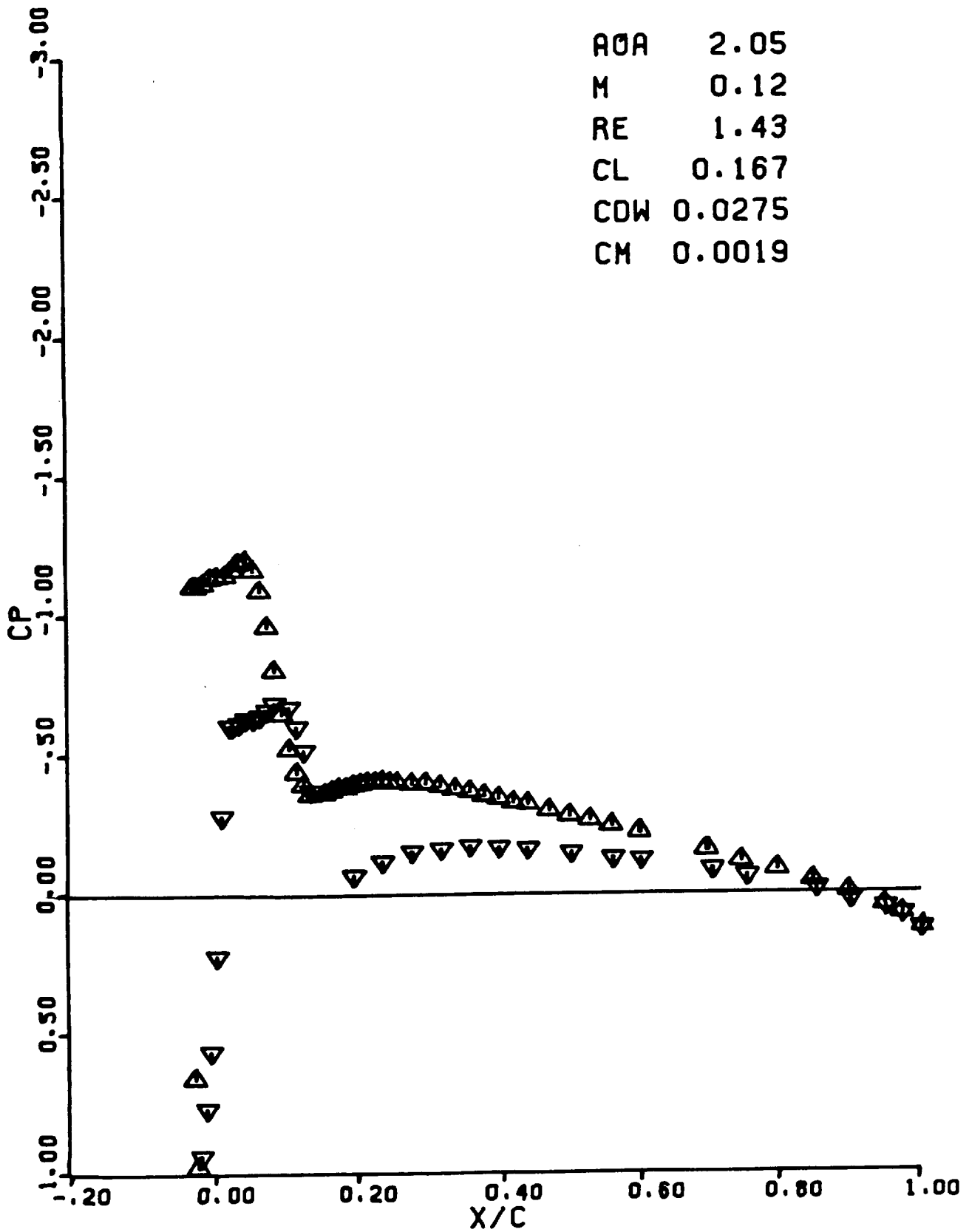
RUN 0440

AOA 1.01  
M 0.12  
RE 1.43  
CL 0.066  
CDW 0.0254  
CM -.0050



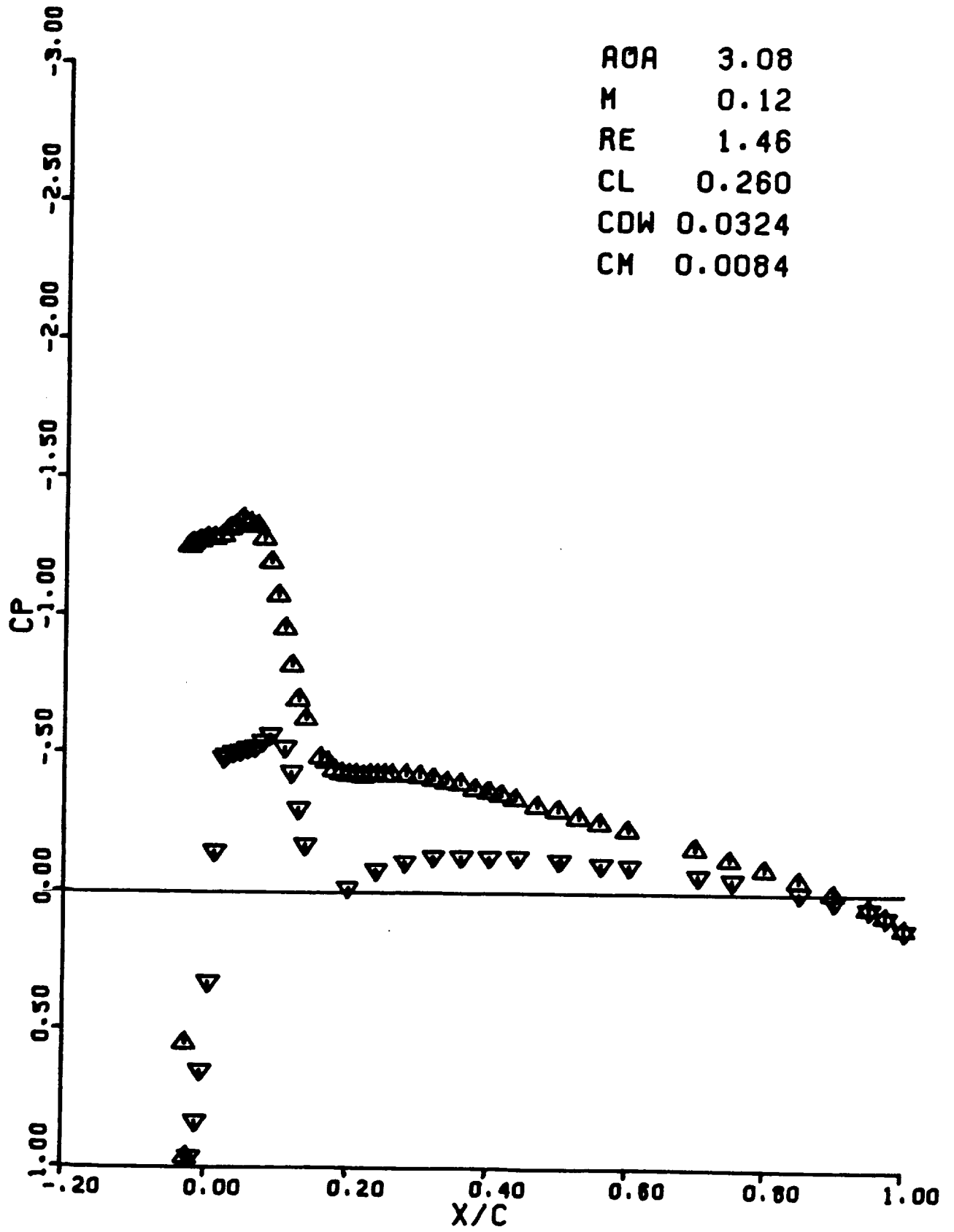
RUN 0441

AOA 2.05  
M 0.12  
RE 1.43  
CL 0.167  
CDW 0.0275  
CM 0.0019



RUN 0442

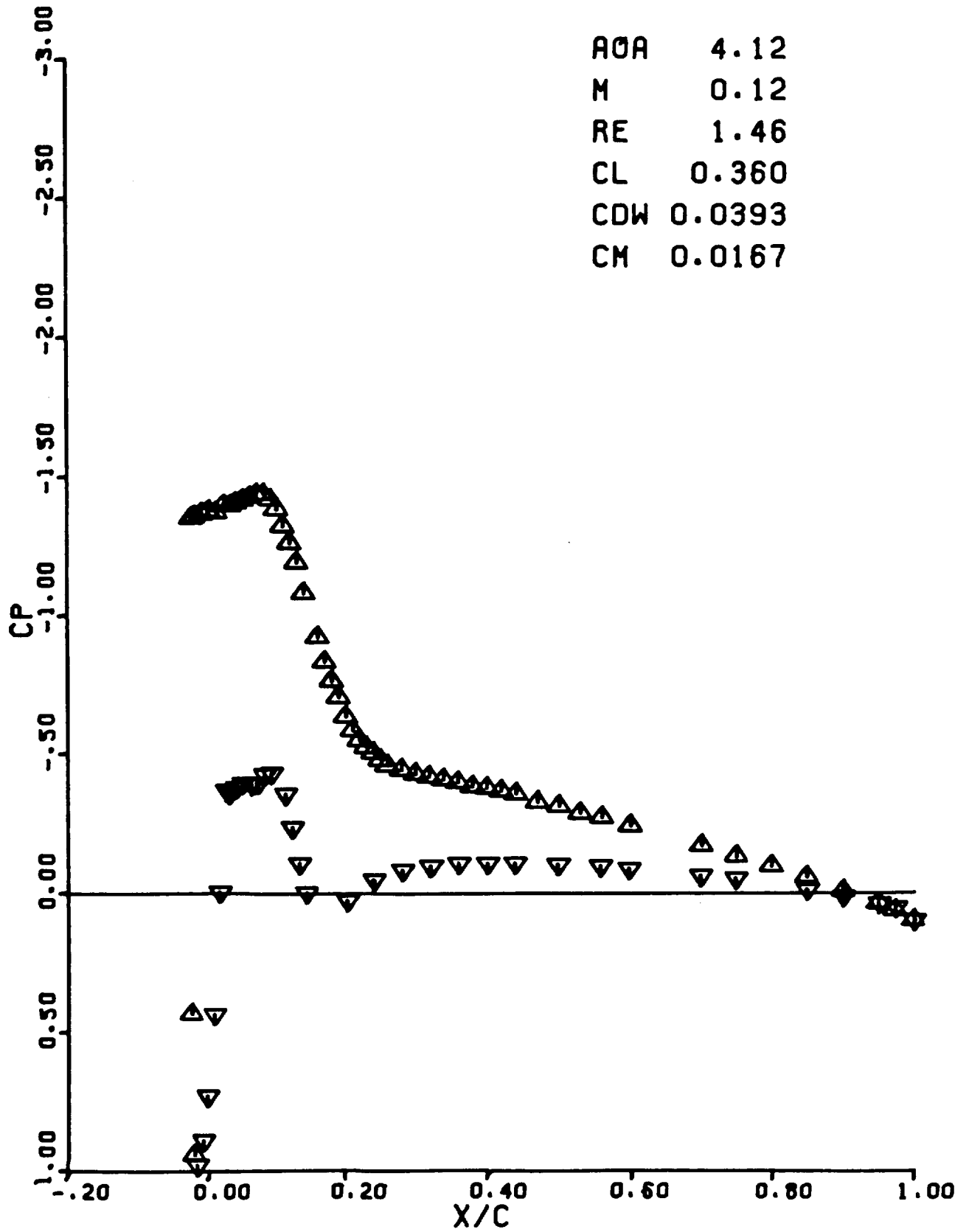
AOA 3.08  
M 0.12  
RE 1.46  
CL 0.260  
CDW 0.0324  
CM 0.0084





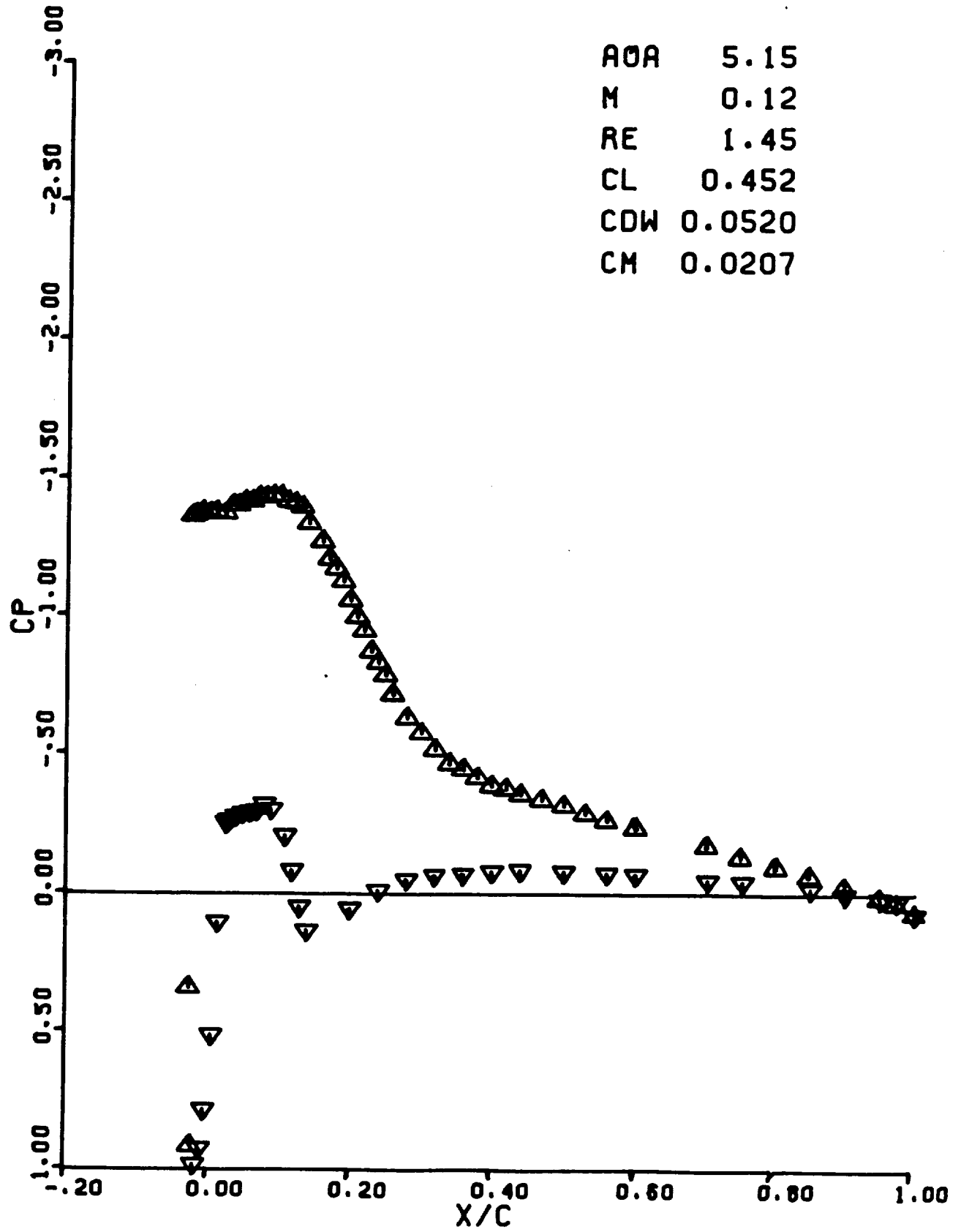
RUN 0443

AOA 4.12  
M 0.12  
RE 1.46  
CL 0.360  
CDW 0.0393  
CM 0.0167



RUN 0444

AOA 5.15  
M 0.12  
RE 1.45  
CL 0.452  
CDW 0.0520  
CM 0.0207



RUN 0445

AOA 6.16

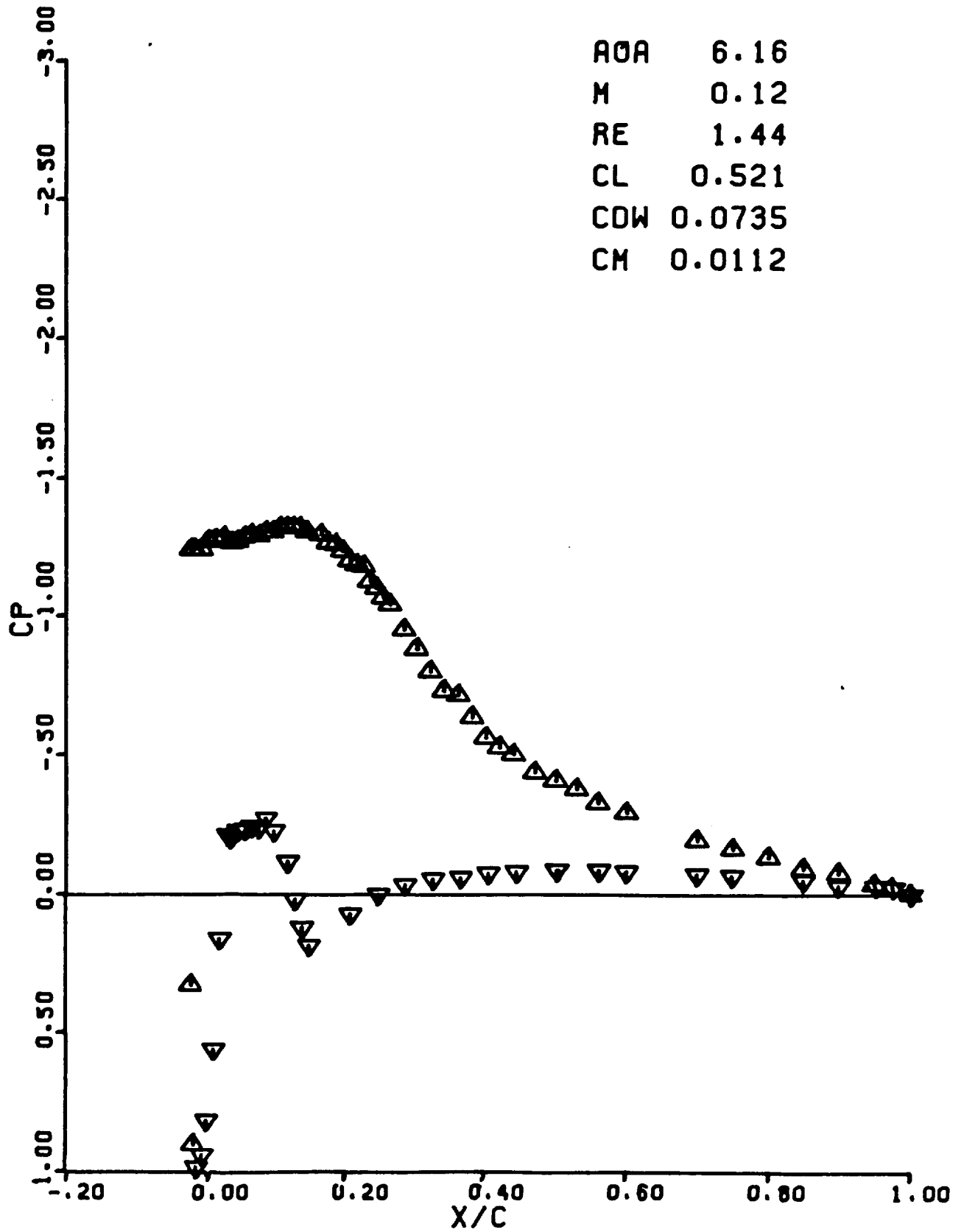
M 0.12

RE 1.44

CL 0.521

CDW 0.0735

CM 0.0112



RUN 0446

AOA 7.14

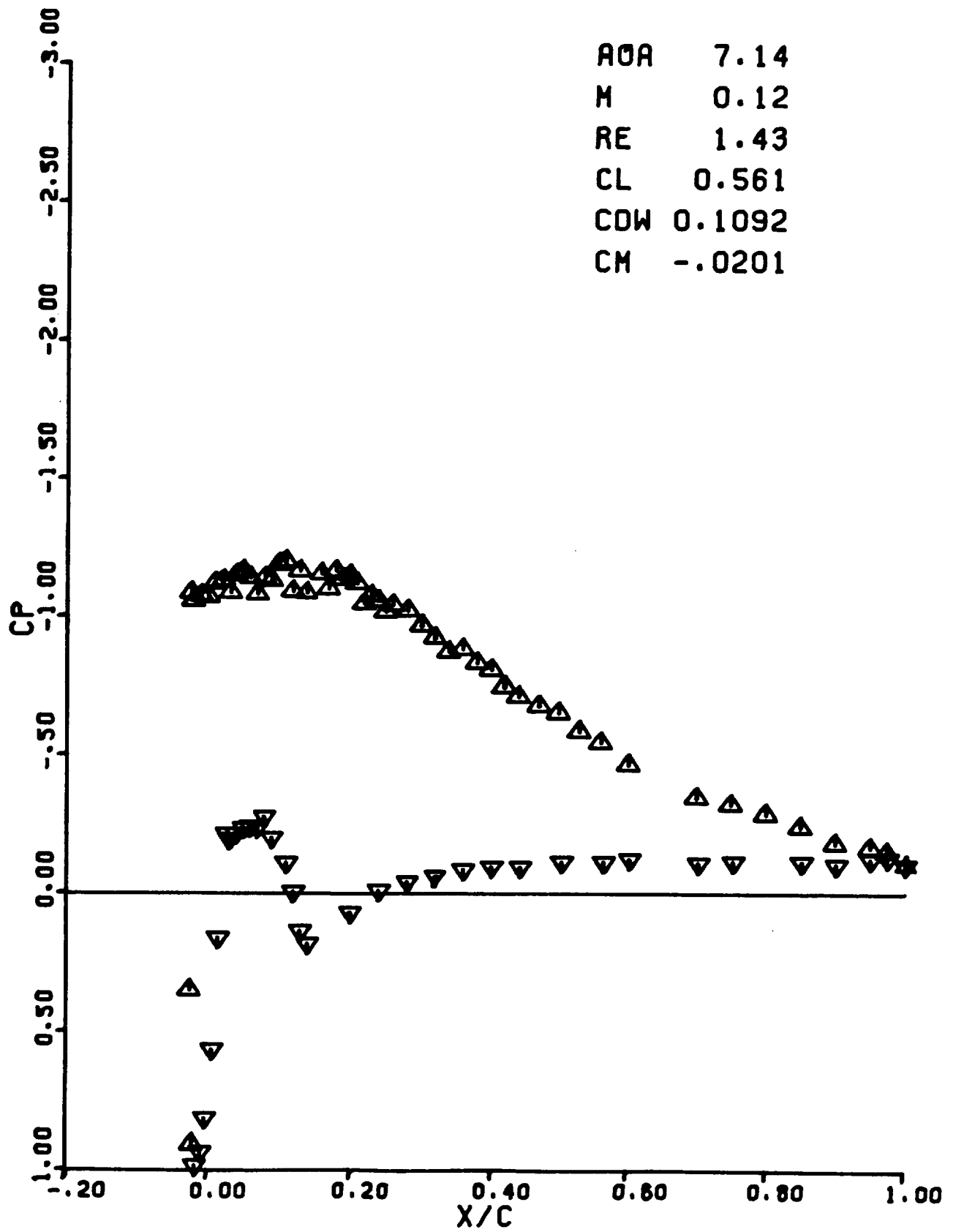
M 0.12

RE 1.43

CL 0.561

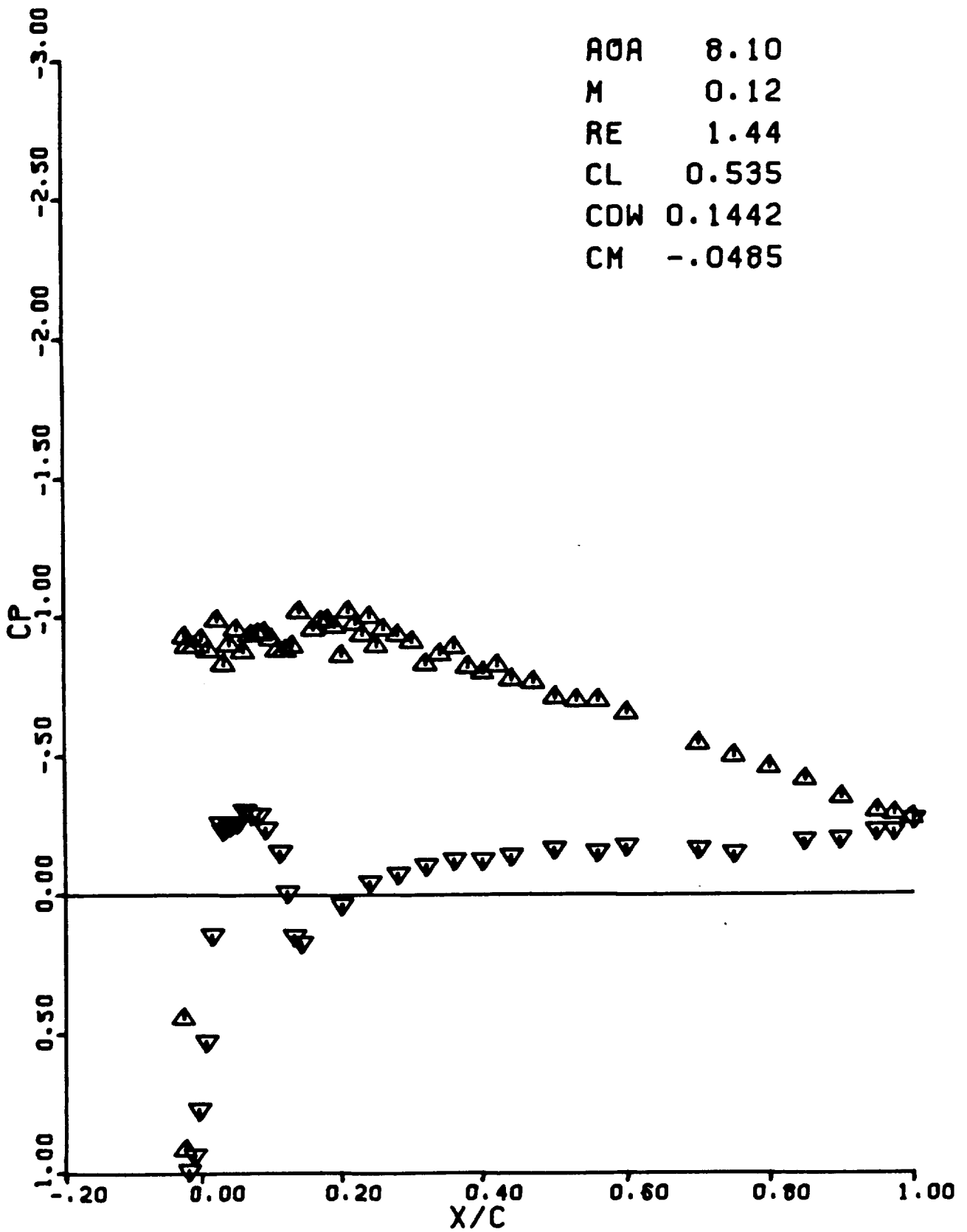
CDW 0.1092

CM -.0201



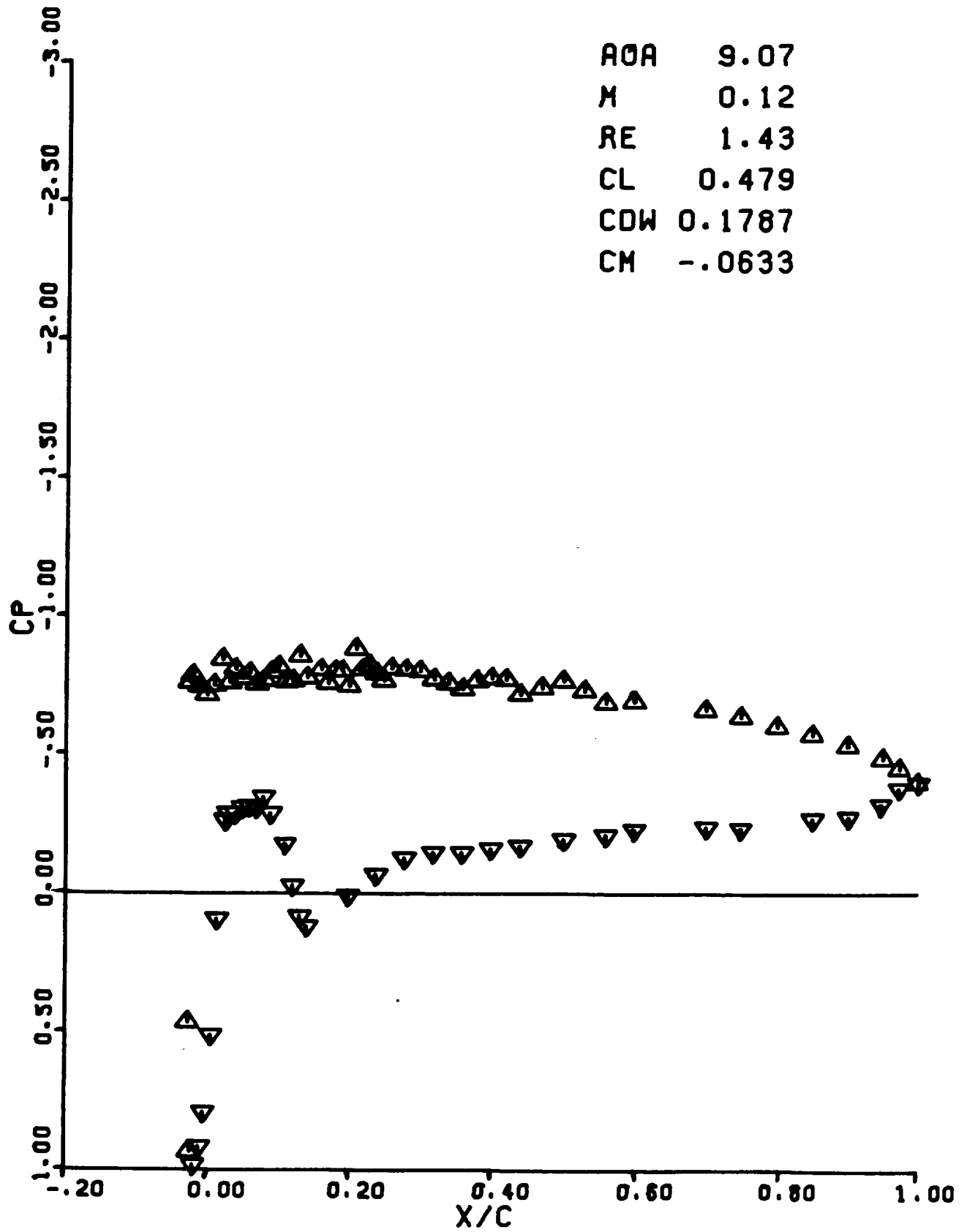
RUN 0447

AOA 8.10  
M 0.12  
RE 1.44  
CL 0.535  
CDW 0.1442  
CM -.0485



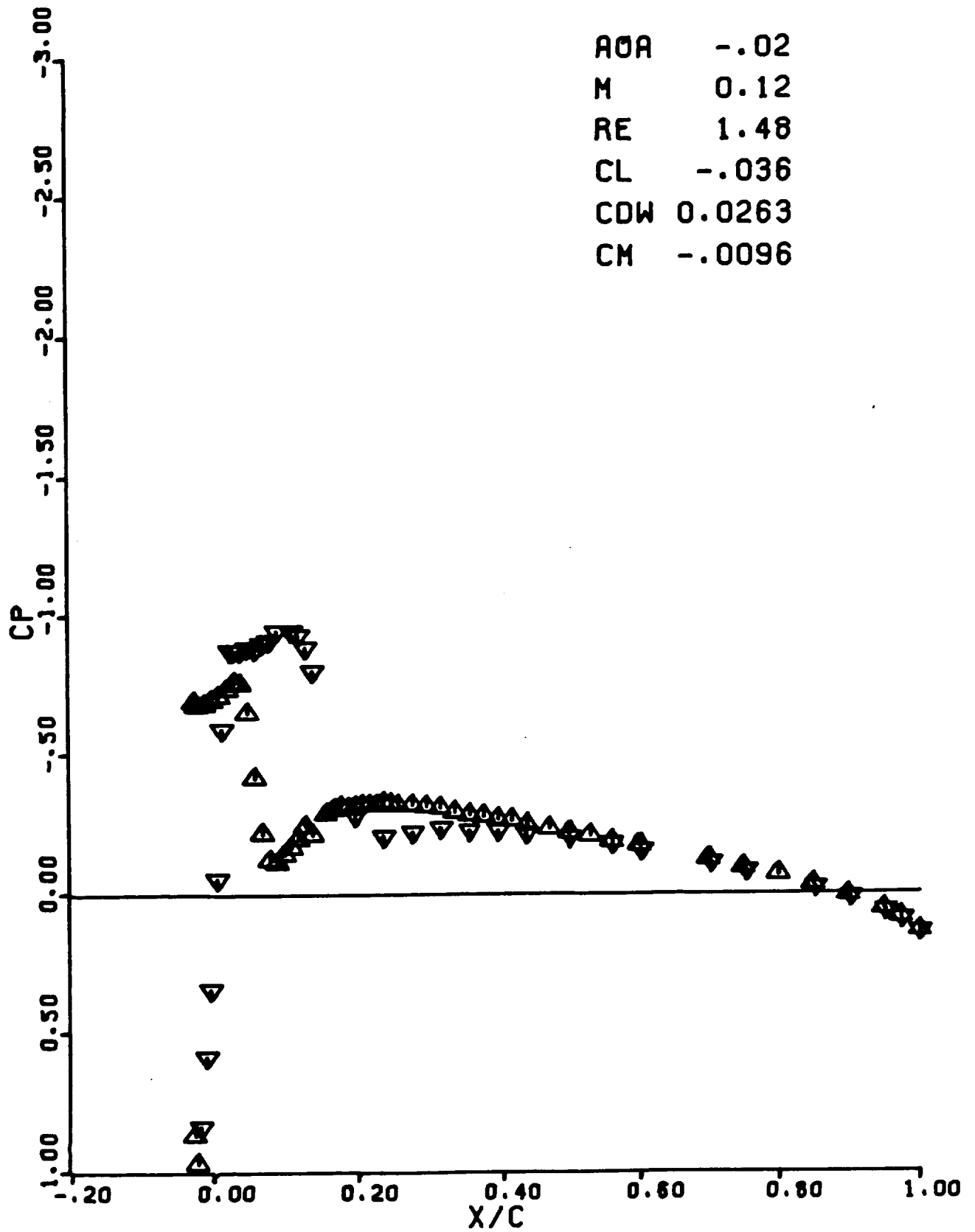
RUN 0448

AOA 9.07  
M 0.12  
RE 1.43  
CL 0.479  
CDW 0.1787  
CM -.0633



RUN 0449

AOA -.02  
M 0.12  
RE 1.48  
CL -.036  
CDW 0.0263  
CM -.0096



RUN 0450

AOA -2.09

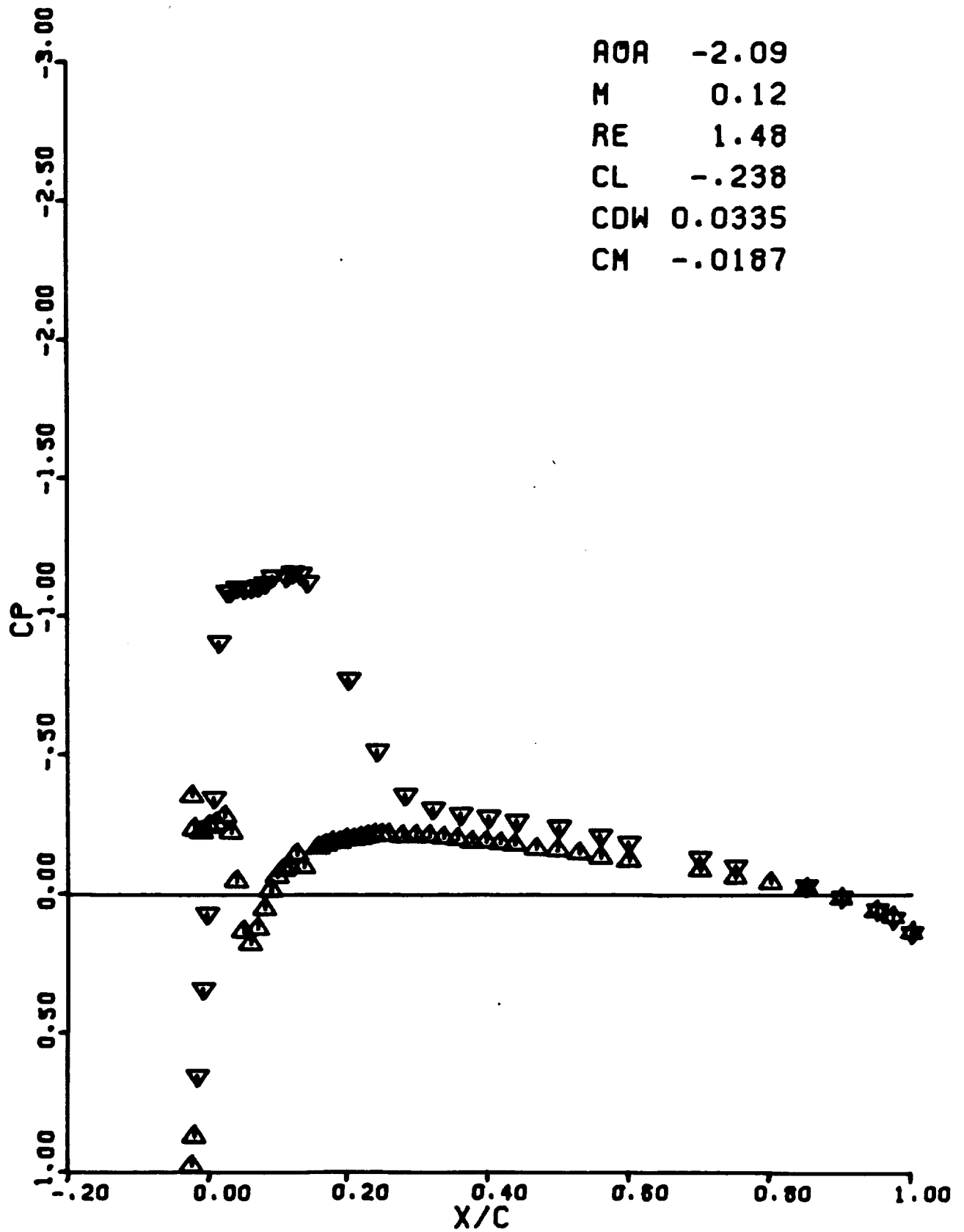
M 0.12

RE 1.48

CL -.238

CDW 0.0335

CM -.0187





RUN 0451

AOA -4.14

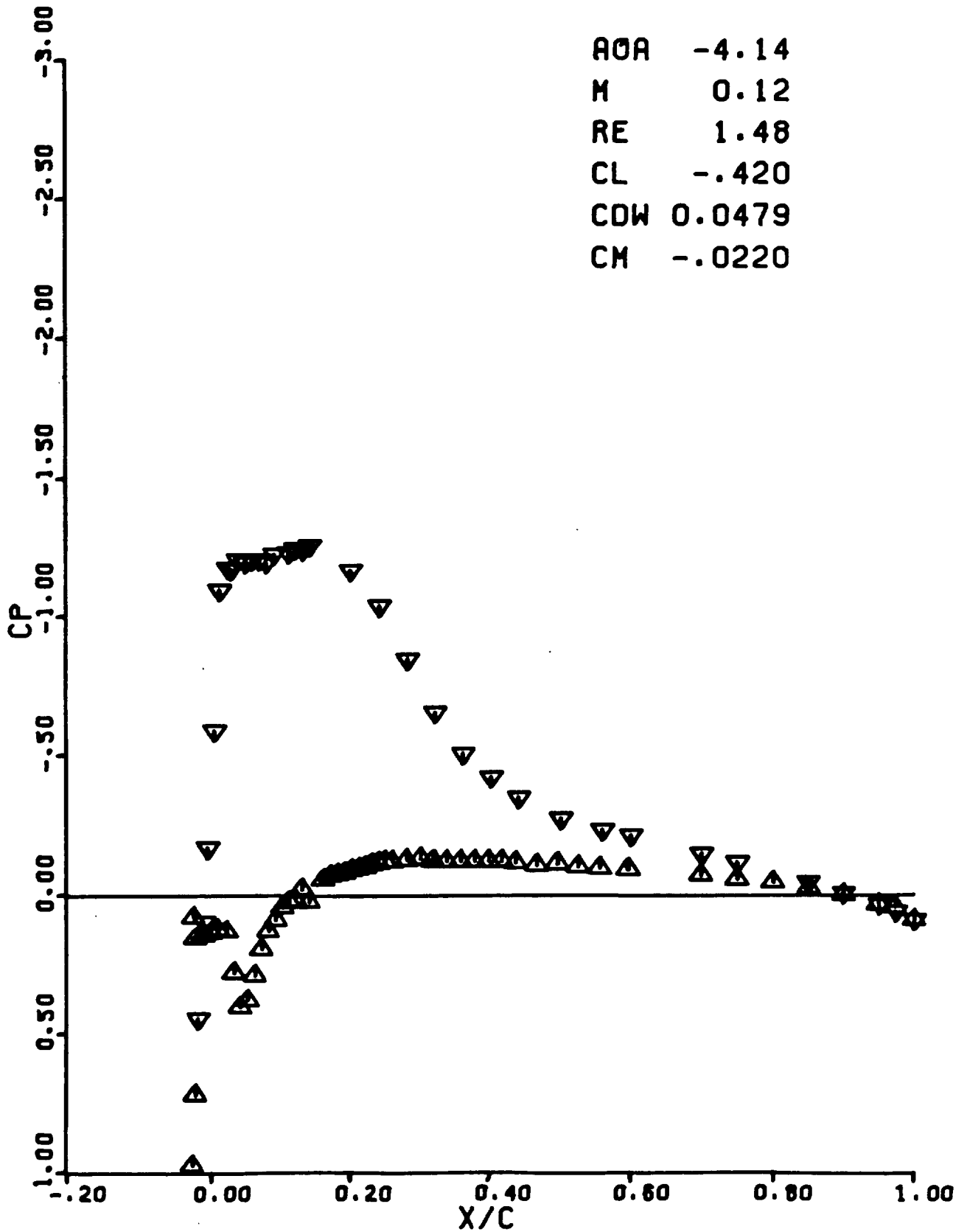
M 0.12

RE 1.48

CL -.420

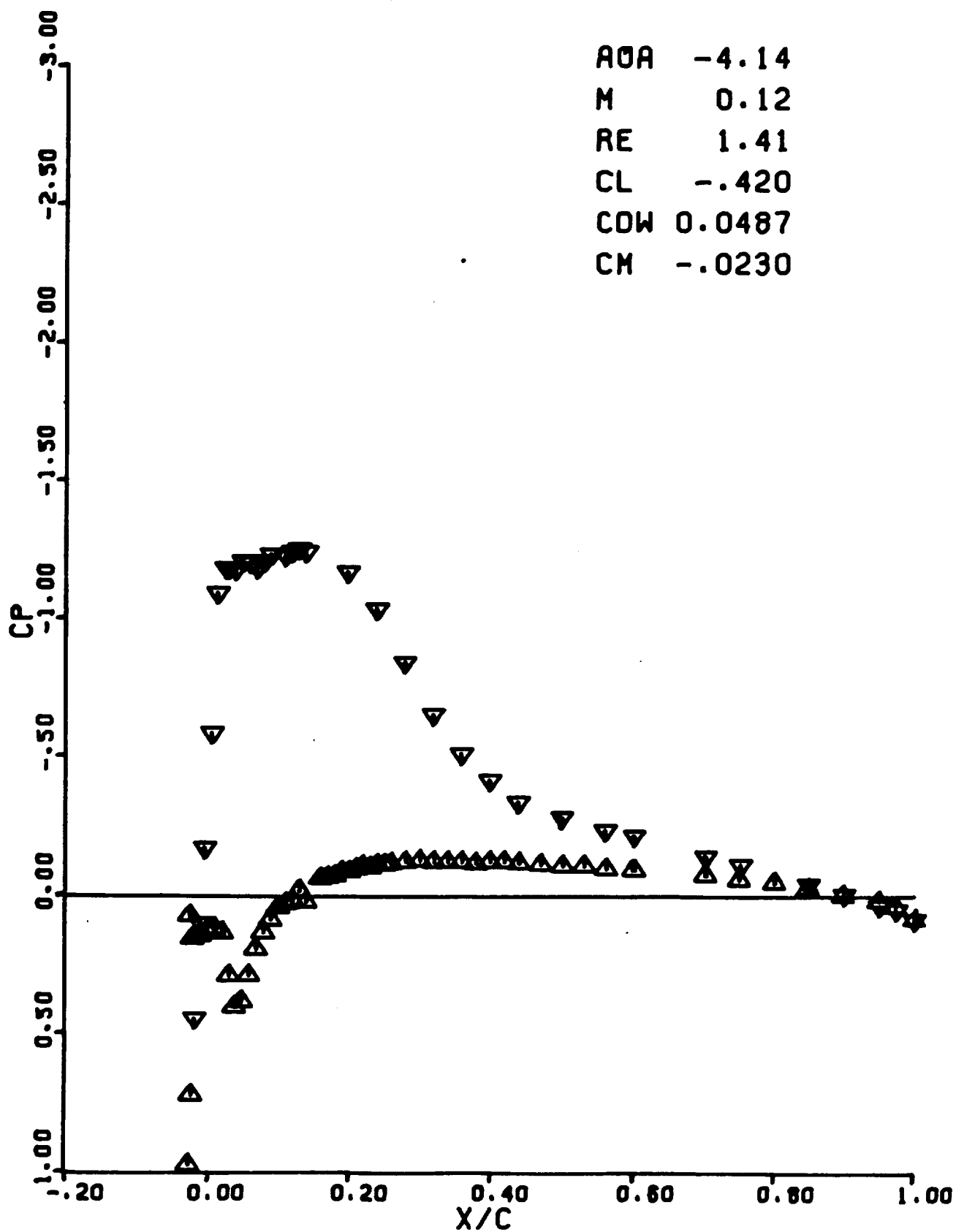
CDW 0.0479

CM -.0220



RUN 0452

AOA -4.14  
M 0.12  
RE 1.41  
CL -.420  
CDW 0.0487  
CM -.0230



RUN 0453

AOA -6.13

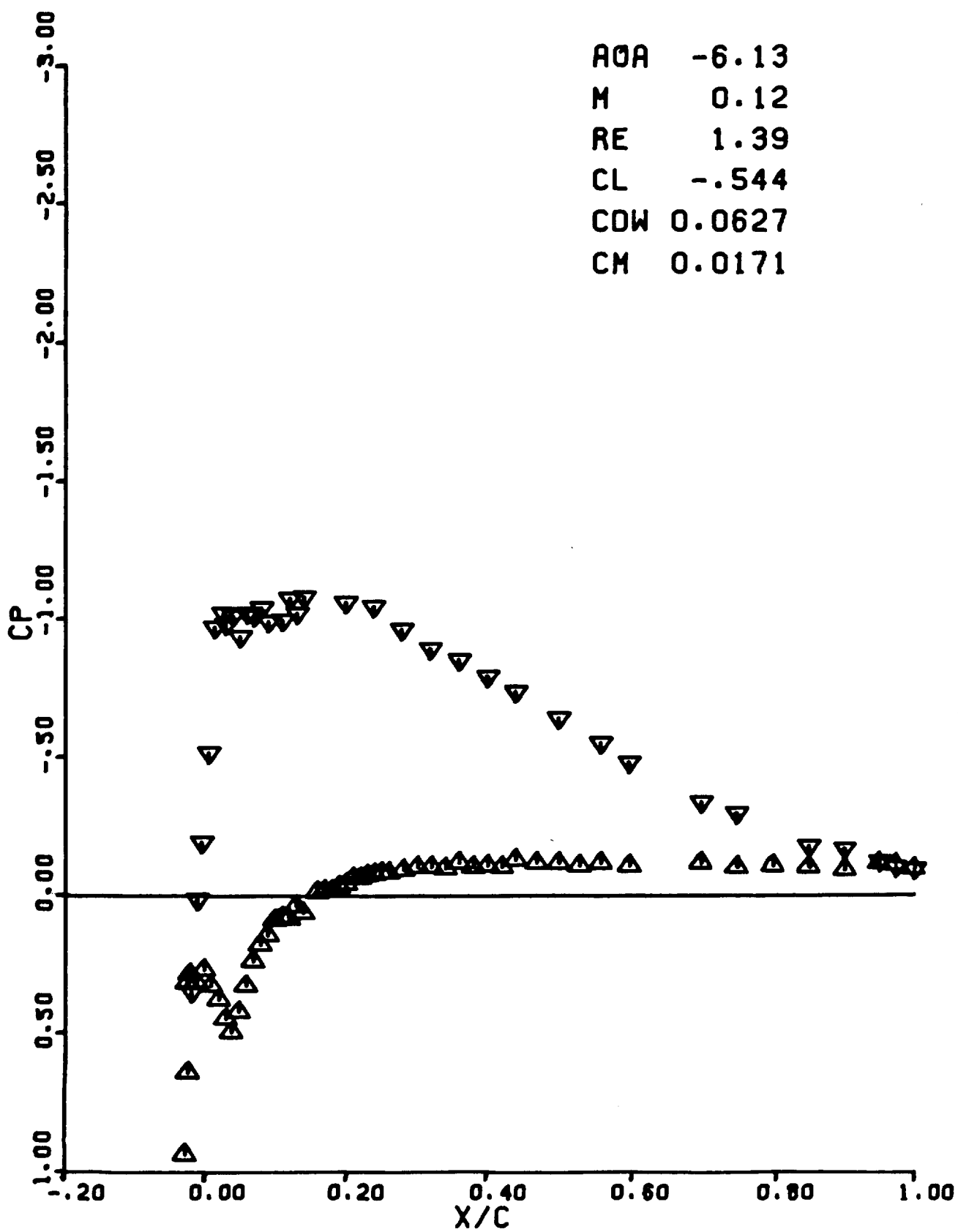
M 0.12

RE 1.39

CL -.544

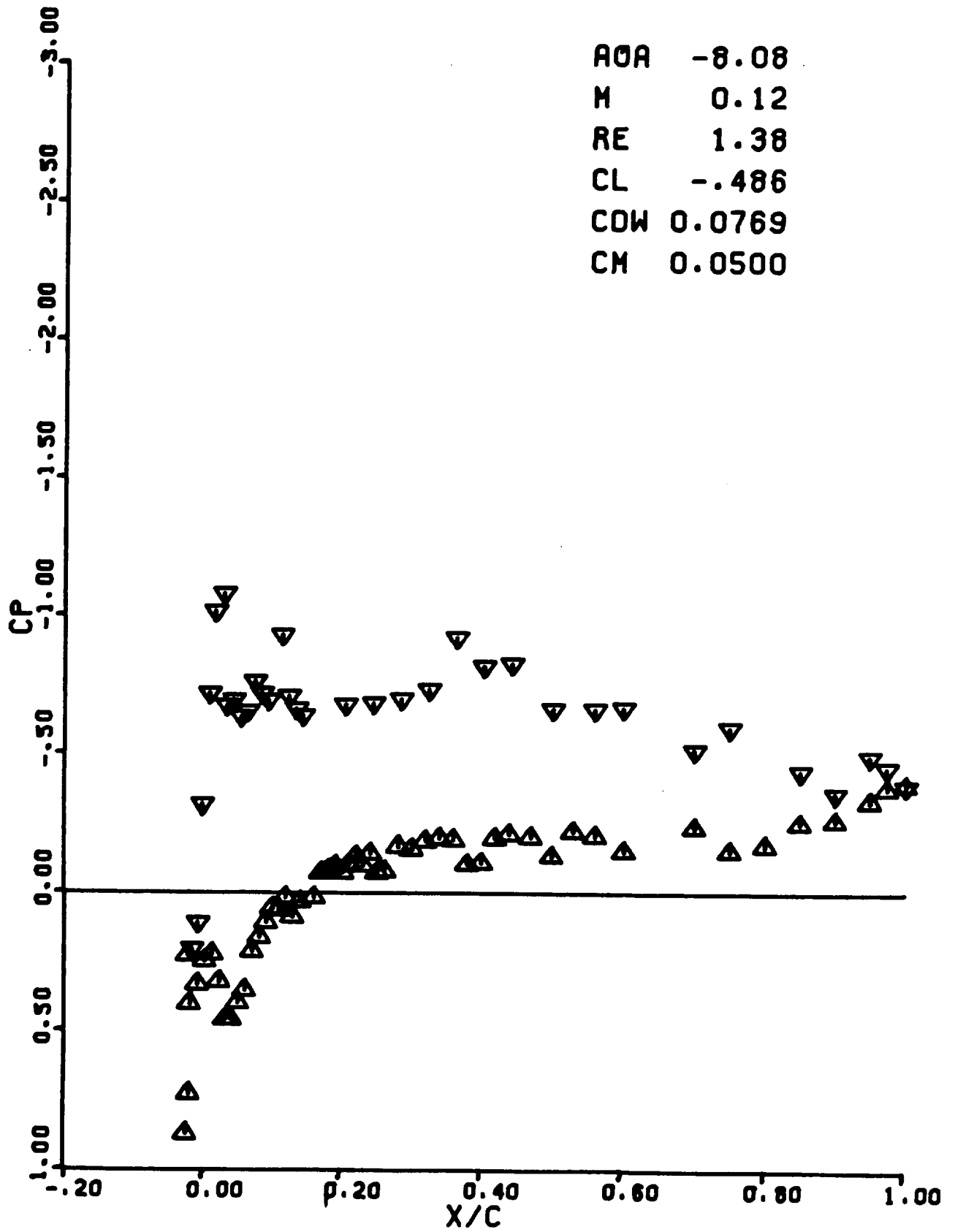
CDW 0.0627

CM 0.0171



RUN 0454

AOA -8.08  
M 0.12  
RE 1.38  
CL -.486  
CDW 0.0769  
CM 0.0500



RUN 0455

AOA -7.11

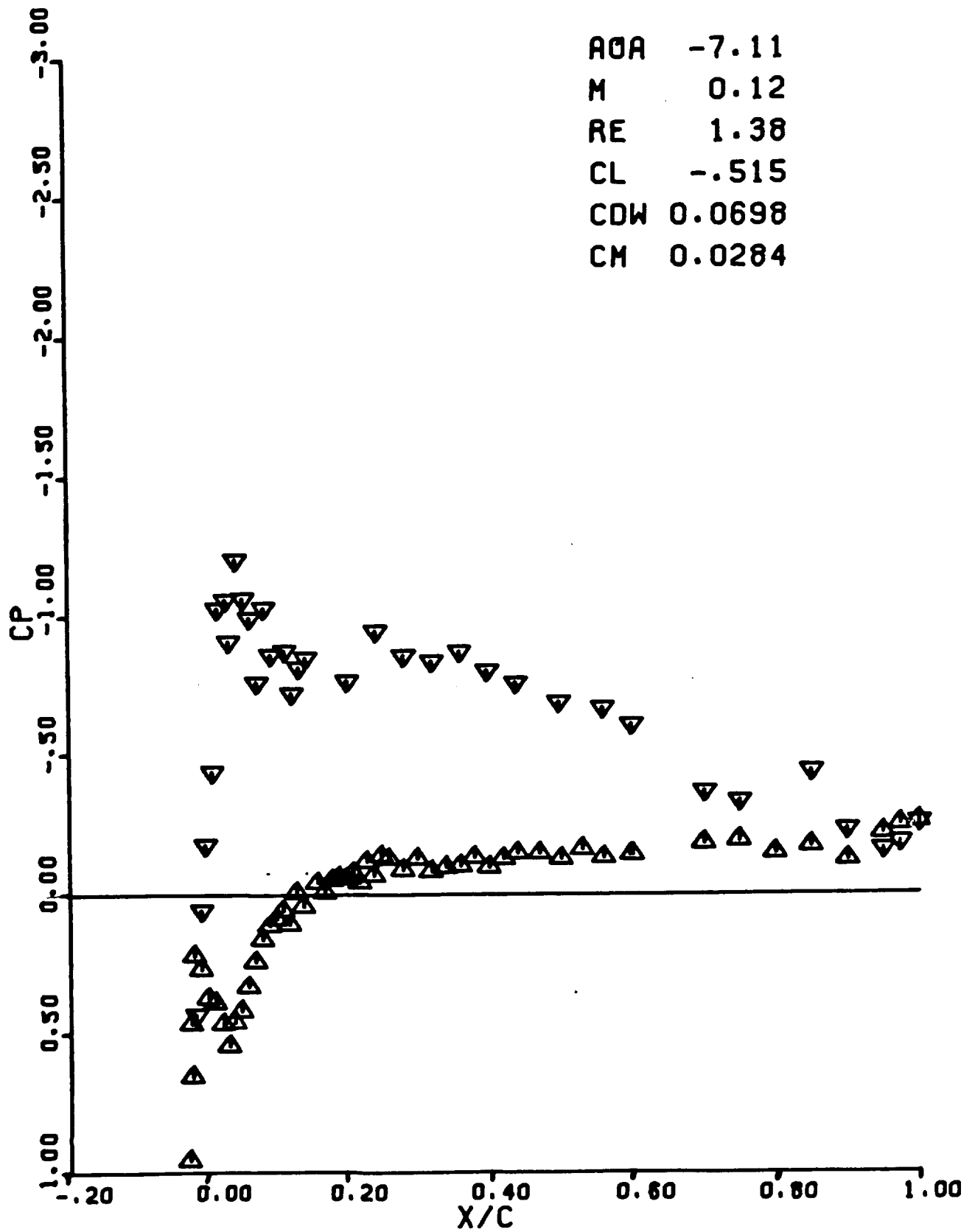
M 0.12

RE 1.38

CL -.515

CDW 0.0698

CM 0.0284



RUN 0456

AOA -6.13

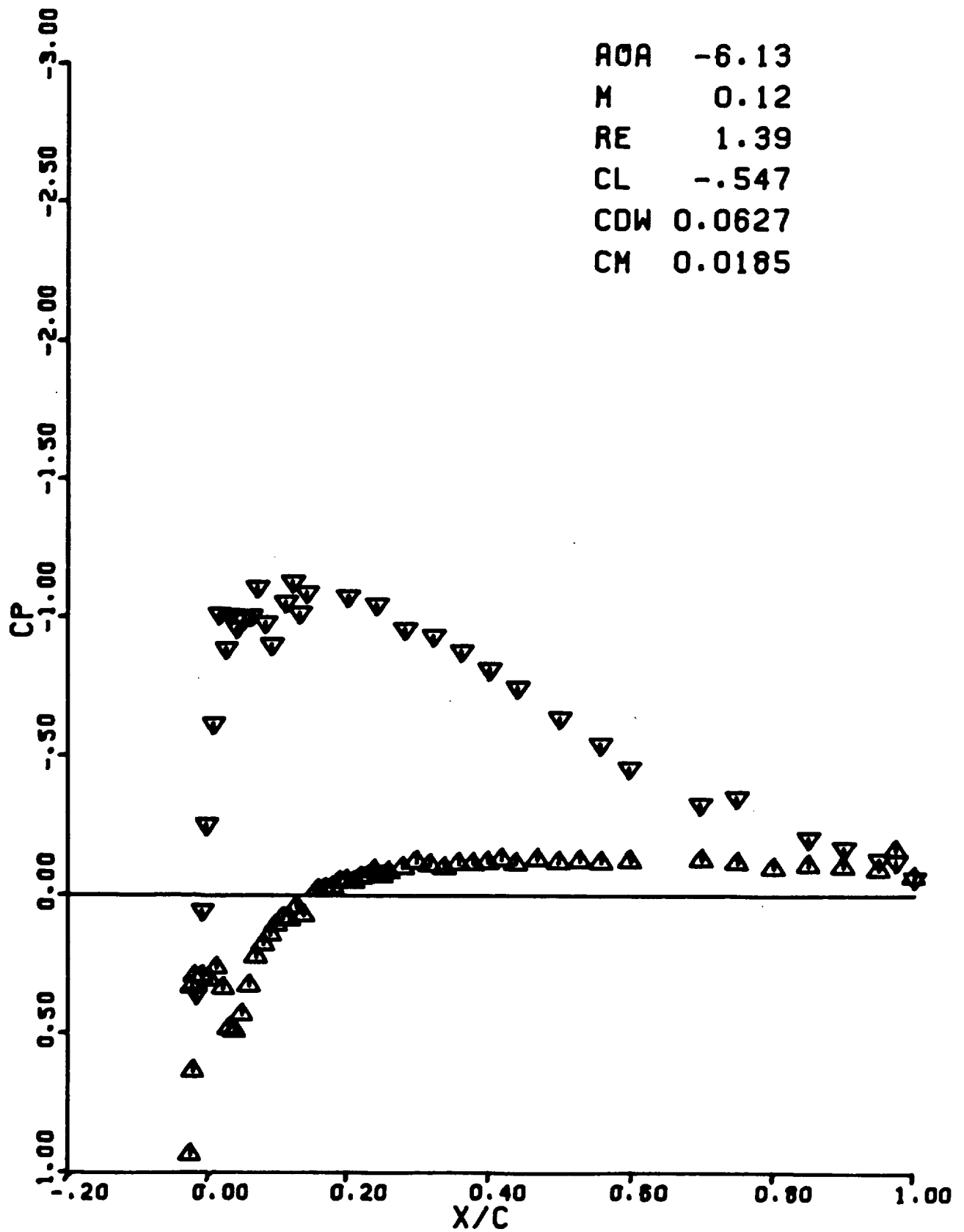
M 0.12

RE 1.39

CL -.547

CDW 0.0627

CM 0.0185



RUN 0457

AOA -5.15

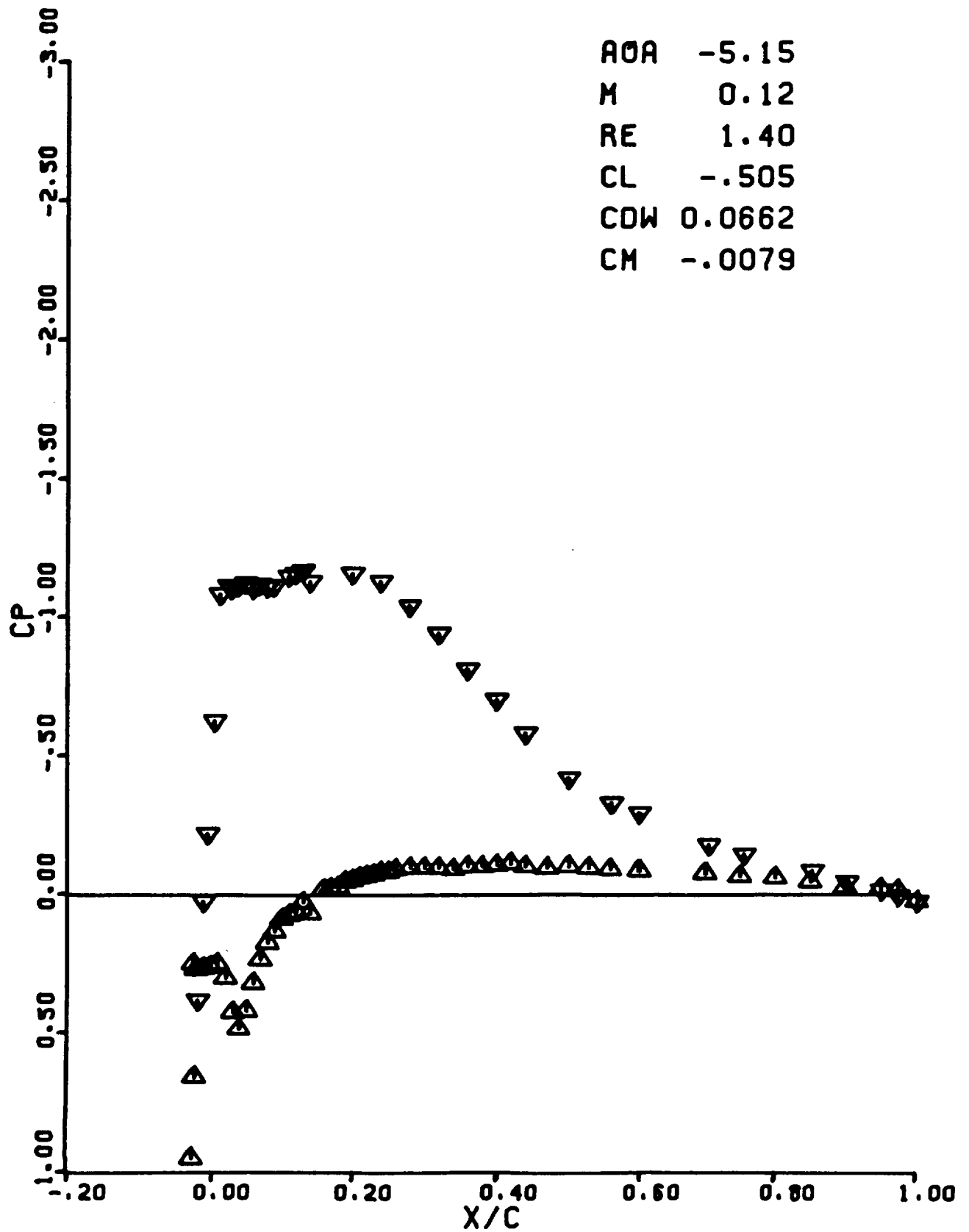
M 0.12

RE 1.40

CL -.505

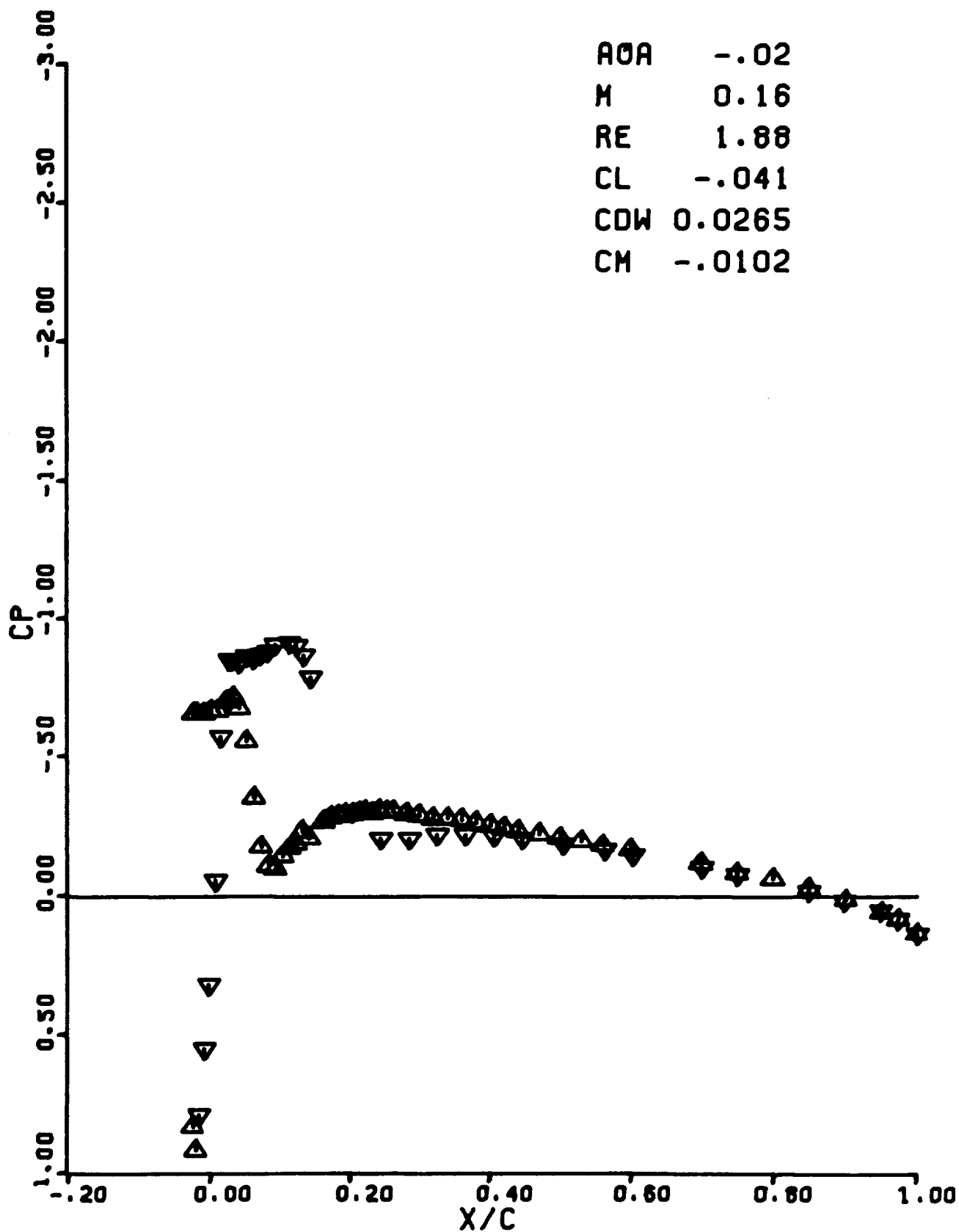
CDW 0.0662

CM -.0079



RUN 0458

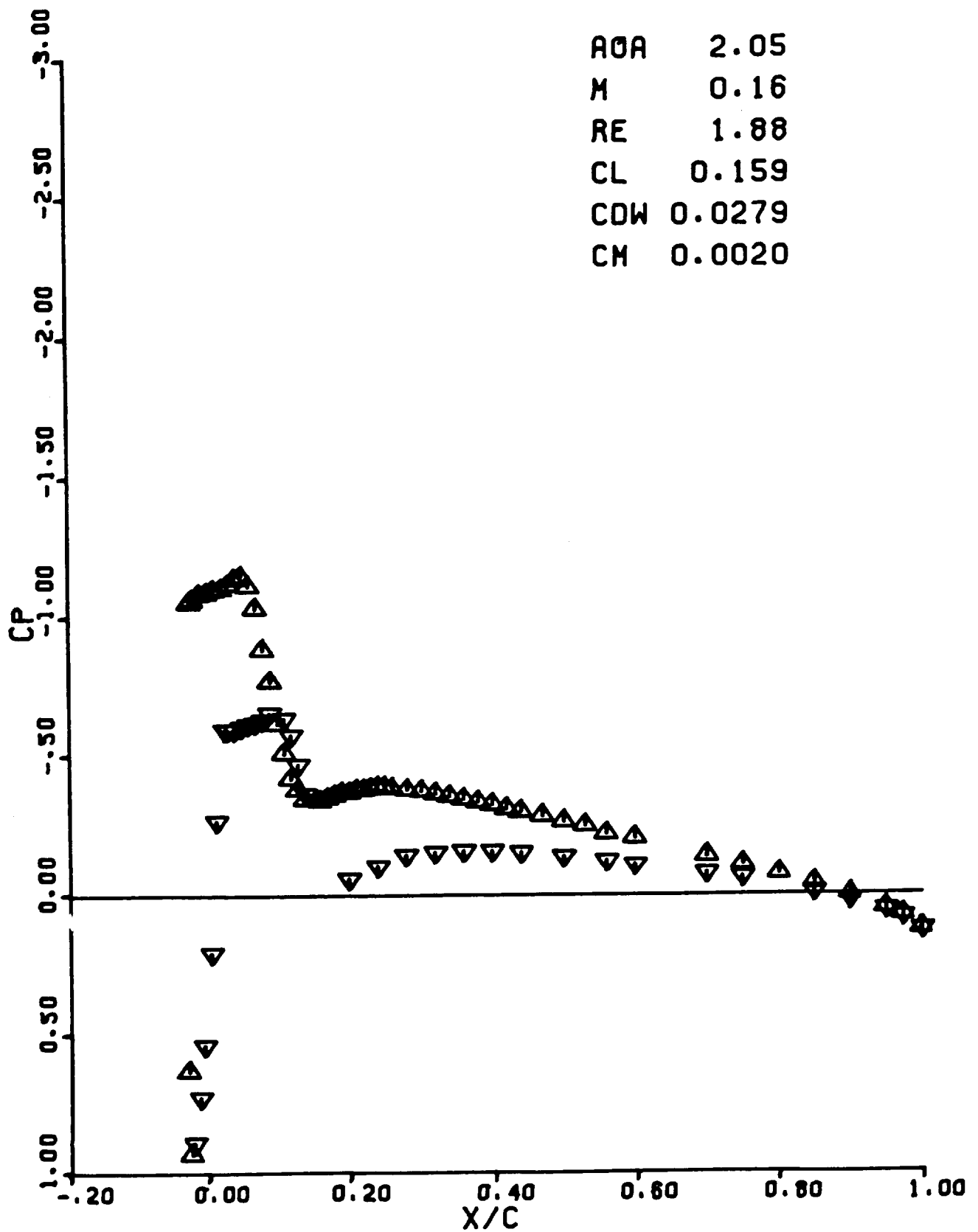
AOA -.02  
M 0.16  
RE 1.88  
CL -.041  
CDW 0.0265  
CM -.0102





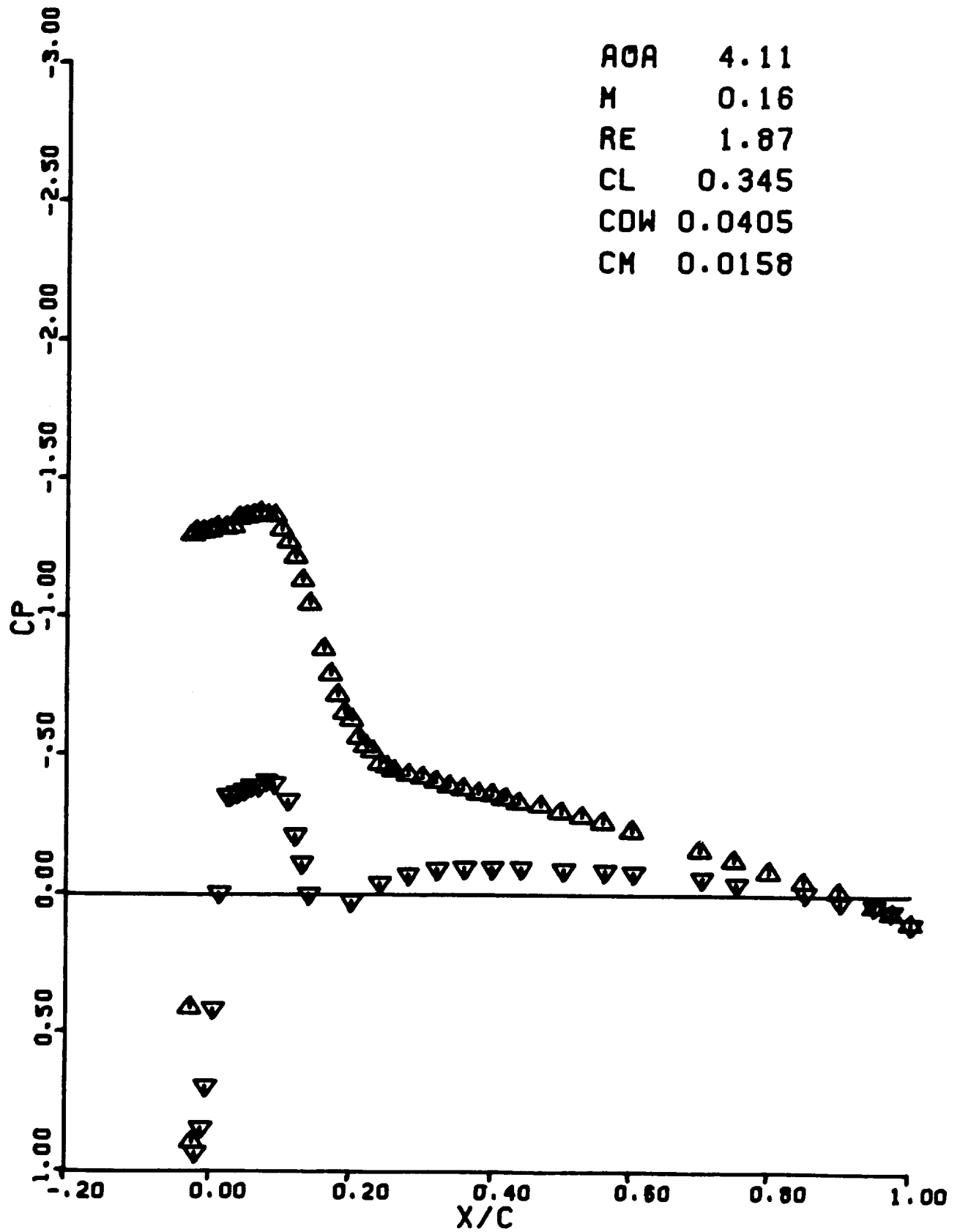
RUN 0459

AOA 2.05  
M 0.16  
RE 1.88  
CL 0.159  
CDW 0.0279  
CM 0.0020

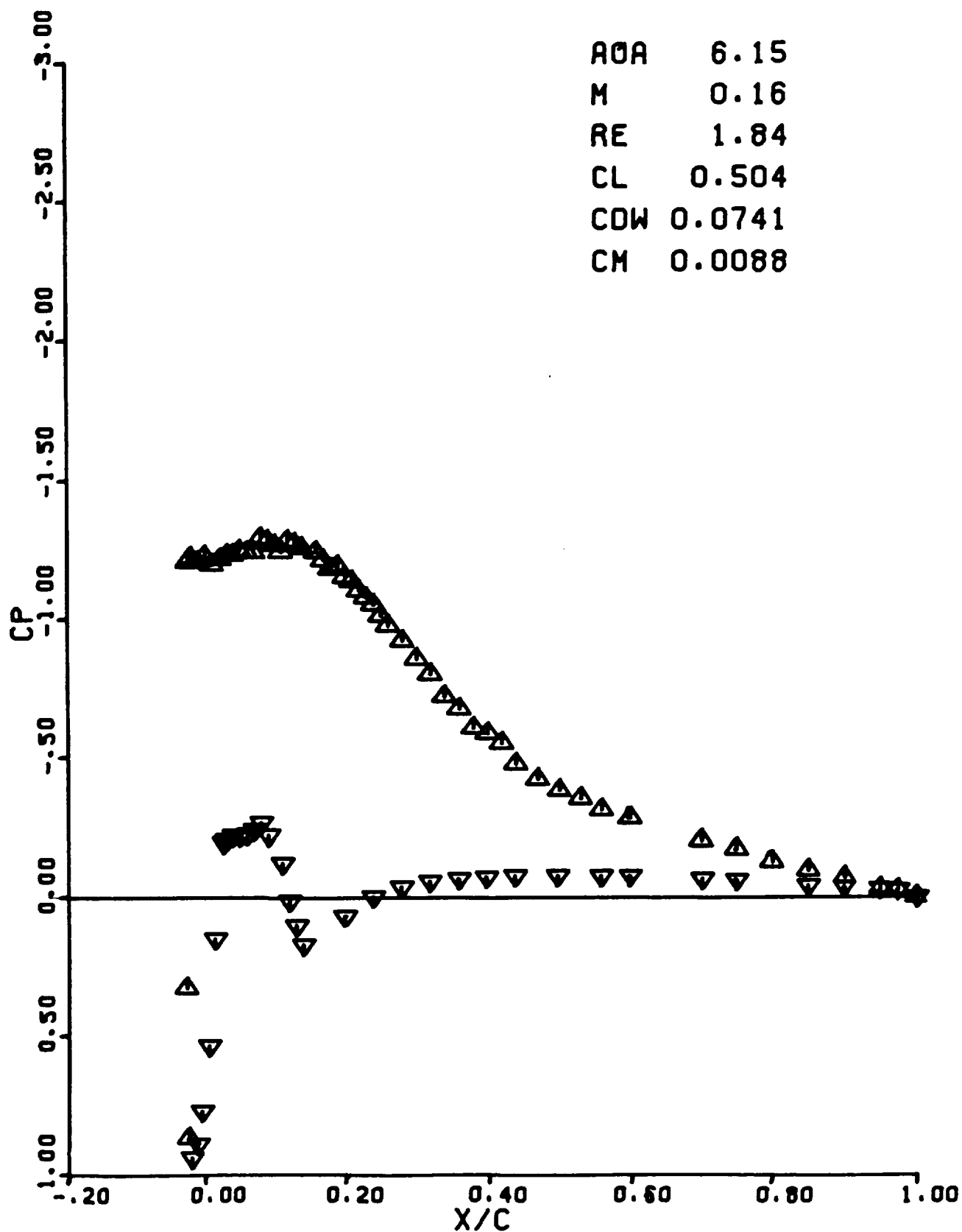


RUN 0460

AOA 4.11  
M 0.16  
RE 1.87  
CL 0.345  
CDW 0.0405  
CM 0.0158



RUN 0461



RUN 0462

AOA 8.11

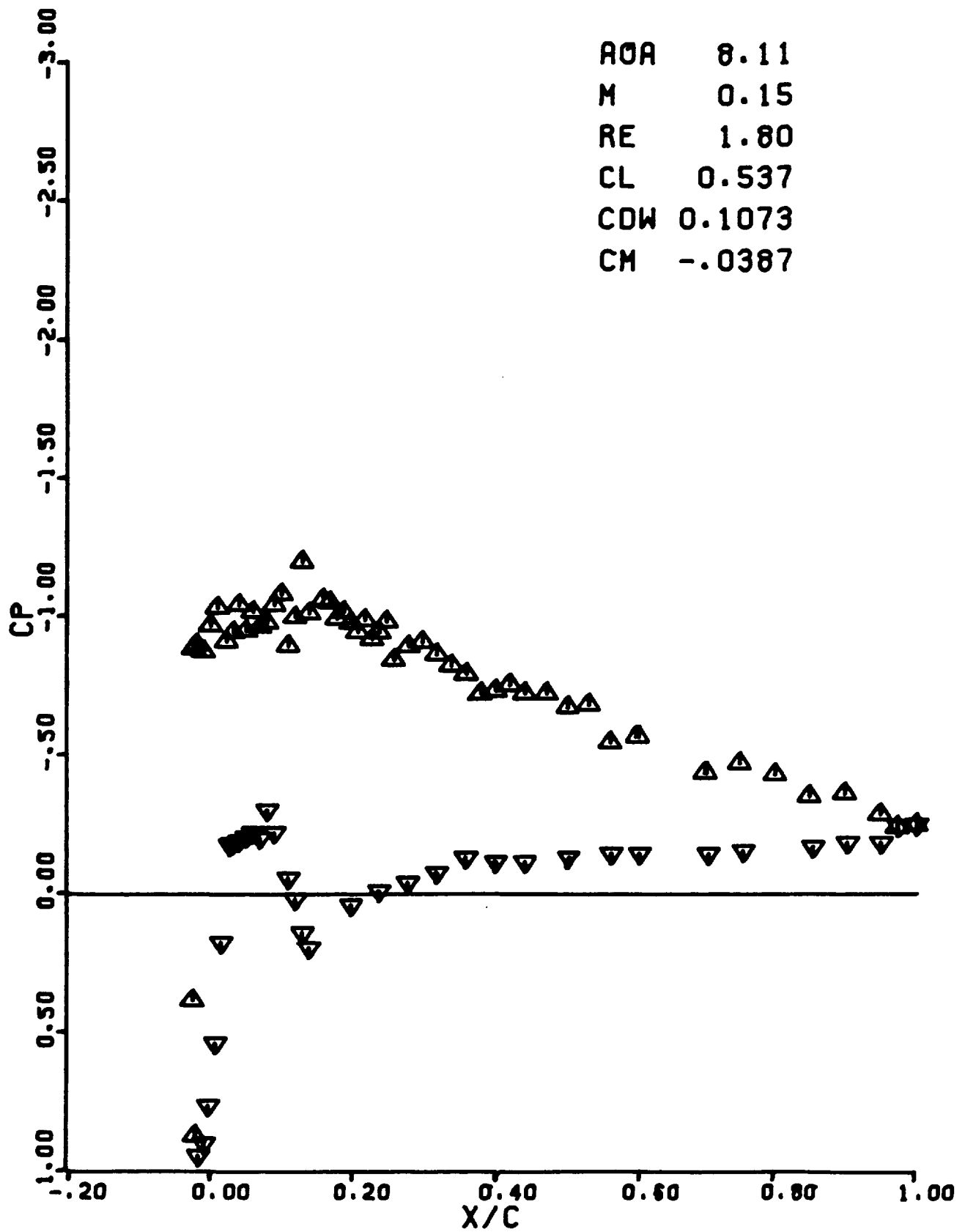
M 0.15

RE 1.80

CL 0.537

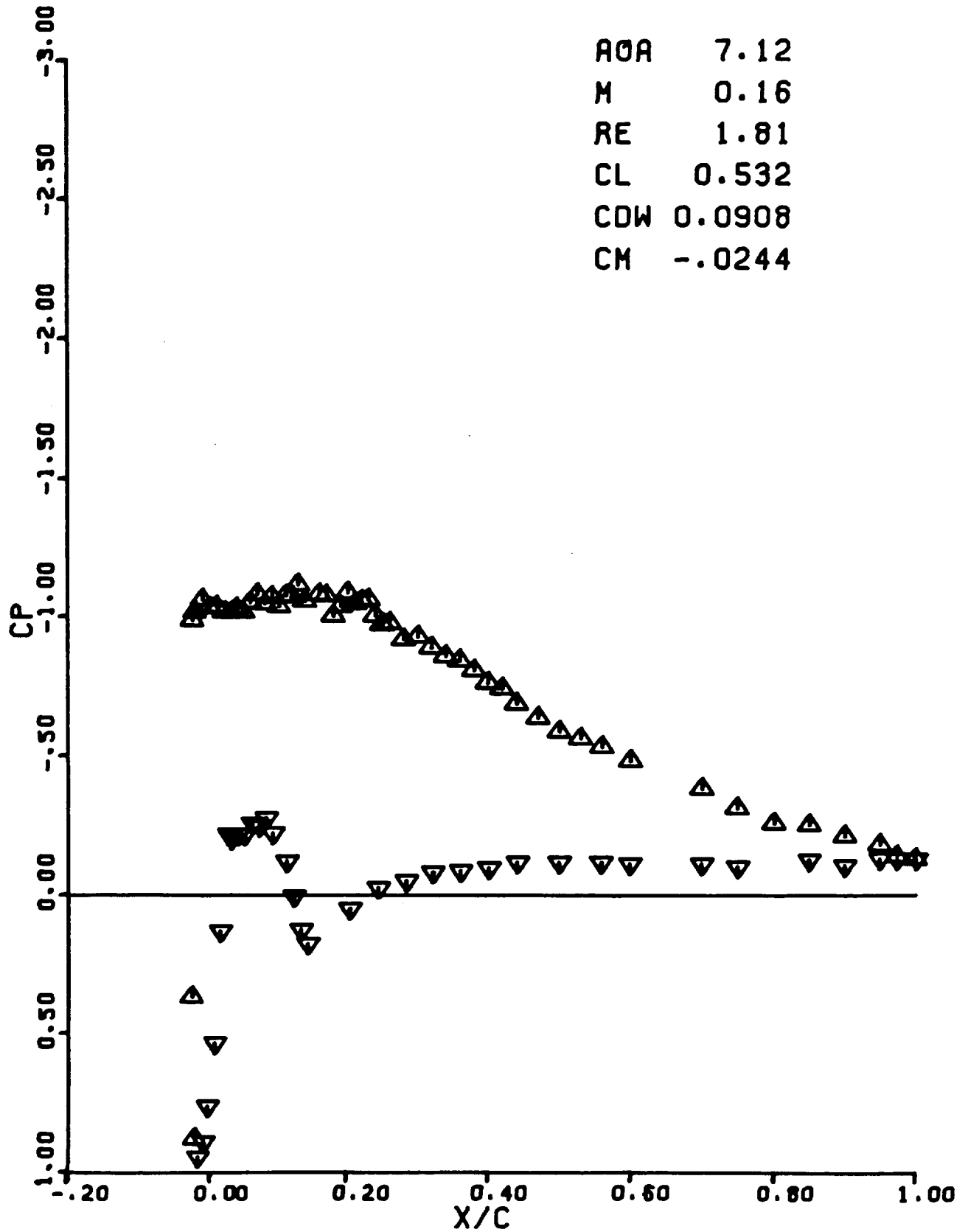
CDW 0.1073

CM -.0387



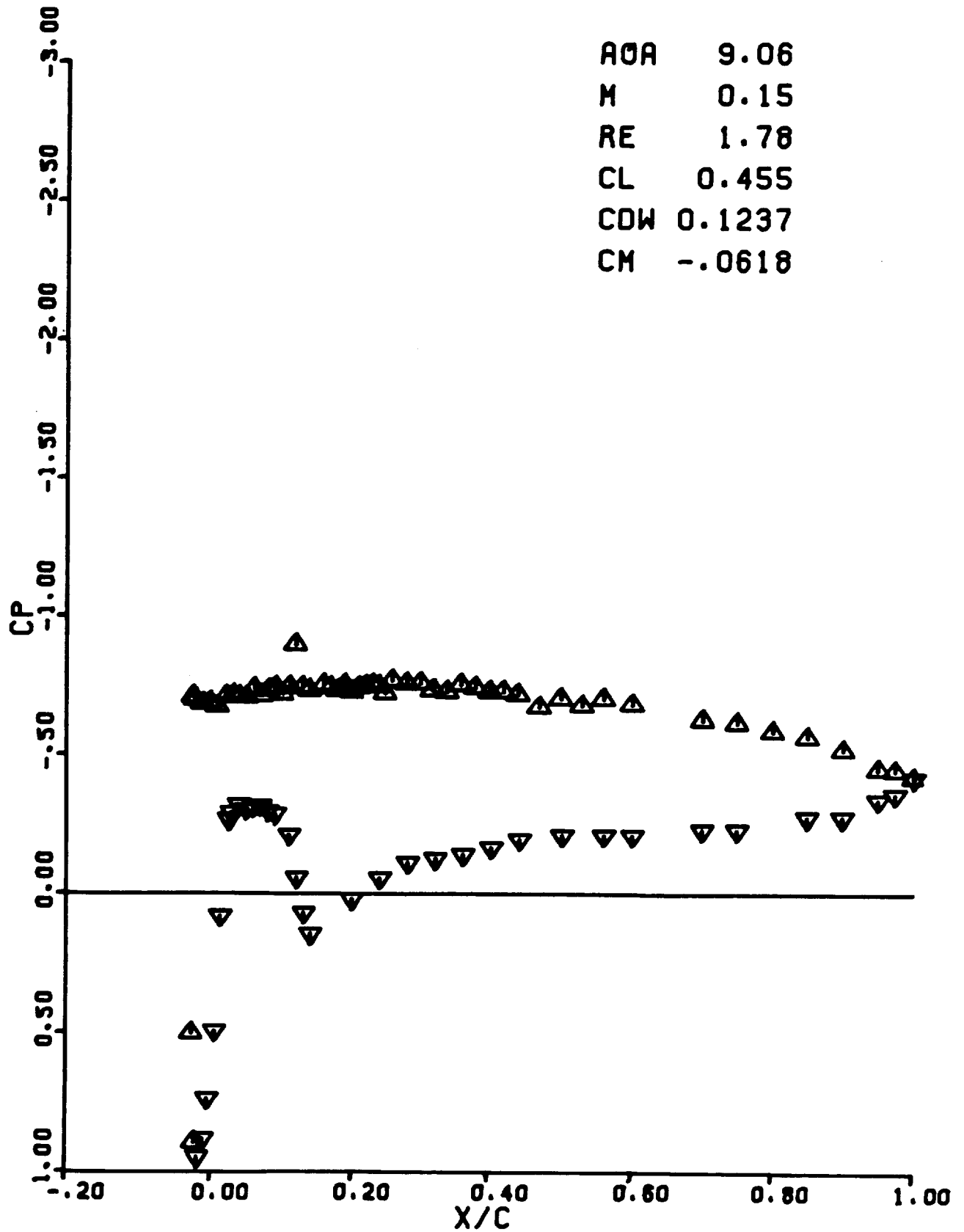
RUN 0463

AOA 7.12  
M 0.16  
RE 1.81  
CL 0.532  
CDW 0.0908  
CM -.0244



RUN 0464

AOA 9.06  
M 0.15  
RE 1.78  
CL 0.455  
CDW 0.1237  
CM -.0618



RUN 0465

AOA -2.08

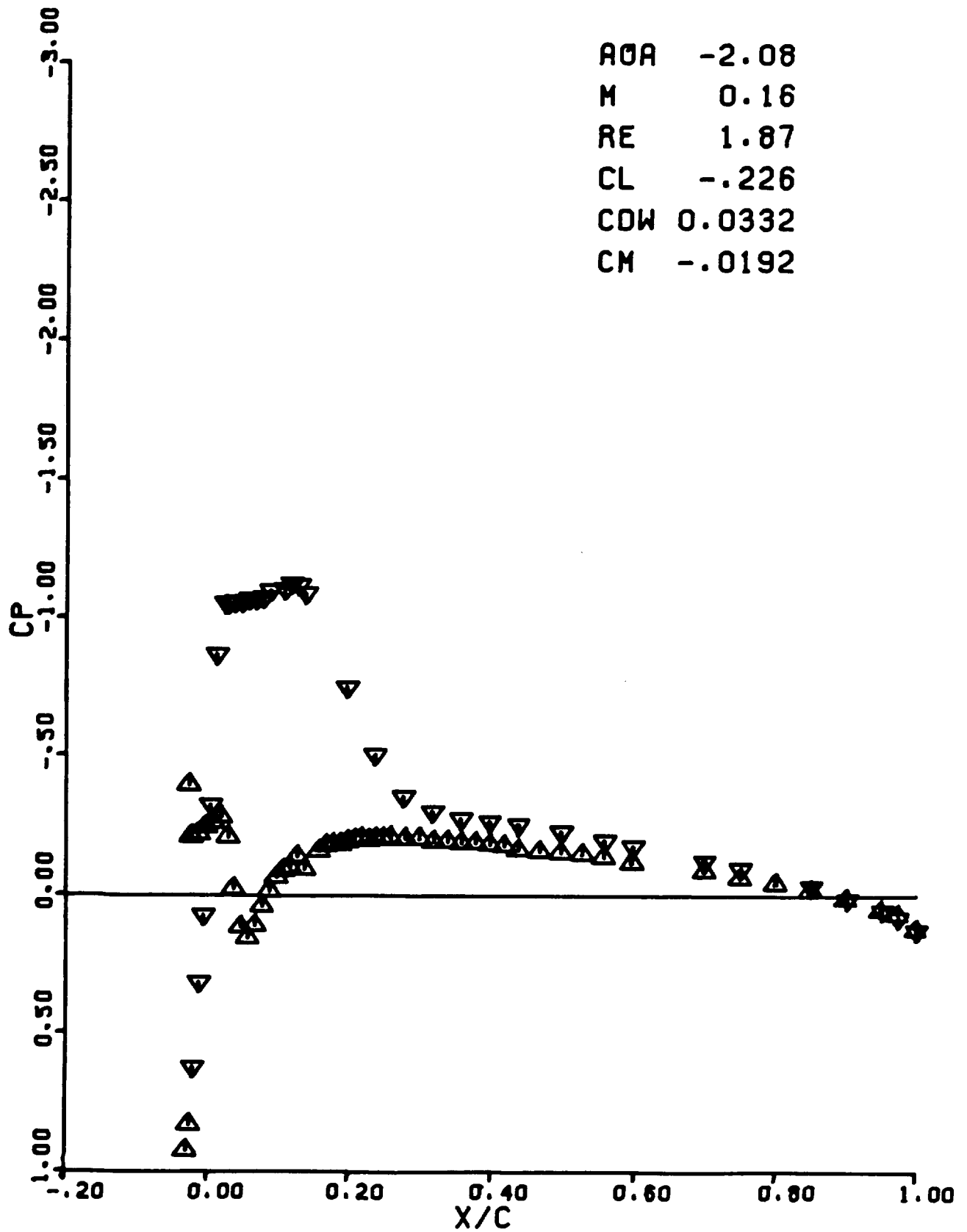
M 0.16

RE 1.87

CL -.226

CDW 0.0332

CM -.0192



RUN 0466

AOA -2.09

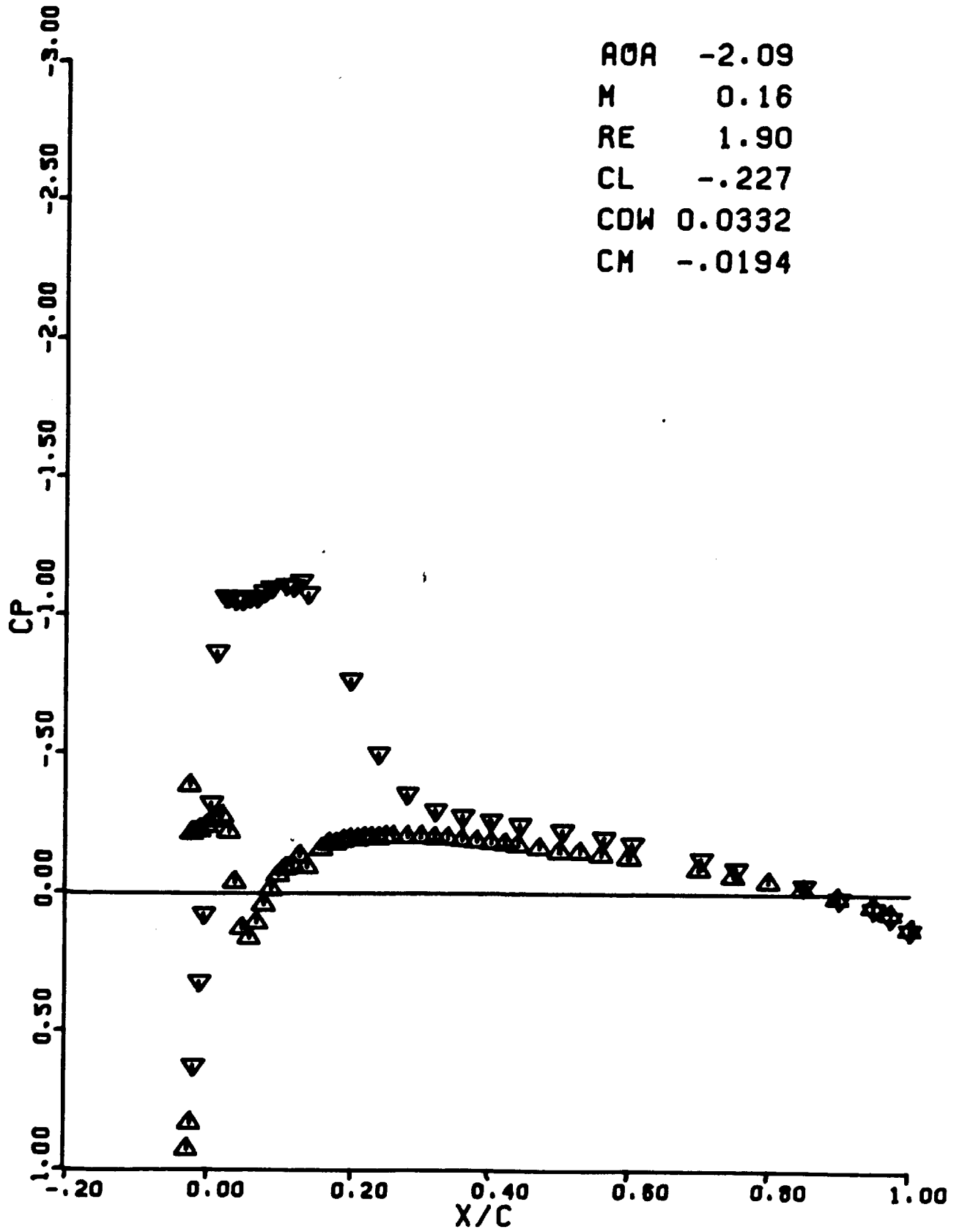
M 0.16

RE 1.90

CL -.227

CDW 0.0332

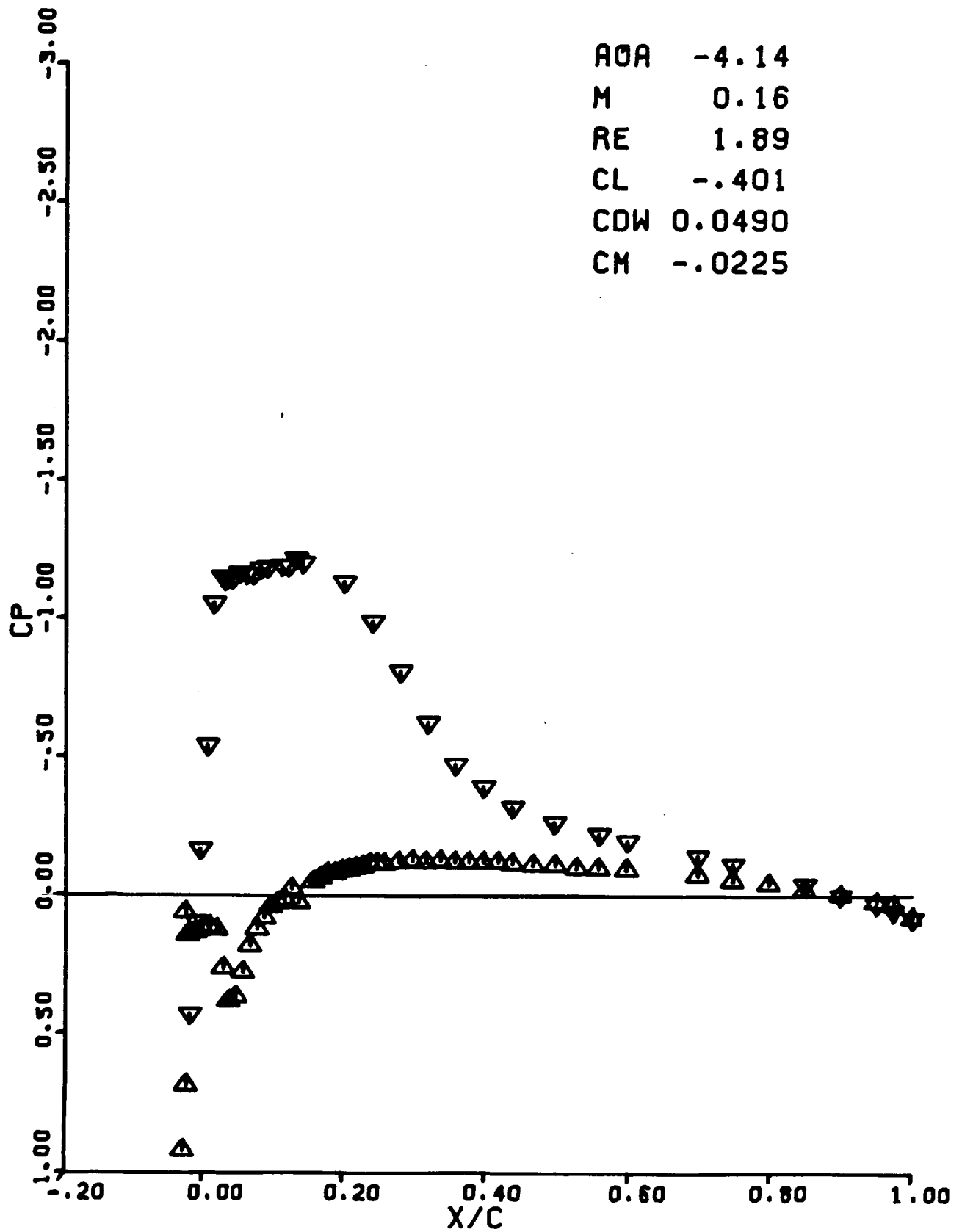
CM -.0194





RUN 0467

AOA -4.14  
M 0.16  
RE 1.89  
CL -.401  
CDW 0.0490  
CM -.0225



RUN 0468

AOA -6.15

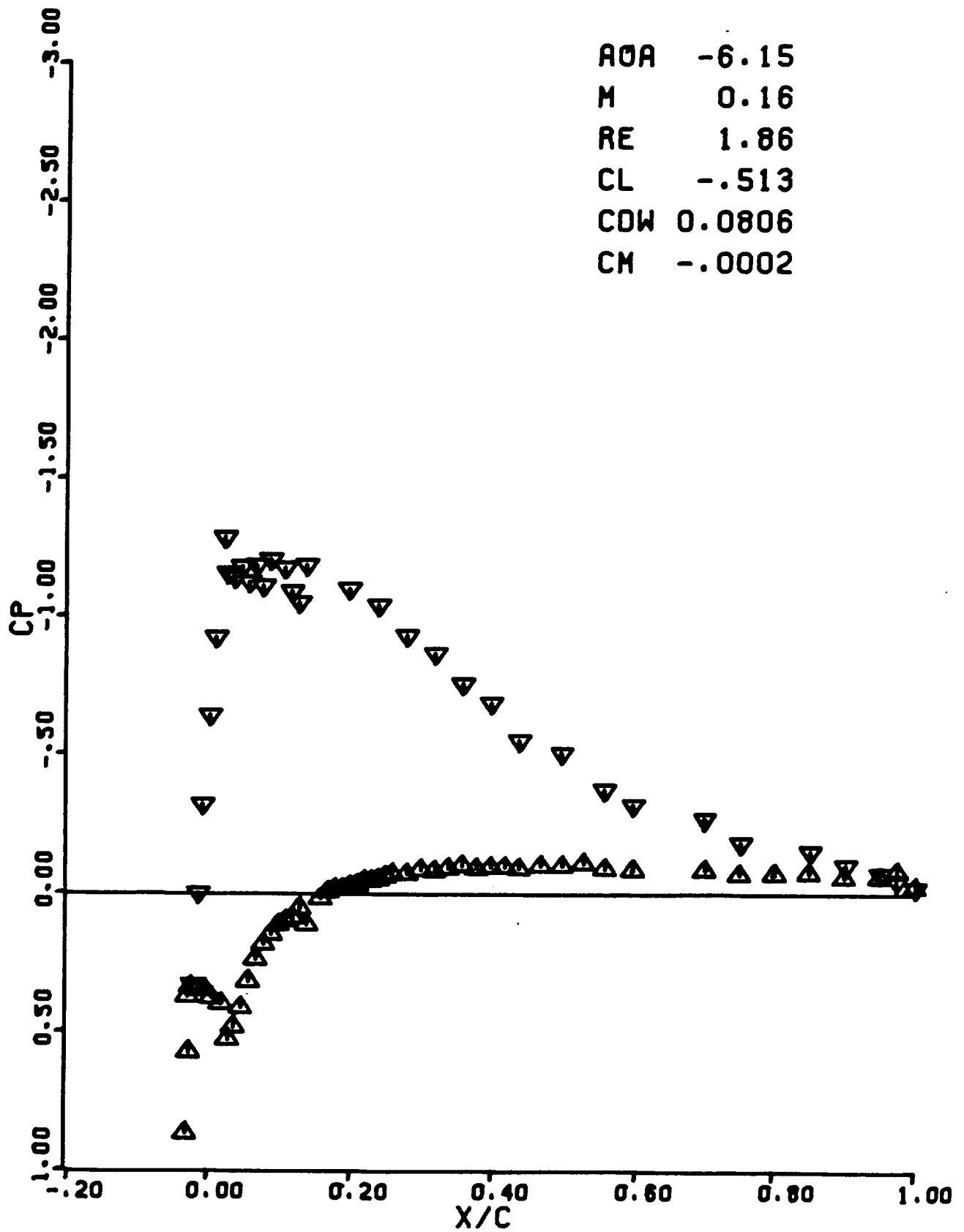
M 0.16

RE 1.86

CL -.513

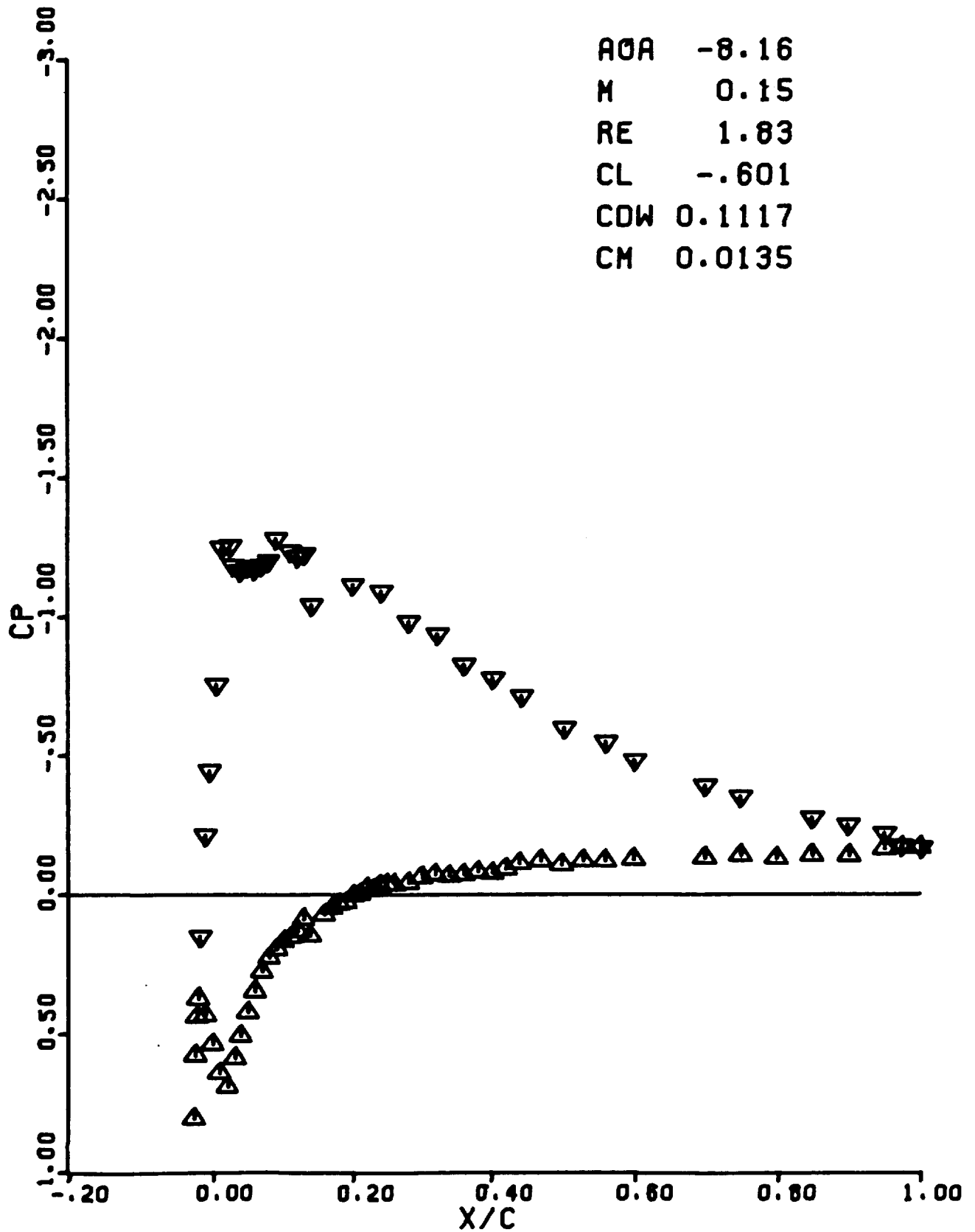
CDW 0.0806

CM -.0002



RUN 0469

AOA -8.16  
M 0.15  
RE 1.83  
CL -.601  
CDW 0.1117  
CM 0.0135



RUN 0470

AOA -9.16

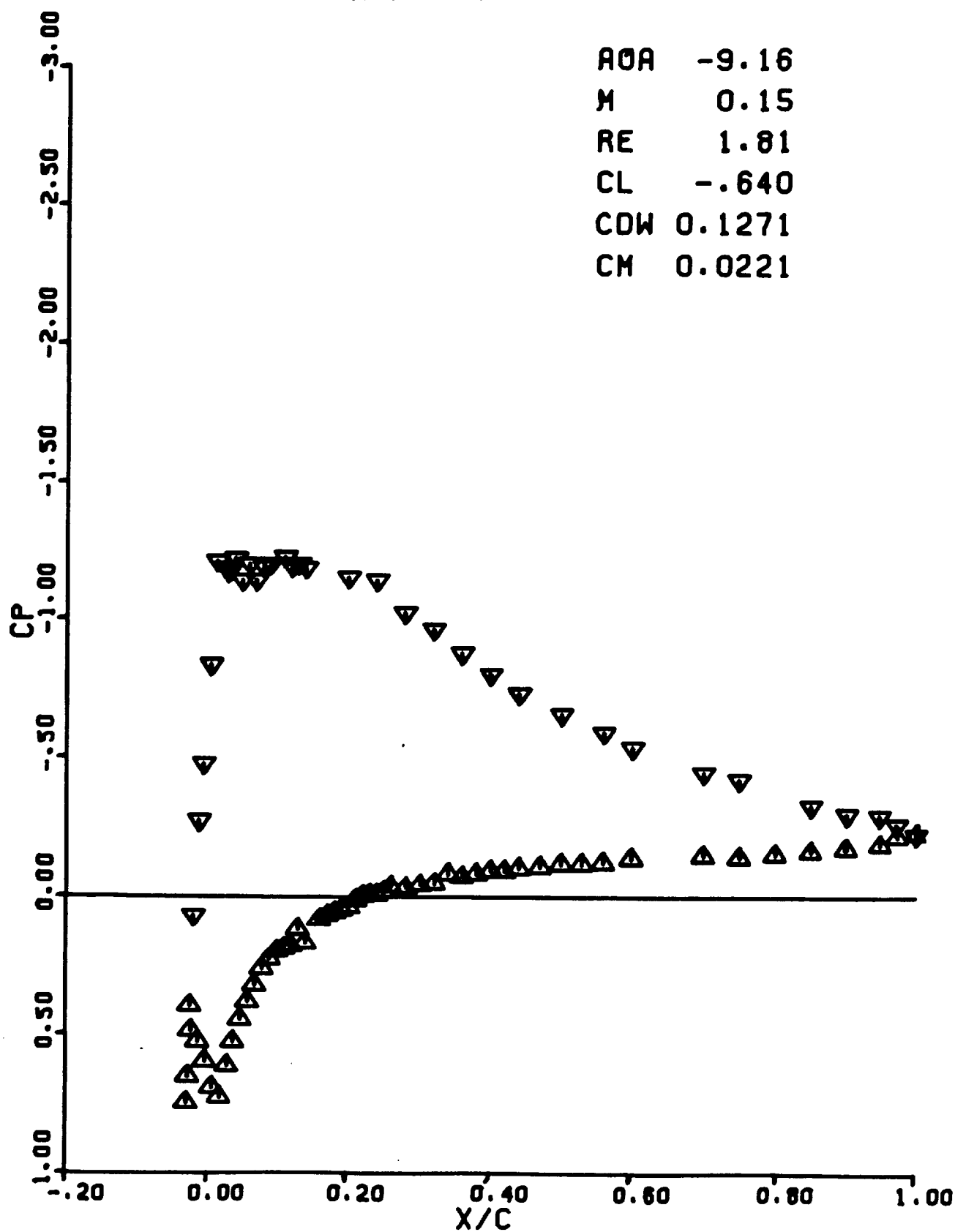
M 0.15

RE 1.81

CL -.640

CDW 0.1271

CM 0.0221



RUN 0471

AOA -10.16

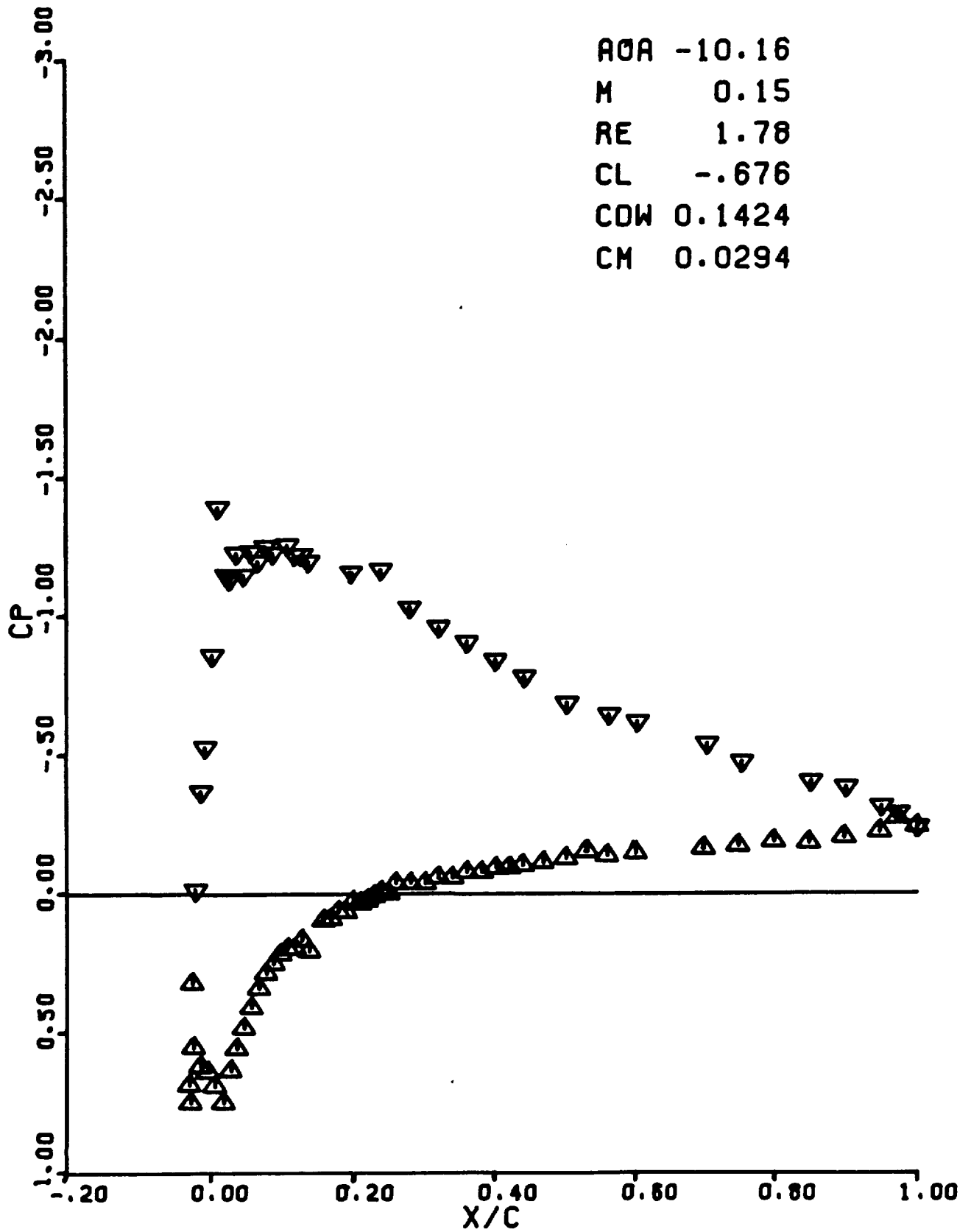
M 0.15

RE 1.78

CL -.676

COW 0.1424

CM 0.0294



RUN 0472

AOA -10.05

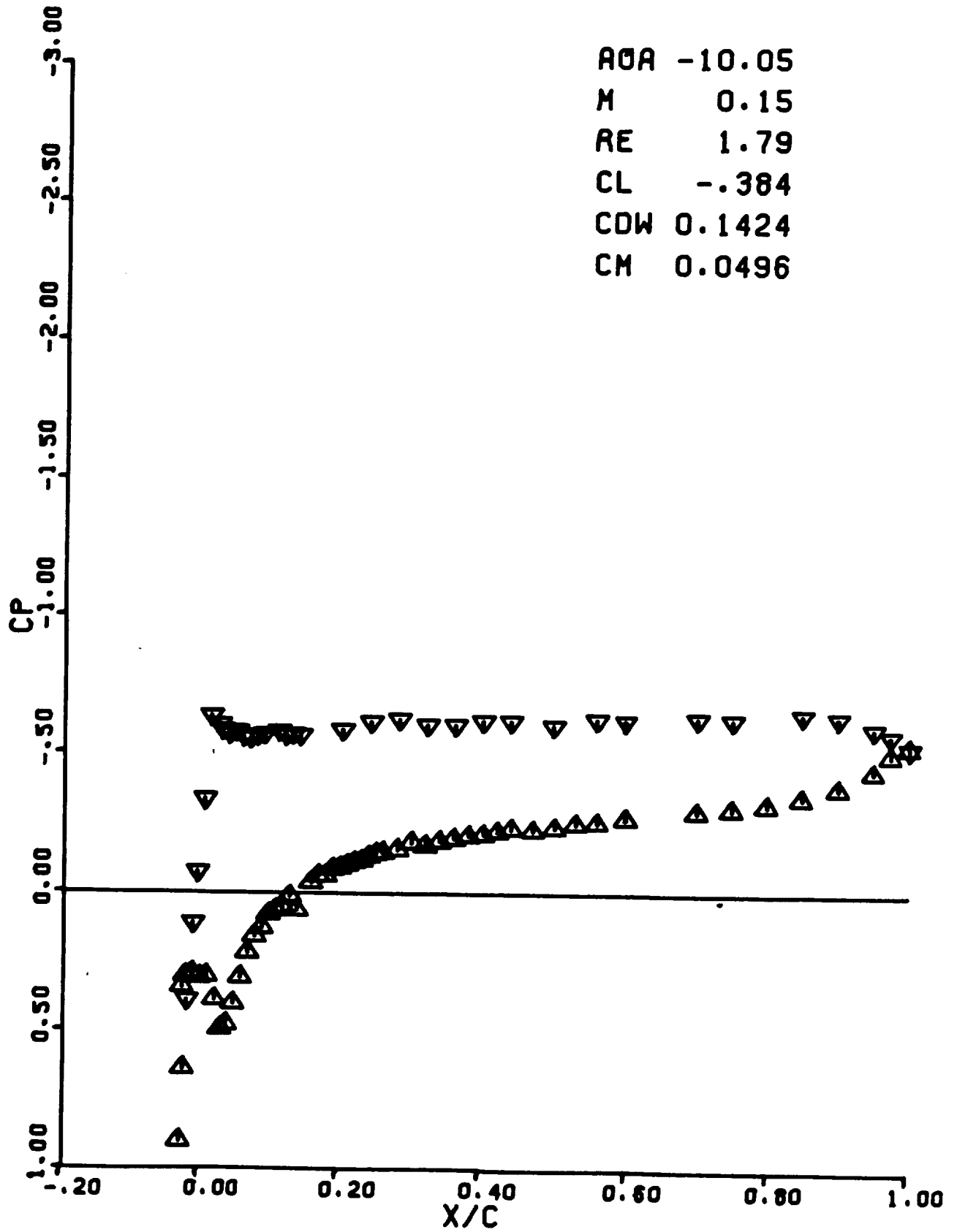
M 0.15

RE 1.79

CL -.384

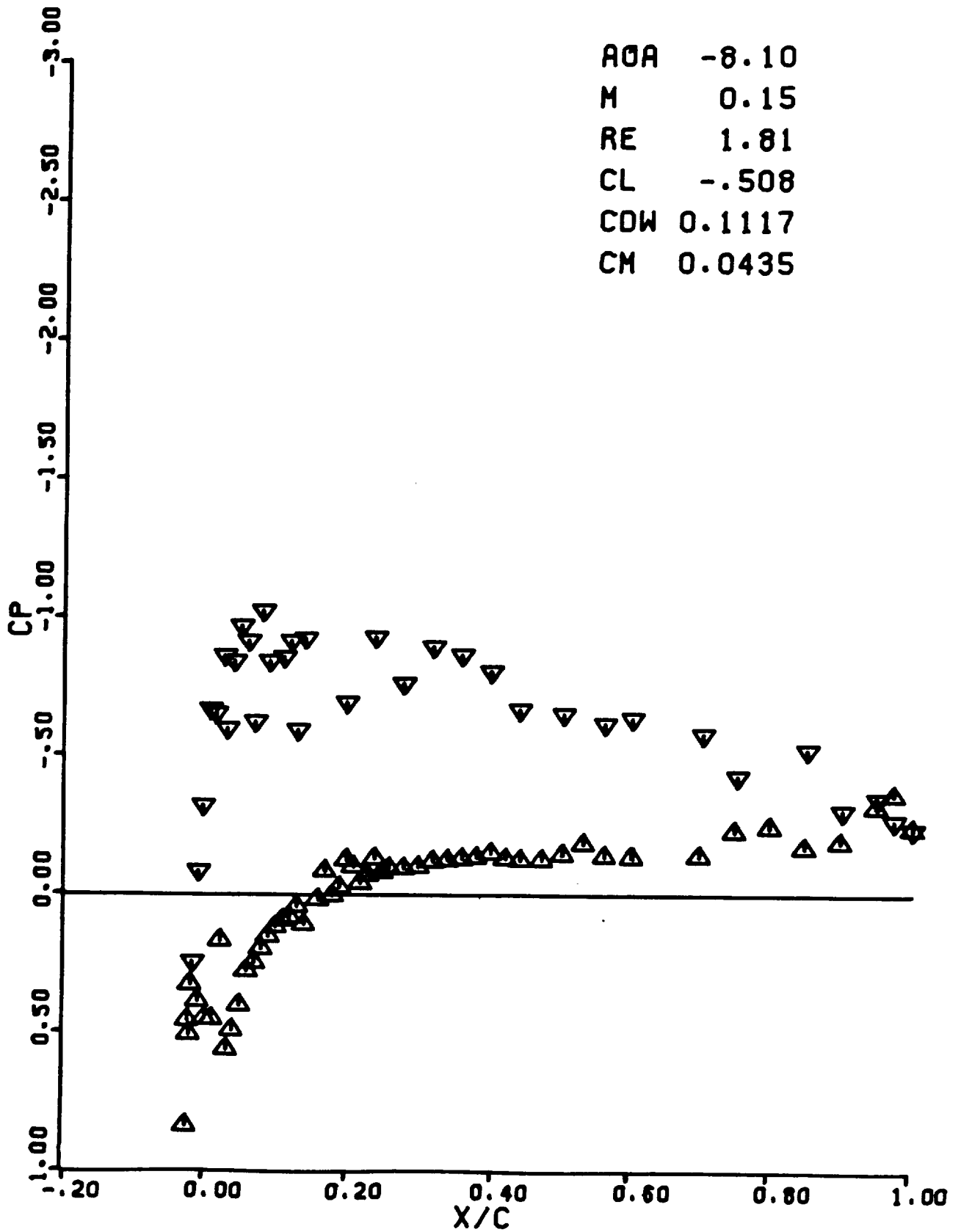
CDW 0.1424

CM 0.0496



RUN 0473

AOA -8.10  
M 0.15  
RE 1.81  
CL -.508  
CDW 0.1117  
CM 0.0435



RUN 0474

AOA -6.13

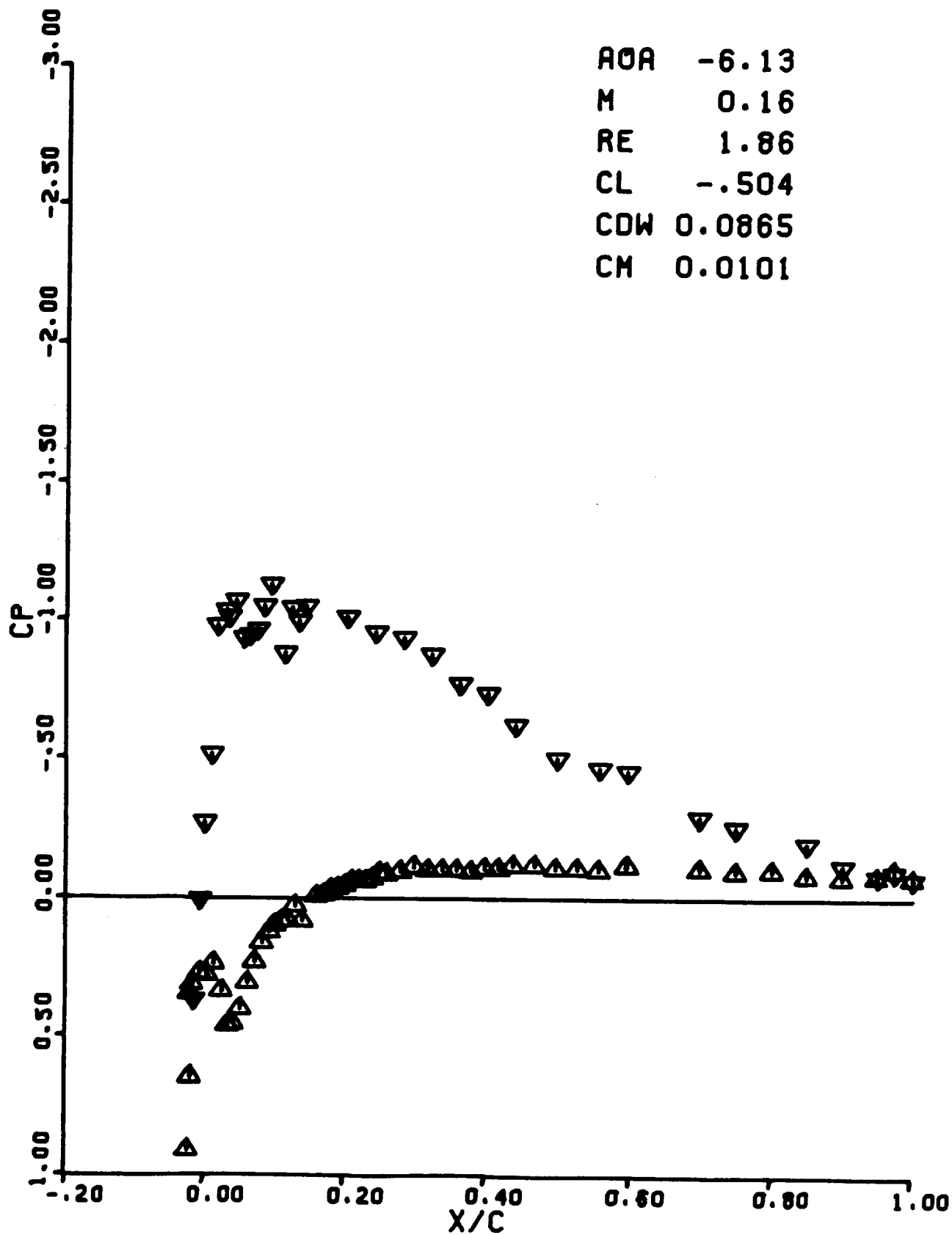
M 0.16

RE 1.86

CL -.504

CDW 0.0865

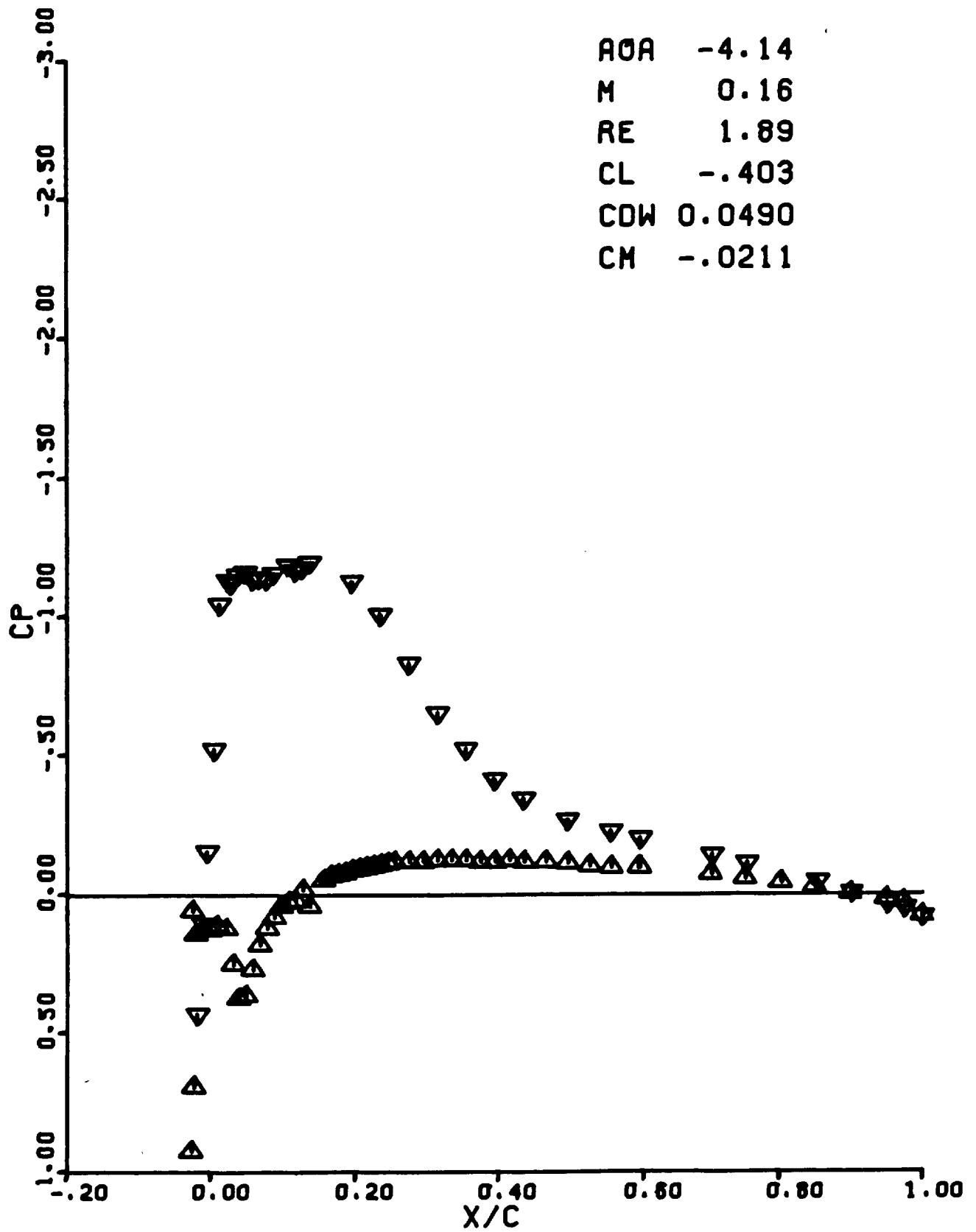
CM 0.0101





RUN 0475

AOA -4.14  
M 0.16  
RE 1.89  
CL -.403  
CDW 0.0490  
CM -.0211



RUN 0476

AOA -7.13

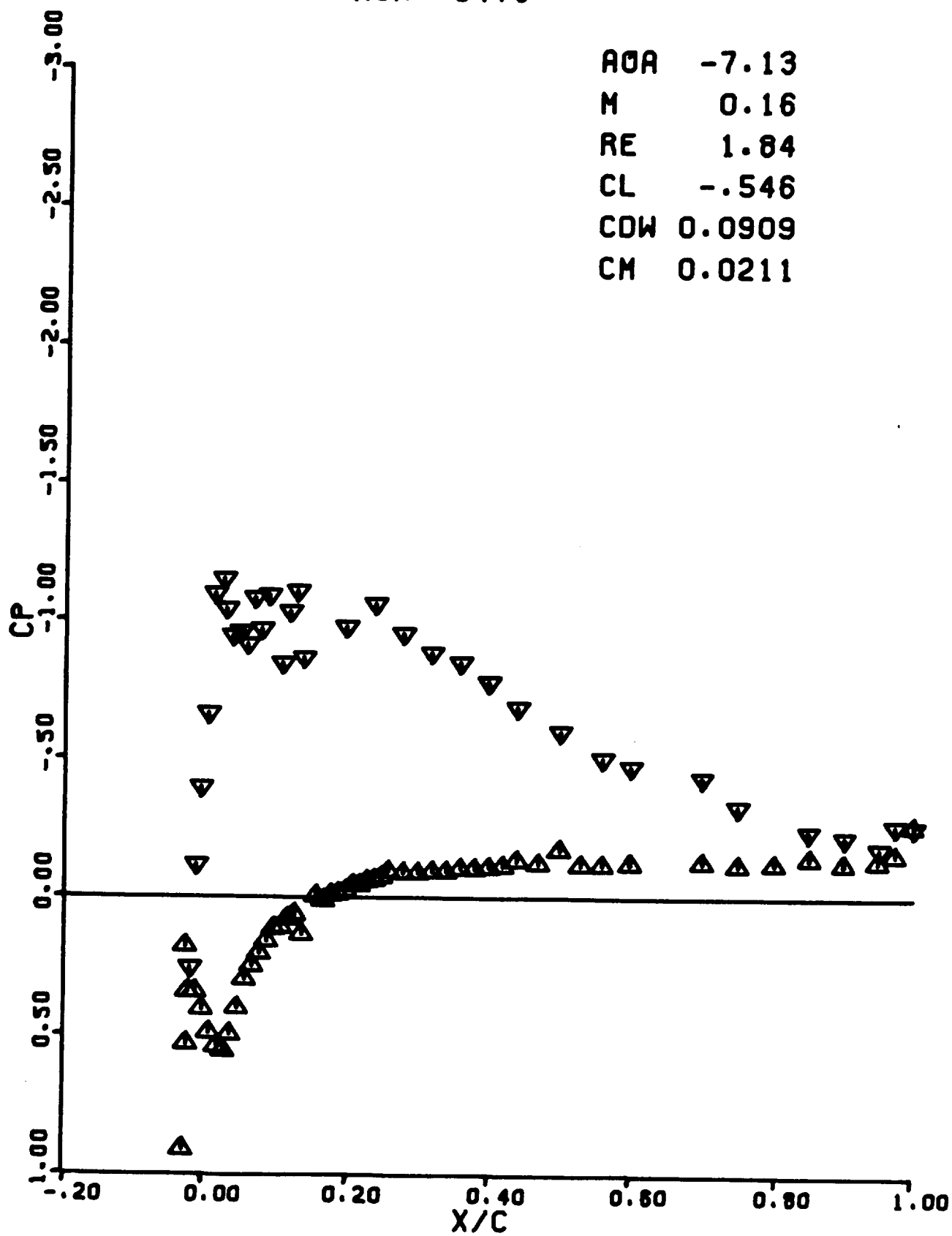
M 0.16

RE 1.84

CL -.546

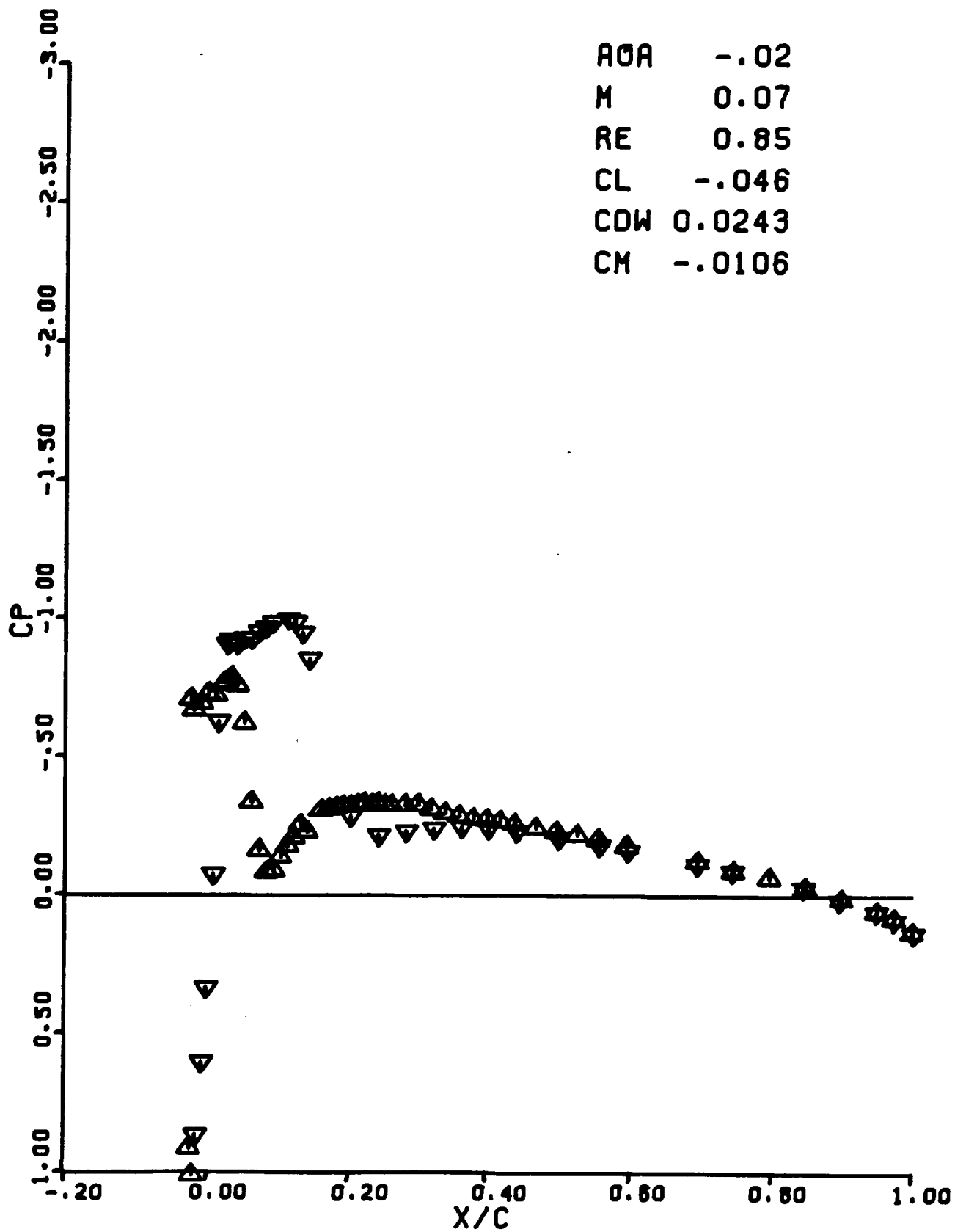
CDW 0.0909

CM 0.0211



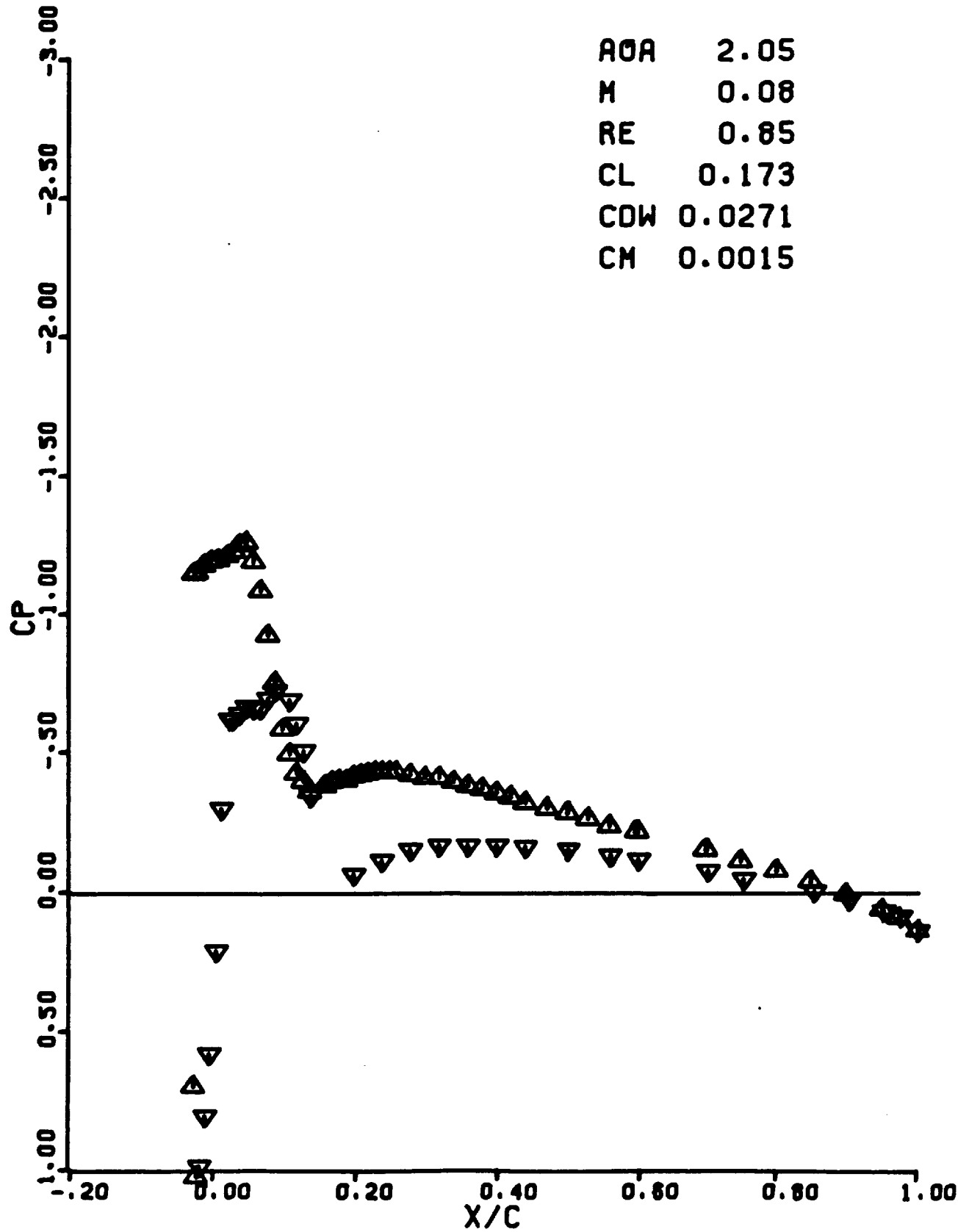
RUN 0477

AOA -.02  
M 0.07  
RE 0.85  
CL -.046  
CDW 0.0243  
CM -.0106



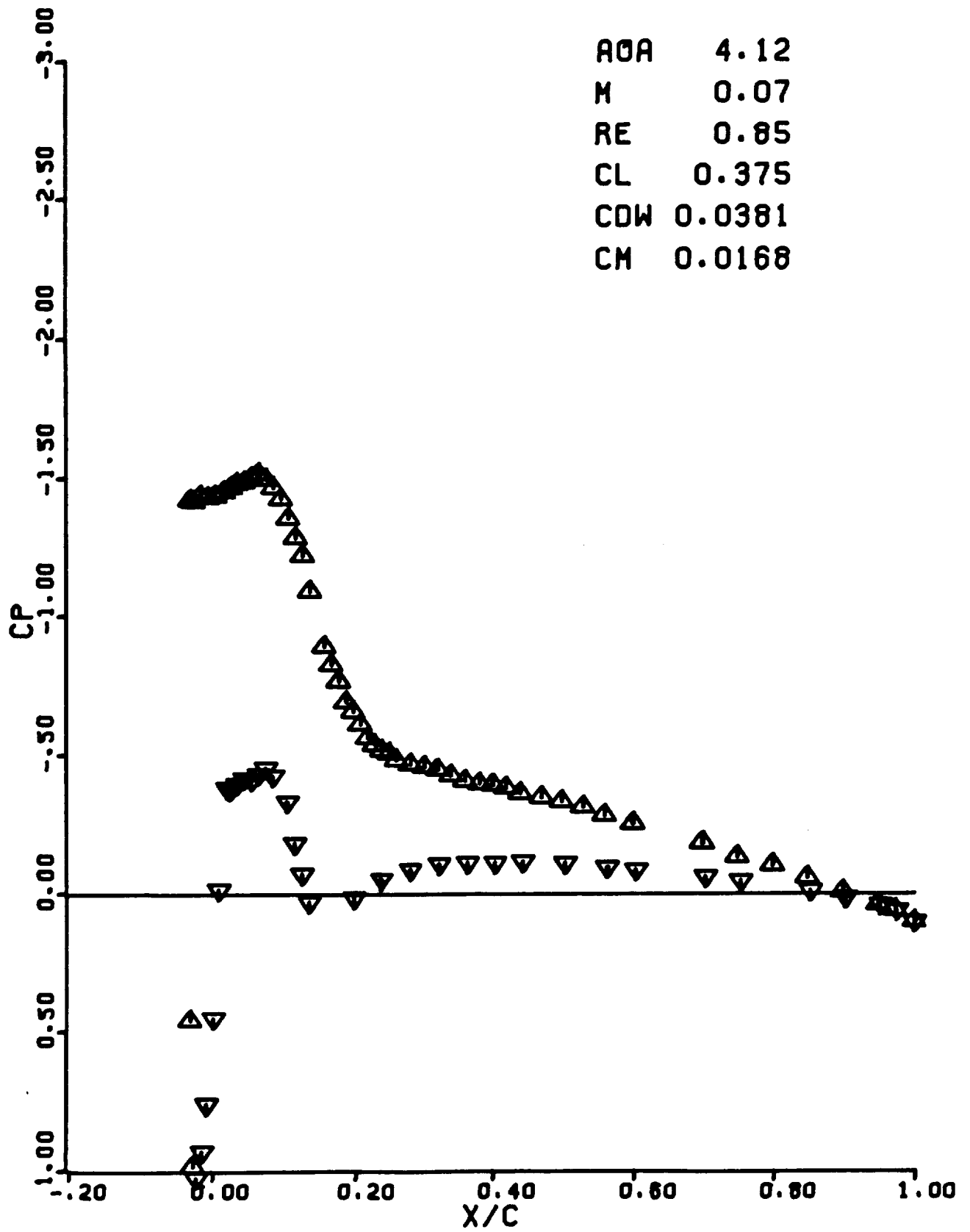
RUN 0478

AOA 2.05  
M 0.08  
RE 0.85  
CL 0.173  
CDW 0.0271  
CM 0.0015



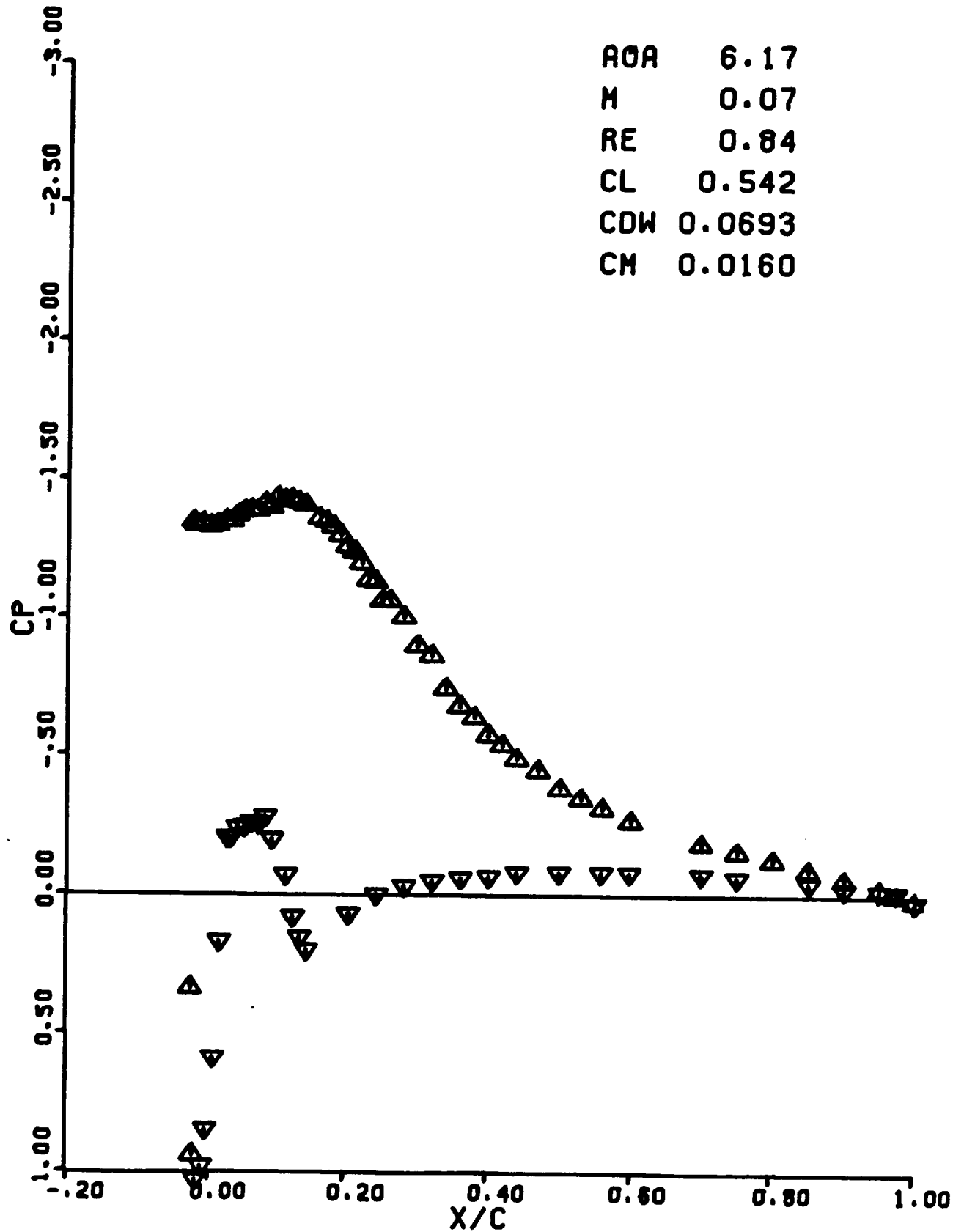
RUN 0479

AOA 4.12  
M 0.07  
RE 0.85  
CL 0.375  
CDW 0.0381  
CM 0.0168



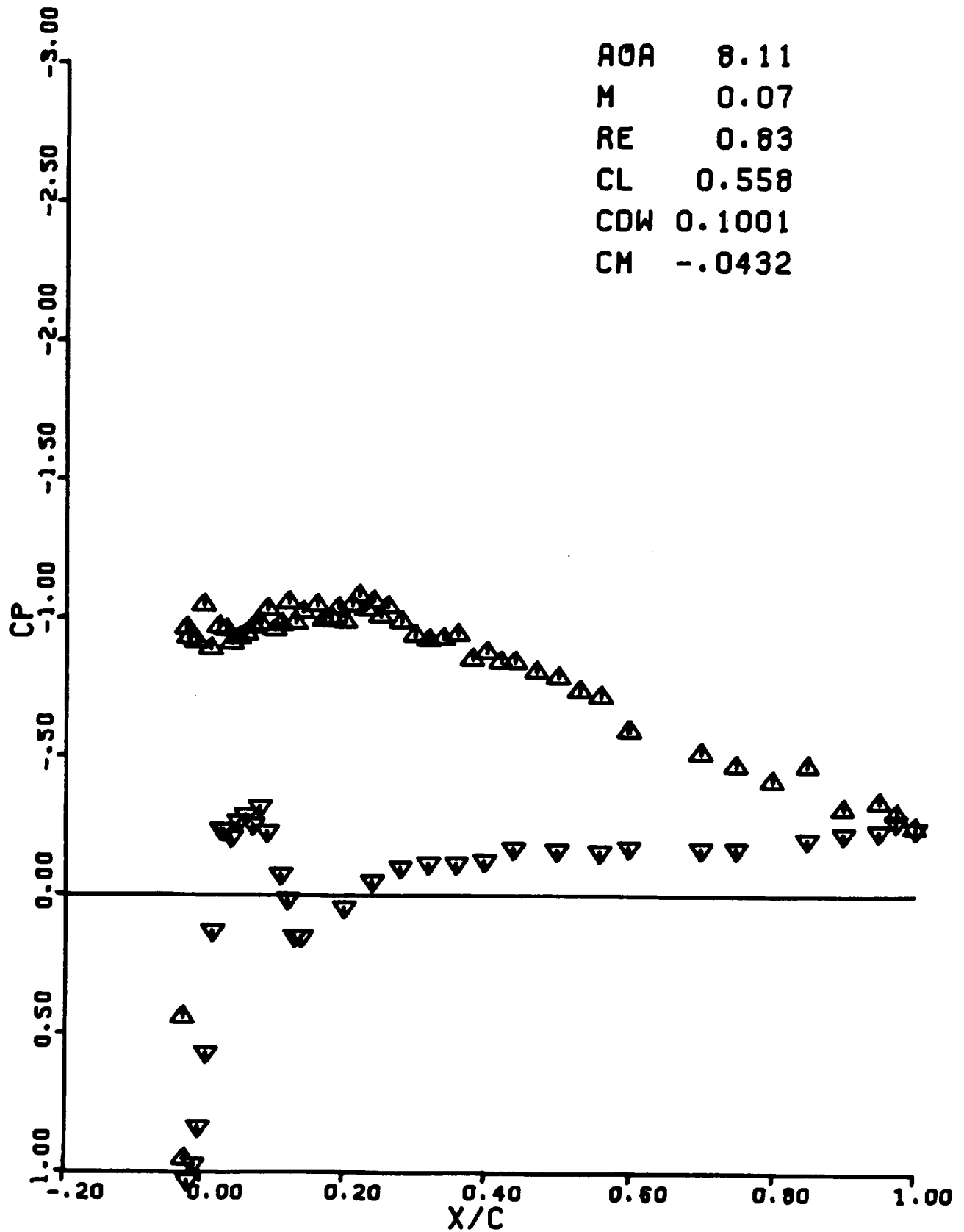
RUN 0480

AOA 6.17  
M 0.07  
RE 0.84  
CL 0.542  
CDW 0.0693  
CM 0.0160



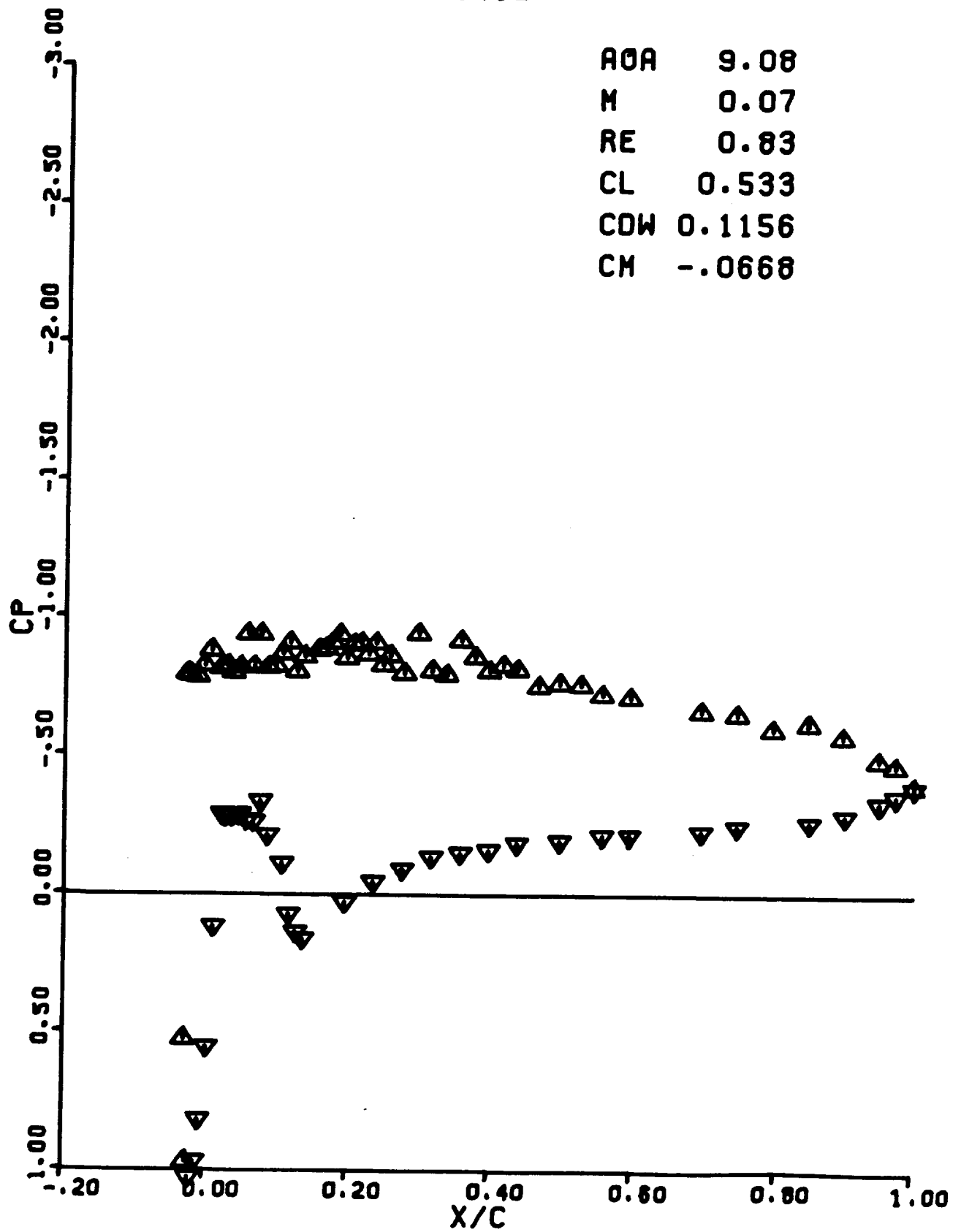
RUN 0481

AOA 8.11  
M 0.07  
RE 0.83  
CL 0.558  
CDW 0.1001  
CM -.0432



RUN 0482

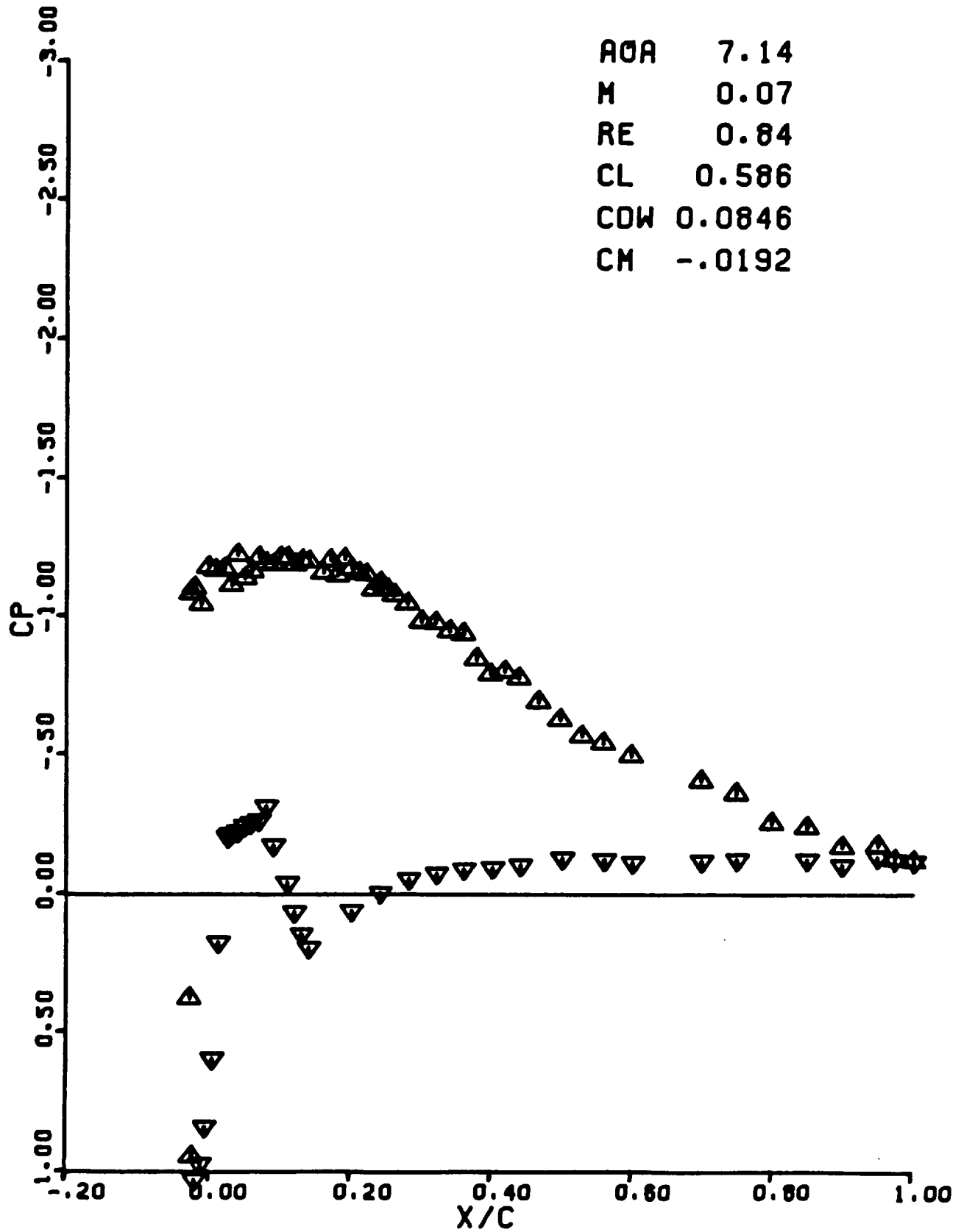
AOA 9.08  
M 0.07  
RE 0.83  
CL 0.533  
CDW 0.1156  
CM -.0668





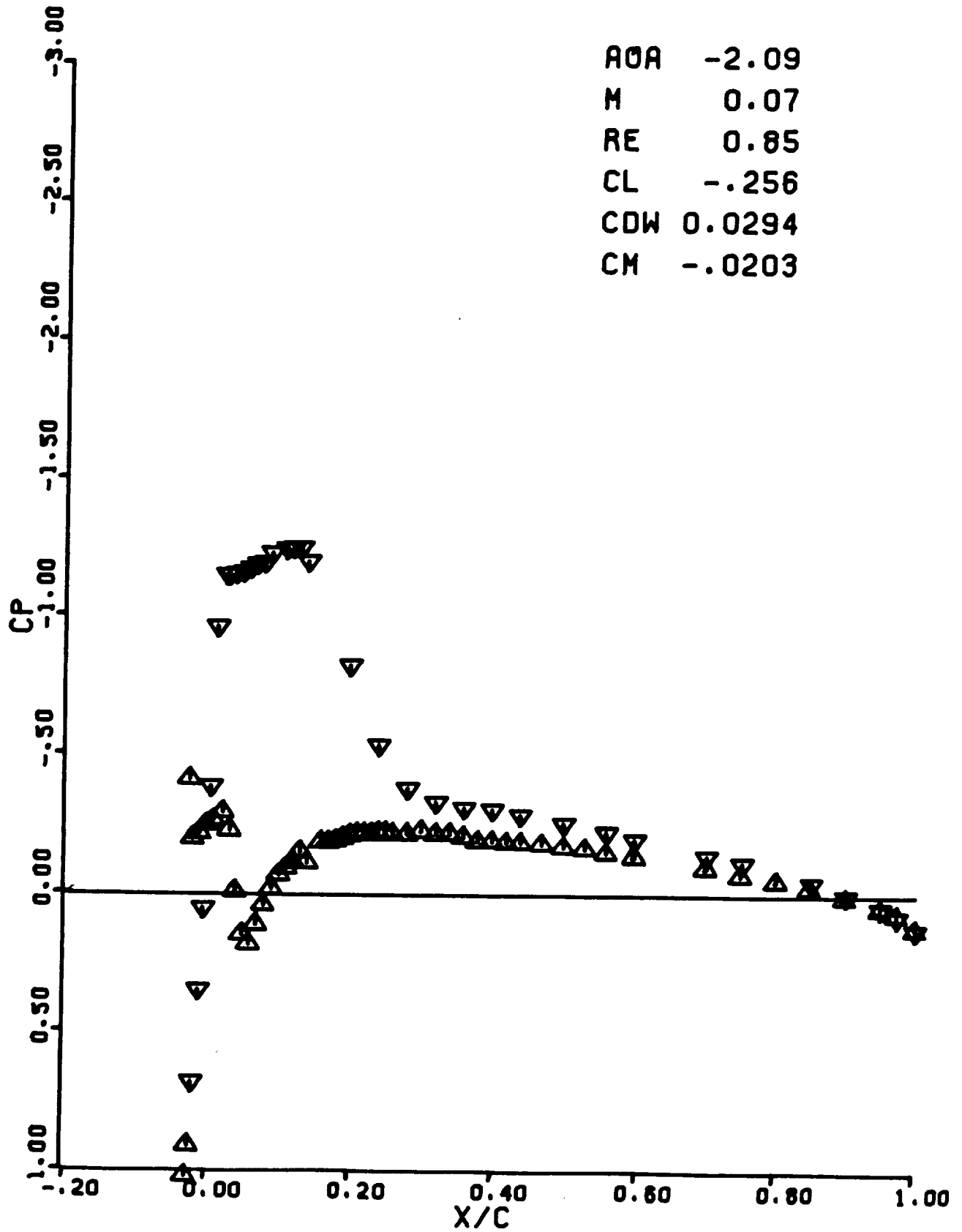
RUN 0483

AOA 7.14  
M 0.07  
RE 0.84  
CL 0.586  
CDW 0.0846  
CM -.0192



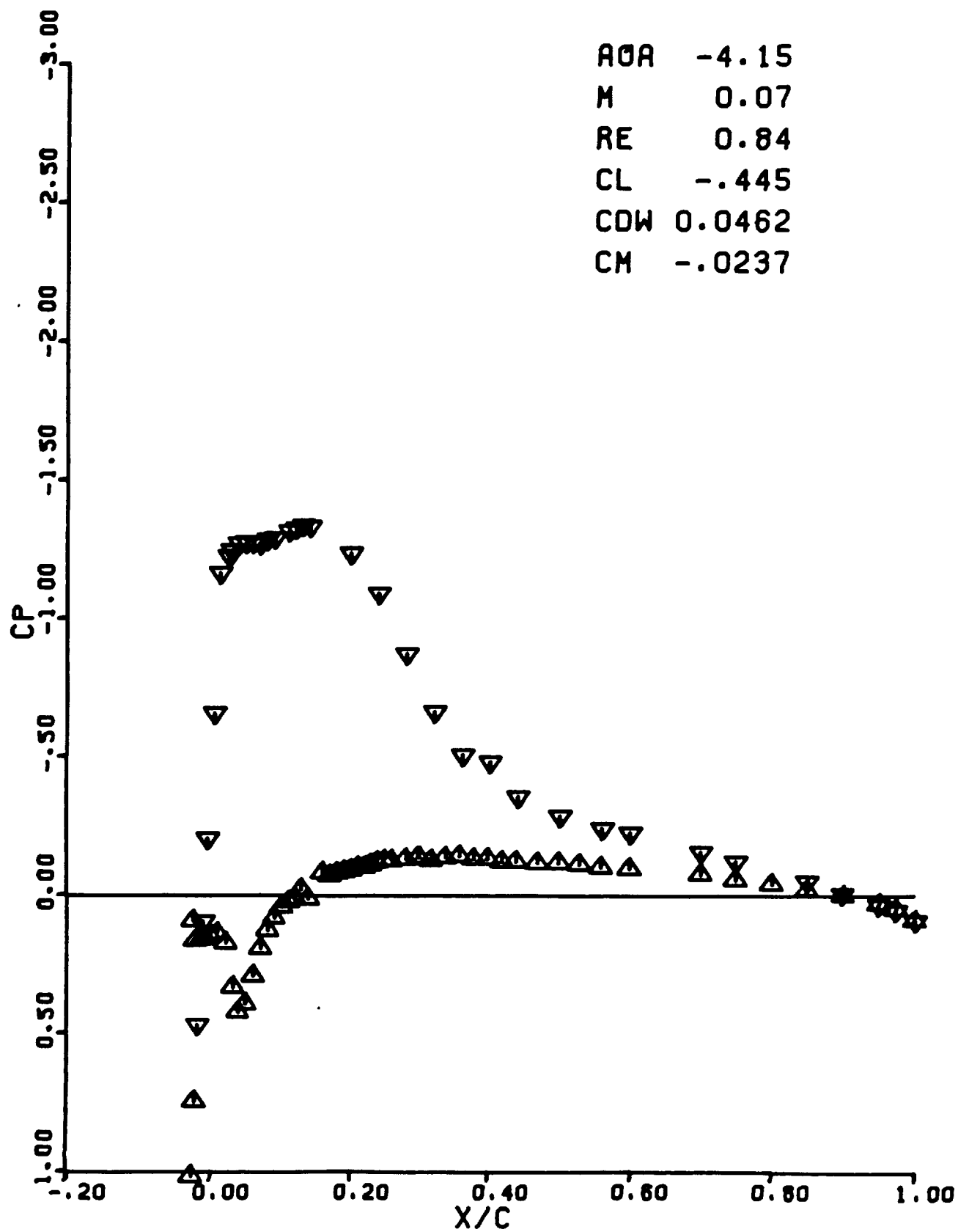
RUN 0484

AOA -2.09  
M 0.07  
RE 0.85  
CL -.256  
CDW 0.0294  
CM -.0203



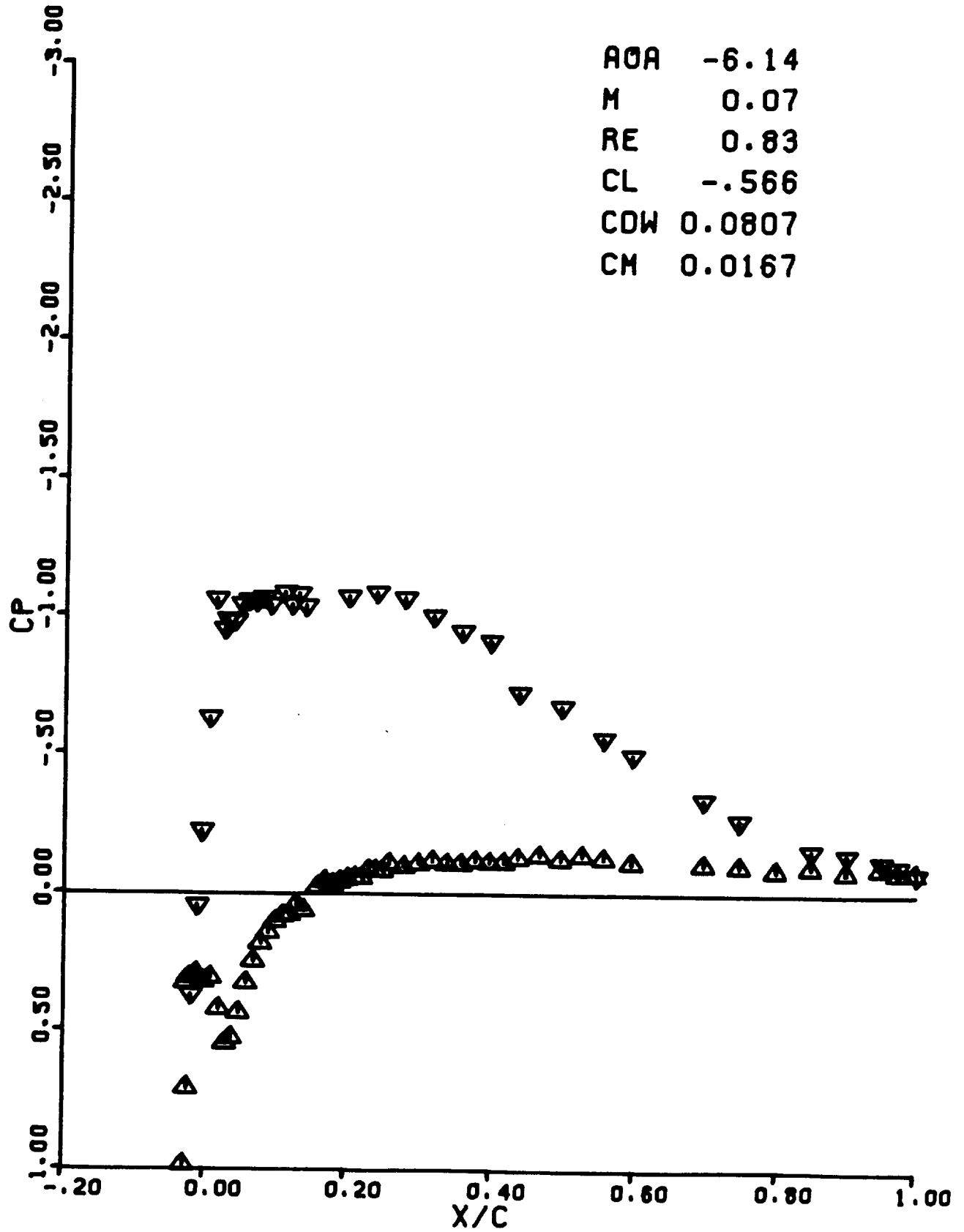
RUN 0485

AOA -4.15  
M 0.07  
RE 0.84  
CL -.445  
CDW 0.0462  
CM -.0237



RUN 0486

AOA -6.14  
M 0.07  
RE 0.83  
CL -.566  
CDW 0.0807  
CM 0.0167



RUN 0487

AOA -8.07

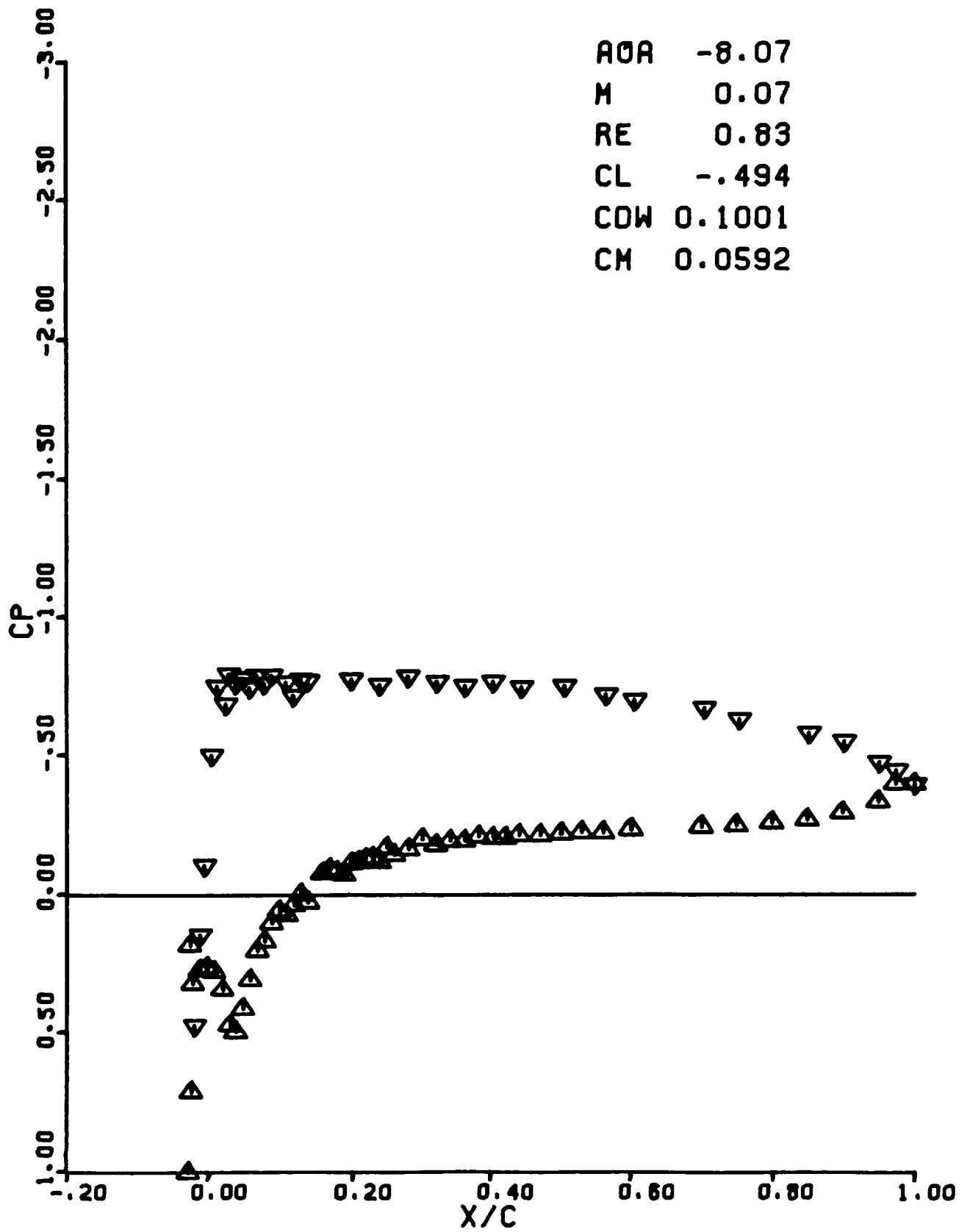
M 0.07

RE 0.83

CL -.494

CDW 0.1001

CM 0.0592



RUN 0488

AOA -7.10

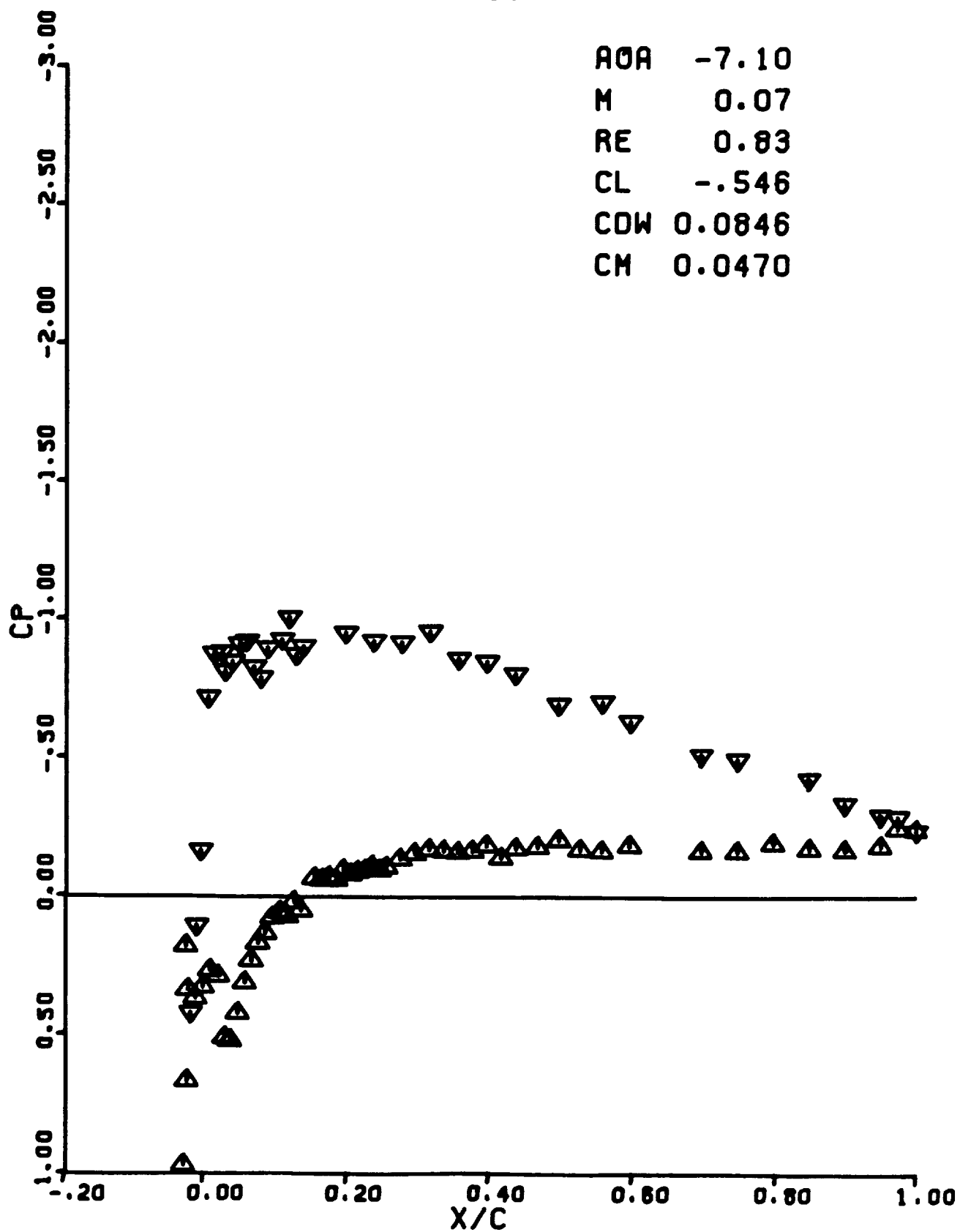
M 0.07

RE 0.83

CL -.546

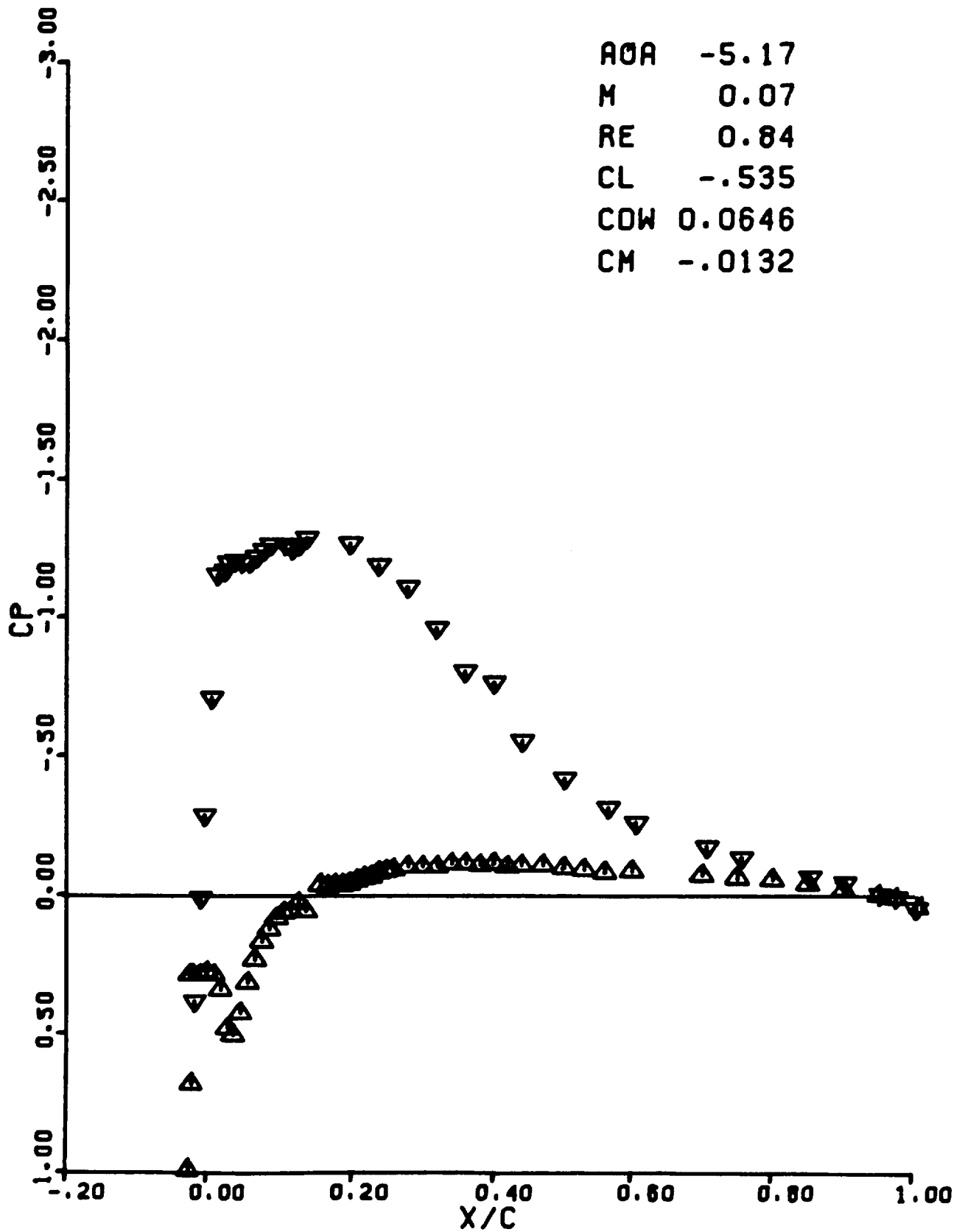
CDW 0.0846

CM 0.0470



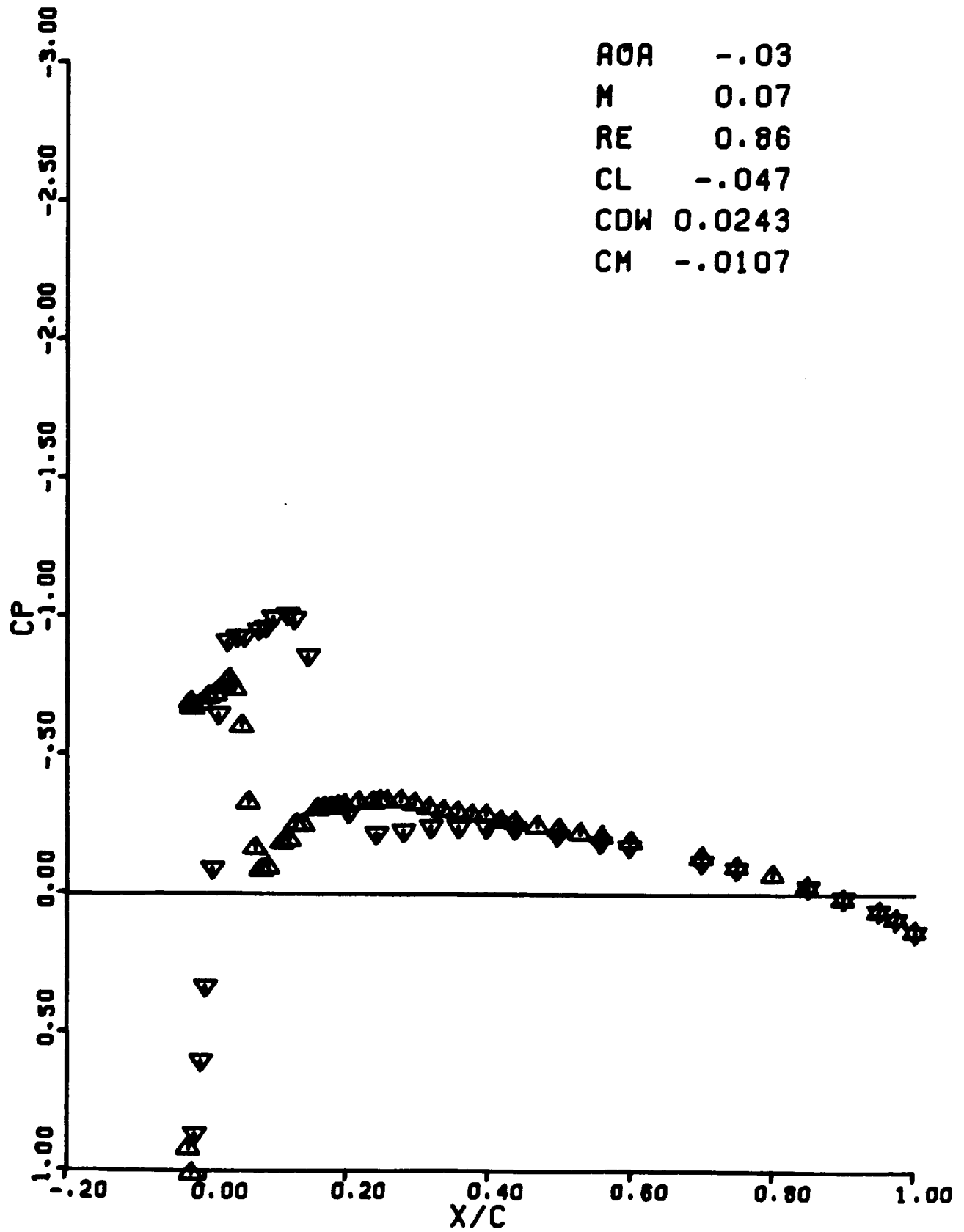
RUN 0489

AOA -5.17  
M 0.07  
RE 0.84  
CL -.535  
CDW 0.0646  
CM -.0132



RUN 0490

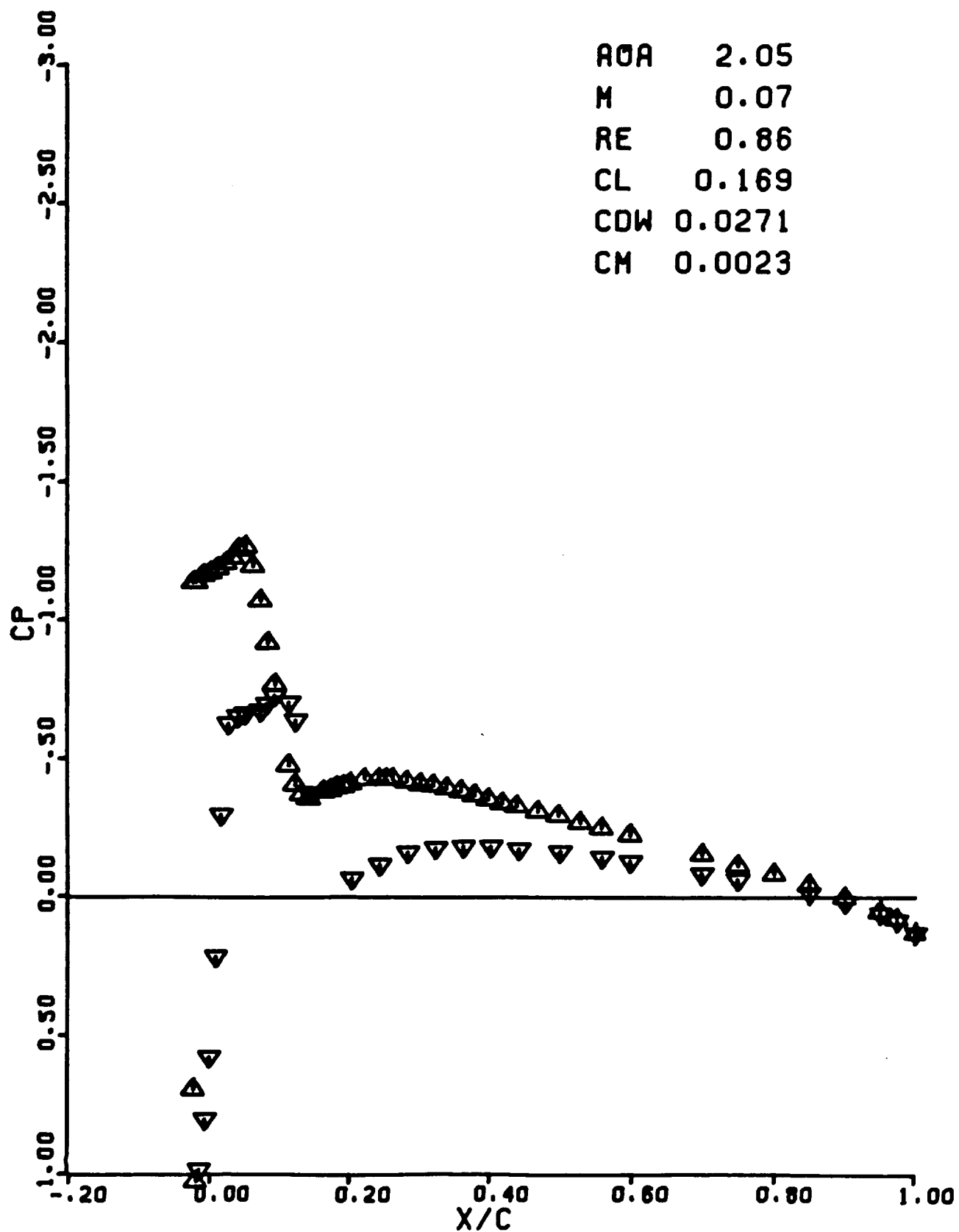
AOA -.03  
M 0.07  
RE 0.86  
CL -.047  
CDW 0.0243  
CM -.0107





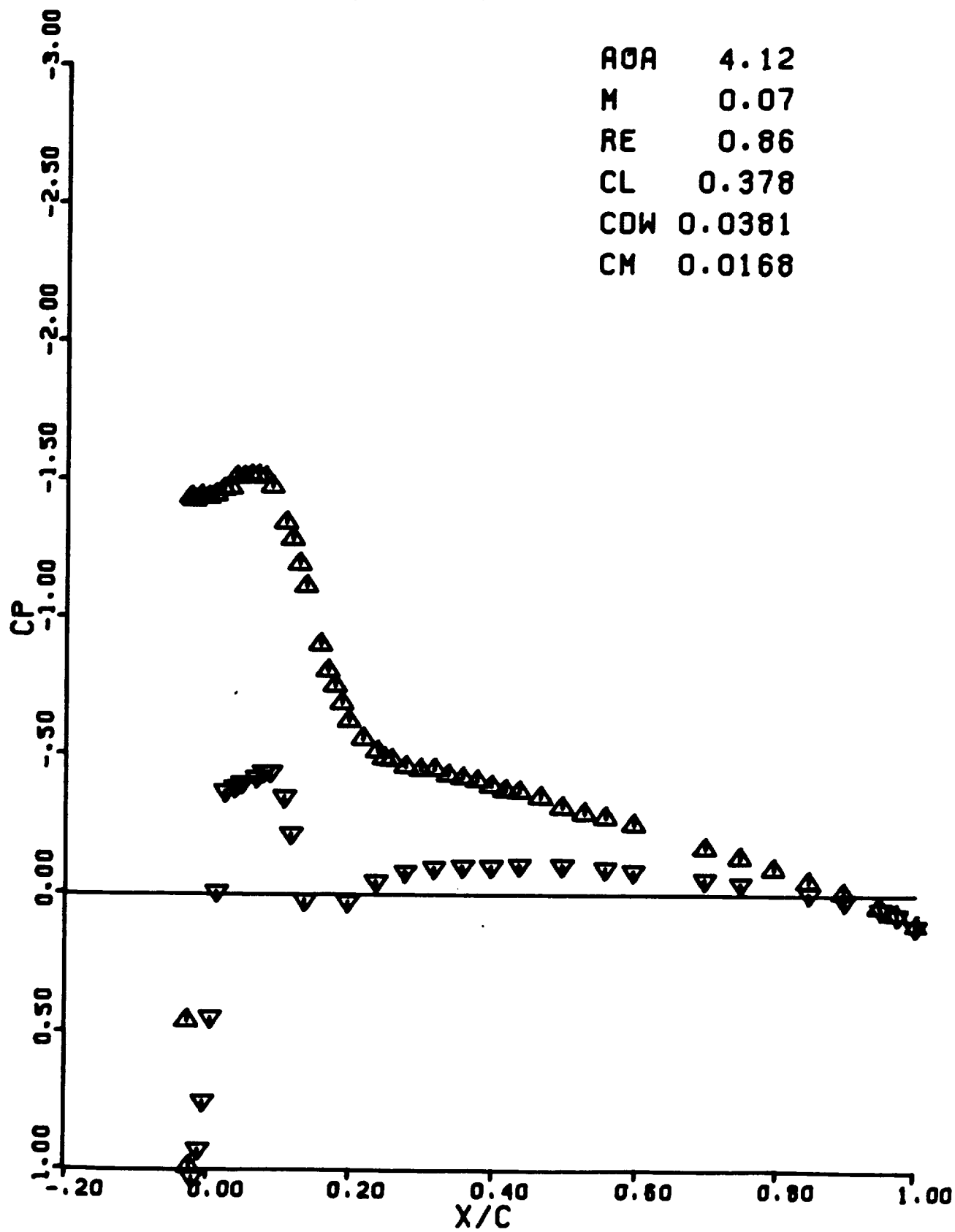
RUN 0491

AOA 2.05  
M 0.07  
RE 0.86  
CL 0.169  
CDW 0.0271  
CM 0.0023

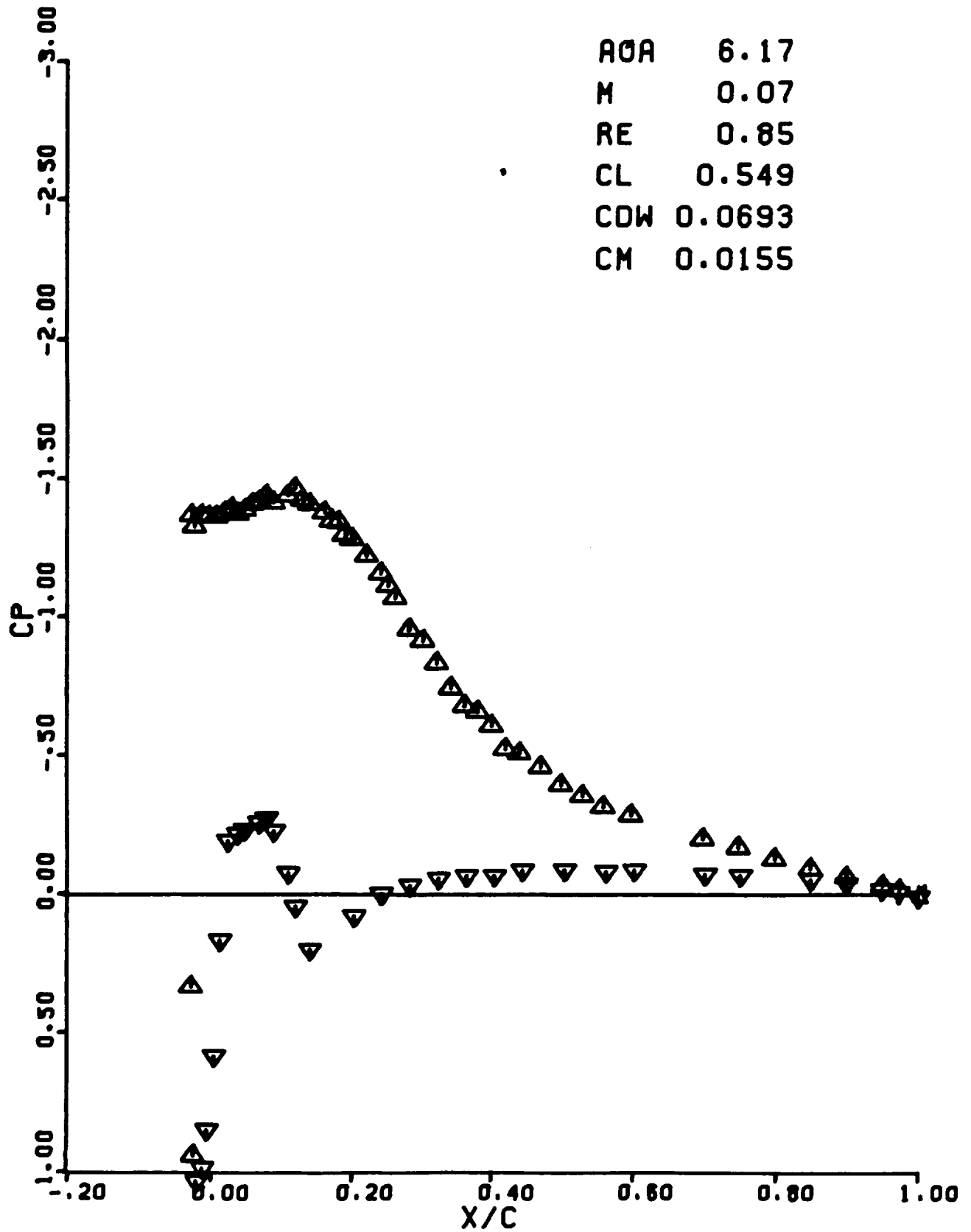


RUN 0492

AOA 4.12  
M 0.07  
RE 0.86  
CL 0.378  
CDW 0.0381  
CM 0.0168

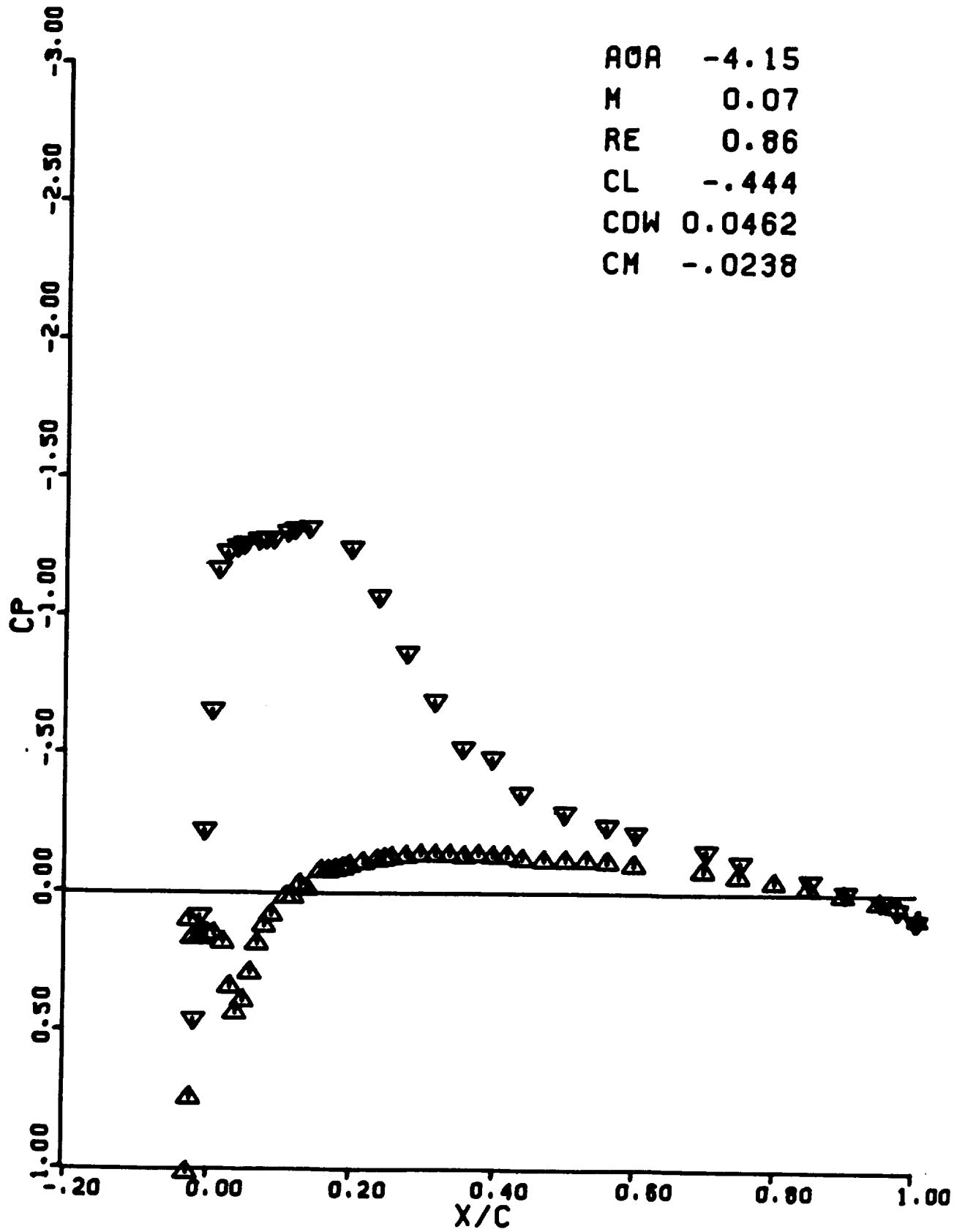


RUN 0493



RUN 0494

AOA -4.15  
M 0.07  
RE 0.86  
CL -.444  
CDW 0.0462  
CM -.0238



RUN 0495

AOA -2.09

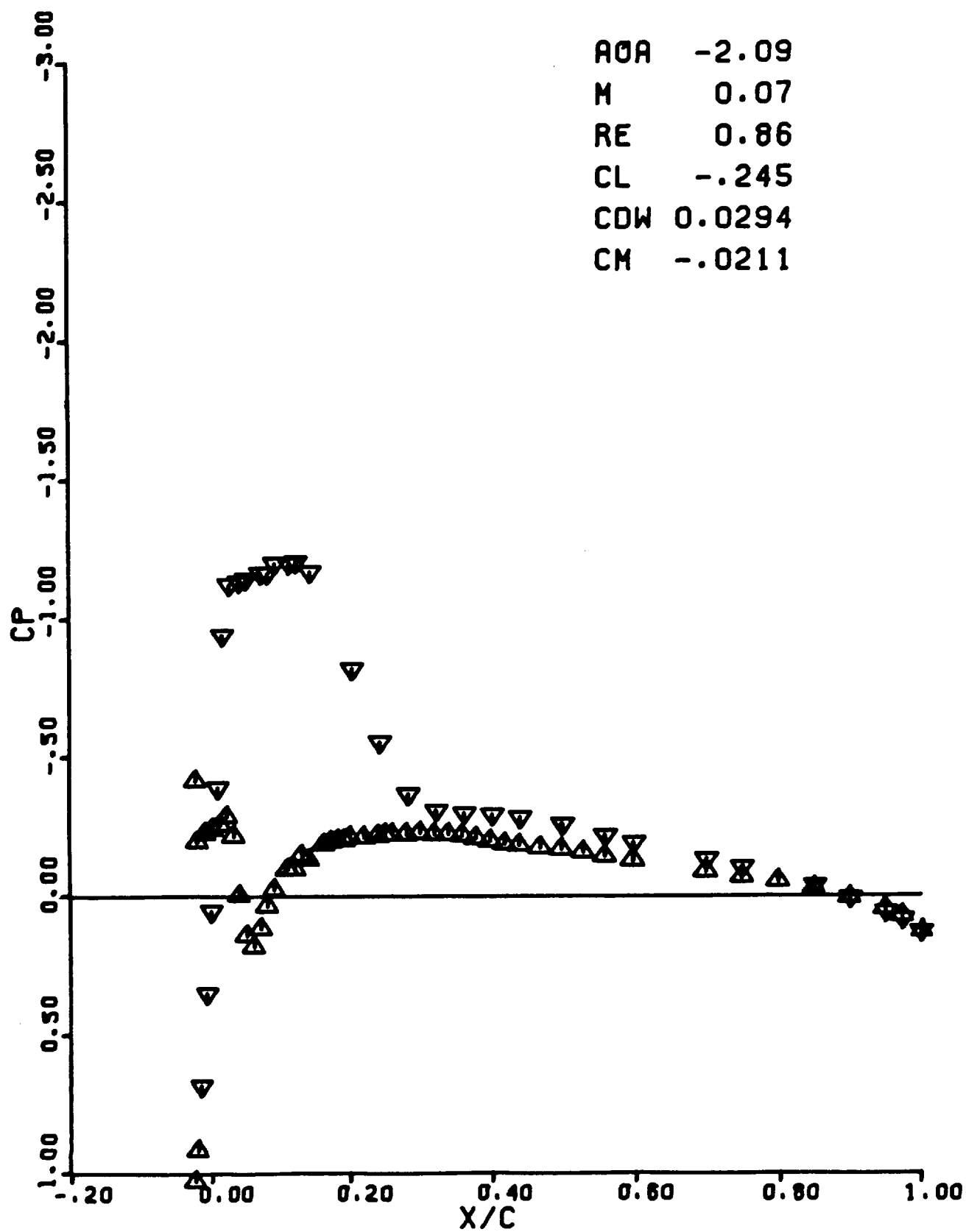
M 0.07

RE 0.86

CL -.245

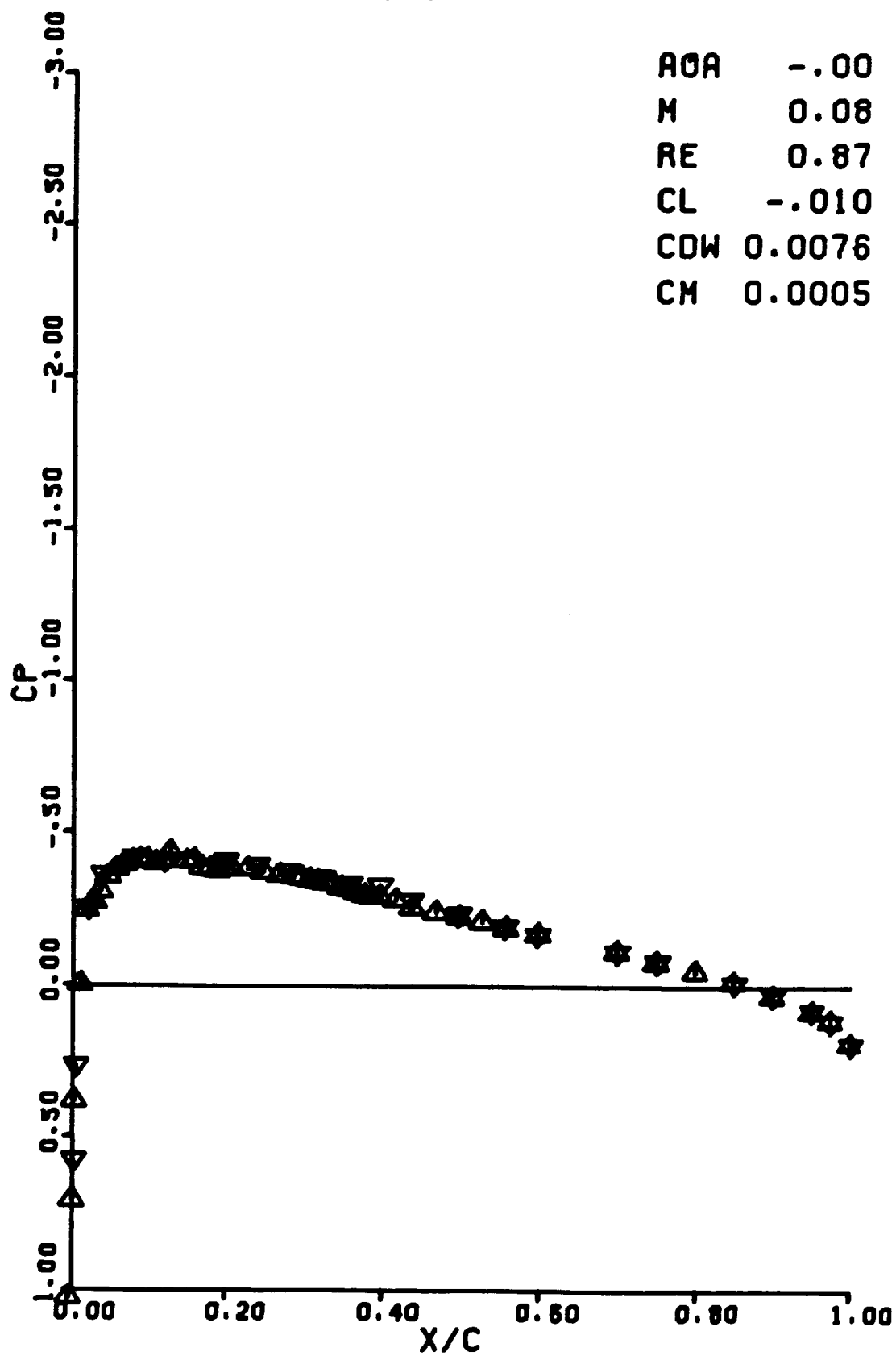
CDW 0.0294

CM -.0211



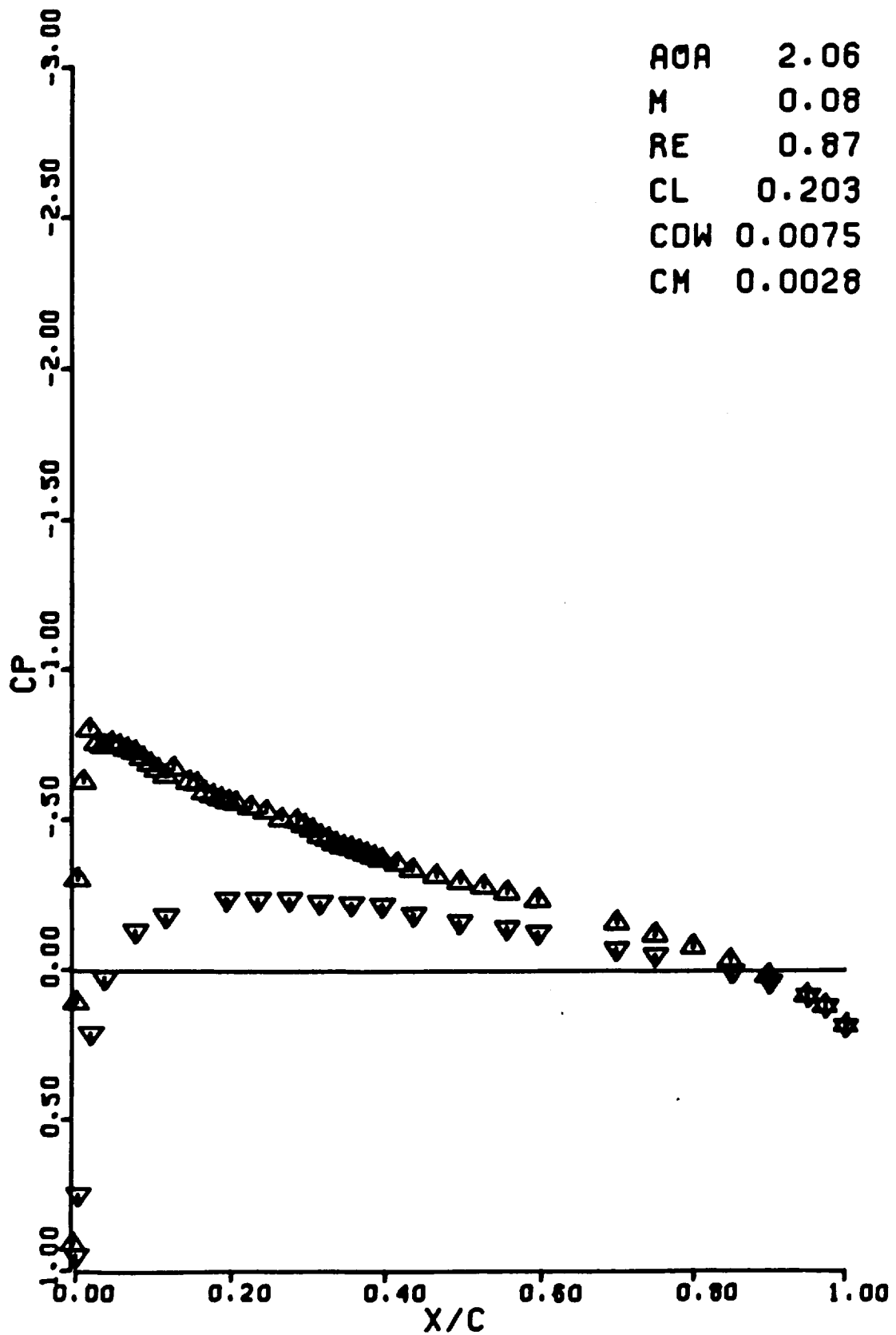
RUN 0500

AOA -.00  
M 0.08  
RE 0.87  
CL -.010  
CDW 0.0076  
CM 0.0005



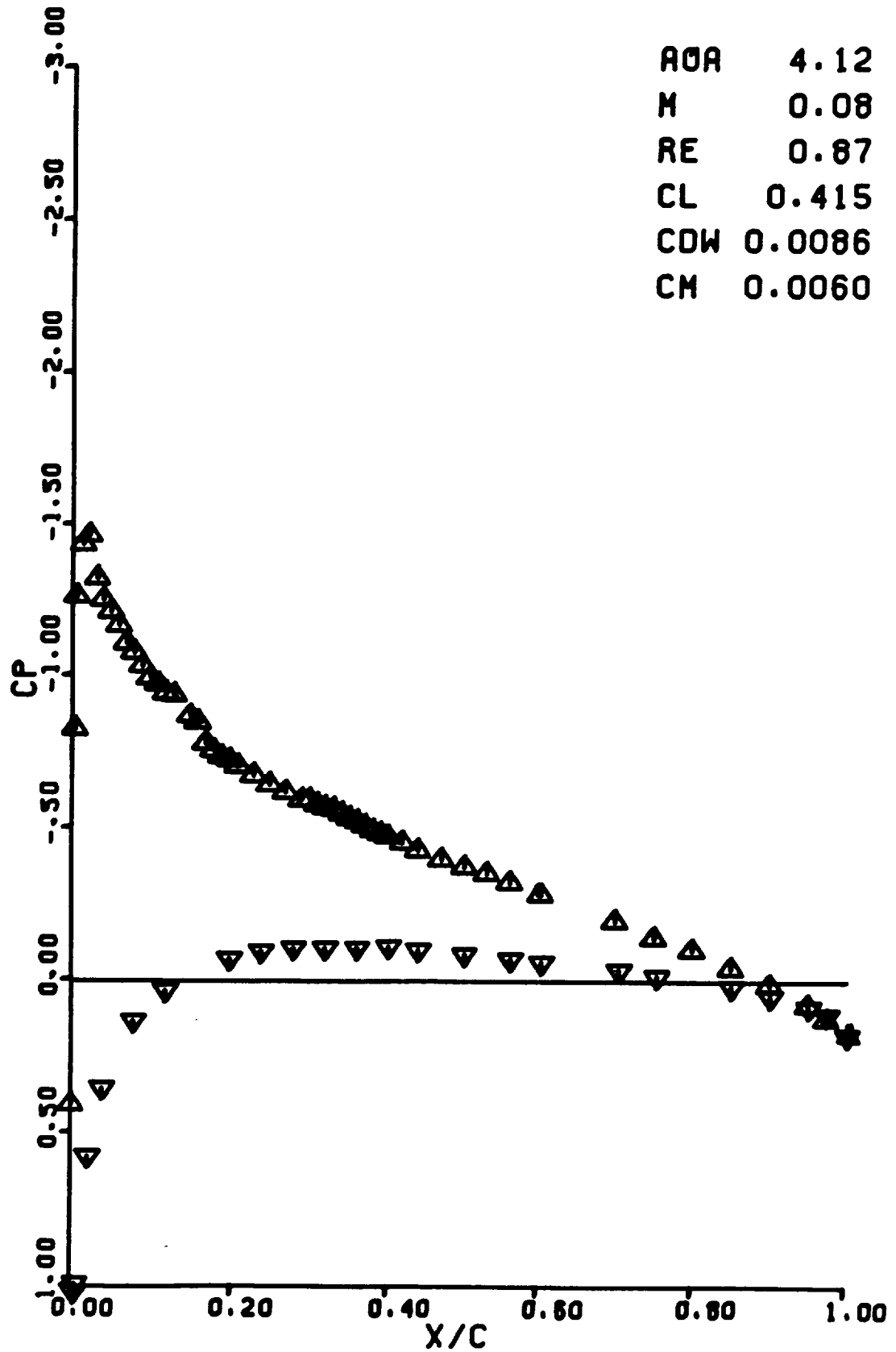
RUN 0501

AOA 2.06  
M 0.08  
RE 0.87  
CL 0.203  
CDW 0.0075  
CM 0.0028



RUN 0502

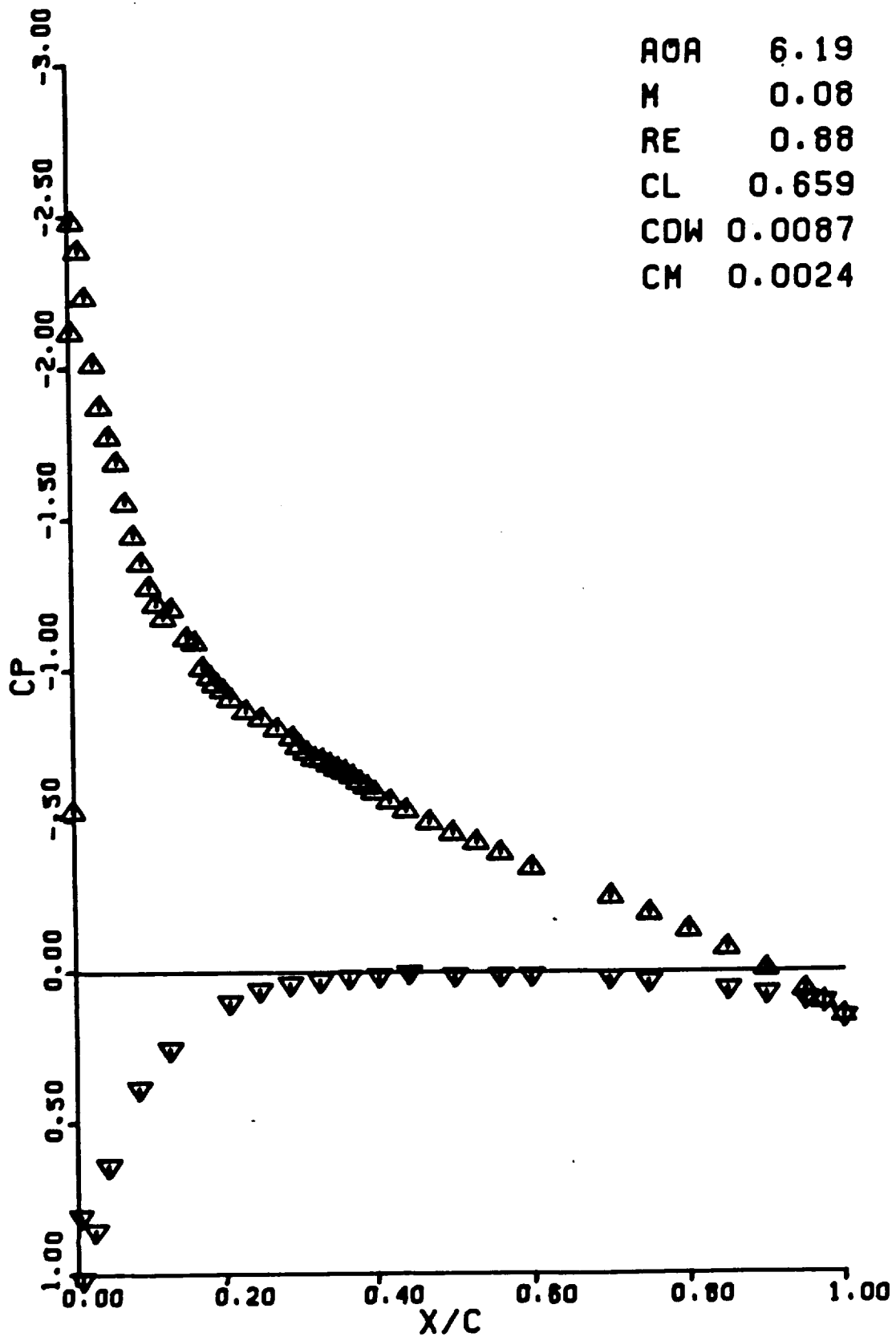
AOA 4.12  
M 0.08  
RE 0.87  
CL 0.415  
CDW 0.0086  
CM 0.0060





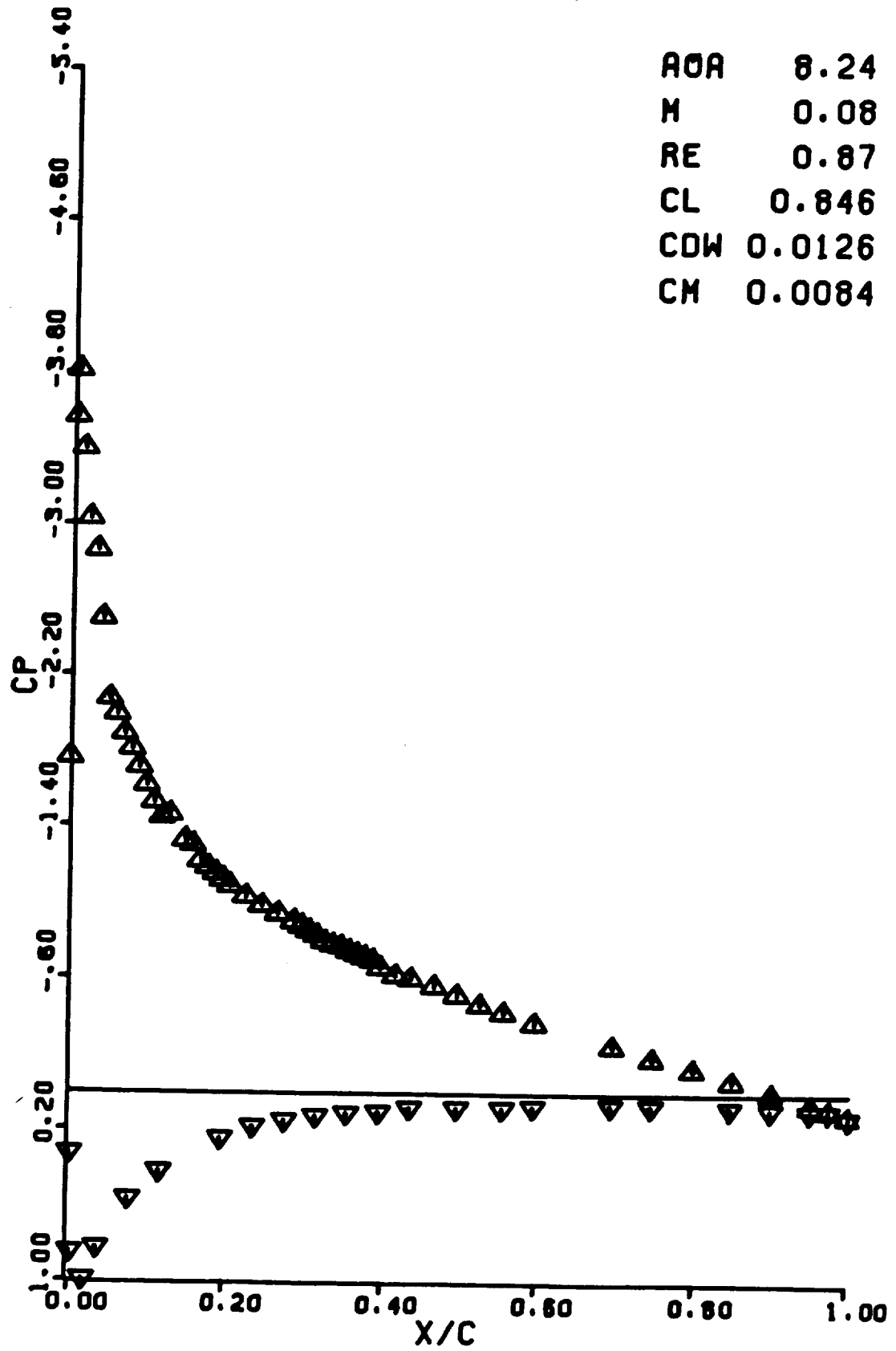
RUN 0503

AOA 6.19  
M 0.08  
RE 0.88  
CL 0.659  
CDW 0.0087  
CM 0.0024



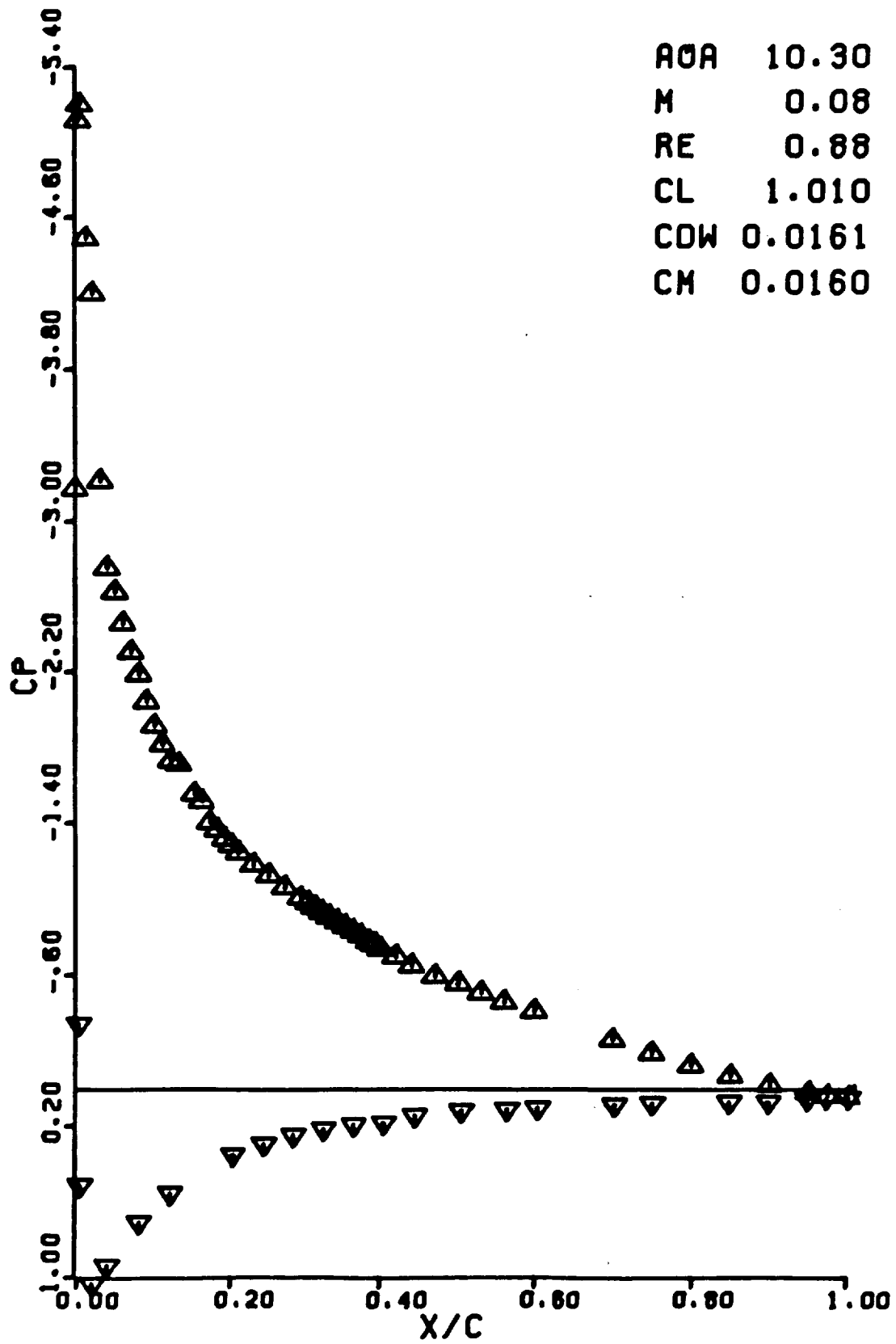
RUN 0504

AOA 8.24  
M 0.08  
RE 0.87  
CL 0.846  
CDW 0.0126  
CM 0.0084



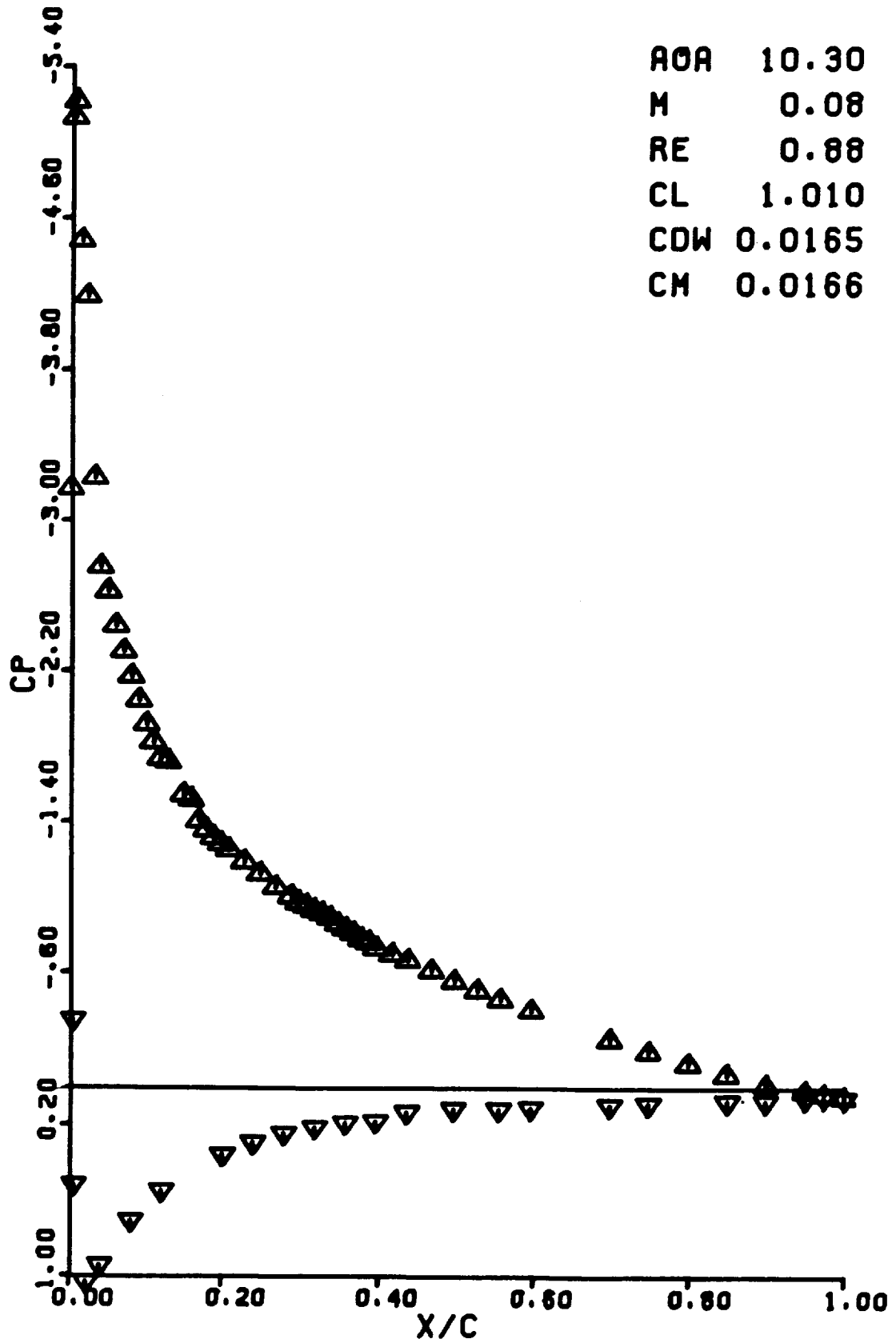
RUN 0505

AOA 10.30  
M 0.08  
RE 0.88  
CL 1.010  
CDW 0.0161  
CM 0.0160



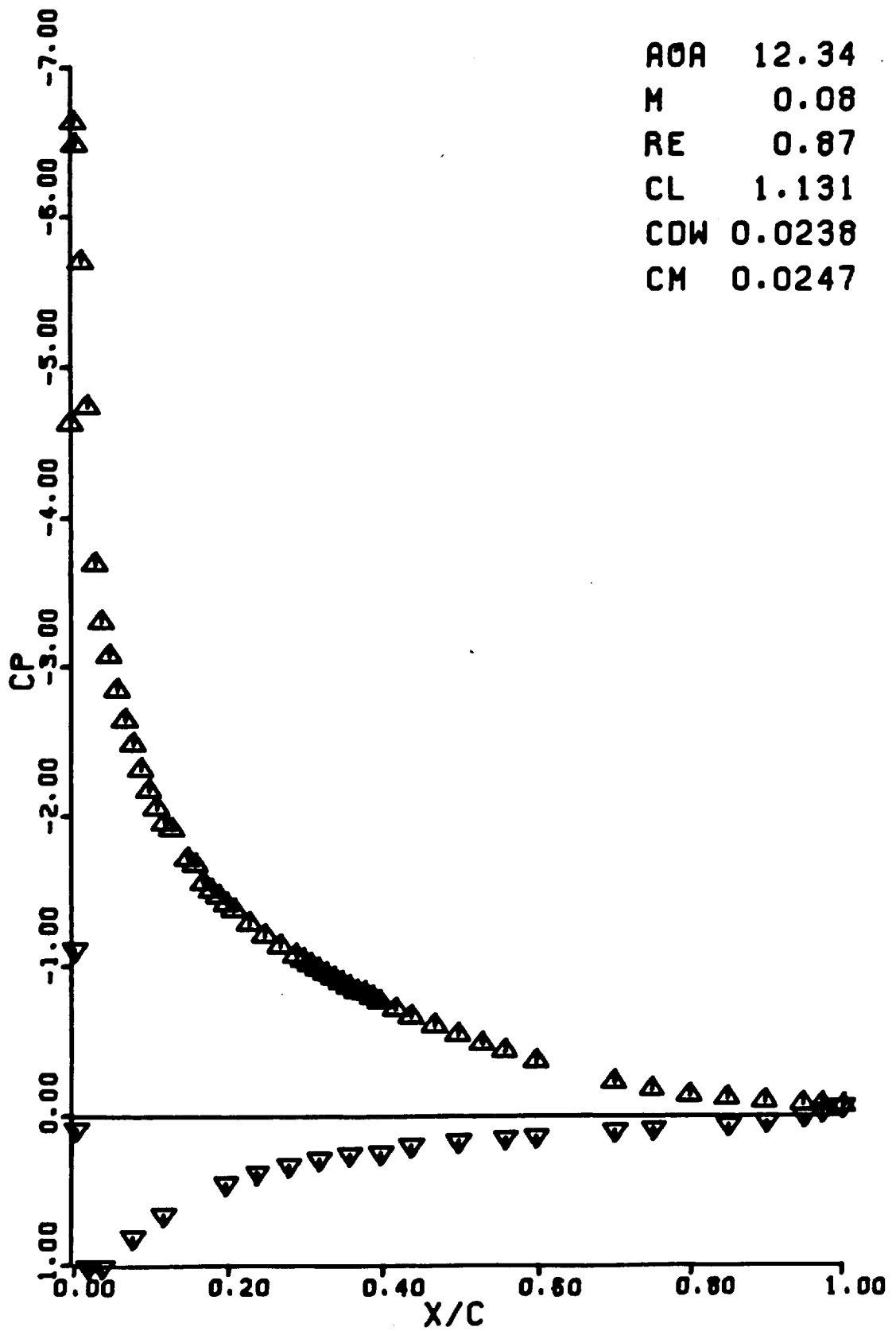
RUN 0506

AOA 10.30  
M 0.08  
RE 0.88  
CL 1.010  
CDW 0.0165  
CM 0.0166



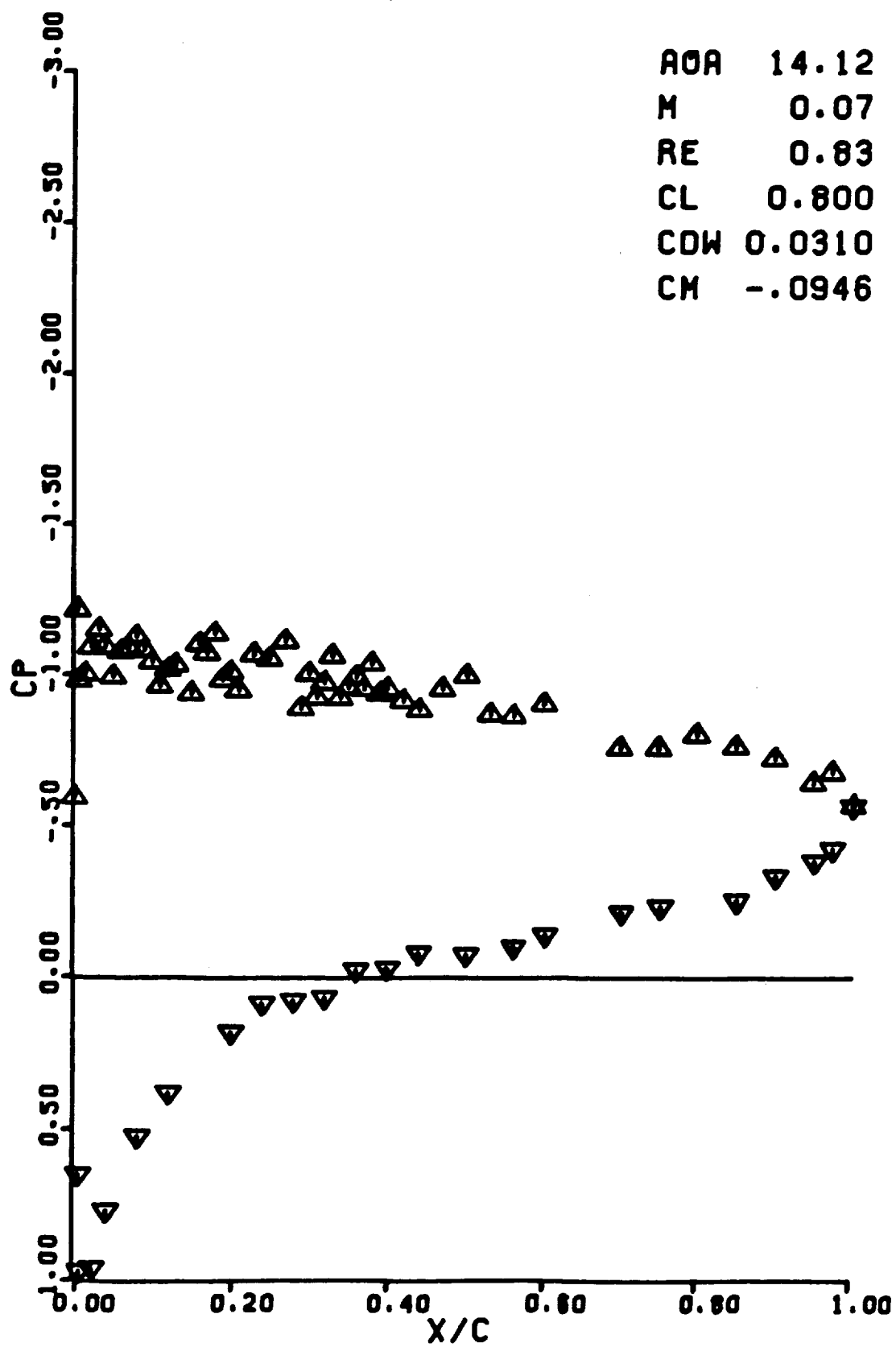
RUN 0507

AOA 12.34  
M 0.08  
RE 0.87  
CL 1.131  
CDW 0.0238  
CM 0.0247



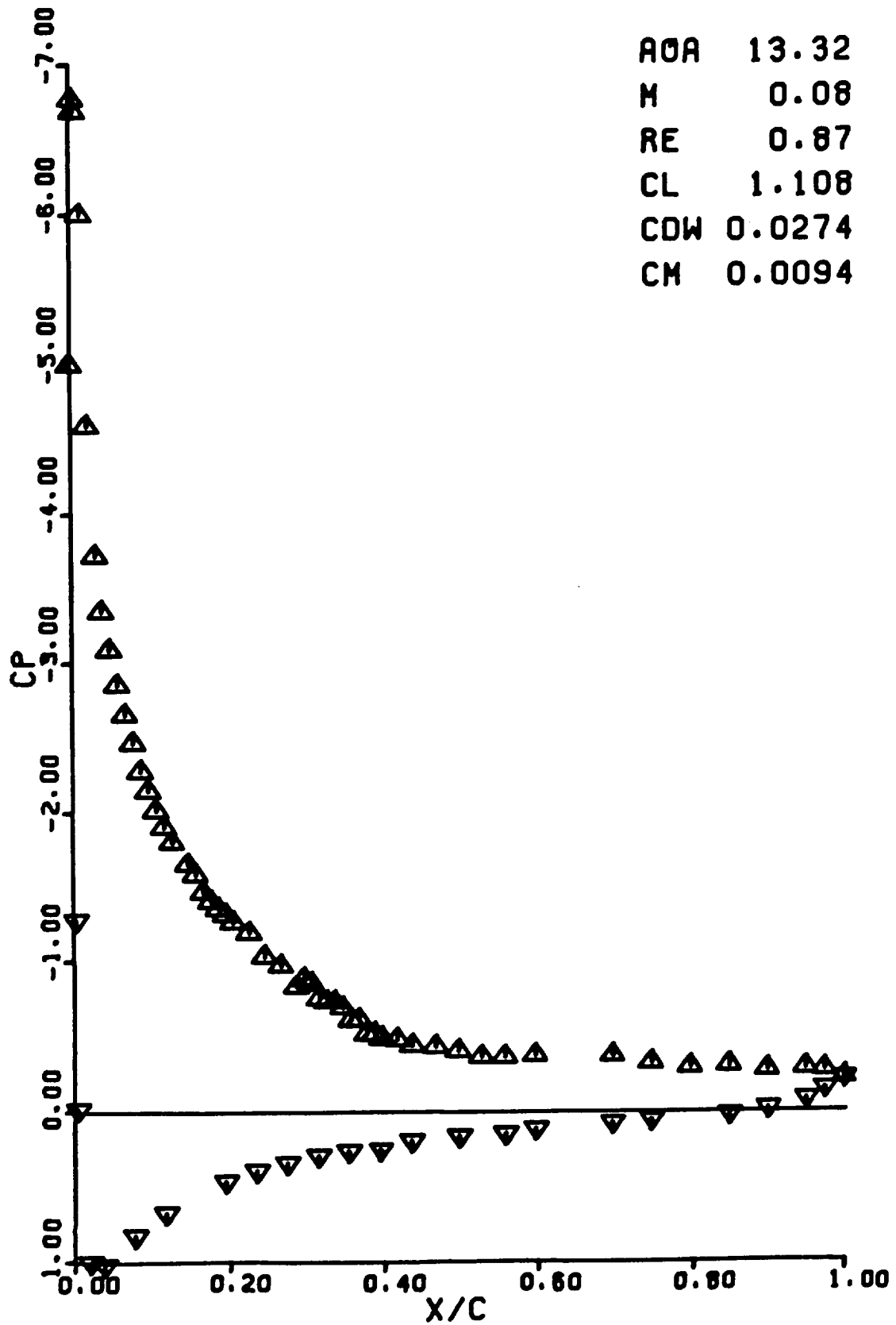
RUN 0508

AOA 14.12  
M 0.07  
RE 0.83  
CL 0.800  
CDW 0.0310  
CM -.0946



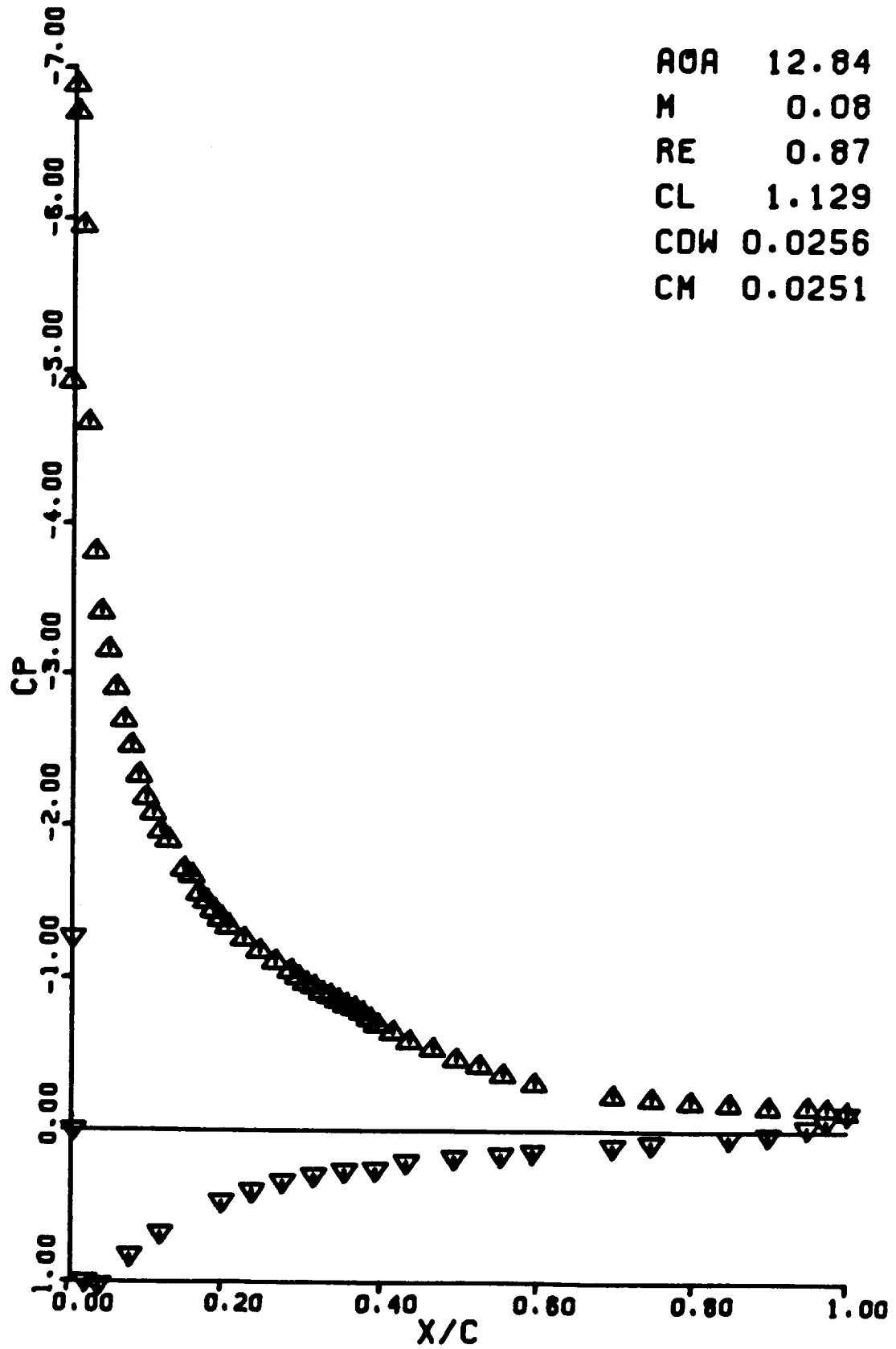
RUN 0509

AOA 13.32  
M 0.08  
RE 0.87  
CL 1.108  
CDW 0.0274  
CM 0.0094



RUN 0510

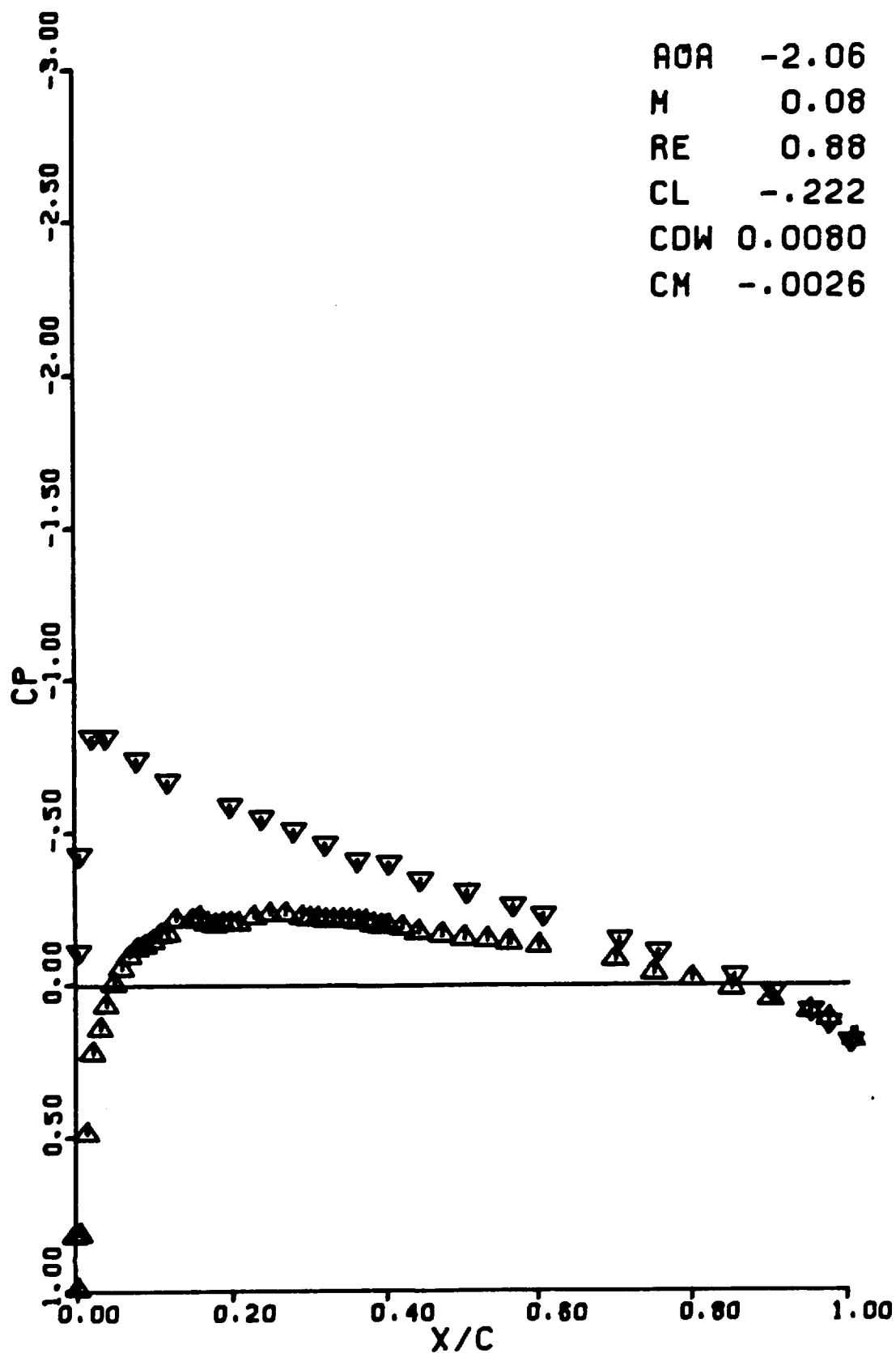
AOA 12.84  
M 0.08  
RE 0.87  
CL 1.129  
CDW 0.0256  
CM 0.0251





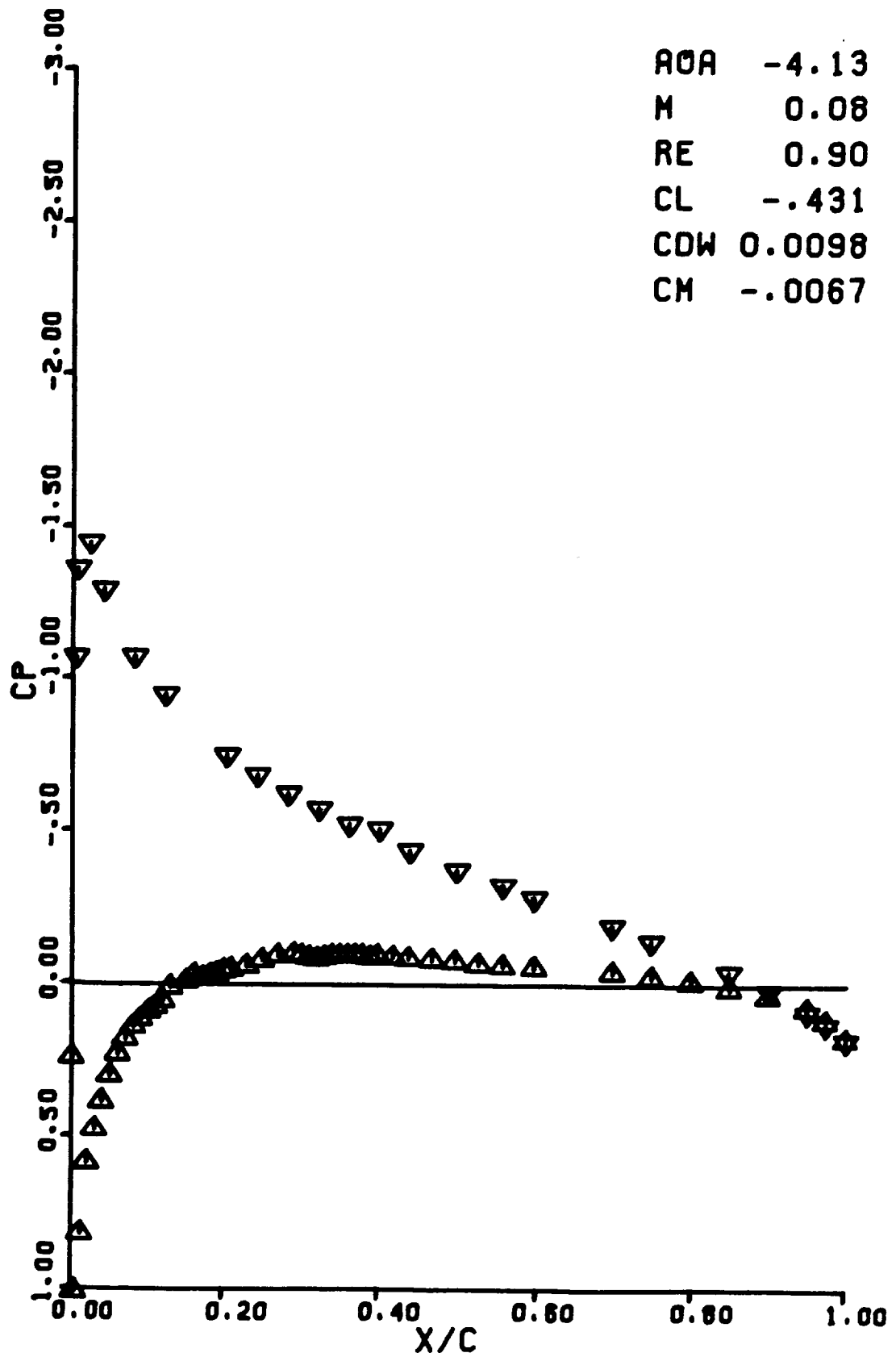
RUN 0511

AOA -2.06  
M 0.08  
RE 0.88  
CL -.222  
CDW 0.0080  
CM -.0026



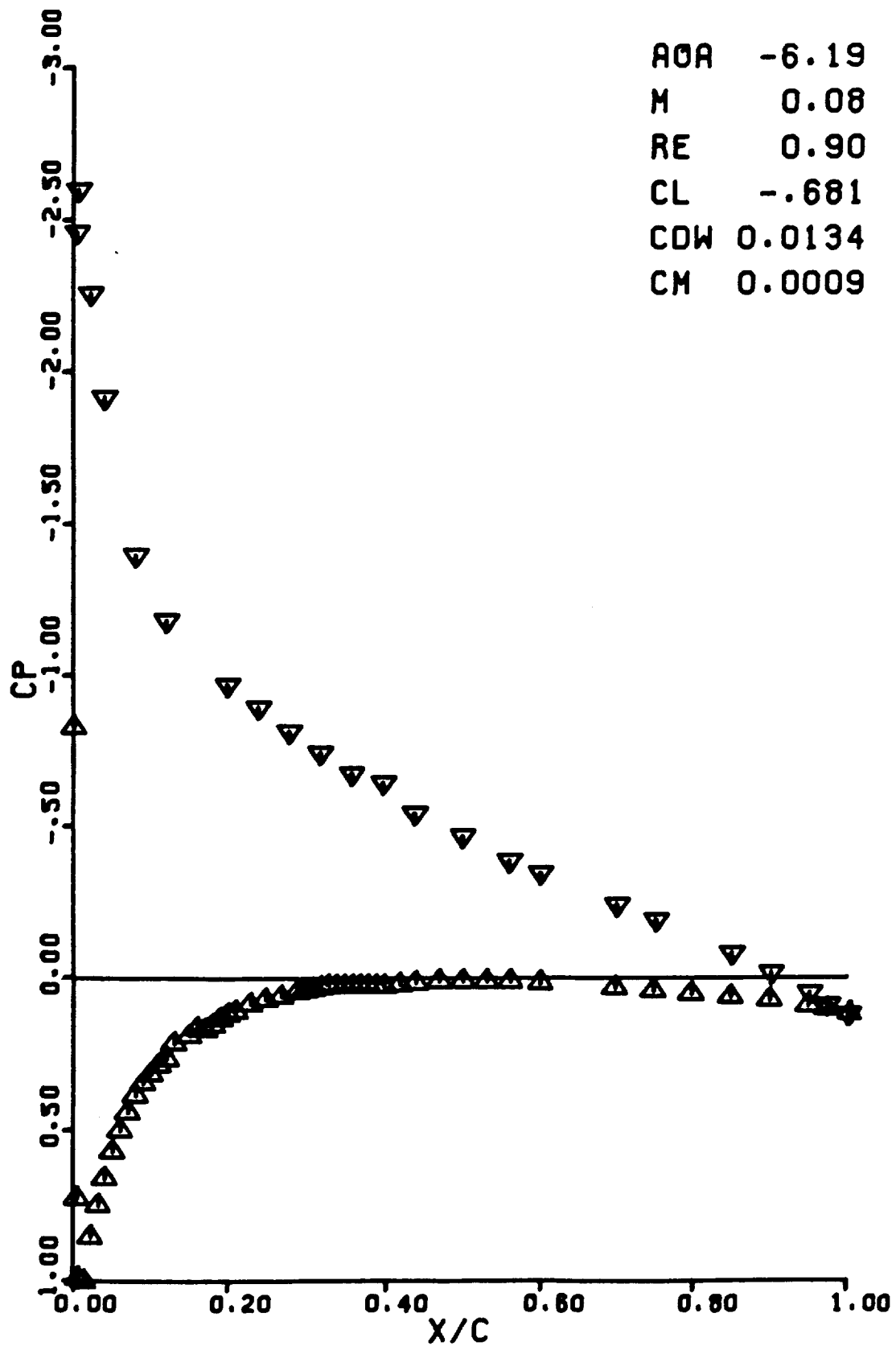
RUN 0512

AOA -4.13  
M 0.08  
RE 0.90  
CL -.431  
CDW 0.0098  
CM -.0067



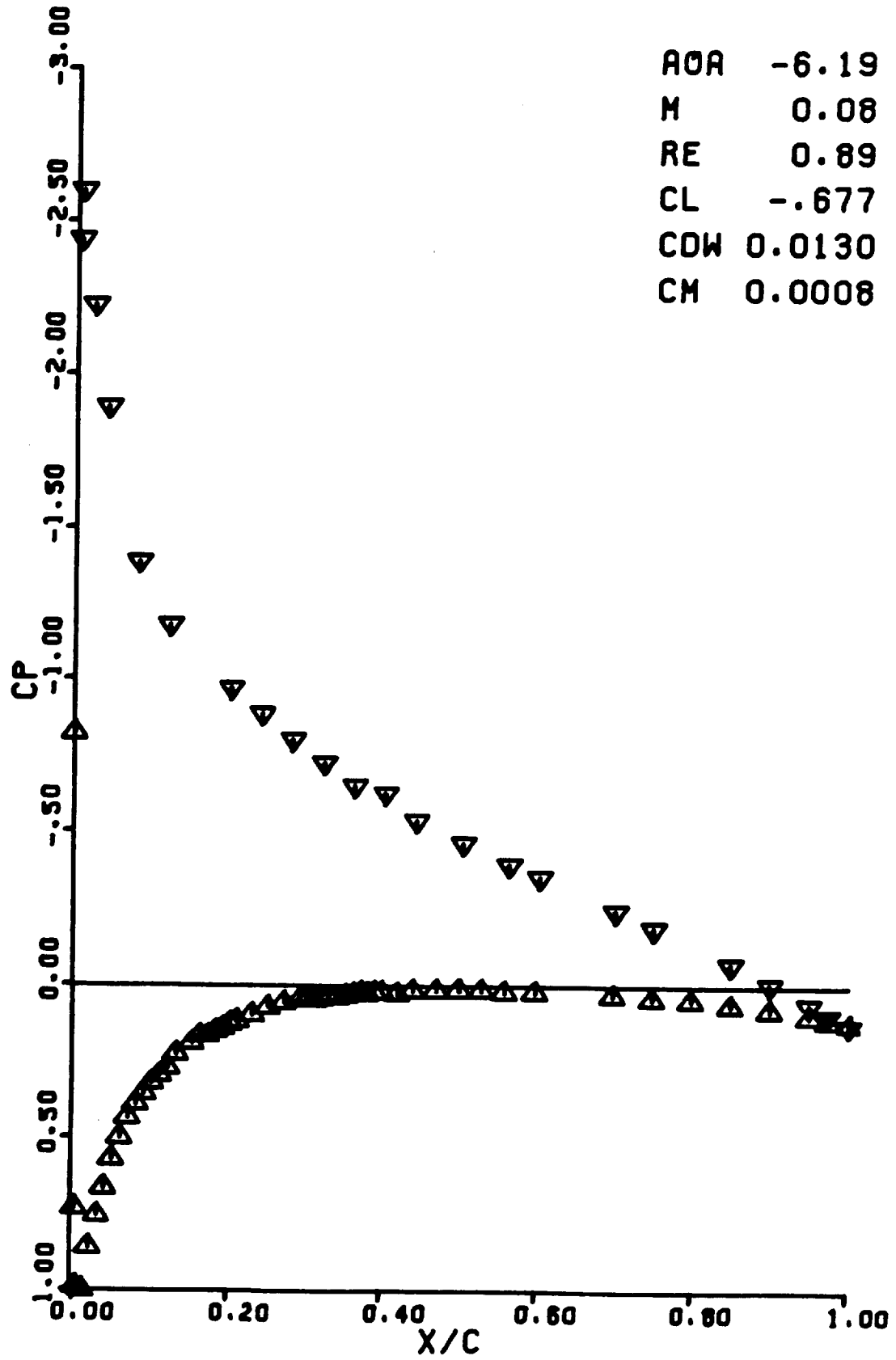
RUN 0513

AOA -6.19  
M 0.08  
RE 0.90  
CL -.681  
CDW 0.0134  
CM 0.0009



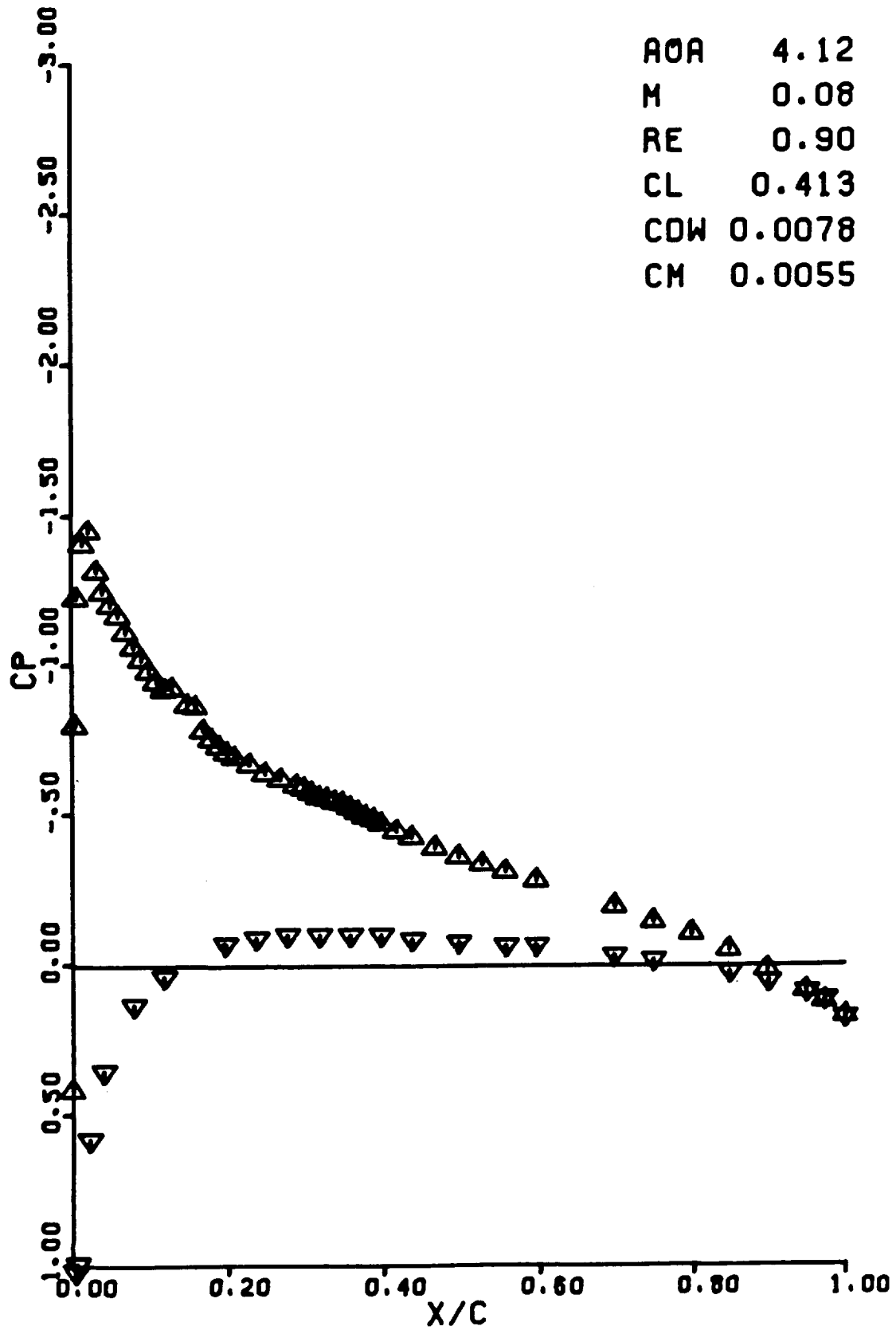
RUN 0514

AOA -6.19  
M 0.08  
RE 0.89  
CL -.677  
CDW 0.0130  
CM 0.0008



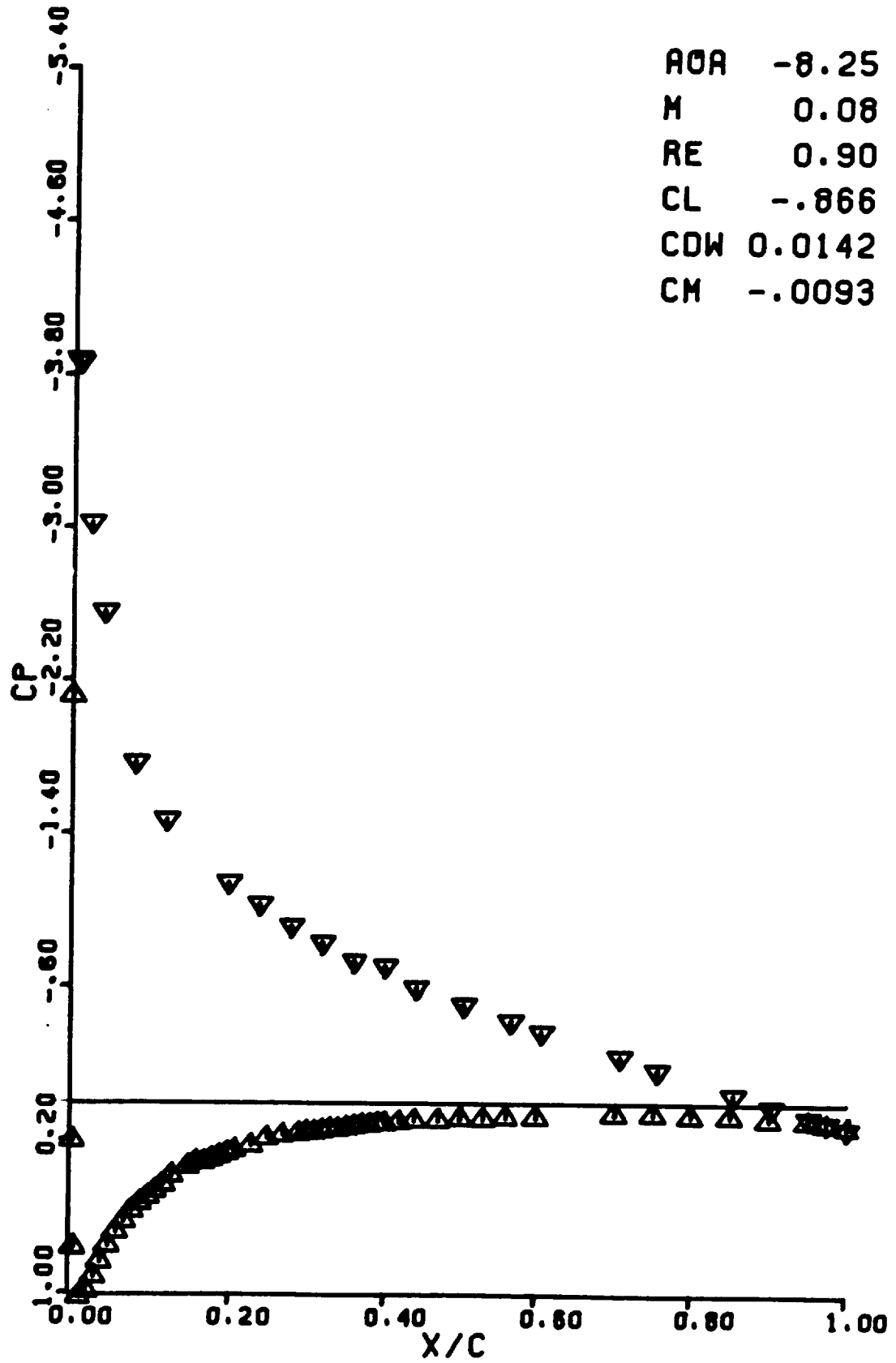
RUN 0515

AOA 4.12  
M 0.08  
RE 0.90  
CL 0.413  
CDW 0.0078  
CM 0.0055



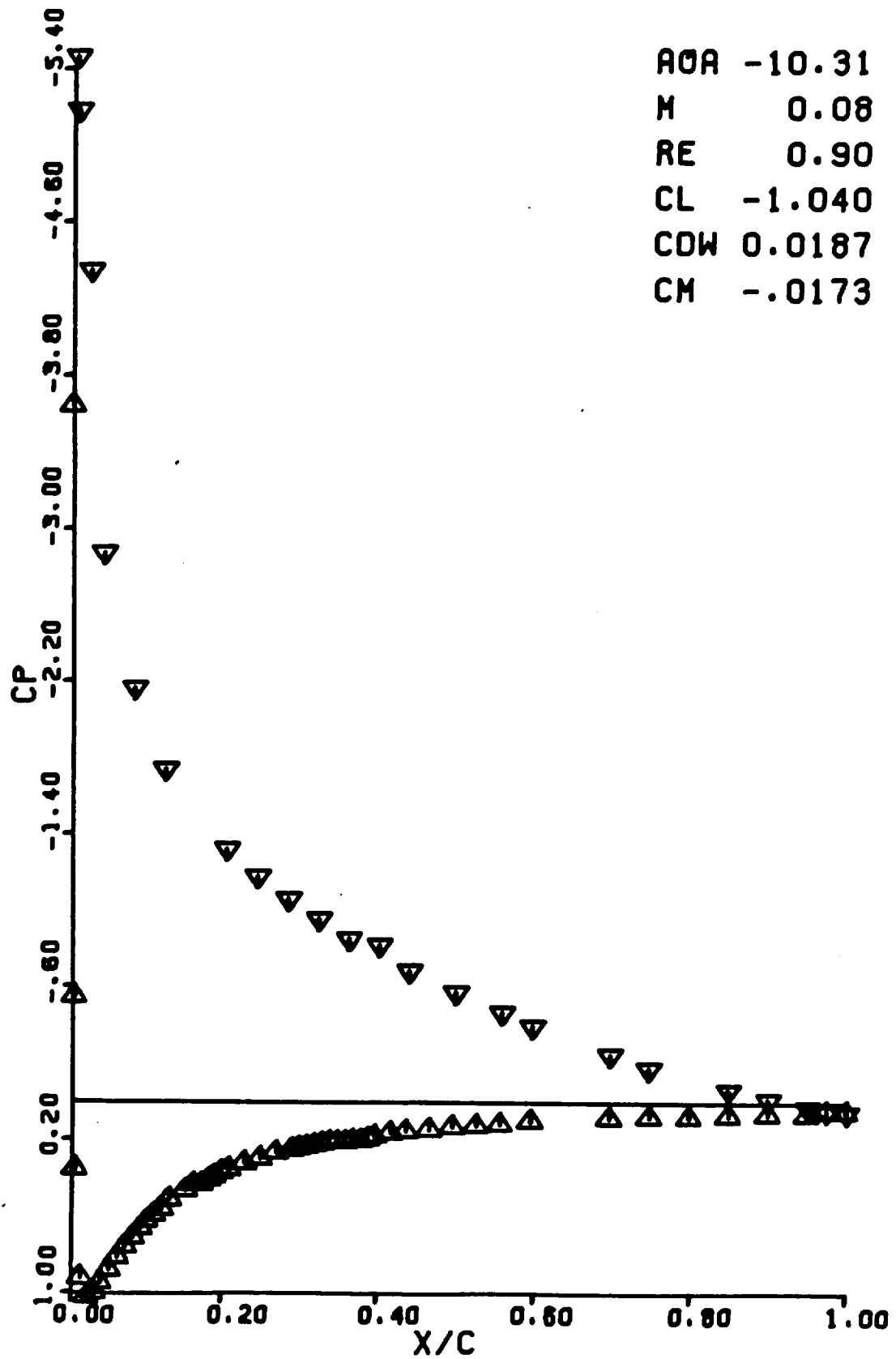
RUN 0516

AOA -8.25  
M 0.08  
RE 0.90  
CL -.866  
CDW 0.0142  
CM -.0093



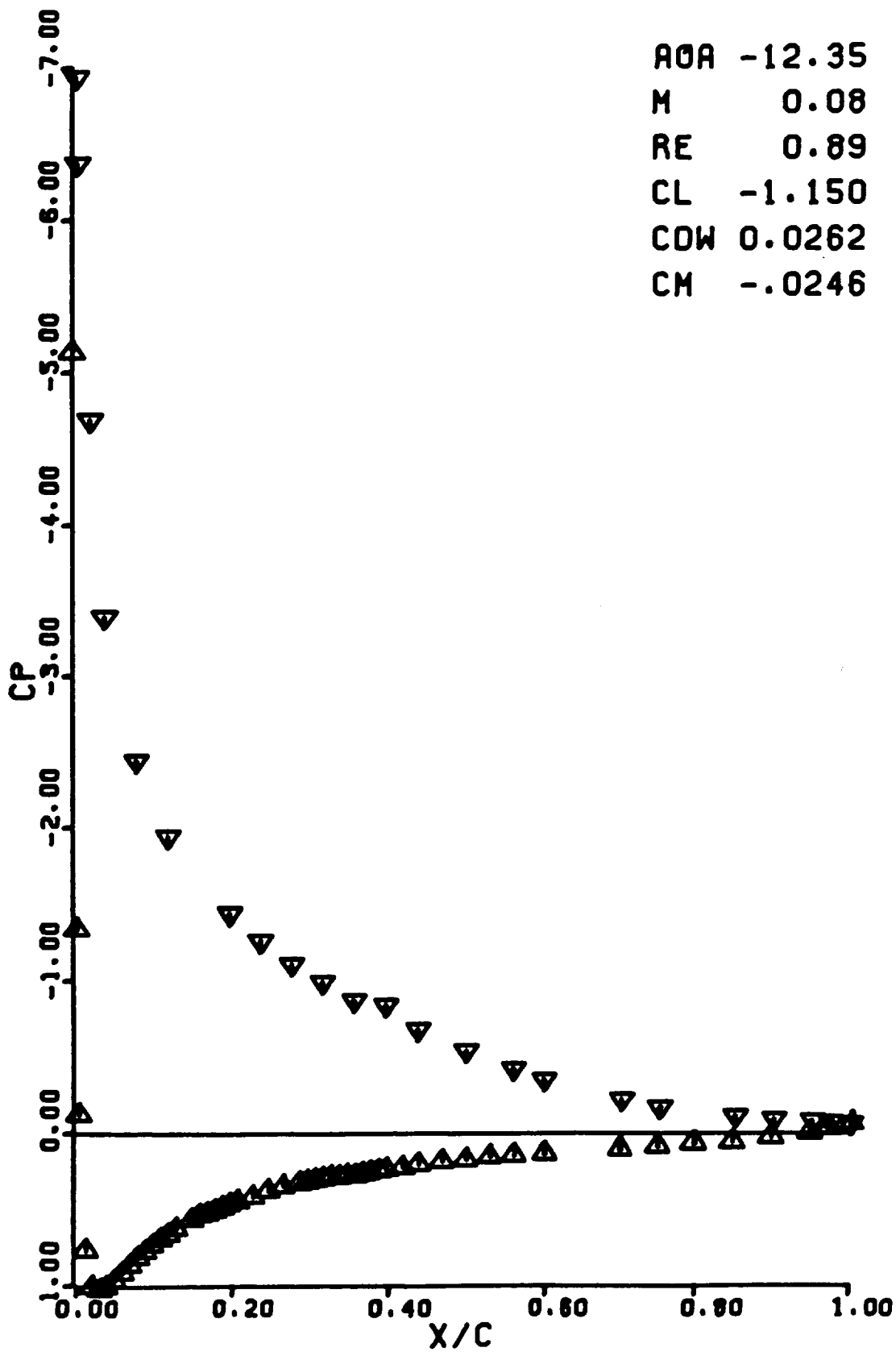
RUN 0517

AOA -10.31  
M 0.08  
RE 0.90  
CL -1.040  
CDW 0.0187  
CM -.0173



RUN 0518

AOA -12.35  
M 0.08  
RE 0.89  
CL -1.150  
CDW 0.0262  
CM -.0246





RUN 0519

AOA -14.12

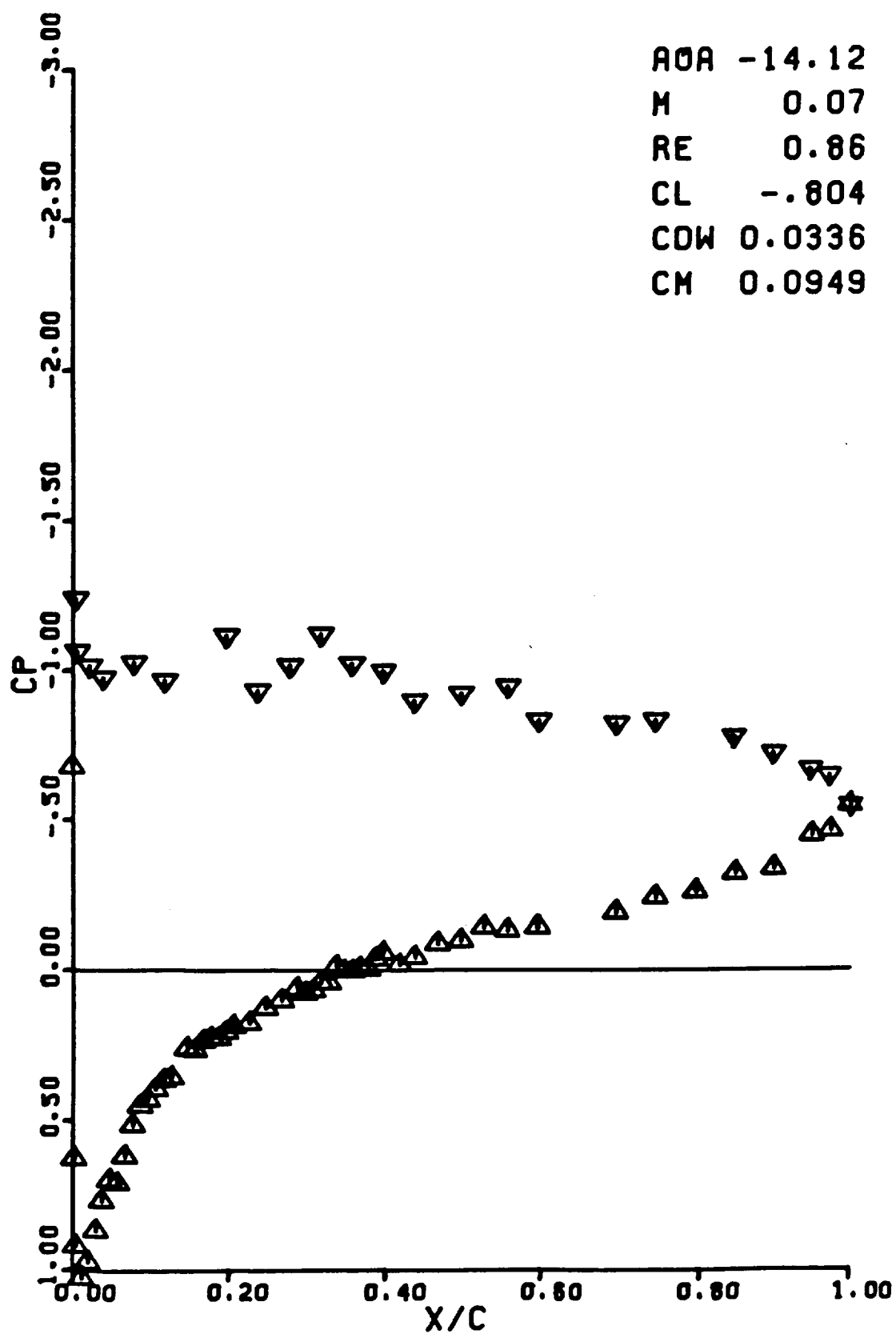
M 0.07

RE 0.86

CL -.804

CDW 0.0336

CM 0.0949



RUN 0520

AOA -13.32

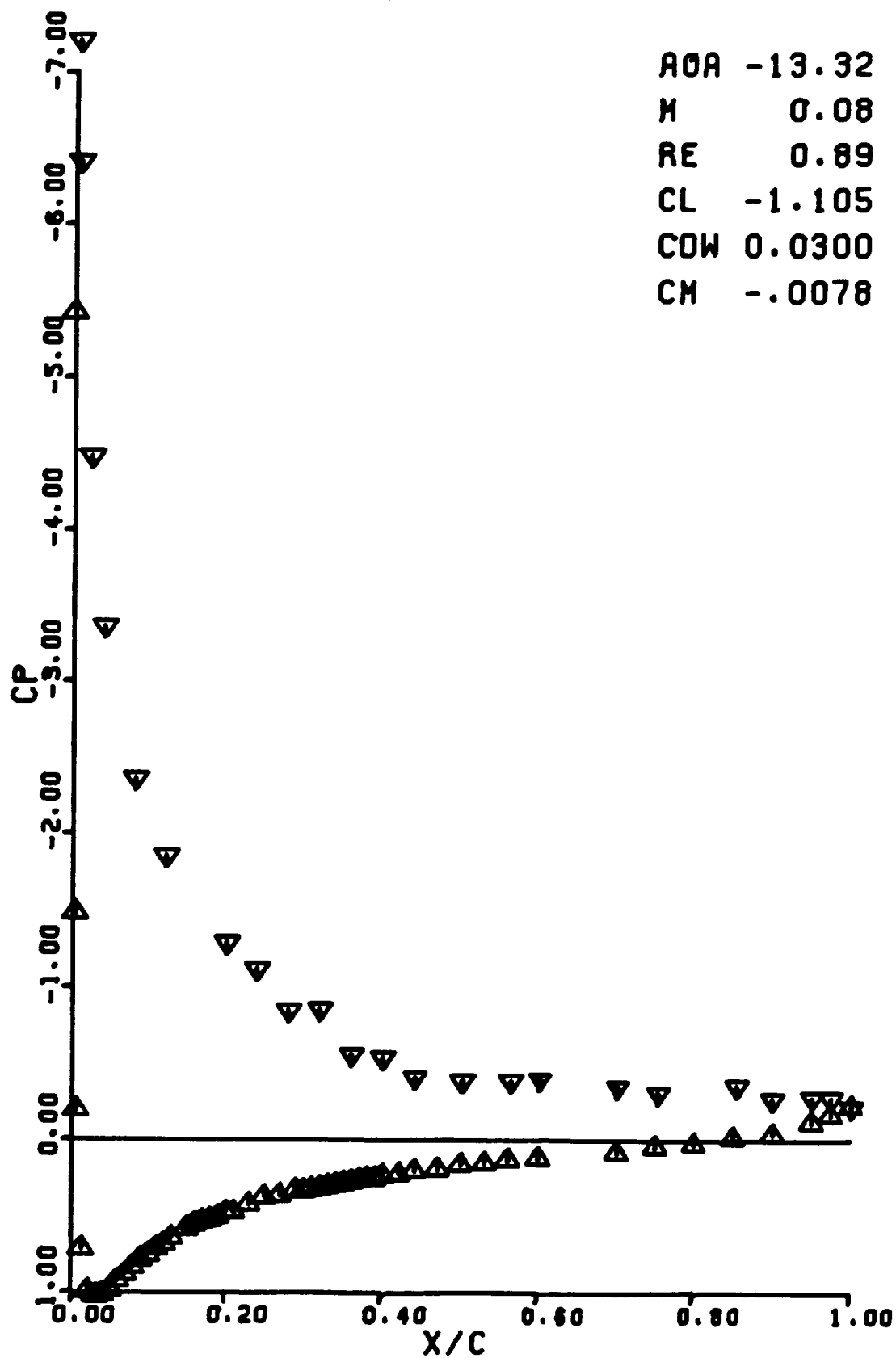
M 0.08

RE 0.89

CL -1.105

CDW 0.0300

CM -.0078



RUN 0521

AOA -12.85

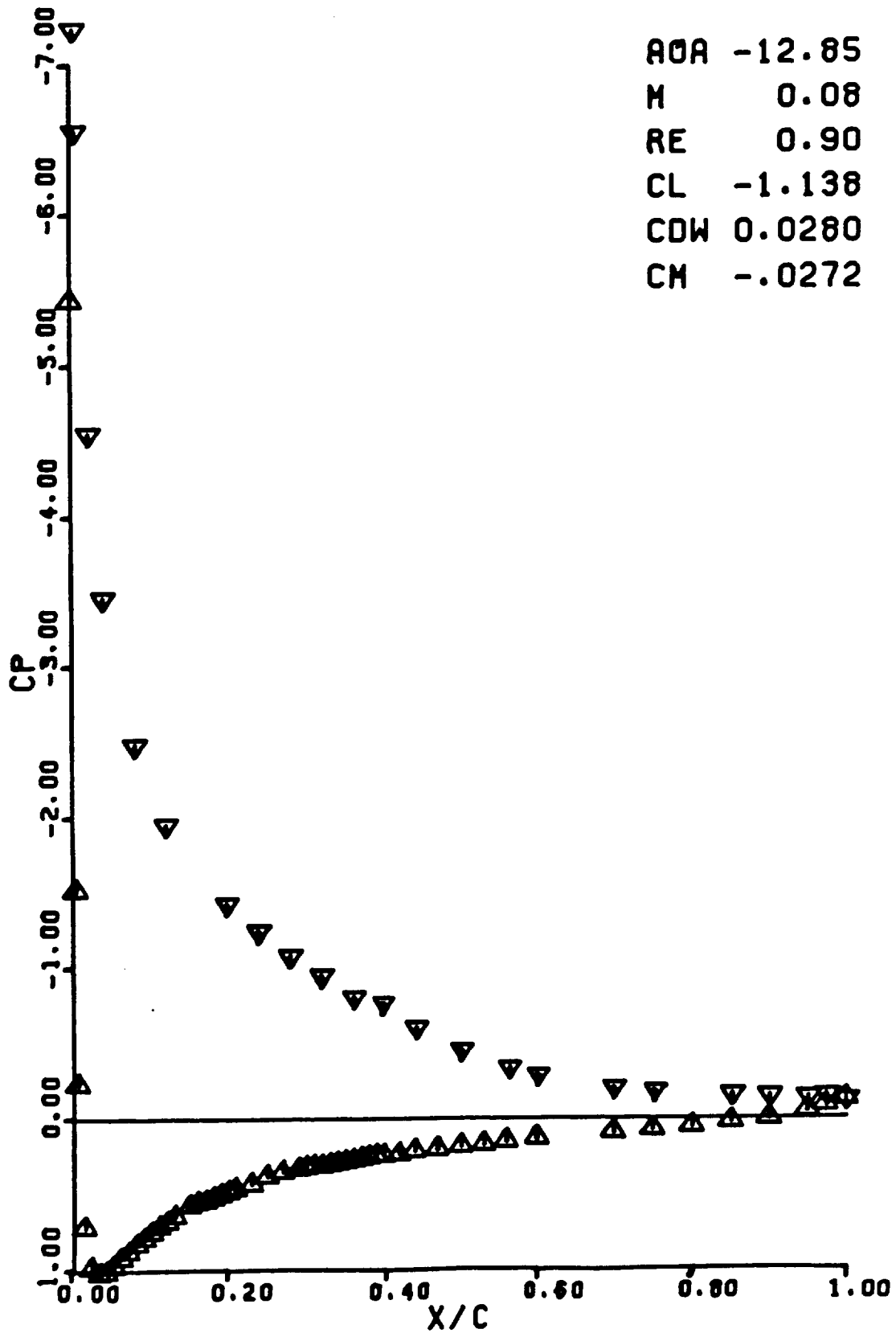
M 0.08

RE 0.90

CL -1.138

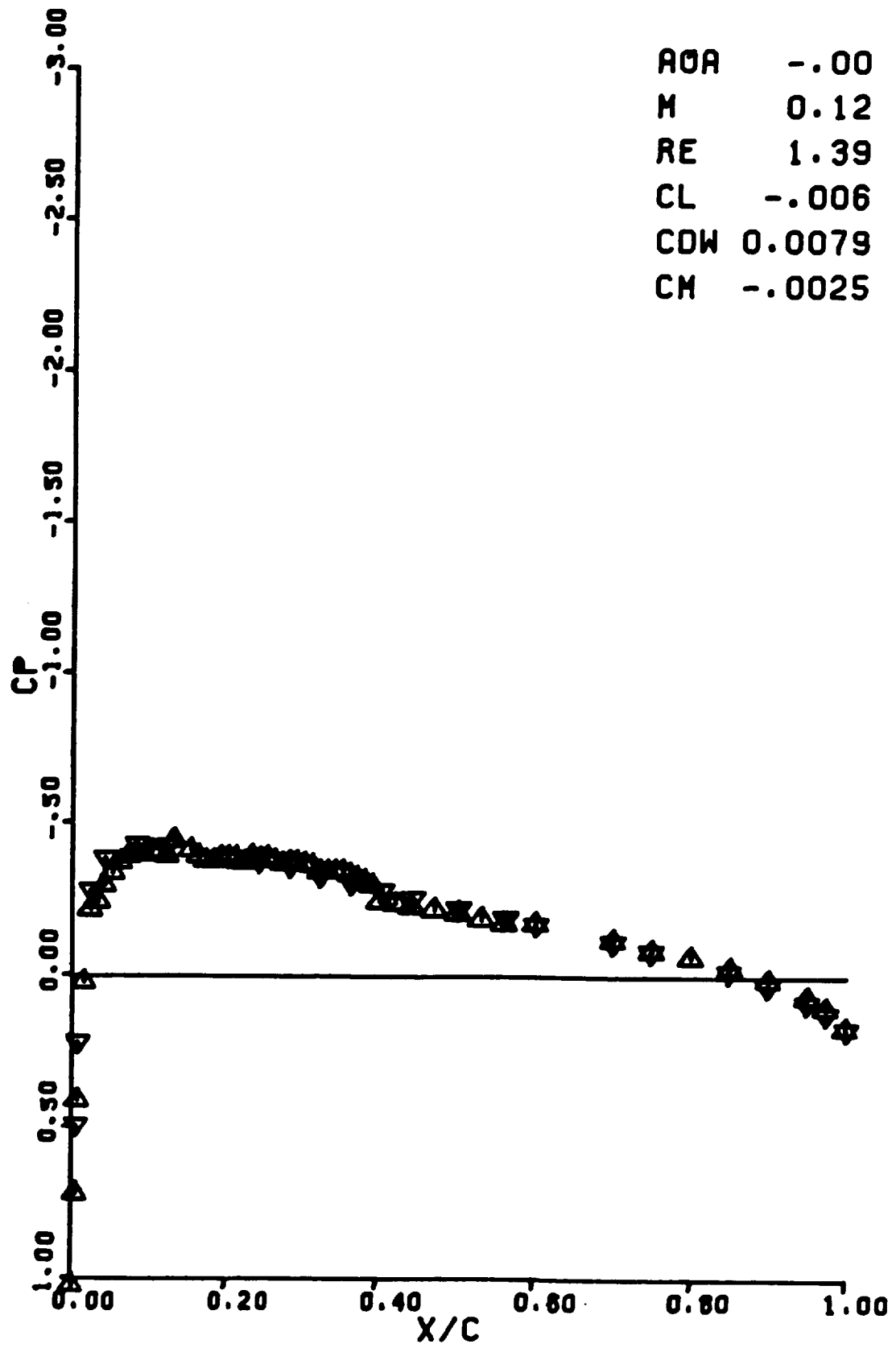
CDW 0.0280

CM -.0272



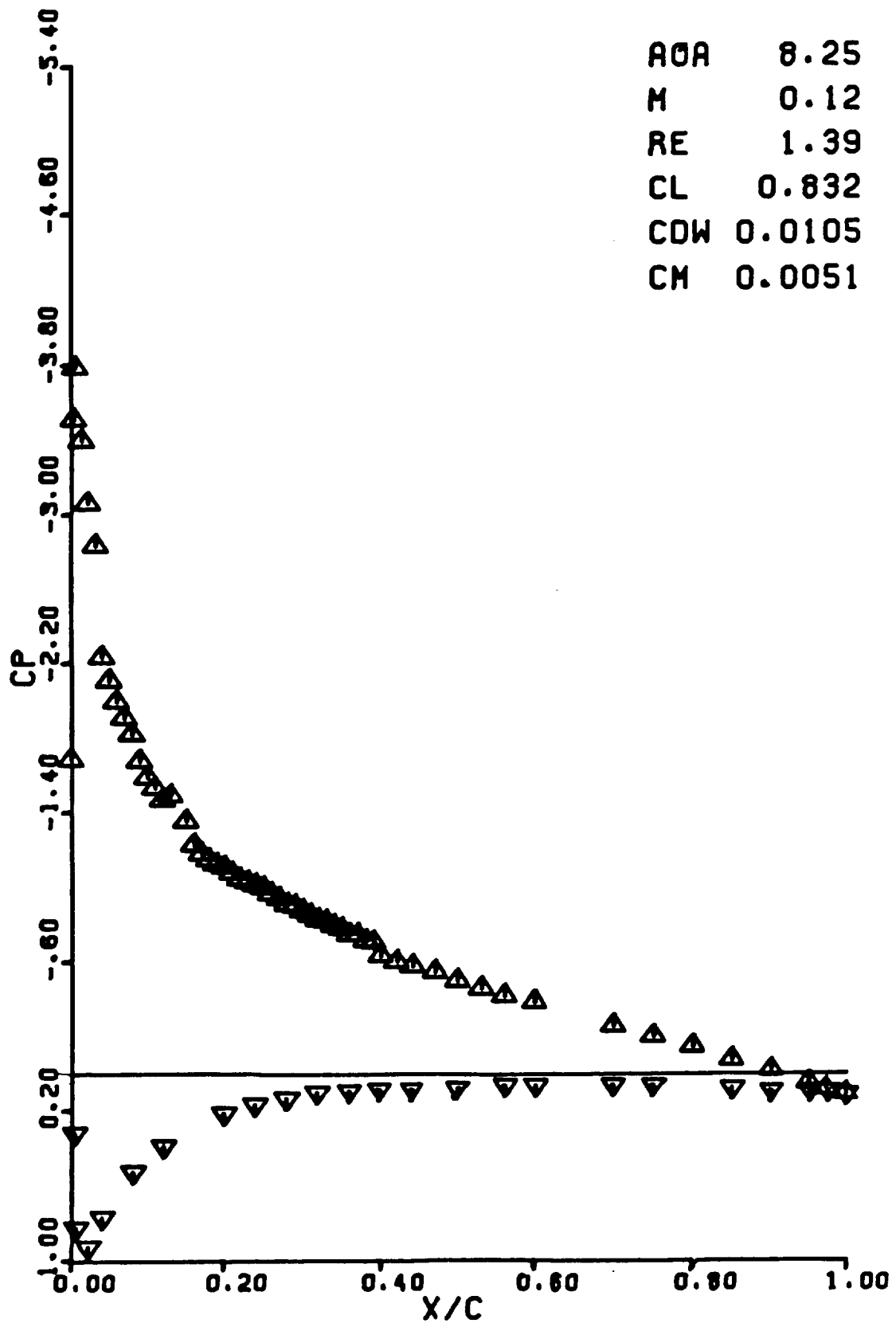
RUN 0748

AOA -.00  
M 0.12  
RE 1.39  
CL -.006  
CDW 0.0079  
CM -.0025



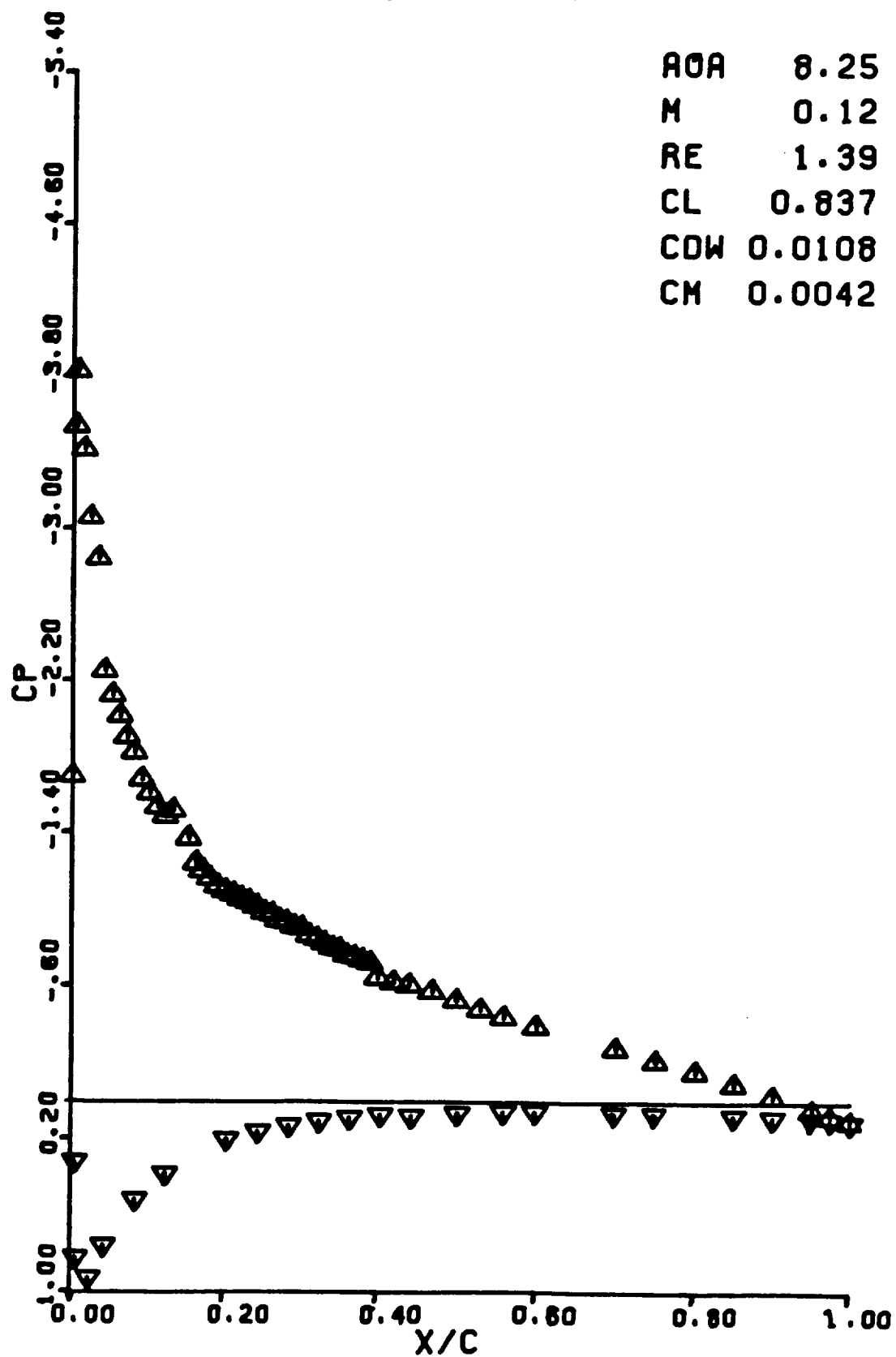
RUN 0749

AOA 8.25  
M 0.12  
RE 1.39  
CL 0.832  
CDW 0.0105  
CM 0.0051



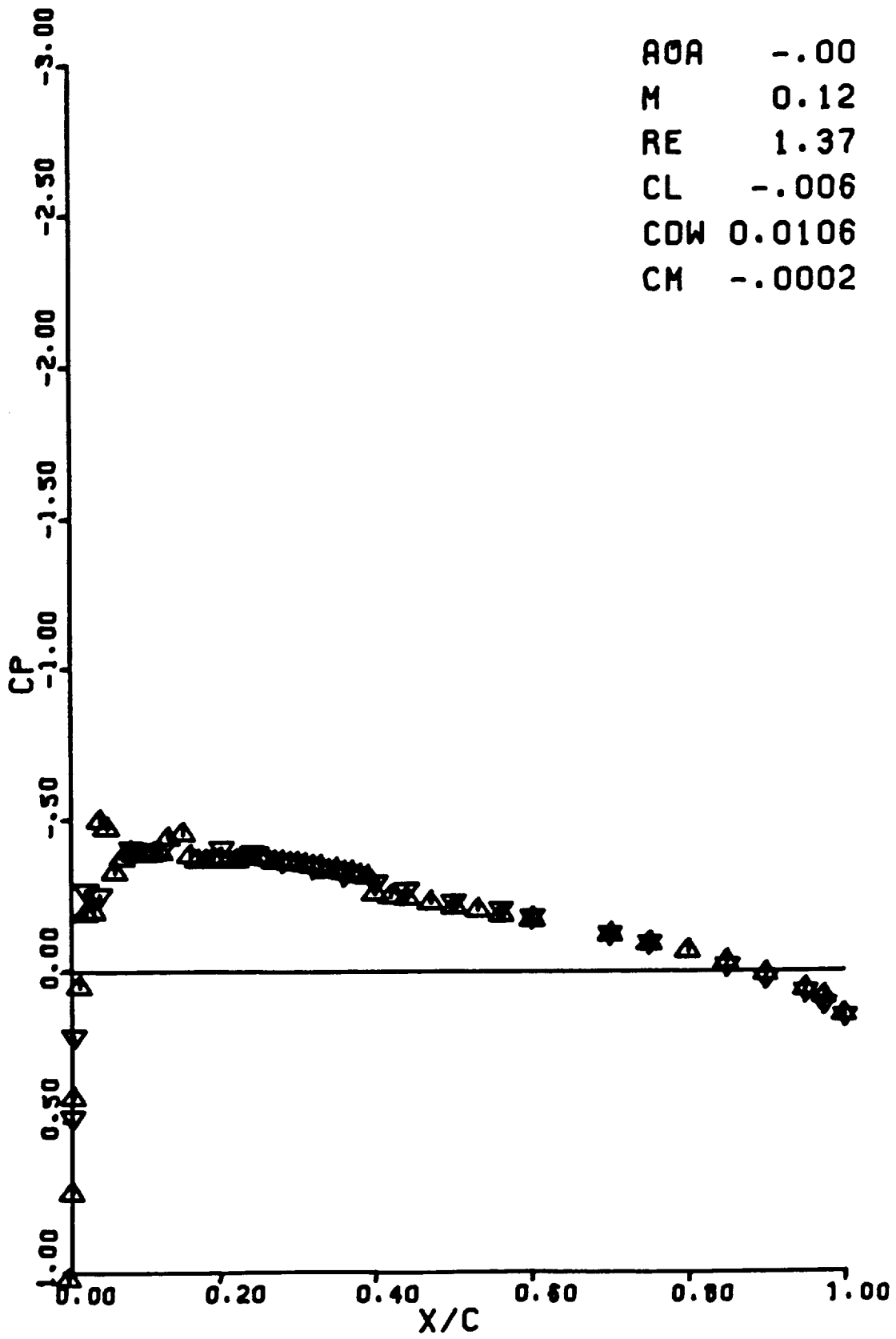
RUN 0750

AOA 8.25  
M 0.12  
RE 1.39  
CL 0.837  
CDW 0.0108  
CM 0.0042



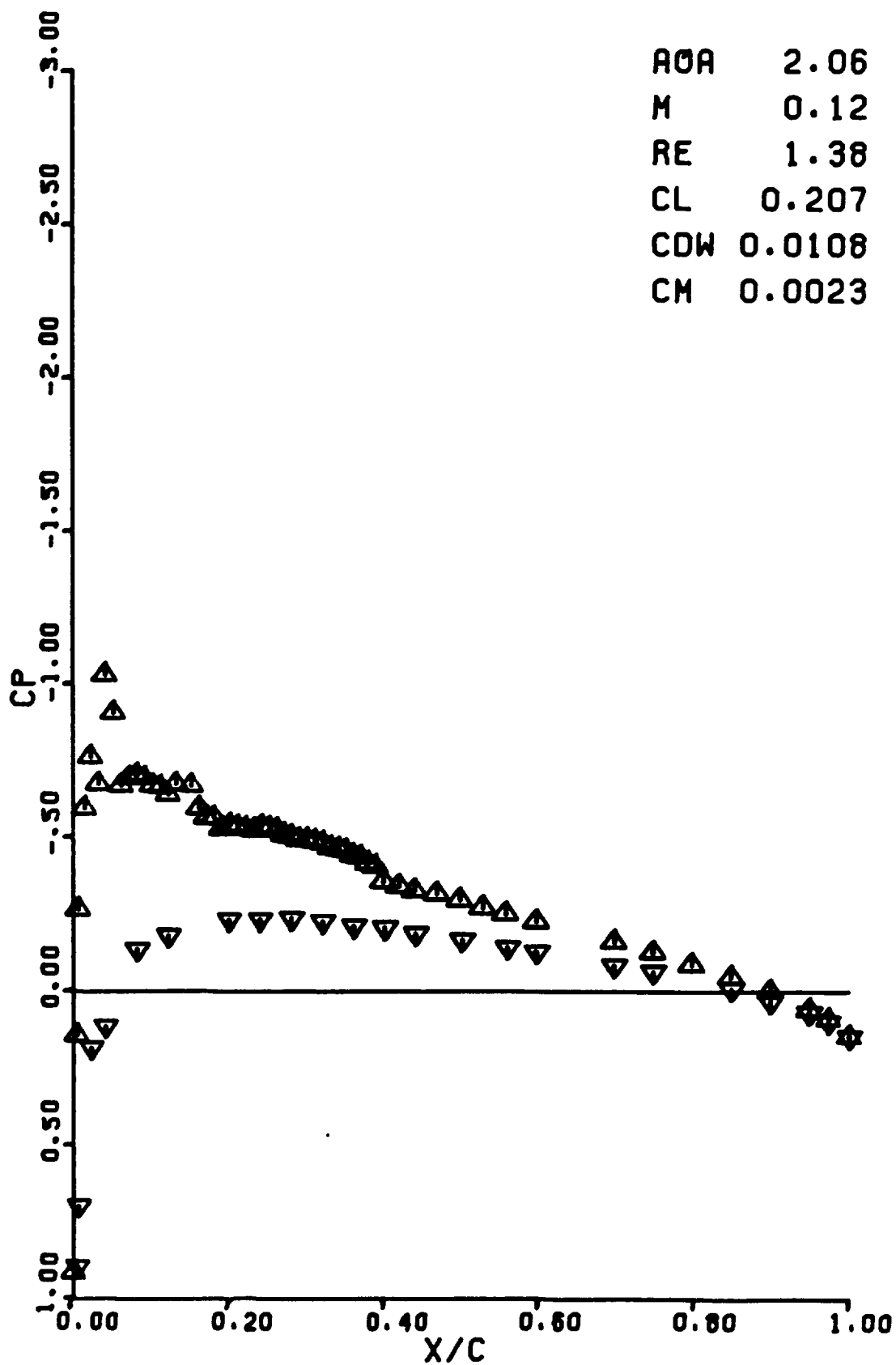
RUN 0751

AOA -.00  
M 0.12  
RE 1.37  
CL -.006  
CDW 0.0106  
CM -.0002



RUN 0752

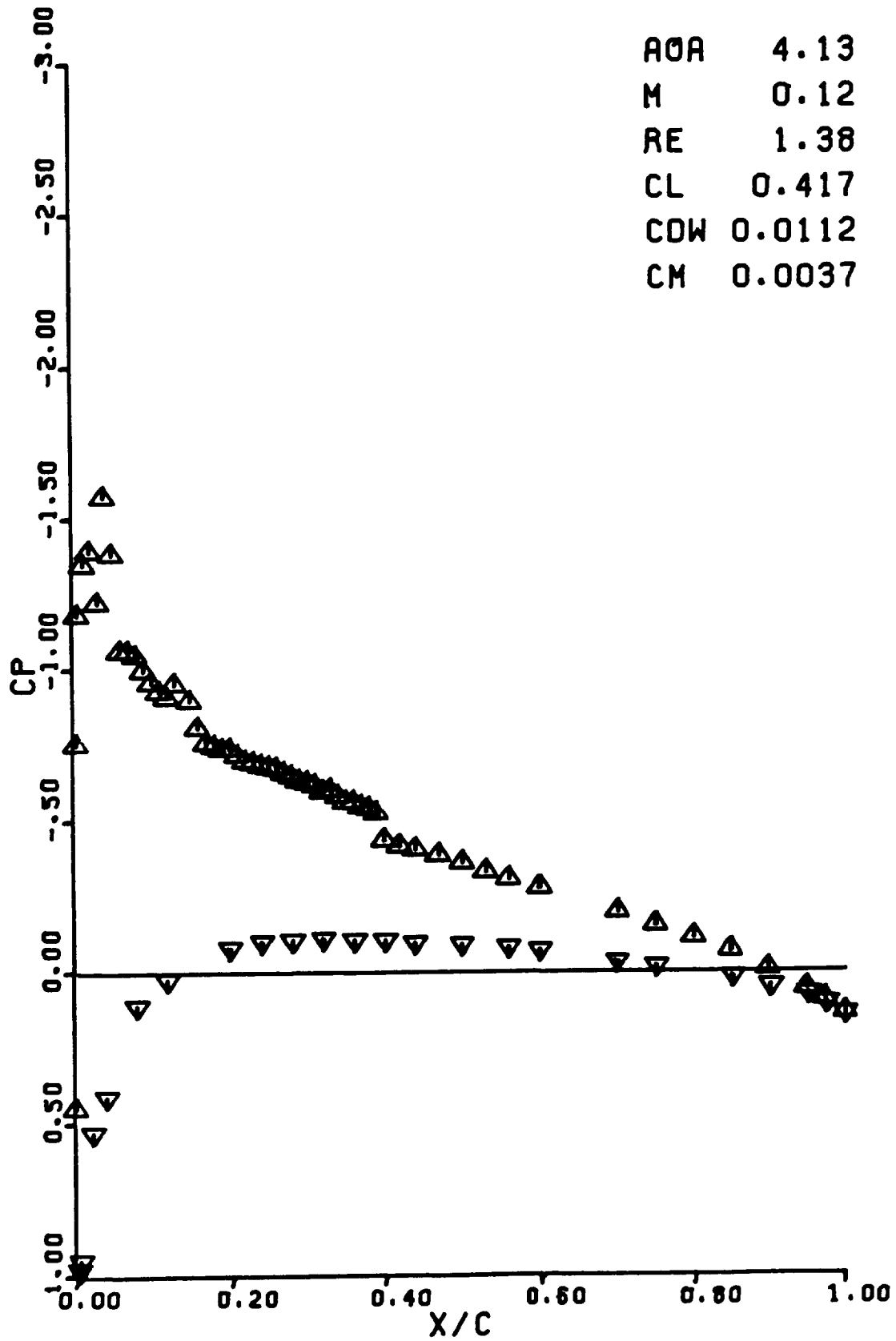
AOA 2.06  
M 0.12  
RE 1.38  
CL 0.207  
CDW 0.0108  
CM 0.0023





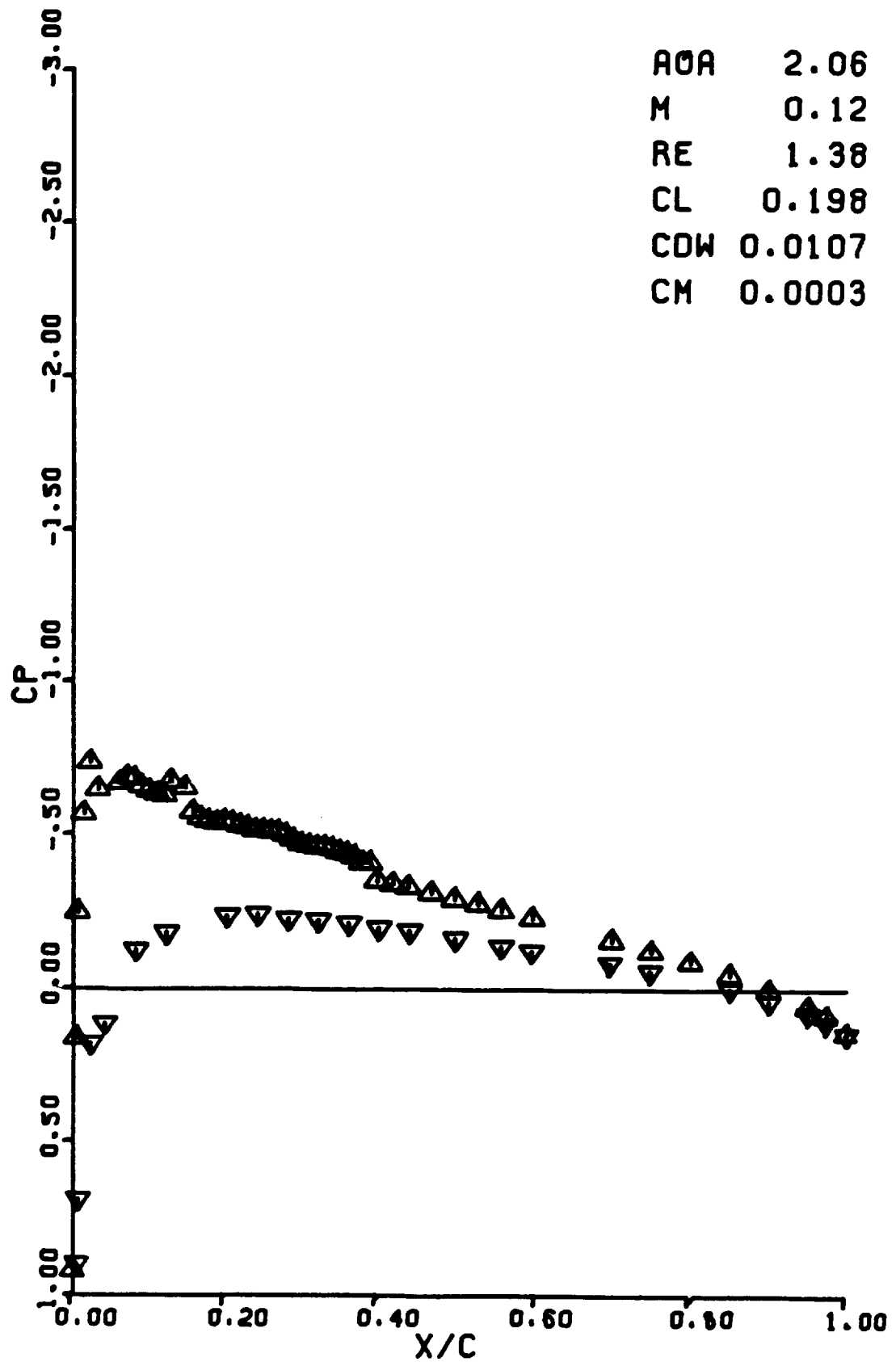
RUN 0753

AOA 4.13  
M 0.12  
RE 1.38  
CL 0.417  
CDW 0.0112  
CM 0.0037



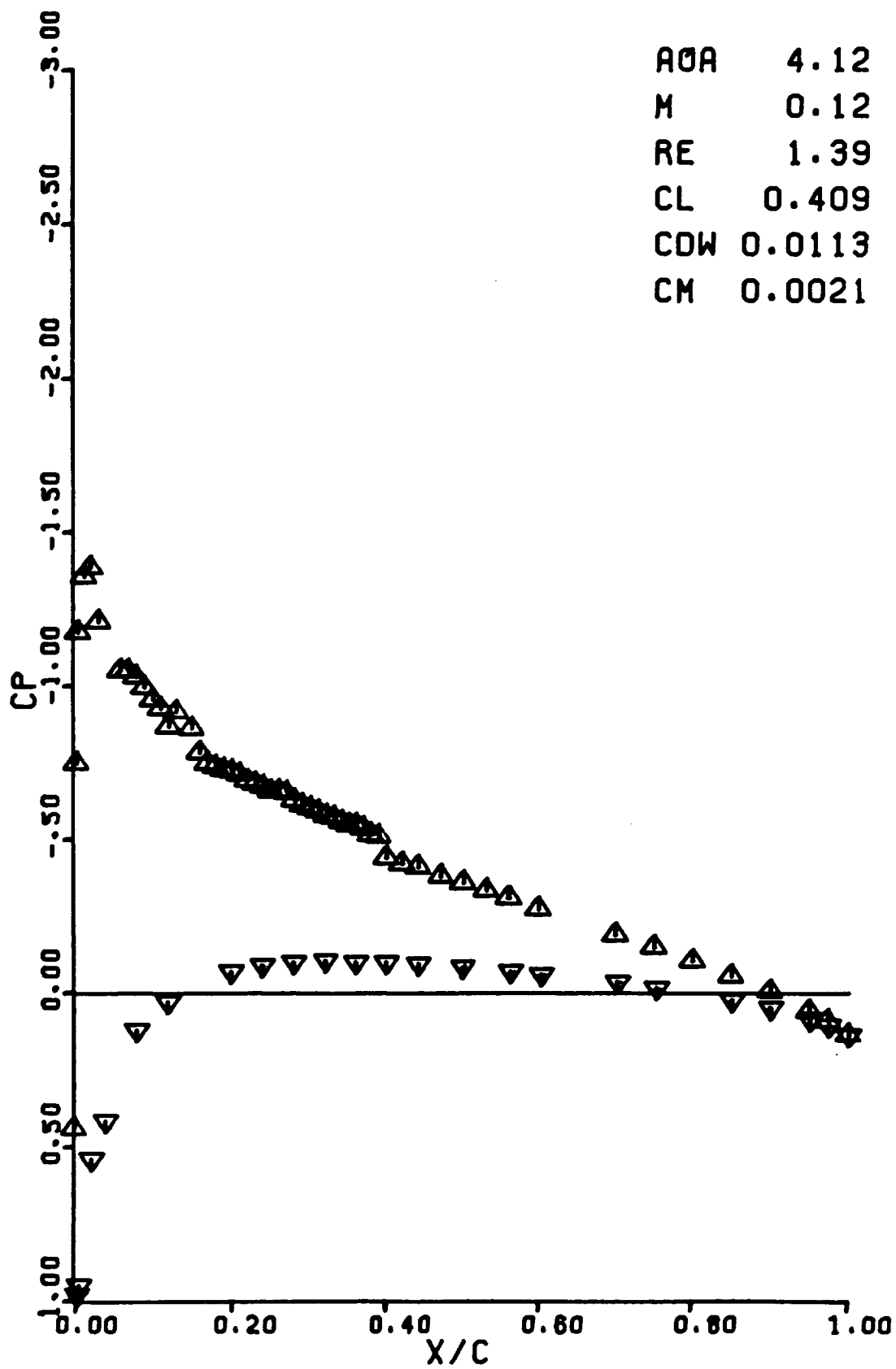
RUN 0754

AOA 2.06  
M 0.12  
RE 1.38  
CL 0.198  
CDW 0.0107  
CM 0.0003



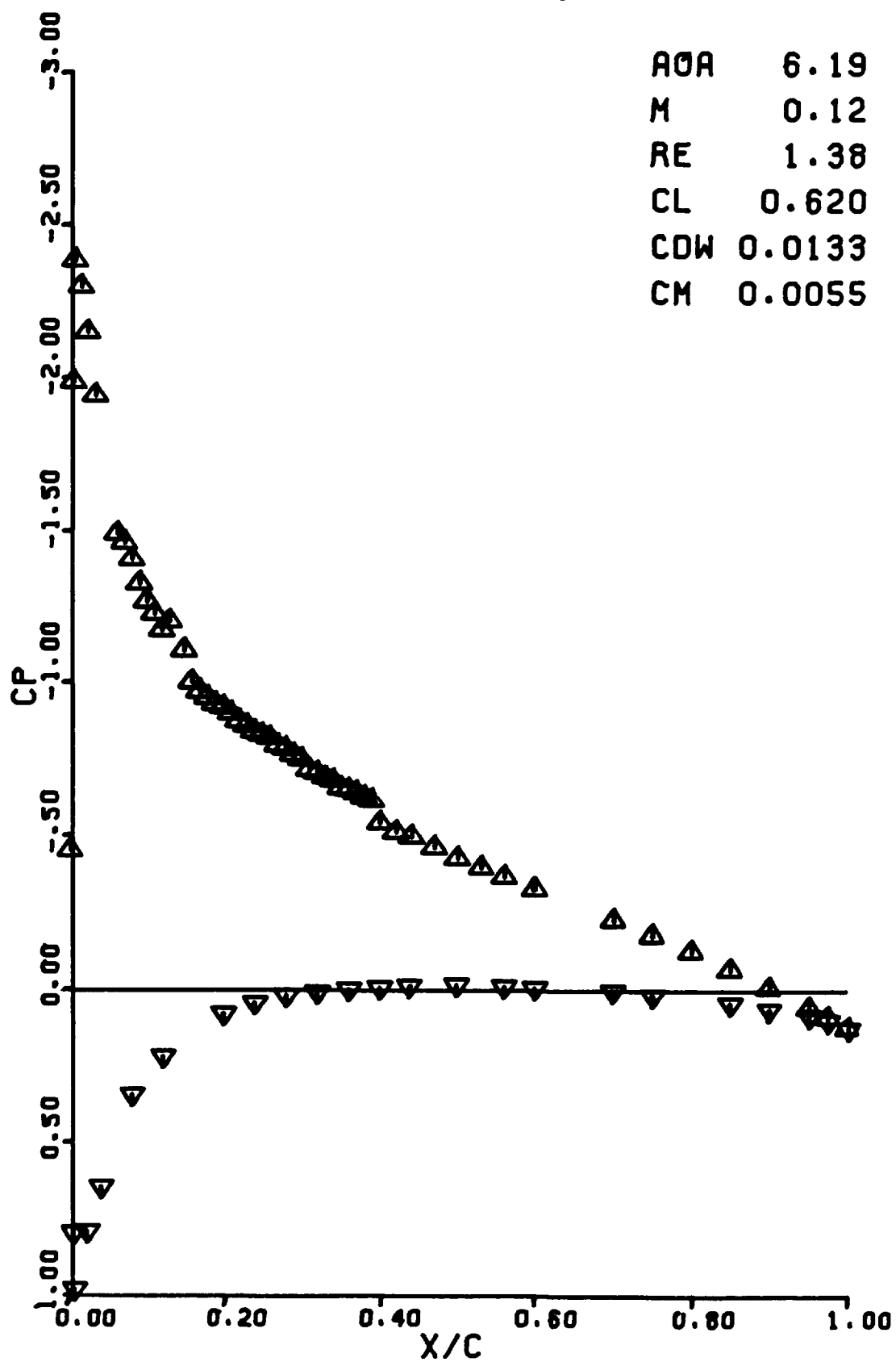
RUN 0755

AOA 4.12  
M 0.12  
RE 1.39  
CL 0.409  
CDW 0.0113  
CM 0.0021



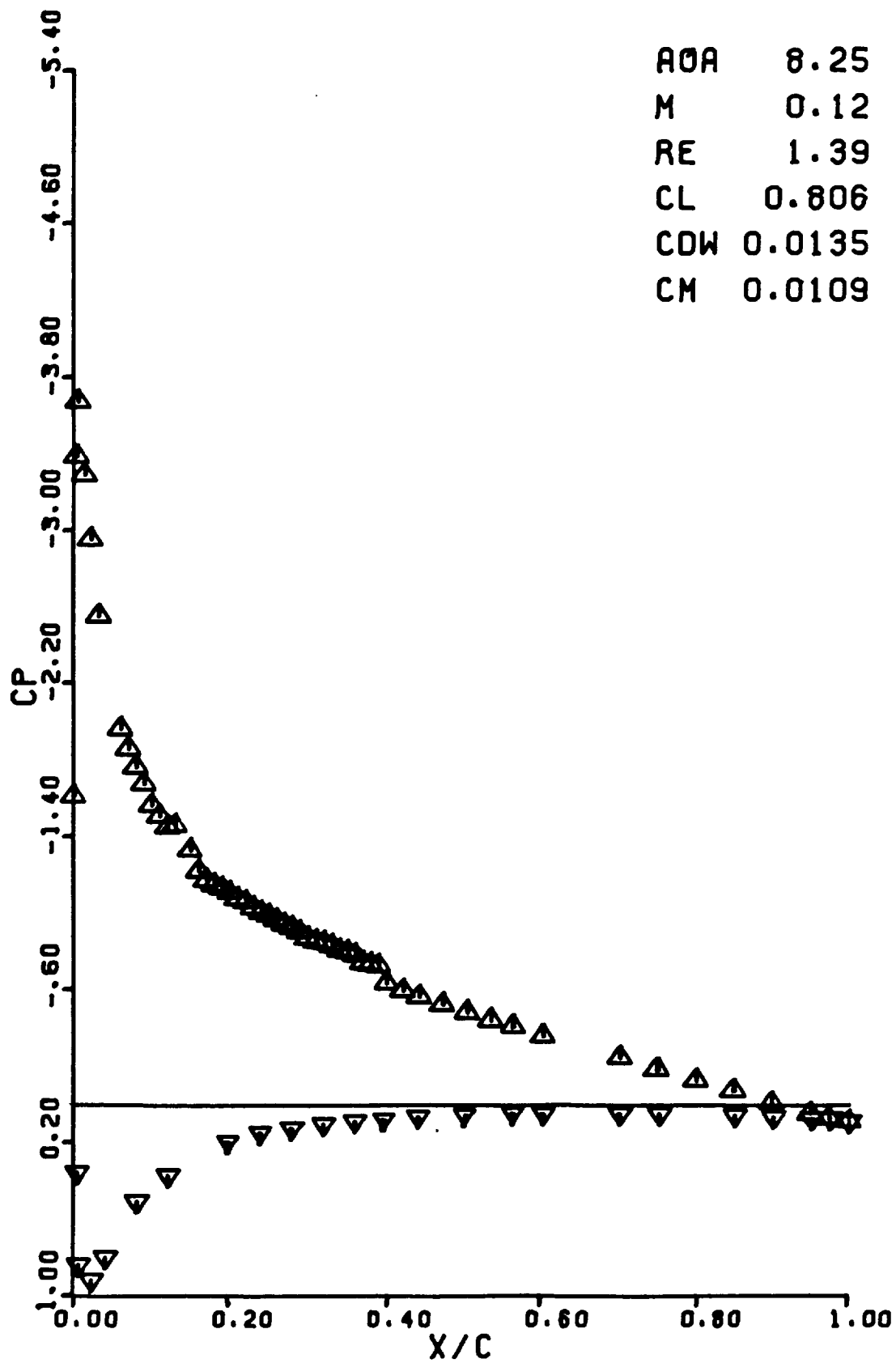
RUN 0756

AOA 6.19  
M 0.12  
RE 1.38  
CL 0.620  
CDW 0.0133  
CM 0.0055



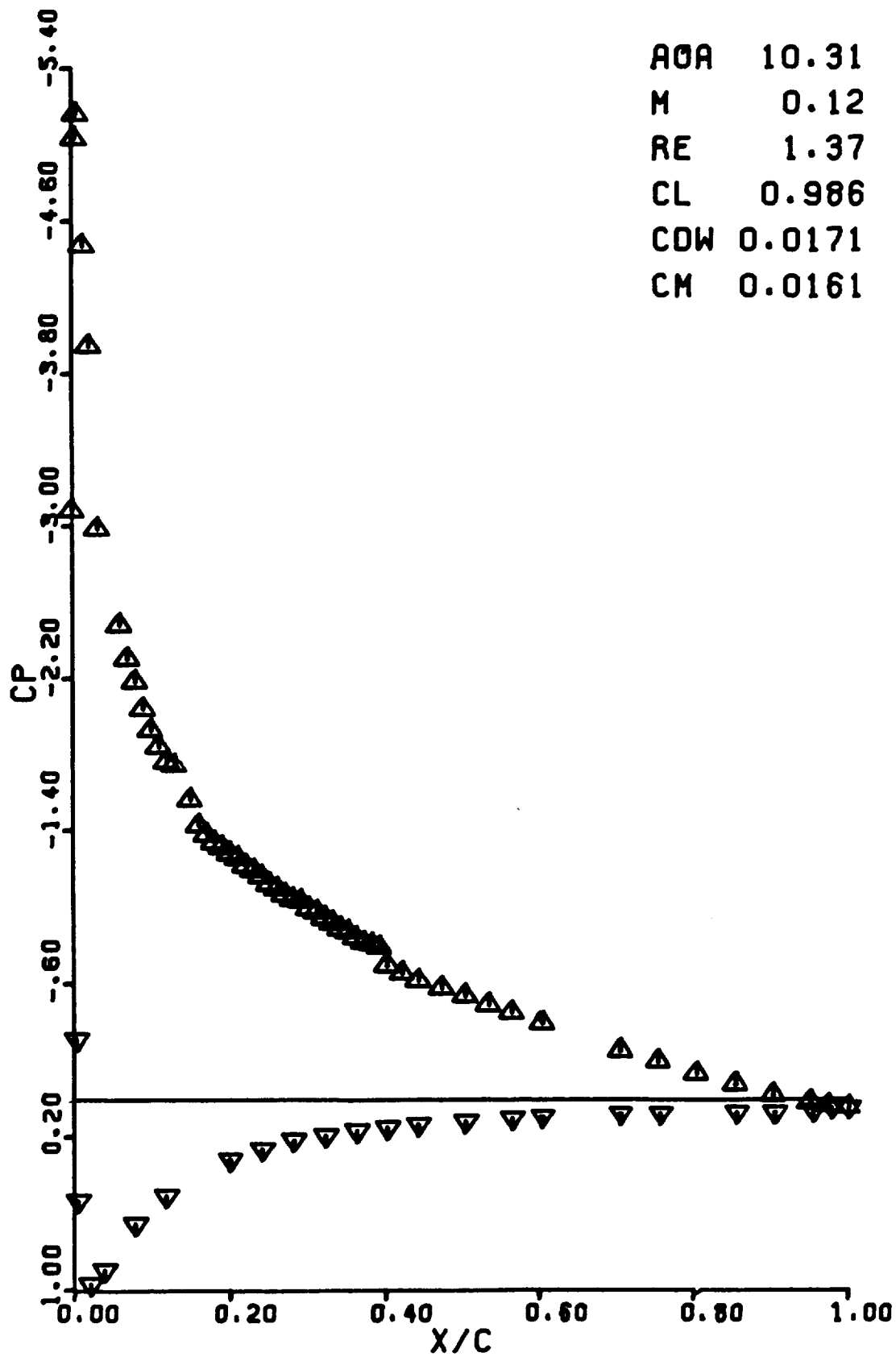
RUN 0757

AOA 8.25  
M 0.12  
RE 1.39  
CL 0.806  
CDW 0.0135  
CM 0.0109

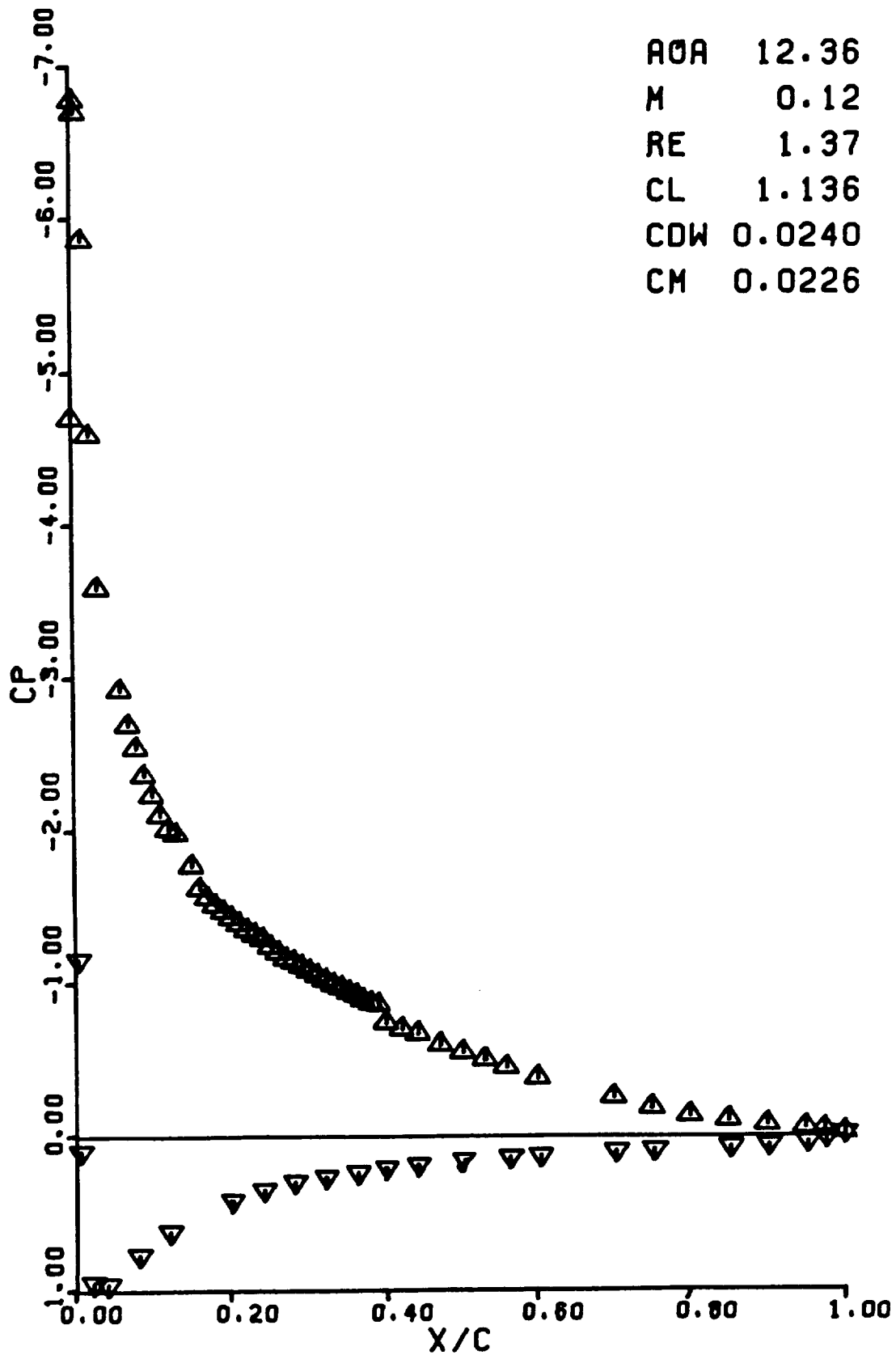


RUN 0758

AOA 10.31  
M 0.12  
RE 1.37  
CL 0.986  
CDW 0.0171  
CM 0.0161

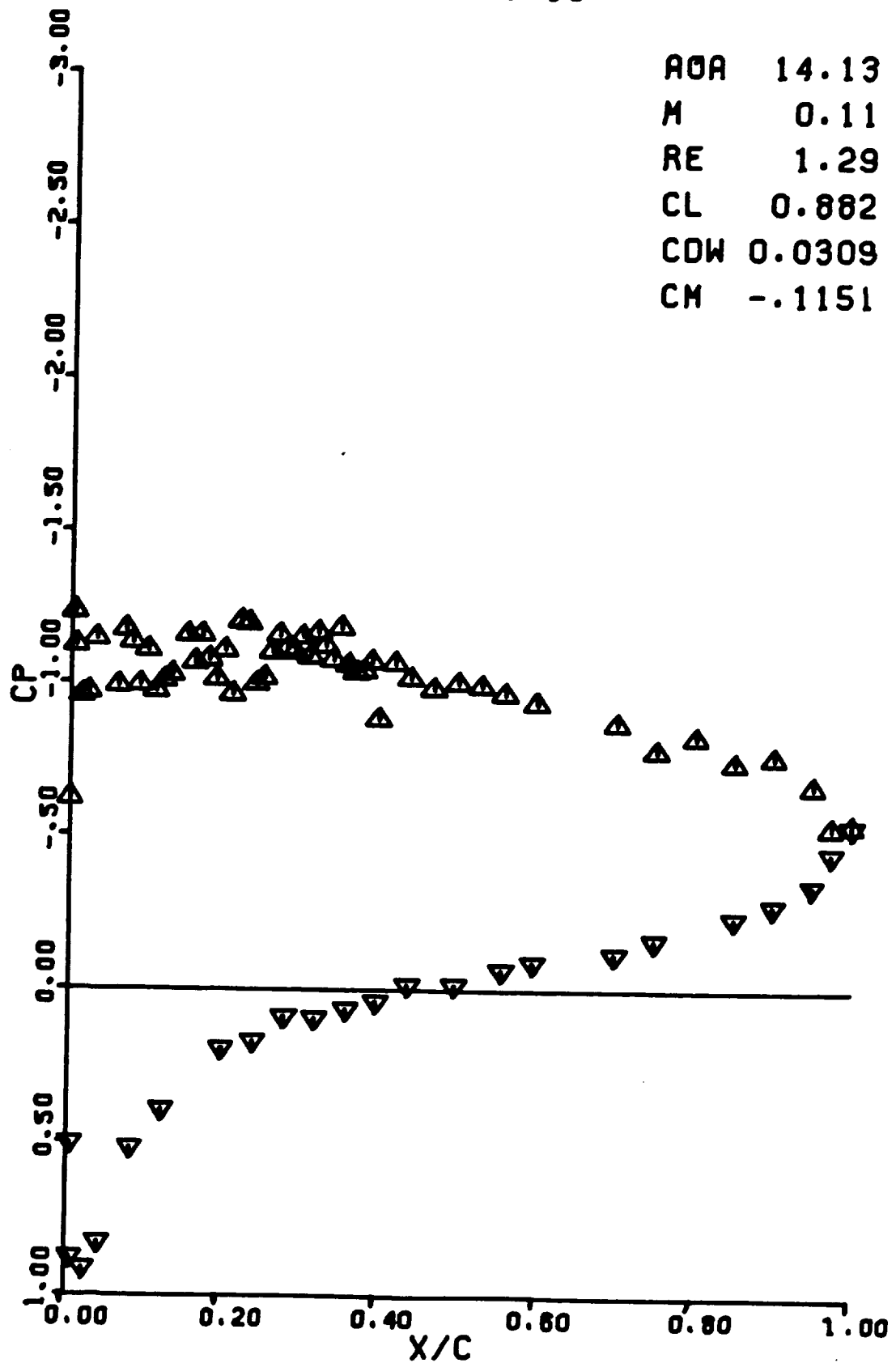


RUN 0759



RUN 0760

AOA 14.13  
M 0.11  
RE 1.29  
CL 0.882  
CDW 0.0309  
CM -.1151





RUN 0761

AOA 13.38

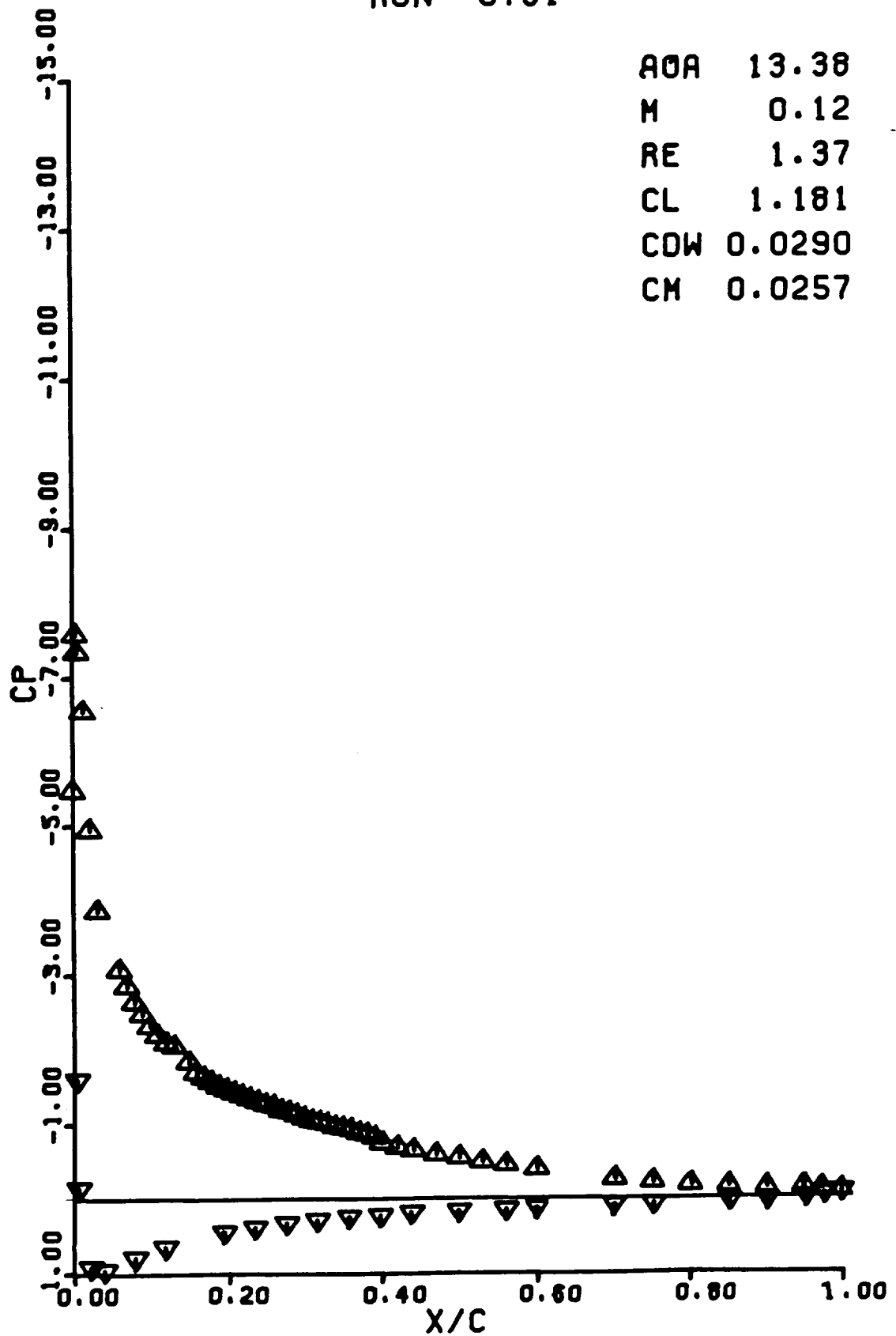
M 0.12

RE 1.37

CL 1.181

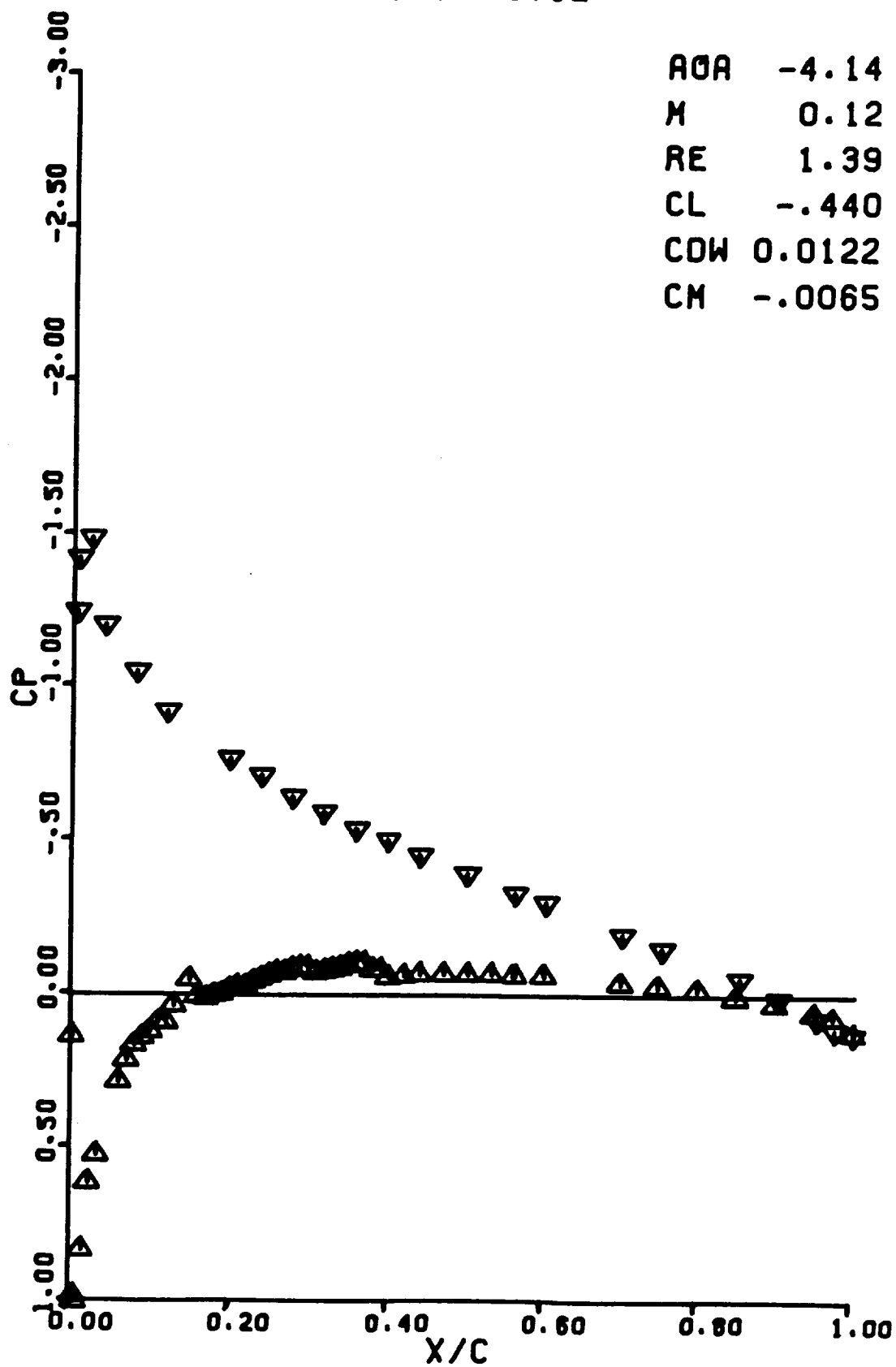
CDW 0.0290

CM 0.0257



RUN 0762

AOA -4.14  
M 0.12  
RE 1.39  
CL -.440  
CDW 0.0122  
CM -.0065



RUN 0763

AOA -8.26

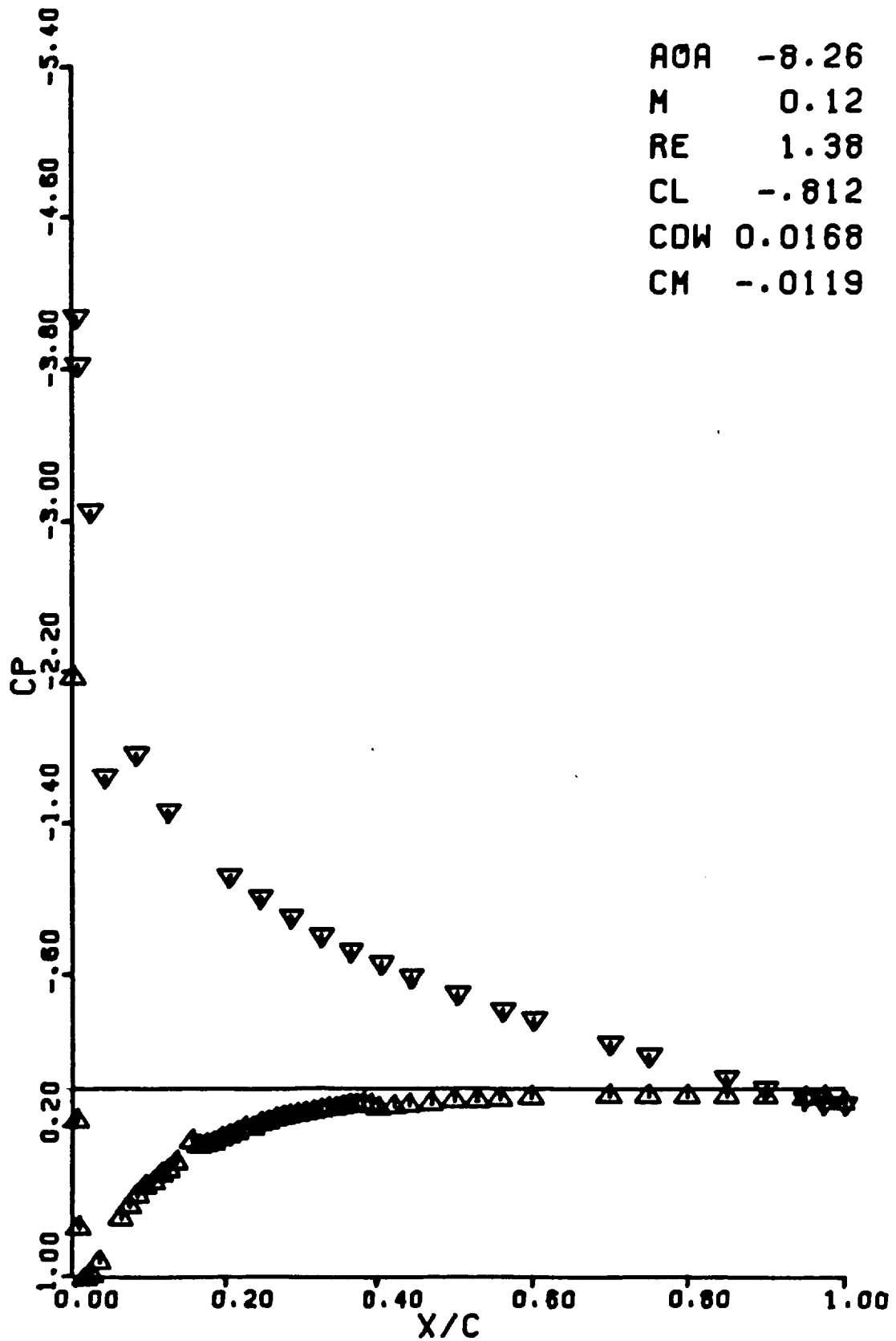
M 0.12

RE 1.38

CL -.812

CDW 0.0168

CM -.0119



RUN 0764

AOA -13.37

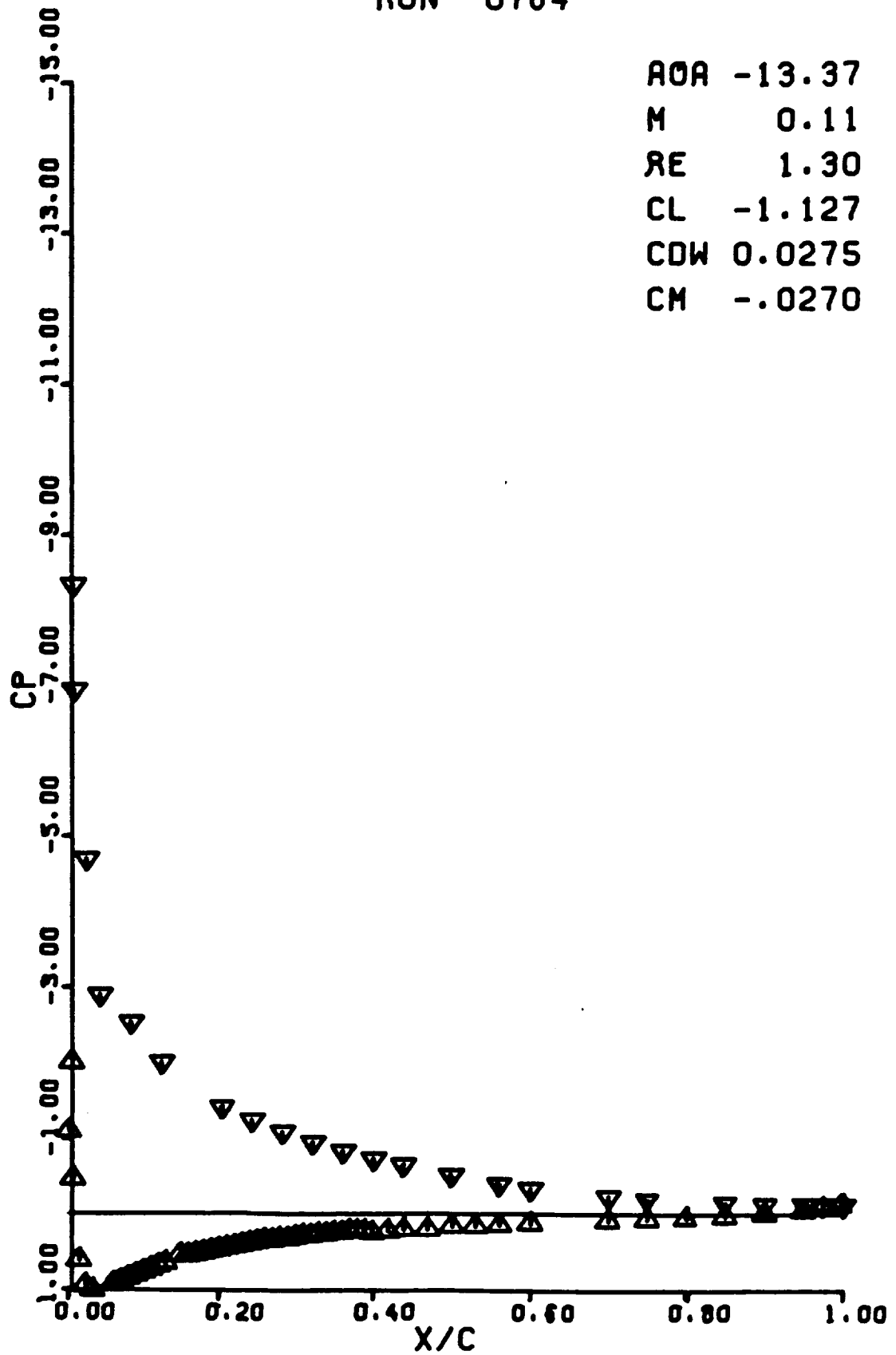
M 0.11

RE 1.30

CL -1.127

CDW 0.0275

CM -.0270



RUN 0765

AOA -14.19

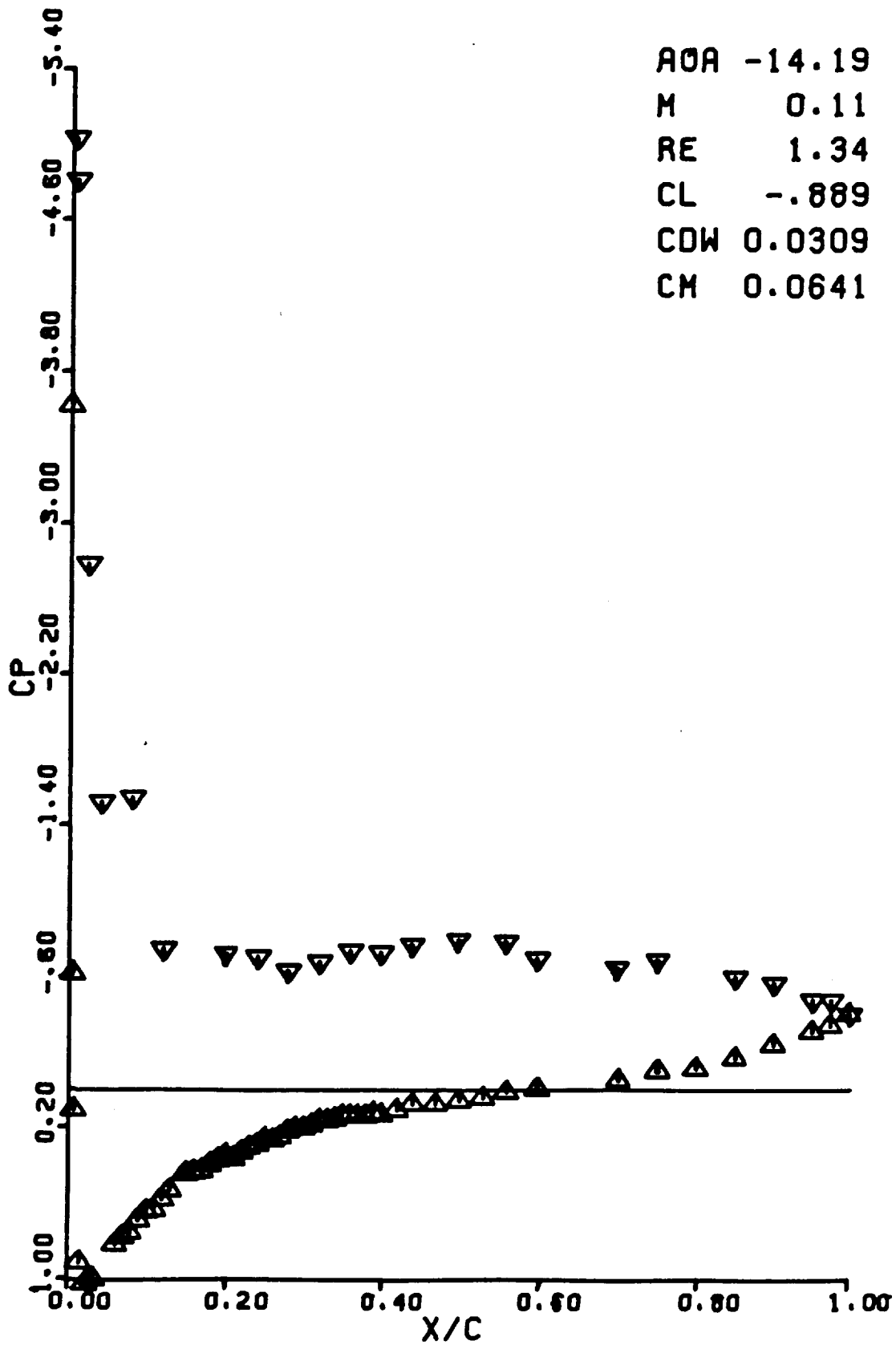
M 0.11

RE 1.34

CL -.889

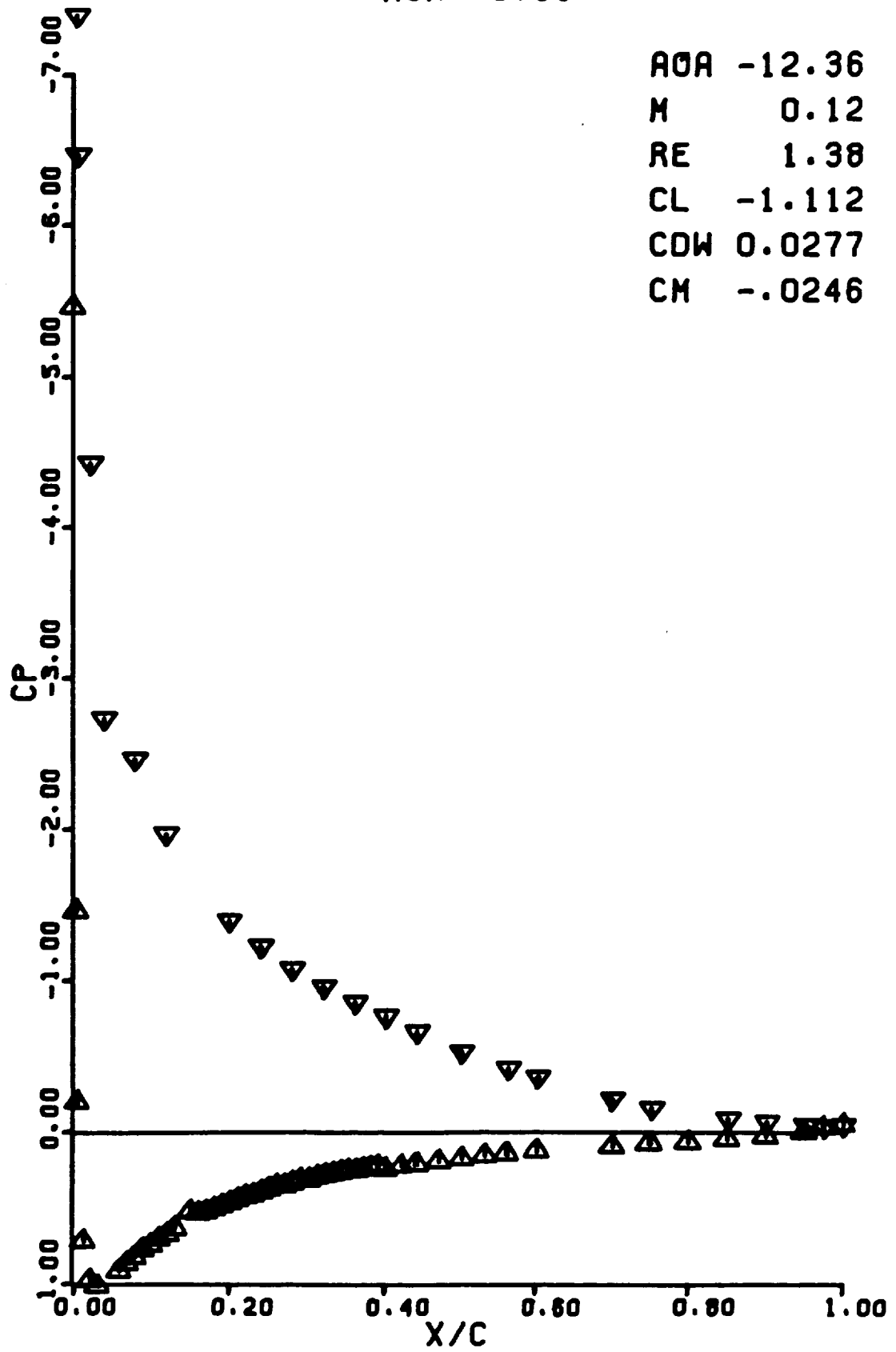
CDW 0.0309

CM 0.0641



RUN 0766

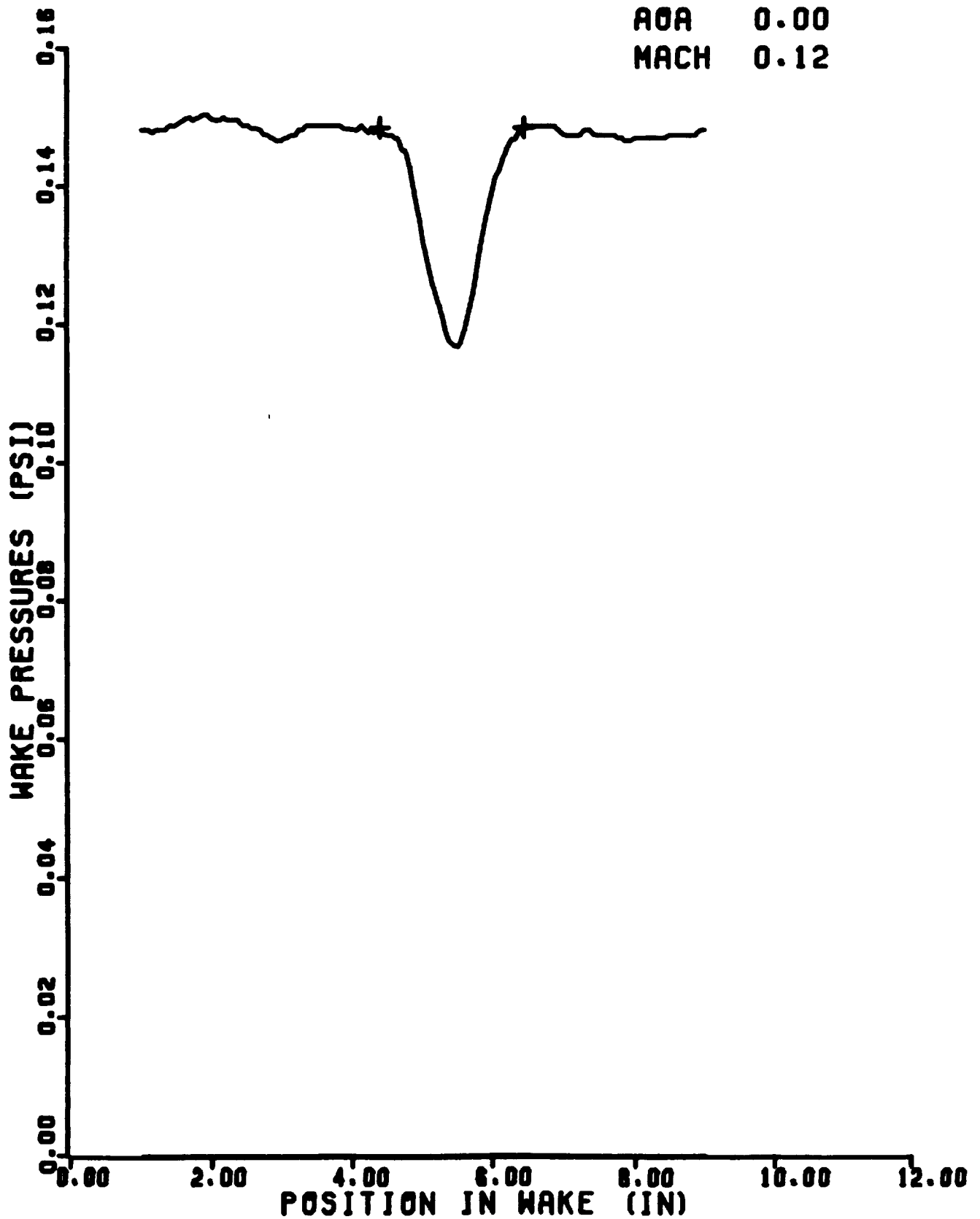
AOA -12.36  
M 0.12  
RE 1.38  
CL -1.112  
CDW 0.0277  
CM -.0246



## APPENDIX C

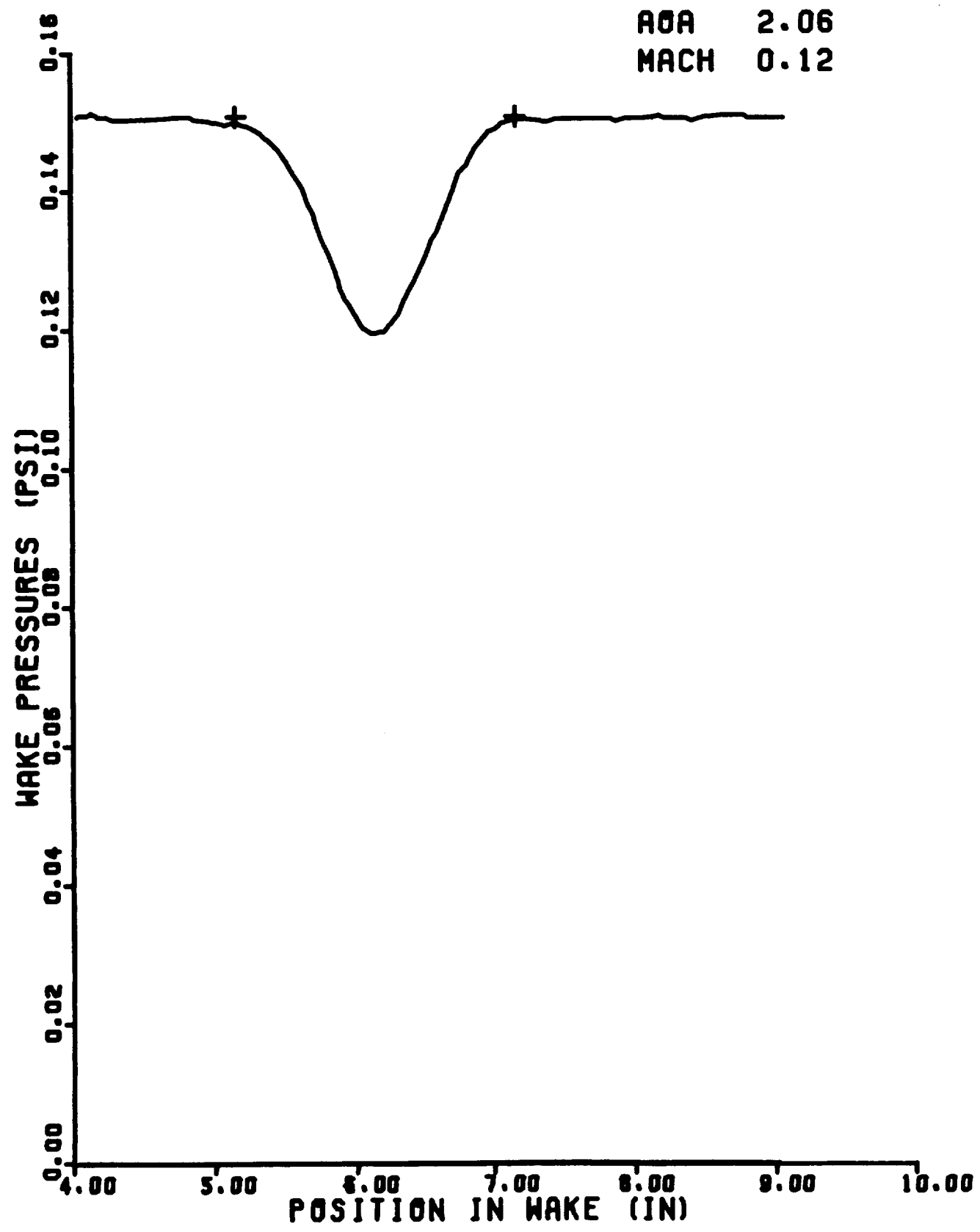
### WAKE SURVEYS

RUN 0365  
CD 0.0076  
AOA 0.00  
MACH 0.12

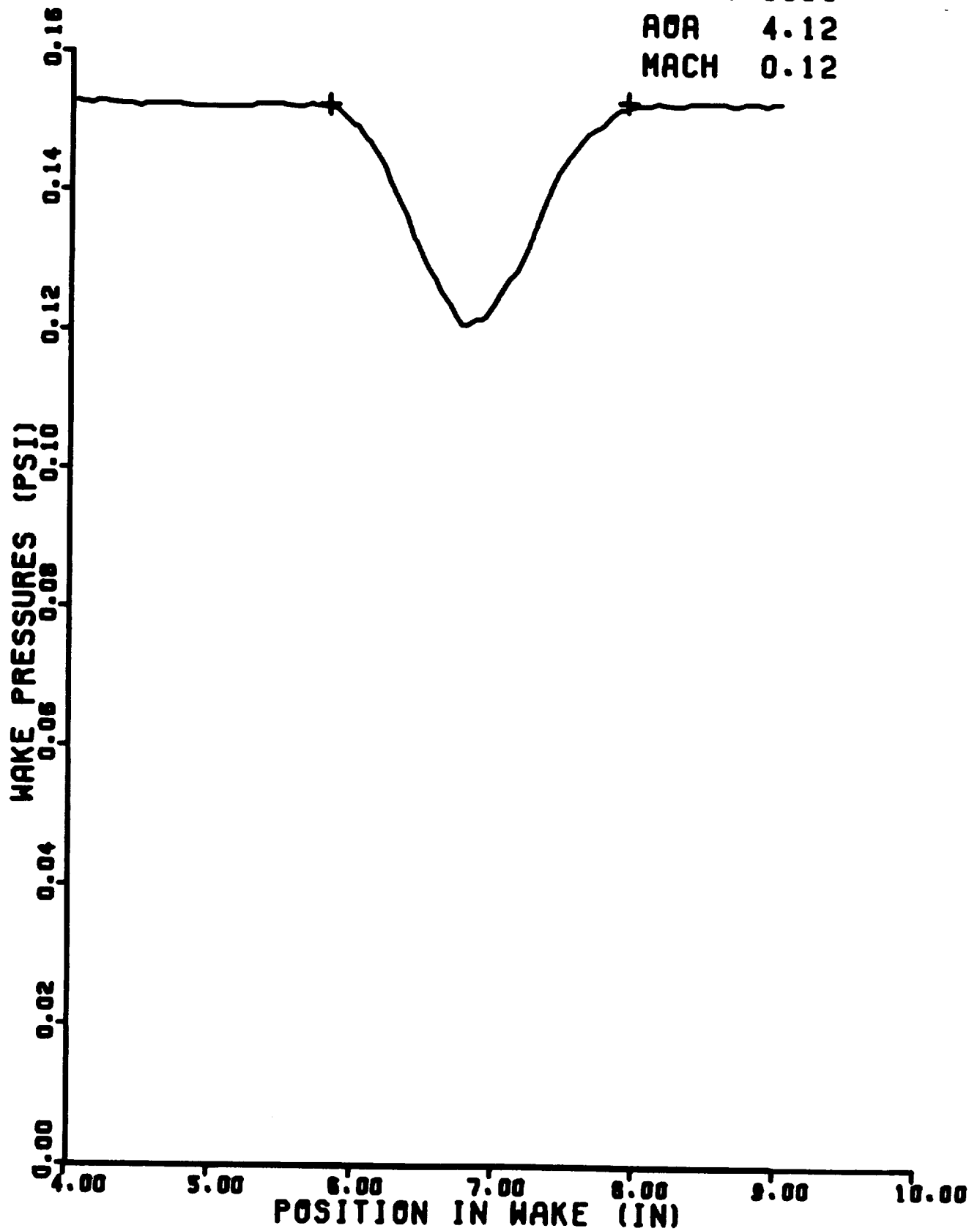




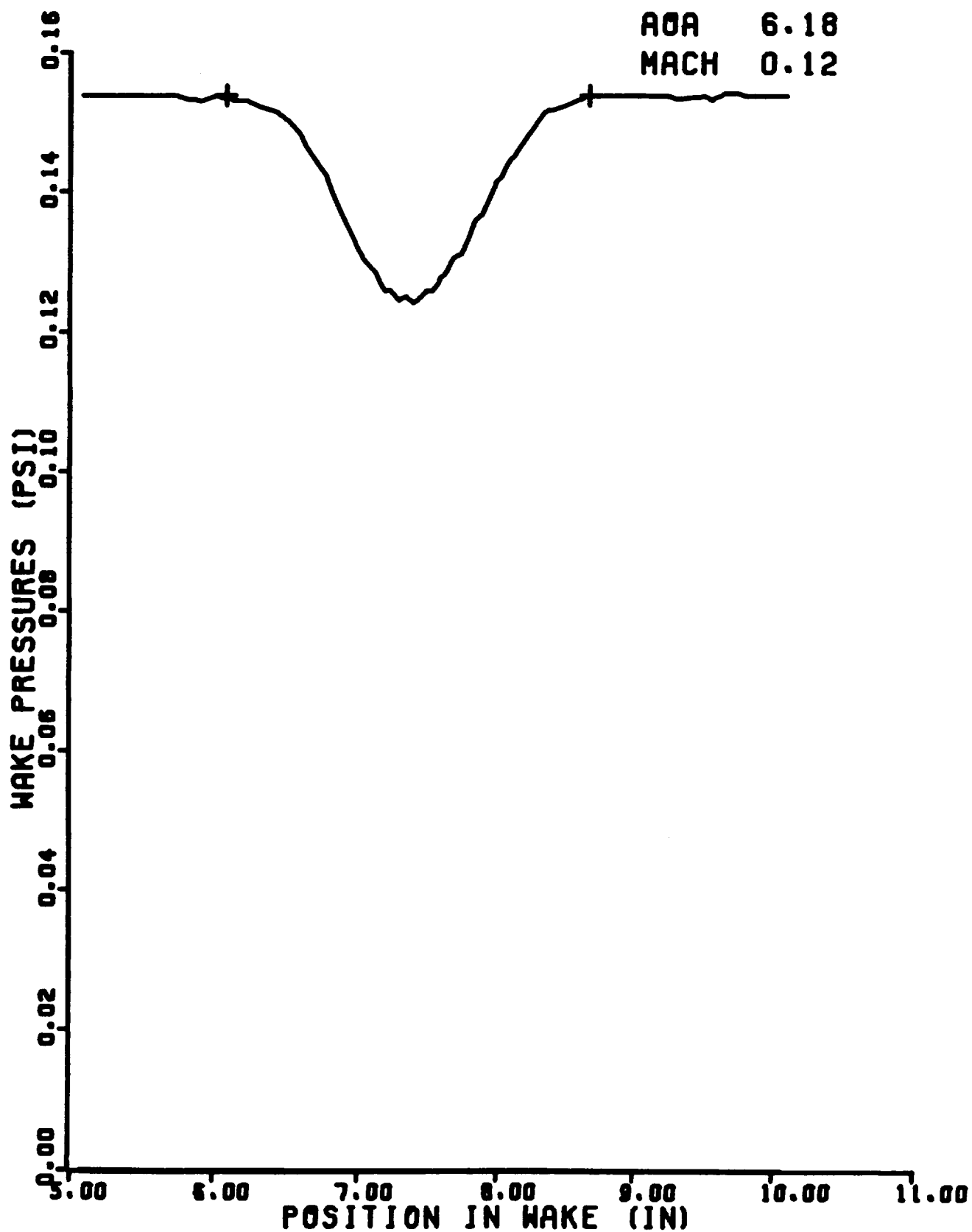
RUN 0367  
CD 0.0081  
AOA 2.06  
MACH 0.12



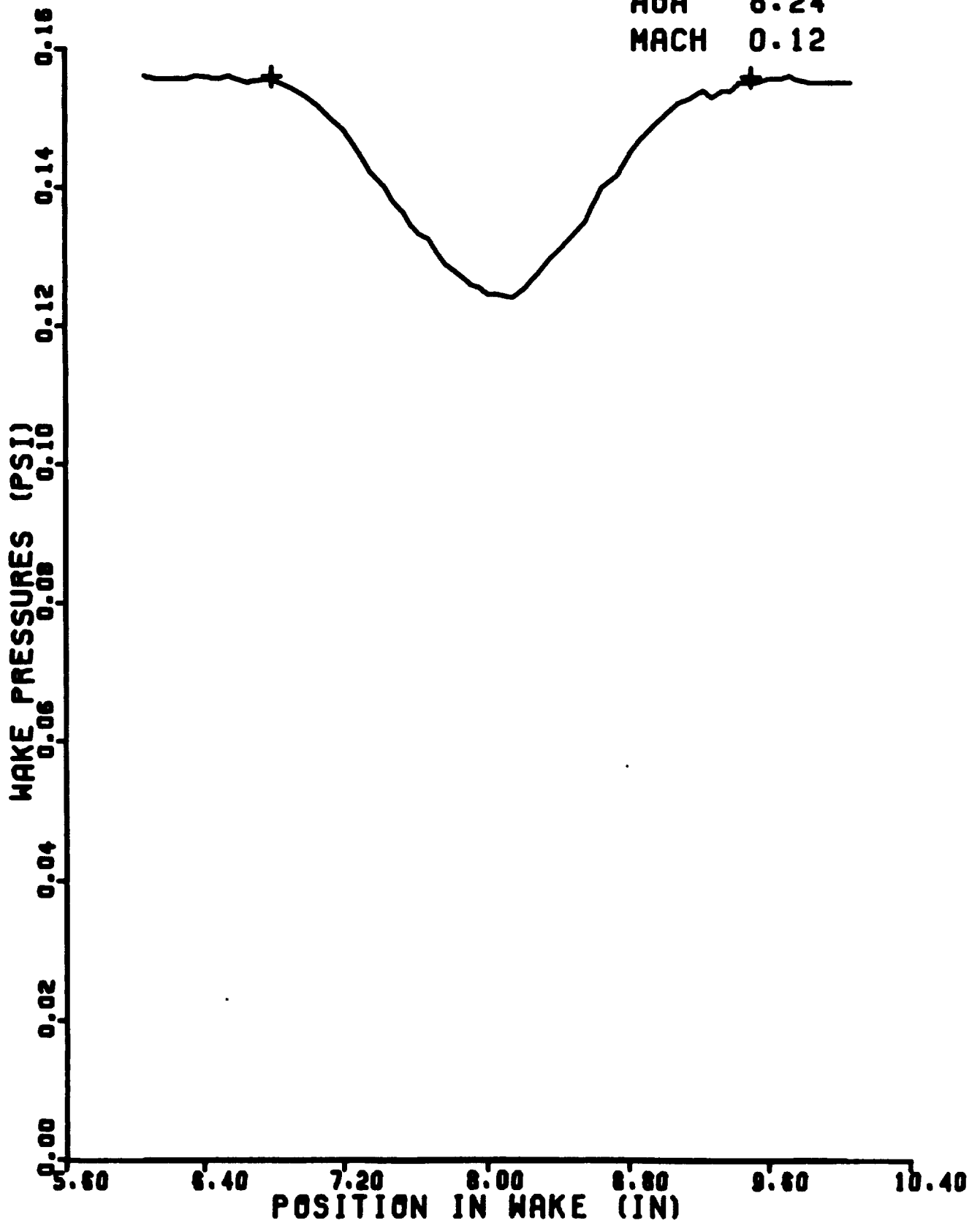
RUN 0369  
CD 0.0090  
AOA 4.12  
MACH 0.12



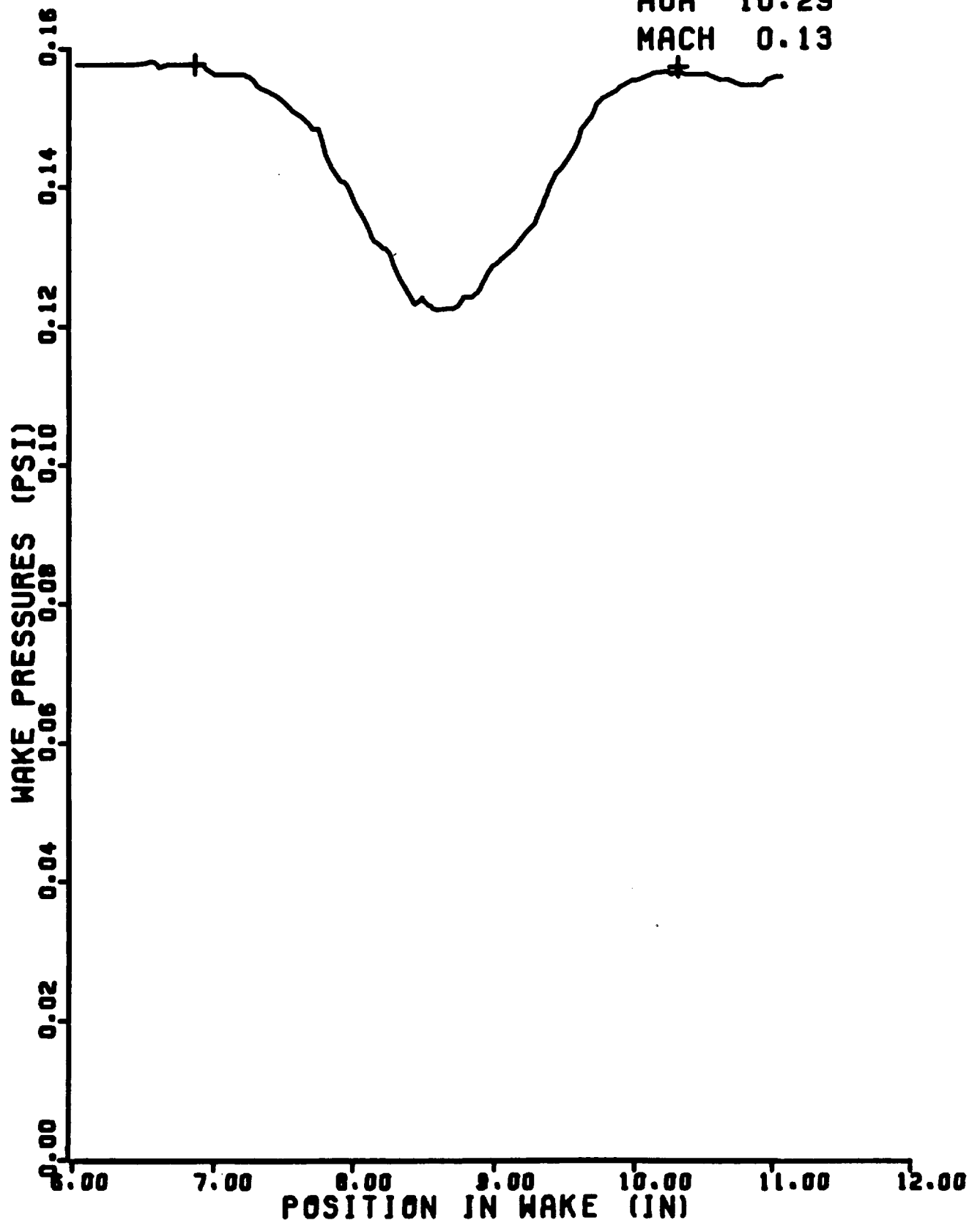
RUN 0371  
CD 0.0096  
AOA 6.18  
MACH 0.12



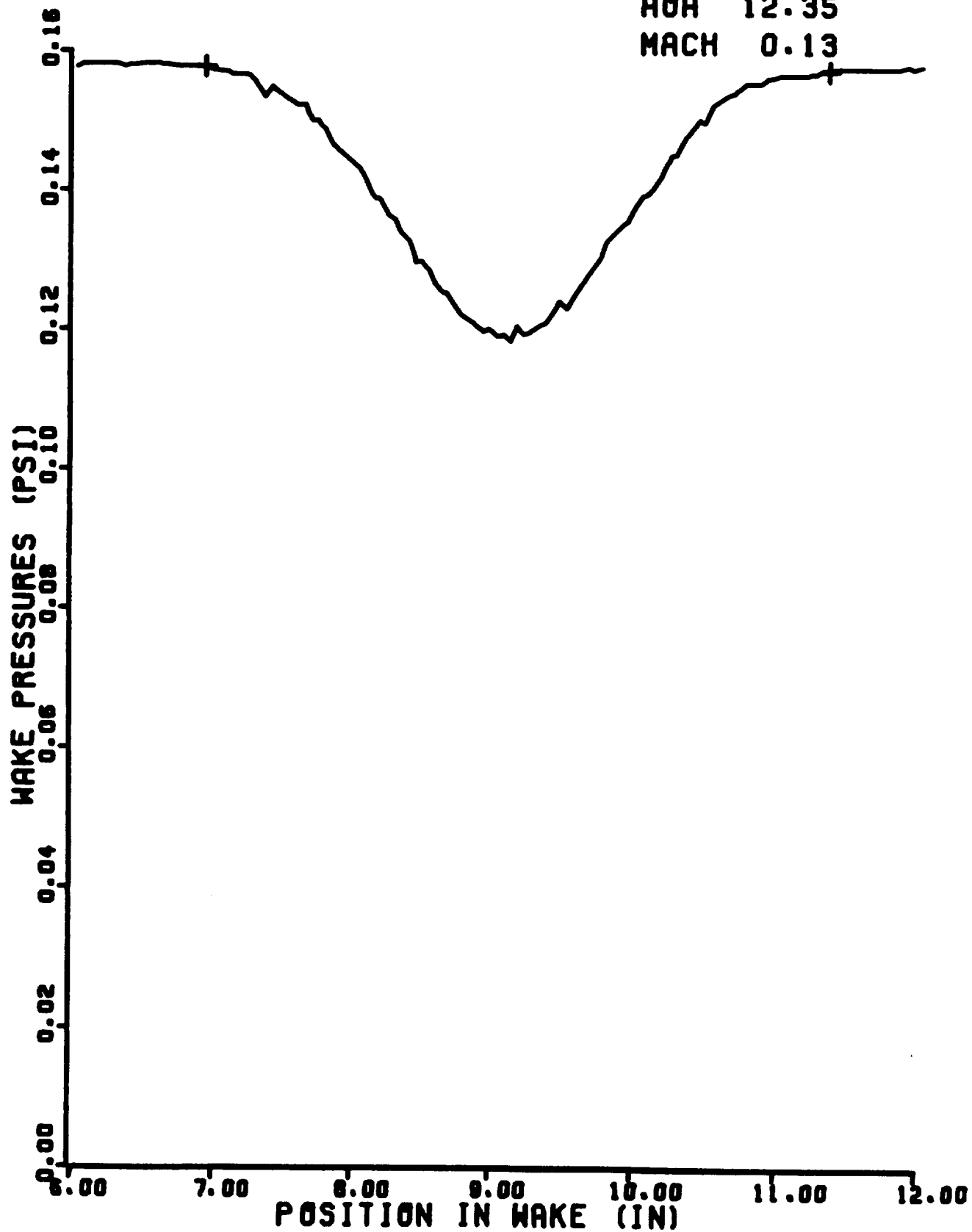
RUN 0373  
CD 0.0111  
AOA 8.24  
MACH 0.12



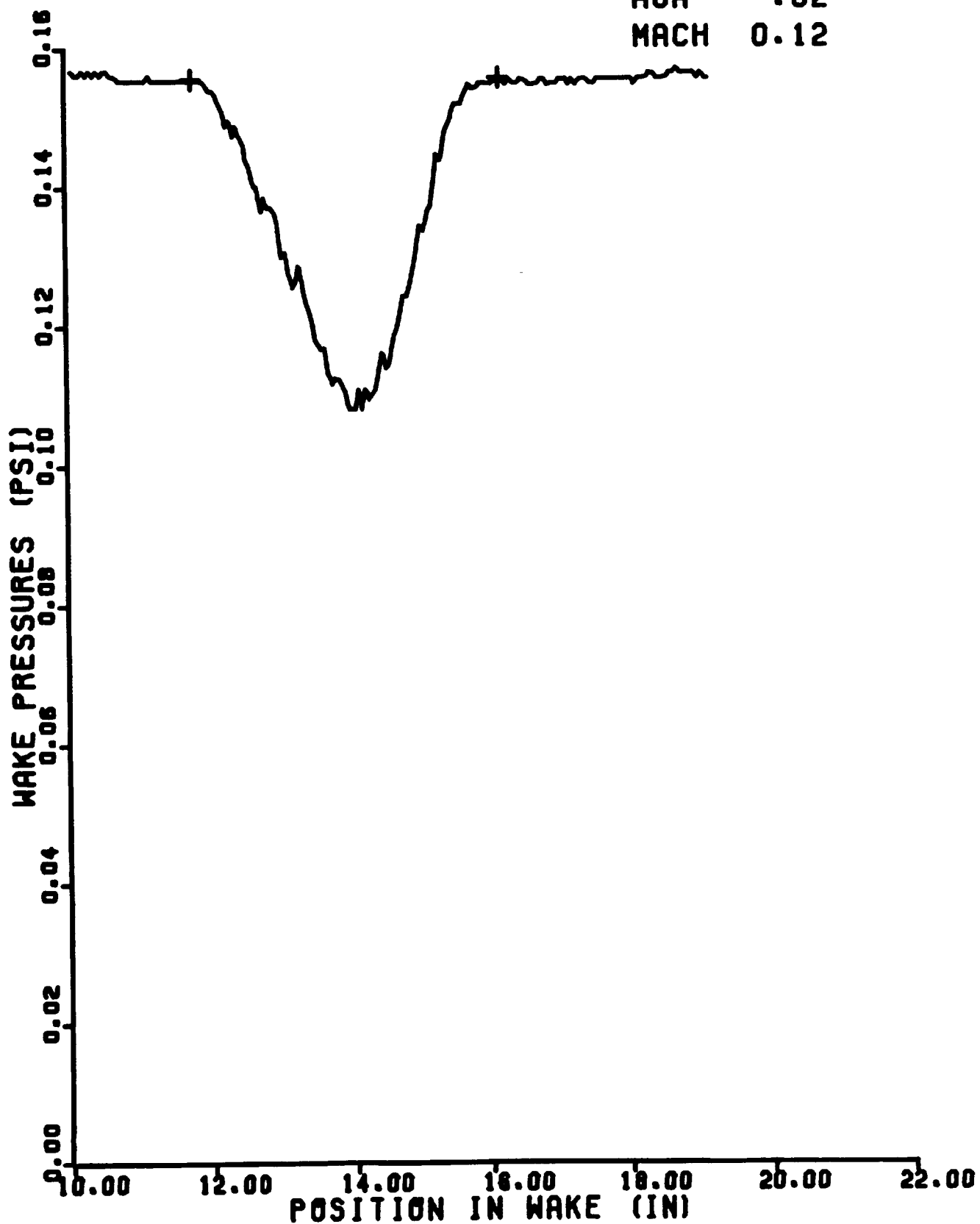
RUN 0375  
CD 0.0139  
AOA 10.29  
MACH 0.13



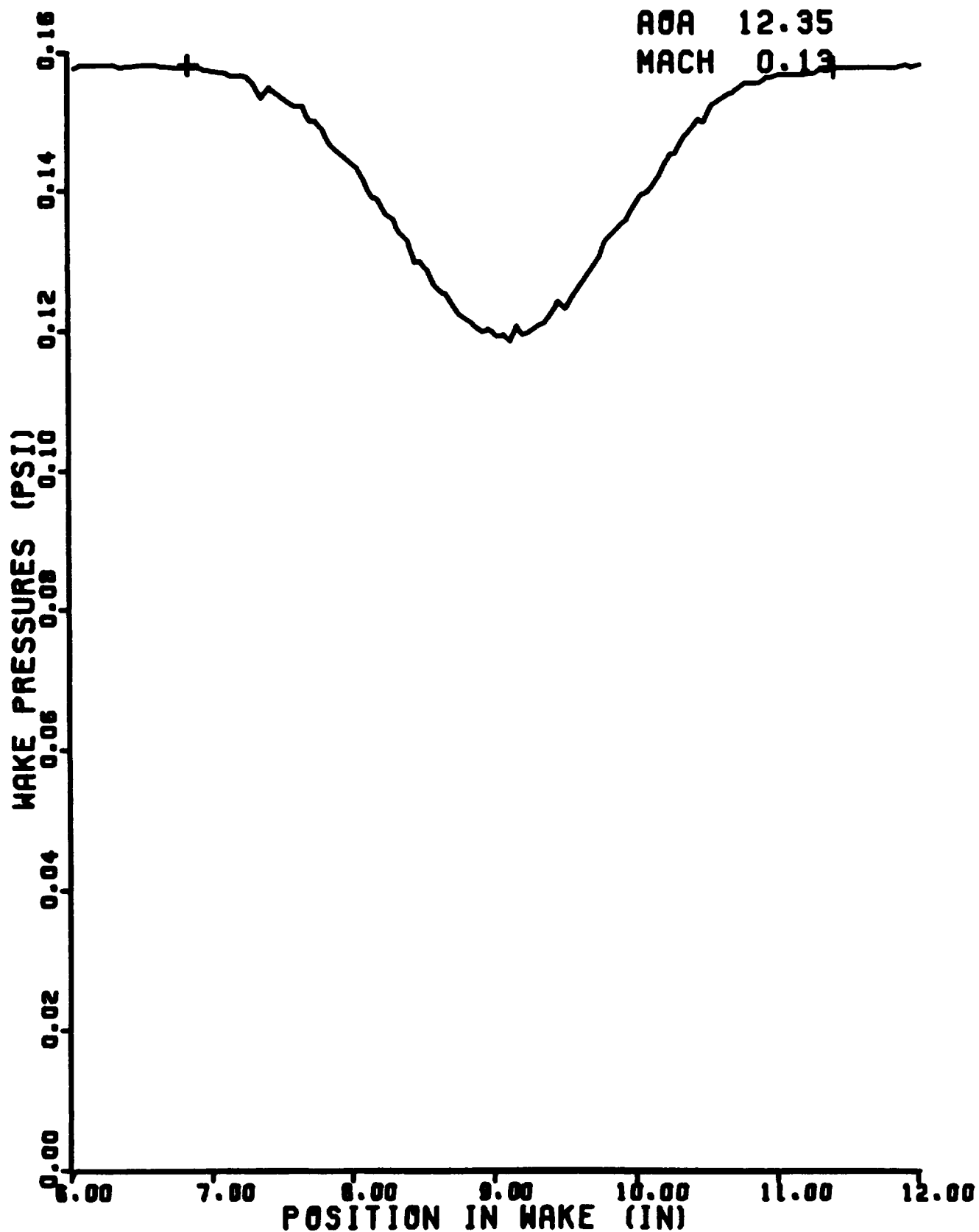
RUN 0377  
CD 0.0200  
AOA 12.35  
MACH 0.13



RUN 0439  
CD 0.0251  
AOA -.02  
MACH 0.12

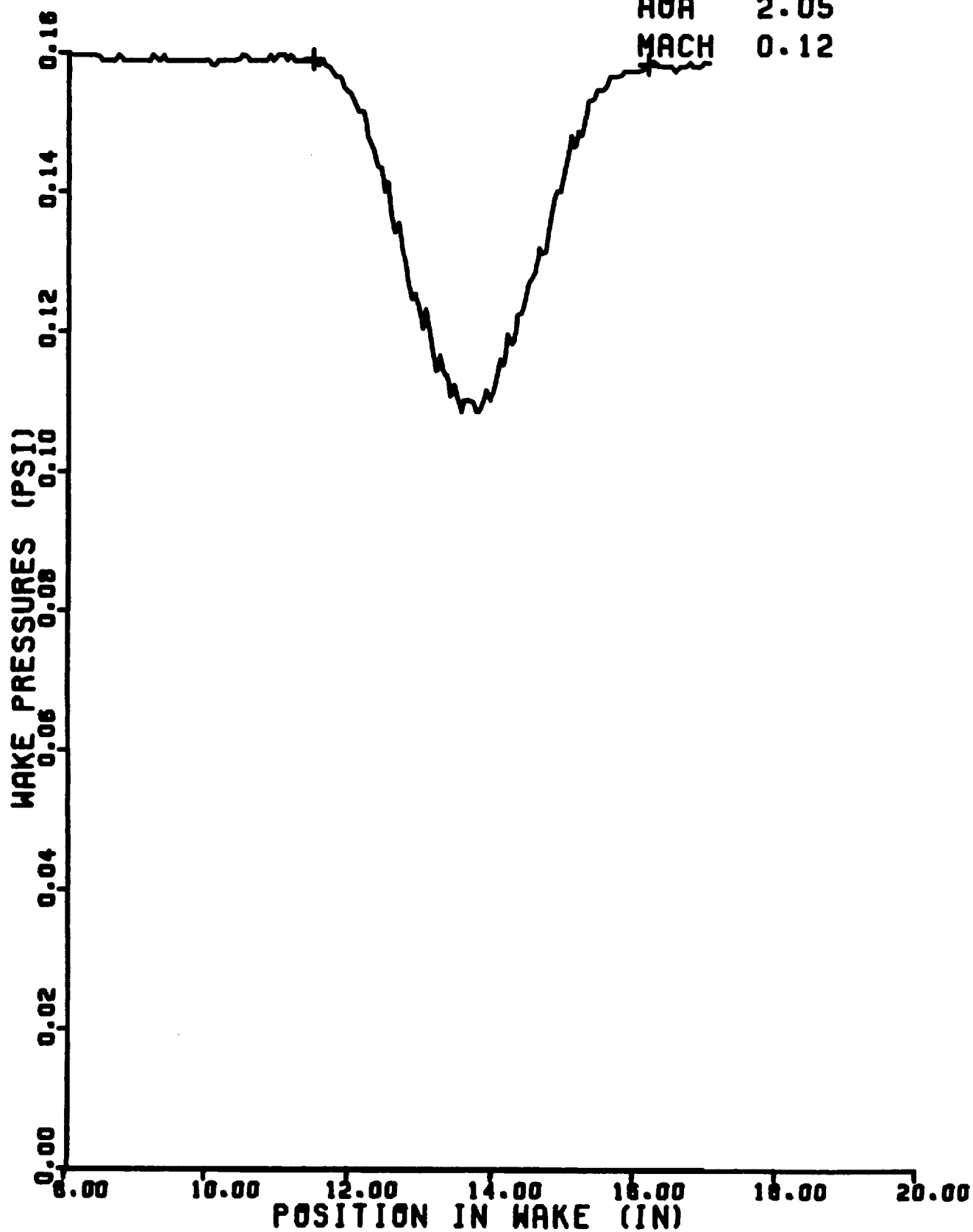


RUN 0377  
CD 0.0200  
AOA 12.35  
MACH 0.13

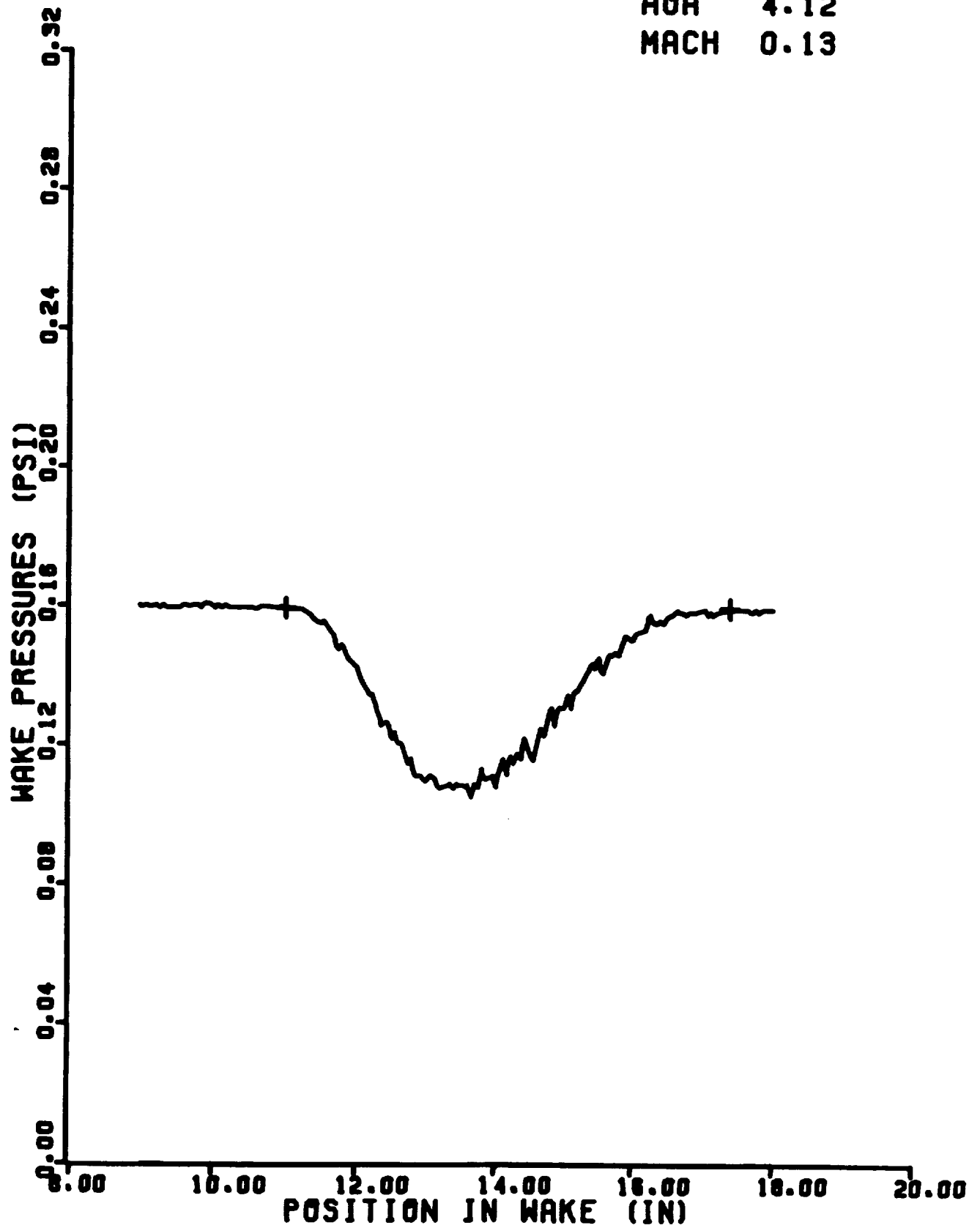




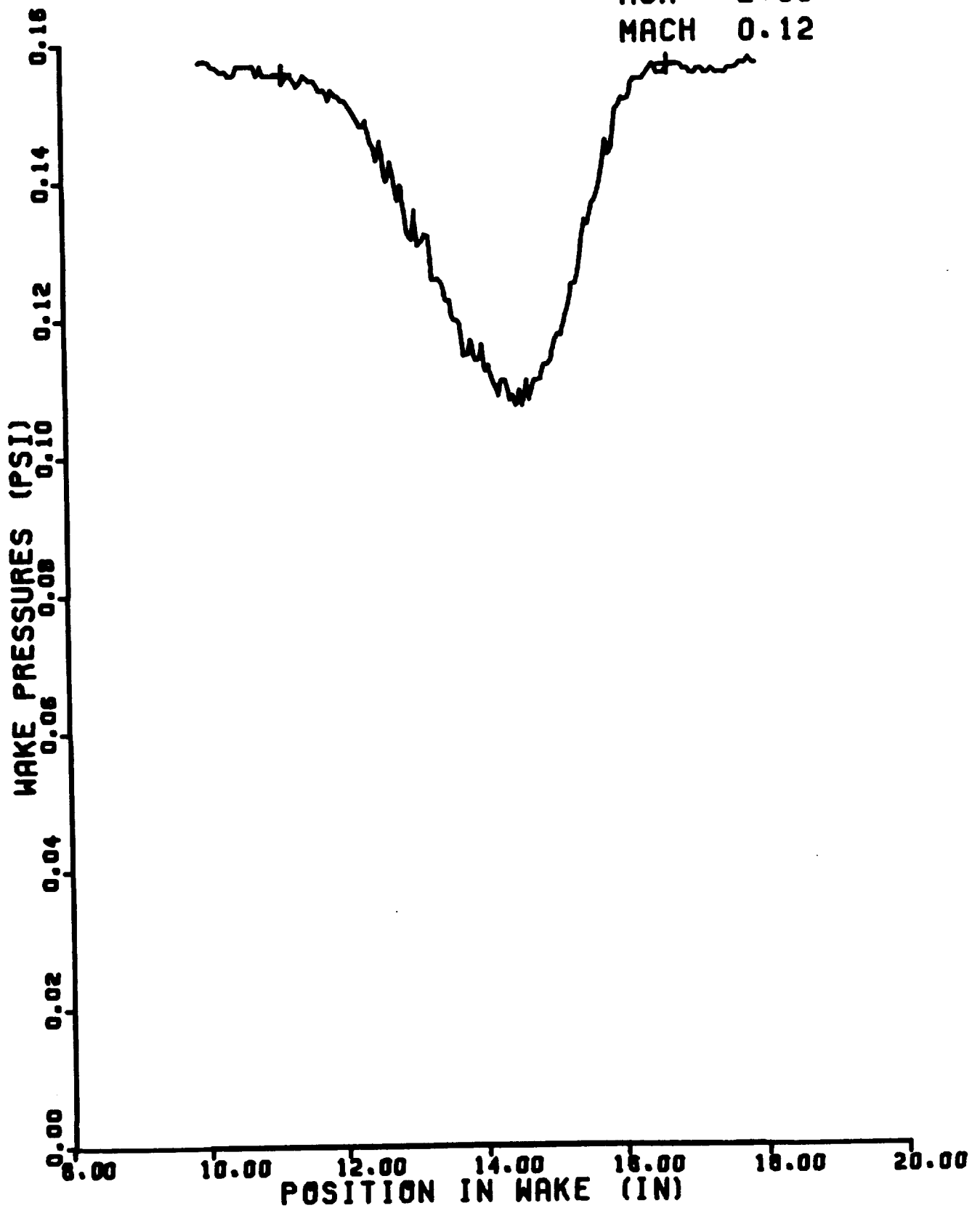
RUN 0441  
CD 0.0275  
AOA 2.05  
MACH 0.12



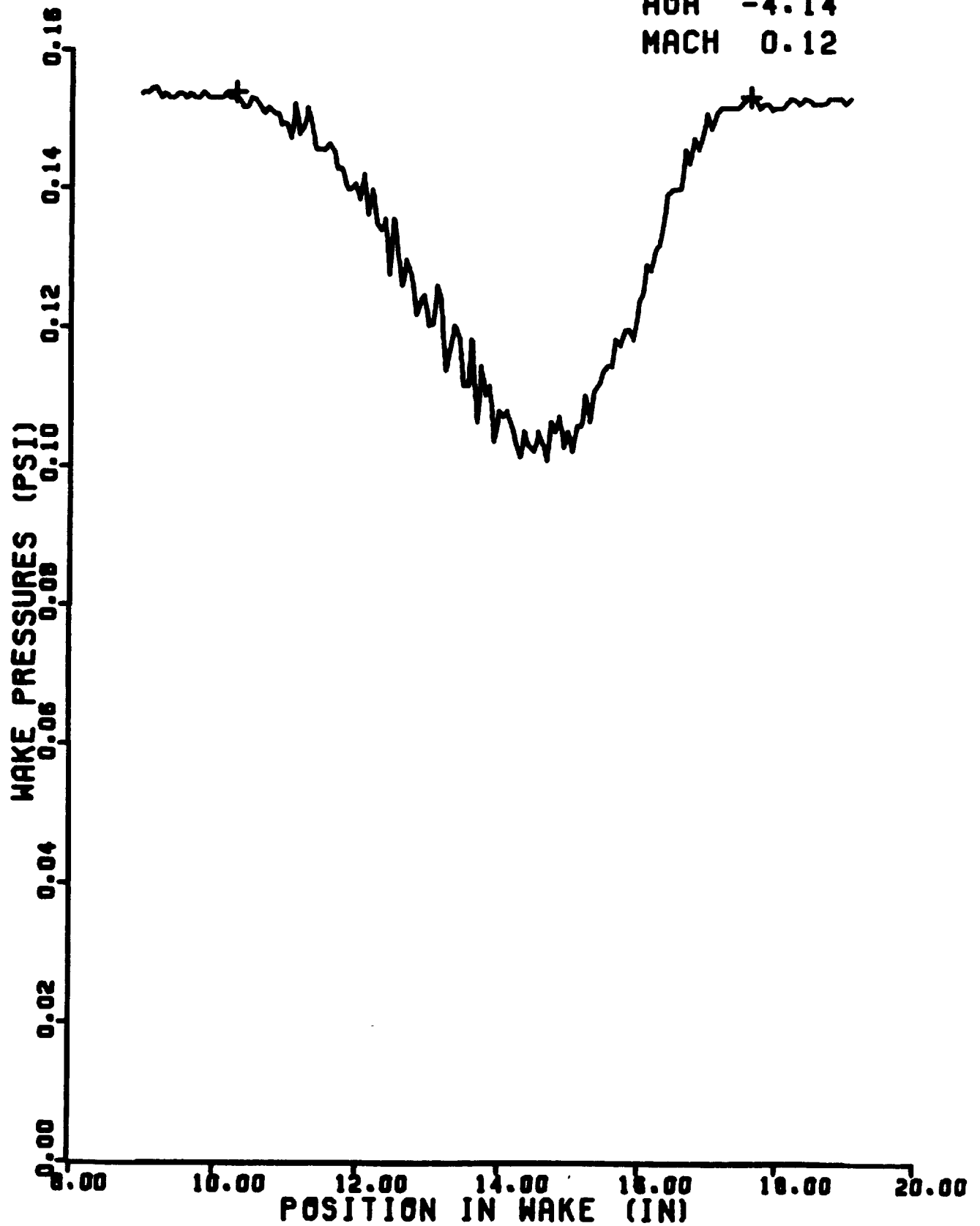
RUN 0443  
CD 0.0393  
AOA 4.12  
MACH 0.13



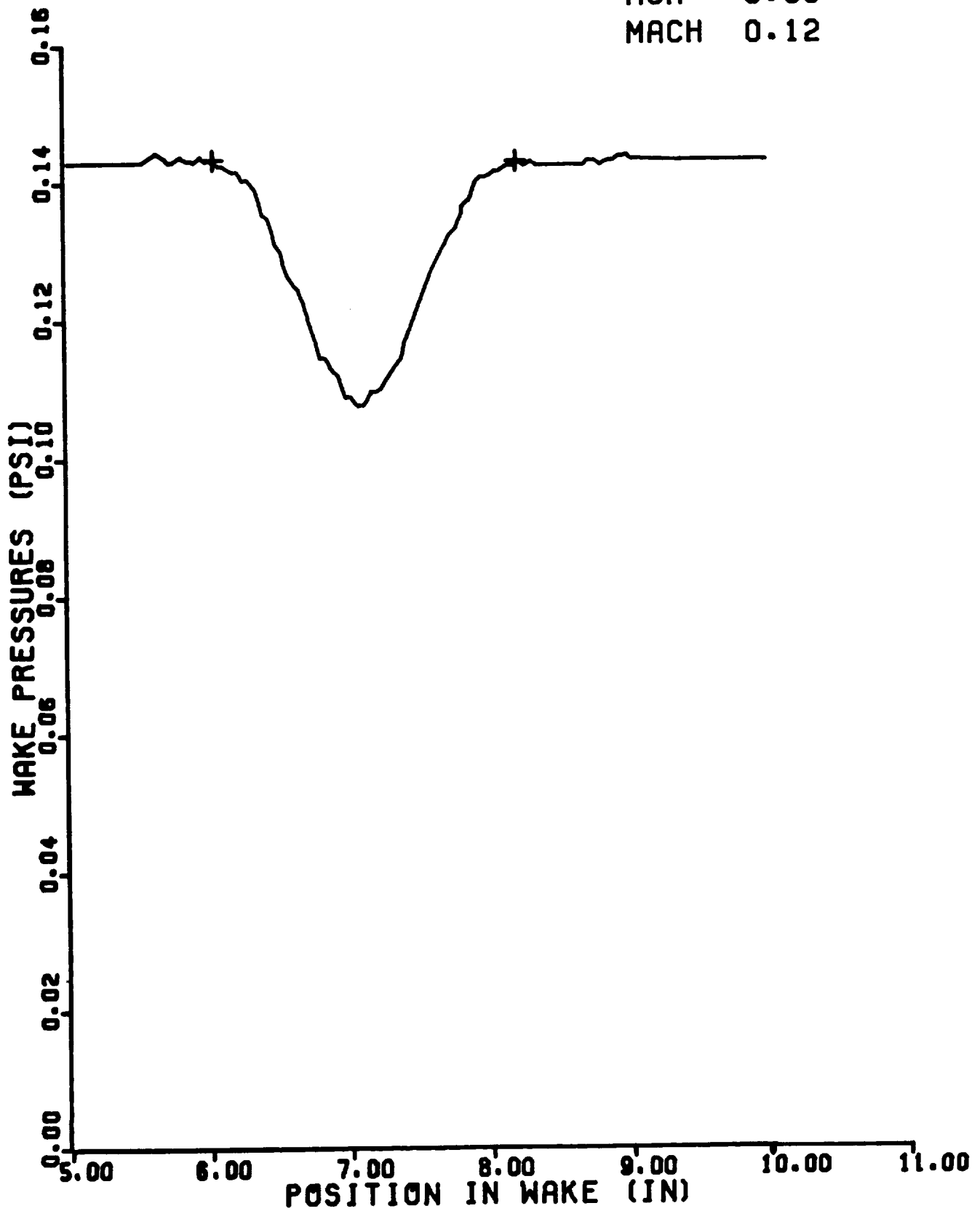
RUN 0450  
CD 0.0335  
AOA -2.09  
MACH 0.12



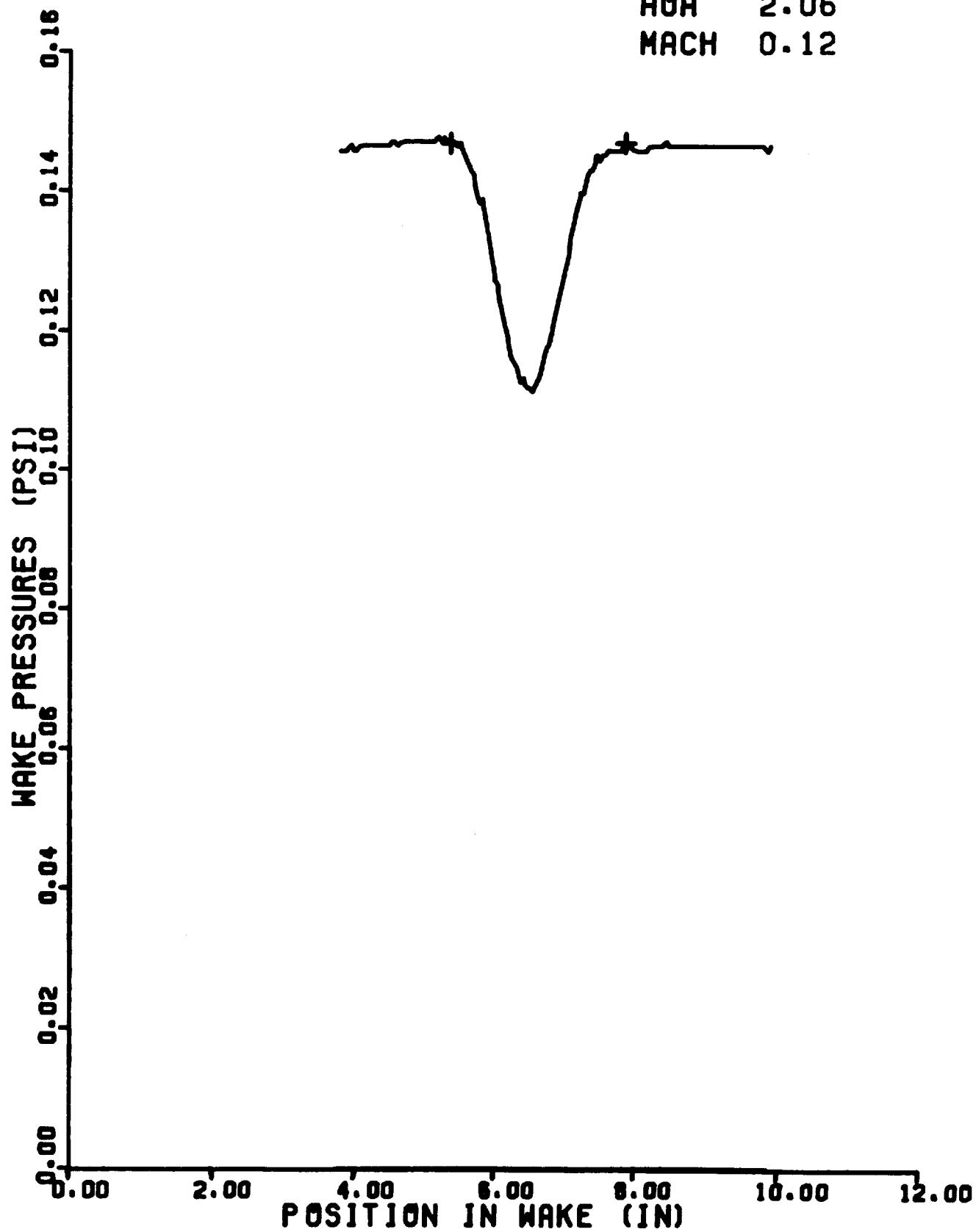
RUN 0451  
CD 0.0479  
AOA -4.14  
MACH 0.12



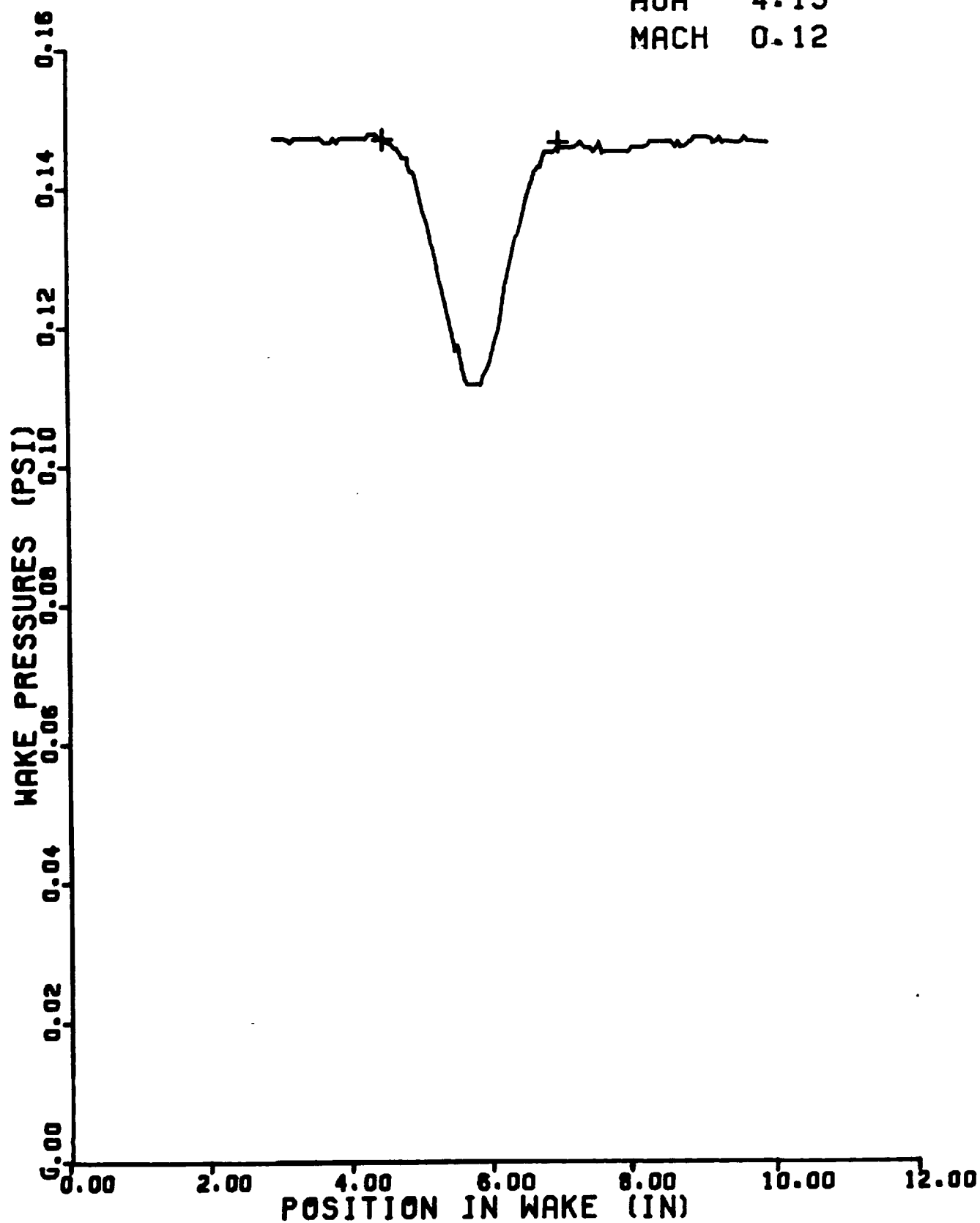
RUN 0751  
CD 0.0106  
AOA 0.00  
MACH 0.12



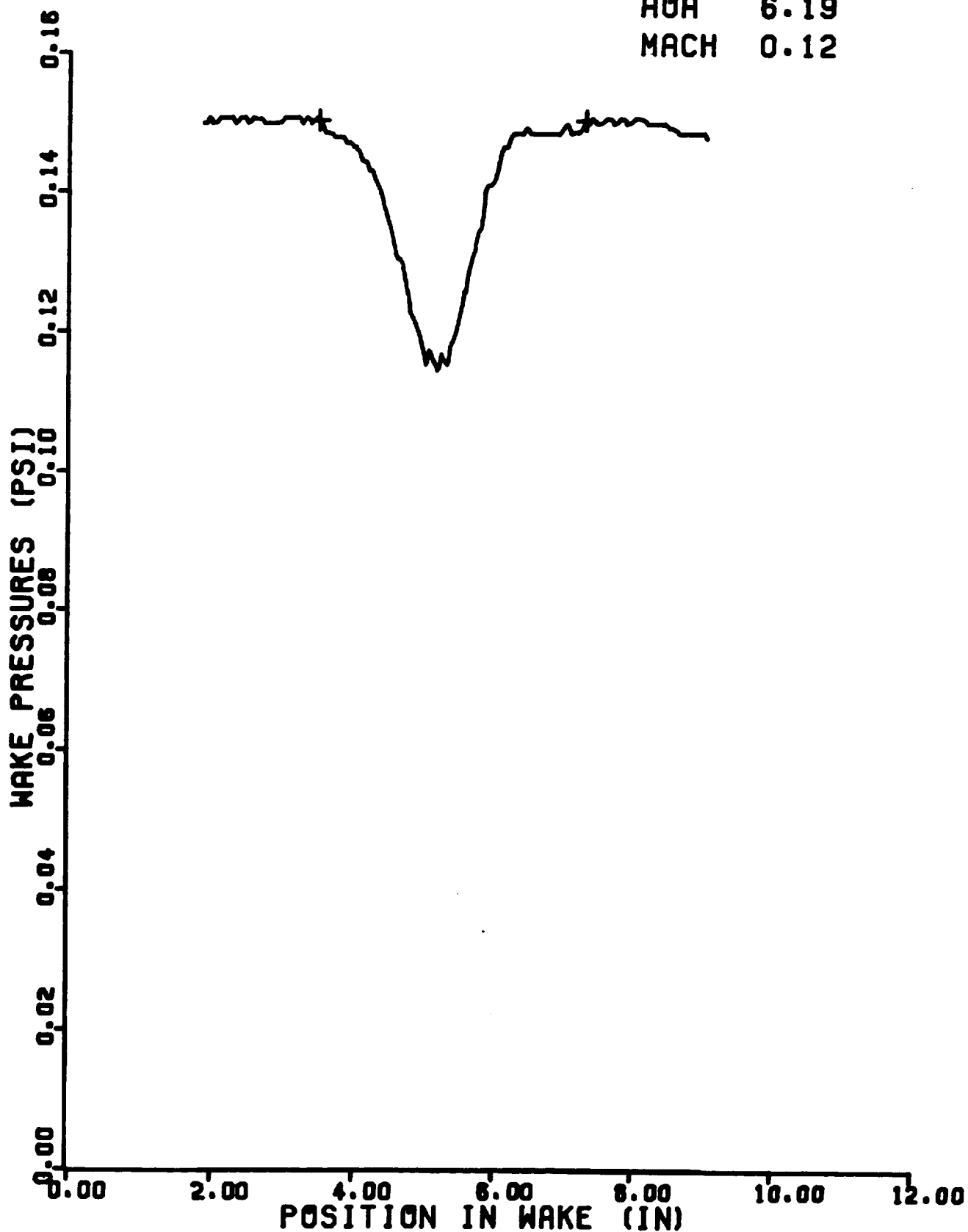
RUN 0752  
CD 0.0108  
AOA 2.06  
MACH 0.12



RUN 0753  
CD 0.1120  
AOA 4.13  
MACH 0.12

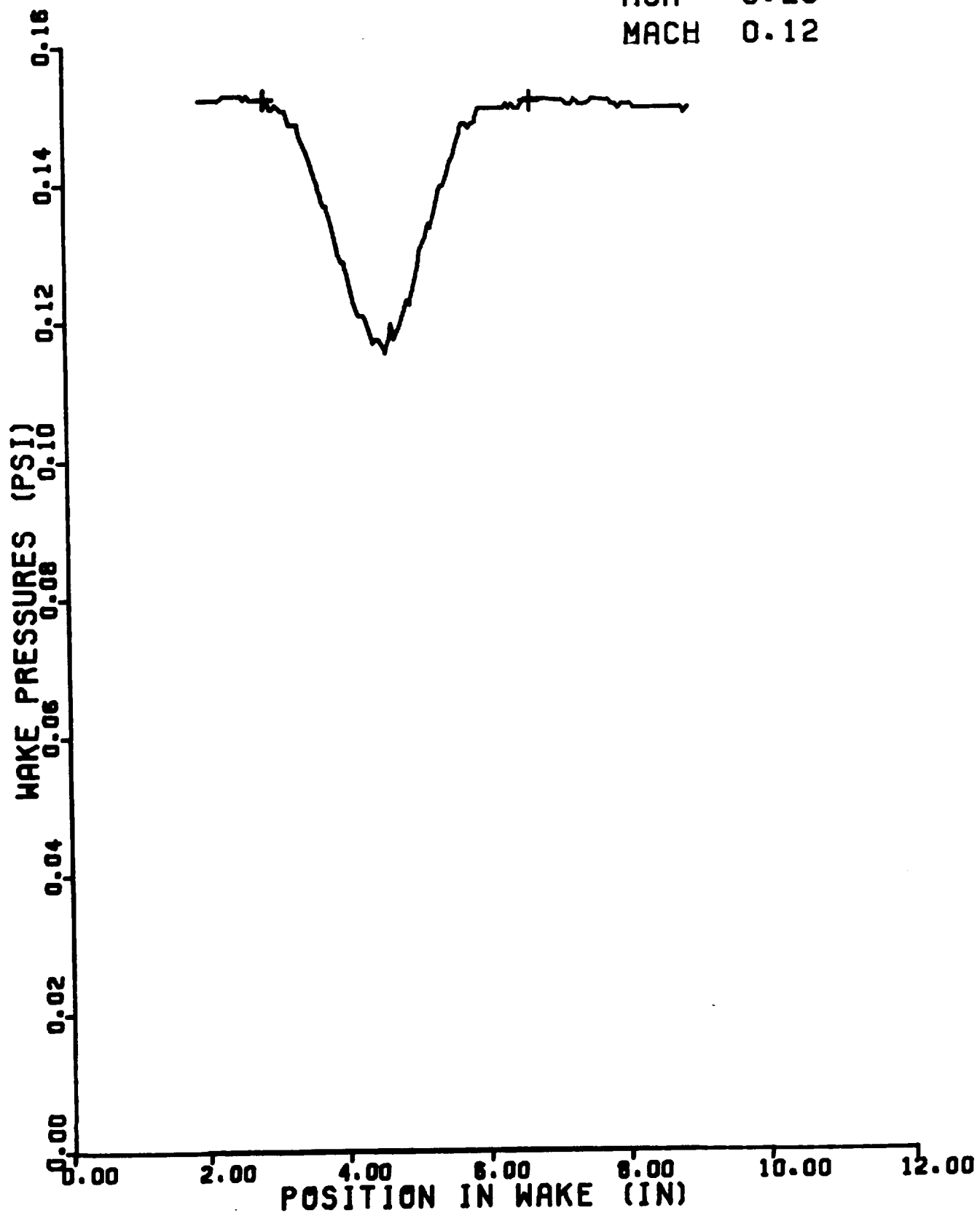


RUN 0756  
CD 0.0133  
AOA 6.19  
MACH 0.12

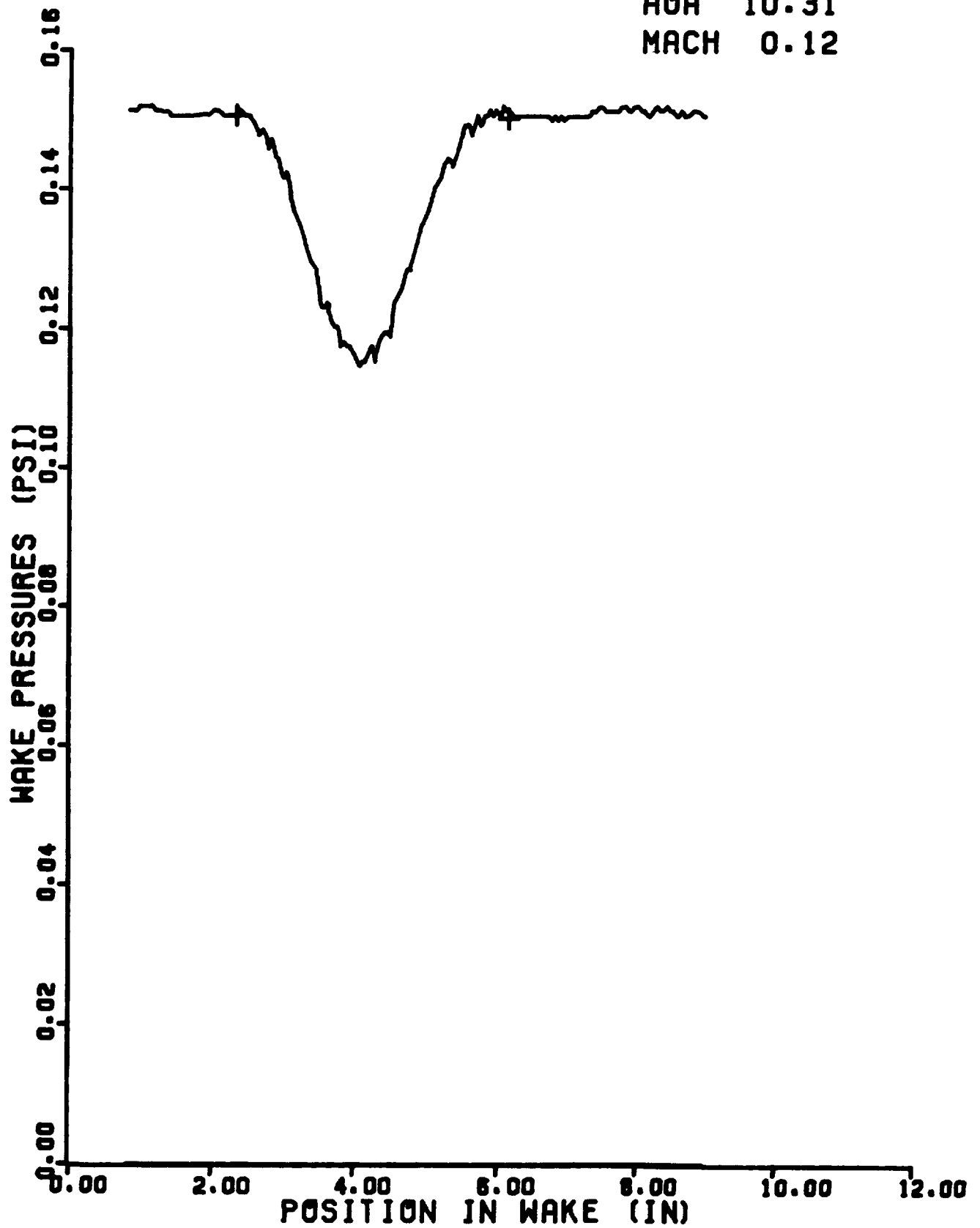




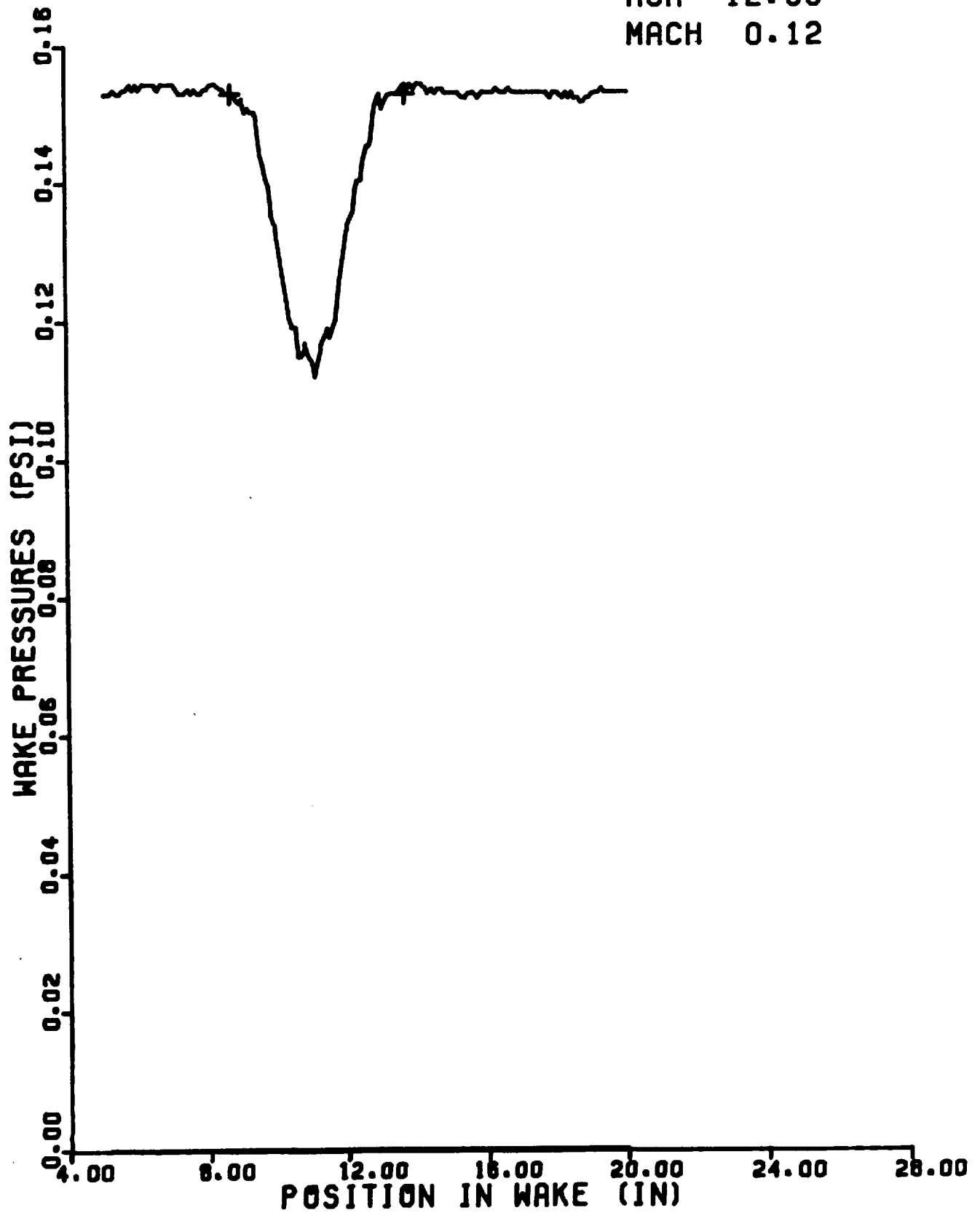
RUN 0757  
CD 0.0135  
AOA 8.25  
MACH 0.12



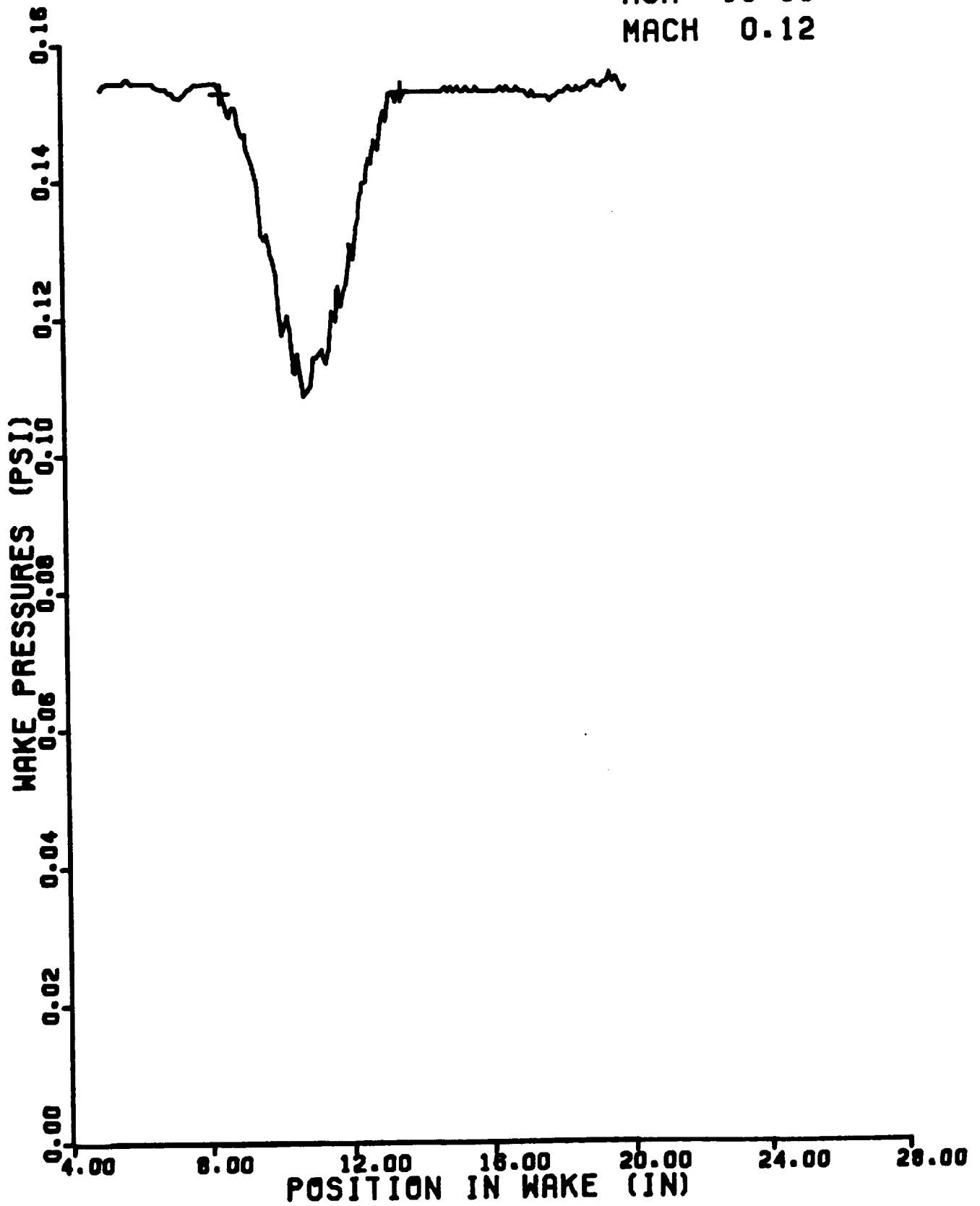
RUN 0758  
CD 0.0171  
AOA 10.31  
MACH 0.12



RUN 0759  
CD 0.0240  
AOA 12.36  
MACH 0.12

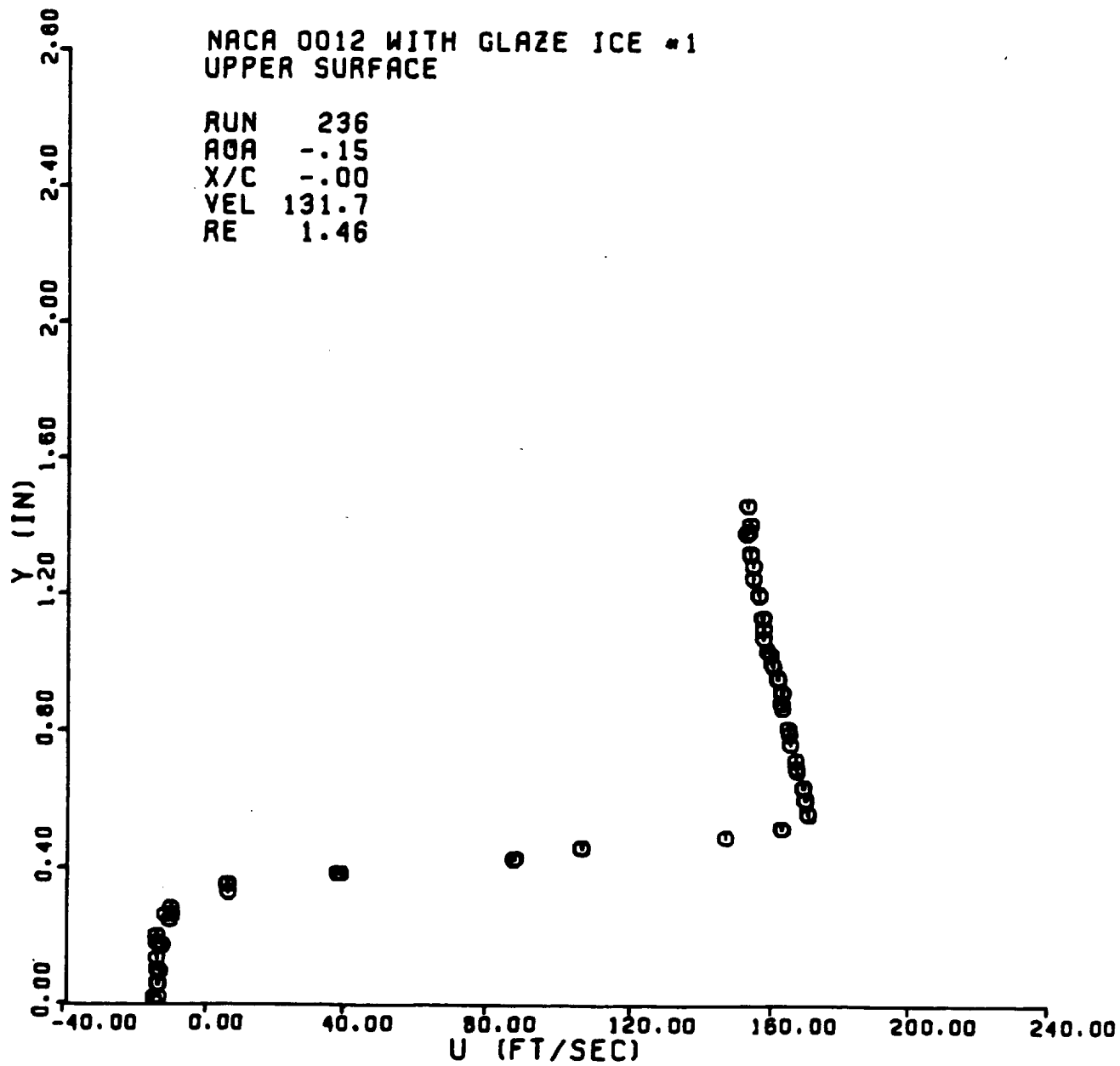


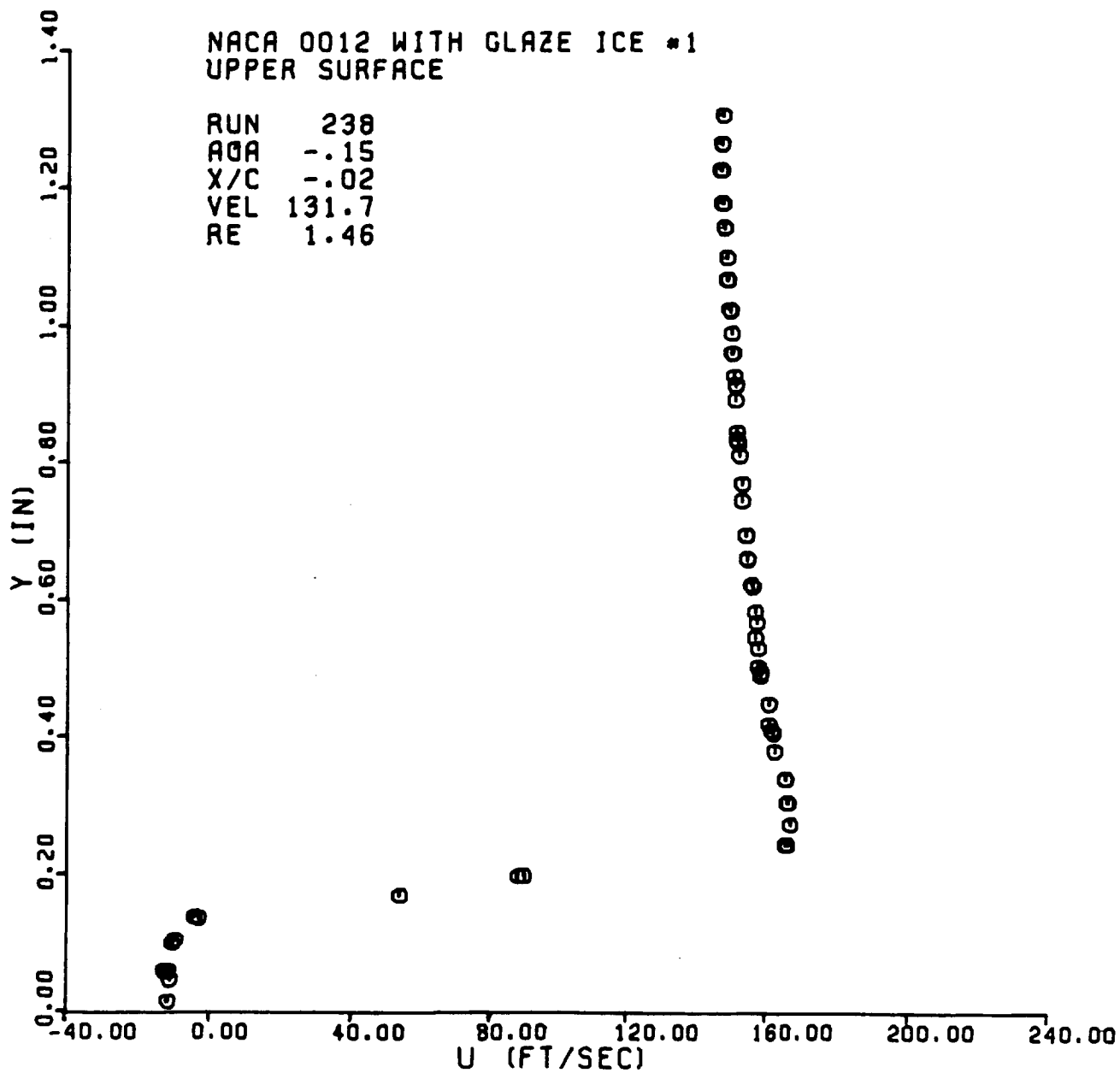
RUN 0761  
CD 0.0290  
AOA 13.38  
MACH 0.12

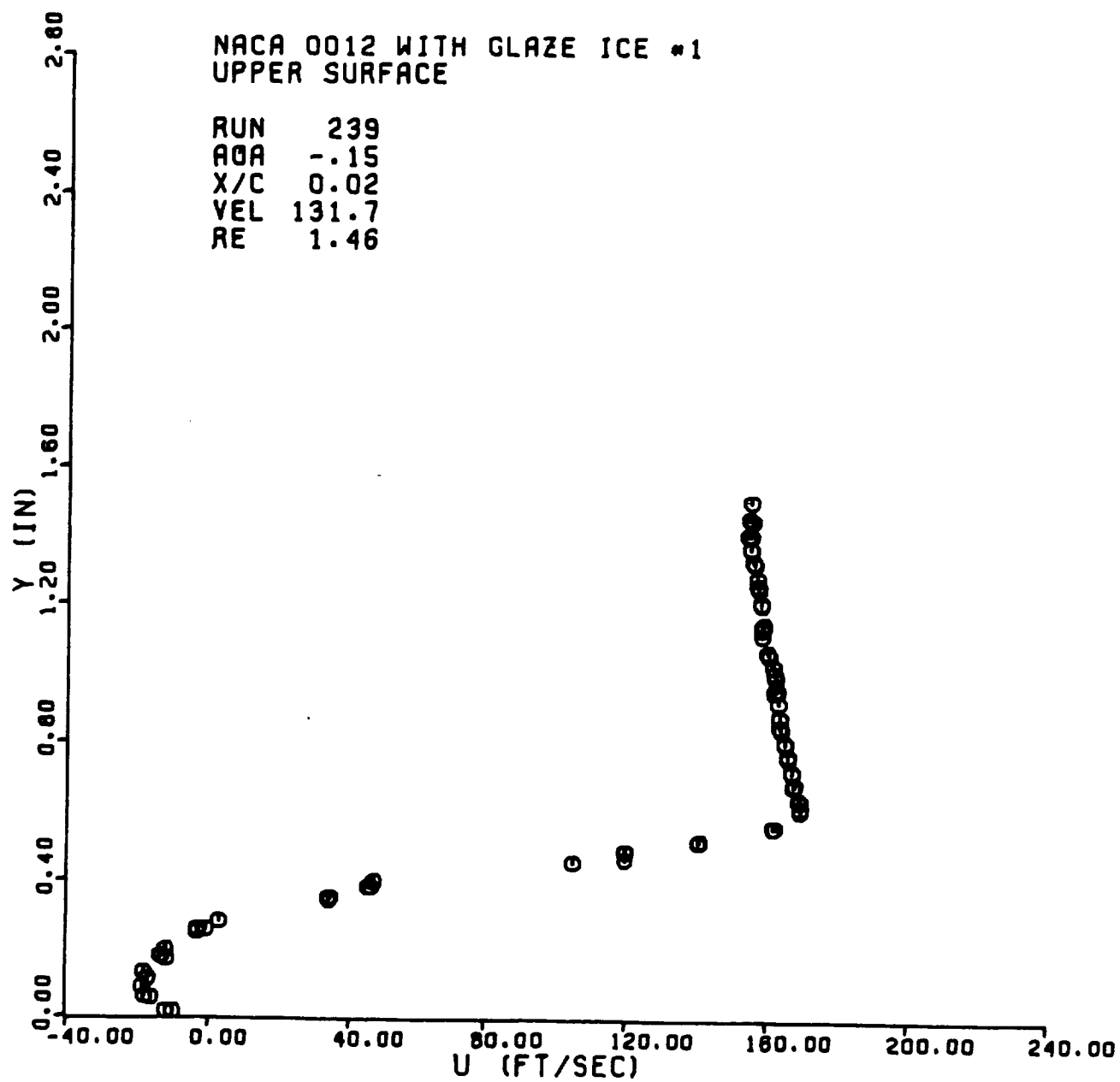


## APPENDIX D

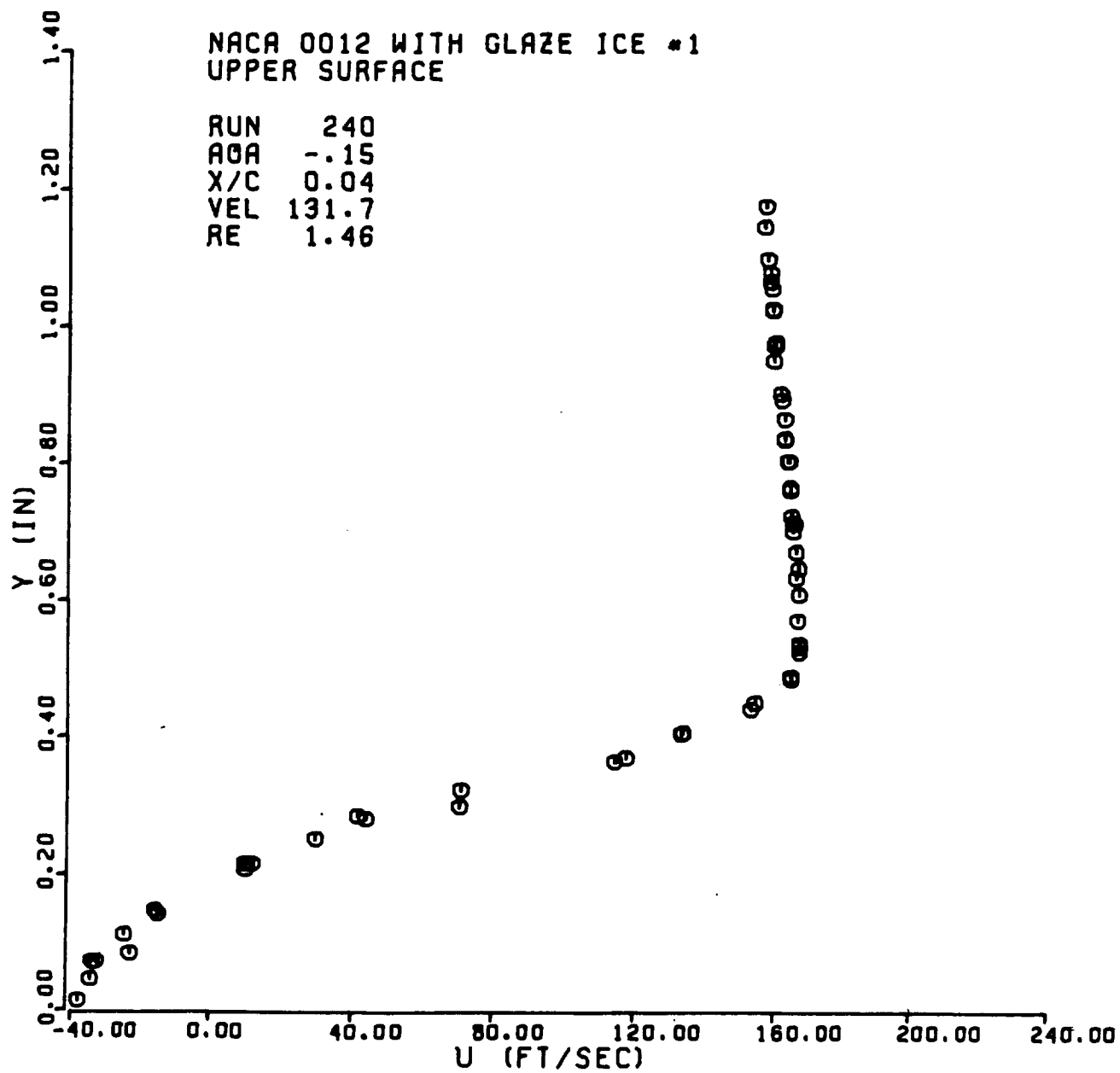
### VELOCITY PROFILES

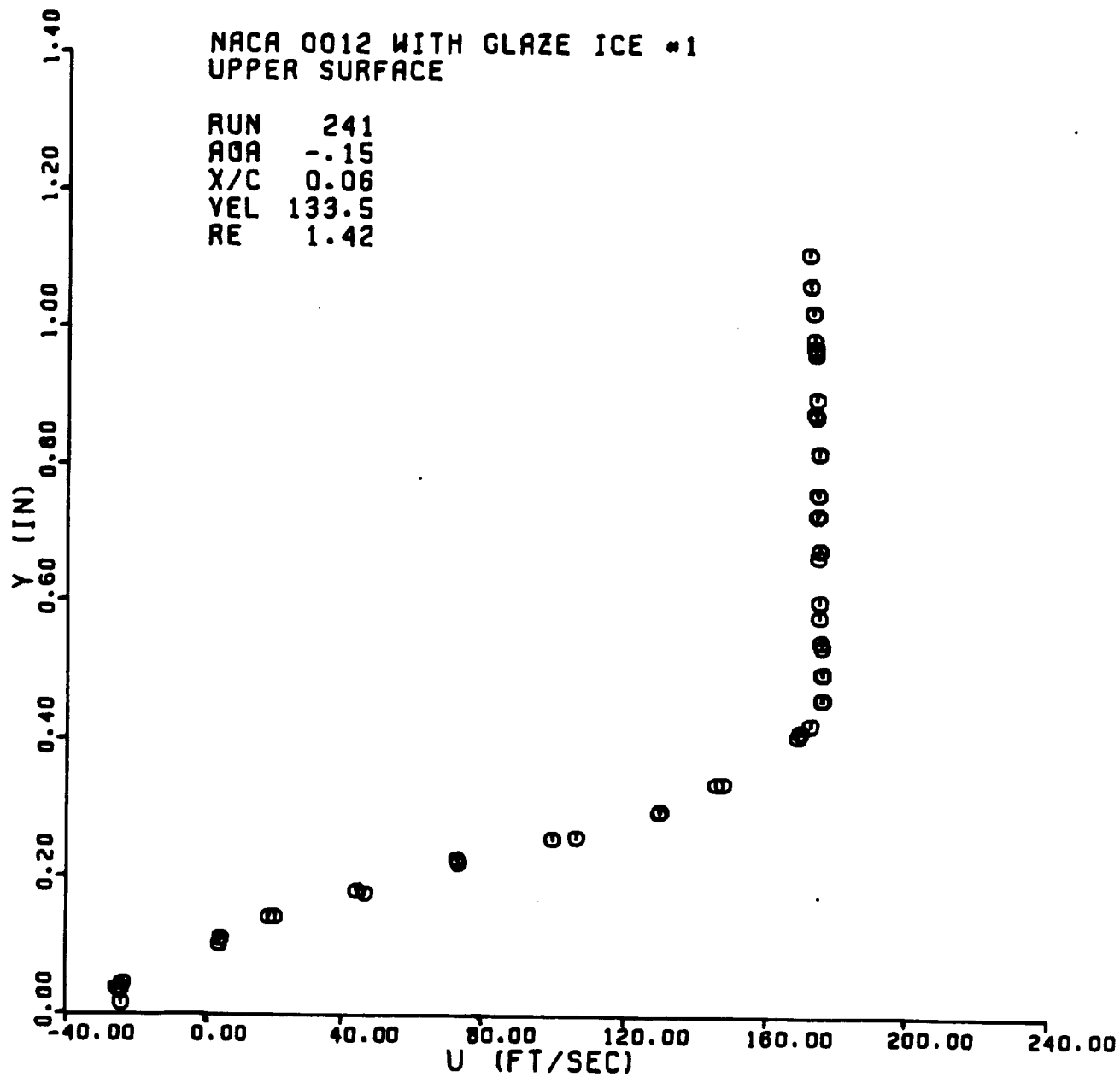


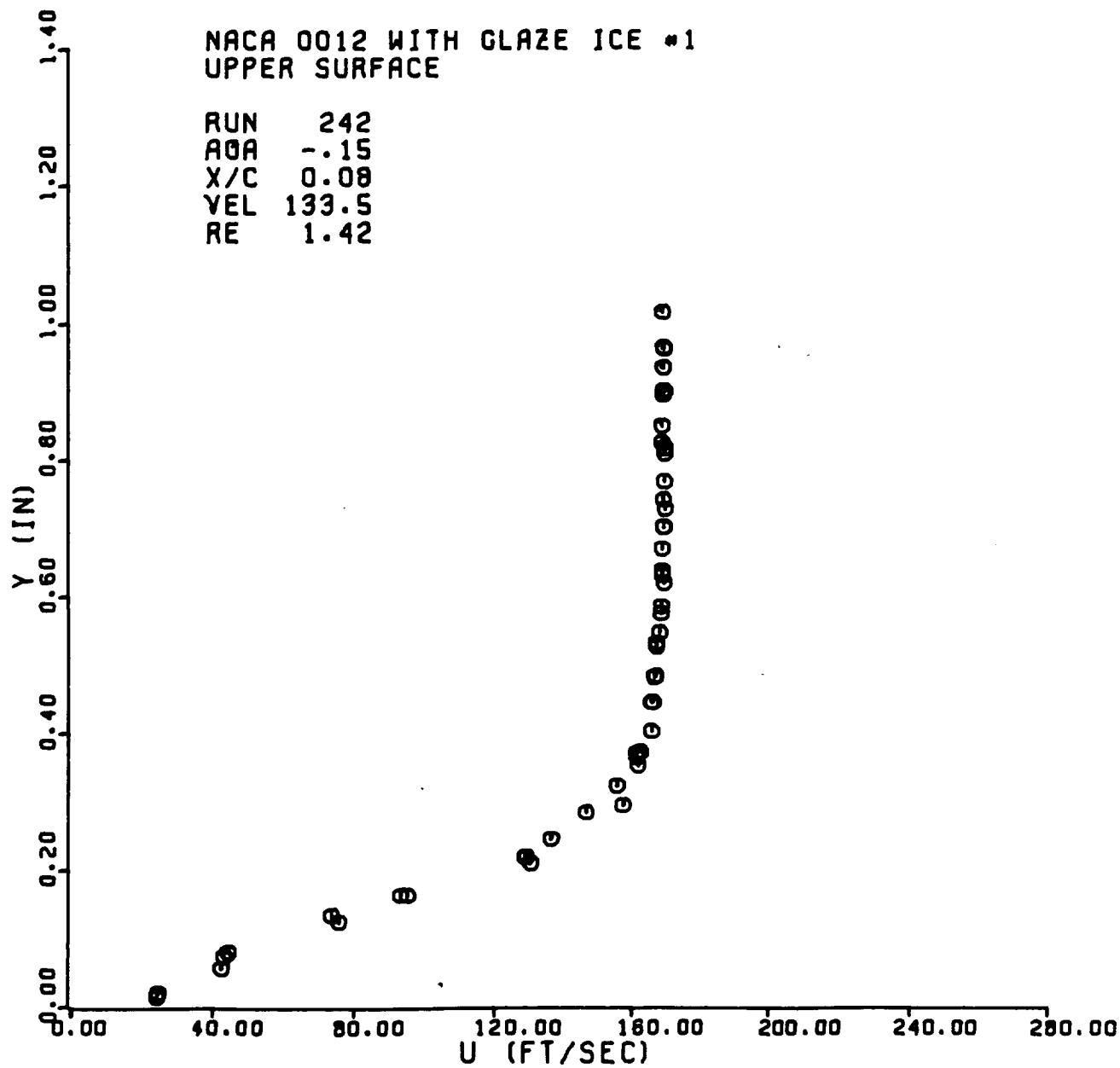


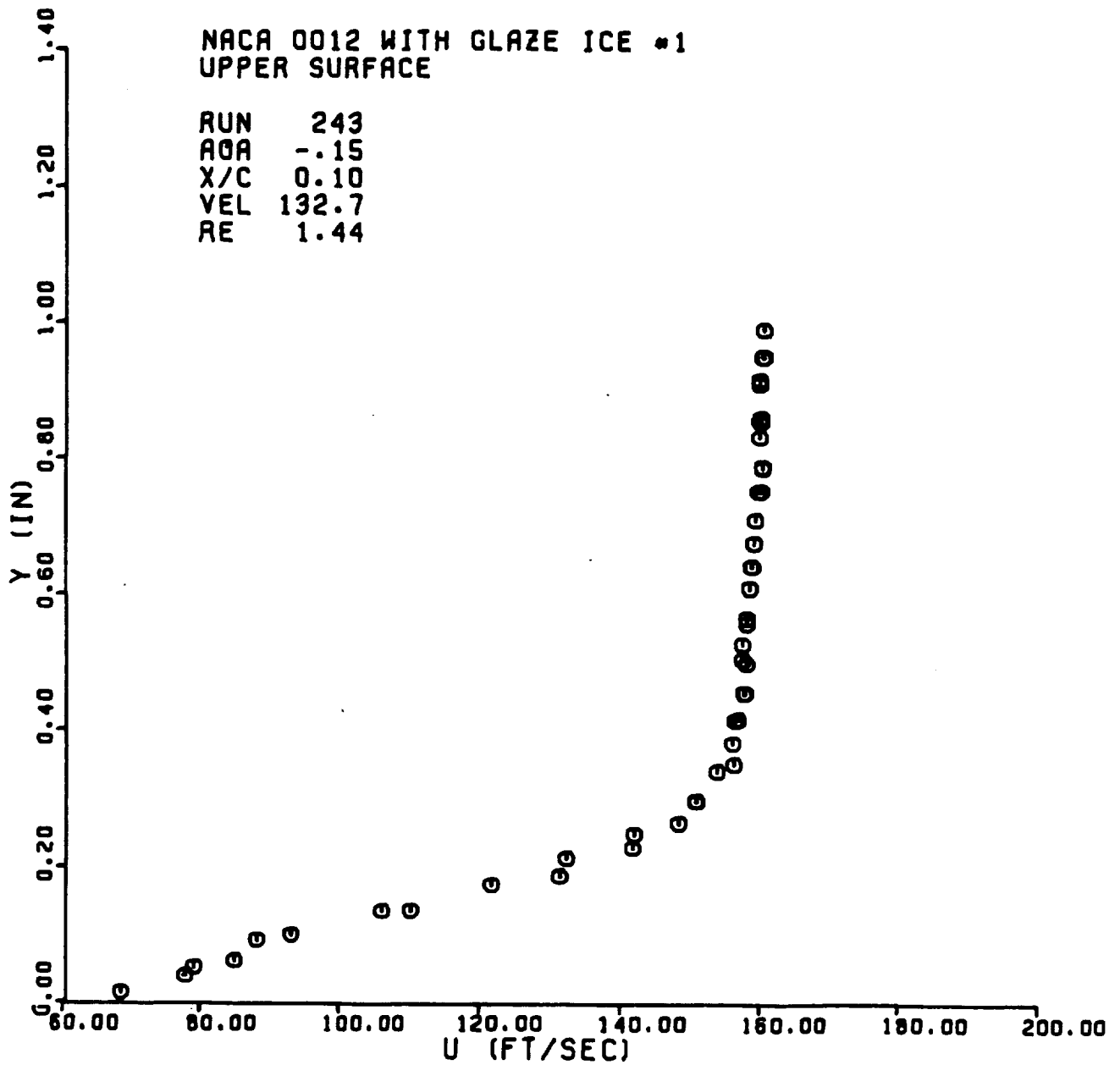


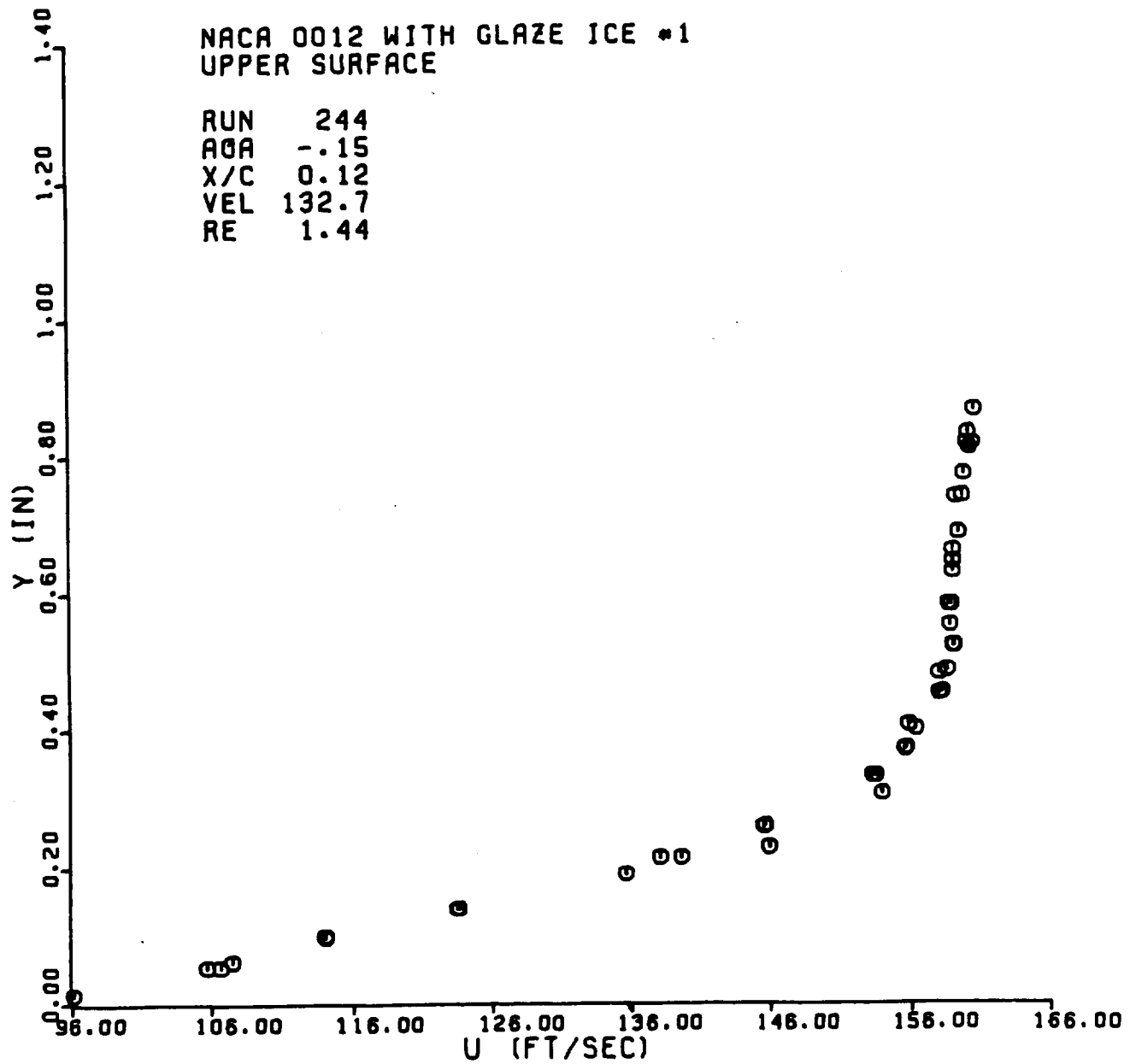


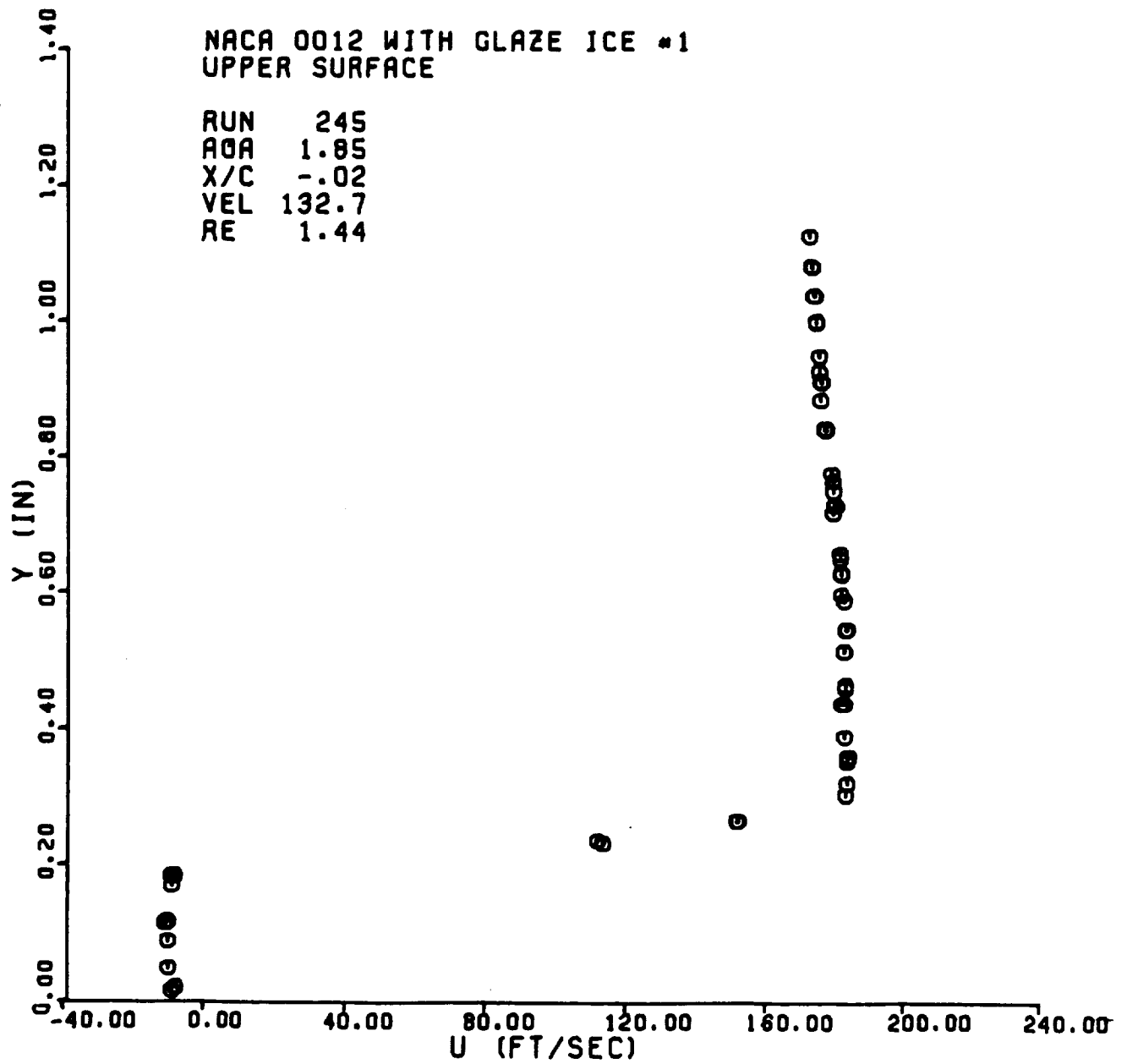


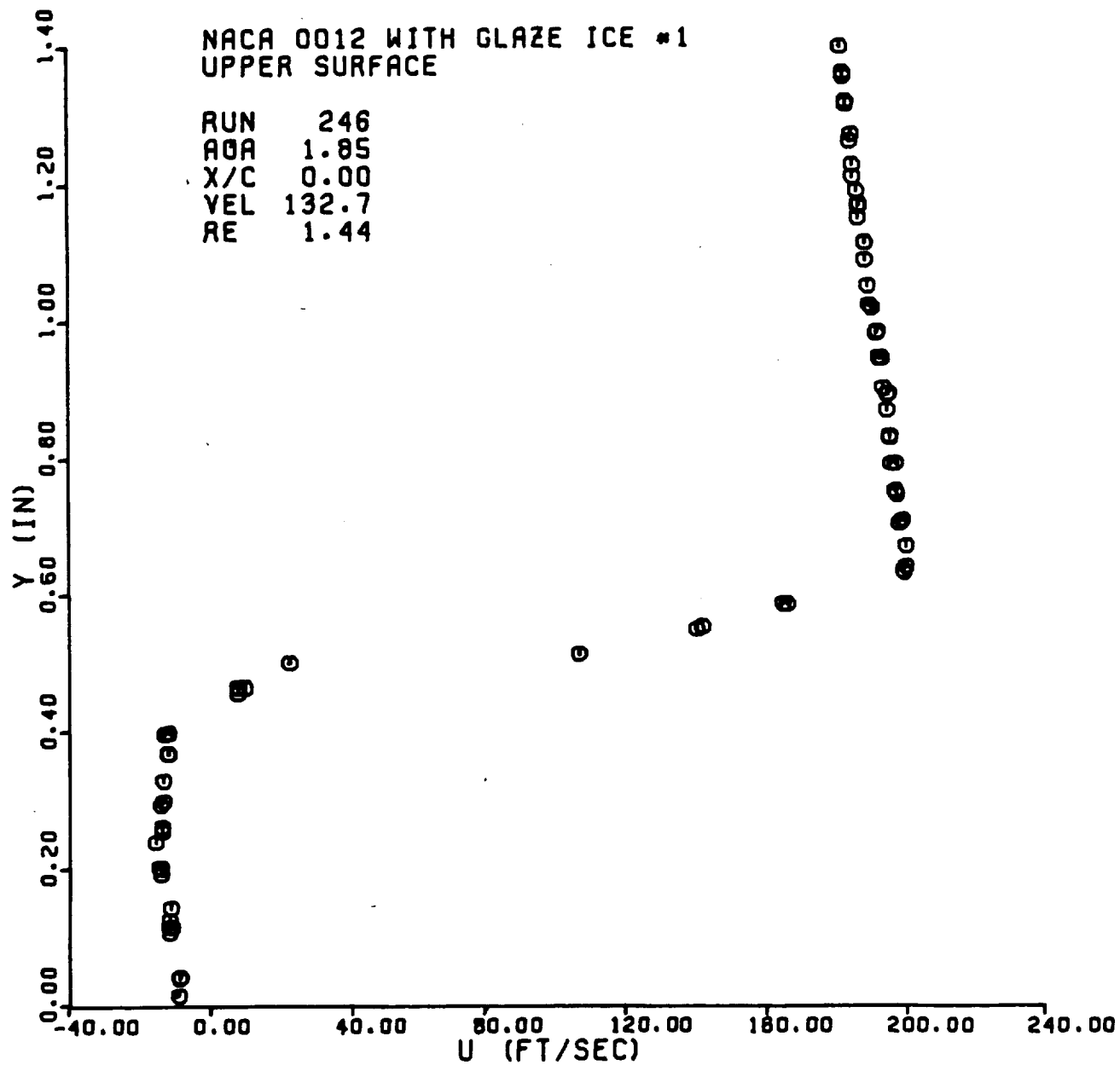


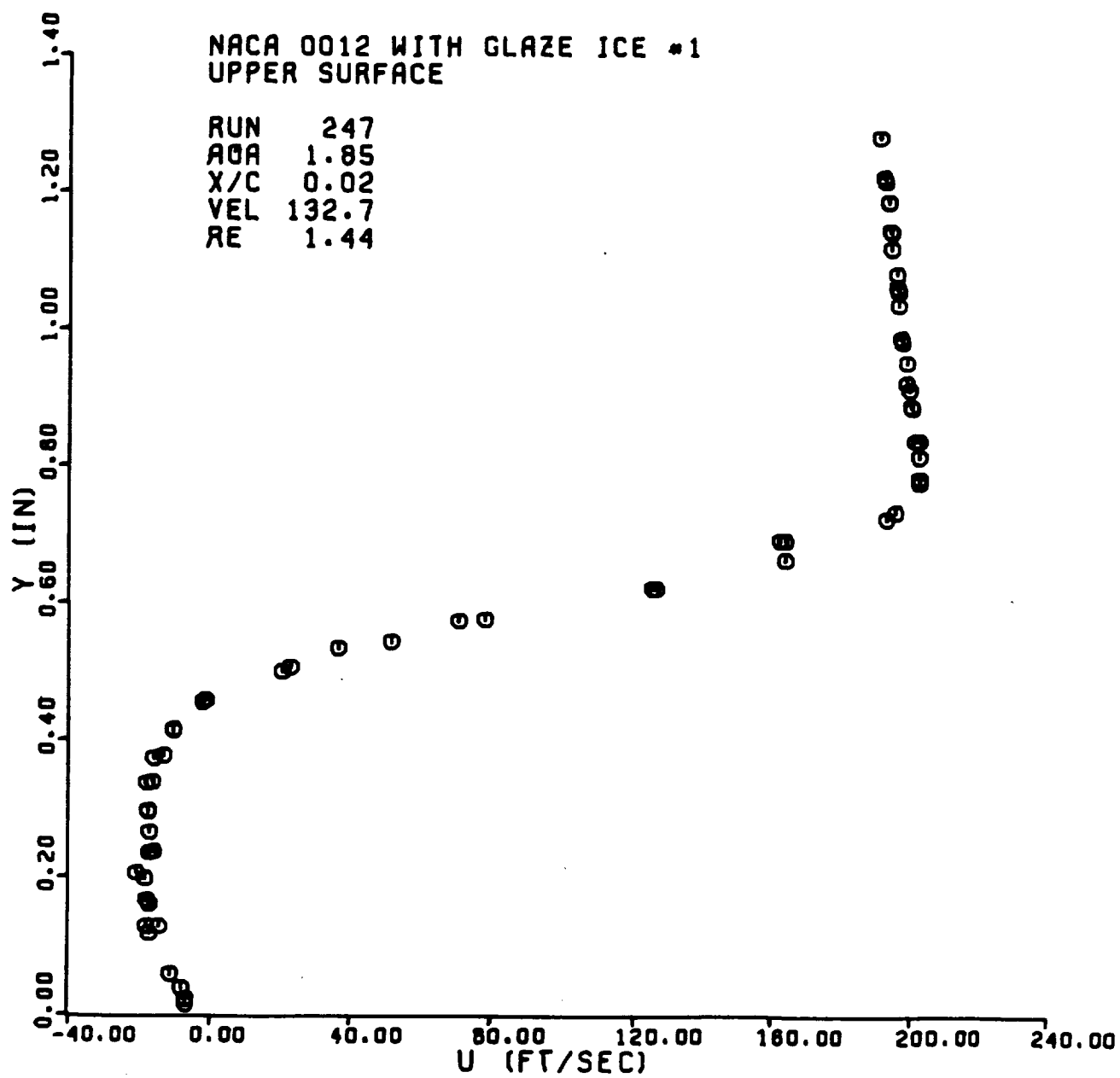




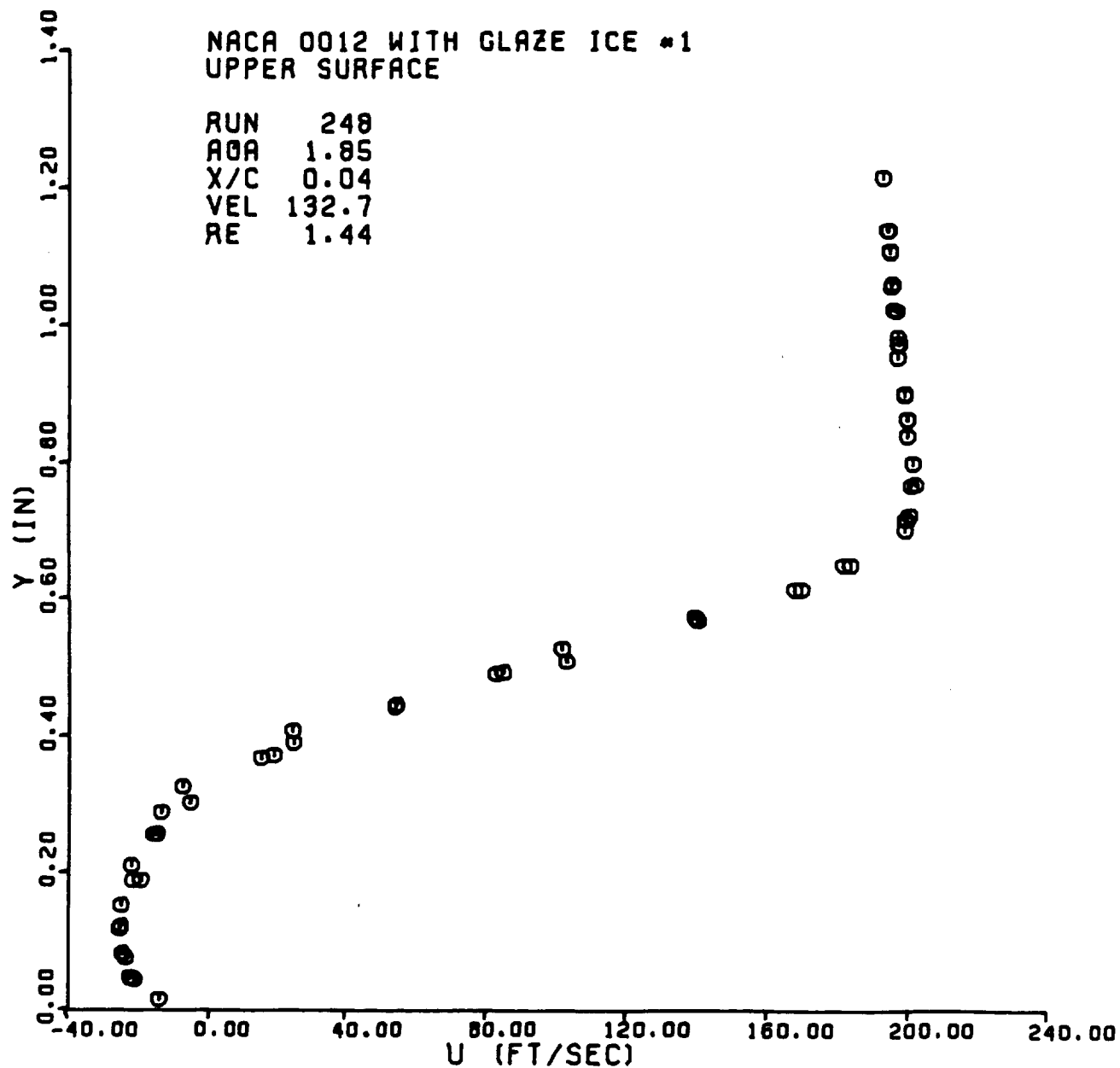


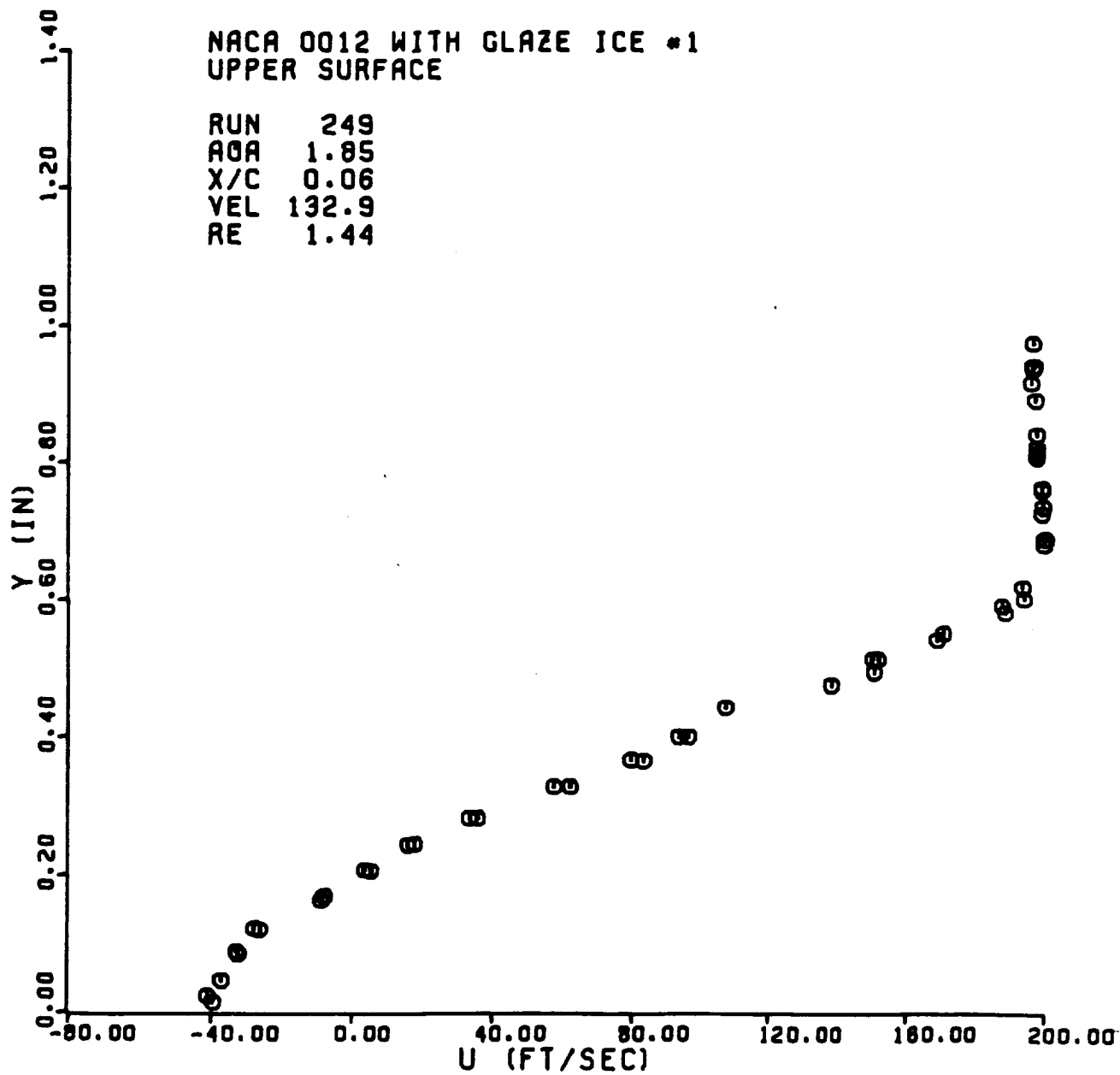


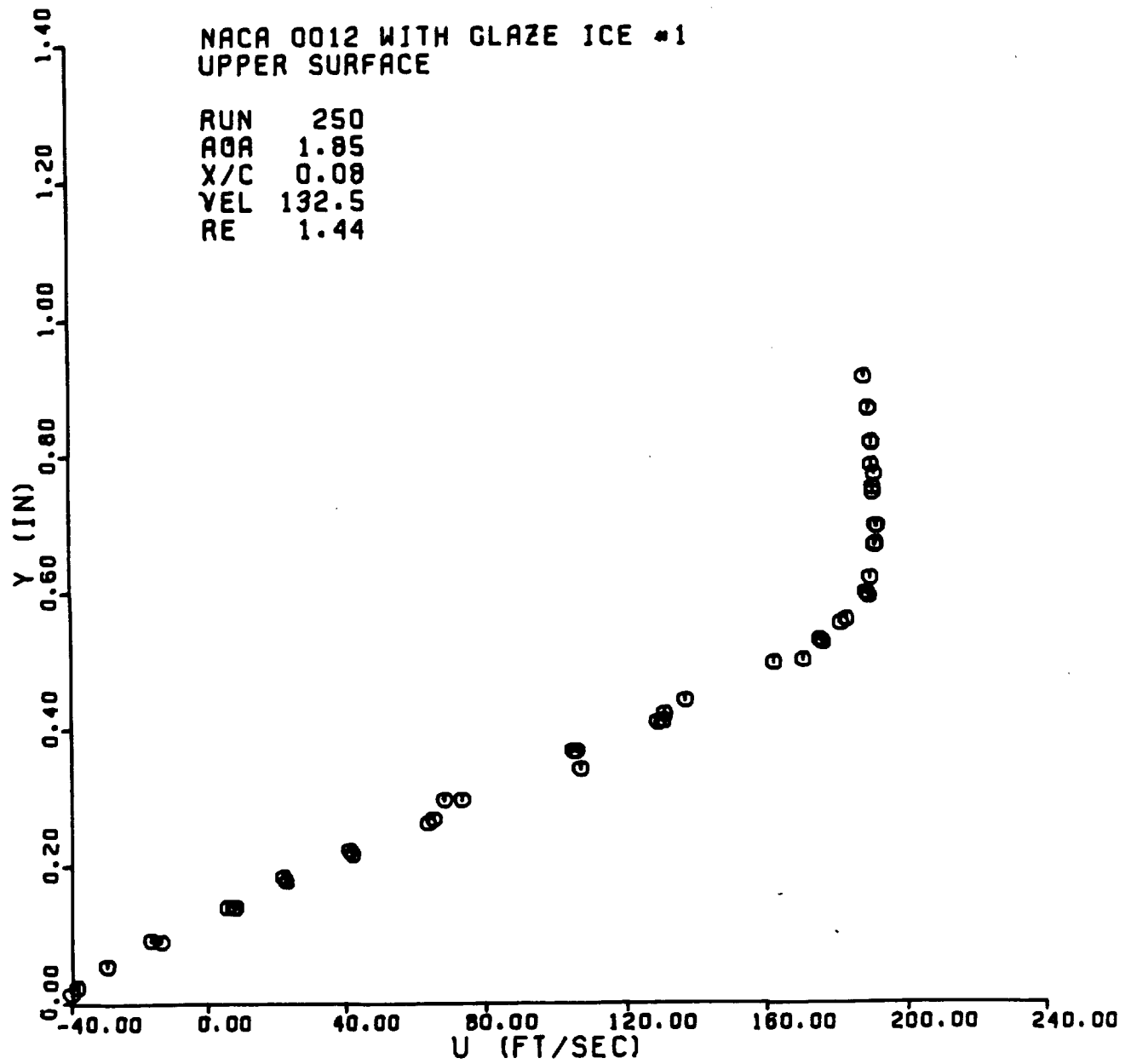


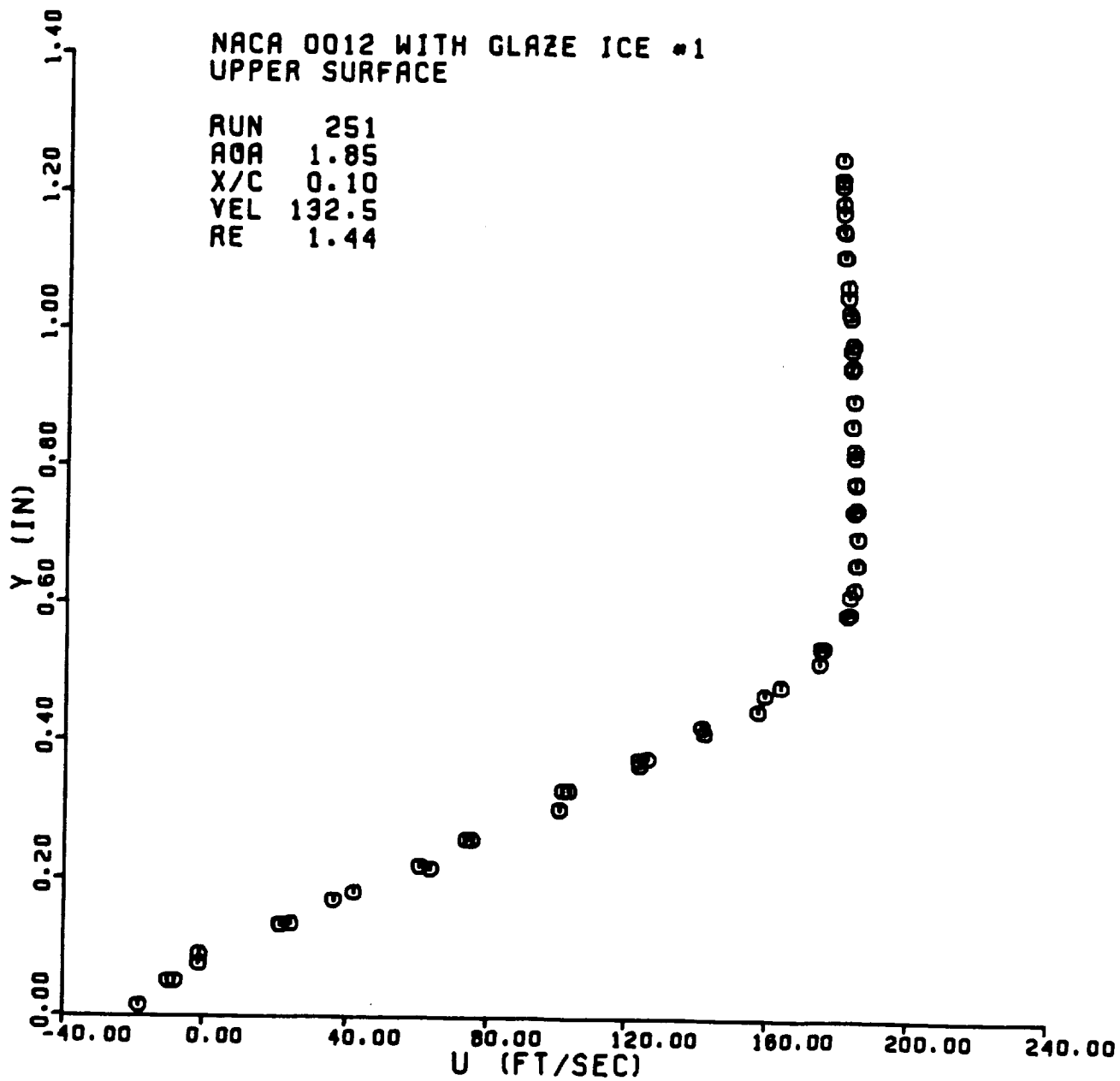


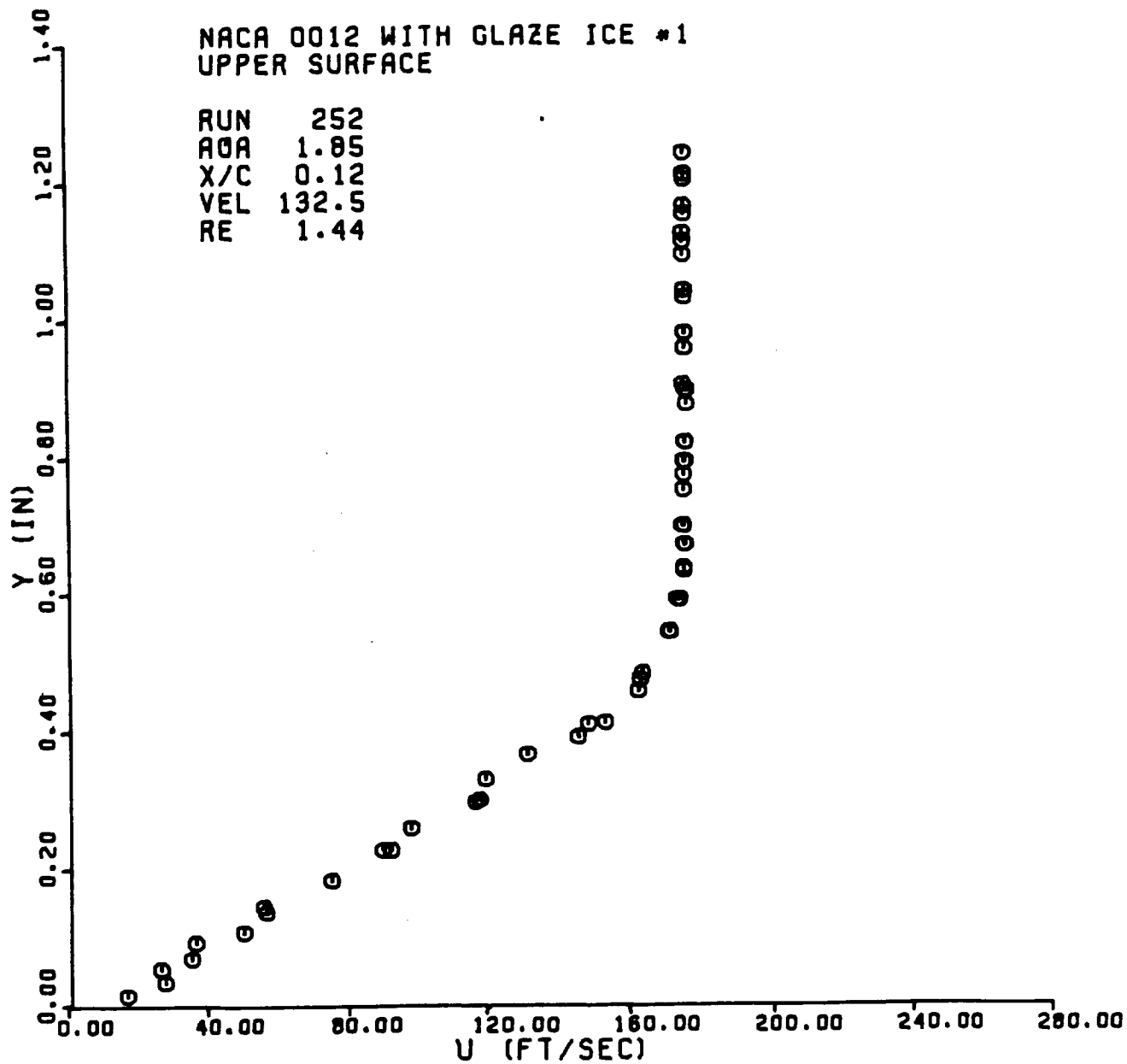


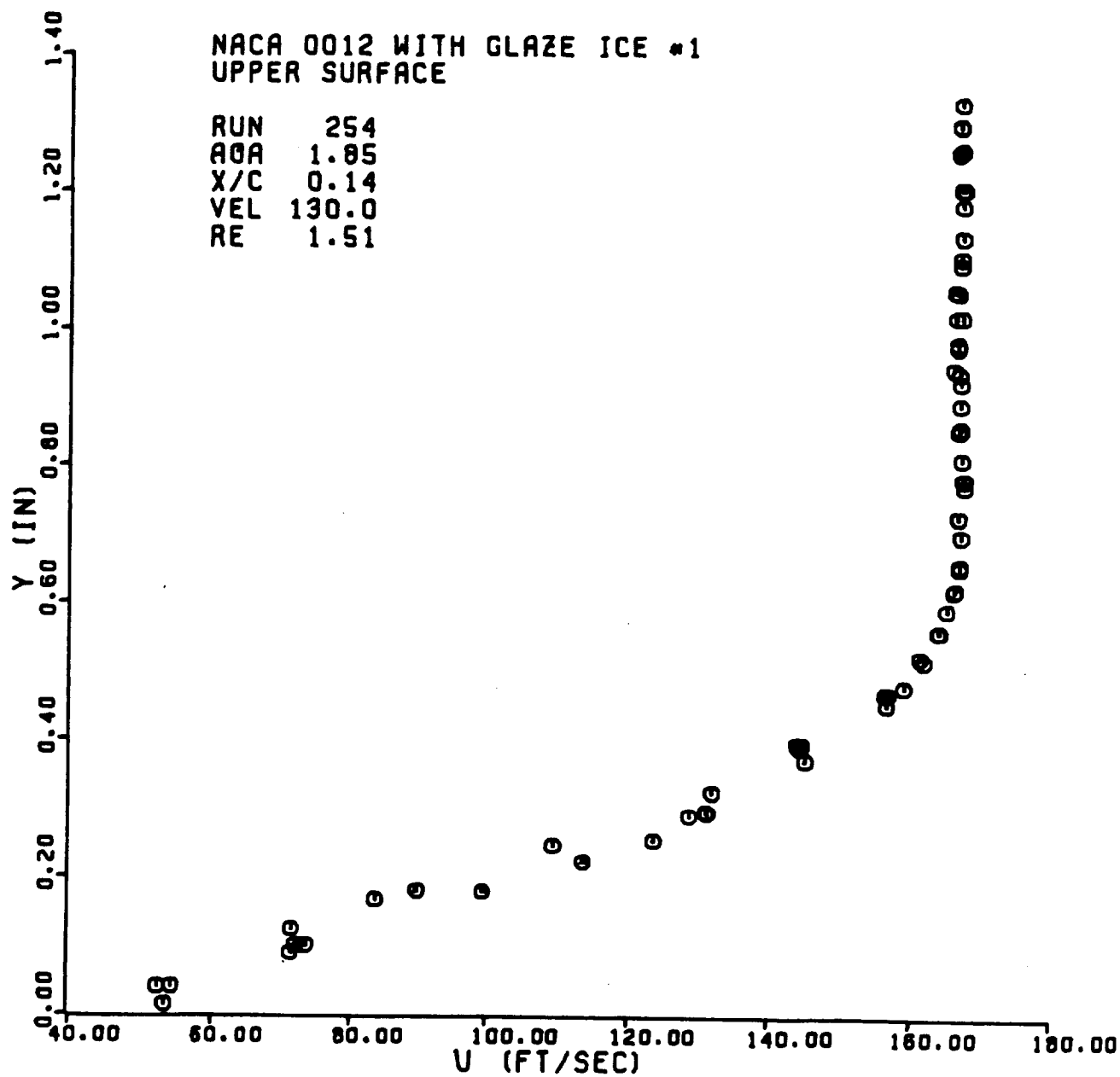


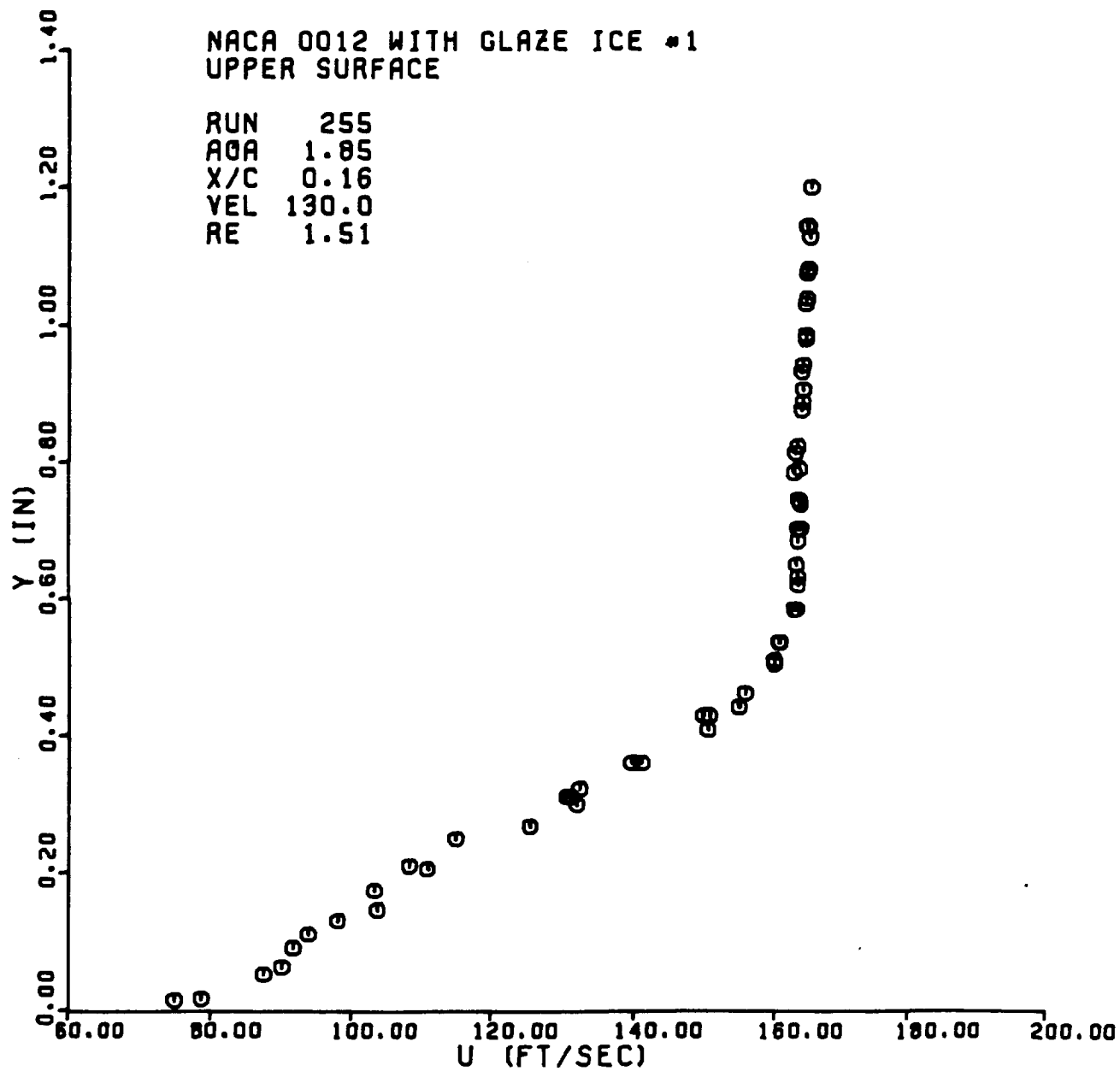


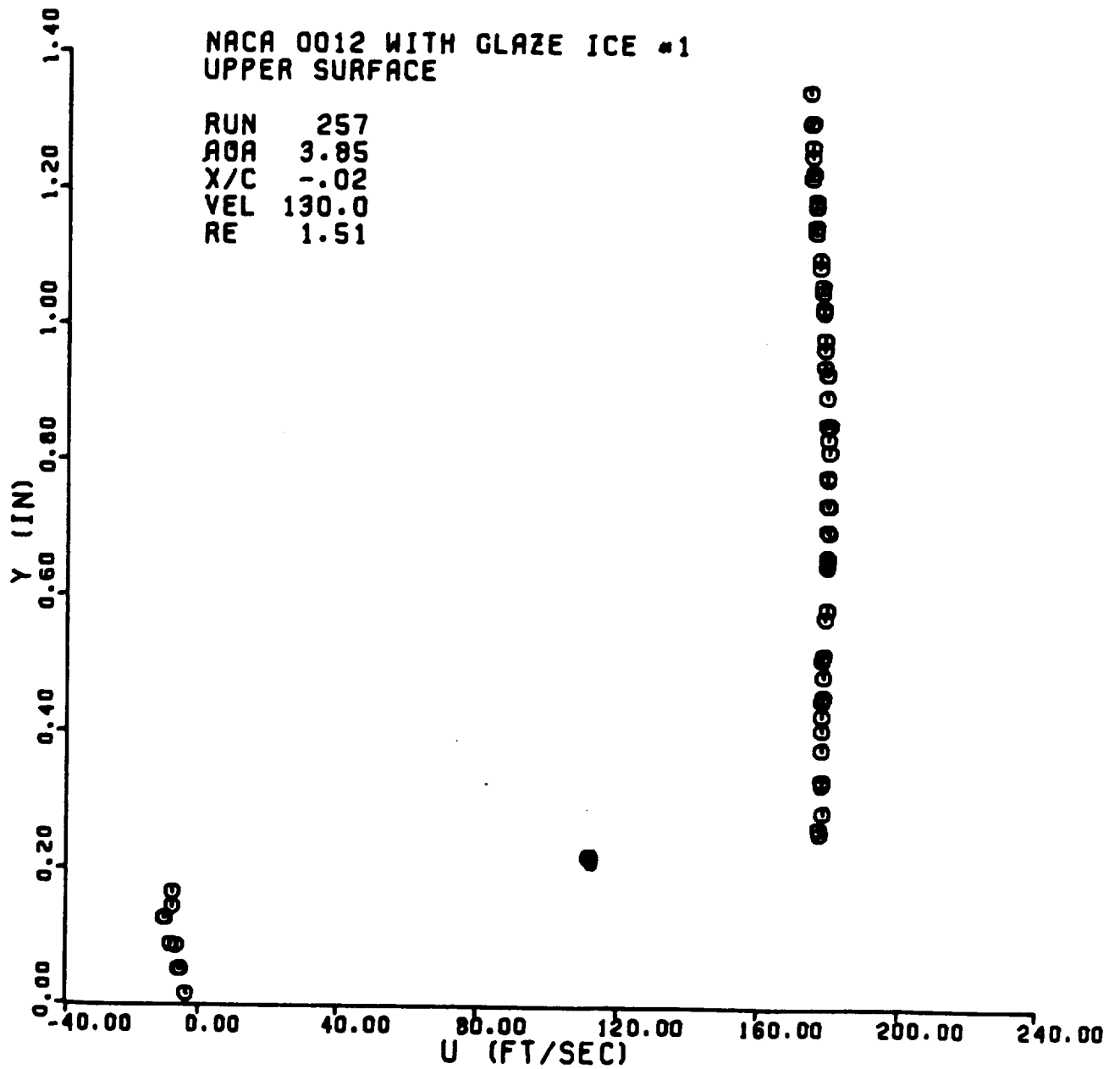




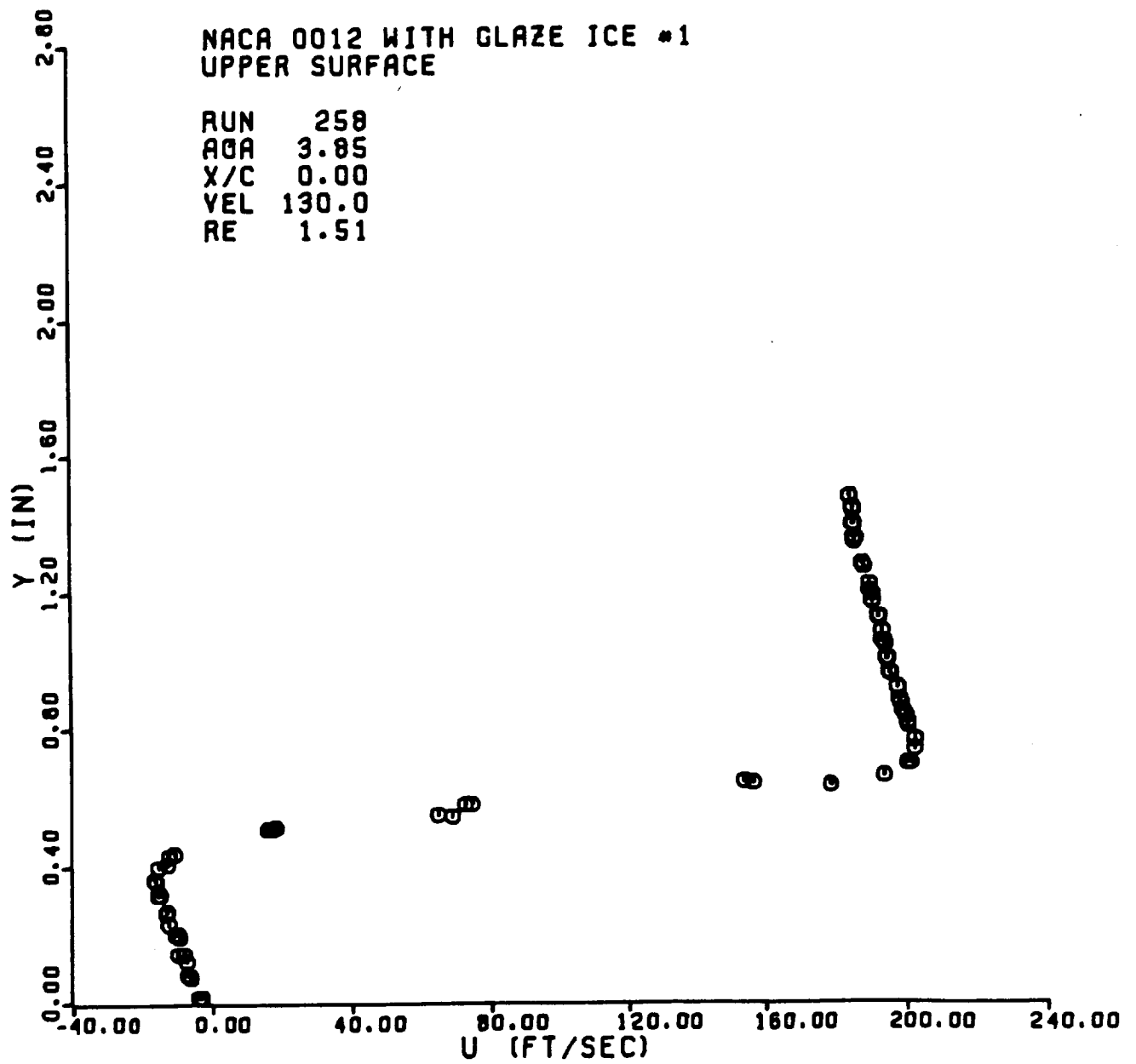


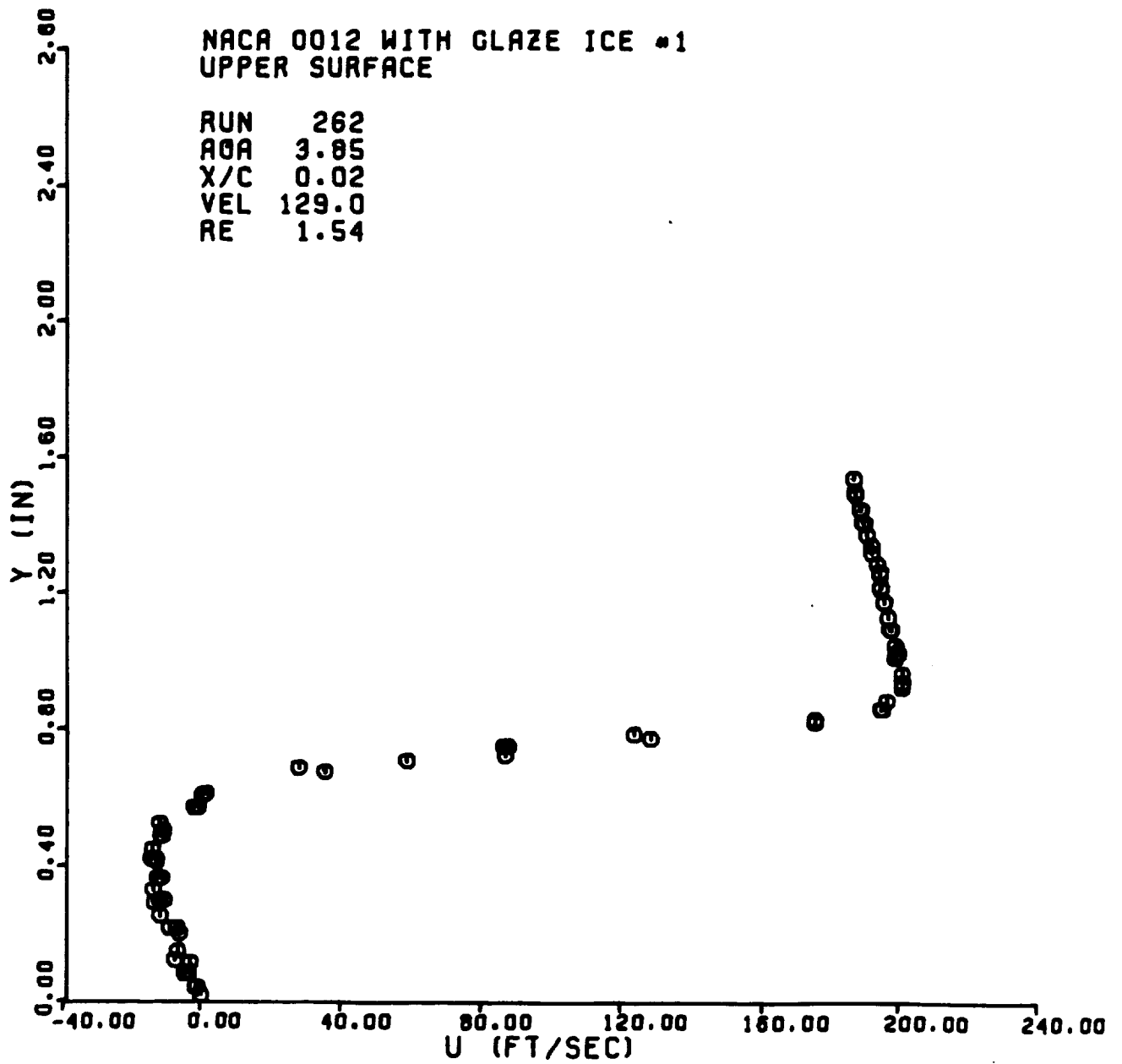


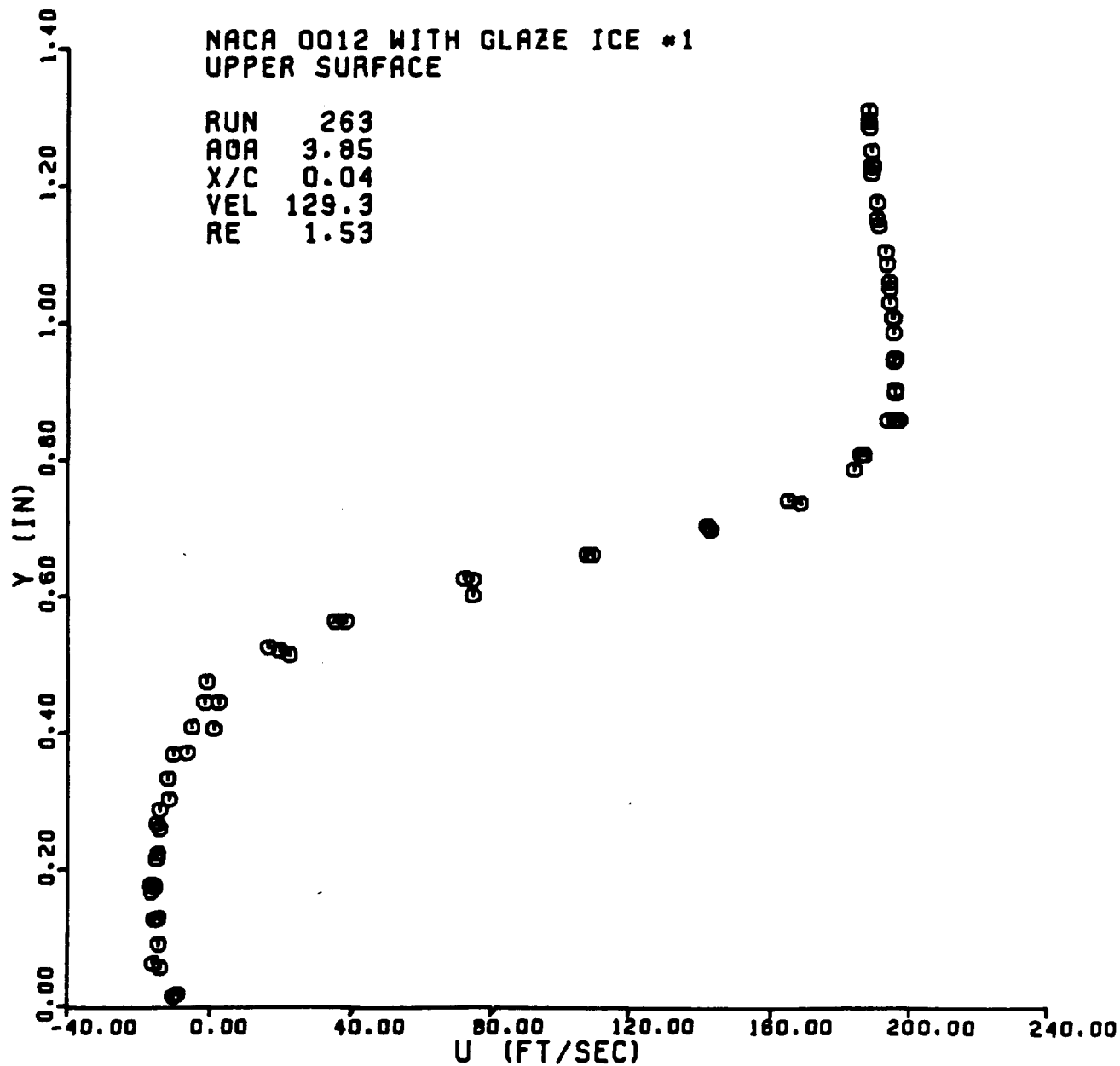


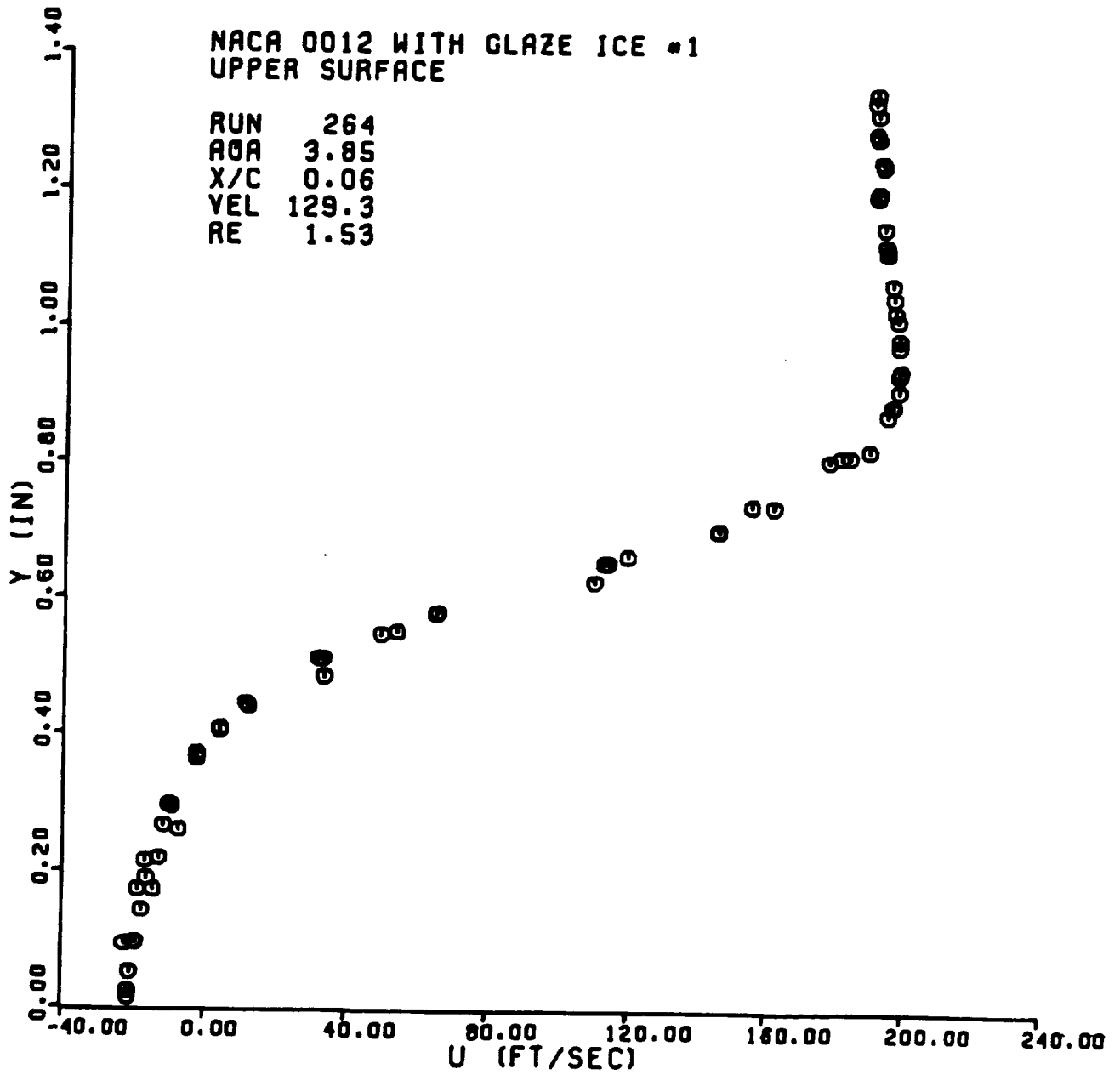


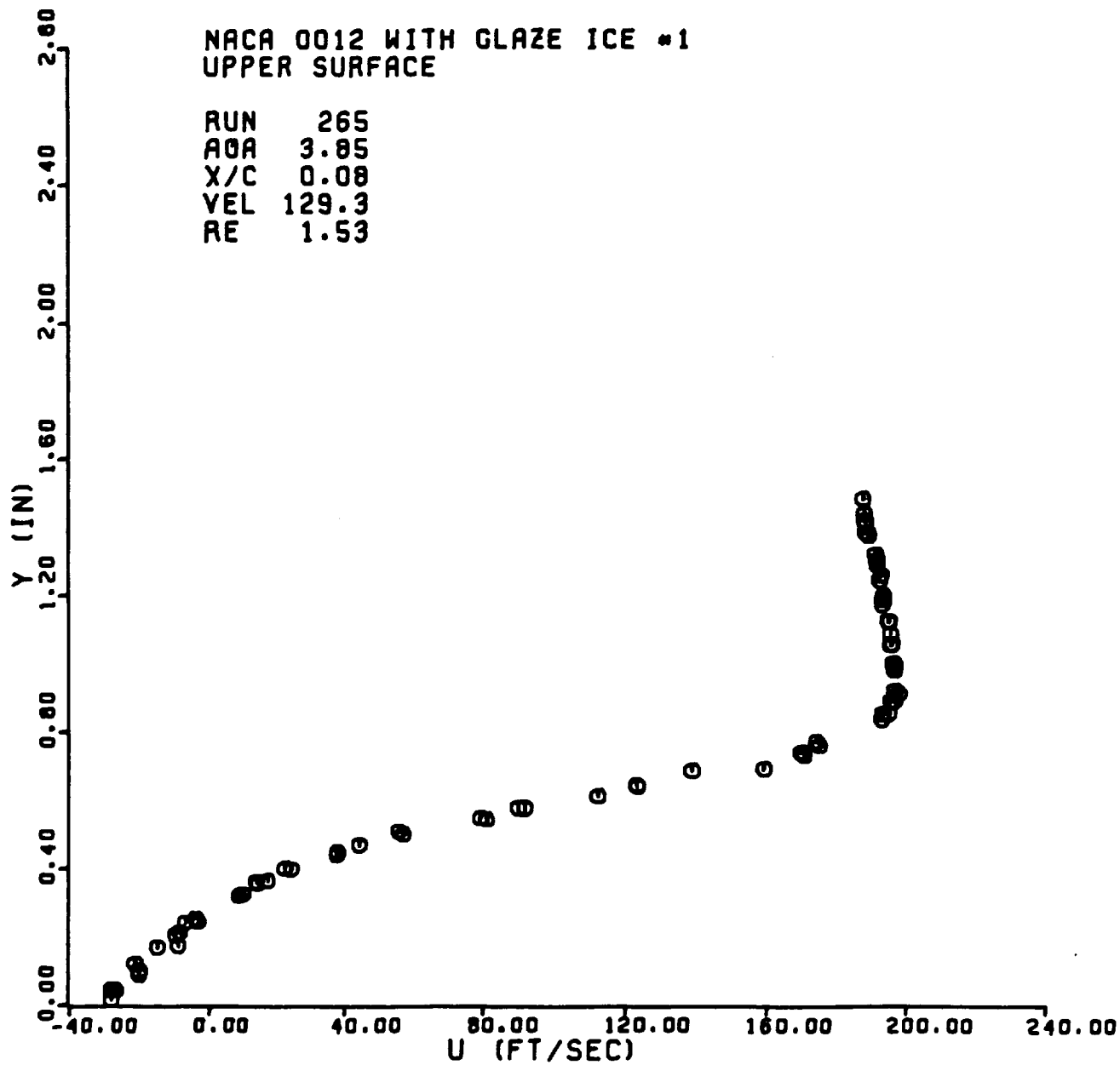


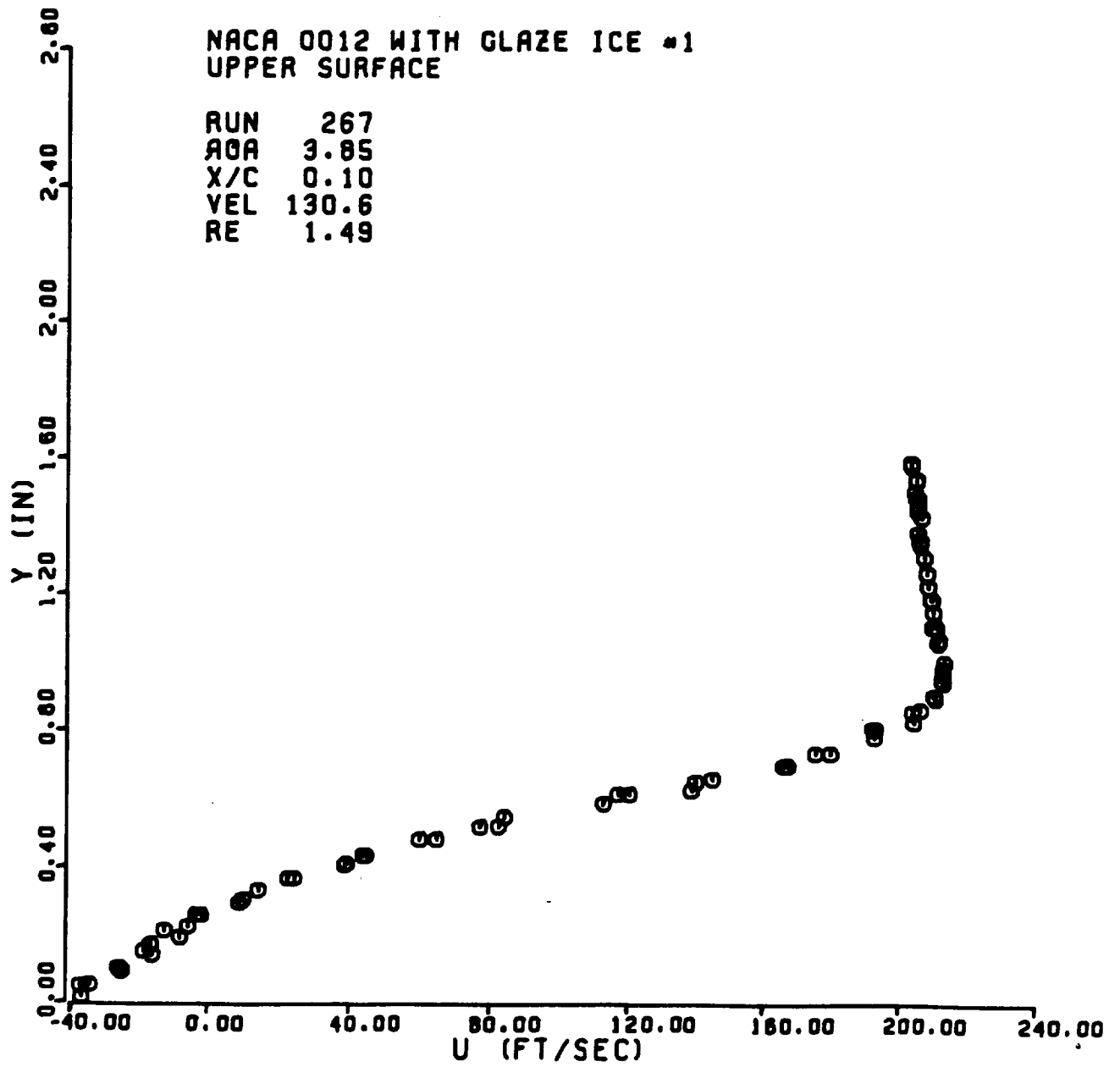


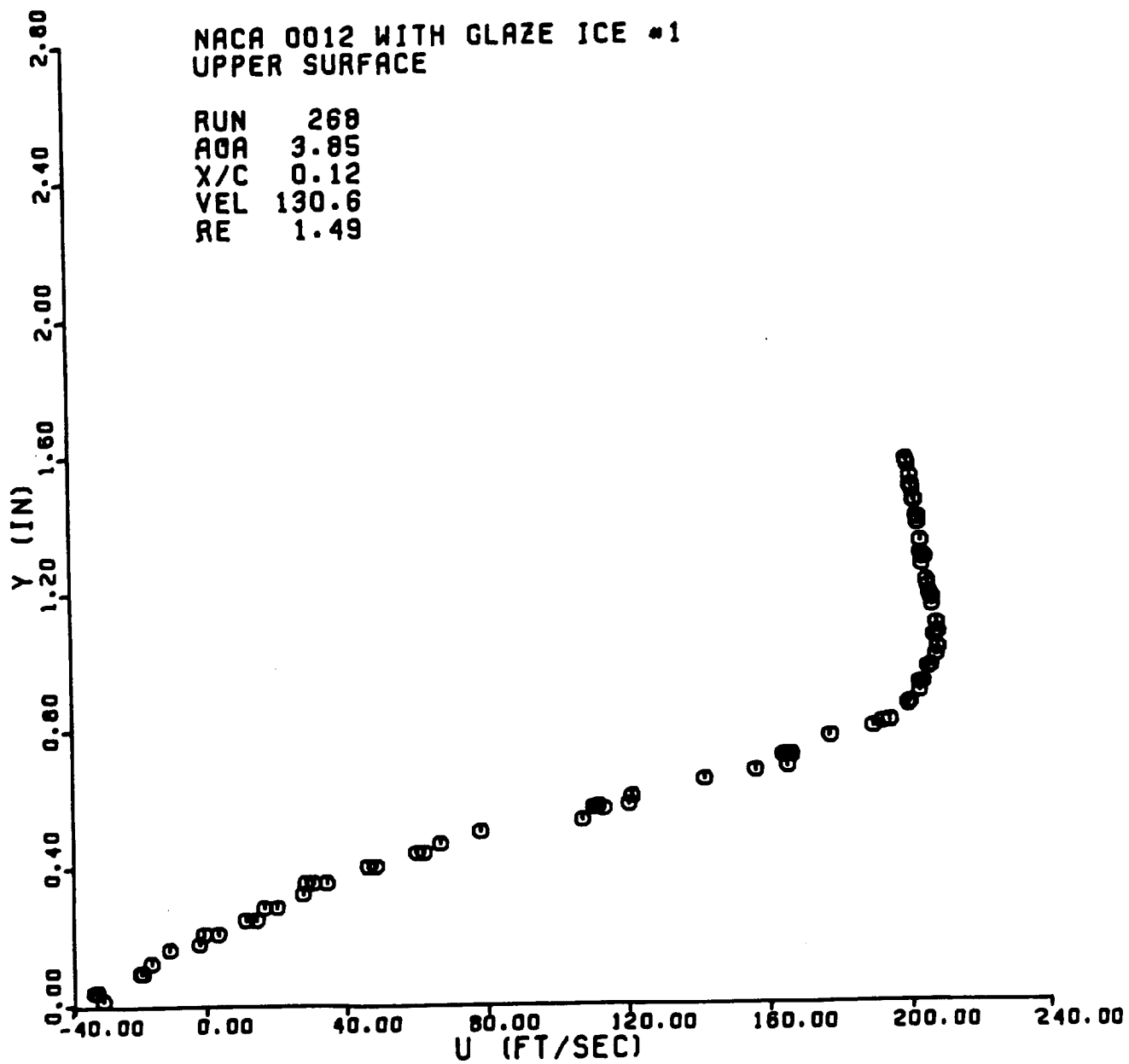


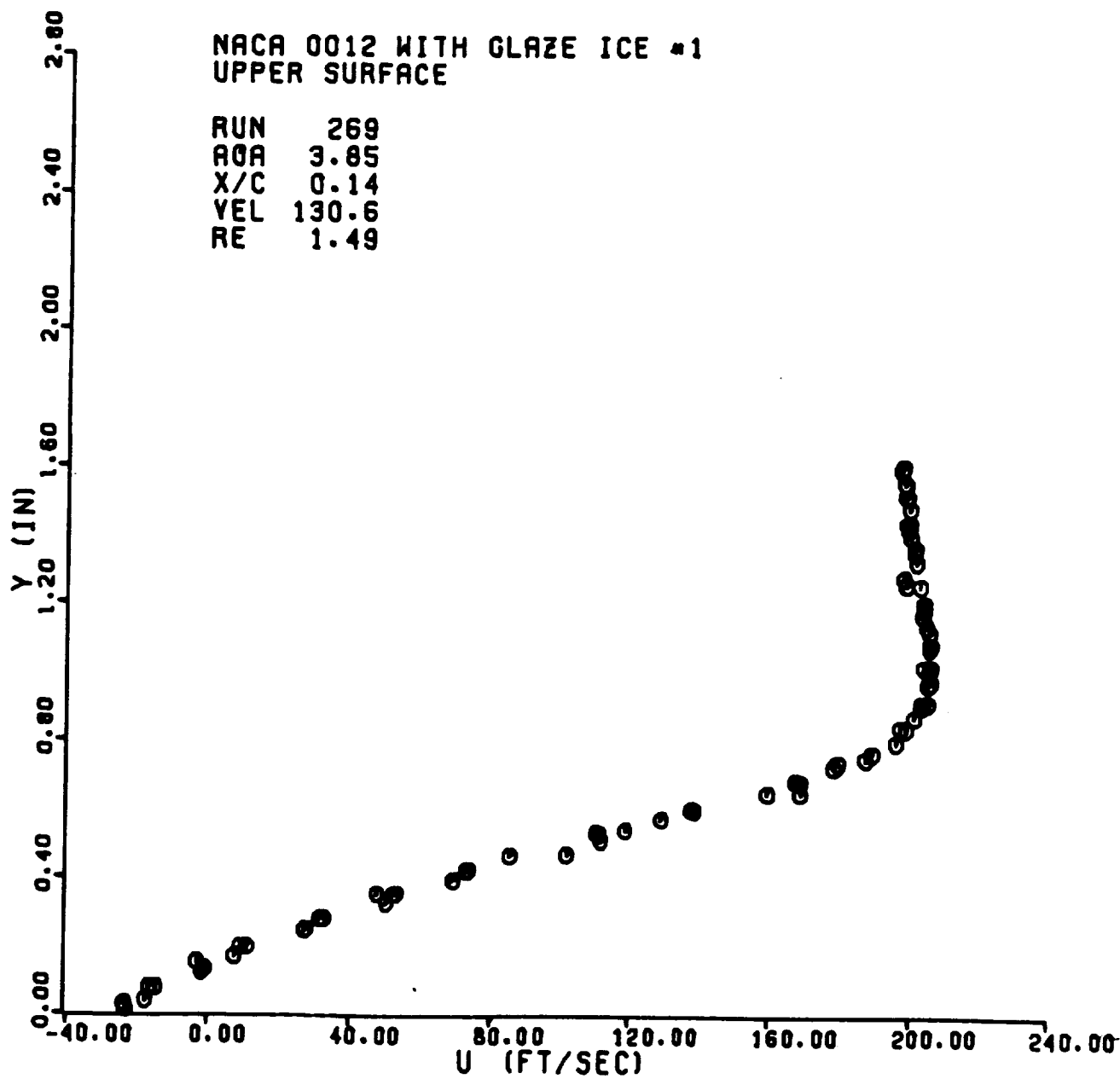




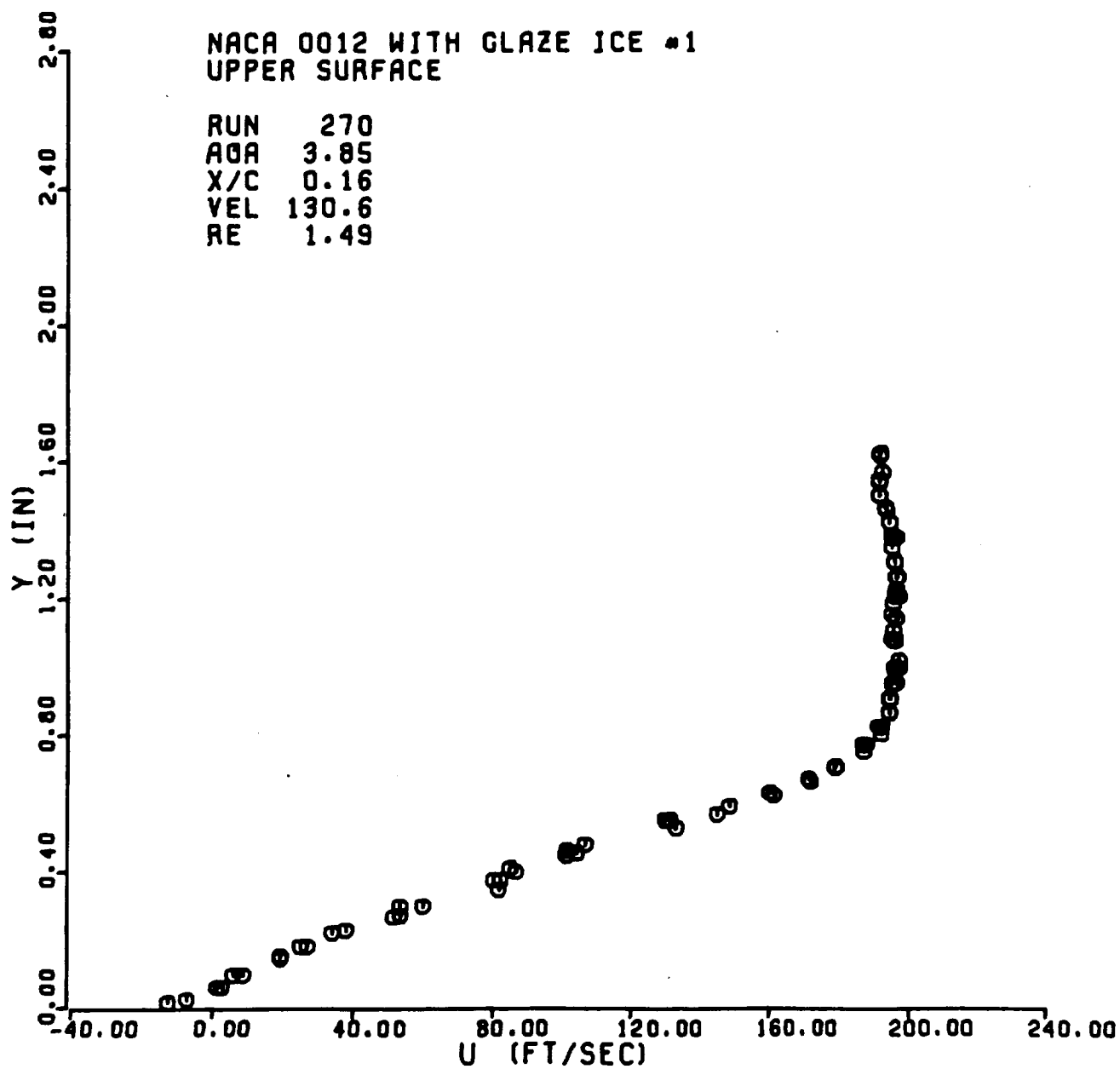


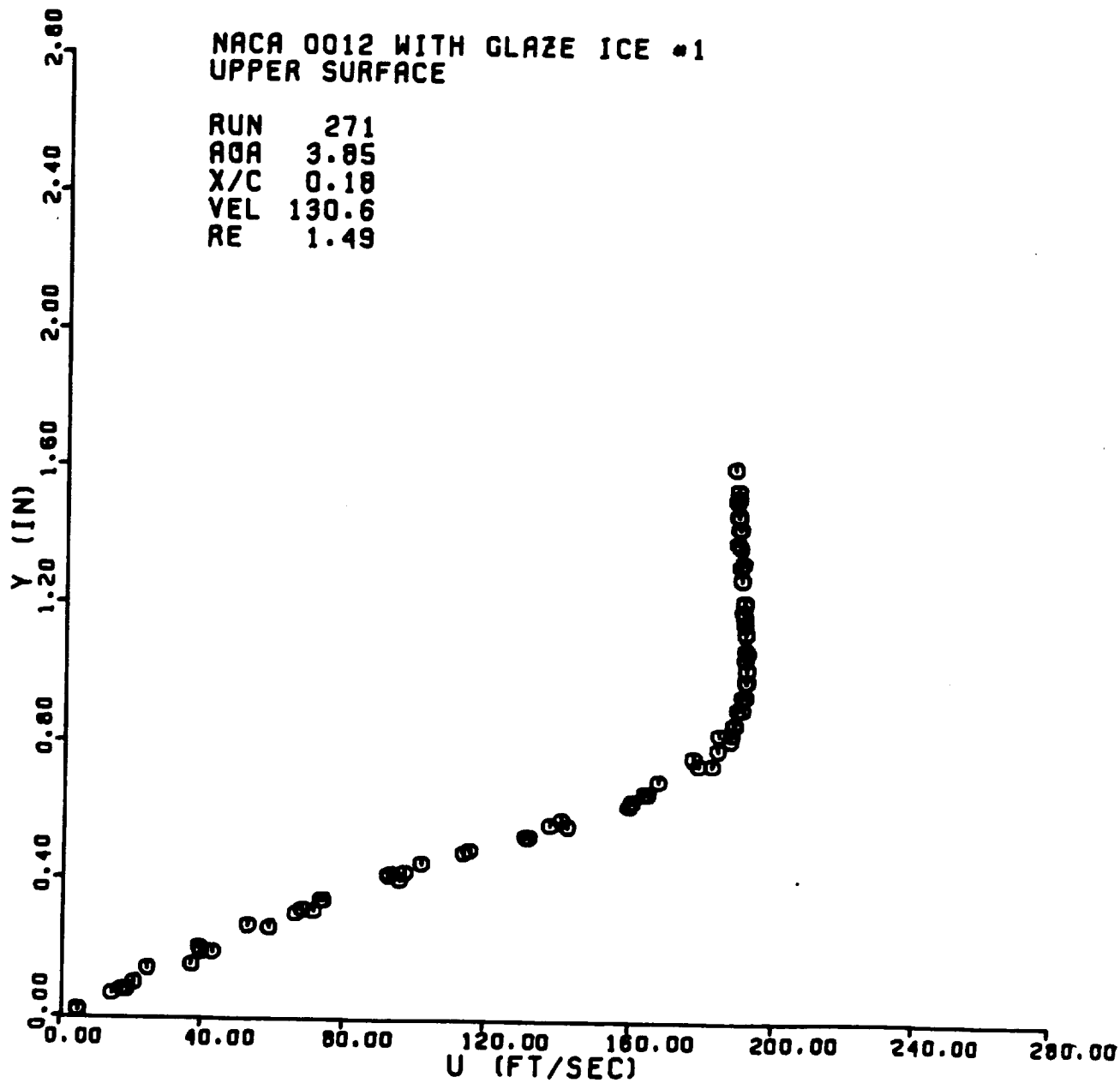


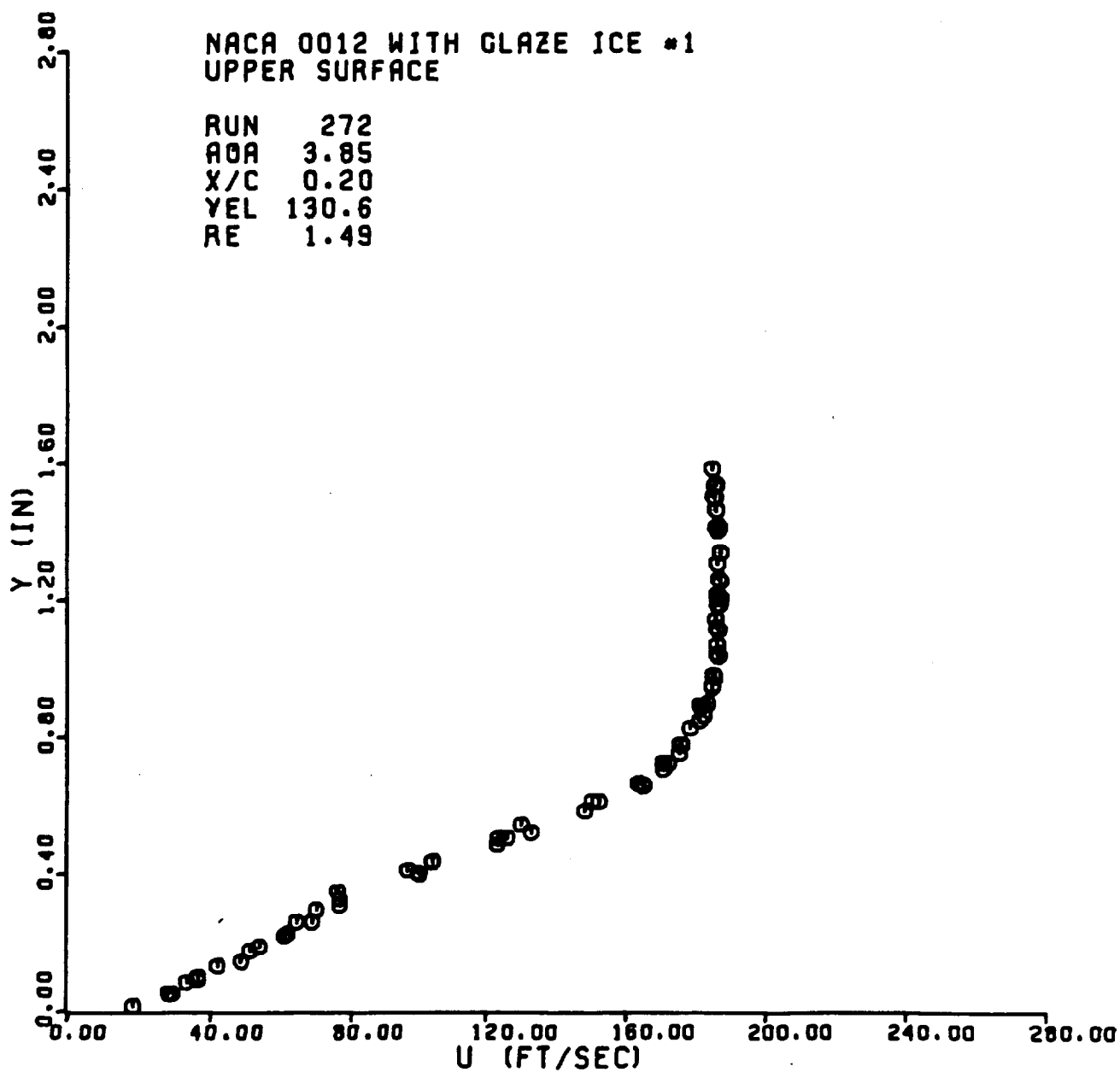


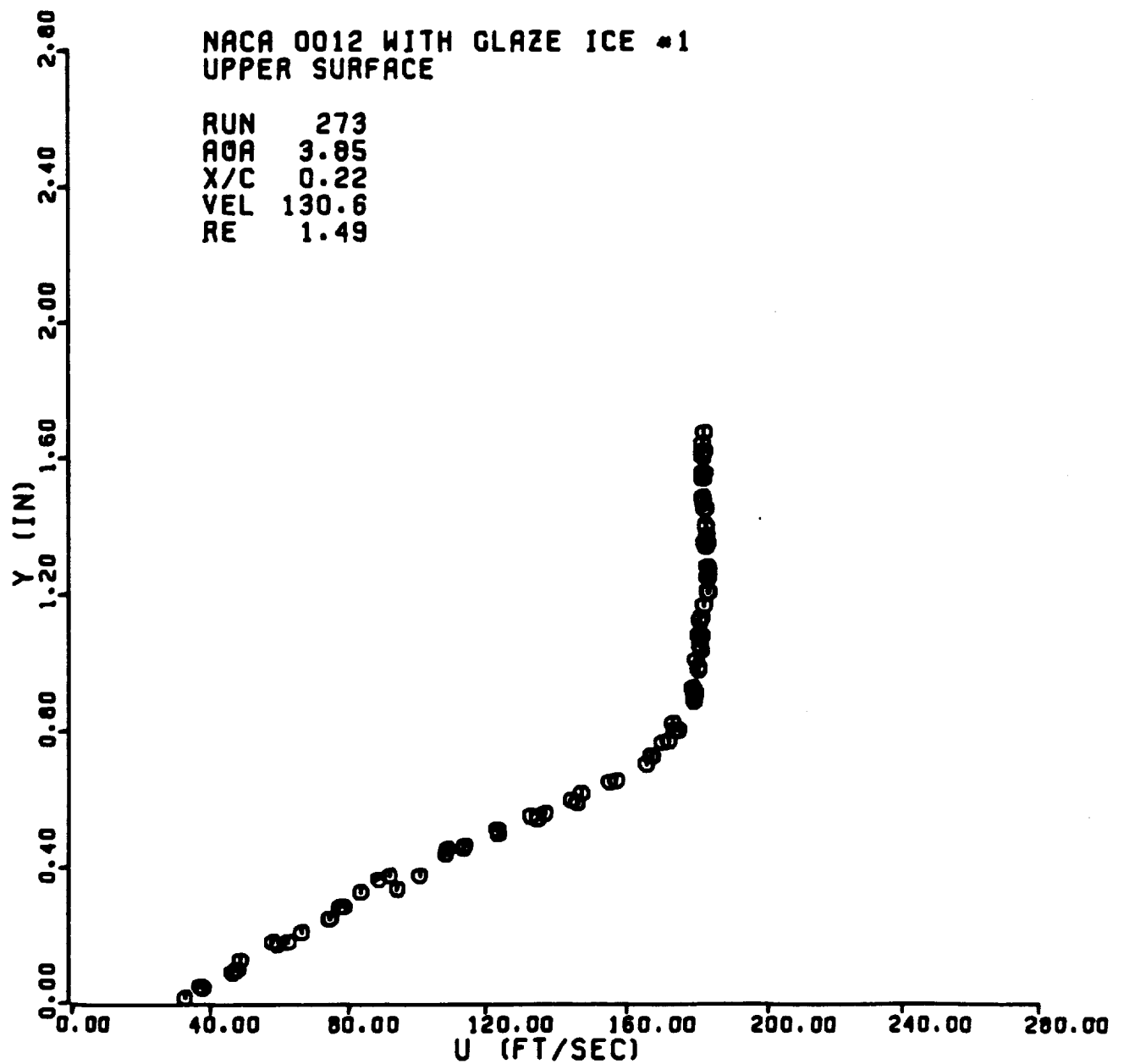


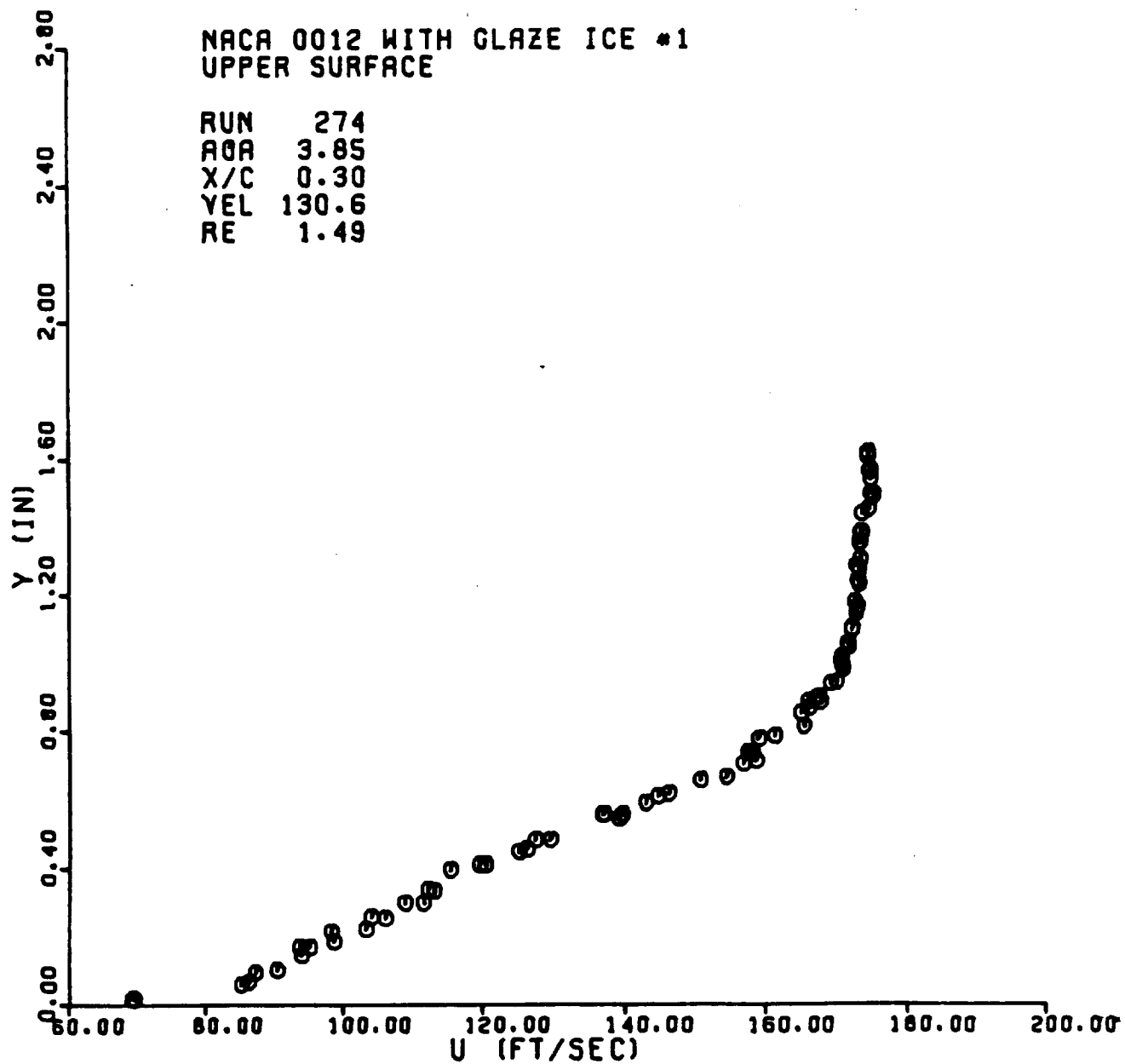


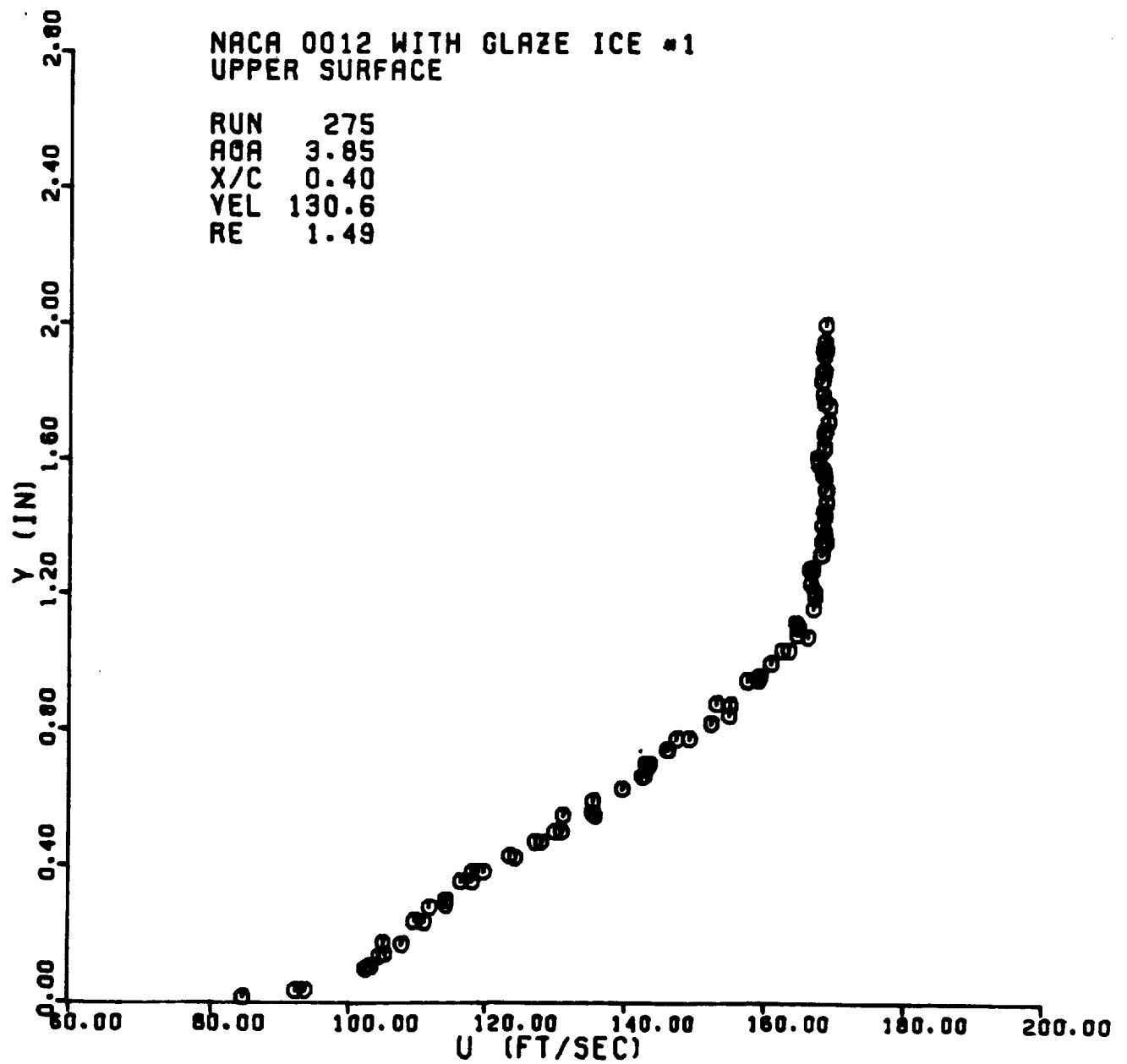


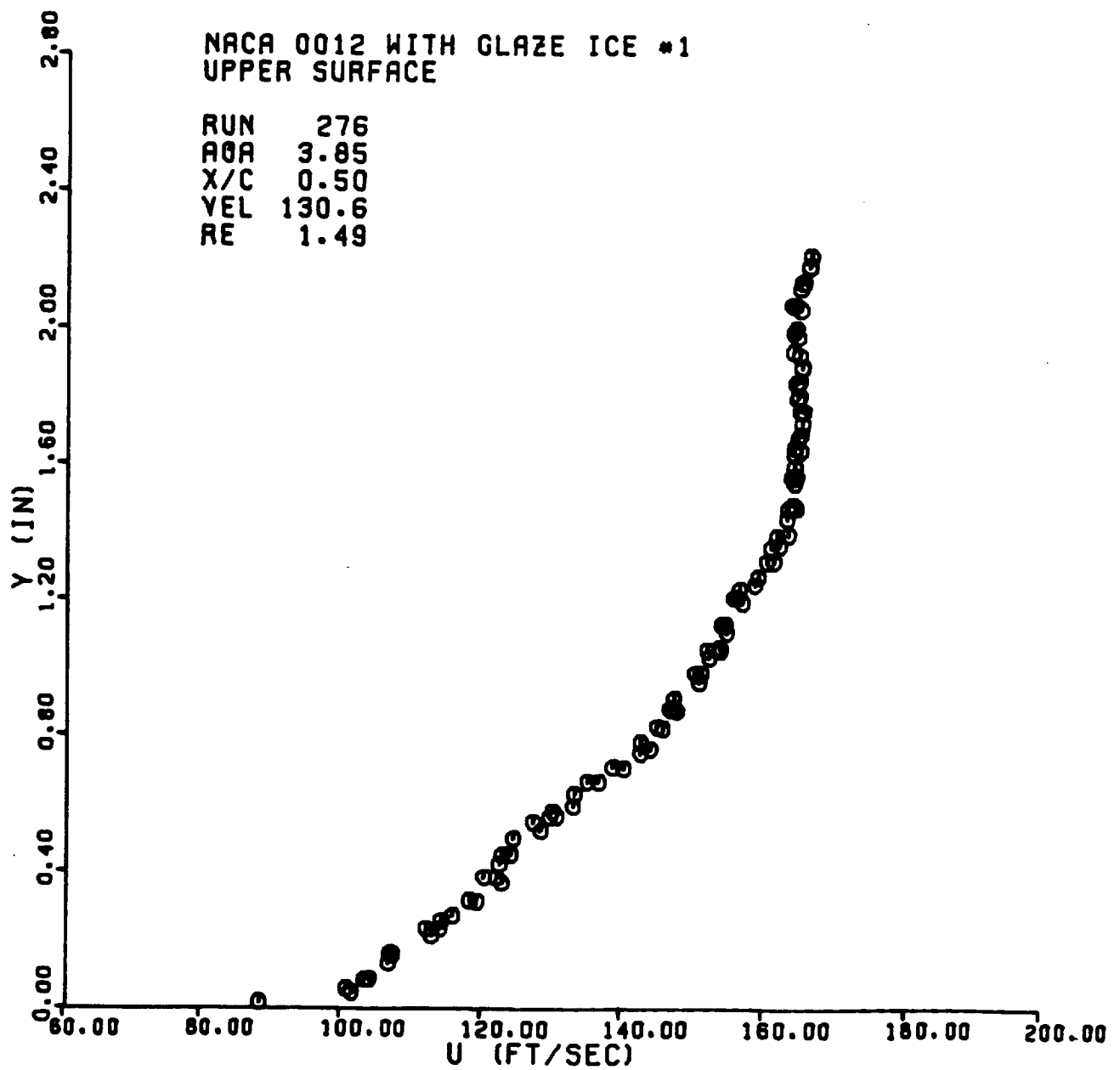


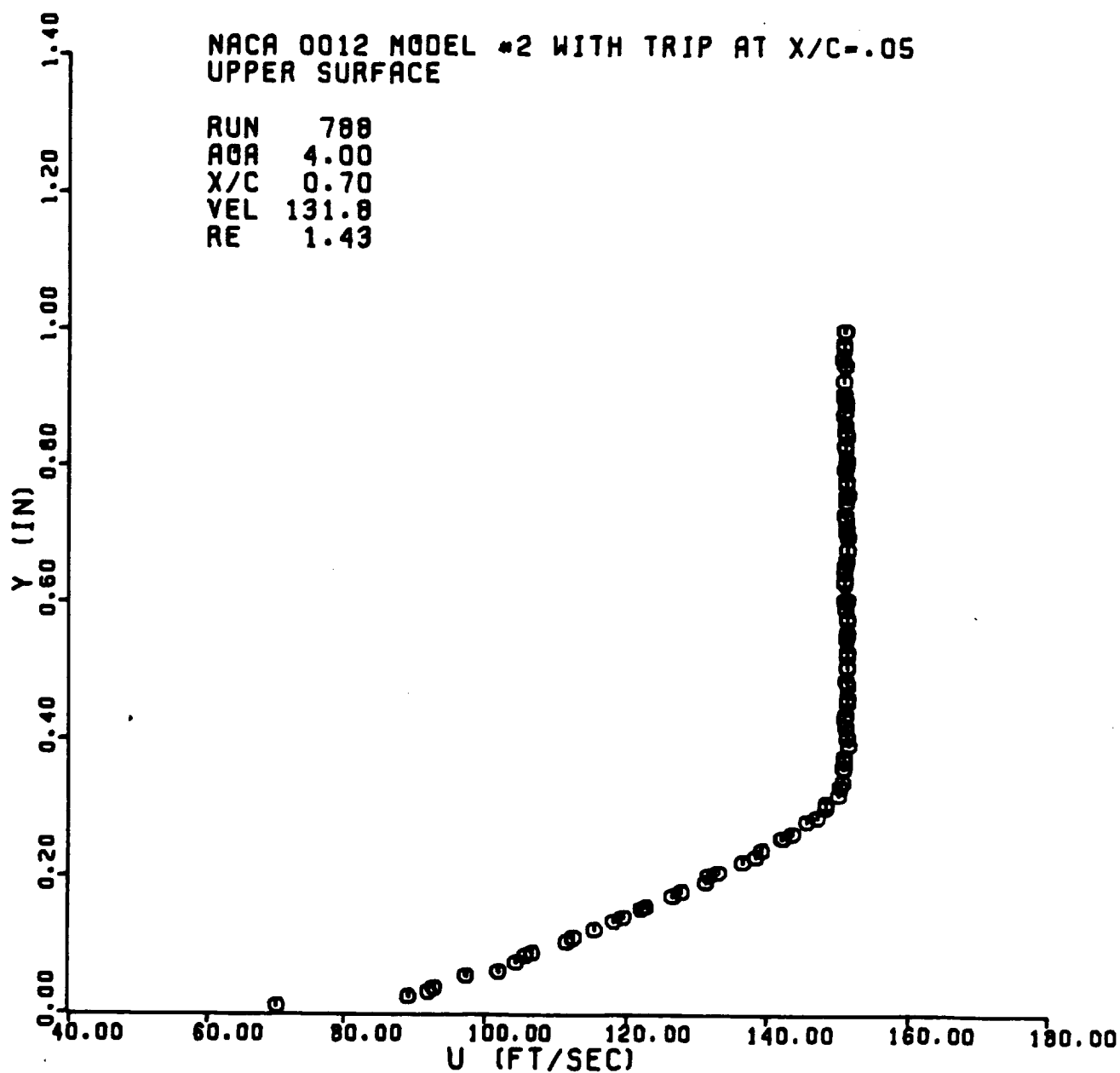














NACA 0012 MODEL #2 WITH TRIP AT X/C=.05  
UPPER SURFACE

RUN 789  
AOA 4.00  
X/C 0.70  
VEL 130.7  
RE 1.41

